

**PYROMETRY STUDIES OF THE COMBUSTION OF LEAD CONCENTRATE
PARTICLES UNDER CONTROLLED CONDITIONS.**

By

Nigel Edwin Tuffrey

B.Sc.(Eng.), The University of London, 1981

M.A.Sc., The University of British Columbia, 1984

A THESIS SUBMITTED IN PARTIAL FULFILLMENT OF
THE REQUIREMENTS FOR THE DEGREE OF
DOCTOR OF PHILOSOPHY

in

THE FACULTY OF GRADUATE STUDIES
(Department of Metals and Materials Engineering)

We accept this thesis as conforming
to the required standard

THE UNIVERSITY OF BRITISH COLUMBIA

September 1989

© Nigel Edwin Tuffrey, 1989

In presenting this thesis in partial fulfilment of the requirements for an advanced degree at the University of British Columbia, I agree that the Library shall make it freely available for reference and study. I further agree that permission for extensive copying of this thesis for scholarly purposes may be granted by the head of my department or by his or her representatives. It is understood that copying or publication of this thesis for financial gain shall not be allowed without my written permission.

Department of Graduate Studies

The University of British Columbia
Vancouver, Canada

Date 18th Sept 1989

Abstract

An investigation of the combustion of lead sulphide concentrates under controlled conditions has been carried out. A fast response, two-wavelength radiation pyrometer and a "laminar flow" furnace were constructed to facilitate the measurement of the temperature of individual particles during combustion. Chemical analysis and electron microscopy studies of the reaction products were also performed.

The combustion of galena, pyrite, pyrrhotite, sphalerite and two commercial concentrates (Brunswick and Sullivan) at 1130K was investigated. The effects of particle size between 63-125 μ m and gaseous oxygen concentration between 10 and 100% were examined.

For combustion in both air and oxygen a number of different combustion pulses were identified which corresponded to the combustion of different mineral species or to different physical phenomena. An analogous series of pulse classifications was identified for combustion in oxygen however they reflected the greater intensity and temperature of the reactions. The form of combustion was strongly dependent on oxygen concentration. From the results it was not possible to identify the effect of particle size on combustion behaviour.

The vaporisation of lead sulphide appears important to the mechanism of galena combustion. In air the temperature of combustion appears limited to 1500-1700K (cf boiling point PbS of 1609K); whereas in oxygen, massive vaporisation results in a heating arrest at 1700-2000K and disintegration into droplets which combust at 2000-2400K. Transition from air-type to oxygen-type combustion occurs at oxygen concentrations between 40 and 65% and is thought to be due to the transition from a liquid to gaseous phase PbO reaction product.

The initial stage of pyrite reaction is thermal decomposition to porous pyrrhotite. The ignition of this porous pyrrhotite was more rapid than dense pyrrhotite, but once molten, the combustion of the two was indistinguishable and the peak temperature

observed was very reproducible. In air the peak combustion temperatures of 2400-2600K appeared to coincide with a sudden expansion of the particle, possibly due to the inflation of thin-walled iron oxide cenospheres. In oxygen the reactions are more intense and disintegration typically occurs on reaching a peak temperature of 3000-3400K. Between ~10 and 35% oxygen the maximum combustion temperature increased linearly, but at higher concentrations remained constant at 3000-3400K. The results suggest the maximum temperature reached is limited by the occurrence of a physical phenomenon possibly associated with the vaporisation of iron.

Sphalerite did not ignite at the temperatures considered, but shells of zinc oxide were observed in the reaction products.

For the commercial concentrates pulses of intermediate combustion characteristics and a wide range of combustion temperatures (typically intermediate to those of PbS and FeS) were observed, as well as many pulses similar to those of the constituent minerals. The former were considered to be due to the combustion of agglomerations of many smaller individual particles. The effect of the mineral composition was evident in the combustion results, with increased quantities of iron sulphide tending to result in more intense reactions. The results suggest that metallic lead formation occurs during the initial stages of reaction, probably after melting as the result of reaction between the surface oxides/sulphates and unreacted PbS.

A simple reaction model for iron sulphide combustion suggests that the reaction of the molten drop is controlled by gas-phase oxygen mass transfer with the measured heating rates consistent with the formation of wustite and sulphur dioxide.

Table of Contents

	<u>Page</u>
Abstract	ii
Table of Content	iv
List of Tables	ix
List of Figures	xi
List of Symbols	xxiii
Acknowledgements	xxvi
CHAPTER 1 Introduction	1
1.1 Pyrometallurgical Production of Lead	1
1.1.1 New Pyrometallurgical Processes for Lead Smelting	2
1.2 Lead Flash Smelting	3
1.2.1 The KIVCET Process	4
1.3 Area of Study	5
CHAPTER 2 Literature Review	8
2.1 Thermodynamics of Flash Smelting Reactions	8
2.1.1 General	8
2.1.2 Vapour Phase Species	9
2.1.3 Pb-S-O System	10
2.1.4 The Effects of Other Mineral Species	13
2.2 Kinetics of Lead Flash Smelting Reactions: Pilot and Industrial Plant Studies	14
2.3 Kinetics of Lead Flash Smelting Reactions: Laboratory Studies	17
2.3.1 DTA Experiments and Ignition Studies	17
2.3.2 Solid State Oxidation	19
2.3.3 Flame Studies	20
2.3.4 Laminar Flow Furnace Studies	20
2.3.5 Particle Temperature Measurements	22
2.4 Modelling Studies of Flash Smelting Reactions.	24
2.4.1 Particle Reaction Models	24
2.4.2 Flash Smelting Models	26
2.5 Summary -Justification for the Present Research	26
2.6 Figures - Chapter 2	28
CHAPTER 3 Objectives and Scope of the Experimental Series	38

- CHAPTER 4 Experimental 40**
- 4.1 Experimental Apparatus 40
 - 4.1.1 Laminar Flow Furnace 41
 - 4.1.1.1 Electrical Power Supply 41
 - 4.1.1.2 Ancillary Equipment 42
 - 4.1.2 Particle Feeder 42
 - 4.1.3 Two Wavelength Radiation Pyrometer 43
 - 4.1.4 Data Acquisition and Analysis 44
 - 4.1.5 Solid Sampling Devices 45
- 4.2 Laminar Flow Furnace Characteristics 46
 - 4.2.1 Gas Flow Characteristics 46
 - 4.2.2 Laminar Flow Furnace Temperature Profile 46
- 4.3 Experimental Measurements 48
 - 4.3.1 Pyrometer Output Signals 48
 - 4.3.2 Solid Samples 48
- 4.4 Feed Materials -Chemical, Mineralogical and Physical Properties 49
- 4.5 Experimental Series Conducted 53
- 4.6 Particle Residence Times Calculations 56
- 4.7 Figures - Chapter 4 59
- CHAPTER 5 Pyrometer Design and Calibration 70**
- 5.1 Pyrometer Calibration 70
 - 5.1.1 Previous Designs 70
 - 5.1.2 Design Requirements 72
 - 5.1.3 Optical Component Design 72
 - 5.1.4 Pyrometer Detector Selection 73
 - 5.1.5 Optical Filter Selection 74
 - 5.1.6 Electronics 76
 - 5.1.7 Final Pyrometer Design Specifications and Construction 76
- 5.2 Pyrometer Calibration 77
 - 5.2.1 Photomultiplier Tube Calibration. 77
 - 5.2.2 Noise Performance 78
 - 5.2.3 Temperature Calibration Theory 80
 - 5.2.4 Temperature Calibration Results 80
 - 5.2.4.1 Blackbody Cavity Temperature Source Calibration 81
 - 5.2.5 Pyrometer Viewing Volume 85
 - 5.2.5.1 Measured Temperature Variation Across the Viewing Volume 87

5.2.6 Pyrometer Response	89
5.2.7 Apparent Particle Area Calculations	91
5.2.7.1 Relative Apparent Particle Area	91
5.2.7.2 Apparent Particle Area Calculations	91
5.2.8 Pyrometer Accuracy	92
5.3 Figures - Chapter 5	95
CHAPTER 6 Results	103
6.1 Preliminary Observations-Photographs of Combusting Particles	103
6.2 AIR EXPERIMENTS	105
6.2.1 Classification of Particle Combustion Peaks	105
6.2.1.1 Galena - "Type A1" Combustion Pulses	106
6.2.1.2 Pyrite and Pyrrhotite - "Type A3" Combustion Pulses	108
6.2.1.3 Sphalerite	110
6.2.1.4 Brunswick and Sullivan Concentrates - "Type A2" Combustion Pulses	110
6.2.1.5 Material Ejection or Sparks - "Type A4" Pulses	111
6.2.1.6 Periodic Energy Fluctuations - "Type A5 " Pulses	112
6.2.2 Temperature Measurement Experiments	112
6.2.2.1 Air Experiments - Galena	113
6.2.2.1.1 Galena - Effect of Particle Size	115
6.2.2.2 Air Experiments - Pyrite and Pyrrhotite	119
6.2.2.3 Air Experiments - Sullivan Concentrate	121
6.2.2.4 Air Experiments - Brunswick Concentrate	123
6.2.3 Air Experiments - Heating and Cooling Rates	125
6.2.4 Summary of Results of Air Experiments	127
6.3 OXYGEN EXPERIMENTS	127
6.3.1 Oxygen Combustion Pulse Classification	128
6.3.1.1 Galena Combustion - "Type O1" Pulses	128
6.3.1.2 Pyrite and Pyrrhotite Combustion - "Type O3" Pulses	129
6.3.1.3 Brunswick and Sullivan Concentrate Combustion - "Type O2" Pulses	130
6.3.1.4 Material Ejection and Sparks - "Type O4" Pulses	131
6.3.2 Temperature Measurement Experiments for Combustion in Oxygen	132
6.3.2.1 Galena	132
6.3.2.2 Pyrite and Pyrrhotite	133
6.3.2.3 Sullivan Concentrate	135
6.3.2.4 Brunswick Concentrate	136

6.3.2.5 Summary of the Results of the Oxygen Experiments	138
6.4 The Effect of Oxygen Concentration on the Combustion of Pyrite and Galena	138
6.4.1 Galena Combustion	138
6.4.1.1 Variation in Pulse Shape	138
6.4.1.2 Temperature Measurement Results	138
6.4.2 Pyrite Combustion	140
6.4.2.1 Variation in Pulse Shape	140
6.4.2.2 Temperature Measurement Results	140
6.5 Reaction Product Analysis	142
6.5.1 Chemical Analysis/X-ray Diffraction Results	142
6.5.1.1 Air Experiments	143
6.5.1.2 Oxygen Experiments	145
6.5.2 Scanning Electron Microscopy (SEM), Energy and Wavelength Dispersive X-ray Spectroscopy (EDX/WDX) Studies	146
6.5.2.1 Air Experiments	146
6.5.2.2 Oxygen Experiments	150
6.6 Tables - Chapter 6	153
6.7 Figures - Chapter 6	169
CHAPTER 7 Discussion of Results	252
7.1 Important Findings in the Experimental Results	252
7.1.1 Comparison of the Pyrometer Results with Previous Studies	257
7.2 Particle Heating and Reaction Prior to Ignition	259
7.2.1 Time to Ignition	260
7.2.2 Sphalerite Reaction	263
7.3 Combustion Mechanisms	263
7.3.1 Galena	263
7.3.1.1 Metallic Lead Formation	264
7.3.1.2 Reaction Mechanism	265
7.3.1.3 Comparison With Salomon de Friedberg Combustion Model ...	268
7.3.2 Pyrite/Pyrrhotite	269
7.3.2.1 Combustion Model	275
7.3.2.2 Combustion Model Predictions	277
7.3.2.3 Overall Pyrite/Pyrrhotite Reaction Model	284
7.3.3 Commercial Concentrates	285
7.4 Figures -chapter 7	292
CHAPTER 8 Conclusions	309

References	313
APPENDIX 1 Two-Wavelength Pyrometry	323
A.1.1 Theory	323
A.1.2 Calculation of Relative Apparent Object Area	325
A.1.3 Pyrometer Accuracy	326
APPENDIX 2 Mathematical Model of the Two-Wavelength Radiation Pyrometer	327
A.2.1 General	327
A.2.2 Model Outline	328
A.2.2.1 Energy Transmitted Through the Filter	328
A.2.2.2 Power Incident on the Detectors	329
A.2.2.3 Calculated Measurement Error in Pyrometer Temperature	330
A.2.2.4 Apparent Particle Area Calculation	330
APPENDIX 3 Particle Terminal Velocity and Residence Time Calculations	333
A.3.1 Particle Terminal Velocity	333
A.3.2 Particle Residence Time Calculations	334
APPENDIX 4 Combusting Particle Modelling	337
A.4.1 Particle Heat Balance	337
A.4.2 Heat Transfer Correlations	337
A.4.3 Mass Transfer Correlations	338
A.4.3.1 The Effects of Non-Equimolar Diffusion on Mass Transfer	339
A.4.4 Estimate of Relative Magnitude of Gas Phase and Liquid Phase Mass Transfer	341
APPENDIX 5 Pyrometer Calibration	344
A.5.1 Calibrated Temperature Sources Available	344
A.5.2 Blackbody Temperature Sources	345
A.5.3 Copper Freezing Point Blackbody	347
A.5.4 Low Temperature Resistance Heated Blackbody Furnace	348
A.5.5 High Temperature Induction Heated Blackbody Furnace	349
A.5.6 Calibration Accuracy	350
APPENDIX 6 Tungsten Emissivity Data	359

List of Tables

<u>Table</u>	<u>Page</u>
2.1 Selected thermodynamic properties of lead species	10
4.1 Chemical composition of the different mineral species and size fractions tested	50
4.2 Screen Analysis of the Brunswick and Sullivan concentrate.....	51
4.3 Size analyses of feed materials	51
4.4 Experimental series conducted	55
4.5 Calculated residence times as a function of furnace position for different mineral species in air and oxygen @1130K	57
5.1 Details of two-colour pyrometers developed to measure the surface temperature of particles	71
5.2 Photomultiplier tube calibration- measured photomultiplier sensitivity vs. photomultiplier gain setting	78
5.3 Noise level on pyrometer output signal	79
5.4 Summary of pyrometer calibration data	82
5.5 Measured and calculated pyrometer calibration constants	84
5.6 Theoretical blackbody temperature error associated with various C_{VAL} errors	85
5.7 Variation of 710nm Detector output signal across the pyrometer field of view for various lamp and lens tube settings	87
5.8 Intensity and measured temperature variation across the pyrometer measuring volume	88
6.1 Classifications of pyrometer output signal pulses recorded during particle combustion in air	153
6.2 Average temperature pulse lengths and calculated particle diameter of the different pulse classifications for the combustion of the different feed materials in air	154
6.3 Summary of air series pyrometry results	155
6.4 Classifications of pyrometer output signal pulses recorded during particle combustion in oxygen	156
6.5 Average temperatures, pulse lengths and calculated particle diameters of the different pulse classifications for the combustion of the different feed materials in oxygen	157

6.6	Summary of oxygen series pyrometry results	158
6.7	Compiled results of the experiments examining the effects of oxygen concentration on the combustion of 74-88 μ m galena particles	159
6.8	Compiled results of the experiments examining the effects of oxygen concentration on the combustion of 74-88 μ m pyrite particles	161
6.9	Averaged results of the experiments examining the effects of oxygen concentration on the combustion of 74-88 μ m galena particles	163
6.10	Measured particle expansions, heating rates and cooling rates for the combustion of 74-88 μ m galena in different oxygen concentrations	164
6.11	Averaged results of the experiments examining the effects of oxygen concentration on the combustion of 74-88 μ m pyrite particles	165
6.12	Chemical analyses of the galena, Sullivan and Brunswick concentrates combusted in air and oxygen	166
6.13	Results of chemical analyses of the galena, Sullivan and Brunswick concentrates in air and oxygen	167
6.14	X-ray diffraction analysis of reacted material.....	168
7.1	Comparison of calculated time to reach ignition temperature and observed combustion zone	261
A.5.1	Pyrometer calibration test data - copper freezing point calibration test	351
A.5.2	Pyrometer calibration test data - resistance heated blackbody	352
A.5.1	Pyrometer calibration test data - induction heated blackbody	354

List of Figures

<u>Figure</u>	<u>Page</u>
1.1	Schematic Diagrams of a) Sinter Strand/Blast Furnace and b) Kivcet Lead Smelting Processes (from Reimers et al. [4]). 7
2.1	Vapour pressure of lead species above the pure compounds (from $F^*A^*C^*T$ [30]), and $S_{2(g)}$ vapour pressure above equilibrium PbS (from Sharma et al. [34]) 28
2.2	PbO - $PbSO_4$ binary phase diagram (from Kellogg et al. [39]). 28
2.3	Pb - S - O predominance area diagram (after Tuffley et al. [40-41]). a) P_{SO_2} - P_{O_2} at 600°C, b) P_{SO_2} - P_{O_2} at 1200°C, c) P_{SO_2} - P_{PbS} at 600°C and d) P_{SO_2} - P_{PbS} at 1200°C. 29
2.4	The effect of P_{O_2} and temperature on the Pb - S - O system at 1atm SO_2 . (from Rosenqvist [46]) 30
2.5	The Pb - S binary phase diagram (from Kullerud [35]). 30
2.6	The PbS - FeS and PbS - ZnS binary phase diagrams (from Hofman [2]). 30
2.7	Typical flash-smelting results. a) a plot of temperature, desulphurisation and metallic lead formation down a Kivcet flash-smelting shaft (from Willis [49]), b) temperature profile along the U.B.C. pilot plant shaft (2kg/min Sullivan concentrate, 40% excess oxygen, from Shook et al.[27]). 31
2.8	Nomograph of the effects of feed concentration of lead flash-smelting. (from Sychev [28]) 32
2.9	Typical U.B.C. pilot plant flash-smelting results. a) desulphurisation and b) ratio of mols Pb to mols S (2kg/min Brunswick concentrate stoichiometric oxygen). (from Shook et al.[27]). 33
2.10	Sulphur elimination from various sulphide minerals (37-53 μ m screen fraction air) a) as function of time, and b) as a function of temperature $\tau=0.1$ s. (from Jorgensen [69]) 34
2.11	Laminar flow furnace and two-wavelength pyrometer of Jorgensen et al. (from Jorgensen et al. [82]). 34
2.12	Average temperature measurements of a) galena, chalcopyrite and pyrite combustion in 900°C air, and b) lead concentrate in oxygen. (from Happ et al. [43]). 35
2.13	Effect of screen fraction on the average combustion temperature of pyrite and chalcopyrite combustion in air at 700°C (from Jorgensen [80]). 36

2.14	Pyrometer output signal and measured temperature for a single combusting pyrite particle (37-53 μm screen fraction in air at 700°C) and b) maximum individual and average particle temperatures as a function of oxygen concentration. (from Jorgensen [79,81]).	36
2.15	Calculated reaction times and temperatures for the combustion of a 100 μm galena particles in air and oxygen at 978K (from Salomon de Friedberg [44]).	37
4.1	Schematic diagram of the experimental furnace, temperature measurement and data acquisition equipment.	59
4.2	The laminar flow furnace a) photograph and b) cross-section.	60
4.3	Schematic diagram of the particle feeder.	61
4.4	The two-wavelength radiation pyrometer, a) schematic diagram and b) pyrometer and associated electronics.	62
4.5	Solid sampler.	63
4.6	Diagram detailing the location of the three furnace tube thermocouples (T_{F1} - T_{F3}) and feed delivery tube surface thermocouples (T_{FDT1} - T_{FDT3}).	64
4.7	Measured furnace tube and feed delivery tube surface temperatures a) versus furnace power setting ($L_f=95\text{mm}$) and b) as a function of feed delivery tube position (power setting=8). (gas flowrate= $0.2 \times 10^{-3} \text{ms}^{-1}$, water flowrate= $0.01 \times 10^{-3} \text{ms}^{-1}$)	65
4.8	Commercial concentrate feed material particles (Brunswick concentrate 105-125 μm screen fraction); a) unsectioned agglomerate, b) sectioned agglomerate, c) agglomeration around a large pyrite grain and d) sectioned agglomerate containing a large pyrite grain.	66
4.9	Pure mineral feed materials (74-88 μm screen fraction) a) pyrite, b) pyrrhotite and c) galena.	67
4.10	Calculated velocity profiles in the feed delivery tube and furnace tube indicating the calculated effect of particle size, gas composition and material density.	68
4.11	Calculated particle residence times in the furnace tube, a) calculated variation within a screen fraction and b) calculated effect of gas composition, particle size and density.	69
5.1	Blackbody spectral radiance (from Reference [116]).	95
5.2	Calculated relative power transmitted though various 10nm band-pass interference filters of different centre wavelengths (see Appendix 2).	95
5.3	Radiant sensitivities and associated quantum efficiencies of different commercially available photomultiplier tubes (Hamamatsu Ltd.).	96

5.4	Calculated relative photomultiplier response for different 10nm bandpass filters vs that for the 810nm interference filter (the product of the power transmitted and photomultiplier quantum efficiencies at the different filter wavelengths).	96
5.5	Calculated minimum measurable temperature and associated measurement errors a) as a function of detector resolution (W) and b) as a function of particle size. (710nm and 810nm interference filters with 10nm band width).....	97
5.6	Photomultiplier tube calibration results.	98
5.7	Pyrometer Blackbody calibration test results. a) natural logarithm of the detector output signal vs inverse of blackbody temperature, b) Calibration constants (C_{VAL}) vs Blackbody temperature (gain settings $G_{710}=8.23$ $G_{810}=9.9$).	99
5.8	Variation in detector output signal across the viewing volume with pyrometer-object distance, X_1 , and lens tube distance, X_2 (see Figure A.2.1 for definitions).	100
5.9	Variation in a) detector output signals and b) measured lamp temperatures across the pyrometer measuring volume.	100
5.10	Schematic diagram of the range of different energy and temperature pulses obtainable from a single combustion peak.	101
5.11	Pyrometer response to a series of drilled holes in a plate rotated between the 6mm blackbody cavity and pyrometer lens at a velocity equivalent to 11ms^{-1}	102
6.1	Time exposure photographs of galena combustion in air and oxygen a)63-74 μm screen fraction, Air, $T_{FURNACE}=1123\text{K}$ $t_{exp}=0.125\text{s}$, and b)63-74 μm screen fraction, Oxygen, $T_{FURNACE}=1023\text{K}$ $t_{exp}=0.067\text{s}$	169
6.2	Time exposure photographs of pyrite and pyrrhotite combustion in air and oxygen. a)Pyrite, 74-88 μm screen fraction, air, $T_{FURNACE}=1023\text{K}$, $t_{exp}=0.125\text{s}$, b)Pyrrhotite, 74-88 μm screen fraction, air, $T_{FURNACE}=1123\text{K}$, $t_{exp}=0.125\text{s}$, c)Pyrite, 74-88 μm screen fraction, oxygen, $T_{FURNACE}=1023\text{K}$ $t_{exp}=0.067\text{s}$	170
6.3	Time exposure photographs of Sullivan concentrate combustion in air and oxygen. a)63-74 μm screen fraction, air, $T_{FURNACE}=1123\text{K}$ $t_{exp}=0.125\text{s}$, b)63-74 μm screen fraction, oxygen, $T_{FURNACE}=1023\text{K}$ $t_{exp}=0.125\text{s}$	171
6.4	Time exposure photographs of Brunswick concentrate combustion in air and oxygen. a)63-74 μm screen fraction, air, $T_{FURNACE}=1023\text{K}$ $t_{exp}=0.125\text{s}$, b)63-74 μm screen fraction, oxygen, $T_{FURNACE}=1023\text{K}$ $t_{exp}=0.067\text{s}$, c)105-125 μm screen fraction, oxygen, $T_{FURNACE}=1023\text{K}$ $t_{exp}=0.067\text{s}$	172
6.5	A1 combustion pulse recorded during the combustion of galena in air. a)pyrometer output and b)measured temperature. (63-74 μm , $T_{FURNACE}=1130\text{K}$, $C_{VAL}=1.42$, data#=G237.dat).	173

- 6.6 A1 combustion pulse recorded during the combustion of galena in air. a)pyrometer output and b)measured temperature. (63-74 μ m, $T_{\text{FURNACE}}=1130\text{K}$, $C_{\text{VAL}}=1.42$, data#=G352.dat). 174
- 6.7 Variation in apparent relative area from the A1 galena combustion pulse shown in Figure 6.5. Particle area calculated relative to that at 7.4ms. (63-74 μ m, $T_{\text{FURNACE}}=1130\text{K}$, $C_{\text{VAL}}=1.42$, data#=G237.dat)..... 175
- 6.8 A3 combustion pulse recorded during the combustion of pyrrhotite in air, a)pyrometer output, b)measured temperature and c)apparent area relative to that at 5ms. (74-88 μ m, $T_{\text{FURNACE}}=1130\text{K}$, $C_{\text{VAL}}=1.01$, data#=PH126.dat)..... 176
- 6.9 A3 combustion pulse recorded during the combustion of pyrite in air. a) pyrometer output, b) measured temperature and c)apparent area relative to that at 8ms. (74-88 μ m, $T_{\text{FURNACE}}=1130\text{K}$, $C_{\text{VAL}}=0.81$, data#=PY201.dat)..... 177
- 6.10 A3 combustion pulse recorded during the combustion of Brunswick concentrate in air a)pyrometer output, b)measured temperature and c)apparent area relative to that at 11.6ms. (74-88 μ m, $T_{\text{FURNACE}}=1130\text{K}$, $C_{\text{VAL}}=1.01$, data#=NB414.dat)..... 178
- 6.11 A3I combustion pulse recorded during the combustion of pyrrhotite in air. a)pyrometer output and b)measured temperature. (63-74 μ m, $T_{\text{FURNACE}}=1130\text{K}$, $C_{\text{VAL}}=1.42$, data#=PH81.dat). 179
- 6.12 A3I combustion pulse recorded during the combustion of pyrrhotite in air, a)pyrometer output and b)measured temperature. (74-88 μ m, $T_{\text{FURNACE}}=1130\text{K}$, $C_{\text{VAL}}=1.01$, data#=PH176.dat). 180
- 6.13 A2 combustion pulse recorded during the combustion of Sullivan concentrate in air, a)pyrometer output, b) measured temperature and c) apparent area relative to that at 8.0ms. (105-125 μ m, $T_{\text{FURNACE}}=1130\text{K}$, $C_{\text{VAL}}=1.42$, data#=S436.dat). 181
- 6.14 A2 combustion pulse recorded during the combustion of Brunswick concentrate in air, a)pyrometer output, b)measured temperature and c)apparent area relative to that at 10.0ms. (63-74 μ m, $T_{\text{FURNACE}}=1130\text{K}$, $C_{\text{VAL}}=1.42$, data#=NB284.dat)..... 182
- 6.15 A2 combustion pulse recorded during the combustion of Sullivan concentrate in air. a)pyrometer output and b)measured temperature. (88-105 μ m, $T_{\text{FURNACE}}=1130\text{K}$, $C_{\text{VAL}}=1.42$, data#=S266.dat). 183
- 6.16 A2 combustion pulse recorded during the combustion of Brunswick concentrate in air. a)pyrometer output and b)measured temperature. (74-88 μ m, $T_{\text{FURNACE}}=1130\text{K}$, $C_{\text{VAL}}=1.42$, data#=NB313.dat)..... 184
- 6.17 A4 combustion pulse recorded during the combustion of galena in air, a)pyrometer output and b)measured temperature. (74-149 μ m, $T_{\text{FURNACE}}=1130\text{K}$, data#=G70.dat). 185

6.18	A5 combustion pulse recorded during the combustion of Sullivan concentrate in air, a)pyrometer detector output, b)measured temperature and c)apparent area relative to that at 16.5ms. (63-74 μ m, $T_{\text{FURNACE}}=1130\text{K}$, $C_{\text{VAL}}=1.42$, data#=S234.dat).	186
6.19	Combustion of galena 63-74 μ m in air at $T_{\text{FURNACE}}=1130\text{K}$ - pulse type, temperature and relative frequency as a function of furnace combustion distance.	187
6.20	Combustion of galena 63-74 μ m in air at $T_{\text{FURNACE}}=1130\text{K}$; a)pulse length and b)calculated particle diameter, as a function of furnace combustion distance.	188
6.21	Combustion of galena 63-74 μ m in air at $T_{\text{FURNACE}}=1130\text{K}$ - apparent particle diameter versus measured particle temperature.	189
6.22	Combustion of galena 74-88 μ m in air at $T_{\text{FURNACE}}=1130\text{K}$ - pulse type, temperature and relative frequency as a function of furnace combustion distance.	189
6.23	Combustion of galena 88-105 μ m in air at $T_{\text{FURNACE}}=1130\text{K}$ - pulse type, temperature and relative frequency as a function of furnace combustion distance.	190
6.24	Combustion of galena 105-125 μ m in air at $T_{\text{FURNACE}}=1130\text{K}$ - pulse type, temperature and relative frequency as a function of furnace combustion distance.	190
6.25	Pulse type averaged combustion pulse data as a function of feed size for galena combustion in air, a)pulse temperatures, b)pulse lengths and c)apparent diameters ($T_{\text{FURNACE}}=1130\text{K}$).	191
6.26	Combustion of galena 105-125 μ m in air at $T_{\text{FURNACE}}=1130\text{K}$ - apparent particle diameter versus measured particle temperature.....	192
6.27	A1 combustion pulse recorded during the combustion of 88-105 μ m galena in air showing the presence of energy spikes, a)pyrometer output and b)measured temperature. (74-88 μ m, $T_{\text{FURNACE}}=1130\text{K}$, $C_{\text{VAL}}=1.42$, data#=G156.dat).	193
6.28	Combustion of 74-88 μ m pyrrhotite in air at $T_{\text{FURNACE}}=1130\text{K}$ - pulse type, temperature and relative frequency as a function of furnace combustion distance.	194
6.29	Combustion of 74-88 μ m pyrite in air at $T_{\text{FURNACE}}=1130\text{K}$ - pulse type, temperature and relative frequency as a function of furnace combustion distance.	194
6.30	Pulse type averaged combustion pulse data for pyrite and pyrrhotite combustion in air, a)pulse temperatures, b)pulse lengths and c)apparent diameters. ($T_{\text{FURNACE}}=1130\text{K}$).	195
6.31	Calculated apparent particle expansion for A3 combustion pulses recorded during the combustion of pyrite(Py), pyrrhotite(Ph), galena(G) and Brunswick(NB) concentrate in air at $T_{\text{FURNACE}}=1130\text{K}$, as a function of an arbitrary data#.	196

6.32	Combustion of a)63-74 μ m and b)74-88 μ m Sullivan concentrate in air at $T_{\text{FURNACE}}=1130\text{K}$ - pulse type, temperature and relative frequency as a function of furnace combustion distance.....	197
6.33	Combustion of a)88-105 μ m and b)105-125 μ m Sullivan concentrate in air at $T_{\text{FURNACE}}=1130\text{K}$ - pulse type, temperature and relative frequency as a function of furnace combustion distance.....	198
6.34	Pulse type averaged combustion pulse data as a function of feed size for Sullivan concentrate combustion in air, ($T_{\text{FURNACE}}=1130\text{K}$). a)pulse temperatures, b)pulse lengths and c)apparent diameters.	199
6.35	Combustion of 63-74 μ m Sullivan concentrate in air at $T_{\text{FURNACE}}=1130\text{K}$ - apparent particle diameter versus measured particle temperature.	200
6.36	Combustion of a)63-74 μ m and b)74-88 μ m Brunswick concentrate in air at $T_{\text{FURNACE}}=1130\text{K}$ - pulse type, temperature and relative frequency as a function of furnace combustion distance.....	201
6.37	Combustion of a) 88-105 μ m and b) 105-125 μ m Brunswick concentrate in air at $T_{\text{FURNACE}}=1130\text{K}$ - pulse type, temperature and relative frequency as a function of furnace combustion distance.....	202
6.38	Pulse type averaged combustion pulse data as a function of feed size for Brunswick concentrate combustion in air, ($T_{\text{FURNACE}}=1130\text{K}$).a)pulse temperatures, b)pulse lengths and c)apparent diameters.....	203
6.39	Combustion of 63-74 μ m Brunswick concentrate in air at $T_{\text{FURNACE}}=1130\text{K}$ - apparent particle diameter versus measured particle temperature.	204
6.40	Heating and cooling rates of the A1 combustion pulses recorded during the combustion of the galena(G), Sullivan(S) and Brunswick(NB) feed materials in air at $T_{\text{FURNACE}}=1130\text{K}$ (plotted vs an arbitrary data number).	205
6.41	Heating and cooling rates of the A3 combustion pulses recorded during the combustion of Pyrite(Py), Pyrrhotite(Ph), galena(G), Sullivan(S) and Brunswick(NB) feed materials in air at $T_{\text{FURNACE}}=1130\text{K}$ (plotted vs an arbitrary data number).....	206
6.42	Heating and cooling rates of the A2 combustion pulses recorded during the combustion of galena(G), Sullivan(S) and Brunswick(NB) feed materials in air at $T_{\text{FURNACE}}=1130\text{K}$ (plotted vs an arbitrary data number).....	207
6.43	O1T combustion pulse recorded during the combustion of galena in oxygen, a)pyrometer output and b)measured temperature. (63-74 μ m, $T_{\text{FURNACE}}=1130\text{K}$, $C_{\text{VAL}}=1.42$, data#=G316.dat).	208
6.44	O1T combustion pulse recorded during the combustion of galena in oxygen, a)pyrometer detector output, b)measured temperature and c)apparent area relative to that at 4ms. (105-125 μ m, $T_{\text{FURNACE}}=1130\text{K}$, $C_{\text{VAL}}=1.42$, data#=G455.dat).	209

6.45	O3 combustion pulse recorded during the combustion of pyrrhotite in oxygen, a)pyrometer output, b)measured temperature and c)apparent area relative to that at 4ms. (74-88 μ m, $T_{\text{FURNACE}}=1130\text{K}$, $C_{\text{VAL}}=0.81$, data#=PH224.dat).....	210
6.46	O3 combustion pulse recorded during the combustion of pyrite in oxygen, a)pyrometer output, b)measured temperature and c)apparent area relative to that at 2.8ms. (74-88 μ m, $T_{\text{FURNACE}}=1130\text{K}$, $C_{\text{VAL}}=0.81$, data#=PY84.dat).....	211
6.47	O2 combustion pulse recorded during the combustion of Sullivan concentrate in oxygen, a)pyrometer output and b)measured temperature. (63-74 μ m, $T_{\text{FURNACE}}=1130\text{K}$, $C_{\text{VAL}}=1.42$, data#=S324.dat).....	212
6.48	O2 combustion pulse recorded during the combustion of Brunswick concentrate in oxygen, a)pyrometer output and b)measured temperature. (105-125 μ m, $T_{\text{FURNACE}}=1130\text{K}$, $C_{\text{VAL}}=1.01$, data#=NB669.dat).....	213
6.49	O2S combustion pulse recorded during the combustion of Sullivan concentrate in oxygen, a)pyrometer output and b)measured temperature. (63-74 μ m, $T_{\text{FURNACE}}=1130\text{K}$, $C_{\text{VAL}}=1.01$, data#=S303.dat).....	214
6.50	Combustion of 63-74 μ m galena in oxygen at $T_{\text{FURNACE}}=1130\text{K}$ - pulse type, temperature and relative frequency as a function of furnace combustion distance.	215
6.51	Combustion of a) 74-88 μ m and b) 105-125 μ m galena in oxygen at $T_{\text{FURNACE}}=1130\text{K}$ - pulse type, temperature and relative frequency as a function of furnace combustion distance.....	216
6.52	Pulse type averaged combustion pulse data as a function of feed size for galena combustion in oxygen, a)pulse temperatures, b)pulse lengths and c)apparent diameters. ($T_{\text{FURNACE}}=1130\text{K}$).....	217
6.53	Combustion of 63-74 μ m galena in oxygen at $T_{\text{FURNACE}}=1130\text{K}$ - apparent particle diameter versus measured particle temperature.....	218
6.54	Heating and cooling rates of the O1 combustion pulses recorded during the combustion of galena(G), Sullivan(S) and Brunswick(NB) feed materials in oxygen at $T_{\text{FURNACE}}=1130\text{K}$ (plotted vs an arbitrary data number).....	219
6.55	Combustion of 74-88 μ m a)pyrrhotite and b)pyrite in oxygen at $T_{\text{FURNACE}}=1130\text{K}$ - pulse type, temperature and relative frequency as a function of furnace combustion distance.....	220
6.56	Pulse type averaged combustion pulse data for the combustion of pyrrhotite and pyrite in oxygen, a)pulse temperatures, b)pulse lengths and c)apparent diameters. ($T_{\text{FURNACE}}=1130\text{K}$).....	221

6.57	Heating and cooling rates of the O ₃ combustion pulses recorded during the combustion of pyrite(Py), pyrrhotite(Ph), galena(G) and Brunswick(NB) feed materials in oxygen at $T_{\text{FURNACE}}=1130\text{K}$ (plotted vs an arbitrary data number).....	222
6.58	Combustion of a)63-74 μm and b)105-125 μm Sullivan concentrates in oxygen at $T_{\text{FURNACE}}=1130\text{K}$ - pulse type, temperature and relative frequency as a function of furnace combustion distance.....	223
6.59	Pulse type averaged combustion pulse data as a function of feed size for Sullivan concentrate combustion in oxygen, a)pulse temperatures, b)pulse lengths and c)apparent diameters. ($T_{\text{FURNACE}}=1130\text{K}$).	224
6.60	Heating and cooling rates of the O ₂ combustion pulses recorded during the combustion of the commercial concentrates in oxygen at $T_{\text{FURNACE}}=1130\text{K}$ (plotted vs an arbitrary data number).....	225
6.61	Combustion of a)63-74 μm and b)105-125 μm Brunswick concentrates in oxygen at $T_{\text{FURNACE}}=1130\text{K}$ - pulse type, temperature and relative frequency as a function of furnace combustion distance.....	226
6.62	Pulse type averaged combustion pulse data as a function of feed size for Brunswick concentrate combustion in oxygen, a)pulse temperatures, b)pulse lengths and c)apparent diameters. ($T_{\text{FURNACE}}=1130\text{K}$).....	227
6.63	A/O ₁ T combustion pulse recorded during the combustion of 74-88 μm galena in 40% oxygen, a)pyrometer output and b)measured temperature. ($T_{\text{FURNACE}}=1130\text{K}$, $C_{\text{VAL}}=1.42$, data#=G520.dat).....	228
6.64	A/O ₁ T combustion pulse recorded during the combustion of 74-88 μm galena in 50% oxygen, a)pyrometer output and b)measured temperature. ($T_{\text{FURNACE}}=1130\text{K}$, $C_{\text{VAL}}=1.42$, data#=G535.dat).....	229
6.65	The effect of oxygen concentration on the combustion of 74-88 μm galena at $T_{\text{FURNACE}}=1130\text{K}$ - combustion pulse type and temperature.	230
6.66	The effect of oxygen concentration on the combustion of 74-88 μm galena at $T_{\text{FURNACE}}=1130\text{K}$ - combustion pulse length.....	230
6.67a	The effect of oxygen concentration on the combustion of 74-88 μm galena at $T_{\text{FURNACE}}=1130\text{K}$ - calculated apparent particle diameter.....	231
6.67b	The effect of oxygen concentration on the combustion of 74-88 μm galena at $T_{\text{FURNACE}}=1130\text{K}$ - calculated apparent particle diameter vs particle temperature.	231
6.68	A ₃ combustion pulse recorded during the combustion of 74-88 μm pyrite in 10% oxygen, a)pyrometer detector output and b)measured temperature. ($T_{\text{FURNACE}}=1130\text{K}$, $C_{\text{VAL}}=1.12$, data#=PY267.dat).....	232
6.69	Temperatures of A ₃ and O ₃ combustion pulse recorded during the combustion of 74-88 μm pyrite at various oxygen concentrations at $T_{\text{FURNACE}}=1130\text{K}$	233

6.70a	The effect of oxygen concentration on the combustion of 74-88 μ m pyrite at $T_{\text{FURNACE}}=1130\text{K}$ - combustion pulse type and temperature....	234
6.70b	The effect of oxygen concentration on the combustion of 74-88 μ m pyrite at $T_{\text{FURNACE}}=1130\text{K}$ - combustion pulse length.....	234
6.71a	The effect of oxygen concentration on the combustion of 74-88 μ m pyrite at $T_{\text{FURNACE}}=1130\text{K}$ - calculated apparent particle diameter.....	235
6.71b	The effect of oxygen concentration on the combustion of 74-88 μ m pyrite at $T_{\text{FURNACE}}=1130\text{K}$ - calculated apparent particle diameter vs particle temperature.	235
6.72	The effect of oxygen concentration on the combustion of 74-88 μ m pyrite at $T_{\text{FURNACE}}=1130\text{K}$ - calculated apparent particle expansion.....	236
6.73	The effect of oxygen concentration on the combustion of 74-88 μ m pyrite at $T_{\text{FURNACE}}=1130\text{K}$ on the heating and cooling rates.	237
6.74	Chemical analyses of the reaction products of galena combustion in air at $T_{\text{FURNACE}}=1130\text{K}$, a)74-88 μ m and b)105-125 μ m screen fractions. Sulphur, lead and product weight as percentage of original, metallic lead as percent of total lead.	238
6.75	Chemical analyses of the reaction products of Sullivan concentrate combustion in air at $T_{\text{FURNACE}}=1130\text{K}$, a)74-88 μ m and b)105-125 μ m screen fractions. Sulphur, lead and product weight as percentage of original, Fe(II) and metallic lead as percent of species total.	239
6.76	Chemical analyses of the reaction products of Brunswick concentrate combustion in air at $T_{\text{FURNACE}}=1130\text{K}$, a)74-88 μ m and b)105-125 μ m screen fractions. Sulphur, lead and product weight as percentage of original, Fe(II) and metallic lead as percent of species total.	240
6.77	Chemical analyses of the reaction products of 63-74 μ m galena combustion in oxygen at $T_{\text{FURNACE}}=1130\text{K}$. Sulphur, lead and product weight as percentage of original, metallic lead as percent of total lead.	241
6.78	Chemical analyses of the reaction products of 74-88 μ m screen fractions of a) Sullivan, and b) Brunswick concentrate, combustion in oxygen at $T_{\text{FURNACE}}=1130\text{K}$. Sulphur, lead and product weight as percentage of original, Fe(II) and metallic lead as percent of species total.	242
6.79	SEM photomicrographs of reaction products of galena combustion in air at $T_{\text{FURNACE}}=1130\text{K}$. a)74-149 μ m screen fraction, b) and c) (74-88 μ m) back-scattered electron image showing sulphur deficient Pb cores (light areas) and d) (74-88 μ m) zinc oxide shells.	243
6.80	SEM photomicrographs of partially reacted pyrite and pyrrhotite grains prior to melting (74-88 μ m, air, $T_{\text{FURNACE}}=1130\text{K}$). a) porous pyrrhotite surrounding pyrite core, b) Relative sulphur concentration across particle in a), c) partially thermally decomposed pyrite grains, and d) pyrrhotite grains.	244

6.81	SEM photomicrographs of iron oxide reaction products of 74-88 μ m screen fraction pyrite and pyrrhotite combustion in air at $T_{\text{FURNACE}}=1130\text{K}$	245
6.82	SEM photomicrographs of commercial concentrate combustion in air at $T_{\text{FURNACE}}=1130\text{K}$. a)Sullivan Pb-Fe-S melt (105-125 μ m), b)Sullivan, iron oxide shells (105-125 μ m), c)Brunswick, partially reacted iron sulphide particles (74-88 μ m), and d)Brunswick iron oxide shells (74-88 μ m).....	246
6.83	SEM photomicrographs of iron oxide shells found in the products of 74-88 μ m Brunswick concentrate combustion in air at $T_{\text{FURNACE}}=1130\text{K}$	247
6.84	SEM photomicrographs of the reaction products of 63-74 μ m screen fraction galena combustion in oxygen at $T_{\text{FURNACE}}=1130\text{K}$. a)unsectioned, b)part-reacted particles (light) in fume clump, c)B-S image of Pb rich core in PbS drop, d) B-S images of a partially melted PbS particle, unmelted material fractured, original surface oxide (light patches).	248
6.85	SEM photomicrographs of the reaction products of 74-88 μ m screen fraction pyrite and pyrrhotite combustion in oxygen at $T_{\text{FURNACE}}=1130\text{K}$. a),c)-d))pyrite, and b) pyrrhotite.....	249
6.86	SEM photomicrographs and x-ray maps of a sectioned, partially reacted, Pb-Fe-Zn-S particle. Sullivan feed, 74-88 μ m, oxygen, $T_{\text{FURNACE}}=1130\text{K}$	250
6.87	SEM photomicrographs of the products of 74-88 μ m screen fraction of Brunswick concentrate combustion in oxygen at $T_{\text{FURNACE}}=1130\text{K}$	251
7.1a	Calculated heating rates for various size particles of density equivalent to galena ($\rho=7500\text{ kgm}^{-3}$, $\epsilon=0.7$ and $T_{\text{FURNACE}}=1130\text{K}$).	292
7.1b	Calculated heating rates for particles of different densities, different furnace gas temperatures and furnace gas compositions ($d_p=74\mu\text{m}$, $\rho=7500\text{ kgm}^{-3}$, $\epsilon=0.7$ and $T_{\text{FURNACE}}=1130\text{K}$).....	292
7.2	The sulphur-oxygen potential diagram for Pb-S-O system at 1473K (from Yazawa [38]).	293
7.3	Schematic diagram of the galena combustion mechanism in air and oxygen at 1130K.....	294
7.4	Oxygen-sulphur dioxide/sulphur potential diagrams for the Fe-S-O system at several temperatures (from F*A*C*T [30]).	295
7.5	The FeS-FeO-SiO ₂ system ternary phase diagram at 1473K (from Biswas et al. [134]).	296
7.6	Binary phase diagrams a) Fe-S and b) Fe-O systems (from [136]).	297

7.7	Calculated temperature histories for 65 μ m FeS particles combusting in air ($T_{\text{FURNACE}} = 1130\text{K}$, $\epsilon=0.7$) considering the formation of different reaction products (after Jorgensen [79])	298
7.8	Calculated heating and cooling rates as a function of particle temperature for variations in reaction mechanism, particle emissivity and diameter for particles combusting in air at $T_{\text{FURNACE}} = 1130\text{K}$ and $\epsilon=0.7$ (unless otherwise stated).....	299
7.9	A comparison of calculated thermal histories for the combustion of FeS particles in air ($dp=65\mu\text{m}$, $T_{\text{FURNACE}} = 1130\text{K}$ and $\epsilon=0.7$) and measured A3I combustion pulses for 74-88 μ m pyrrhotite particles. ..	300
7.10	Calculated thermal histories for 30 and 65 μ m FeS particles combusting in air ($T_{\text{FURNACE}} = 1130\text{K}$, $\epsilon=0.7$) and the effect of a) emissivities variations ($\epsilon=0.7$ and 1) and b)x2.5 diameter increase on cooling.	300
7.11	Measured and predicted combustion temperatures for specific FeS particles in air ($\epsilon=0.7$) (a) NB414 $dp=69\mu\text{m}$ inflation x1.7, (b) PY123 $dp=55\mu\text{m}$ inflation x2.8 and (c) PY201 $dp=53\mu\text{m}$ inflation x2.5.	301
7.12	Calculate temperature histories for 65 μ m FeS particles combusting in oxygen considering the formation of different reaction products ($T_{\text{FURNACE}} = 1130\text{K}$, $\epsilon=0.7$).	302
7.13	Measured and predicted combustion temperatures for specific FeS particles in oxygen ($\epsilon=0.7$, x1 inflation) (a) PH224 $dp=60\mu\text{m}$, (b) PH222 $dp=61\mu\text{m}$ and (c) PY216 $dp=68\mu\text{m}$	303
7.14	Calculated and measured maximum temperatures for 65 μ m FeS particles as a function of oxygen concentration considering the formation of different reaction products ($T_{\text{FURNACE}} = 1130\text{K}$, $\epsilon=0.7$). ...	304
7.15	A comparison of calculated and measured heating rates at peak combustion temperature as a function of oxygen concentrations ($dp=65\mu\text{m}$, $T_{\text{FURNACE}} = 1130\text{K}$ and $\epsilon=0.7$).	305
7.16	Measured cooling rates of the A3 combustion pulses as a function of combustion temperature. The calculated cooling rates for 65 μ m FeS particles considering x1 and x2.5 particle inflation ($T_{\text{FURNACE}} = 1130\text{K}$, $\epsilon=0.7$) are also included for comparison.....	305
7.17	Schematic diagram of pyrite/pyrrhotite combustion in air and oxygen at 1130K.	306
7.18	Superimposed oxygen-sulphur dioxide potential diagrams for the Fe-S-O and Pb-S-O systems at 1500K.	307
7.19	Schematic diagram of the combustion lead-iron-zinc sulphide agglomerates in air and oxygen at 1130K.	308
A.2.1	Schematic diagram of the pyrometer optics.....	332

A.5.1	Theoretical blackbody emissivity as a function of cavity L/D ratio and surface emissivity (from Brandsetter [121]).	356
A.5.2	Schematic diagram of copper freezing point blackbody cavity.	357
A.5.3	Typical variation in measured temperature and derived calibration constant observed with the copper freezing point blackbody cavity (for $G_{710}=8.23$ $G_{810}=9.9$).	357
A.5.4	Schematic diagram of low temperature, resistance heated, blackbody cavity.	358
A.5.5	Schematic diagram of high temperature, induction heated, blackbody cavity.	358
A.6.1a	Variation in the monochromatic emissivity of tungsten with temperature (from Latyev et al. [124]).	360
A.6.1b	Variation in the ratio of the monochromatic emissivity of tungsten at 710 and 810nm, and associated measured temperature error as a function of temperature (from Latyev et al. [124]).	360

List of Symbols

Symbols

a_x	activity of species x relative to the standard state
a	acceleration (ms^{-2})
A	area (m^2)
B	constant
c	velocity of light (m/s)
c_g	molar density of gas ($molm^{-3}$)
c_A	molar concentration of species A of gas ($molm^{-3}$)
C_1	1st radiation constant 3.74×10^{-16} (Wm^2)
C_2	2nd radiation constant 1.438×10^{-2} (mK)
C_D	drag coefficient
C_p	specific heat capacity at constant volume ($Jmol^{-1}K^{-1}$)
C_{val}	experimentally determined pyrometer constant
C_o	constant
D_{A-B}	binary diffusion coefficient of species A in B (m^2s^{-1})
d	diameter (real or apparent) (m)
E_a	activation energy (J)
F	force (N)
F_{dp}	particle-detector view factor
$F_{0-\lambda,T}$	fraction of blackbody radiation in spectrum between wavelengths of 0 and λ
g	gravitational acceleration 9.8 (ms^{-2})
ΔG_f^0	Gibb's free energy of formation ($kJmol^{-1}$)
G	overall pyrometer gain (V/W)
GS	detector gain setting
ΔH_f^0	standard enthalpy of formation ($kJmol^{-1}$)
h	Plank's constant 6.6262×10^{-34} (Js)
h	heat transfer coefficient ($Wm^{-2}K^{-1}$)
ID	inside diameter (mm)
k	Boltzmann's constant 1.3806×10^{-23} (JK^{-1})
k	thermal conductivity ($Wm^{-1}K^{-1}$)
K_g	gas phase mass transfer coefficient (ms^{-1})
K_l	liquid phase mass transfer coefficient (ms^{-1})

K_R	equilibrium constant
$K_{1,2,\dots,n}$	constant
L_f	latent heat of fusion ($kJmol^{-1}$)
m	mass (kg)
M	mols (mol)
n_s	stoichiometry factor
N_A	molar flux of species A ($molm^{-2}s^{-1}$)
NEP	noise equivalent power (W)
Nu	Nusselt number (hd/k)
OD	outside diameter (mm)
P	power (W)
P_x	vapour pressure of species x (atm)
P	pulse length (s)
Pr	Pandtl number ($C_p/\mu k$)
Re	Reynolds number ($\rho ud/\mu$)
S	detector sensitivity ($V\mu m^{-1}$)
S_2	aperture stop
Sc	Schmidt number ($\mu/\rho D_{A-B}$)
Sh	Sherwood number (kl/D_{A-B})
t	time (s)
T	temperature (K)
T_m	measured temperature (K)
u	velocity (ms^{-1})
u_t	particle terminal velocity (ms^{-1})
V	pyrometer detector output voltage (V)
W	intensity of radiation (radiant emittance) (Wm^{-2})
W_λ	spectral radiance (Wm^{-3})
X_1	pyrometer-object distance (mm)
X_f	pyrometer focal length (mm)
X_2	lens tube distance (mm)
X_A	mol fraction of species A
Y_{bl}	boundary layer thickness (m)
Y	object position (mm)
α_λ	absorptivity at wavelength λ
α	constant

δ_l	liquid boundary thickness (m)
$\Delta\lambda$	optical bandwidth (nm)
ΔV	detector resolution (V)
ϵ_λ	monochromatic emissivity (or band pass equivalent)
λ	wavelength (nm)
μ	viscosity ($kgm^{-1}s^{-1}$)
ρ	density (kgm^{-3})
ρ_λ	reflectivity at wavelength λ
σ	Stefan's constant, 5.6697×10^{-8} ($Wm^{-2}K^{-4}$)
σ	surface tension (Nm^{-1})
τ_λ	transmittivity at wavelength λ

Subscripts

a	ambient
bb	blackbody
f	formation
g	gas
$f1-f3$	furnace tube thermocouple identifier
$fdt1-fdt3$	feed delivery tube thermocouple identifier
l	liquid
p	particle
r,R	reaction
s	solid
T	temperature
min,max	bandpass wavelength limits
λ_1	interference filter 1 centre wavelength
λ_2	interference filter 2 centre wavelength
710	centre wavelength of interference filter 1 (nm)
810	centre wavelength of interference filter 2 (nm)

Acknowledgments

I would like to acknowledge my supervisors Dr. Greg Richards and Dr. Keith Brimacombe.

Cominco LTD and Brunswick Mining and Smelting are also acknowledged for supplying the feed materials and for the assaying services provided.

I am also grateful to NSERC Canada for providing financial support.

CHAPTER 1

Introduction

1.1 Pyrometallurgical Production of Lead

The main pyrometallurgical route followed for the production of lead from concentrates is the sinter strand/lead blast furnace process [1-3]. Over 85% of the world's lead concentrates are treated by this method [4], a process in which little has changed since its introduction late last century. A schematic diagram of the process is given Figure 1.1a. The lead concentrates are first mixed with flux and roasted on a sinter strand such that the lead sulphide is converted to oxides, sulphates and basic sulphates. The sinter is then crushed, sized and, together with coke, fed into a squat blast furnace in which the lead oxides are reduced by the coke and the CO generated in the blast air. The lead forms a bullion into which most of the base impurities and precious metals collect. A molten slag is also tapped off from which zinc can be fumed.

The gradual trend towards increased energy efficiency, better industrial hygiene and stricter pollution controls has forced the lead industry to look at new technology [4-7]. In the sinter strand-blast furnace process the heat of oxidation of the sulphides is lost during sintering. The process has difficulty in meeting the present or proposed limits for sulphur dioxide emissions [4] due to the sinter off-gas being of relatively low sulphur dioxide concentration (2-6.5%), and therefore costly to scrub. It is also difficult to prevent emissions from the various unit operations such that lead levels within the work environment exceed the newer requirements for industrial hygiene.

The ideal requirements for any new pyrometallurgical lead smelting process are as follows [4,7]:

- i) the sulphide concentrates should be fed directly to the reactor such that the sinter strand step is eliminated and the heat of oxidation of the sulphides provides the maximum proportion of the process energy requirements;

- ii) the process should produce a continuous stream of off-gas of high sulphur dioxide concentration;
- iii) any required lead reduction steps should use low cost reductants such as coal or coke breeze;
- iv) recirculation of lead dusts should be minimised;
- v) the gases and dusts within the process must be well contained such that future emission standards for lead into the work environment can be achieved.

The recent generally depressed state of the base metal industry and the lack of proven technology has, however, delayed the construction of plants based on new technology until very recently [8-10].

1.1.1 New Pyrometallurgical Processes for Lead Smelting

A considerable number of new pyrometallurgical processes for lead smelting have been developed over the last three decades [4-23]. Most of the proposed new processes are based on the smelting of lead concentrates to metallic lead according to the overall partial oxidation reaction:



The problem [5] with this smelting route is that in order to produce a low sulphur bullion, high oxidation potentials are required which result in a high lead oxide content in the slag. Low *PbO* slag contents are, however, necessary for high lead recoveries. The new lead processes therefore require two regions of different process conditions to produce low sulphur bullion and low lead slags. The two different steps may be carried out as separate stages, as in the Boliden [4-5], Boliden Kaldor [4,6-7], Outokumpu [4-7,11-14], Cominco [5], St. Joe Mineral Corp. [5,15-16] and the Isasmelt process [17], or incorporated in the same reactor as with the Kivcet [4-9,18-23], and QSL [4,6-7,10] processes.

Few of these new processes have been taken beyond the pilot plant stage and it is the two processes in which both stages are carried out in a single reactor, namely the Kivcet and QSL processes, which have become commercial realities. These two processes differ considerably in the methods used for sulphur elimination and slag reduction. In the Kivcet process a flash smelting shaft is used for the initial sulphur elimination step and the slag reduction is carried out with coke in an attached electric arc furnace. In the QSL process both the sulphur elimination and *PbO* reduction are carried out as bath reactions in a single vessel. By injecting oxygen and coal in the bath at opposing ends, regions of high and low oxidation potential are produced at the different ends of the reactor. A commercial plant based on the Kivcet process has been constructed and operated since February 1987 by Nuova Samin (ENI) at Portovesme Sardinia [8-9]. Plants based on the QSL process are being constructed at Cominco Ltd. Trail, B.C. and in China.

1.2 Lead Flash Smelting

Flash smelting has become accepted practice in the non ferrous industry for the smelting of copper and nickel concentrates. Due to the fast rates of reaction, high throughput, high utilisation of process heat and high sulphur dioxide off-gas can be achieved. Considerable interest exists in applying this technology to the processing of other materials. Of the new pyrometallurgical processes for lead, the Kivcet, Outokumpu, Cominco and Boliden processes [4-5] all utilise a flash smelting shaft for the primary sulphur elimination step.

In flash smelting, the concentrates are combusted as a finely divided dispersion of particles in a jet of air or oxygen. In most cases the sulphide concentrates are introduced through a burner nozzle at the top of the flash smelting shaft. Combustion occurs as the particles travel down the shaft producing a lead rich condensed phase (which impinges on the molten bath below) and a high sulphur dioxide containing off-gas (up to 60% SO_2).

The very large surface areas of commercial concentrates and the good mixing between the particles and gas allow very high rates of reaction to occur [24-25] and therefore very high throughput can be achieved. This encourages the use of tonnage oxygen which increases the intensities of reactions and allows a higher proportion of the total energy requirements to be produced, also a high SO_2 off gas is produced.

The high vapour pressures of the lead species at the smelting temperatures (1500-1700K) is possibly the most serious problem associated with the flash smelting of lead concentrates. Pilot plant [18-23,26-27] and industrial studies[28] indicated that up to 30% of the lead feed can report to the dust and require recycling.

1.2.1 The KIVCET Process

A description of the Kivcet process is helpful in understanding the role of the flash smelting chamber in relation to the overall system. The Kivcet process (see Figure 1.1b) uses a flash smelting shaft for the sulphur elimination step and the oxide present in the molten product is then reduced in an adjoining electric arc furnace. Maximum sulphur elimination is required in the flash smelting shaft and therefore the oxygen-to-feed ratio is controlled such that the lead species enter the bath as a mixture of oxides and metallic lead [18-23,28]. For concentrates with greater than 17% sulphur and less than 1% moisture the process is autogeneous. Galena contains 13.4 wt% S, so that a higher fraction of sulphur in the concentrate is generally due to the presence of other metal sulphides, of which, copper and iron sulphides tend to have a greater heat of combustion. Recent data from the commercial plant at Portovesme [8] suggests the process can be autogenous for feeds with as low as 14% sulphur and containing 8% oxidised material and 7% battery pastes. The process can run on less exothermic feeds if fuel is also added in the burner.

At the operating temperature of 1625-1675K volatilisation of the lead species can be significant [5,22,28]. It has been reported that the volatilisation of lead regulates the temperature of the flash smelting shaft [28] which can result in 30 % of the charge mass

being recycled. Recycle from Portovesme [8] was, however, found to be only 5%. Recycle dusts are primarily lead sulphate which, on recycling decomposes endothermically to lead oxide in the flame. For highly exothermic feeds the addition of a thermal load such as sulphate battery slimes can be beneficial in reducing lead fume recycle [8-9].

It is reported that the shaft temperature must be maintained between 1625-1675K to foster endothermic reactions that occur between the molten droplets and the coke layer floating on the bath [8].

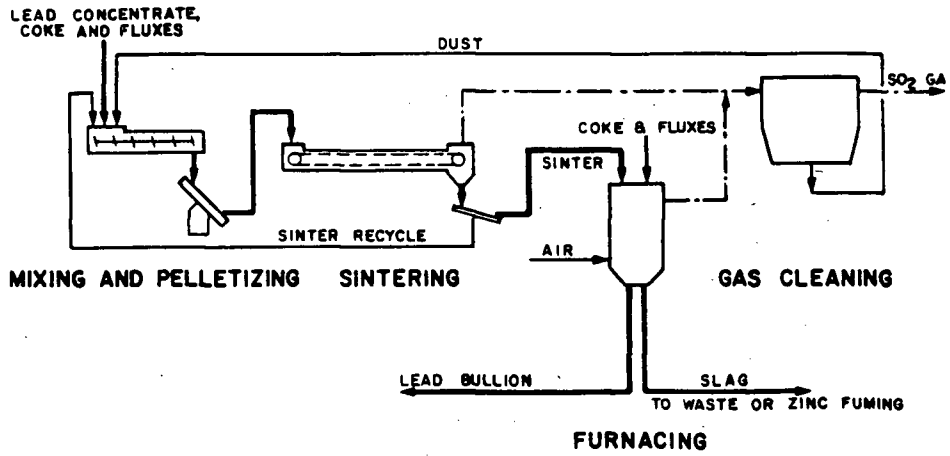
Flux additions of lime and silica are added with the feed to produce a slag composition of typically 39% FeO , 38% SiO_2 and 23% CaO [8]. On entering the bath at the bottom of the flash smelting shaft the metallic lead and PbO rich slag separate and flow under a water-cooled partition wall into the submerged arc furnace. The high lead content in the slag is reduced by the addition of coke breeze to the electric furnace. The slag and bullion are tapped at opposite ends of the furnace. Typically the bullion, tapped at 1100K, contains 0.1% sulphur and the slag contains ~2% lead and 5-10% zinc.

The 80 000 tonnes (lead bullion) per year (tpy) plant at Portovesme operates at a throughput of 50 tonnes of charge per square metre of shaft per day [8-9,26]. The dimensions of this flash smelting shaft have not been reported. The 50 000 tpy plant constructed by KHD Humboldt Wedag AG for ENAF/COMIBOL Bolivia (but never commissioned) [18-22] had a Shaft Height of 4.8m and a hearth area of 6.0m².

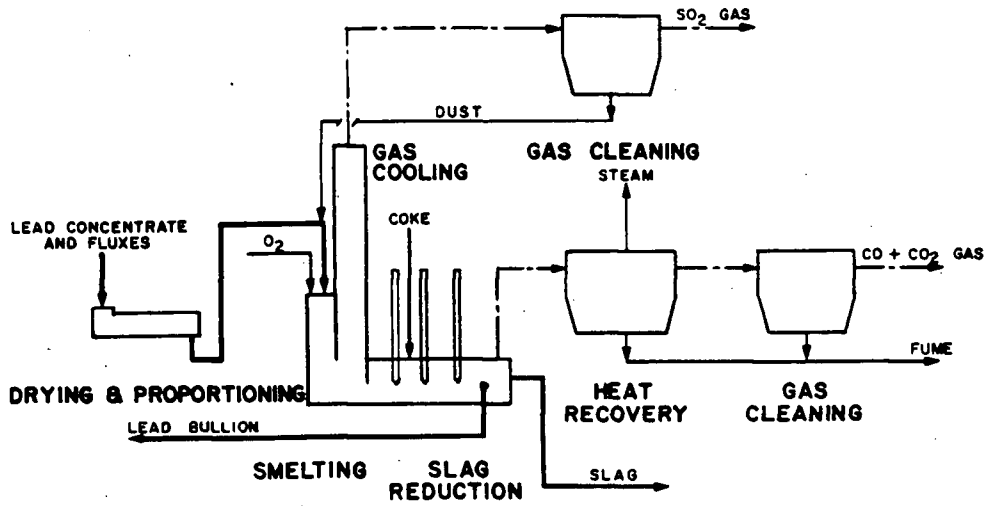
1.3 Area of Study

The reaction of particles in the flash smelting shaft is complex and not clearly understood. Our knowledge of the behaviour of reacting particles in a turbulent jet is incomplete. Similarly, little work has been done at a fundamental level examining the behaviour of individual particles during combustion under flash smelting conditions. The dearth of information is especially true for the flash smelting of lead concentrates.

Any attempt to increase our understanding of the fundamentals of metal sulphide combustion processes will be useful even if its direct applicability to industrial operation is not apparent. This thesis presents the results of an experimental programme examining the combustion of lead concentrate particles under controlled conditions.



(a)



(b)

Figure 1.1 Schematic Diagrams of a) Sinter Strand/Blast Furnace and b) Kivcet Lead Smelting Processes (from Reimers et al. [4]).

CHAPTER 2

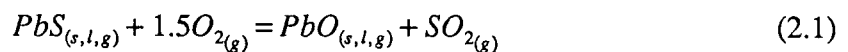
Literature Review

During flash smelting the individual particles and the gas phase surrounding them experience rapid and transient changes in temperature and composition. The exact conditions experienced by the individual particles and the reactions occurring have not been clearly identified. A literature review of the thermodynamics of the species involved in the flash smelting reactions is, however, necessary to define the theoretical limits of what is possible. Similarly a review of the published data on the kinetics of the different gas-solid, liquid-solid and gas-liquid reactions which occur during the brief history of the particles in the furnace is necessary.

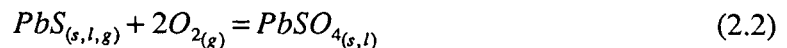
2.1 Thermodynamics of Flash Smelting Reactions

2.1.1 General

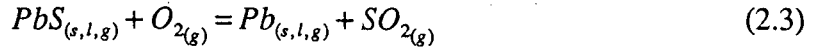
In the flash smelting shaft the individual lead concentrate particles are oxidised to different degrees. Oxides and sulphates of lead (Reactions 2.1 and 2.2) can be considered the main oxidation reaction products. Up to 20% of the lead, however, enters the bath in the metallic form [28]. It is possible that the metallic lead is the result of direct reaction under specific condition in the shaft (as given in Equation 2.3); or it could be the result of the reactions between oxidised species and unreacted sulphides in the shaft or after mixing in the bath (Reaction 2.4 and 2.5).



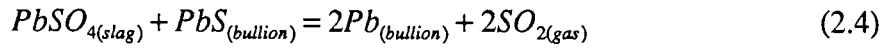
$$\Delta G_{R\ 1500K}^{\circ} = -260\ kJ \quad \Delta H_{R\ 1500K}^{\circ} = -421\ kJ$$



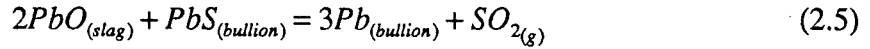
$$\Delta G_{R\ 1500K}^{\circ} = -312\ kJ^* \quad \Delta H_{R\ 1500K}^{\circ} = -799\ kJ^*$$



$$\Delta G_R^{\circ}_{1500K} = -218 \text{ kJ} \quad \Delta H_R^{\circ}_{1500K} = -239 \text{ kJ}$$



$$\Delta G_R^{\circ}_{1500K} = -124 \text{ kJ}^{* **} \quad \Delta H_R^{\circ}_{1500K} = +321 \text{ kJ}^{* **}$$



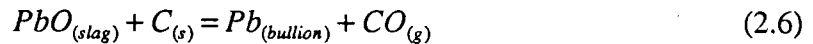
$$\Delta G_R^{\circ}_{1500K} = -63 \text{ kJ}^{**} \quad \Delta H_R^{\circ}_{1500K} = +122 \text{ kJ}^{**}$$

(Reference 30)

* $PbSO_{4(s)}$ considered ** all species considered at unit activity

At the process temperatures (1500-1625K), some equilibration between the slag and bullion in the bath will also tend to occur through the roast reactions [5] given by Equations 2.4 and 2.5.

The lead oxides in the slag are then reduced in a second step, by the addition of carbon according to the overall reaction given in Equation 2.6, to produce a discardable slag of typically less than 2% lead.



2.1.2 Vapour Phase Species

The vapour pressures of PbS , PbO and Pb are relatively high, and their boiling points of 1609, 1745 and 2017K respectively (see Table 2.1 [29-33]), are relatively low with respect to flash smelting temperatures. The significant quantities of fume observed attests to the importance of the volatile lead species. The reported vapour pressures of Pb , PbS and PbO above the pure species are shown in Figure 2.1. The interactions between the various components in the condensed phases means that the activities and hence the vapour pressures of the above species may differ from that at standard state depending on the composition.

Also shown in Figure 2.1 is the vapour pressure of sulphur in equilibrium with PbS and Pb phases at unity activity as determined by Sharma et al. [34]. Considering a point defect model, a much higher sulphur pressure ($\sim \times 1000$ greater) above

TABLE 2.1 Selected Thermodynamic Properties of Lead Species

Species	m.pt. (K)	L_f m.pt. (kJ/mol)	b.pt. (K)	L_{vap} b.pt. (kJ/mol)	$L_{subl.}$ sb.pt. (kJ/mol)	Reference
Pb	600.4	4.81±0.12	2017	178±2.1	194±2.5	29
PbO	1158 -	24.4±2.5 -	- 1745	- 213	- -	29 33
PbS	1385 1392	36.4±3.3 36.4	(1553) 1609.5	- 167.3	(229) -	29,33 30
PbSO ₄	1363 1443	(40.19) -	- -	- -	- -	29 39
PbSO ₄ .PbO	1248	-	-	-	-	39
PbSO ₄ .2PbO	1234	-	-	-	-	39
PbSO ₄ .4PbO	1168	-	-	-	-	39

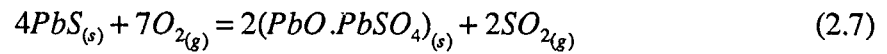
stoichiometric *PbS* was calculated, and considered to result in slight non-stoichiometry of the solid. The predicted bulk sulphur losses from the formation of non-stoichiometric *PbS* are calculated to be in the order of 0.001% and would be insignificant to the overall combustion behaviour.

2.1.3 Pb-S-O System

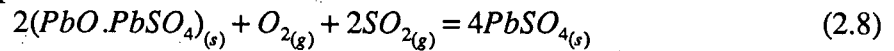
The *Pb-S-O* system is the most important with respect to the flash smelting of lead sulphide concentrates. The thermodynamics of the system have been examined by several authors with respect to lead smelting [5,36-38] and lead sulphide roasting [39-41]. For the *Pb-S-O* system at the compositions and temperatures (>800K) of interest the condensed phases which exist are *Pb*, *PbS*, *PbO*, *PbSO₄* and a series of basic lead sulphates. The basic sulphates known to exist are *PbO.PbSO₄*, *2PbO.PbSO₄* and *4PbO.PbSO₄* [39]. A phase diagram of the *PbO-PbSO₄* binary system is given in Figure 2.2. *2PbO.PbSO₄* is reported unstable below 889K. Kellogg and Basu [39] have determined the heats and free energies of formation of the solid basic sulphates; however the thermodynamic data for the liquid phases must be estimated [29,30,42].

Using the thermodynamic data for the solid phases and assuming sulphur dioxide and oxygen are the only species in the gaseous phase, it is possible to construct stability diagrams for the *Pb-S-O* system. The thermodynamic stability of the species with respect to the gas phase P_{SO_2} and P_{O_2} can be determined. Typical equilibria considered are:

"Oxidation" Type Equilibria



"Sulphation" Type Equilibria



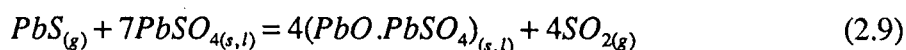
Kellogg et al.[39] and Tuffley and Russell [40-41] have published a series of these diagrams for temperatures between 873 and 1473K. examples of which are given in Figures 2.3a and 2.3b. Thermodynamic data available on the F*A*C*T Data system [30] allows similar diagrams to be prepared for specific conditions.

The diagrams are useful in suggesting which phases may form or exist under flash smelting conditions. If the partial pressure of lead species is small the oxygen and sulphur dioxide partial pressures are linked through the total atmosphere pressure of effectively one bar (or some fraction of it if nitrogen is present). The permissible composition variation corresponds to a line, such as line a (for oxygen), in Figure 2.3b. If the gas composition can be estimated, the changes in the thermodynamically stable phases which exist at increasing temperatures can be taken as a guide to what phases may form during reaction. This very superficial analysis is most suited to considering solid phase oxidation or rapid equilibration between two condensed phases. The diagrams suggest that sulphates and basic sulphates will tend to be the low temperature products of oxidation. With increasing temperature their stabilities decline with respect to *PbO*, *Pb* and *PbS*. This is in general agreement with the behaviour of the lead fume and dust recycle. Sychev [28] reports that the *PbO* fume generated during galena combustion sulphates in the off-gas on cooling below 1000K. Similarly, the recycled sulphate fume is reported [22,28] to decompose endothermically to basic sulphates or oxides in the flash smelting

flame.

The diagrams indicate that under typical flash smelting conditions PbO and PbS , in their standard state, cannot coexist in equilibrium but should react to form liquid lead.

At higher temperatures neglecting the volatile lead species can be unrealistic. These species adds considerable complexity to the diagram and therefore, to date, have not been calculated. Tuffley and Russell [40-41] have, however, plotted an analogous diagram to the previous considering SO_2 and PbS as the stable gas species. A typical reduction equilibrium considered would be:



Examples of this type of predominance area diagram are given in Figures 2.3c and 2.3d. Line b represents the maximum vapour pressure of PbS above the pure species at the given temperature and therefore the region to the right of the line is theoretical at normal pressures. The stability of lead oxide and liquid lead (at higher P_{PbS}) increases with increasing temperature under reducing conditions. The presence of a lead sulphide vapour front around particles during combustion has been speculated upon by several researchers [43,44]. Under such circumstances the reduction of any surface sulphates present to metallic lead may be expected.

The results of roasting experiments carried out by Tuffley and Russell [40-41] indicated that PbS vapour reduction reactions occur. Their findings suggest that the PbS vapour prevents the complete sulphation of the low temperature oxidation products, and at temperatures above 1100K the basic lead sulphates are reduced to metallic lead. Unlike roasting, it is improbable that the particles travelling through the flash smelting shaft will pass through regions in the gas phase where lead sulphide vapour exists in sufficient quantity to allow reduction reactions to occur. Instead the presence of metallic lead observed by many researchers [18-22,28] could be due to either oxygen depletion at the particle surface at relatively high reaction temperatures encouraging the formation of metallic lead (Reaction 2.3) or interaction between oxide and sulphide particles allowing

the "roast reactions" to occur (Reactions 2.4 and 2.5). From an examination of the interaction of pellets of lead sulphate and lead sulphide within briquettes, Hsiao et al. [45] reports that metallic lead formation was observed on the site of the sulphate pellets by vapour phase transport of *PbS*. Roast reactions producing metallic lead were also observed in pellets containing sphalerite, pyrrhotite and chalcopyrite, instead of galena. These reactions, however, did not appear to occur by the vapour phase transport of the sulphide species with instead, the oxygen from the lead sulphate appearing to transfer to the sulphide. This is reported possibly to occur through the decomposition of the lead sulphate to a basic lead sulphate. Later reaction occurs through point contact and molten material.

By redrawing the predominance area diagram for a fixed sulphur dioxide partial pressure, the effect of temperature on the stability of the phases can be seen. The diagram shown in Figure 2.4 [46] is plotted for a partial pressure of sulphur dioxide of one atmosphere. Above ~1150K a molten lead phase can form by a roast reaction. Above the melting point of *PbS*, molten lead and *PbS* are completely miscible [47-48]. The *Pb-S* binary phase diagram reported by Kullerud [35] is given in Figure 2.5, which shows a relatively flat liquidus and miscibility gap at 5-7 wt% S. Schuhmann et al. [36] and Esdaile [48] have determined that the liquidus data of the *Pb-PbS* binary system correlate well to a regular solution model. Using this information, the activities of the species in solution and the vapour pressure of the volatile lead species above the melt can be determined. The theoretical total pressure of the volatile species above the melt (P_{TOT}) is plotted in Figure 2.4.

2.1.4 The Effects of Other Mineral Species

Lead concentrate feed is typically a mix of the sulphides of lead, iron and zinc, and therefore, the reaction and thermodynamics of multicomponent melts is of importance.

Similarly, as silica and lime fluxes are mixed with the feed before smelting, metal-slag systems resulting from the interaction of particles in the shaft are of importance. Not surprisingly little of this information is available in the literature.

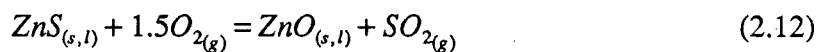
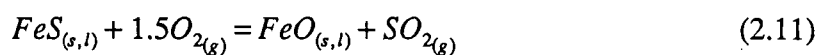
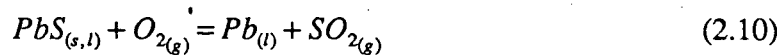
Phase diagrams for the *PbS-FeS* and *PbS-ZnS* binary systems [2] (see Figures 2.6a and 2.6b) indicate that eutectics exist at 30wt% *FeS* and 8wt% *ZnS* at temperatures of 1136K and 1317K respectively. The formation of lower temperature melts could enhance reaction rates by encouraging the generally more rapid gas-liquid reactions.

2.2 Kinetics of Lead Flash Smelting Reactions: Pilot and Industrial Plant Studies

The kinetics of both the oxidation and vaporisation reactions are of considerable importance to the understanding of lead flash smelting. The reactions involved and the effects of process variables on the reactions have not been clearly identified. Pilot plant information from the industry is sparse and generally of a qualitative nature [12,18-19,28]. Preliminary results from the U.B.C. lead flash smelting pilot plant have recently been published by Shook et al.[27].

From Willis [49] a typical temperature profile down the shaft of a commercial smelter, is given in Figure 2.7a. Similarly a typical centreline gas temperature profile from the 2kg/min U.B.C. furnace [27] is given in Figure 2.7b. In both cases, despite the differences in the scale of operation the peak temperatures of about 1673K (1400°C) were measured ~1m down the shaft.

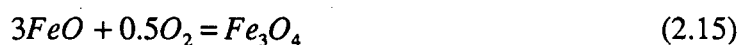
The primary reactions reported in the shaft [18-22,28] are:



where Reaction 2.13 represents the formation of silicates from the metal oxides.

The reactions are reported to occur primarily in the liquid phase at temperatures between 1525-1625K [49]. Thermodynamics indicates that, at the smelting temperatures, metallic lead is only stable at low oxygen partial pressures. The formation of metallic lead in the smelter shaft has, however, been reported by several authors [18-19,27,49], with up to 20% of lead being present (see Figure 2.7a) in the metallic form. This suggests that either localised conditions of oxygen depletion around the particles are occurring or the "Roast reactions" (Equations 2.4 and 2.5) are of considerable importance.

Further down the shaft the secondary reactions reported are:



Chauduri et al. [18-19] and Sychev [28] reveal that in the first 500mm of the shaft the concentrate is heated to ~1000K during which time a small amount (<10%) of desulphurisation occurs. Melting of the particles then occurs, followed by rapid liquid-gas reactions. The rates of reactions suggest that there is little limitation from the inherent chemical reaction kinetics [49]. The large quantities of lead fume reported suggests lead sulphide vaporisation may be limiting the rate of reaction of the lead species for some period [43,44]. The temperature reaches about 1525K 1000mm down the shaft, and metallic lead formation is the predominant lead oxidation reaction. Intensive sulphur oxidation occurs 1500mm down the shaft with the temperature reaching a maximum of ~1675K. Here metallic lead formation reaches a maximum (~40-45% of the lead feed) and the formation of lead oxide and lead silicates begins to predominate. At greater distances the shaft temperature declines as the intensity of the oxidation reactions decrease.

Sychev [28] has reported the effects of concentrate composition on the ignition and reaction of lead concentrates; his findings are summarised in the nomograph given in Figure 2.8. The ignition temperatures have been found by Sychev [28,51-52] to increase

in order of decreasing enthalpy of oxidation such that $CuFeS_2 < FeS_2 < PbS < ZnS$. Increasing concentrations of sulphides of lower ignition temperatures were found to lower the ignition temperature of the lead concentrate and vice versa.

The results from Shook et al. [27] for the reaction of Brunswick concentrate (Pb 34%, S 32%, Fe 21% and Zn 6%) are interesting (see Figure 2.9). At 200mm down the reaction shaft 90% of the sulphur was removed; however, the molar ratio of $Pb:S$ increased to 2.8. This suggests most of the iron had reacted and also much of the sulphur associated with the lead was removed. During this period most of the lead was still present. Between 200 and 700mm, a ten-fold decrease in the $Pb:S$ ratio but a ~50% increase in the percentage of sulphur present is reported. This strongly suggests considerable lead volatilisation has occurred. The increasing $Pb:S$ ratio further down the shaft is thought [27] to be due to the deposition of lead sulphate fume on the sampler. The results of Shook et al. [27] comparing the combustion of Sullivan concentrate (Pb 62%, S 18%, Fe 9.5% and Zn 5.5%) with that of Brunswick, found that increasing the iron content of the feed did not significantly increase the maximum furnace temperature but did shift the main region of combustion slightly towards the burner. Considerably more recycle (fume products and entrained material) was observed with the high iron concentrates. This could be due either to increased lead volatilisation as the result of increased heat input or due to more physical carry-over due to the increased gas volume with the Brunswick concentrate or as a result of changes in the furnace vacuum. Increasing the oxygen-to-feed ratio seemed to increase the amount of fume produced. Finally the effects of burner design were highlighted. Radial distribution of the concentrate discharging from a straight burner pipe was found to be poor and oxygen starvation at the centre of the jet was indicated by the chemical assays. Poor sulphur elimination was observed in the centre whereas towards the edges over-oxidation tended to occur.

Sychev [28] reports the fume produced in the flash smelter to be nominally lead sulphate of 3 to 6 μ m in diameter. It is reported that the lead oxide reaction product reacts with sulphur trioxide below ~1000K, to form lead sulphate [28]. Similarly the recycled lead sulphate flue dusts are reported to decompose by the reverse mechanism on heating in the flame. Cordina et al. [50] reports the formation of a sulphur trioxide fume during the fluidised bed drying of a lead concentrate at ~600K.

It is apparent from the pilot plant results that the reaction mechanisms and the effects of process variables have not been established clearly. The behaviour of the particles in the reaction shaft is not fully understood. The nature of the feed material has not been identified, with both strongly [56] and loosely [57] bonded agglomerates being reported. Similarly, particles have been observed [58-63] both to disintegrate and to coalesce. Controversy also exists as to whether small particles oxidise to a greater extent than larger particles [58-63]. It is clear that the geometric design of the burner and furnace can have a significant effect on the particle behaviour [62].

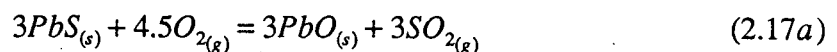
Many researchers have attempted small scale experiments under controlled conditions to identify reaction mechanisms and the effects of process variables. Owing to the complexity of the hydrodynamics within the flash smelter, it is difficult to relate these small scale experiments to what is occurring in the flash smelting shaft. Notwithstanding this shortcoming, some useful information can be obtained from a review of laboratory studies.

2.3 Kinetics of Lead Flash Smelting Reactions: Laboratory Studies

2.3.1 DTA Experiments and Ignition Studies

A considerable number of DTA/TGA studies of the ignition of sulphide concentrates have been conducted [50-55]. It is debatable, however, if most of these findings can be applied directly to the kinetics of flash smelting as the low heating rates used (often <10K/sec) probably allow low temperature solid products to form to a much greater extent than in flash smelting where the heating rates are considerably higher

(10^4 - 10^5 K/s) [24-25]. It is probable that the ignition temperature is not an intrinsic property of the mineral but is the result of the combined influence of heat and mass transfer in addition to the intrinsic reaction kinetics [53,54]. A recent paper by Nakamura et al. [53] examining the combustion of lead sulphide concentrates at heating rates up to $200^\circ\text{C}/\text{min}$ suggests that the location of the DTA peaks for reaction in air is strongly dependent on the heating rate for rates below $\sim 100^\circ\text{C}/\text{min}$. At low heating rates ($<20^\circ\text{C}/\text{min}$.) two exothermic reaction peaks at $\sim 1000\text{K}$ and $\sim 1050\text{K}$, considered to be due to the formation of basic lead sulphates, were observed. With increasing heating rates the temperature at which the main reaction peak was observed increased, until at a heating rate of $200^\circ\text{C}/\text{min}$ a single combustion peak at 1195K was recorded. With increasing heating rates, increasing amounts of lead oxide (PbO) was found associated with the basic lead sulphates. From this, the overall reaction given in Equation 2.16 was considered to consist of two intermediate reactions, with the sulphur dioxide generation in Equation 2.17a being kinetically faster than the sulphation reaction in Equation 2.17b such that at high heating rate unsulphated PbO was found.



Nakamura et al. [53] also examined the reaction of three commercial concentrates containing between 4.5 and 19.7% iron as sulphides and concluded that the amount of iron (sulphide) present is important to the temperature at which the samples reacted. The presence of iron resulted in a reaction peak, in air, of ~ 850 - 900K with sometimes also a later lead sulphide reaction peak being observed. Sychev et al. [51,52] report DTA experiments at heating rates of 10 - $70^\circ\text{C}/\text{min}$., examining the effects of particle composition, size and slag additions on the oxidation of sulphide concentrates in oxygen. The temperature of PbS reaction varied from 700 - 850K and was most strongly dependent

on the particle size. Small lead sulphide particles ($<10\mu\text{m}$) were found to oxidise in a single step to lead oxide. Larger particles tended first to sulphate, and then on melting reacted rapidly forming of PbO at temperatures above 1175K.

Salomon de Friedberg [44,68] has studied the ignition of galena and two commercial concentrates in air and oxygen. The particles were dropped into a hot furnace and therefore heated very rapidly (10^4 - 10^5K/s). The ignition temperatures for galena in air and oxygen were 980K and 880K respectively. The temperatures appear similar to those recorded by Sychev et al. [51,52] and also to the laminar flow furnace results of Jorgensen [69], but less than those measured by Nakamura et al. [53]. The effect of increasing iron (and sulphur) composition was found (similar to the work of Nakamura et al. [53]) to lower the ignition temperature. The ignition temperatures of Sullivan concentrate (Fe 9.5%, S 18%) in air and oxygen were 863 and 793K respectively; and those of Brunswick concentrate (Fe 21%, S 32%) in air and oxygen were 823 and 663K respectively.

Salomon de Friedburg [44,68] observed only galena (PbS) and anglesite ($PbSO_4$) in the product of galena combustion. From microscopic analysis it was proposed that during combustion the galena particles form molten spheres which react and gradually shrink due to lead sulphide vaporisation. For particles containing sulphides of iron and zinc, as well as lead, a different reaction mechanism was proposed [44]. On heating, porosity within the particle was postulated to form due to PbS vaporisation as the particle reaches high temperatures; the oxides of iron and zinc melt and PbS vapour entrapped within results in the formation of a thick walled hollow sphere (cenospheres).

2.3.2 Solid State Oxidation

Gray et al. [70-71] have examined the sulphation of single crystals of galena between 969 and 1073K with set gas compositions. The rate of sulphation was found to be related linearly to the logarithm of the sulphur trioxide partial pressure with an

activation energy of 167 ± 40 kJ/mol. It was proposed that the overall sulphation reaction (Equation 2.2) is controlled by the outwards diffusion of Pb^{2+} through the sulphate layer and that absorbed SO_3 provided the potential gradient causing outward diffusion of Pb^{2+} .

The reaction of the solid oxidation products with lead sulphide on melting is probably of some importance. However, according to Willis [49] and Fuller [15] the reactions are slow below 1475K.

2.3.3 Flame Studies

Wuth and co-worker [63-65] have examined the combustion of several sulphide mineral (including galena) concentrates using a laboratory-scale burner. Using a feed rate of ~ 10 g/min a 150-200mm flame was produced, and the reaction products were quenched in a water trough. Many partially reacted particles were collected indicating the presence of separate metallic or oxide phases within the quenched sulphide droplets. The presence of metallic lead was observed with the galena concentrates [64]. These dense phases (metallic lead, copper, magnetite, ferrites etc) were usually found at the centre of the sulphide droplets. Studies of the composition and morphology of quenched samples from commercial and laboratory reactors have also been published by Hagni et al. [66,67].

2.3.4 Laminar Flow Furnace Studies

Jorgensen et al. [43,56,69,72-83] and others [84-85] have examined the combustion of dilute suspensions of concentrates in a laminar flow of gas, however little of the published work has been carried out on galena. Jorgensen has published a brief examination of the combustion of galena [69] and recently Happ and Jorgensen [43] have published a more extensive study of the combustion of Broken Hill lead concentrate. From the preliminary study, the effect of reaction time and gas temperature on the combustion of galena, in comparison with other minerals is given in Figure 2.10. Above the ignition temperature (~ 1000 K) very rapid sulphur elimination occurs from the molten particles and the reactions are completed in less than 50 milliseconds. The final sulphur content and its decrease with increasing gas temperature is consistent with the formation

of the experimentally observed basic sulphates [43] which are thermodynamically stable at these temperatures and oxygen partial pressures. During combustion, however, the particle temperature can rise several hundred degrees above the gas temperature and therefore the observed products could be due to post-combustion equilibration. Lead losses increased with increasing gas temperature [69,43]. The formation of metallic lead during the experiments was not reported.

Some of the results from studies of the combustion of other minerals reported by Jorgensen [56,69,72-83], may also be of significance. With chalcopyrite, considerable particle disintegration was observed [61-62,80]. Jorgensen [80] determined that, in air, particles larger than $40\mu\text{m}$ tended to a final particle size of $40\mu\text{m}$ irrespective of their initial size. Average reacted particle size was found to decrease gradually with increasing oxygen concentration to a limiting value of about $30\mu\text{m}$ at 40% oxygen or more. Size reduction was reported to be due primarily to the pinching off of liquid during melting. Jorgensen, however, also reports [81] that high speed cinetography studies indicated that during the reaction of pyrite, explosions typically resulted in the formation of 3-4 particles. High speed cinetography studies of the combustion of copper concentrates by Otero et al. [88] also suggest that 2-4 particles are produced by disintegration during copper concentrate (CuFeS_2) combustion and a reaction front or vapour shroud about twice the particle size is often observed. For pure chalcocite (Cu_2S), however, the reactions terminate with a violent disintegration producing many tens of particles.

Jorgensen observed [69,78-79,81,83] large thin-walled magnetite cenospheres present in the reaction products of pyrite combustion in air. The diameter of the cenospheres was typically 2-3 times greater than the average particle size of the feed material and inside the cenospheres there was often a large number of small oxide or sulphide particles. Energy traces from two wavelength pyrometry studies [81,83] suggests cenosphere formation is due to the rapid inflation and freezing of a thin iron

oxide film. Jorgensen [81] also reports that material ejection is often observed during both the initial period of reaction where molten particles are reacting violently and also during the period of rapid cooling after peak combustion temperatures have been reached.

Kim and Themelis [61-62] have proposed that both particle disintegration and cenosphere formation are due to an impervious oxide skin forming around the molten sulphide core trapping gaseous sulphur or sulphur dioxide resulting in explosions and the ejection of molten sulphide material.

2.3.5 Particle Temperature Measurements

A considerable number of researchers [43,69,78-83,86-87,89-95] have used two-wavelength radiation pyrometry techniques (often in conjunction with a laminar flow furnace) to measure the temperature of individual particles during combustion under controlled conditions. The combustion of sulphide concentrates has been examined by Jorgensen et al. [43,69,78-83]. Coal combustion has been examined by Timothy et al. [89], Ayling et al. [90-91] and others [92-95]. Themelis and Gauvin [87] examined the reduction of iron oxide with two wavelength pyrometry.

A schematic diagram of the experimental set-up used by Jorgensen [82] to measure the temperature of combusting particles is given in Figure 2.11. The particles are carried down the reactor in a gas stream of velocity typically of 3.8m/s and are observed by the pyrometer for the few milliseconds (typically 4-6) they spend in front of the pyrometer lens. Although the thermal history and peak temperature of the combusting particles can be determined from the pyrometer output signal, Jorgensen presents most results as the average of a large number of individual measurements [43,69,78-83].

Average temperatures of combusting particles of Broken Hill lead concentrate have been published recently by Happ and Jorgensen [43]. The concentrate is relatively pure galena containing only 3.3% *Zn* and 2.3% *Fe*. The average particle temperature for the combustion of this lead concentrate in air and oxygen (and as a function of gas and wall temperature) is given in Figure 2.12. In oxygen very high average particle

temperatures were attained (1800-1950K) and complete reaction occurred in 20-40 milliseconds. Typically the peak average particle temperatures were 600-700 degrees above the gas temperature [43]. Higher furnace temperatures resulted in an increased maximum temperature, a shortened time to ignition and shorter combustion times. In air the average particle temperature was considerably lower (~1600K) and the time for complete reaction was longer. The average particle temperature for galena was considerably lower than for either chalcopyrite or pyrite (see Figure 2.12a) and again this was attributed to the volatility of the lead species [43]. The average particle temperatures measured in oxygen are considerably above the boiling point of pure lead sulphide (1609K); this may suggest that either the temperature of a combusting cloud of lead sulphide surrounding the particles is being measured or, other lead species are involved in the vaporisation reactions.

The initial particle size of the feed material appears also to affect the reaction time and average particle temperature, as indicated by the results for the combustion of pyrite and chalcopyrite shown in Figure 2.13 [82]. With increasing feed particle size the reaction time and range over which ignited particles are observed appears to increase. It is possible that the relatively small apparent decrease in combustion temperature with increasing feed size is the result of averaging the temperature measurements.

A typical thermal history of a 37-53 μ m pyrite particle combusting in air, recorded by Jorgensen [79] is given in Figure 2.14. The dotted line shows the variation of one of the pyrometer signals during the combustion pulse, and it is suggested that the large increase in signal intensity towards the end of the pulse is due to the formation of an iron oxide cenosphere. The maximum temperature reached by the individual particles appears to depend on the oxygen partial pressure. From Figure 2.14b the maximum temperature reached by the individual 40 μ m pyrite particles reacted in a furnace at 973K, increased from ~1900K at 8% oxygen to temperatures in excess of 2650K in pure oxygen [79]. Similarly the maximum combustion temperature of the individual particles in air was

found to increase modestly with increasing furnace temperatures from ~2000K for surrounding temperatures of 873K to ~2450K for temperatures in excess of 1200K. The maximum temperature of the individual particles is typically 400 to 700 degrees higher than the average of the measured particle temperatures and 1000 to 1700 degrees higher than the gas and furnace wall temperature.

2.4 Modelling Studies of Flash Smelting Reactions.

2.4.1 Particle Reaction Models

Calculations by Jorgensen [78-80] and Themelis et al. [24] for pyrite and chalcopyrite suggest that the reactions are limited by oxygen mass transport. From heat balance calculations, considering oxygen mass transport to be rate controlling, Jorgensen [79] found that better agreement was obtained between predicted and measured particle temperatures if sulphur monoxide rather than sulphur dioxide was considered to be the primary gaseous product at the reaction interface. The SO would then combust at some distance from the particle. Model predictions for pyrite combustion considering SO and SO_2 as the main reaction products and the measured reaction temperatures are given in Figure 2.14b. At higher oxygen potentials both the simple models predicted peak temperatures in excess of those measured.

The initial reaction rate for galena may also be oxygen mass transfer controlled. During the later stages of reaction measured particle temperatures are, however, relatively low and high vapour pressure of the lead species probably exists which suggests that the particle temperature is being limited by the vaporisation of lead species. Similar observations of copper fume and limited maximum temperatures during chalcopyrite combustion in oxygen [80], suggest that particle temperature is often limited by vaporisation reactions.

Salomon de Friedberg [44] has attempted to model the combustion of a single lead sulphide particle. The oxidation reaction was considered to be the direct formation of lead sulphate as given by Equation 2.2, with all of the heat of reaction being absorbed by the particle. Combustion was considered to consist of four stages:

- i) Chemically controlled solid state oxidation and particle heating;
- ii) *PbS* vaporisation and oxygen mass transfer which are rate limiting. The chemical reaction is considered to occur instantaneously at an interface in the gas boundary layer. At some stage during this regime the particle melts. The particle temperature gradually increases until it reaches the boiling point of lead sulphide.
- iii) The particle remains at the boiling point of lead sulphide and the reaction rate is dependent on the net rate of heat input. The *PbS* gas envelope quickly expands and reacts increasingly rapidly. The liquid particle core is consumed and gradually shrinks.
- iv) On complete evaporation of *PbS*, oxygen diffuses rapidly inwards and reacts with the vapour cloud.

The model was fitted to experimental mass loss data through an Arrhenius type equation for the chemically controlled solid state reaction. The model was found to be very sensitive to the value of the pre-exponential constant (k) and the activation energy E_a .

Predicted temperatures for a 100 μ m particle reacted in air and oxygen are given in Figure 2.15. The thermal arrests correspond to the melting and boiling of lead sulphide. The furnace temperature used for these calculations is very close to the ignition temperature of galena in air and therefore it is difficult to compare these results with the temperatures measured by Happ and Jorgensen [43]. The predicted time for complete reaction in oxygen at 978K (~90 ms) is longer than the region of combustion at 1073K (~60 ms) measured by Happ and Jorgensen [43] for lead concentrate.

2.4.2 Flash Smelting Models

Several attempts have been made to model, mathematically, both the hydrodynamics of, and the reactions occurring in flash smelting shafts. To date the models have been concerned with copper [61-62,96-99] and iron sulphide [100-101] flash smelting and no attempt has been made to model lead flash smelting. Models have been developed by Kim and Themelis [61-62], Hahn and Sohn [96-98] and Ruottu [99] for copper; and by Funkunaka et al. [100] and Asaki et al. [101] for pyrite and pyrrhotite. Various degrees of complexity and numbers of defining equations, with respect to the hydrodynamics, have been considered. All the models, however, suffer from the limitations of there being insufficient experimental data to justify the level of complexity being attempted. Similarly the reaction models considered are generally simple, although the treatment of particle fragmentation and material ejection by Kim and Themelis [61-62] is of interest. Recent assessment of modelling studies to date [61] has emphasized our present incomplete understanding of the interaction of individual particles in the flash smelting shaft. Similarly most industrial flash smelters do not have tall thin cylindrical smelting shafts with an axi-symmetrical burner, but usually have several burners. The importance of the burner in distributing the concentrate evenly within the flash space also needs to be modelled more realistically.

2.5 Summary -Justification for the Present Research

It is obvious that our understanding of the oxidation kinetics of lead sulphide is incomplete. Similarly, even less is known about the combustion of the complex mixtures of sulphides found in commercial concentrates. The importance of the volatile lead species is understood but the role of these species in the reactions is not.

The review of the literature indicates that on all levels of investigation more information are required. More pilot and industrial plant data is needed to determine the fluid dynamics, temperature and composition profiles within the flash smelting shaft; and to determine the amount and role of interacting particles within the furnace. Fundamental

data about the species and mechanisms involved in the combustion of lead concentrate particles especially under flash smelting conditions are necessary. Finally modelling studies which realistically address the phenomena occurring in the flash smelting shaft need to be developed.

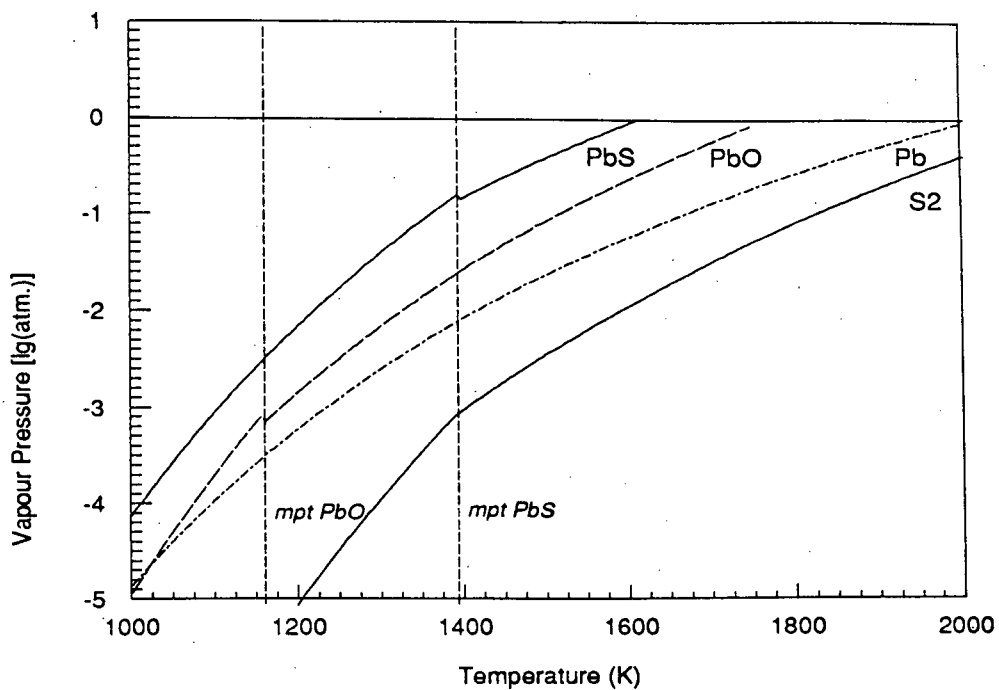


Figure 2.1 Vapour pressure of lead species above the pure compounds (from F*A*C*T [30]), and $S_{2(g)}$ vapour pressure above equilibrium PbS (from Sharma et al. [34])

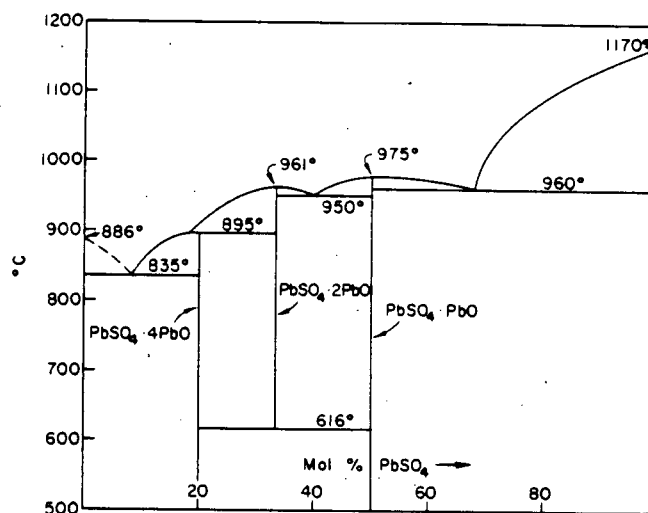


Figure 2.2 PbO - $PbSO_4$ binary phase diagram (from Kellogg et al. [39]).

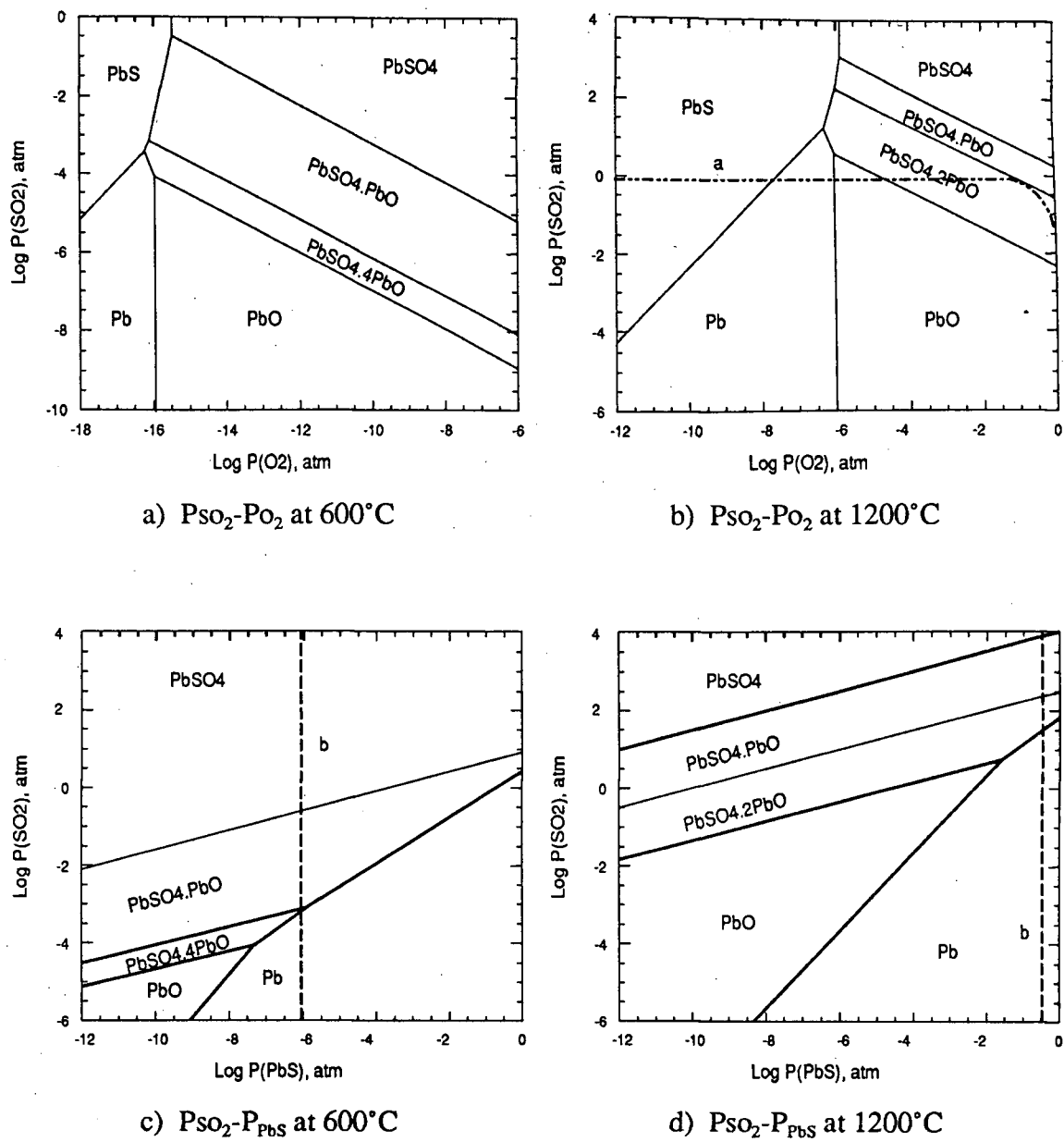


Figure 2.3 Pb-S-O predominance area diagrams (after Tuffley et al. [40-41]).

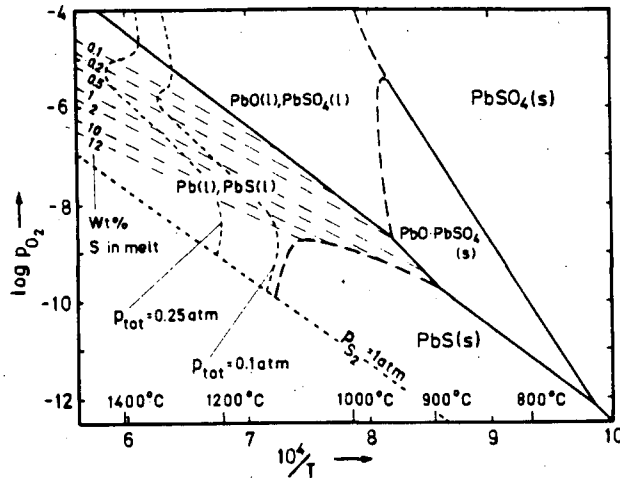


Figure 2.4 The effect of P_{O_2} and temperature on the $Pb-S-O$ system at $1 \text{ atm } SO_2$. (from Rosenqvist [46])

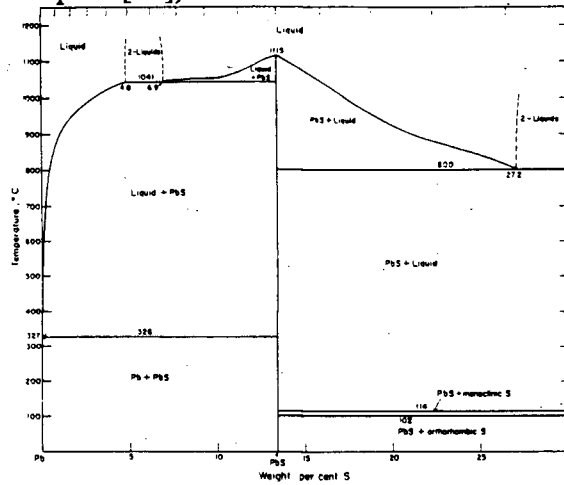


Figure 2.5 The $Pb-S$ binary phase diagram (from Kullerud [35]).

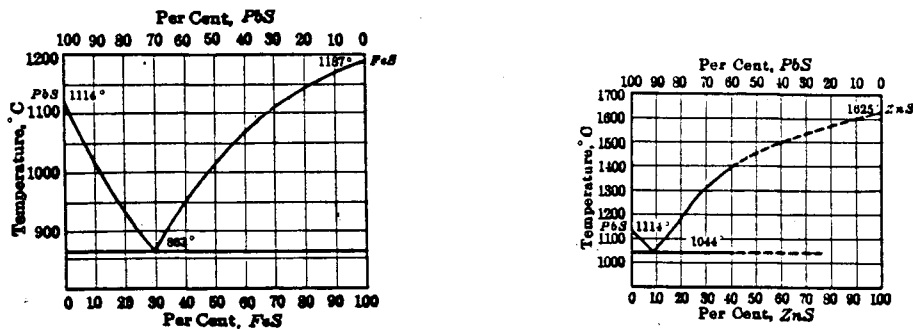
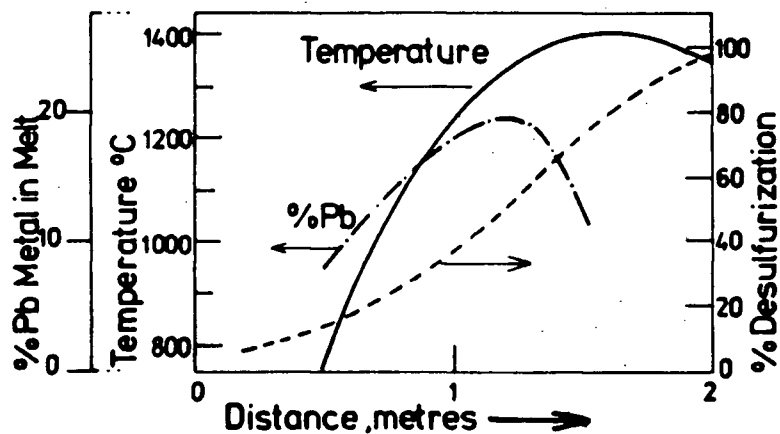
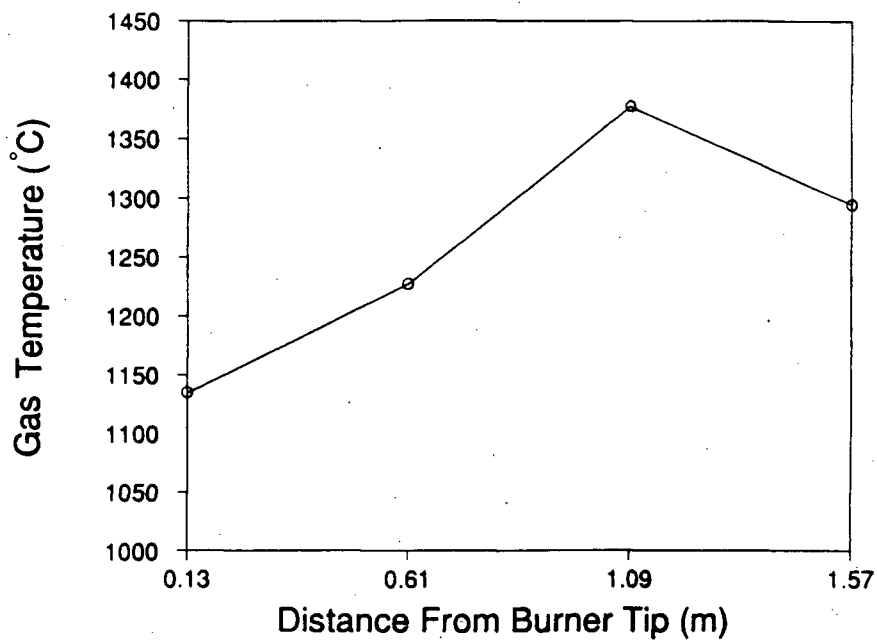


Figure 2.6 The $PbS-FeS$ and $PbS-ZnS$ binary phase diagrams (from Hofman [2]).



(a)



(b)

Figure 2.7 Typical flash-smelting results.
 a) a plot of temperature, desulphurisation and metallic lead formation down a Kivcet flash-smelting shaft (from Willis [49])
 b) temperature profile along the U.B.C. pilot plant shaft (2kg/min Sullivan concentrate, 40% excess oxygen, from Shook et al.[27]).

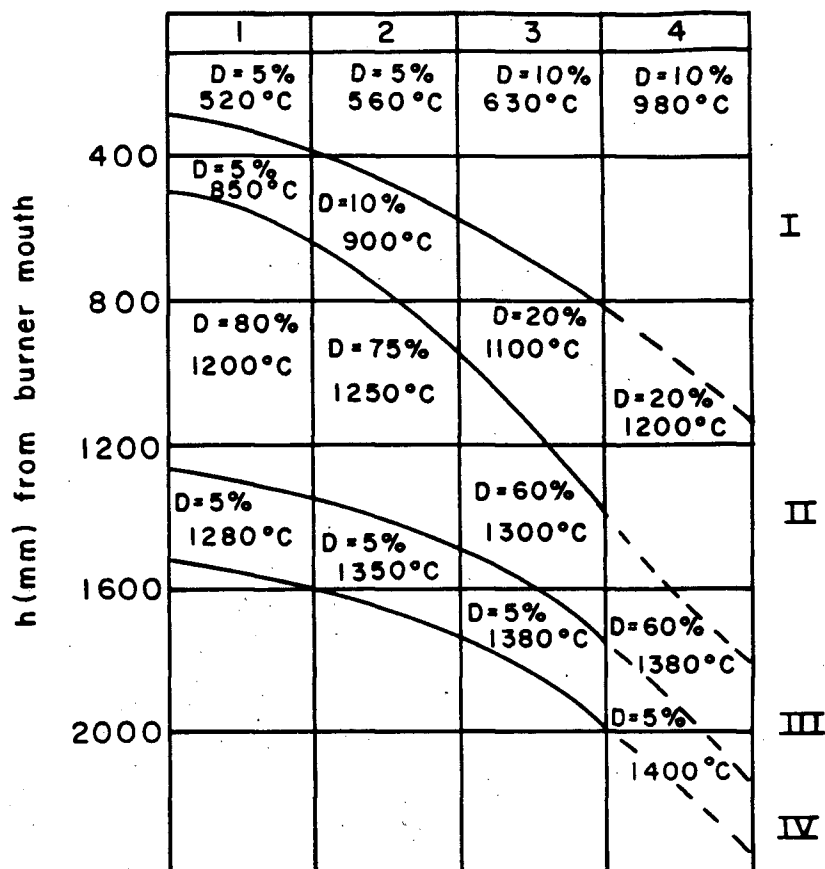


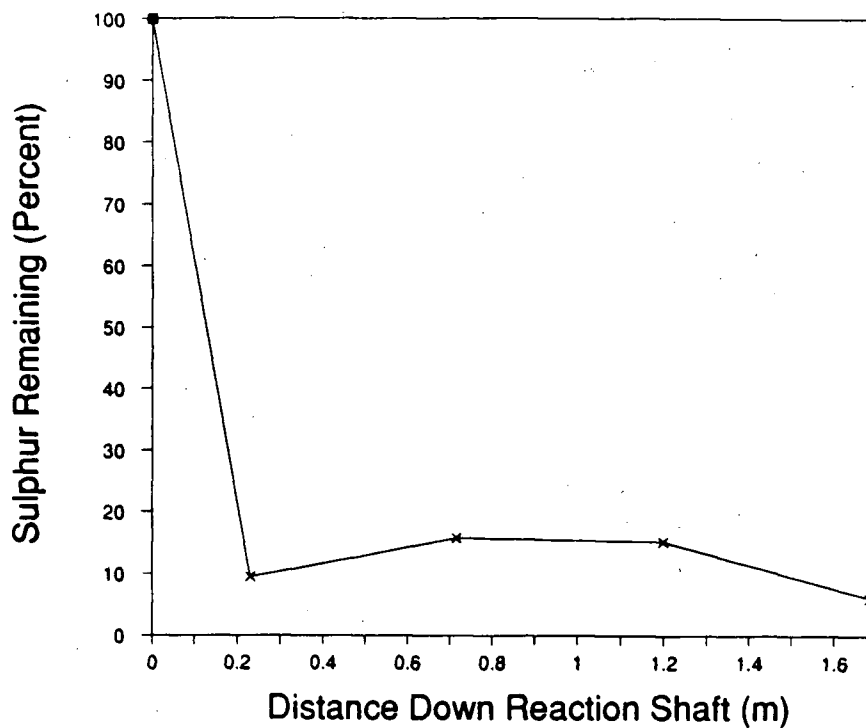
Figure 2.8 Nomograph of the effects of feed concentration of lead flash-smelting. I- solid-phase oxidation, II- melting and oxidation, III- gas-liquid reactions and IV- silicate formation. D- desulphurisation.

1 - 61%Pb, 4.4%Zn and 6.6%Fe.

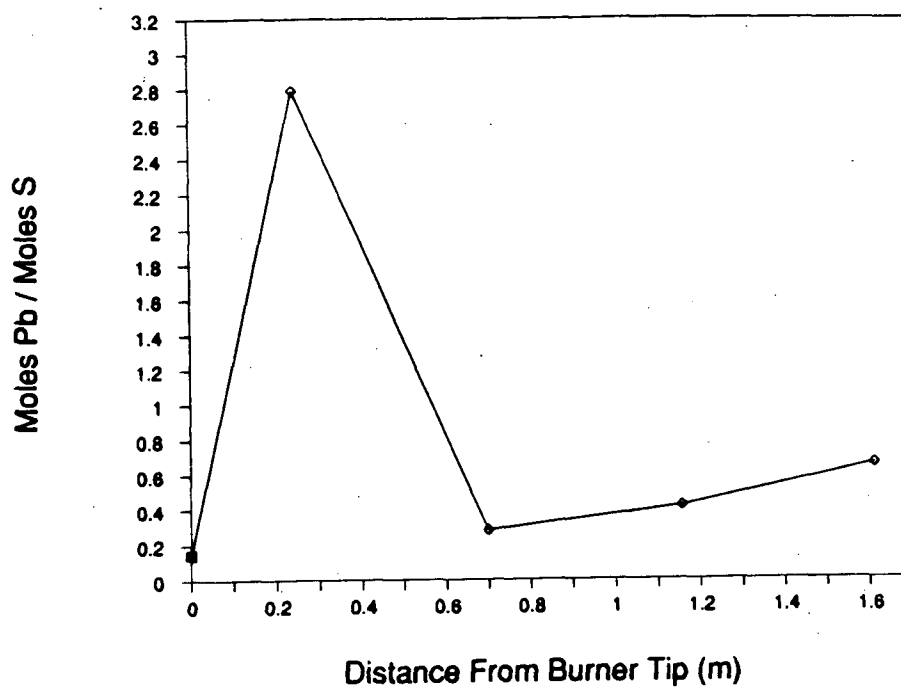
2 - 54%Pb, 10%Zn and 8.1%Fe.

3 - 26%Pb, 38%Zn and 4.7%Fe.

4 - 15%Pb, 38%Zn and 8.3%Fe. (from Sychev [27])



(a)



(b)

Figure 2.9 Typical U.B.C. pilot plant flash-smelting results.
 a) desulphurisation and b) ratio of mols *Pb* to mols *S* (2kg/min Brunswick concentrate stoichiometric oxygen).
 (from Shook et al.[27]).

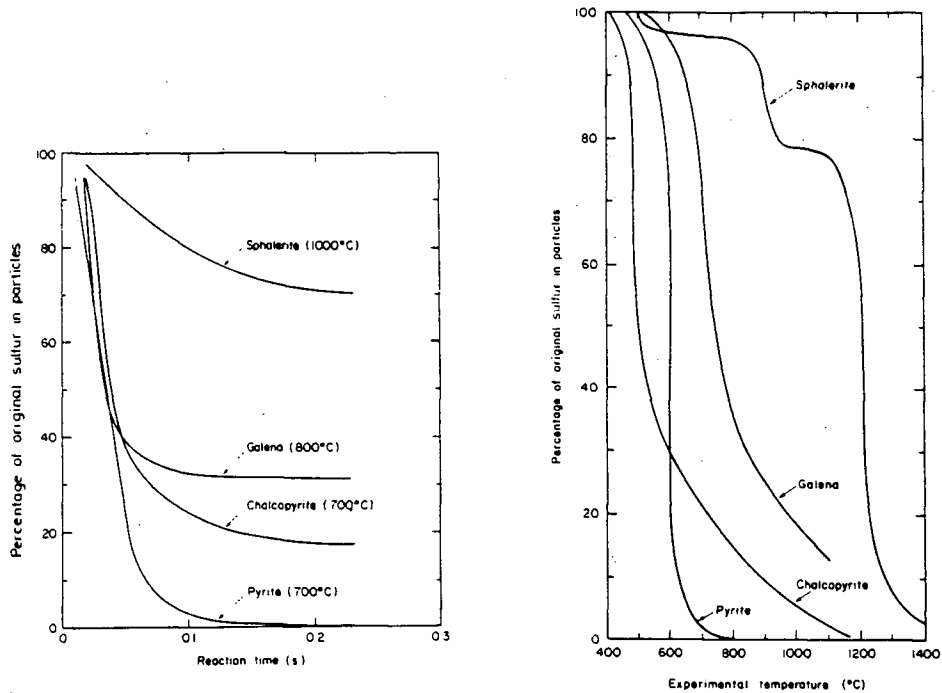


Figure 2.10 Sulphur elimination from various sulphide minerals (37-53 μ m screen fraction air) a) as function of time, and b) as a function of temperature $\tau_{res}=0.1s$. (from Jorgensen [69])

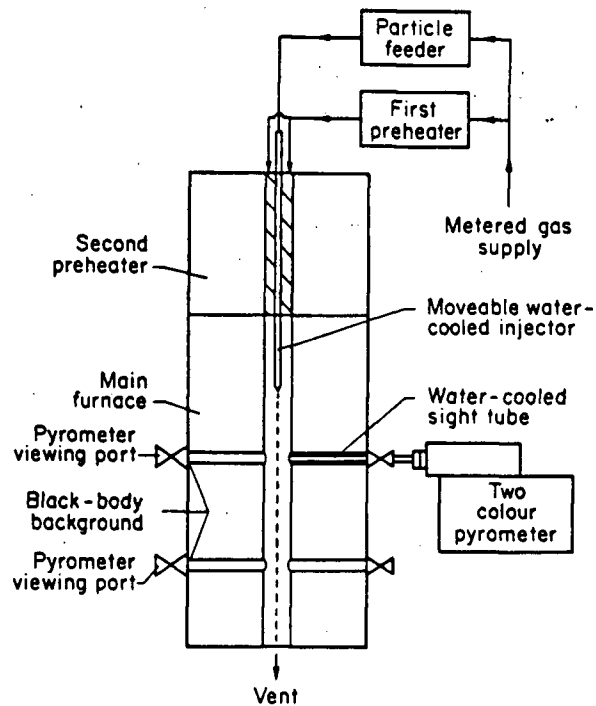
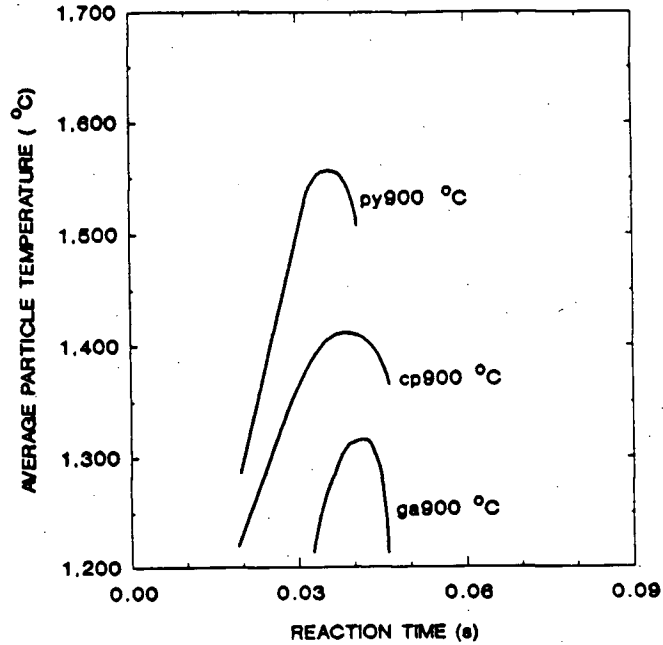
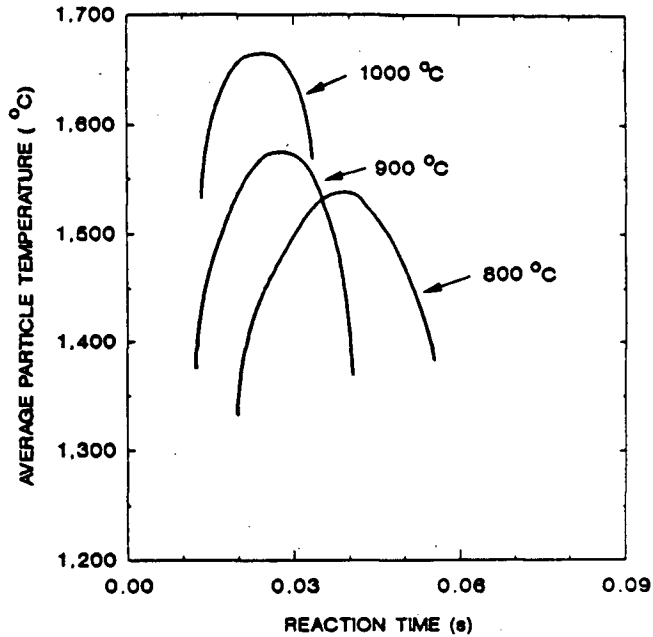


Figure 2.11 Laminar flow furnace and two-wavelength pyrometer of Jorgensen et al. (from Jorgensen et al. [82]).



(a)



(b)

Figure 2.12 Average temperature measurements of a) galena, chalcopyrite and pyrite combustion in 900°C air, and b) lead concentrate in oxygen. (from Happ et al. [43]).

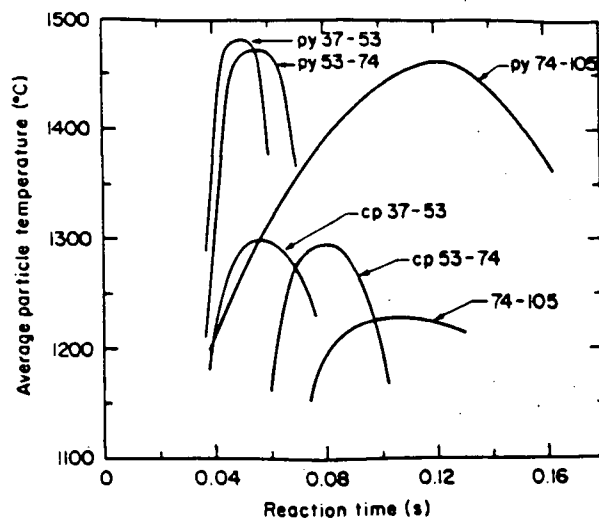


Figure 2.13 Effect of screen fraction on the average combustion temperature of pyrite and chalcopyrite combustion in air at 700°C (from Jorgensen [80]).

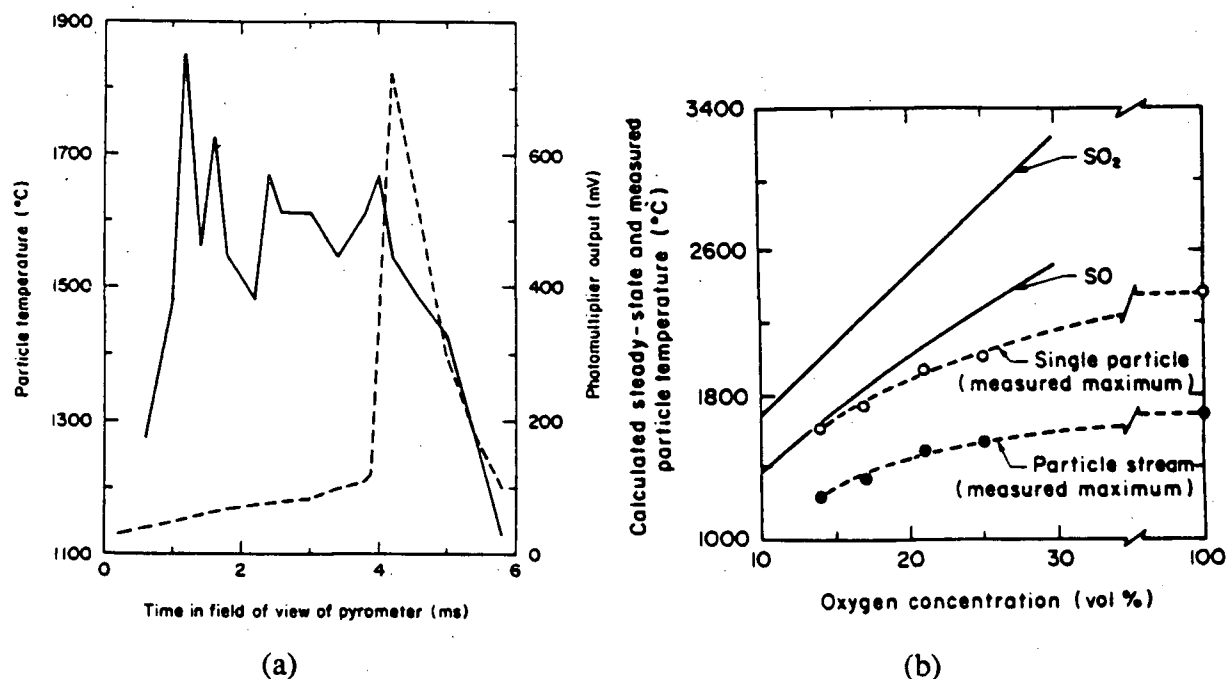


Figure 2.14 Pyrometer output signal and measured temperature for a single combusting pyrite particle (37-53 μ m screen fraction in air at 700°C) and b) maximum individual and average particle temperatures as a function of oxygen concentration. (from Jorgensen [79,81]).

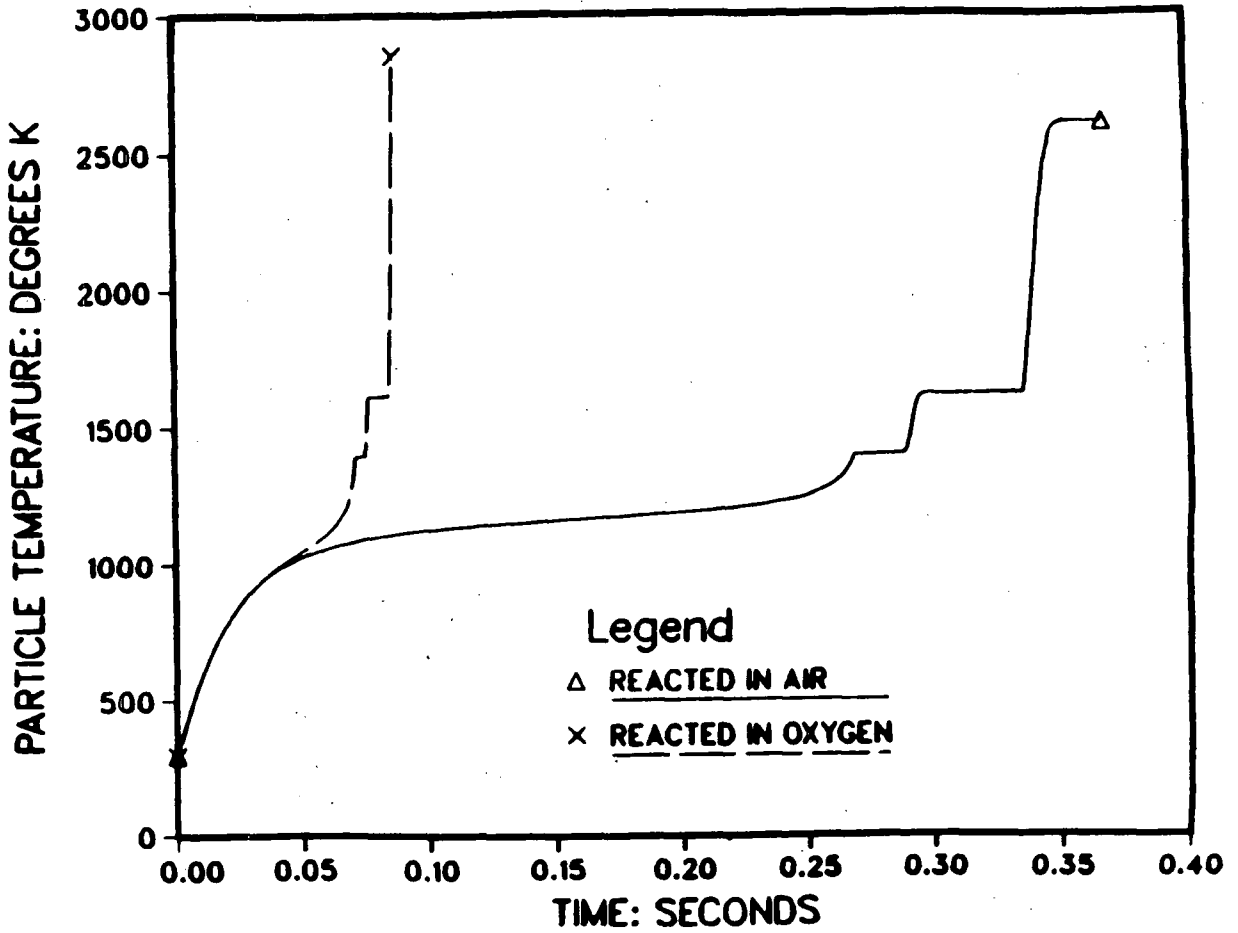


Figure 2.15 Calculated reaction times and temperatures for the combustion of a $100\mu\text{m}$ galena particles in air and oxygen at 978K (from Salomon de Friedberg [44]).

CHAPTER 3

Objectives and Scope of the Experimental Series

This research was undertaken as a first step to increasing our understanding of the mechanism and the kinetics of lead concentrate combustion. The areas where our knowledge of lead concentrate combustion and lead flash smelting is incomplete are many, and far beyond the scope of a single research project. An experimental series has, therefore, been conducted to identify the important physical characteristics of combustion and to obtain some preliminary quantitative data on temperatures, heating rates etc. The effects of reaction variables such as mineral species, particle diameter and oxygen concentration have also been investigated. To deduce information about the reaction kinetics it is necessary to know the local conditions of temperature, fluid dynamics and species concentration within, and surrounding, each of the individual combusting particles. In an attempt to satisfy these requirements the combustion of very dilute suspensions of particles in a "Laminar Flow" furnace has been examined; and similar to the work of Jorgensen et al. [82,83], temperature measurements of the individual particles during combustion have been made.

Particle temperature measurements were undertaken with a fast response, two-wavelength radiation pyrometer. The combustion of several pure minerals and lead concentrates of different chemical composition was investigated. The effects of particle size, partial pressure of oxygen and reaction time on the measured particle temperature and the observed combustion pulses were examined. The chemical, mineralogical and morphological nature of the feed materials and reaction products also was investigated.

The research has been aimed at identifying and classifying the physical manifestations of lead concentrate combustion, as observed by the experimental techniques applied and attempting to link these to the process variables investigated. In this way the research provides information which is both new and fundamental to the

understanding of the kinetics of single particle combustion of lead concentrates. The information obtained also should prove useful in formulating the reaction kinetics for a mathematical model of the lead flash smelting process.

CHAPTER 4

Experimental

4.1 Experimental Apparatus

A schematic diagram of the experimental apparatus employed in this study is given in Figure 4.1 and an overall view of the equipment is shown in Figure 4.2a. The equipment can be considered to consist of four different components: i) the laminar flow furnace, ii) the particle feeder and feed delivery tube, iii) the two-wavelength radiation pyrometer and blackbody cavity, and iv) data collection, storage and analysis equipment.

Particles are introduced into a preheated, downward flowing stream of reaction gas and are carried axially through the furnace past the pyrometer viewing port. Radiation from the combusting particles passing the pyrometer lens is measured and the output signals from the pyrometer detectors are recorded by the data acquisition system for subsequent particle temperature calculations.

The particles are introduced into the furnace, via the feed delivery tube, at a very low mass rate by the vibratory feeder. The particles fall under gravity through the stagnant gas in the water cooled feed delivery tube before entering the hot gas stream in the reactor. The residence time of the particles in the furnace is varied by raising and lowering the feed delivery tube within the laminar flow reactor tube. In this way, residence times of typically between 50 and 400 milliseconds were obtained. Owing to the relatively short length of the reactor tube, the gas flow is changing from laminar annular flow to laminar pipe flow throughout the reactor tube. In this case therefore, the term "Developing Laminar Pipe Flow Furnace" would probably be a more apt description of the laboratory reactor.

Samples of the reaction products were taken with two different solid sampling devices (see Section 4.1.5), which were introduced into the reactor tube from the bottom.

4.1.1 Laminar Flow Furnace

A schematic diagram of the laminar flow furnace showing the materials of construction is given in Figures 4.2b. The furnace consisted of a 813mm x 600mm OD mild steel vessel lined with 150mm of insulating refractory. Low thermal conductivity, yet impermeability to gas, was obtained by casting 50mm of refractory (Thermolite 26, Clayburn Refractories Ltd.) onto a backing of 100mm of insulating blanket (Fibrefrac blanket, Carborundum Ltd.). The castable liner was supported by mild steel "V" anchors. This insulated chamber formed the gas preheating annulus within which was located an outer 102mm OD mullite tube and the inner 50.8mm ID reactor tube. The furnace power was supplied by three silicon carbide heating elements located in the gas preheating annulus. Preheated gas from this annulus then passed down the annulus between the reactor tube and the 34mm OD insulated Feed Delivery Tube before entering the open reactor tube beyond the tip of the feed delivery tube.

The 438mm x 50mm ID axial reactor tube was located above the 38.1mm ID side port for the watercooled pyrometer lens. Below the pyrometer port was located a 50mm ID Chromel wound resistance furnace. This lower heating source was found to be necessary to offset the heat losses and temperature gradients, which would otherwise occur in this region.

4.1.1.1 Electrical Power Supply

The main heat supply to the furnace was from the three silicon carbide "globar" heating elements (Carborundum Ltd.) located in the gas preheating annulus. SGR bayonet type heating elements with dimensions of 762mm x 38.1mm diameter (457mm heating length) were used. The individual heating elements were mounted in flanged, closed one end, 711 x 70mm OD alumina tubes.

A variable tap three-phase AC transformer (#12948Y Hammond Manufacturing Co. Canada) was used to supply power to the three globars wired in a "Closed Delta" load configuration. The power to the transformer was controlled by a SCR power controller

(Research Inc. Control Systems Minneapolis) which was in turn operated by a 4-20mA control signal. Up to 12 kW of power can be supplied by the three heating elements. The furnace power (and temperature) was manually controlled.

The 180mm x 50.8mm ID lower chromel wound resistance furnace positioned below the pyrometer viewing port was controlled manually by a 0-120V variac transformer and could supply up to 1 kW of power.

4.1.1.2 Ancillary Equipment

Gas and water trains were constructed to supply gas and cooling water to the various components in the experimental system. A proportionating flow train, using calibrated flow meters, was constructed for mixing air, oxygen and nitrogen to supply carrier gas of the required oxygen potential. Argon was used to purge the outer pyrometer lens and also as a quenching gas in the solid sampling probe. Air was used to cool the electrical connections in the globar head caps. Cooling water was required for the feed delivery tube, the pyrometer lens tube, the blackbody cavity and the solid sampling probe.

4.1.2 Particle Feeder

In order to observe the combustion of individual particles, it was necessary to construct a feeder capable of introducing concentrates into the furnace at very low flow rates such that the interaction between individual particles and also with reaction products was minimised. After several attempts, a design based on a vibrating trough was found most suitable for the purpose. A schematic diagram of the feeder is given in Figure 4.3. An electromagnet controlled by a Variac transformer was utilised to vibrate a pivoted steel spatula. The flow of particles was restricted by a series of constrictions in the spatula in an attempt to obtain a relatively even feed rate. Flow rates of less than 0.05 g/min. were obtainable; however, under these conditions, considerable fluctuation in the feed rate was found. The feed rate fluctuations were not a serious problem, since particle dispersal rather than absolute feed rate was most important. Lower feed rates were

obtained by momentarily exciting the vibrator. The particle feeder was raised and lowered on a laboratory jack to accommodate the changes in the position of the feed delivery tube required to vary the residence time of the particles in the furnace. The particle feeder is connected to the feed delivery tube by a flexible rubber hose. The feed delivery tube consists of a 1000mm long, 4.5mm ID, feed tube surrounded by a 12.5mm OD cooling water annulus. The cooling water annulus is thermally insulated from the hot furnace gas by a 3mm thick, 34mm OD outer mullite tube with an inner 7.6mm thick layer of Fiberfrax between the two. A smooth alumina tip with a cone angle of 65° was cemented to the end of the tube in an attempt to minimise the turbulence generated during the gas transition from the annular flow to flow in an unrestricted pipe in this region of the reactor tube.

With this specific feeder design it was not possible to introduce particles smaller than approximately $50\mu\text{m}$, into the furnace as individual particles. Smaller particles tended to enter the furnace as loosely associated clumps. In consequence only screen fractions in excess of $63\mu\text{m}$ (+230 mesh) were used for the experiments. For galena, a feed rate of 0.05g/min. would represent ~ 850 particles of $63\mu\text{m}$ diameter per second and ~ 100 particles of $125\mu\text{m}$ diameter per second. If these particles were evenly dispersed, one would pass the pyrometer every ~ 1 and 10ms respectively for 63 and $125\mu\text{m}$ diameter particles. It is, therefore, quite common to observe only a single particle for the whole time it is in front of the pyrometer lens (typically 10 to 20ms).

4.1.3 Two Wavelength Radiation Pyrometer

Optical radiation pyrometry is one of the few techniques suitable for measuring the temperature of individual combusting particles. To measure the temperature directly by this technique, it is necessary to know both the particle area and emissivity. Particle emissivity is generally unknown, and for this type of study, the precise particle area is also unknown and small in comparison with the area viewed. In an attempt to overcome these problems, two-wavelength radiation pyrometry, which compares the ratio of energy

radiated at two closely spaced wavelengths, is used. Provided the emissivity of the object at the two different wavelengths is the same, the temperature of the particle can be determined without knowing either the object emissivity or area. The theory and limitations of use of two-wavelength pyrometers are given in Appendix 1.

Examination of the commercially available two-wavelength radiation pyrometers revealed that they had neither the sensitivity, nor the speed of response, required to determine the temperature of particles from the small transient energy pulses produced during combustion. It was therefore necessary to design and construct a suitable instrument. The details of the pyrometer design, construction and calibration are given in Chapter 5.

A schematic diagram of the pyrometer design is given in Figure 4.4. The 300mm long watercooled section of the lens tube was inserted into the pyrometer port in the laminar flow furnace (see Figure 4.1). The temperature measured by a two-wavelength radiation pyrometer is a function of the temperature, and area, of all the objects viewed by the pyrometer. The pyrometer was therefore sighted into a watercooled blackbody cavity to give a stable low intensity background, against which the combusting particles could be resolved. The blackbody cavity consisted of a 25.4mm OD cone tapering to a 10mm ID, 150mm long cavity coated with ultra flat black paint.

4.1.4 Data Acquisition and Analysis

The schematics of the data acquisition system is shown in Figure 4.1. The output signals (0 to +10V and common ground), from the pyrometer's two photomultiplier detectors were connected to the terminals of the DT2828 DMA Data Acquisition Board (Data Translation Inc. Marlborough, MA). The data acquisition board itself, was mounted in an IBM AT personal computer and controlled using ASYST software (Macmillan Software Co. Inc.). The pyrometer output signal was also displayed on an oscilloscope connected in parallel with the data acquisition board.

The DT2828 DMA board is capable of simultaneously sampling and storing the two output signals from the pyrometer at a rate of up to 50kHz per channel. The high sampling rate is necessary to measure the rapidly changing signal intensities observed during combustion, and the simultaneous sampling is necessary to accurately determine the particle temperature from the ratio of the two detector output signals. The 0 to +10V common ground inputs are converted to 12 bit resolution digital signals and, using Direct Memory Access (DMA) mode, transferred directly to the computer memory. Owing to software limitations, the data collection was limited to 16K samples per channel which at the fastest sampling rate corresponded to 0.32 seconds of continuous data collection.

A control and analysis programme written in ASYST (a variant of FORTH) was used to collect the data, locate any combusting particle peaks, and then calculate and display, the detector output voltages and apparent particle temperature versus time. If suitable, the data for the combustion peak was stored and the energy and temperature traces printed.

4.1.5 Solid Sampling Devices

Two different solid sample devices were constructed to collect quenched samples from the reactor. Both devices consisted of 25.4mm OD stainless steel probes which were inserted from the bottom of the furnace to the level of the pyrometer viewing port. The initial probe consisted of a simple 20mm deep thimble attached to the top of the water cooled probe. The larger particles tend to collect in the thimble, with those that were molten impacting and freezing onto those below. With this probe the small particles, especially lead sulphate reaction fume, were deflected with the gas and tended to deposit on the water cooled sides of the sampler. In an attempt to collect this fume and also to freeze the particles in their molten shape a second probe based on the principle of isokinetic gas sampling was constructed.

A schematic diagram of the isokinetic sampling probes and associated particle collection apparatus is shown in Figure 4.5. Quenching gas is introduced at the tip of the collector and the probe suction was adjusted such that the particle-gas mixture from the furnace and the quenchant are sucked down the 10.9mm ID water-cooled central tube. Very careful adjustment was required to achieve isokinetic gas-solid sampling. Typically a flow rate of argon four times that of the gas removed from the furnace was used. As well as quenching the particles, this curtain of argon helps, together with an electro-mechanical vibrator, to prevent the particles from sticking to the collection cone. The larger reaction product particles collect in the first sample trap below the probe. Smaller particles were collected in a 25.4mm diameter cyclone and the very fine fume was collected in a 100mm diameter 1 μ m Nomex filter.

4.2 Laminar Flow Furnace Characteristics

4.2.1 Gas Flow Characteristics

Initial experiments examining the combustion of lead sulphide indicated the presence of turbulence in the gas flowing down the reactor tube at Reynolds numbers well below 2000. The movement of the fine fume produced by the reaction gave a good indication of the flow in the laminar flow furnace tube. Without bulk gas flow, recirculation patterns between the hot reactor tube and cooler feed delivery tube were observed. With the introduction of increasing amounts of gas, the flow appeared to be laminar up to tube Reynolds numbers of about 200, above which eddy separation from the feed delivery tube tip was observed. This restriction limited gas flow rates of the experiments to less than about $\sim 2.6 \times 10^{-4} m^3 s^{-1}$ (NTP) which typically corresponds to superficial gas velocities of less than $0.5 ms^{-1}$.

4.2.2 Laminar Flow Furnace Temperature Profile

To determine the temperature profile along the length of the reactor tube three thermocouples were attached to both the main reactor tube and the feed delivery tube. The position of these thermocouple (relative to the centre line of the pyrometer port are

indicated in Figure 4.6. Three Type-S (Pt-Pt/10%Rh) thermocouples were mounted on the reactor tube at the positions indicated ($T_{f1} - T_{f3}$). Holes were drilled through the outer insulation and mullite annulus to allow the thermocouple to be cemented directly to the back of the 3.2mm thick mullite reactor tube. Three 0.13mm diameter Type-K (chromel-alumel) thermocouples ($T_{fd1} - T_{fd3}$) were cemented to the surface of the feed delivery tube at the positions indicated in Figure 4.6. A Type-S thermocouple enclosed in a narrow bore alumina sheath was mounted in the head space above the reactor tube to facilitate suction thermocouple measurements of the gas temperature (T_{gas}) entering the reactor tube. Another Type-S thermocouple was cemented to the outside of the alumina sheath, surrounding the heating element.

The temperature of the laminar flow furnace was controlled manually from the reactor tube thermocouples. Due to the large thermal mass of the furnace it was relatively easy to control the furnace temperature; however, temperature gradients were observed along the reactor tube. Typical differences between the temperature measured at the various locations and power setting are shown in Figure 4.7. In order to minimise temperature gradients within the laminar flow furnace:

- i) a portion of the carrier gas was introduced into both the top and the bottom of the gas preheating annulus, and:
- ii) the power supply to the lower resistance heated furnace was varied.

Temperature gradients of <30K were obtainable in the reactor tube below the level of the feed delivery tube, with the centre of the reactor tube (T_{f2}) usually being the hottest. The surface of the feed delivery tube was typically 100K lower than the outside wall of the reactor tube and it is possible this results in slight cooling of the gas adjacent to it.

Suction thermocouple measurements of the gas temperature within the reactor tube, taken below the level of the feed delivery tube, however, revealed little change in bulk gas temperature from that at the inlet.

The effect of varying the length of the feed delivery tube within the reactor, on the furnace temperature, is given in Figure 4.7b. As would be expected, overall furnace temperature declines as the length of the feed delivery tube in the furnace is increased. The temperature of the upper most feed delivery tube thermocouple (T_{fd1}) decreases as the feed delivery tube is withdrawn, because the thermocouple is withdrawn into the roof insulation.

The maximum furnace operating temperature is limited to about 1700K by the upper service limit of the insulating castable refractory.

4.3 Experimental Measurements

4.3.1 Pyrometer Output Signals

The output signals obtained from the two detectors of the pyrometer were used to calculate the apparent particle temperature and its variation with time. The combustion pulse data was stored and later analysed for relative changes in area, apparent particle area, peak shape, heating and cooling rates etc. using a series of ASYST and LOTUS 1-2-3 programmes.

4.3.2 Solid Samples

The solid samples collected were analysed by several techniques. The specimens were first analysed by x-ray diffraction to determine the crystallographic phases present. Samples of the specimens then were examined by scanning electron microscopy (SEM, Hitachi S-570) using the secondary electron and backscattered electron analysis facilities attached to the SEM. Semi-quantitative and quantitative analyses of the elements present were made using Energy and wavelength Dispersive x-ray spectroscopy (EDX -Kevex 8000 and Microspec WDX). Chemical analyses of the samples for total/metallic lead, total/Fe(II), zinc, and total/sulphate sulphur were carried out by Cominco.

4.4 Feed Materials -Chemical, Mineralogical and Physical Properties

The combustion of Sullivan concentrate (supplied by Cominco) and Brunswick concentrate (supplied by Brunswick Mining and Smelting Co.) was examined. The chemical compositions of different size fractions of these two concentrates are given in Table 4.1. For both, the concentration of iron, zinc and sulphur decreases, and that of the galena increases with increasing feed size [102-104]. Brunswick concentrate has a significantly higher iron (and sulphur) content which is present predominantly as pyrite [102,103]. Pyrrhotite, on the other hand, is the main iron mineral present in the Sullivan concentrate [26,104]. From x-ray analysis the main mineral species present for the two concentrates were found to be:

Sullivan concentrate - galena (PbS), pyrrhotite ($Fe_{1-x}S$) and marmatite ($Zn_xFe_{1-x}S$);

Brunswick concentrate - pyrite (FeS_2), galena and marmatite (~6% Fe).

Sphalerite, chalcopyrite, quartz and, also, pyrite and pyrrhotite (where it is not a major form) are reported to be present in minor amounts.

Sullivan concentrate is reported to be finely divided with 95% -325 mesh (~<44 μ m) [26,104], and counter to the chemical analyses results stated above, Surges [102] and Bazin [103] report the following for the Brunswick concentrate:

1. The lead concentrate is substantially finer than 63 μ m with up to 97% reported to be -270 mesh (~<53 μ m).
2. Approximately 50% of the galena in the concentrate is present as free grains while 43% of the galena is associated with pyrite. Only 7% is associated with sphalerite and a very small percentage as ternary galena-pyrite-sphalerite grains. More specifically it was observed that 58% of the marmatite and 65% of the pyrite in the +74 μ m fraction are present as free grains. The rest is present mainly as binary particles of pyrite, galena and marmatite.

Table 4.1 Chemical Composition of the Different Mineral Species and Size Fractions Tested.

Material	Size Fraction	%Pb	%S	%Fe	%Zn	%S as Sulphate
Galena	63-74	84.8	13.4	0.6	0.7	<0.1
	74-88	84.8	13.9	0.8	0.8	<0.1
	88-105	84.1	14.2	0.8	0.6	<0.1
	105-125	84.1	14.0	1.0	1.1	<0.1
Pyrite	74-88	0.31	49.5	43.2	1.0	1.6
Pyrrhotite	74-88	2.9	38.6	53.7	4.0	0.1
Sullivan	63-74	59.9	18.7	10.0	6.2	0.6
	74-88	61.3	18.2	9.5	5.4	0.7
	88-105	62.3	18.0	9.0	4.9	0.6
	105-125	62.4	18.0	8.9	4.5	0.8
Brunswick	63-74	29.1	31.4	19.0	12.1	2.0
	74-88	30.0	31.1	18.4	11.7	1.9
	88-105	32.9	29.1	17.7	9.1	2.3
	105-125	34.4	28.8	17.8	7.2	2.4

3. The proportion of free galena increases significantly with decreasing particle size.

The marmatite content in the lead concentrate is greater in the coarser size fractions.

The pyrite content in the concentrate is similar in all size fractions.

4. The dominant mineral in all size fractions is pyrite, although in the $-37\mu\text{m}$ size

fraction the galena content may approach or exceed the pyrite content depending on the lead concentrate grade.

The dry screen analyses and Coulter-counter results for the different size fractions of the commercial concentrates are given in Tables 4.2 and 4.3 respectively.

The results indicate that a much larger proportion of the concentrate is associated with size fractions of greater than $63\mu\text{m}$ than reported by Surges [102] and Bazin [103]. Microscopic analysis of the particles (see Figure 4.8) indicated that, at these larger size fractions, most of the grains were made up of agglomerates of many smaller particles.

Table 4.2 Screen Analysis of the Brunswick and Sullivan Concentrate

Screen Fraction	Size ($\mu\text{m.}$)	Sullivan %Retained	Brunswick %Retained
+100	>150	9.4	27.0
+120-100	125-150	1.7	2.9
+140-120	105-125	3.0	2.8
+170-140	88-105	4.7	13
+200-170	74-88	1.2	0.1
+230-200	63-74	7.6	4.0
-230	<63	72.9	49.5

TABLE 4.3 Size Analyses of Feed Materials

Feed Material	Size Fraction (μm)	Coulter Counter Results (volume average)				SEM Results	
		10th Percentile (μm)	25th Percentile (μm)	Mean Particle Size (μm)	75th Percentile (μm)	Mean Particle Size (μm)	L/D Ratio
Galena	63-74	-	-	-	-	80	1.4
	74-88	44	57	65	82	96	1.3
	88-105	58	65	75	95	101	1.6
	105-125	57	82	92	115	109	1.5
Pyrite Pyrrhotite	74-88	-	-	-	-	85	1.3
	74-88	-	-	-	-	80	1.5
Sullivan	63-74	29	40	43	52	-	-
	74-88	52	70	78	100	-	-
	88-105	82	103	114	141	-	-
	105-125	84	112	120	150	-	-
Brunswick	63-74	51	55	59	67	-	-
	74-88	54	59	66	73	-	-
	88-105	57	75	78	100	-	-
	105-125	55	86	92	117	-	-

Generally, random clumping of the different mineral species found in the concentrates was observed. Agglomeration probably accounts for the increase in the lead concentration with increasing size fraction. Individual grains of zinc and iron sulphide (as reported by Surges[102] and Bazin[103]) are probably more prevalent in the 63-74 μm screen fraction; but with increasing size fraction the proportion of agglomerate particles (with higher lead content) increases. For the Brunswick concentrate, agglomeration

around a larger grain of pyrite or marmatite, as shown in Figure 4.8c and d, was also occasionally observed. The bonding between the individual particles in the agglomerates appears quite strong; from the coulter-counter results small particles (see Table 4.3) typically accounted for less than 10% (by volume) of the total recorded. Similarly a large amount of particle disintegration did not appear to occur during wet screening. This type of agglomerate has been observed by others [56] and is thought, possibly, to be the result of surface sulphation during the rotary drying of the concentrates (typically from 10 wt% moisture to <1 wt%). The amount of sulphate present (see Table 4.1) was typically ~0.6-0.8% for the Sullivan concentrate and ~1.9-2.4% in the Brunswick concentrate. It is also possible that some flocculation of the concentrate could occur in the bulk (lead-dezincing) and zinc flotation circuits where high lime additions are made [102]. Agglomerates would presumably be present in smelter feeds in proportions similar to those determined in Table 4.2, and therefore, dry screened fractions of these larger fractions of the commercial concentrates were used.

To identify the behaviour of the different mineral constituents of the commercial concentrates, the combustion of several of the pure minerals present was examined. Relatively pure galena, pyrite, pyrrhotite and sphalerite feed materials (supplied by Cominco) were tested. The chemical and size analyses of the different species are given in Tables 4.1 and 4.3. The chemical analyses indicate that the minerals were relatively pure forms and from x-ray diffraction analysis the only significant impurity present in the pyrite, pyrrhotite and galena feed materials was small quantities of sphalerite. From electron microscopy, the particles in the 74-88 μm screen fraction of both pyrite and pyrrhotite, tended to be lozenge shape (see Figure 4.9) with two similar dimensions and an average length to width ratio of ~1.3 and ~1.5 respectively. It was calculated that the average equivalent spherical diameter of the two materials is ~85 and ~80 μm respectively. The chemical composition of the Pine Point galena varied relatively little with increasing size fraction between 63-74 and 105-125 μm . Some sphalerite was

observed in the feed either intimately associated with galena or as discrete grains and a few particles of iron sulphides were also found. From Figure 4.9c the cubic cleavage of the galena particle can be seen; two of the particle dimensions are typically similar, and the average lengths to width ratios of the different size fraction particles, given in Table 4.2, were 1.3 to 1.6. The particle sizes in the different screen fractions were determined both with a Coulter-counter and manually from SEM micrographs of the particles. The agreement between the two methods was poor. The manually determined results suffer from the relatively small sample size examined (<100) and error could also be introduced by assuming, in the calculations, that the particles are cuboids, with the two smaller dimensions being equal. Inaccuracies, however, also exist in the Coulter Counter results due to the particles being near the upper limit of the measurement range. Marmatite samples, also supplied by Cominco, were found to have a variable chemical composition at the larger size fractions and, therefore, their combustion was not examined. The combustion of sphalerite was examined instead. In all cases the relatively pure mineral species were ground to liberate new surface and then wet screened before use.

4.5 Experimental Series Conducted

A series of experiments was conducted to examine the effect of feed composition, particle size and partial pressure of oxygen on the combustion of lead concentrate particles.

All the experiments were conducted at a furnace and gas temperature of 1130K. This temperature is much lower than the typical flash smelting temperatures of 1500 to 1700K, and was chosen primarily because the amount of background thermal radiation from the walls and fume reaction products (in the gas stream) entering the pyrometer became excessive at higher temperatures. The gas flow rate was maintained at $2 \times 10^{-4} m^3 s^{-1}$ (NTP), which corresponds to a superficial gas velocity of $\sim 0.37 ms^{-1}$ at furnace temperature. The position of the feed delivery tube within the reactor tube was

varied such that the distance between the feed delivery tube tip and the pyrometer port (combustion distance) varied between 50 and 350mm. This nominally corresponded to calculated particle residence times of between 50 and 400 ms.

The conditions used for the experimental series conducted are given in Table 4.4. For the commercial concentrates and galena air screened size fractions of +230-200, +200-170, +170-140 and +140-120 mesh were examined. For pyrite, pyrrhotite and sphalerite, combustion of the +200-170 mesh (74-88 μ m) size fraction was examined. All the experiments were conducted at 1 atmosphere pressure with a mole fraction of oxygen between 0.1 and 1.

Table 4.4 Experimental Series Conducted.
 $T_f = 1130\text{K}$, Gas Flow rate = $0.2 \times 10^{-3} \text{ms}^{-1}$ (NTP)

T = Temperature Measurements Made

S = Solid Samples Taken

Feed Material	Oxygen Concentration (%)	Nominal	Screen	Size	Fraction
		63-74 μm	74-88 μm	88-105 μm	105-125 μm
Brunswick	21	T	T,S	T	T,S
Sullivan	21	T	T,S	T	T,S
Galena	21	T	T,S	T	T,S
Pyrite	21	-	T,S	-	-
Pyrrhotite	21	T	T,S	-	-
Sphalerite	21	-	No Reaction	-	-
Brunswick	100	T	T,S	-	T
Sullivan	100	T	T,S	-	T
Galena	100	T,S	T	-	T
Pyrite	100	-	T,S	-	-
Pyrrhotite	100	-	T,S	-	-
Sphalerite	100	-	No Reaction	-	-
Galena	10	-	T	-	-
	21	-	T	-	-
	30	-	T	-	-
	40	-	T	-	-
	50	-	T	-	-
	65	-	T	-	-
	80	-	T	-	-
Pyrite	10	-	T	-	-
	15	-	T	-	-
	21	-	T	-	-
	25	-	T	-	-
	30	-	T	-	-
	40	-	T	-	-
	50	-	T	-	-
	65	-	T	-	-
	80	-	T	-	-
100	-	T	-	-	

4.6 Particle Residence Times Calculations

The experimental conditions used in the laminar flow furnace are such that both the gas velocity and particle terminal velocity are significant to the particles residence time in the furnace. For the mean bulk gas velocity of 0.37ms^{-1} maintained throughout the experimental series, and for the range of particle sizes ($63\text{-}125\mu\text{m}$) used, the theoretical terminal falling velocities of the particles are in the order of $0.3\text{-}2.0\text{ms}^{-1}$ [105]. As well as the particle size, the particle density, the gas composition and gas temperature influence the particle terminal velocity. The range of mineral species within the industrial concentrates, with their different densities and shapes, would be expected to result in a range of particle terminal velocities. Chemical reaction and particle disintegration may also result in changes in particle density or size (and consequently particle velocity during flight). These variations indicate the necessity for calculation of the particle terminal velocity, and also indicate the limitations of applying calculated particle terminal velocities to bulk materials.

The particles, on introduction into the furnace, are considered to enter gas flowing at mean bulk velocity (0.37ms^{-1}), whereas in reality the gas velocity will vary due to the transition from annular flow to pipe flow followed by the development of a parabolic flow profile ($u_{\text{max}} = 2\bar{u}$). The relatively short length of the reaction tube as compared to the entrance length effect (est $\sim 0.6\text{m}$ [106]) and the relatively flat initial profile [107] resulting from the transition suggest, however, that this is a reasonable first approximation.

The residence times of particles in the furnace were calculated based on the method outlined in Appendix 3, and using the conditions specific to these experiments. Examples of the calculated variation in particle velocity with size, density and gas composition are given in Figure 4.10 and Table 4.5. For the initial 0.8m the particle is assumed to be travelling through a stagnant gas in the feed delivery tube, after which the particle enters the flowing gas in the reactor tube. Due to the decrease in the calculated particle terminal

Table 4.5 Calculated Residence Time as a Function of Furnace Position for Different Mineral Species in Air and Oxygen @1130K.

i) Air

$$\bar{u}_{gas} = 0.37ms^{-1}$$

* particle terminal velocity in static gas

Mineral Species	Density (kg/m^3)	Particle Diameter (μm)	Terminal Velocity* (m/s)	Furnace Residence Time (ms)			
				$L_F=50mm$	$L_F=100mm$	$L_F=200mm$	$L_F=300mm$
Galena	7500	69	0.43	61	122	246	370
		82	0.61	50	101	202	304
		97	0.86	41	82	163	244
		116	1.23	34	67	132	195
Pyrite	5000	82	0.41	66	131	259	387
Pyrrhotite	4740	69	0.29	80	157	311	480
		82	0.38	67	134	266	397

ii) Oxygen

Mineral Species	Density (kg/m^3)	Size Fraction (μm)	Terminal Velocity* (m/s)	Furnace Residence Time (ms)			
				$L_F=50mm$	$L_F=100mm$	$L_F=200mm$	$L_F=300mm$
Galena	7500	69	0.38	65	131	264	396
		82	0.54	54	109	219	329
		116	1.08	36	72	142	212
Pyrite	5000	82	0.36	71	140	277	413
Pyrrhotite	4740	82	0.34	72	141	283	437

velocity with increasing gas temperature, relatively small increases (or even decreases) in particle velocities may be predicted to occur on entering the flowing gas in the furnace.

The differences in velocity predicted for particles of different diameters and densities, therefore result in different particle residence times (see Figures 4.11a and 4.11b).

Considerable variation in the particle velocity is predicted both, between particles in the different size fractions, and for the extremes of particle size within each size fraction (see Figure 4.11a). The ideal variation in particle velocity predicted within the individual size fractions is calculated to be about 15-20%, and increases with increasing feed size.

The effect of different mineral compositions, due to density differences, is also shown. For the conditions shown the magnitude of the effect is similar to that due to size variations in the size fractions. The effect of differences in furnace gas composition on the predicted particle residence times (see Figures 4.10 to 4.11) is relatively small. For the commercial concentrates especially, the mixture of minerals would tend to give a large range of observed particle residence times at any furnace position

After reaction the variation in particle residence times would be further increased due both to the effect of reaction on particle properties (size, density, velocity etc.) and its effect on the fluid dynamics [108].

Due to the general uncertainties in the accuracy of the calculated residence times, and the large range of particle sizes and physical properties present in the feed materials, the experimental results have been plotted against distance travelled in the furnace (combustion distance), but reference has also been made to the calculated particle residence times given in Table 4.5.

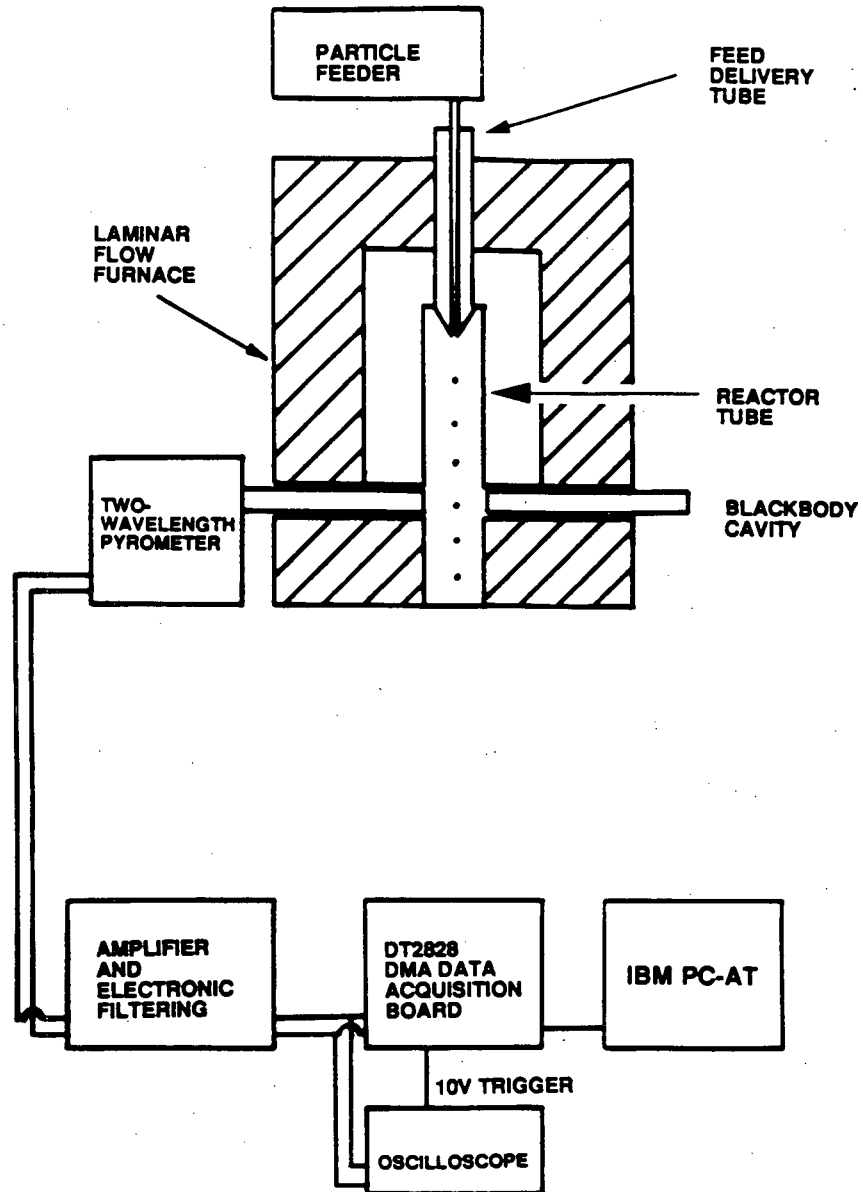


Figure 4.1 Schematic diagram of the experimental furnace, temperature measurement and data acquisition equipment.

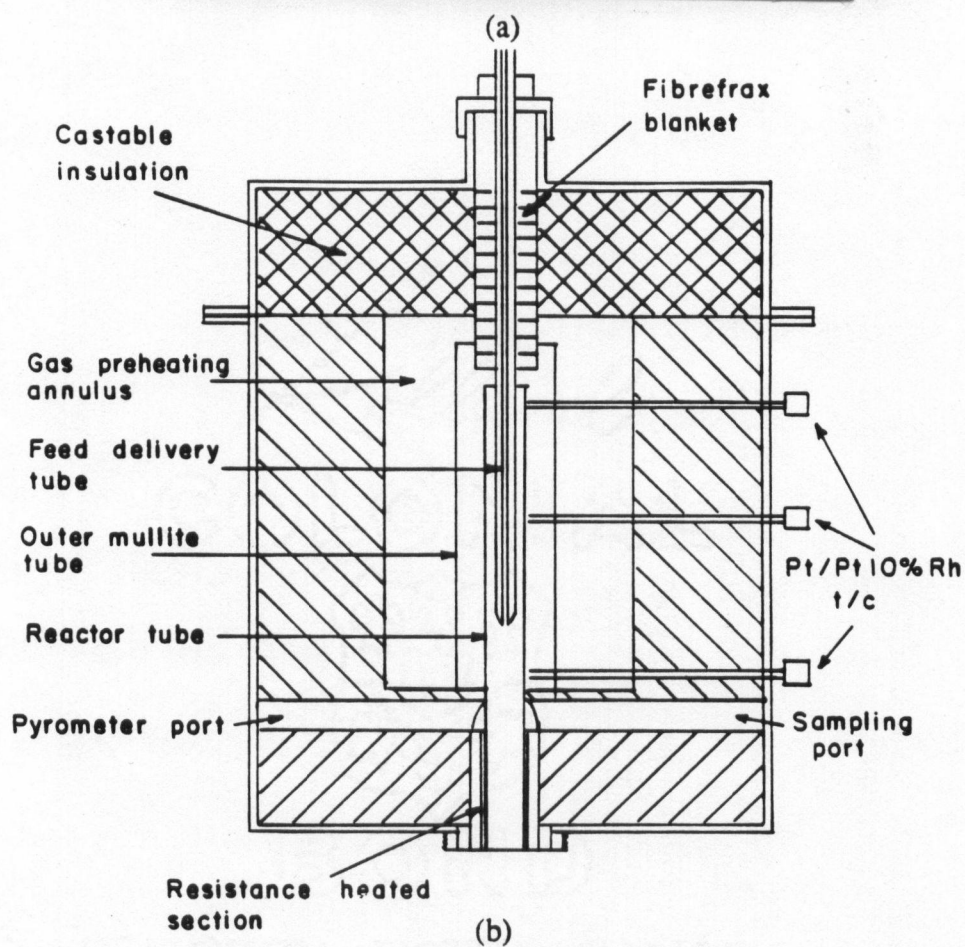
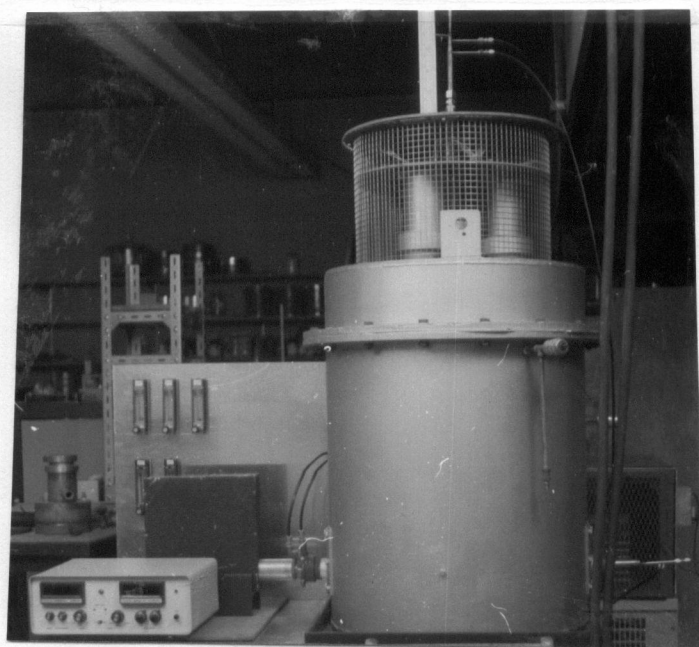


Figure 4.2 The laminar flow furnace a) photograph and b) cross-section.

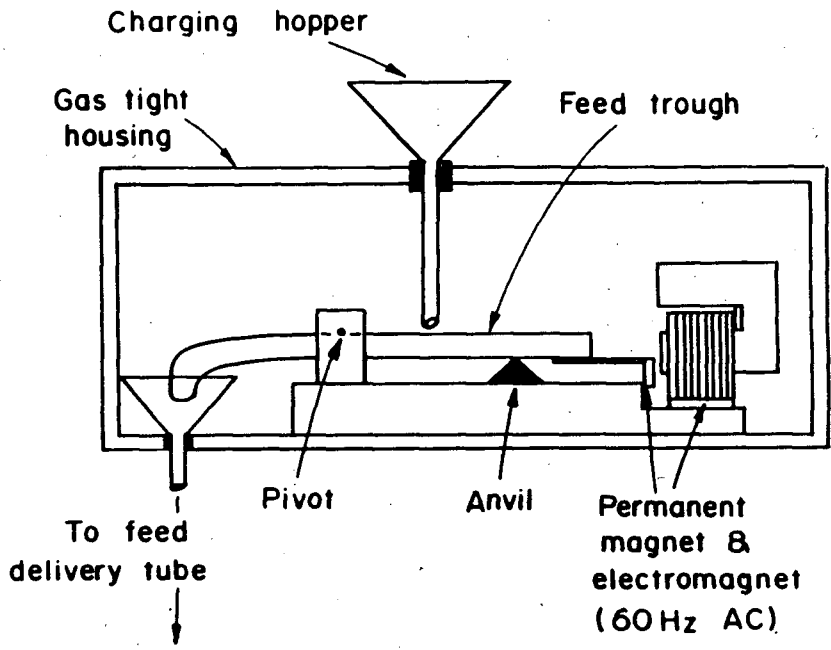
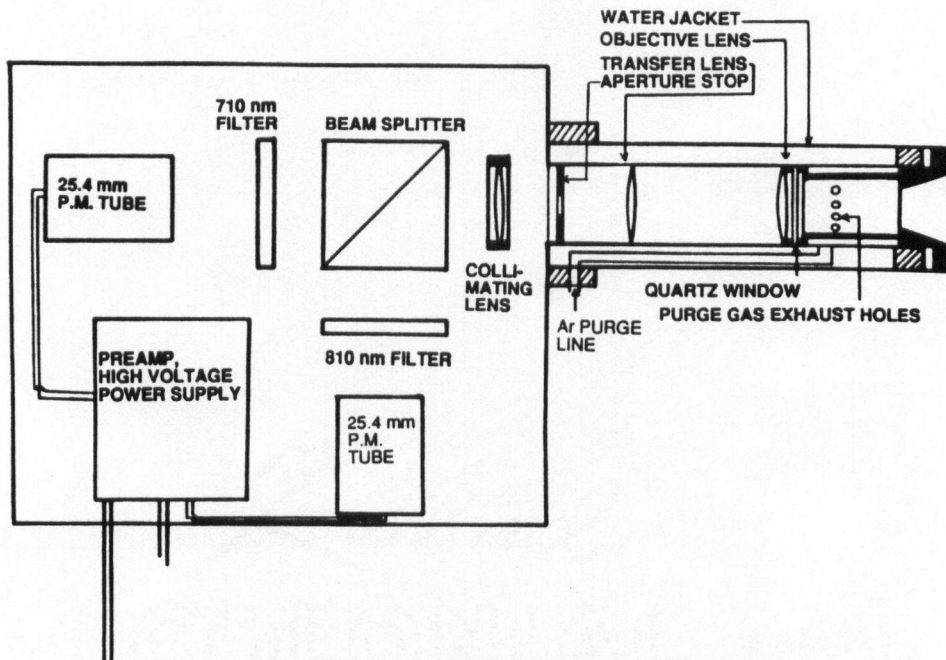
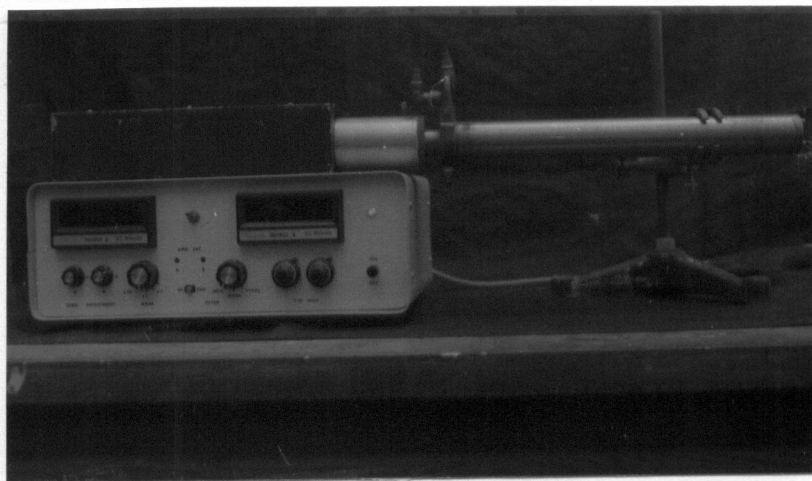


Figure 4.3 Schematic diagram of the particle feeder.



(a)



(b)

Figure 4.4 The two-wavelength radiation pyrometer, a) schematic diagram and b) pyrometer and associated electronics.

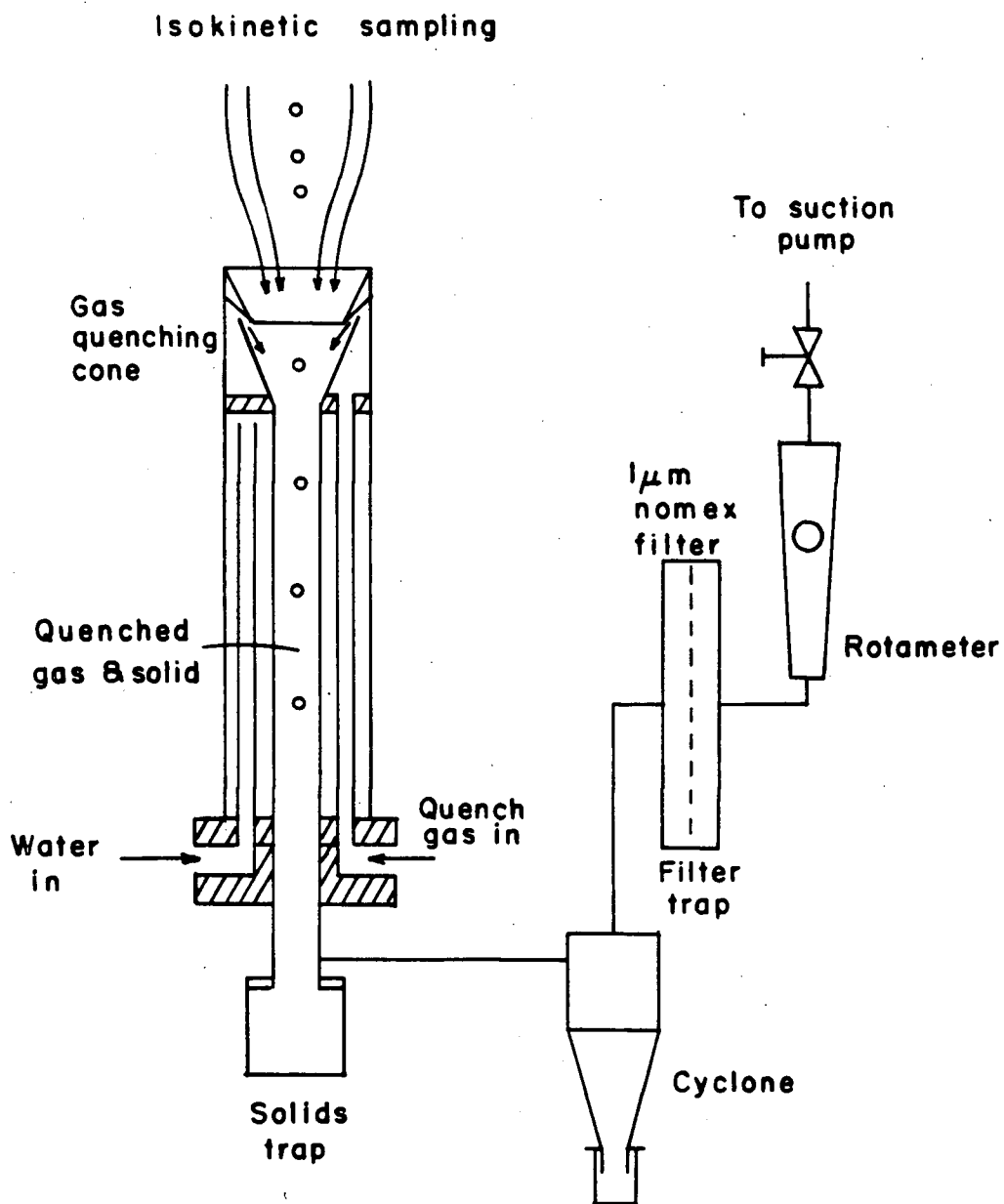
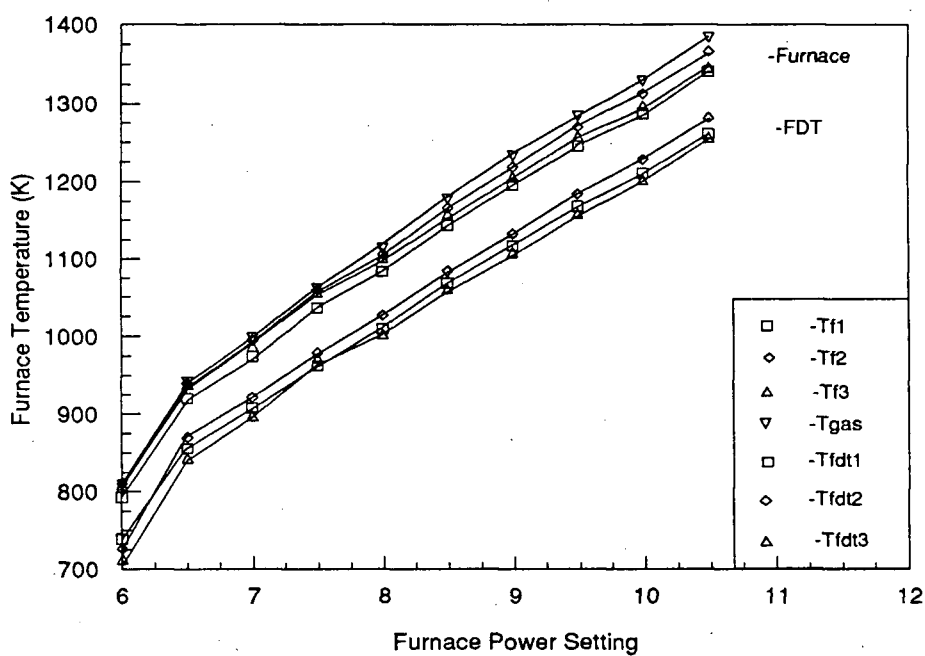
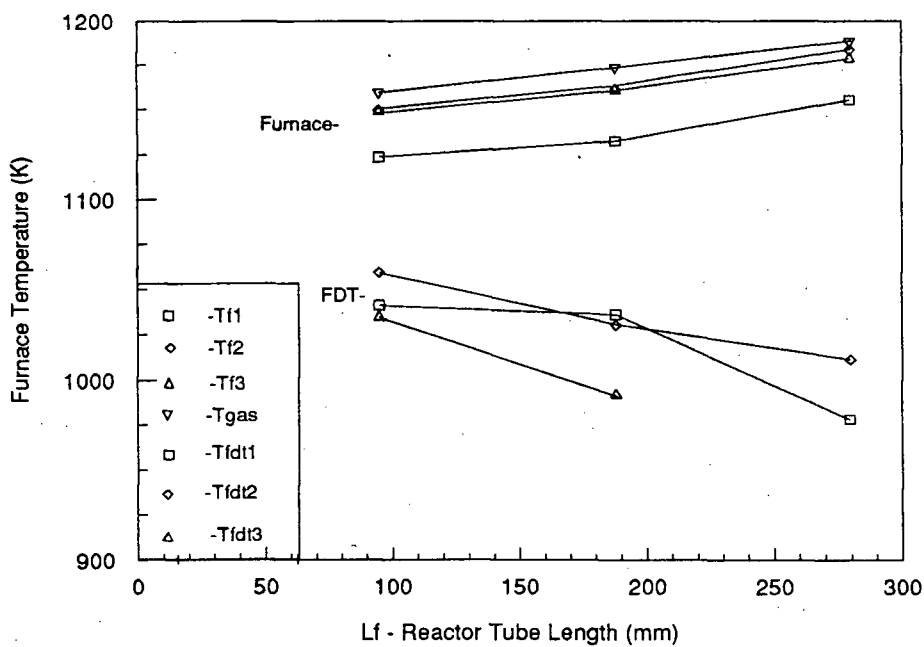


Figure 4.5 Solid sampler

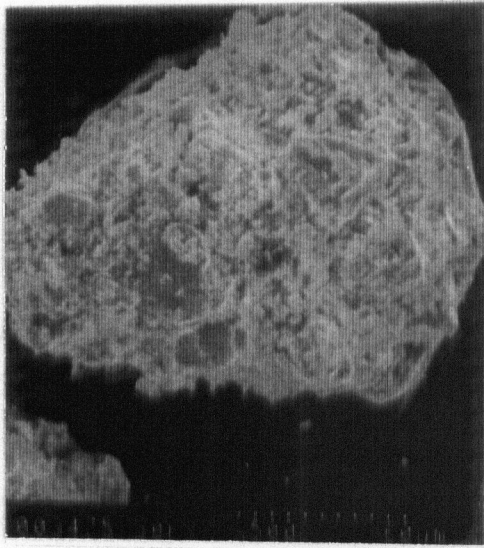


(a)

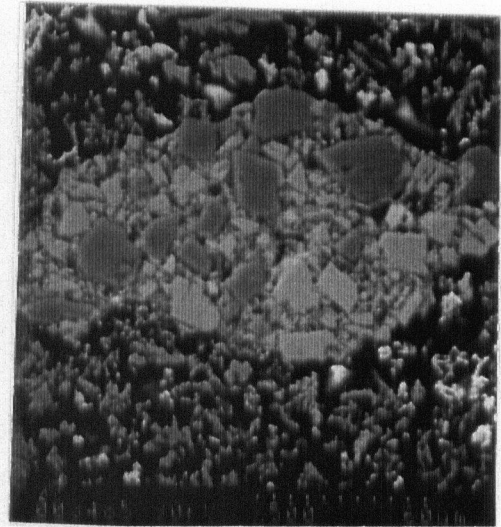


(b)

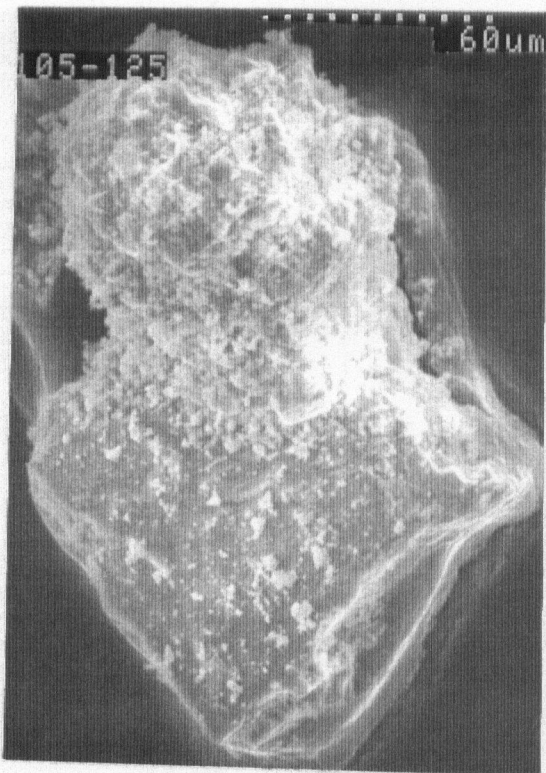
Figure 4.7 Measured furnace tube and feed delivery tube surface temperatures a) versus furnace power setting ($L_f=95\text{mm}$) and b) as a function of feed delivery tube position (power setting=8). (gas flow rate= $0.2 \times 10^{-3} \text{ms}^{-1}$, water flow rate= $0.01 \times 10^{-3} \text{ms}^{-1}$)



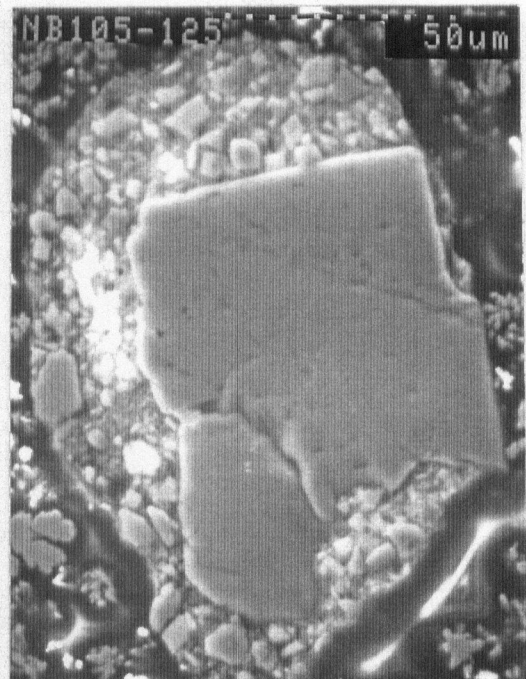
(a)



(b)



(c)

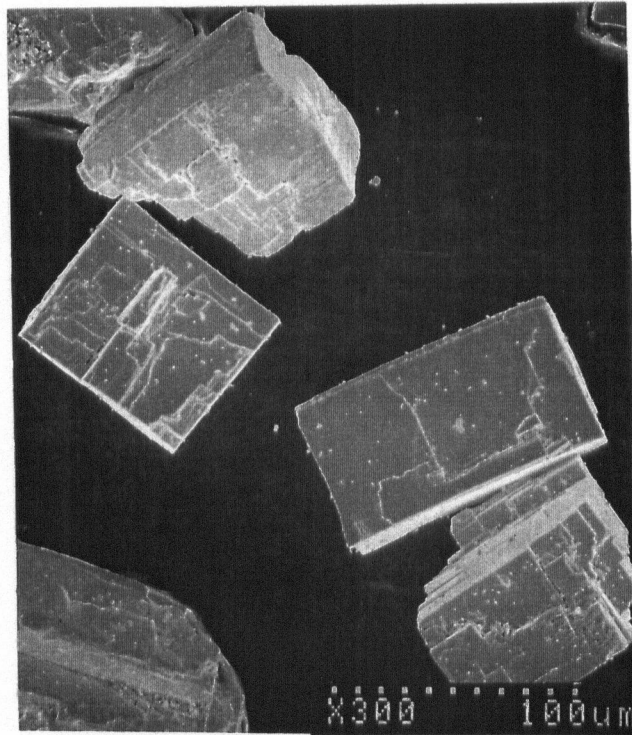
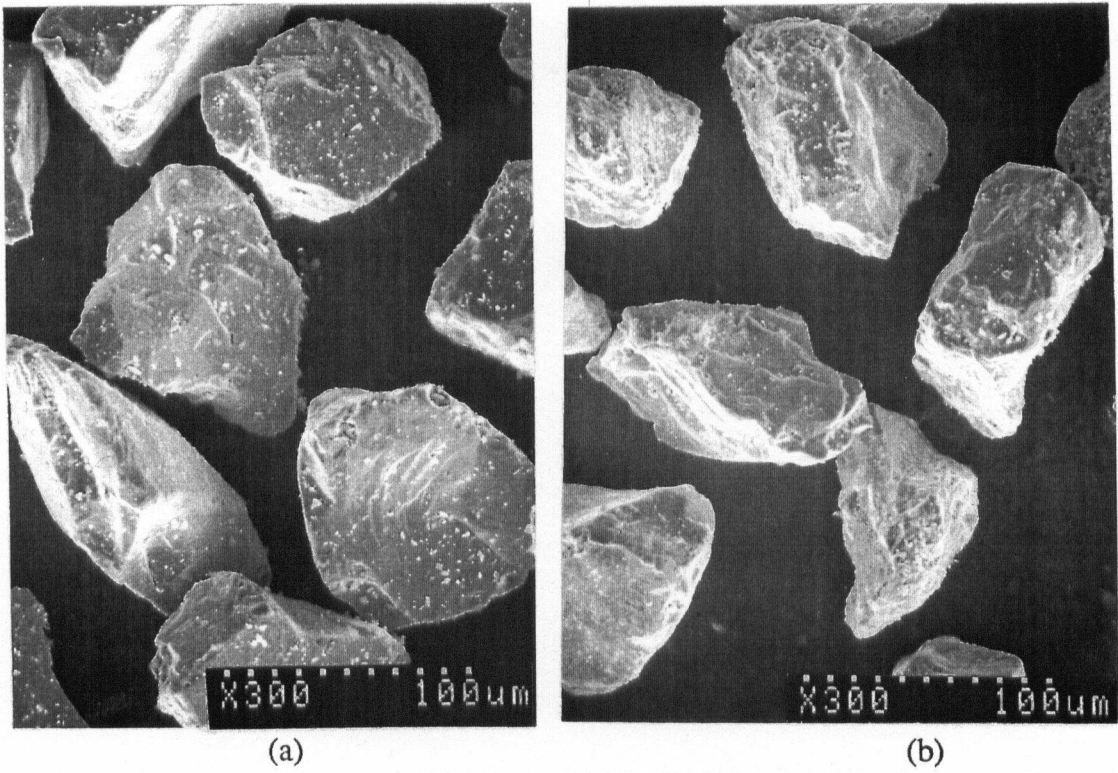


(d)

Figure 4.8

105-125 μ m screen fraction Brunswick concentrate feed material.

a) unsectioned agglomerate, b) sectioned agglomerate, c) agglomeration around a large pyrite grain and d) sectioned agglomerate containing a large pyrite grain.



(c)
Figure 4.9 Pure mineral feed materials: a) pyrite, b) pyrrhotite and c) galena. (74-88 μm screen fraction).

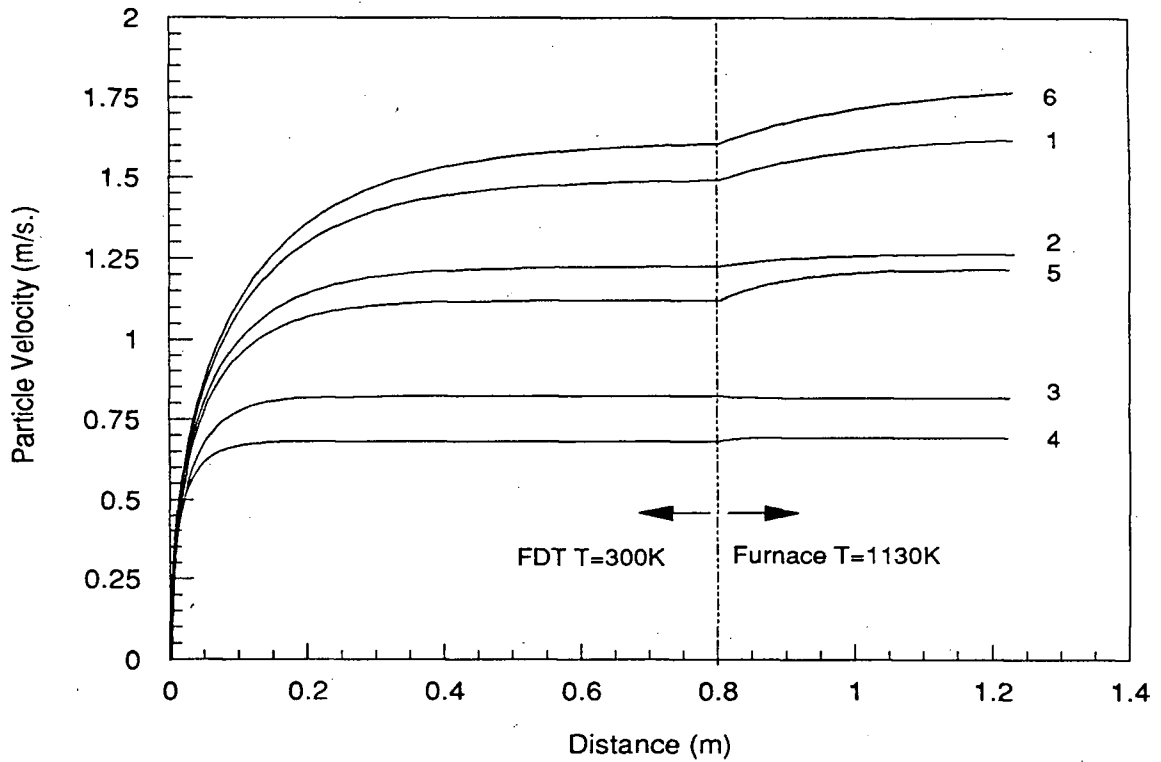


Figure 4.10 Calculated velocity profiles in the feed delivery tube and furnace tube indicating the calculated effect of particle sizes, gas composition and material density.

1 $dp=125\mu\text{m}$, $\rho=7500\text{kgm}^{-3}$, oxygen;

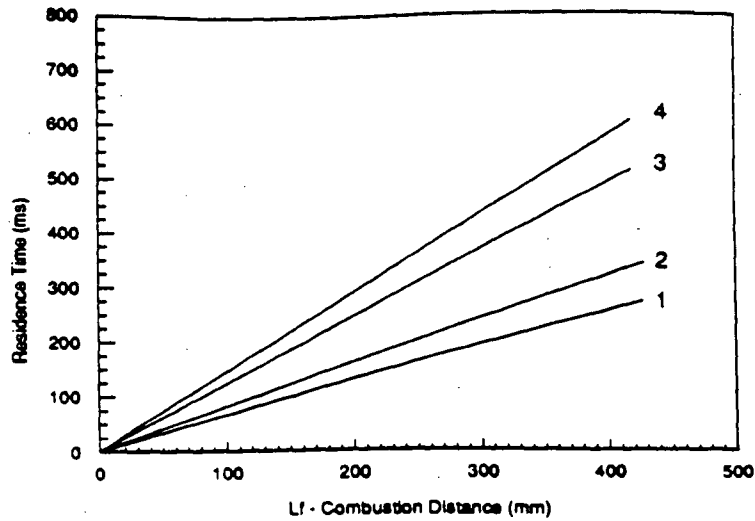
2 $dp=105\mu\text{m}$, $\rho=7500\text{kgm}^{-3}$, oxygen;

3 $dp=74\mu\text{m}$, $\rho=7500\text{kgm}^{-3}$, oxygen;

4 $dp=63\mu\text{m}$, $\rho=7500\text{kgm}^{-3}$, oxygen;

5 $dp=125\mu\text{m}$, $\rho=5000\text{kgm}^{-3}$, oxygen;

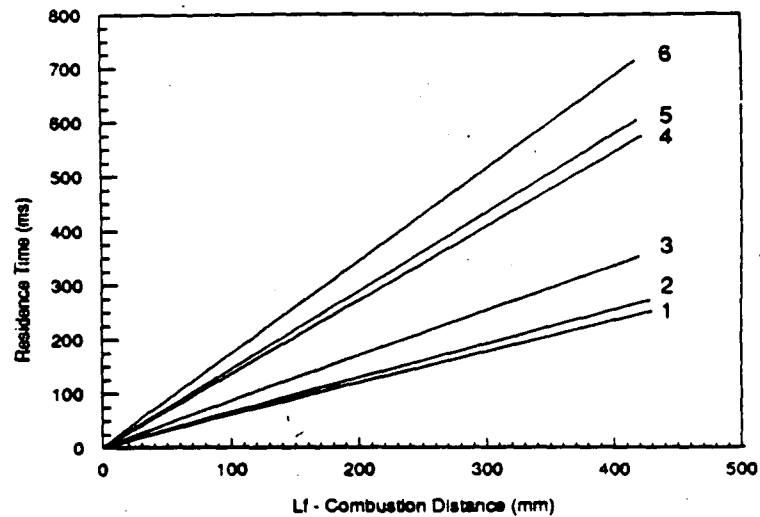
6 $dp=125\mu\text{m}$, $\rho=7500\text{kgm}^{-3}$, air;



(a)

1 $dp=125\mu\text{m}$, $\rho=7500\text{kgm}^{-3}$, oxygen;
 3 $dp=74\mu\text{m}$, $\rho=7500\text{kgm}^{-3}$, oxygen;

2 $dp=105\mu\text{m}$, $\rho=7500\text{kgm}^{-3}$, oxygen;
 4 $dp=63\mu\text{m}$, $\rho=7500\text{kgm}^{-3}$, oxygen;



(b)

1 $dp=125\mu\text{m}$, $\rho=7500\text{kgm}^{-3}$, air;
 3 $dp=125\mu\text{m}$, $\rho=5000\text{kgm}^{-3}$, oxygen;
 5 $dp=63\mu\text{m}$, $\rho=7500\text{kgm}^{-3}$, oxygen;

2 $dp=125\mu\text{m}$, $\rho=7500\text{kgm}^{-3}$, oxygen;
 4 $dp=63\mu\text{m}$, $\rho=7500\text{kgm}^{-3}$, air;
 6 $dp=63\mu\text{m}$, $\rho=5000\text{kgm}^{-3}$, oxygen;

Figure 4.11 Calculated particle residence times in the furnace tube, a) calculated variation within a screen fraction and b) calculated effect of gas composition, particle size and density.

CHAPTER 5

Pyrometer Design and Calibration

5.1 Pyrometer Calibration

5.1.1 Previous Designs

A considerable number of researchers have designed and constructed two (or more) wavelength radiation pyrometers [43,69,89-95,87,89-95,109-115] for measuring rapid temperature changes. The requirements for such pyrometers are that they have a rapid response and high sensitivity such that the thermal history of particles can be determined from the short energy pulses produced during combustion.

A brief outline of the theory and accuracy of two-wavelength radiation pyrometry is given in Appendix 1. Most of the two-wavelength pyrometers reported in the literature have similar basic designs. Radiation from a combusting particle is collected by a lens system and then filtered at two (or more) different wavelengths. The relative intensity of the energy at the two wavelengths is then measured and, from the ratio of the two signals, the object temperature is determined.

The characteristics of a number of pyrometers used in particle studies have been analysed by Jorgensen and Zuiderwyk [82] and the results are presented in Table 5.1. The design of a pyrometer may be considered to consist of four parts:

- i) the method of splitting the incident radiation into two beams,
- ii) the filters,
- iii) the detectors and
- iv) the electronics and signal processing.

Most pyrometers use narrow bandpass filter pairs with central wavelengths between 0.45 and 1 μ m and employ two silicon photodiode or photomultiplier tube detectors. The

response times of the pyrometer vary from 20 to <1 ms.

Temperature measurements of between 1000 and 2500K for particles between 10 and 500 μ m diameter have been reported.

Before discussing the actual pyrometer design selected the requirements of the design should be outlined.

TABLE 5.1 Details of Two Colour Pyrometers Developed to Measure The Surface Temperature of Particles.
(from Jorgensen et al. reference 82)

Light Splitting	Filters	Detectors	Temperature Range (K)	Response Time (ms.)	Application	Reference
Rotating filter (133 Hz)	0.51 and 0.58 μ m.	1-PMT*	1073-1473	~10	Iron oxide in H ₂ <100 μ m.	Themelis & Gauvin (1962) [87]
Rotating filter (50 Hz)	Three filters	1-PMT	1173-3273	~20	Stationary coal 500 μ m	Babii & Ivanova (1968) [94]
Rotating filter (50 Hz)	0.55 and 0.65 μ m.	1-PMT	1400-2200	~20	coal 6-78 μ m	Ayling & Smith (1972) [90-91]
Oscillating filter (100 Hz)	3.1 and 4.5 μ m.	1-Indium antimonide	500-1900	~10	Stationary coal 250 μ m	Bach et al. (1970) [95]
Partially silvered mirror	Filter pairs 0.51, 0.545, 0.581 and 0.63 μ m.	2-PMT	1273-2773	~0.5	FeS ₂ , PbS, & CuFeS ₂ 35-105 μ m	Jorgensen et al. (1980-88) [43, 78-83]
Bifurcated fibre optics	0.45 and 0.55 μ m.	2-PMT	1250-2500	~1	coal 44-66 μ m	Timothy et al (1982) [89]
Partially silvered mirror	0.5 and 0.8 μ m.	2-PMT	<1200	~0.5	sphero carb 113-153 μ m	Tichenor et al. (1984) [92]
Trifurcated fibre optics	0.45, 0.55 and 0.65 μ m.	3-PMT	1000-4000	<1	alumina 10-100 μ m	Spjut et al (1988) [113-115]

*PMT - Photomultiplier Tube

5.1.2 Design Requirements

The following requirements were specified for the pyrometer design:

- i) the lower limit of resolvable particle temperature should be 1000K and preferably less, and it should be capable of measuring temperatures up to ~3000K,
- ii) the temperature of particles between 150 and 50 μm or smaller should be resolvable,
- iii) temperature changes of $\sim 10^6$ degrees per second should be measurable,
- iv) the particles should be viewed for as long as possible during combustion in the laminar flow furnace.

Not all of the specifications are independent of each other.

5.1.3 Optical Component Design

The physical specifications of the pyrometer were, to an extent, limited by the design of the laminar flow furnace. It was felt that a 38mm watercooled lens tube was the largest practical without causing excessive heat loss from either the furnace or the combusting particles. The total energy collected from the combusting particle was, therefore, limited by the objective lens size and proximity to the combusting particle. A 23mm diameter objective lens was selected. The closest it could be positioned to the particles combusting on the axis was 76mm owing to the need for a gas purge chamber to prevent fume from depositing on the pyrometer lens. The relationship between the position of the pyrometer lens and the combusting particles can be inferred from Figures 4.1, 4.3 and A.2.1.

The maximum pyrometer viewing area (perpendicular to the lens tube axis), on the axis of the reactor tube was about 15mm in diameter due to the need to sight into a watercooled blackbody and this dictated the focal lengths of the lenses. The total viewing time of the particles is then determined by their velocity down the laminar flow furnace and was estimated to be between 10 and 20 milliseconds.

Several different methods have been adopted by previous researchers (see Table 5.1 [82]) to split the incident beam. Use of a single detector and a rotating disc containing the different filters [87,90-91,94-95] is not a satisfactory method for particle temperature measurement due to the relatively slow speed of sampling and the fact the two different wavelengths are sampled at different times. Bifurcated fibre optics [89,112-115] is one possible method of collecting and proportioning the radiation to the two detectors; however, the relatively narrow diameters available and losses in the fibres result in reduced signal intensity. Following an examination of the previous designs, it was decided to split the radiation into two beams using a partially silvered mirror beam splitter [82,92]. The resultant beams were then filtered at two different wavelengths before being focussed onto separate detectors. The physical layout of the pyrometer decided on is given in Figure 4.4 and A.2.1.

5.1.4 Pyrometer Detector Selection

The two main alternatives for the pyrometer detectors were silicon photodiodes and photomultiplier tubes [116]. Typical photodiodes have radiant sensitivities of ~ 0.5 amps per watt. From a preliminary study of the pyrometer electronics [117] it was estimated that for silicon photodiodes a system noise equivalent power [NEP] of 10^{-11} watts rms over a 1 to 16 kHz bandwidth was possible. Although rise times of $1\mu\text{s}$, are possible a trade-off between amplifier noise and bandwidth is necessary. Photodiodes are relatively cheap, have stable properties and are resistant to mechanical shock.

The radiant sensitivities of photomultipliers are much higher than photodiodes. Typically a photomultiplier tube with extended red sensitivity has a radiant sensitivity of about 2×10^4 amps per watt at 810nm, an NEP of 3×10^{-14} watts over a 16 kHz bandwidth and response time of 15 ns. Photomultipliers are, however, much more expensive than photodiodes, have less stable characteristics and require magnetic shielding.

Despite the desirable properties of photodiodes preliminary calculations suggested that the faster response time and higher sensitivity of photomultiplier tubes would be advantageous and therefore photomultiplier tubes with extended red sensitivity were selected for the pyrometer detectors.

5.1.5 Optical Filter Selection

Having chosen the geometry of the optics and detector type, the optical filters then were selected with the aid of the computer model presented in Appendix 2. The optimum filter specifications are determined, to an extent, by the characteristics of the specific detectors used and also the temperature range required. The selection of the correct filter pair is a compromise between:

- i) the selected wavelengths being as near one another as possible to minimise emissivity variations and as far apart as possible to have as large a detector output ratio as possible;
- ii) having as narrow a band pass as possible to reduce the error associated with energy over a range of wavelengths being transmitted to the detectors and having as large a bandpass as possible to maximise the amount of energy reaching the detectors;
- iii) locating the wavelengths as a compromise between the region of maximum radiation energy and maximum detector sensitivity and also placing them in a region where selective absorption by the gases and vapours in the system does not occur.

Figure 5.1 gives the variation in blackbody spectral radiance with wavelength for a range of temperatures. The temperature of the object is obtained from the ratio of energies measured at two different filter wavelengths. Maximum sensitivity of temperature measurement is achieved by locating the two closely spaced narrow bandpass filter wavelengths on the left-hand portion of the curves (where Wien's Law approximation is valid) given in Figure 5.1. Since temperature measurements between 1000 and 3000K are required this suggests that the wavelengths chosen should be between 100 and 1000nm. The upper limit of the photomultiplier tube sensitivity is about 900nm, and therefore, interference filters of centre wavelength above this wavelength

were not considered. The calculated amount of energy transmitted to the detectors relative to that transmitted at 810nm, with a 10nm bandpass, is given in Figure 5.2. As indicated in Figure 5.1, in relative terms, at low temperatures very much more energy is transmitted at longer wavelengths than at higher temperatures.

The sensitivity of two different photomultiplier tubes with extended red sensitivity, are shown in Figure 5.3. Above 500nm the sensitivity of the photomultiplier tube detectors falls rapidly; however at 1000K the spectral radiance declines rapidly with decreasing wavelength below 1000nm (see Figure 5.1). By considering i) both the variation of the quantum efficiency and radiant sensitivity of a photomultiplier tube (from Figure 5.3) with wavelength; and ii) the variation in the radiant power transmitted through a specific bandpass filter, with object temperature (Figure 5.2), the variation in detector output signal can be calculated. The calculated detector output signal intensity obtained using different wavelength interference filters, relative to the output signal obtained using a 810nm filter is shown in Figure 5.4. The 710nm and 810nm interference filters (with 10nm bandpass) gave the largest output signals for object temperatures below ~2000K (the region of particular importance), and this filter pair was, therefore, chosen as a compromise between the various requirements and limitations.

The effect of variation in the detector resolution, as calculated by the model outlined in Appendix 2, is shown in Figure 5.5a. For each detector resolution, there is a minimum temperature below which the error in particle temperature measurement becomes unacceptably large. The actual limit depends on the filter wavelengths and bandpass chosen and therefore Figure 5.5 is plotted for those which were finally selected.

The calculated effect of variation in particle size on the particle error is shown in Figure 5.5b. The variation in calculated temperature error over the range of particle sizes used in the experiments (63-125 μm) is relatively small. Size diminution may, however, take place during the reactions and, therefore, the temperature resolution of smaller particles may also be important.

Radiation and absorption by the gaseous medium is another factor which must be considered. The literature was examined to see if selective absorption of energy has been reported to occur at wavelengths between 710 and 810nm for any of the gaseous reactants or reaction products. Owing to the symmetrical nature of the nitrogen and oxygen molecules, these gases are effectively transparent to radiation. For sulphur dioxide absorption maxima are reported at 280nm [118] and in the infrared region (7340, 8690 and 19200nm due to molecular bond vibration) [119]. No information is available for the absorption spectra of the volatile lead species PbS and PbO.

5.1.6 Electronics

From Figure 5.1 it can be seen that for the pyrometer wavelengths chosen (710 and 810nm) the spectral radiance varies by a factor of 10^6 between 1000 and 3000K. Most researchers [82,89,113-115] have therefore used logarithmic converters to allow four decades of useful range. Although logarithmic converters would probably have been preferable, in this case linear converters were used. The two decades of range obtainable was found to be satisfactory due to the relatively noisy background signal and to the limited time for which the reacting particles were observed. In this case the pyrometer sensitivity was varied by altering the photomultiplier tube voltage (gain).

A 0-10 volt pyrometer output signal was required to match the range of the data acquisition board input. Suitable electronic filtering was necessary to remove white noise. Low pass filtering down to 5kHz was considered possible without affecting the transient combustion pulse.

5.1.7 Final Pyrometer Design Specifications and Construction

The following were specified as the final design specifications for the two wavelength radiation pyrometer

Energy Collection and Transfer:	Quartz and Glass Lenses and Beam Splitter
Filters:	710nm and 810nm
Filter Bandpass:	10nm

Detectors:	2-extended red sensitivity photomultiplier tubes
Electronic Filtering:	5, 10 and 20 kHz Low Pass Filters
Output Signal	0-10 Volt

From these specifications, a two-wavelength radiation pyrometer was constructed by Canatech Electronics Research Corporation of Richmond B.C. [117].

5.2 Pyrometer Calibration

5.2.1 Photomultiplier Tube Calibration.

The radiant sensitivities of the individual photomultiplier tubes vary considerably and it is, therefore, necessary to determine the sensitivity of the individual photomultiplier tubes. Maximum overall pyrometer sensitivity is obtained by matching the interference filters and the photomultiplier tubes.

The sensitivity of the photomultiplier tubes was determined by measuring the radiation incident on the detectors from a calibrated spectral irradiance lamp placed at a known distance (26.26m). The pyrometer output signals were recorded for a range of photomultiplier tube gain settings. The pyrometer was calibrated without the optical tube assembly and the lamp was observed directly through the beam splitter and interference filters. To extend the measurements to the higher sensitivity ranges of the photomultipliers, it was necessary to reduce the lamp voltage and use the values of sensitivities overlapping the previous range to determine the new lamp spectral irradiance. The results of the tests are reported in Table 5.2 and Figure 5.6.

An exponential relationship exists between the setting (GS) of the photomultiplier gain potentiometer (which controls the photomultiplier tube grid voltages) and the photomultiplier tube sensitivities.

TABLE 5.2 Photomultiplier tube calibration - measured photomultiplier sensitivity vs. photomultiplier gain setting.

Gain Setting	710nm V/ μ W	810nm V/ μ W
2	2.1	0.6
3	7.5	1.8
4	31.6	5.4
5	127	17.6
6	496	53.3
7	2012	120
7.7	5705	469
8	8684	561
8.9	-	1678
9	40209	1611
10	173253	6267

For the 710nm filter detector

$$S_{710} = \exp_{10}[0.615(GS_{710}) - 0.9607] \quad (V/\mu W) \quad (5.1a)$$

and for the 810nm filter detector

$$S_{810} = \exp_{10}[0.500(GS_{810}) - 1.2600] \quad (V/\mu W) \quad (5.1b)$$

5.2.2 Noise Performance

The background noise level determines the ultimate resolution and usable sensitivity of the instrument. The noise on the output signal was measured, using 5kHz low pass filtering, with the lens opening covered and the digital panel meters turned off. The peak-to-peak and rms noise level for the range of gain settings is given in Table 5.3. The minimum noise levels were obtained at the highest photomultiplier tube sensitivities, and were 2.25×10^{-14} and $2.17 \times 10^{-13}W$ (noise equivalent power) for the 710 and 810nm detectors respectively. The actual minimum signal resolvable may be considerably larger than this if the signal component due to fluctuating background radiation is large.

TABLE 5.3 Noise level on pyrometer output signal.Preamplifier feedback resistor.....100 k Ω

Filter Setting.....5 kHz

Gain Setting	V ₇₁₀ (mV)	V ₇₁₀ rms (mV)	NEP (watts)	V ₈₁₀ (mV)	V ₈₁₀ rms (mV)	NEP (watts)
0	0.4	0.14	-	0.4	0.14	-
1	0.4	0.14	3.23(-10)	0.4	0.14	7.98(-10)
2	0.4	0.14	8.11(-11)	0.5	0.18	3.06(-10)
3	0.4	0.14	2.04(-11)	0.8	0.28	1.50(-10)
4	0.6	0.21	7.68(-12)	1.0	0.35	5.77(-11)
5	0.8	0.28	2.57(-12)	0.8	0.28	1.42(-11)
6	1.0	0.35	8.08(-13)	0.9	0.32	4.89(-12)
7	1.4	0.49	2.84(-13)	1.2	0.42	2.00(-12)
8	1.6	0.57	8.15(-14)	1.4	0.5	7.16(-13)
9	2.5	0.88	3.20(-14)	2	0.71	3.14(-13)
10	7.0	2.47	2.25(-14)	4.5	1.59	2.17(-13)

5.2.3 Temperature Calibration Theory

The theoretical relationship between the detector output signals and a blackbody object temperature, T_{bb} , is given by (see Equation A.1.9)

$$\ln\left(\frac{V_{\lambda_1}}{V_{\lambda_2}}\right) = -C_{val} + \left(\frac{C_2}{\lambda_2} - \frac{C_2}{\lambda_1}\right) \frac{1}{T_{bb}} \quad (5.2)$$

where

C_{val} = constant specific to the pyrometer with a specific gain setting

C_2 = 2nd Radiation constant ($1.438 \times 10^{-2} mK$)

If the two filters are considered monochromatic at 712 and 812.65nm, the relationship between the object temperature and the ratio of the pyrometer detector output signals is given by

$$T_{bb} = \frac{2501.43}{\ln\left(\frac{V_{\lambda_{810}}}{V_{\lambda_{710}}}\right) + C_{val}} \quad (5.3)$$

For a non-blackbody object the above equation is valid if the ratio of the emissivities at the two wavelengths are equal. The exact value of the gain dependent constant C_{val} must be determined experimentally.

5.2.4 Temperature Calibration Results

To calibrate the pyrometer it is necessary to have a temperature source whose temperature and emissivity are known precisely. This is a considerable problem, because except for the National Standards Laboratories, few standard sources exist that have been calibrated at the wavelengths and temperatures required in this study. The accuracy of temperature measurement is only as good as the primary calibration. The various calibration temperature source options available are detailed in Appendix 5.

The design of the calibration furnaces and the results of the calibration tests are given in Appendix 5. Calibration tests were conducted over the six month period that

5.2.4.1 Blackbody Cavity Temperature Source Calibration

Several furnaces designed to behave as blackbody cavity temperature sources were used to calibrate the pyrometer. The design requirements for a cavity to approximate a blackbody are given in Appendix 5. The temperature of the blackbody cavity was measured using a Pt-Pt/10%Rh thermocouple and therefore it is the accuracy of calibration of this thermocouple which ultimately limits the accuracy of the pyrometer calibration. The thermocouple and pyrometer were initially calibrated using a copper freezing point, blackbody cavity. The calibrated thermocouple was then used in both a low-temperature and high-temperature blackbody furnaces to calibrate the pyrometer. experimental particle temperature measurements were made. The following range of temperature calibrations were made:

- i) copper freezing point blackbody cavity at 1358K
- ii) low temperature resistance-heated graphite blackbody cavity 1000-1550K
- iii) high temperature RF induction-heated graphite blackbody cavity 1450-2000K.

The results of the calibration tests are given in Appendix 5 and a summary of the calibration tests performed is given in Table 5.4.

The slope of 2509(K) is in good agreement with the theoretical slope of 2501 (K) see (Equation 5.3). The difference in object temperature calculated using the theoretical and measured values was typically less than 0.5%; therefore, the experimental results, calculated using the theoretical value, were not corrected.

The mean of the calibration results from all of the groups of tests varied by less than 3% (see Table 5.4). Similarly the standard deviation (S) within the groups was less than 1%. No systematic variation in the calibration results was observed over the six month period the calibration tests were conducted. The results for a series of tests for $GS_{710}=8.23$ and $GS_{810}=9.9$ are shown in Figure 5.7b.

TABLE 5.4 Summary of Pyrometer Calibration Data.

Gain setting 710nm	Gain setting 810nm	Number of data points	Temperature range of test	Average C_{val}	Standard deviation of sample
8.23	9.9	14	1105-1538	1.4098	0.007
		5	1393-1426	1.4298	0.006
		8	1513-1573	1.4167	0.007
		6	1643-1733	1.4294	0.002
		35	1358	1.4146	0.010
7.73	9.4	1	1539	1.3141	-
		5	1593-1673	1.3310	0.0015
7.23	8.9	1	1479	1.2190	-
		5	1703-1793	1.2312	0.002
6.73	8.4	1	1481	1.1110	-
		11	1159-1541	1.1121	0.002
		5	1763-1843	1.1372	0.001
6.23	7.9	2	1482	0.9987	-
		5	1803-1883	1.0267	0.004
5.73	7.4	1	1484	0.9057	-
		5	1833-1893	0.9263	0.002
5.23	6.9	1	1485	0.80145	-
		5	1833-1913	0.8255	0.007
8.57	9.9	5	1483-1573	1.9256	0.003
8.42	9.78	5	1493-1573	1.8580	0.010
7.55	9.3	5	1593-1693	1.1895	0.004
7.4	9.05	5	1683-1743	1.2811	0.006
7.08	8.73	5	1723-1803	1.2114	0.001
6.6	8.2	5	1783-1863	1.1845	0.001

The natural logarithm of the ratio of the detector outputs versus the inverse of blackbody temperature from the various tests conducted at gain settings $G_{710}=8.23$ and $G_{810}=0.99$ are given in Figure 5.7a. There is reasonable agreement between the results from the various tests; the equation of the line as determined from the curve is

$$\ln\left(\frac{V_{\lambda_{810}}}{V_{\lambda_{710}}}\right) = \frac{2509}{T_{bb}} - 1.4183 \quad (5.4)$$

From the photomultiplier sensitivity Equations 5.1a and b, it is possible to calculate the variation in the calibration constant values with photomultiplier gain setting. The calibration constant is the result of a number of parameters, including the pyrometer detector sensitivities, specific to the pyrometer used. From Equations A.1.9 and 5.2, and considering the case of a blackbody, the calibration constant can be written as

$$-C_{val} = \ln \left(\frac{K_{2\lambda_{810}}}{K_{2\lambda_{710}}} \right) \quad (5.5)$$

Where

$$K_{2\lambda_{710or810}} = F_{dp\lambda_{710or810}} G_{\lambda_{710or810}} 2C_1 \frac{\Delta\lambda_{710or810}}{\lambda_{710or810}^5}$$

and

$$G_{\lambda_{710or810}} \propto S_{710or810}$$

The component relating to the pyrometer detector sensitivities can be extracted from the overall calibration constant. The photomultiplier tube sensitivities, S in Equations 5.1a and b, can be considered as a proportional component of the pyrometer gain, G.

Equation 5.5 can then be rewritten as:

$$C_{val} = \ln \left(\frac{K_{2\lambda_{710}}^*}{K_{2\lambda_{810}}^*} \right) + \ln \left(\frac{S_{\lambda_{710}}}{S_{\lambda_{810}}} \right) \quad (5.6)$$

where

$$K_{2\lambda_{710or810}}^* = K_{2\lambda_{710or810}} \text{ with the photomultiplier tube sensitivity } (S_{710or810}) \text{ extracted.}$$

Substituting the detector sensitivities given by Equations 5.1a and b results in the following Equation

$$C_{val} = C_0 + ((1.416 \times GS_{710} - 1.152 \times GS_{810}) + 0.689) \quad (5.7)$$

where

$$C_0 = \ln \left(\frac{K_{2\lambda_{710}}^*}{K_{2\lambda_{810}}^*} \right)$$

It is not possible to derive the value of C_0 directly; it is necessary to solve the equation for known conditions to determine the value. The experimentally measured value of C_{val} , at $G_{710}=8.23$ and $G_{810}=9.9$, were used to fit the pyrometer sensitivity equations (Equations 5.1a and b) and to determine C_0 . Using the pyrometer sensitivities in Equations 5.1a and

b an ~18% error between the calculated and measured C_{val} was obtained. The best fit was obtained with pyrometer sensitivities given by Equations 5.8a and b, from which C_0 was determined to be 1.03574.

For the 710nm filter detector

$$S_{710} = \exp_{10}[0.600(GS_{710}) - 0.95874] \quad (V/\mu W) \quad (5.8a)$$

and for the 810nm filter detector

$$S_{810} = \exp_{10}[0.513(GS_{810}) - 1.26441] \quad (V/\mu W) \quad (5.8b)$$

Equations 5.1 and 5.8 are very similar however the results are very sensitive to the slopes of the photomultiplier tube calibration equations. The final relationship between the detector gain settings and the calibration constant used was therefore;

$$C_{val} = 1.7397 + (1.382 \times GS_{710} - 1.181 \times GS_{810}) \quad (5.9)$$

Using this equation the expected calibration constant at other gain settings were calculated, and the results are reported in Table 5.5.

Table 5.5 Measured and calculated¹ pyrometer calibration constants.
(1 - from Equation 5.9).

Gain Setting		C_{val} (measured)	C_{val} (calculated)
710nm	810nm		
4.73	6.4	0.72	0.72
5.23	6.9	0.81	0.82
5.73	7.4	0.92	0.92
6.23	7.9	1.01	1.02
6.6	8.2	1.19	1.18
6.73	8.4	1.12	1.12
7.08	8.73	1.21	1.21
7.23	8.9	1.23	1.22
7.4	9.05	1.28	1.28
7.55	9.3	1.19	1.19
7.73	9.4	1.32	1.32
8.23	9.9	1.42	1.42*
8.42	9.78	1.86	1.82
8.57	9.9	1.93	1.89

* C_{val} used to fit the photomultiplier tube sensitivity calibration data to the pyrometer calibration data.

The calculated effects of calibration constant error on the measured temperature error for a blackbody object is given in Table 5.6. This has been calculated assuming the actual value of the constant is 1.42. Over-estimation of the value of the constant results in low temperature measurement, and vice versa. This table of calculated errors refers only to blackbody temperature error; the effects of emissivity errors can also be considerable [120-123].

TABLE 5.6 Theoretical blackbody temperature error associated with various C_{val} errors (assuming $C_{val}(\text{actual})=1.42$).

C_{val}	1.38	1.40	1.42	1.44	1.46
True T_{bb} (K)	Theoretical Measured Temperature (K)				
1400	1432	1416	1400	1385	1369
1600	1642	1621	1600	1580	1560
1800	1853	1826	1800	1774	1750
2000	2066	2032	2000	1969	1938
2200	2280	2239	2200	2162	2125
2400	2496	2447	2400	2355	2311
2600	2713	2655	2600	2547	2496
2800	2931	2864	2800	2739	2680
3000	3151	3074	3000	2930	2863

* Calculated from $\frac{1}{T_{actual}} - \frac{1}{T_{measured}} = \frac{C_{val}(\text{actual}) - C_{val}}{2500}$

5.2.5 Pyrometer Viewing Volume

The radiation imaged on the pyrometer detectors is collected from a spatial volume in front of the lens termed the measuring volume. The volume depends on the pyrometer optics, and the cross-sectional area of this volume, perpendicular to the lens will depend on the distance from the pyrometer lens. The optical configuration for this specific pyrometer is given in Figure A.2.1. The area from which radiation is collected can be varied by altering the lens tube distance X_2 (which alters the focal length X_{FL}) and also by varying the size of the aperture stop S_2 . The aperture stop employed was 4.75x4.75mm.

Combusting particles travelling down the laminar flow furnace typically would be 25-50mm from the tip of the pyrometer lens tube. Most particles, however, would be expected to travel on the axis of the furnace axis at a distance of ~38mm from the tip of

the lens tube. The experimentally determined variation of signal intensity across the pyrometer measuring area at different distances from tip of the lens tube, X_1 , and different lens tube distances, X_2 , is given in Table 5.7 and shown in Figure 5.8. The variation in signal intensity was determined by traversing a tungsten filament lamp with a pinhole aperture, of $342\mu\text{m}$ diameter, in front of the pyrometer lens tube. The width of the viewing volume ($Y_{\text{max}}-Y_{\text{min}}$, vertically perpendicular to the lens tube axis) varied from 12 to 20mm and the intensity was fairly constant for the central portion. The viewing distance increased with increasing lamp-to-pyrometer lens distance but the maximum signal intensity decreased. For the lens tube distance, X_2 , a value of $\sim 90\text{mm}$ appeared to give the maximum signal intensity and therefore this distance was used for all the experimental measurements.

TABLE 5.7 Variation of 710nm detector output signal across the pyrometer field of view for various lamp and Lens tube settings.

(Panel LED Meter Readings)

 X_1 =Objective lens-lamp distance X_2 =Objective lens-detector distance as read off lens tube scale

Position Y(mm)	$X_1=37.5$ mm $X_2=90$ mm	$X_1=25$ mm $X_2=90$ mm	$X_1=50$ mm $X_2=90$ mm	$X_1=37.5$ mm $X_2=75$ mm	$X_1=37.5$ mm $X_2=105$ mm
5.0	-	-	0.1	0.1	0
5.5	-	-	0.2	0.1	0.1
5.7	0	-	-	0.2	0.1
6.0	0.3	-	0.4	0.3	0.2
6.25	0.5	-	0.5	0.5	0.3
6.5	0.6	-	1.0	0.6	0.5
6.6	-	-	1.3	-	-
6.7	0.8	0.2	1.5	2.8	1.2
6.8	-	-	36.0	-	-
6.9	-	-	80.0	-	-
7.0	1.9	0.3	81.0	50	1.0
7.1	25.8	0.4	95.0	69	33
7.2	88	0.7	100	84	42
7.25	99	-	-	-	82
7.3	130	0.8	102	120	105
7.4	140	1.2	106	120	102
7.5	146	90	108	132	104
7.6	165	130	110	145	106
7.7	151	160	110	152	108
7.8	174	212	96	162	104
7.9	170	216	101	135	100
8.0	152	223	103	126	95
8.1	150	230	75	114	60
8.2	140	230	81	102	35
8.3	142	220	83	80	12
8.4	108	220	65	77	2
8.5	77	111	38	52	0.6
8.6	1.5	1.8	0.7	38	0.3
8.7	0.9	1.7	0.6	16	0.3
8.8	0.6	1.0	0.6	6	0.2
8.9	0.5	0.7	0.5	0.4	0.2
9.0	0.5	0.5	0.3	0.3	0.1
9.25	0.3	0.3	0.2	0.3	0.1
9.5	0.2	0.2	0.1	0.2	-
9.75	0.1	0.1	0.1	0.1	-
10.0	0.0	0.0	0.1	0.1	-

5.2.5.1 Measured Temperature Variation Across the Viewing Volume

Using the same procedure as for the pyrometer viewing volume determination, the variation in measured temperature across the pyrometer measuring volume was determined. The values of 38mm and 90mm were used for the pyrometer to object

distance (X_1) and optical lens tube distance (X_2) respectively (see Figure A.2.1). The variation in signal intensities of the two detectors and calculated filament temperatures are given in Table 5.8 and Figures 5.9. The measured filament temperature was corrected for the variation in the ratio of the tungsten emissivities at 710 and 810nm [124,125] (see Appendix 6). Due to the use of an AC power supply, the measured filament temperature fluctuates by $\sim 50\text{K}$; however the measured filament temperature of $\sim 2860\text{K}$ is in general agreement with that reported for tungsten filament lamps of 2850-3000K [127,126].

TABLE 5.8 Intensity and measured temperature variation across the pyrometer measuring volume.

$X_1=38\text{mm}$ $X_2=90\text{mm}$ $G_{710}=4.0$ $G_{810}=5.7$ $C_{\text{val}}=0.6503$

Position Y(mm)	V_{710} (V)	V_{810} (V)	T(measured) (K)	T(corrected) for tungsten emissivity (K)	Calculated particle diameter (μm)	Aperture diameter ($342\mu\text{m}$)/ dp(calc)
-0.75	0.027	0.027	3850	3598	12.1	28.3
-0.65	1.306	1.670	2793	2658	227.9	1.50
-0.55	3.040	3.477	3190	3015	221.6	1.54
-0.45	3.306	3.896	3072	2910	261.0	1.31
-0.35	3.694	4.358	3069	2907	276.9	1.23
-0.25	3.999	4.712	3073	2911	286.7	1.19
-0.15	3.967	4.705	3049	2889	293.0	1.17
-0.05	4.080	4.854	3037	2879	301.1	1.14
0.05	4.185	4.973	3041	2882	303.6	1.13
0.15	4.192	4.988	3037	2878	305.3	1.12
0.25	4.377	5.215	3032	2874	313.6	1.09
0.35	4.292	5.129	3021	2864	314.5	1.09
0.45	4.185	5.007	3016	2860	312.1	1.10
0.55	3.445	3.827	3314	3126	209.4	1.63
0.65	1.196	1.560	2733	2603	236.3	1.45
0.75	0.022	0.024	3312	3125	16.8	20.4
0.85	0.027	0.027	3850	3598	12.1	28.3

A rapid rise and decline in the signal intensities is observed during the initial 2mm of detection; over the central 10mm of the viewing distance a gradual increase in signal intensity is observed. The measured temperature calculated from the previously determined calibration constant is fairly constant, declining about 50K over the central region. At the edges, an apparent increase followed by an apparent decrease in measured

temperature is observed. In theory the measured temperature should be independent of the signal intensity. An explanation for the observed edge peaks may be that at the edges of the lens the radiation is unevenly distributed between the two detectors.

Figure 5.10 indicates how the signal variation across the pyrometer lens may effect the pyrometer output signal for a series of hypothetical combustion pulses. For the example considered, the variation in the energy and particle temperature during combustion are considered to be those given in Figure 5.10a. Typically only a fraction of the combustion pulse is recorded as a particle passes in front of the pyrometer lens; therefore, several different combustion pulses, such as P_1 , P_2 and P_3 shown, could be recorded at different times from the same combusting particle. The pyrometer output signals for the different combustion pulses shown in Figure 5.10c, will depend on the combined effects of both i) the real changes in signal intensity which occur during combustion (Figure 5.10a); and ii) the apparent variation in signal intensity and temperature due to the pyrometer optics (see Figure 5.10b). Each of the three different energy and temperature pulses shown in Figure 5.10c could thus be recorded from a single combusting particle. These results indicate that care must be taken in interpreting both the measured energy and temperature results. The distinct nature of the edge effects, may however, aid in identifying the start and end of combustion pulses.

5.2.6 Pyrometer Response

The response of the pyrometer was tested by rotating a disc with holes of varying sizes between the low-temperature blackbody calibration furnace and the pyrometer lens. Holes of 0.342, 0.51, 1.02, 2.01 and 4mm were rotated in front on the pyrometer lens at a velocity equivalent to 11 m/s. The energy intensities and apparent blackbody temperatures measured are shown in Figure 5.11a and 5.11b respectively. The pyrometer response is quite rapid with peak temperatures being reached in ~ 0.1 ms. Increasingly

lower temperatures were measured with decreasing signal intensities. At the very low signal levels, the error due to digitisation of the pyrometer output signal becomes significant.

This experiment does not represent the true conditions of measurement because the temperature source was fixed in space and a pinhole rotated in front of it, therefore, the lens edge effects which can also be considered as part of the pyrometer response [82] were not observed. From the previous pyrometer optics calibration test (see Figure 5.10a) it can be seen that the edge effects account for the initial and final ~15% of the pyrometer viewing distance, and if typically a particle is observed for 10 to 20 milliseconds the pyrometer response time could be considered to be 1-3 milliseconds.

The photomultiplier tube detectors are reported [116] to have response times in the order of ~15ns which is negligible in comparison to the other response errors. A simple experiment to examine the effect of the electronic filtering and data acquisition on the pyrometer response was performed by replacing the photomultiplier output signals by that from a wave form generator. The effect of the electronic filtering was generally small. The filtered output signals of both detectors lagged the input by an amount equal to the low pass frequency filter (ie 0.2ms for the 5kHz low pass filter); as however the same lag was present on both signals this was unimportant. Very rapid changes in signal up to frequencies close to the cut-off frequency were relatively unaffected. In combination with the inaccuracies associated with data acquisition (the two signals were recorded at 50kHz (DMA) using the simultaneous sample and hold capabilities of the DT2828 data acquisition board) some variation in the ratio of the two detector output signals was observed for ~0.1 ms following the rapid signal change of a square wave input. In consequence of this analysis, it was felt that the pyrometer electronics were capable of accurately recording rapid changes in signal of greater than 1ms duration.

5.2.7 Apparent Particle Area Calculations

5.2.7.1 Relative Apparent Particle Area

From the analysis presented in Appendix 1.2, the changes in apparent particle area relative to that at a reference time can be calculated from the detector output signal and measured pulse temperature data. The equation used to determine the relative changes in particle area was derived from Equation A.1.11 (for the 710nm detector output), by substituting for the filter centre wavelength (712nm) and the second radiation constant (C_2):

$$\frac{A(t)}{A(t_0)} = \frac{V_{710}(t)}{V_{710}(t_0)} \cdot \exp\left[20196.6\left(\frac{1}{T(t)} - \frac{1}{T(t_0)}\right)\right] \quad (5.10)$$

For each of the combustion pulses analysed, a suitable reference time, t_0 , was selected, and the temperature and detector output signal at this time were then used to calculate the relative changes in apparent particle area across the combustion pulse. The effects of signal noise on both the detector output signal and calculated temperature were cumulative; therefore to reduce random fluctuations in the calculated relative apparent area the detector output signal was smoothed. An inverse fourier transform filtering routine present in the ASYST "Analysis Module" software (Macmillan Software Co. Inc.) was used.

The relative changes in apparent particle area calculated using the 810nm detector output signal (and the 810nm form of Equation 5.9) were identical to those calculated using the 710nm signal.

5.2.7.2 Apparent Particle Area Calculations

From the mathematical model presented in Appendix 2 it is possible to calculate the apparent size of the radiating object from the magnitude of the pyrometer output signal and the apparent object temperature. It is also necessary to know the object emissivity, and the pyrometer and system characteristics in order to calculate accurately the equivalent spherical diameter of the object. It is possible to calculate the specific

pyrometer characteristics from the calibration test presented in Section 5.2.5.1, because both the experimental conditions and the spectral emissivity of tungsten [124] are known. Based on the pyrometer and system geometry presented in Figure A.2.1, and the experimental data from Table 5.8, the apparent particle diameter was calculated using the model outlined in Appendix 2, and the results reported in Table 5.8. The calculated particle size is in reasonable agreement with the $\sim 342\mu\text{m}$ diameter pinhole aperture in front of the tungsten lamp. The 10-20% difference between the measured and calculated object diameter is much smaller than the actual uncertainties associated with the values of the parameters used in the mathematical model, the radiative properties of the tungsten filament and the geometry of the experimental set-up. The model was, therefore, not corrected for this discrepancy.

The particle emissivity must be known in order to calculate the size of combusting particles accurately. Unfortunately the emissivities of most molten and solid sulphides and oxides are unknown at the specific pyrometer filter wavelengths. Estimating the particle emissivities can, therefore, result in considerable error. The presence of optically thick reaction products (eg fume) may result in over-estimation of the apparent particle size.

5.2.8 Pyrometer Accuracy

It is very difficult to assign an absolute value to the accuracy of temperature measurements made by this or any other radiation pyrometer; because only a part of the total error can be considered intrinsic to the instrument. The rest of the error is due to uncertainties in the properties of the object and system being measured.

The measurement errors associated with the pyrometer can be divide into three parts:

- i) measurement error due to inaccuracies in pyrometer calibration,
- ii) measurement error due to signal variations across the pyrometer lens, and
- iii) signal error due to digitisation of the analogue detector output signals.

The magnitude of the effect of pyrometer calibration constant errors has been examined in Section 5.2.4.1. The relatively good agreement between the large number of calibration constant data points determined indicates the calibration constant and temperature measurement (approximately) have a reproducibility of probably within 3% which would be equivalent to $\pm < 50\text{K}$. Included in this error was also the estimated $< 0.5\%$ error associated with using the theoretical slope (2501(K)) of the calibration equation rather than the one experimentally determined (2509(K)). The error associated with the blackbody calibration furnace was estimated to be $\pm 0.5\%$ (Section A.5.6) which would be additive to the previous error. From Section 5.2.5.1 the variation in measured temperature across the pyrometer lens was determined as $\sim 50\text{K}$ at $\sim 2850\text{K}$ or $\sim 2\%$ over the centre portion of the viewing area; again this error would be additive. It is considered that the signal errors due to data acquisition and electronic filtering were insignificant at all but very low signal intensities and very high pulse frequencies ($< 1\text{ms}$). The estimated maximum total error associated with the pyrometer and its calibration could therefore reach 5% which would represent a temperature error of $\sim \pm 100\text{K}$ at 2000K . Considerably greater errors are, however, associated with measurements near the edges of the pyrometer viewing area.

The main sources of measurement errors due to the system, although unquantifiable, can be identified as:

- i) errors due to fluctuations in background noise,
- ii) errors due to deviation of the ratio at the emissivities at the two detector wavelengths, and
- iii) errors due to preferential absorption of radiation at one of the two detector wavelengths by gases or fume in the system.

The large number of data points taken during the measurement of a single combustion pulse tended to diminish the problems of background error, such that in most cases signal filtering to remove the background noise was not necessary. The experimental conditions

and pyrometer settings were also controlled to minimise the errors associated with the background radiation. The magnitude of the other two effects were unknown but assumed small.

From Appendix 6 the calculated variation in the ratio of the emissivity of tungsten at 710 and 810nm [124] indicates that errors in excess of 5% are possible. These errors are additive to those associated with the pyrometer and for certain materials could be considerably greater.

Notwithstanding the above, the pyrometer temperature measurements recorded during combustion of the different minerals (especially pyrite and pyrrhotite) were quite reproducible often to within 100K. Errors associated with the quantities derived from the measured particle temperature and energy were, however, often considerably larger.

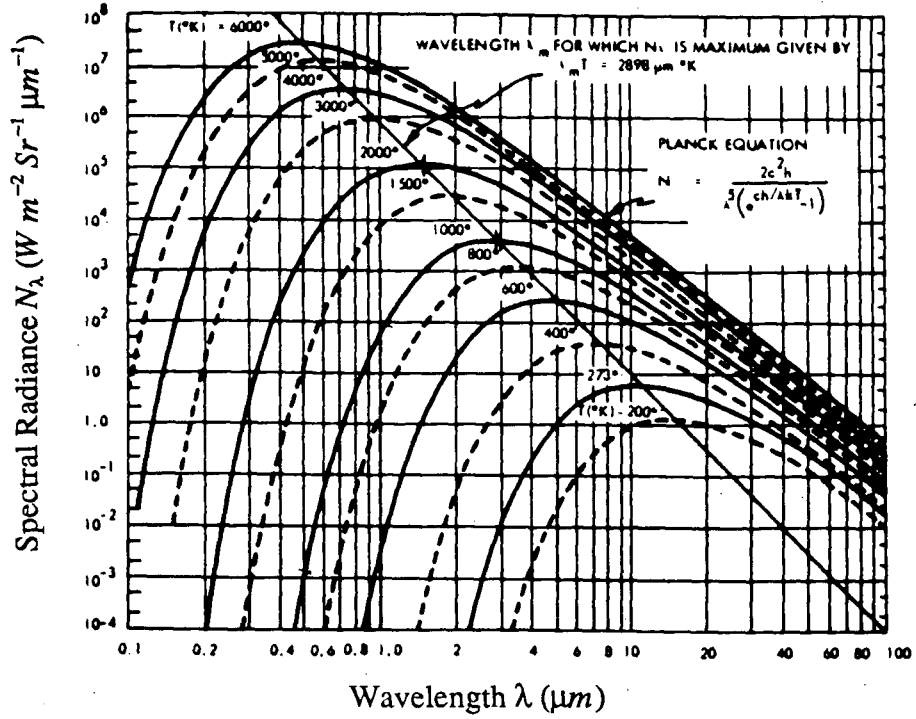


Figure 5.1 Blackbody spectral radiance (from Reference [116])

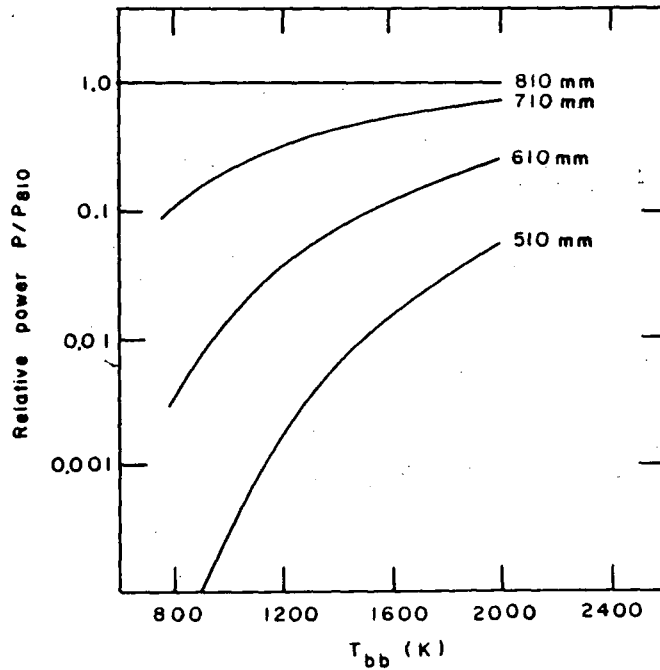


Figure 5.2 Calculated relative power transmitted though various 10nm band-pass interference filters of different centre wavelengths (see Appendix 2).

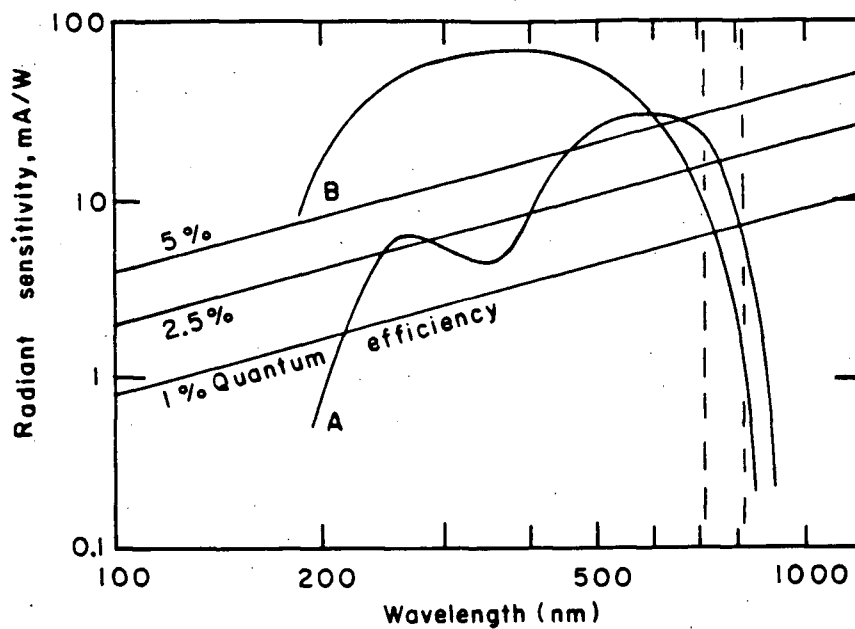


Figure 5.3 Radiant sensitivities and associated quantum efficiencies of different commercially available photomultiplier tubes (Hamamatsu Ltd.).

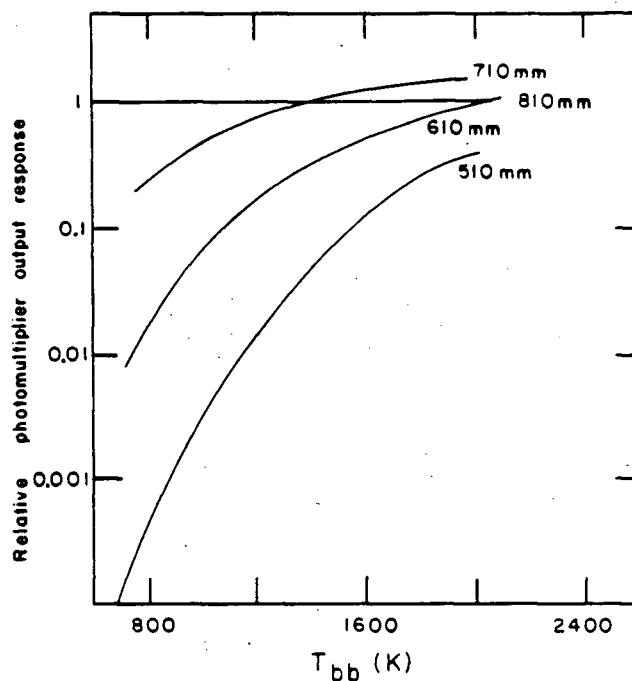
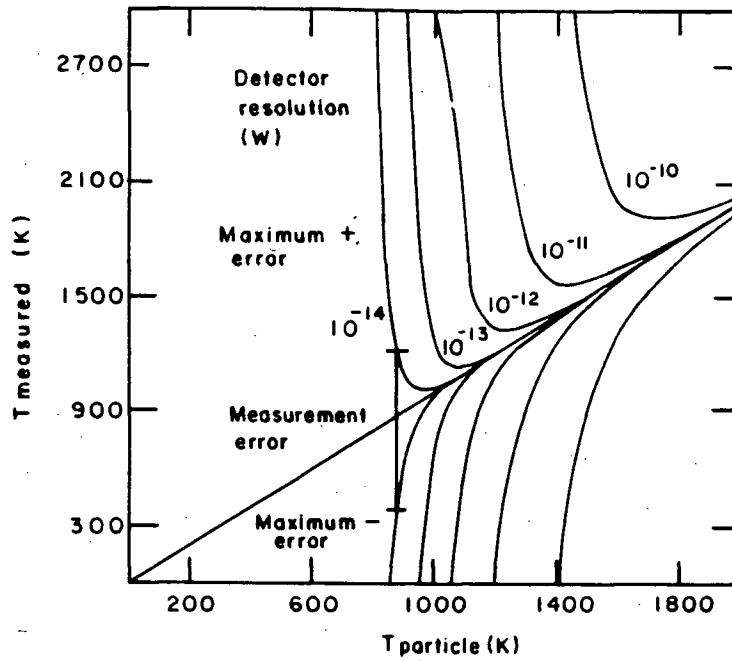
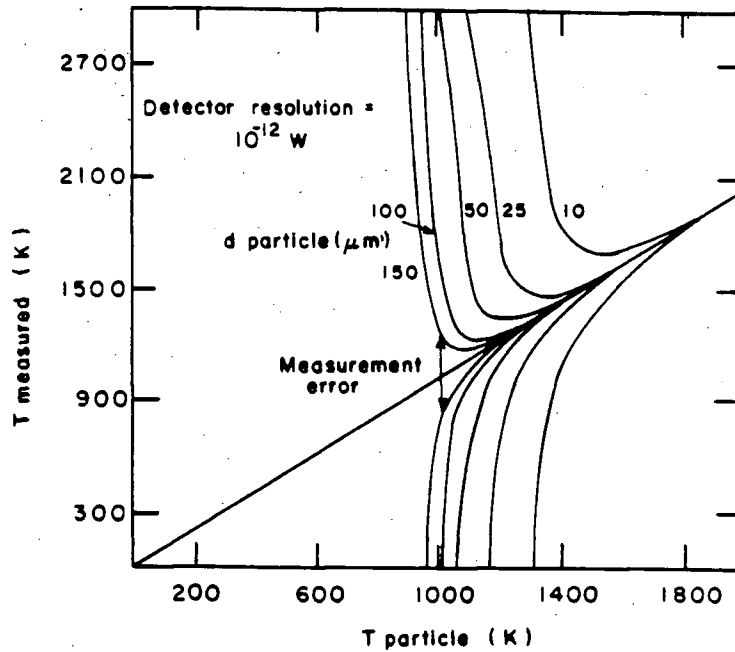


Figure 5.4 Calculate relative photomultiplier response for different 10nm bandpass filters vs that for the 810nm interference filter (the product of the power transmitted and photomultiplier quantum efficiencies at the different filter wavelengths).



(a)



(b)

Figure 5.5 Calculated minimum measurable temperature and associated measurement errors a) as a function of detector resolution (W) and b) as a function of particle size. (710nm and 810nm interference filters with 10nm band width).

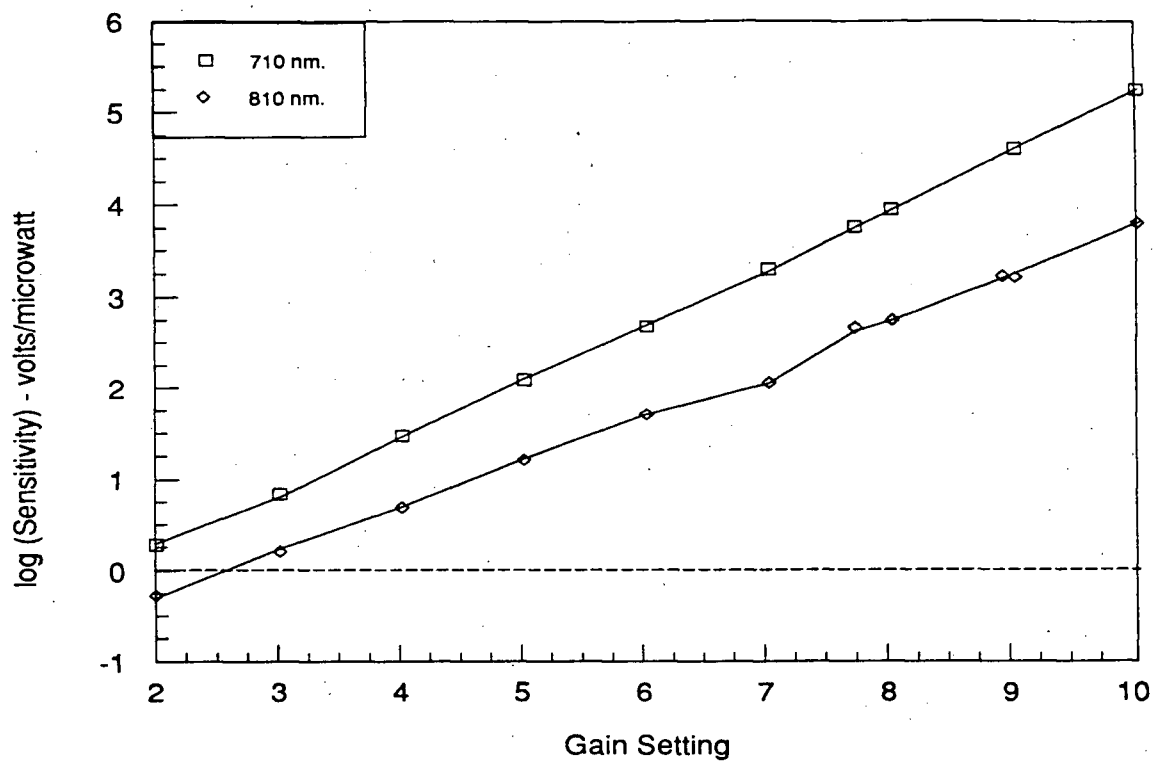
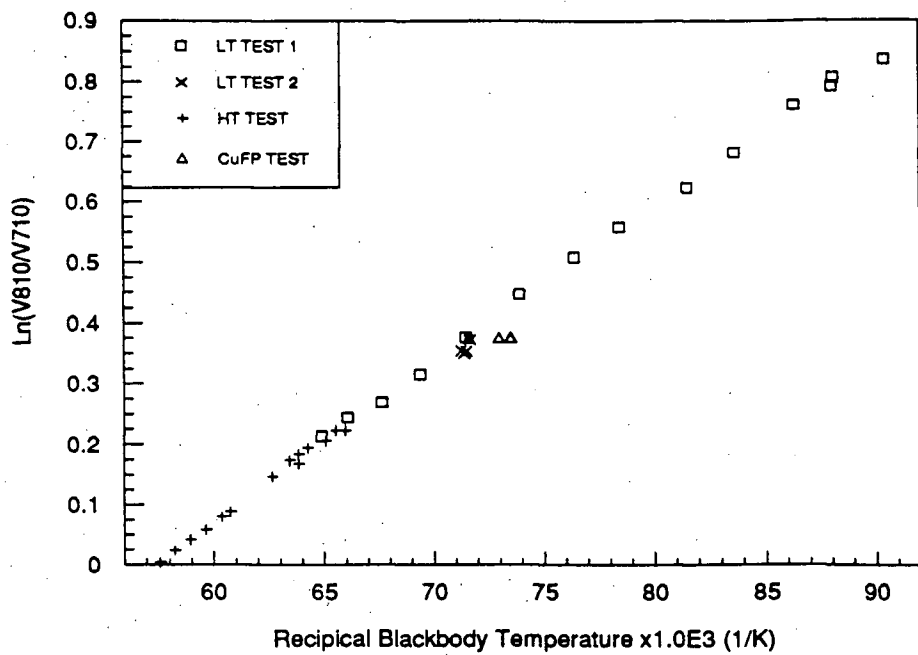
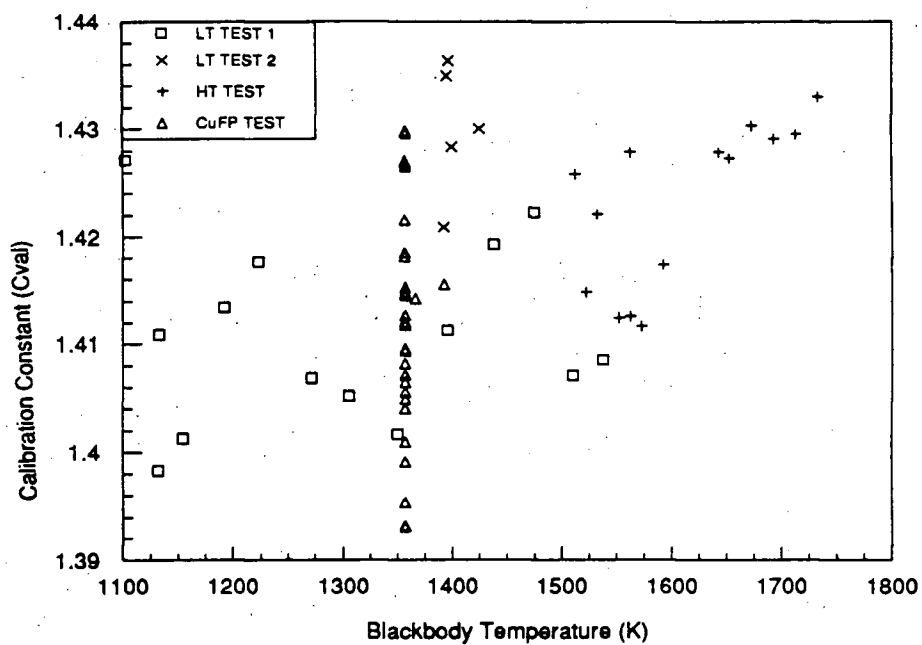


Figure 5.6 Photomultiplier tube calibration results.



(a)



(b)

Figure 5.7 Pyrometer Blackbody calibration test results.
 a) natural logarithm of the detector output signal vs inverse of blackbody temperature,
 b) Calibration constants (C_{VAL}) vs Blackbody temperature (gain settings $G_{710}=8.23$ $G_{810}=9.9$).

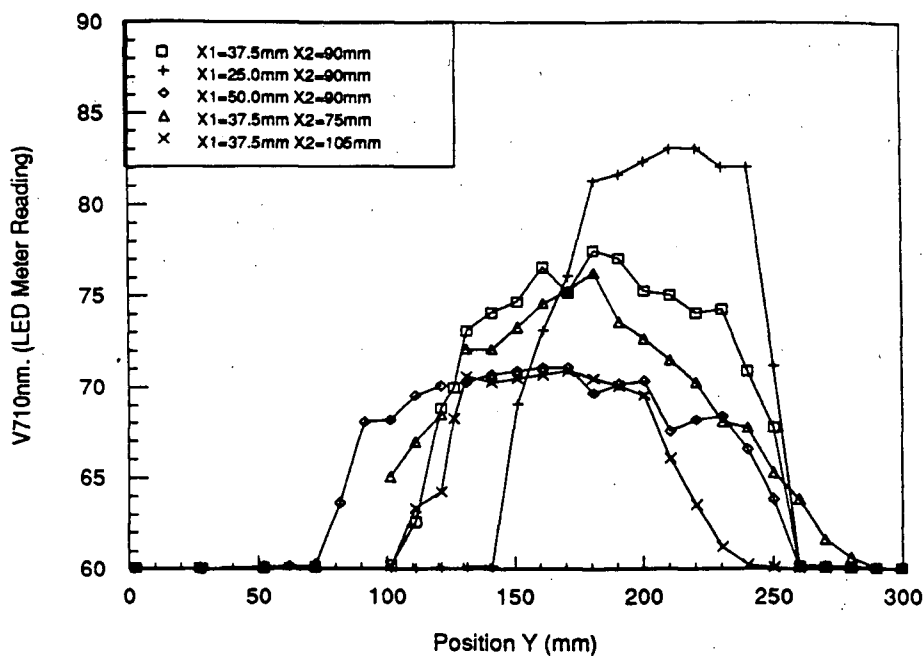


Figure 5.8 Variation in detector output signal across the viewing volume with pyrometer-object distance, X_1 , and lens tube distance, X_2 (see Figure A.2.1 for definitions).

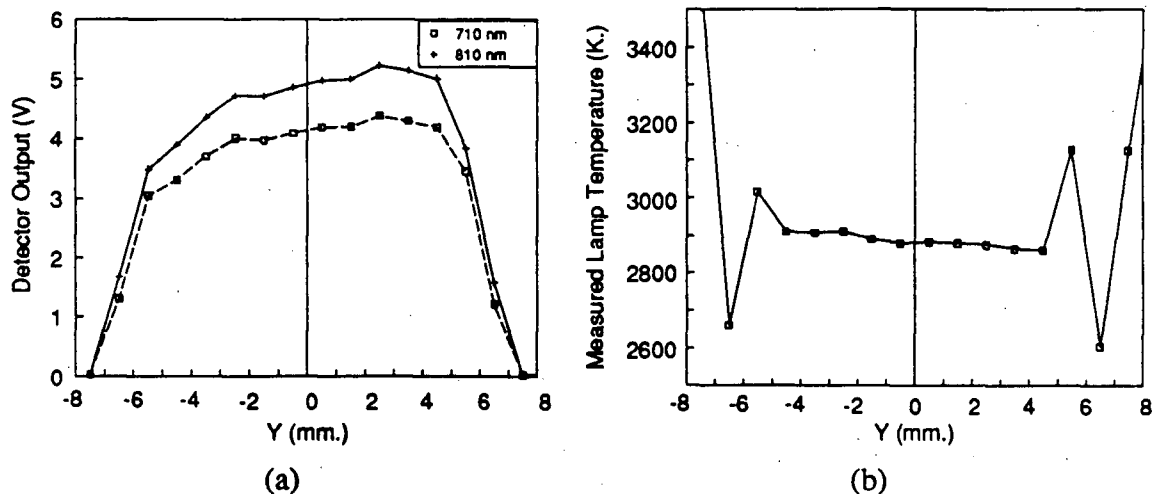


Figure 5.9 Variation in a) detector output signals and b) measured lamp temperatures across the pyrometer measuring volume. ($X_1=37.5\text{mm}$ and $X_2=90\text{mm}$).

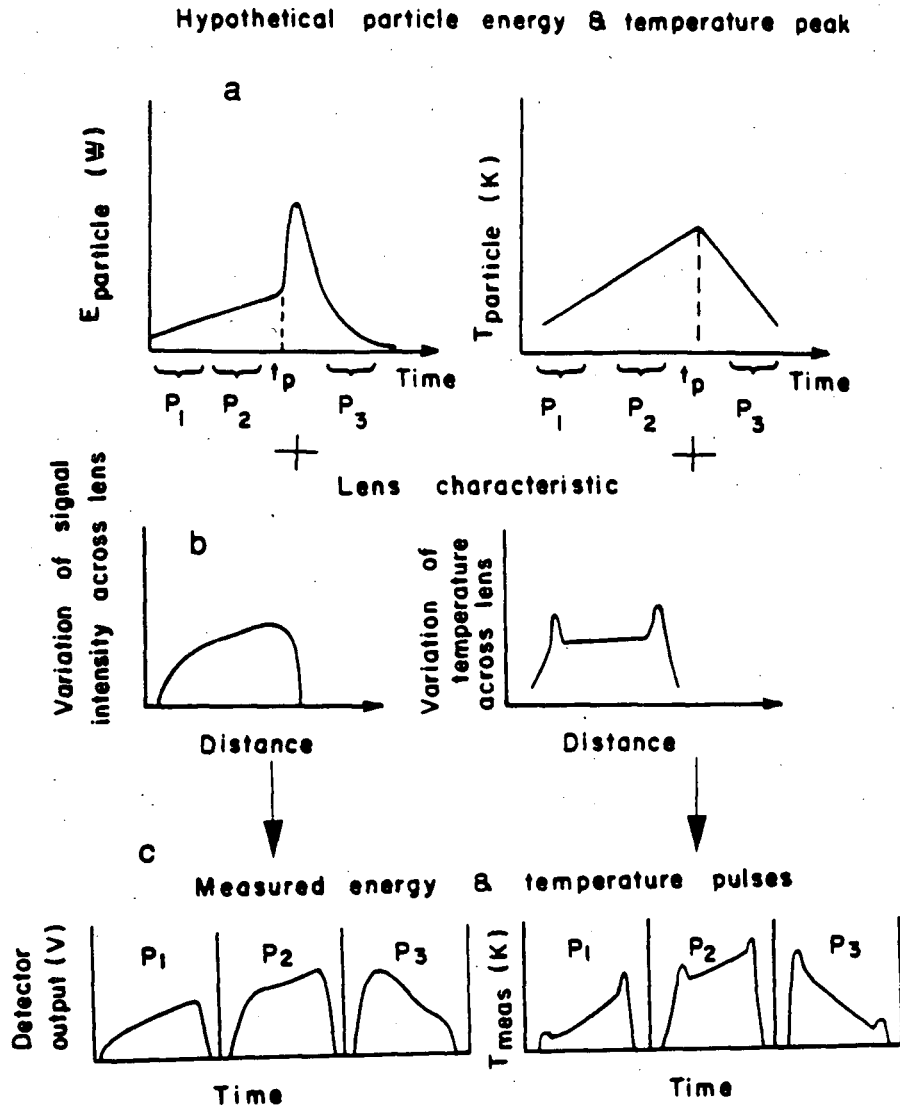
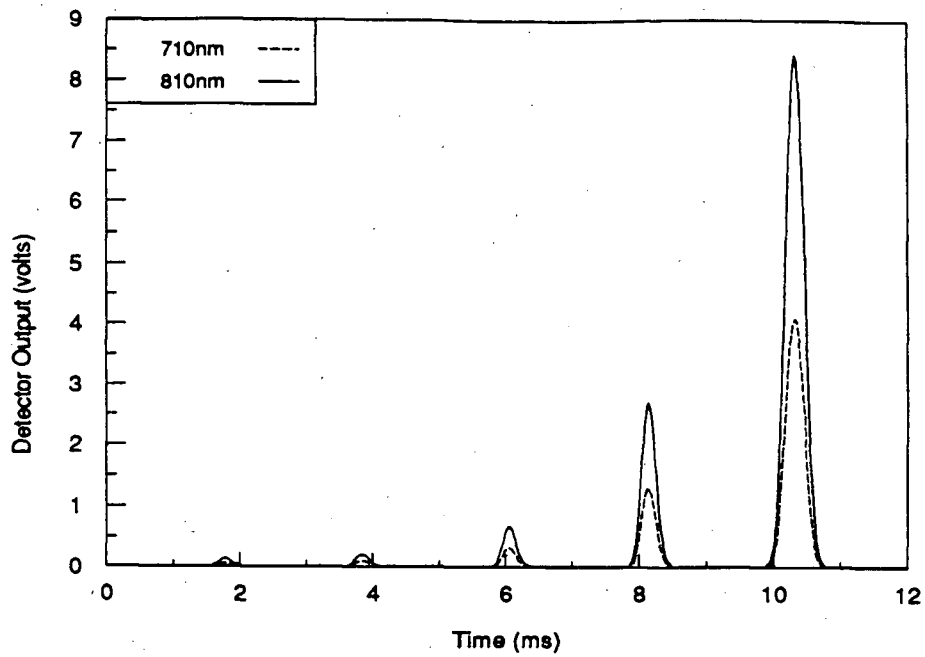
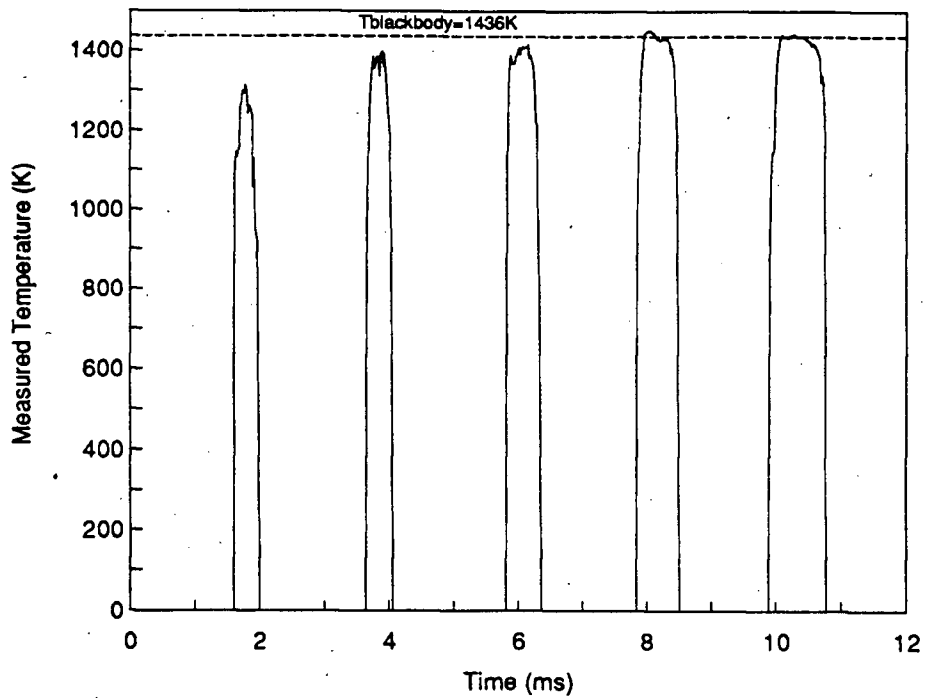


Figure 5.10 Schematic diagram of the range of different energy and temperature pulses obtainable from a single combustion peak.



(a)



(b)

Figure 5.11 Pyrometer response to a series of drilled holes in a plate rotated between the 6mm blackbody cavity and pyrometer lens at a velocity equivalent to 11ms^{-1}

CHAPTER 6

Results

6.1 Preliminary Observations-Photographs of Combusting Particles

A series of photographs were taken of the relatively pure minerals and commercial concentrates during combustion in air and oxygen. The experiments were performed to give a visual indication of the combustion phenomena, using the same stagnant, gas-filled furnace as described by Salomon de Friedberg [44]. The furnace consisted of a 400mm x 76mm ID quartz tube centred in an electrical resistance-heated "clam-shell" furnace with a 40mm wide vertical slit to facilitate viewing. The concentrates were slowly introduced into the stagnant furnace gas and photographs of the combusting particles were taken with a 35mm camera; exposure times of between 1/15 and 1/2 seconds (67-500ms) were used.

Photographs of combusting particles of 63-74 μ m galena in air and oxygen are given in Figure 6.1. The relatively high furnace temperatures of 1123 and 1023K necessary to obtain ignition in air and oxygen respectively, are consistent with those reported by Jorgensen et al. [69] and Salomon de Friedberg [44]. In air, the combusting galena particles appear as short straight low temperature streaks (typically visible for 10-30mm) which were difficult to photograph against the hot furnace background. A white fume reaction product (probably lead oxide or sulphate) was observed to form and rise slowly in the furnace. Considerable variation in the position of combustion of the individual particles was found. With oxygen, the individual combusting particles are quite different, appearing as very short, intense, high temperature bursts of light. These discrete particles often occurred together in clusters, possibly suggesting association prior to combustion. The small clouds of fume formed during reaction rapidly dispersed. Occasionally longer more intense combustion pulses were observed, which were thought due to the combustion of iron sulphide impurities (Pine Point galena-0.6-1% Fe).

The combustion of pyrite and pyrrhotite in air and oxygen is shown in Figure 6.2. The combustion behaviour of pyrite and pyrrhotite was similar, and quite distinct from that of galena. In air, the streaks become brighter (wider) until, towards the end, a sudden increase in intensity is observed. This is followed by a rapid decline in brightness with the point of extinction often coinciding with the rapid ejection of a few very small glowing particles. From the photographs it is not possible to ascertain whether the change in combustion intensity is due to changes in temperature, size or emissivity. It is estimated that the combustion streaks of 74-88 μm pyrrhotite particles in Figure 6.2b correspond to approximately 85ms of reaction (from u_{TERMINAL} Table 4.5). In air, pyrite appears to ignite more rapidly than pyrrhotite. The behaviour of both minerals is quite similar, except for a violet glow observed during the initial reaction of pyrite (see Figure 6.2a), which is thought to be due to the combustion of gaseous sulphur [118] resulting from the thermal decomposition of pyrite. In oxygen the reactions of both pyrite and pyrrhotite are very intense and usually result in disintegration of the very hot particles.

Typical photographs of the combustion of the 63-74 μm screen fraction of Sullivan concentrate in air and oxygen are given in Figure 6.3a and 6.3b. In air, the combustion appears to occur as a mixture of small explosions and low intensity streaks. Fume reaction products are observed trailing the combusting particles. Ignition was found to occur at furnace temperatures similar to those for galena. In oxygen, the Sullivan particles combust more intensely, however the general shape of the combustion streaks is quite similar. The combusting particles rapidly burn-out, terminating as small puffs of fume.

The combustion of 63-74 μm screen fraction Brunswick concentrates in air and oxygen is shown in Figures 6.4a and 6.4b. As with pyrite concentrate, a violet flame is seen during the early stages of combustion in air and many smaller combustion streaks similar to those seen with pyrite are observed. Low intensity streaks, similar to those with

galena, and the formation of lead fume were observed below the pyrite-like combusting particles. Combustion in oxygen appears to consist of violent explosions with small particles of combusting material being hurled rapidly outwards. Small amounts of fume is formed amongst the exploding particles.

6.2 AIR EXPERIMENTS

6.2.1 Classification of Particle Combustion Peaks

As indicated in Figure 5.10 the pyrometer only sees the particle for a fraction of the total time it is combusting and this signal is further distorted by the lens and instrument characteristics. It is therefore necessary to differentiate between the energy and temperature traces recorded by the pyrometer and the actual variation in thermal energy radiating from the particles during combustion. The energy and temperature traces measured by the pyrometer have thus been called combustion pulses whereas those relating to the actual particle temperature and energy have been called combustion peaks.

From the illustrative diagram given in Figure 5.10, it can be seen that the combustion pulses observed at different stages of reaction can be quite different. It was found, however, that the combustion pulses could be grouped into a series of different classifications which appeared to correspond to the different mineral species in the feed or to different physical phenomena. Five main types of pulses were classified for combustion in air. The different pulse types, their main characteristics and the mineral species or phenomena with which they appear to be associated are given in Table 6.1.

Distinctive combustion pulses which seemed to relate to the combustion of lead and iron sulphides were classified as "Type A1" and "Type A3" respectively. A range of combustion pulses with intermediate shape and temperature profiles to these, observed mainly during the combustion of the commercial concentrates, were classified as "Type A2". The "A4" and "A5" types of combustion pulse appear to correspond to different physical phenomena rather than to specific mineral species, and were often observed

superimposed on other energy pulse types. The "Type A4" pulses appear to correspond to material ejection or particle disintegration. "Type A5" pulses are observed as regular oscillations in the energy traces, which may or may not also correspond to oscillations in the calculated particle temperatures. It is thought that these regular fluctuations are due to phenomena such as droplet oscillation, rotation and pulsation. It is also possible that in some cases this could be due to electrical interference.

Notwithstanding these classifications, pulses which are indistinct, or do not appear to fit any classification, were occasionally observed. The measurement of particles which are at an early stage of ignition are sometimes difficult to classify due to the relatively low signal levels and indistinct heating rates. Impurities present in the relatively pure minerals may give spurious results as well.

6.2.1.1 Galena - "Type A1" Combustion Pulses

Typical energy traces from the two pyrometer detectors, recorded as a combusting galena particle passed in front of the pyrometer lens, together with the particle temperatures calculated from this data, are shown in Figures 6.5 and 6.6 for two different particles. Combustion pulses of this type (classified as A1) were essentially the only ones observed during the combustion of 63-74 μm and 74-88 μm galena. Figures 6.5a and 6.6a show the variation of the detector output signal with time. The shape of each pulse is quite similar to that obtained during lens calibration (see Figure 5.9a), which suggests particles of constant intensity and temperature have passed in front of the pyrometer lens. The pyrometer signals are quite noisy due to the high photomultiplier gain settings employed. The corresponding particle temperatures calculated from these data are presented in Figures 6.5b and 6.6b. For both the energy and temperature traces no smoothing of the data was performed. The particle temperatures were not calculated for detector output signal intensities of below 50 digital units ($\sim 0.12\text{V}$) due to significant

round-off errors, and therefore, the temperature traces are sometimes truncated. For the A1 combustion pulses shown, the calculated particle temperature remained relatively constant with an average value typically of between 1550 to 1650K¹ over the time period observed, which can be compared with the boiling point of *PbS* reported as 1609K [30]. The higher temperature spikes sometimes observed at the start and finish of the temperature traces are thought to be due to optical effects at the lens edge.

The significant signal level and lower calculated temperature (~1100K) on the falling edge of the pulse in Figure 6.6a suggest that particulate fume reaction products are trailing behind the combusting particles. This phenomenon was often observed. The presence of increasing quantities of low temperature fume within the viewing volume also could account for the gradual decline in the apparent particle temperature toward the end of this pulse.

Following the method outlined in Section 5.2.7.1 and Appendix 1.3, the relative change in the apparent area of the combusting galena particle shown in Figure 6.5 was calculated and the result presented in Figure 6.7. The change in apparent area has been calculated relative to the area at 7.4ms, using Equation 5.10 and the measured energy and temperature given in Figures 6.5a and b respectively. Due to the considerable signal noise, the 710nm detector output signal was smoothed prior to calculating the relative change in area. The results suggest that the apparent particle area remains relatively constant over the portion of the curve corresponding to the main energy pulse. The low intensity energy (and temperature) signal often seen trailing the A1 combustion pulses (see Figure 6.6), can result in a considerable increase in apparent relative particle area. Such results would be consistent with large quantities of optically thick reaction product trailing the particles.

¹ The accuracy of the temperature measurements depends on the several factors including the mineral species combusting but is probably in the order of $\pm 50\text{K}$ (see Section 5.2.8).

6.2.1.2 Pyrite and Pyrrhotite - "Type A3" Combustion Pulses

Typical A3 pulses observed during the combustion of 74-88 μm pyrite and pyrrhotite in air are shown in Figures 6.8 and 6.9. The detector output signals and the measured particle temperature for the two combustion pulses are initially observed to increase steadily. The heating rates are typically in the order of $1 - 5 \times 10^4 \text{K/s}$ and have been recorded from temperatures below 1800K. The maximum particle temperature achieved, 2300 to 2550K, was quite reproducible. On reaching the maximum temperature, there is a very rapid 5-10 fold increase in the measured energy followed by a rapid decline in both detector output signal and particle temperature. The observed cooling rates were initially very rapid, being typically $10 - 25 \times 10^4 \text{K/s}$, but declined rapidly with decreasing temperature. Typically, the intensities of the iron sulphide combustion pulses are 10-100 times greater than those of galena (calculated from the different gain settings used).

Examples of A3 pulses were also observed during the combustion, in air, of both the Sullivan and Brunswick concentrate and also occasionally during galena combustion. In all cases it is considered that the combustion of iron sulphides was being recorded. Figure 6.10 is an example of a A3 pulse obtained during the combustion of 63-74 μm size fraction of Brunswick concentrate in air.

Figures 6.8c, 6.9c and 6.10c show the changes in apparent relative area calculated to occur during reaction with respect to reference times of 5, 8 and 11.6ms respectively. The sudden increases in pyrometer signal appear to correspond to increases in apparent area of x5, x8 and x3 respectively. For most A3 combustion pulses, the apparent area then appears to remain relatively constant as the particle rapidly cools (Figures 6.8c and 6.10c). These large apparent area increases appear in agreement with the large hollow spheres (typically 2-3 times the feed material diameter) observed in the reaction products

of iron sulphide combustion in this study (see Section 6.5.2.1) and by several other researchers [66,81] which suggest that the sudden expansion and freezing of a thin film is occurring.

Examples of different A3 combustion pulse shapes due to recording only a portion of the overall combustion peaks are shown in Figures 6.11 and 6.12. These pulses represent the earlier period of heating prior to the rapid energy increase (see the schematic diagram in Figure 5.10). In both cases the heating rate is fairly linear at 2.7×10^4 and $1.5 \times 10^4 K/s$ respectively. The maximum temperatures of the region of linear heating of ~ 1900 and $2200K$ respectively are less than the typical maximum temperature of the complete combustion peak ($\sim 2300-2500K$). Including pulses of these types in the A3 classification tends to result in average property calculations not truly representative of the reproducibility of the results. Therefore, for the pyrite and pyrrhotite experiments, the A3 combustion pulses have been split into three sub-classifications; i) "Type A3-increasing" (A3I) corresponding to pulses recorded during the heating period only (eg Figures 6.11 and 6.12 or pulses P_1 and P_2 in Figure 5.10); ii) "Type A3", similar to the pulses shown in Figures 6.8 to 6.10, where both the energy and temperature maxima have been recorded; and iii) "Type A3-decreasing" (A3D) combustion pulses similar to that shown as P_3 in Figure 5.10, where only the period of cooling has been recorded.

Although the combustion of gaseous sulphur from the thermal decomposition of pyrite, during reaction in air, was evident in the photographs (Figures 6.1a and 6.4a), no phenomenon attributable to this was identified in the energy traces recorded by the pyrometer.

It is thought that the small energy arrest sometimes observed on cooling (see Figure 6.9a) may be related to the ejection of materials observed in the photographs. From

Figure 6.9c the small arrest appears to correspond to a transient area increase as may be expected from a few small particles being ejected and rapidly leaving the pyrometer's view.

6.2.1.3 Sphalerite

It was not possible to ignite the 74-88 μ m sphalerite particles at a furnace temperature of 1130K, in either air or oxygen. Therefore no characteristic combustion pulses of sphalerite were obtained.

6.2.1.4 Brunswick and Sullivan Concentrates - "Type A2" Combustion Pulses

During the combustion of the two commercial concentrates many combustion pulses similar to A1 (observed with galena) and A3 (associated with the combustion of iron sulphides) were recorded. A number of pulses which appear to have energy and temperature characteristics intermediate between the two also were observed and classified as "Type A2" pulses. It is thought these pulses are due to the combustion of particles which are complex minerals or agglomerates of individual grains of the different mineral species. Typical examples of A2 pulses are given in Figures 6.13 to 6.16. The pulses in this classification vary from ones quite similar to A1 to those similar to A3 combustion pulses. The combustion pulse temperatures of 1700-2300K were generally intermediate to those of A1 and A3 pulses. Many of the A2 combustion pulses have regions of relatively constant pulse temperatures of 1700-1800K over which energy maxima are also often observed, especially with Sullivan concentrate (see Figures 6.13 and 6.15). This is probably associated with the vaporisation and combustion of a cloud of volatile lead species. The energy maxima tend to correspond to a relative apparent area increases typically of 40-100%.

A2 combustion pulses with spikes of rapid energy and temperature increase are also commonly observed. Examples of this type are shown in Figures 6.14 and 6.16. Usually the sudden increase in energy and temperature occurs during a period of gradual heating and coincides with, or just precedes the temperature maximum, often in excess of 2000K. The subsequent decline in pulse signal intensity and temperature can vary from modest to very rapid. From relative apparent area calculations, such as that given in Figure 6.14c, the energy and temperature spikes often appear to be associated with a large but temporary increase in particle area. This is thought to be due to the ejection of molten material. A2 combustion pulses with characteristics of the higher intensity A3 pulses are more frequently observed during the combustion of Brunswick concentrate than with the Sullivan concentrate. This is probably due to the increased quantity of pyrite present in the former.

The heating and cooling rates of the different A2 combustion pulses varied considerably, from effectively constant temperature (similar to A1 pulses), to the very high heating rates ($\sim 5 \times 10^4 K/s$) and cooling rates ($\sim 10 - 20 \times 10^4 K/s$) seen in A3 pulses.

6.2.1.5 Material Ejection or Sparks - "Type A4" Pulses

A typical example of an A4 combustion pulse is shown in Figure 6.17. The top of the combustion peak is truncated because the pyrometer output signal (including the baseline) exceeded the +10V input limit of the A/D data acquisition board. The characteristic of this type of pulse is a short very intense energy pulse which is often superimposed on another type of energy signal and appears to be due to the ejection of material. Ejected material would be expected to leave the pyrometer field of view as a discrete unit and possibly combust violently during this period. Depending on the size of the energy pulse this might represent anything from small sparks to complete particle disintegration. Determining the true temperature, and relative changes in apparent area, is generally quite difficult due both to the very rapid changes in measured energy and to the

superposition of peaks. The measured temperature over the period of the pulse will be the area-temperature average of both it and the background. Typical temperatures for A4 pulses are 1800-3000K. A4 pulses were observed with all feed materials but appeared most commonly in the larger size fractions of the pure minerals.

6.2.1.6 Periodic Energy Fluctuations - "Type A5 " Pulses

Combustion pulses in which periodic fluctuations in the pyrometer signals were quite rare and classified as A5 pulses. Figure 6.18 shows an example of an A5 pulse, observed during the combustion of 63-74 μ m Sullivan concentrate. Each oscillation the pyrometer signal exceeds the maximum measurable voltage but in this case the results suggest the oscillations are due to apparent area changes (Figure 6.18c) and the frequency of periodic energy oscillation of the combustion pulse shown is \sim 430 Hz. The pyrometer signals were filtered with a 5kHz low pass filter, and therefore, any electrical noise at lower frequencies would not be removed.

This phenomenon was observed most frequently with pulses similar to the A1-type where combustion is occurring at a fairly low, constant temperature. The periodic fluctuations in energy are probably due to either fluctuations in particle temperature or apparent area, or both. Periodic energy and temperature fluctuations could result from several physical phenomena, such as i) periodic ejection of material, ii) oscillation of the viewed area or rotation of the particle and iii) the pulsation of the particle temperature or a gas-phase flame front.

6.2.2 Temperature Measurement Experiments

Since the individual minerals combust at different distances down the furnace, distinct types of combustion pulse often predominate at different locations. Similarly, the relative number of particles combusting at any position within the observed region of combustion varies. Owing to the small number of sampling locations and the relatively small number of combustion pulses measured at each, the main region of combustion

cannot be reliably inferred solely from the pyrometer results. Bias may also exist in the results due to the tendency to record higher intensity pulses. This was especially a problem at longer residence times where interference due to the presence of fume reaction products often made the measurement of the lower intensity combustion pulses difficult. In an attempt to overcome this problem and to define more clearly where in the furnace the particles were combusting, a series of simple measurements were made. The number of particles combusting at various points along the length of the furnace was counted. The pulses were observed on the oscilloscope screen and an attempt was made to give some distinction between those pulses which were of high intensity (in air A3 and A4) and those which were of lower intensity (mainly A1). Those pulses which exceeded the 10V full scale on the oscilloscope scale were classified as high intensity. To allow comparison of the different results, all the measurements were made at pyrometer gain settings of $G_{710}=8.23$ and $G_{810}=9.9$. This corresponds to pulses being arbitrarily considered of high intensity when the energy received by the pyrometer exceeds 10 nW. The number of counts per minute at different furnace positions was recorded. To facilitate comparison at the different feed rates, the results were normalised with the highest count rate being considered unity. The experiments should be considered as a qualitative indicator to where combustion is occurring.

Average results for the combustion pulses recorded in air, tabulated as a function of pulse classification are given in Table 6.2.

6.2.2.1 Air Experiments - Galena

A series of temperature measurements was made at different furnace distances for each of the different concentrate size fractions. The results for the combustion of 63-74 μm galena in air at the furnace temperature of 1130K are shown in Figure 6.19. The individual data points refer to the maximum particle temperature measured during each combustion pulse and the symbol refers to the pulse classification. The two curves shown

refer to the relative number of high and low intensity combustion pulses (relative combustion frequency) measured as a function of combustion distance. A1 combustion pulses were found to predominate, and the measured temperatures were quite similar ranging from ~1400 to 1650K with an overall average of 1535K (see Table 6.2). Trailing fume tails similar to that shown in Figure 6.6 were frequently observed. At the shortest measurement distance (155mm) several higher temperature A4 combustion pulses were observed. The relative frequency of combusting particle curves shown, indicate that mainly low temperature combustion occurs between ~160 and 250mm. This region is estimated to correspond to residence times of 191 and 285ms (calculated assuming the particles to be spheres of galena of the size fraction average diameter of 69 μ m). Considerable fume was observed at distances greater than 200mm. No ignited particles were seen at furnace distances below ~300mm.

The duration of the measured combustion pulses for 63-74 μ m galena in air are given in Figure 6.20a. For A1 particles the combustion pulses are typically between 8 and 15 milliseconds in length, whereas the A4 pulses are much shorter, typically less than 5ms in length. The calculated residence time for a 63 μ m spherical galena particle traversing the 14mm pyrometer viewing area is 19ms. It would be expected that the measured pulses be less than, or equal to, this calculated maximum time, as particles may be ignited for only a fraction of the time in front of the pyrometer. In reality, the measured pulse length would vary further due to variability in feed size, density (see Table 4.5) and also the variation in viewing length with radial distance across the tube. The lengths of the A1 combustion pulses are consistent with the particles typically being ignited for a longer time than viewed by the pyrometer. The shorter pulse lengths of the A4 particles are probably due to high velocity of particles (possibly produced during disintegration).

Using the computer programme outlined in Appendix 2, the apparent diameter of the combusting particles have been calculated from the pulse intensity and measured particle temperature and the results are presented in Figure 6.20b. The calculated particle diameters for the A1 pulses are typically between 60 and 200 μm with an average of $\sim 112\mu\text{m}$ (see Table 6.2). The apparent diameter of the A4 particles also appears to vary considerably, ranging from 15-220 μm . The calculated apparent diameter can only be considered qualitative due to the uncertainties and inaccuracies associated with their calculation (see Section 5.2.7.2). The particle emissivities are not known, and a value of 0.7 was used throughout. It is also probable that large over-estimates of apparent particle diameter are calculated for galena combustion due to the presence of a semi-opaque fume cloud surrounding the particle (as suggested by the larger A1 apparent diameters given in Figure 6.20b).

From Figure 6.21 the apparent particle size appears to be inversely related to the measured particle temperature. This relationship was commonly seen with the galena results and is probably due to the relatively low combustion temperature and the large quantities of reaction fume produced. Since the temperature measured by the pyrometer is an area weighted average of all the objects in view, larger quantities of low temperature fume surrounding a particle will result in lower average temperatures and larger apparent areas. Conversely, as the particle temperature increases, the energy resulting from the fume would become an increasingly smaller proportion of the total and an increasingly accurate apparent area (and temperature) calculation should result.

6.2.2.1.1 Galena - Effect of Particle Size

The effects of particle size on the combustion of galena, in air, of size fractions, 74-88, 88-105 and 105-125 μm are presented in the series of Figures 6.22 through 6.26. From the Figures and Table 6.2 it appears that there is relatively little difference between the results for the different size fractions examined. Combustion appears to be located at

similar furnace positions and the average (see Table 6.2) and individual temperatures of the different combustion pulse classifications appear not to vary greatly with size fraction. The type and relative frequency of the different combustion pulses did, however, alter significantly with feed size.

The relative combustion frequency curves for the different size fractions in Figures 6.19, and 6.22 to 6.24 indicate that the main zones of combustion are located at 160-280, 160-270, 120-300 and 150-360mm respectively for the size fractions increasing from 63-74 to 105-125 μ m. Low intensity (A1) combustion pulses with temperatures between 1400 and 1700K predominate in all cases. The maximum number of combustion pulses were recorded at 225, 197, 233 and 315mm respectively and suggest a slight trend towards combustion occurring at increasing distances with increasing size fraction. The calculated residence times of the particles, due to their increased size, however suggest a decrease in the reaction time with increasing size fractions. The combustion distances of the observed maximum number of combusting particles are calculated to correspond to residence times of 277, 209, 190 and 205ms for mean sizes of 68, 82, 96 and 116 μ m respectively (see Table 4.5). From Table 4.3 it can be seen that the average particle size for the different screen fractions of galena differ considerably from the mesh size. The much larger range of particle sizes in each size fraction would tend to cause some overlap of results. However, an increasing reaction time for the larger size fraction would still be expected.

The measured temperatures and types of combustion pulses recorded with the different size fractions appeared to fit into two groups. For the 74-88 μ m and 63-74 μ m size fractions the results are quite similar being predominantly the low temperature A1 type. The measurements for the 88-105 and 105-125 μ m are also similar, with more higher intensity combustion pulses being recorded than with the smaller size fractions. The proportion of high intensity pulses increases with increasing particle size, however

even with the largest size fraction they represent only a small fraction of the total. In all cases the high intensity combustion pulses were observed at the shorter combustion distances and were a mixture of A4, A3 and a few A2 pulses with temperatures of between 1800 and 2400K. The increasing number A3 pulses observed with increasing size fraction suggest increasing quantities of iron sulphide impurities are present in the larger size fractions. However, the quantity of iron (see Table 4.1) only increases from 0.6% (63-74 μm) to 1% (105-125 μm).

The average pulse temperature results for the different size fractions are presented in Table 6.2 and Figure 6.25a. The average temperatures measured for the individual combustion pulse types were similar for all the size fractions examined. The average temperatures of the A1 and A3 combustion pulses are ~1450-1600K and ~2200-2300K respectively. The large variation in the A4 pulse temperatures is also apparent.

From Figure 6.25b the average measured pulse lengths appear relatively independent of feed size, and except for the A4 combustion pulse, independent of pulse type. Most of the A1 and A3 combustion pulses are between 10 and 20ms, with their relatively long duration suggesting that only a portion of the total combustion peak is generally recorded. The high intensity A4 pulses are generally much shorter (<8ms). Also shown in Figure 6.25b is a series of lines indicating the calculated maximum pulse lengths for galena particles of the screen fraction lower size limit. By virtue of their higher terminal velocities (see Table 4.5), the calculated maximum pulse lengths decreases steadily with increasing feed size from 19ms for a 63 μm particle to ~10.3ms for a 105 μm particle. It is possible that the over-lap of material size in the different size fractions, and the large quantities of fines present (see Table 4.3) are partially responsible for the similar range of pulse lengths measured with all the screen fractions.

No specific trend in the apparent particle diameters calculated for the different galena size fractions is apparent from Figure 6.25c. The apparent diameters are similar, with those determined for the different pulse types mostly being between 50 and 200 μm . The averages for the A1 combustion pulses were typically larger at ~100-140 μm than those for the A3 combustion pulse at ~85 μm . Generally the reacting particle sizes measured are comparable with those of the feed material. The greater apparent diameter for A1 combustion (galena) is probably due to the presence of reaction fume. The standard deviation of the groupings indicate a large spread of results especially for the A4 combustion pulse classification. The apparent diameters calculated for the individual A4 combustion pulses varied from 10 to 300 μm . This large variation is thought to be due to both the ejection of small sparks and the total disintegration of combusting particles being observed.

The relationship between the calculated apparent particle diameter and the pulse temperature for the different size fractions indicates an inverse proportionality especially for the low temperature A1 combustion pulses. This is similar to that observed with the 63-74 μm size fraction shown in Figure 6.21. The apparent particle size versus particle temperature for the 105-125 μm size fraction is shown in Figure 6.26. The generally larger apparent size of A1 classification particles especially at temperatures below 1400K is apparent. The presence of an optically thick reaction product is clearly seen in the furnace during the reaction, which along with the high vapour pressure of both the *PbS* reactant and *PbO* product indicates the importance of lead species vaporisation in the reaction of galena. Experience suggests that those combustion pulses recorded with a high background signal exhibit low pulse temperature. The A3 combustion pulses are mostly of temperatures between 1700-2400K and their apparent size appears relatively independent of temperature. This would be consistent with the A3 combustion pulses

being due to the combustion of iron sulphides; considerably less fume would be produced which, in conjunction with increased particle temperature, would reduce the energy component from the fume to a very low level resulting in a smaller error.

With the 88-105 and 105-125 μm size fractions, single or multiple spiked pulses are often observed superimposed on the flat A1-type energy trace, an example of which is given in Figures 6.27. The energy spikes are 0.5-2ms in duration, but due to the signal noise it is difficult to identify transient temperature increases corresponding to these energy spikes. It is probable that the energy spikes are due to the ejection of molten material.

6.2.2.2 Air Experiments - Pyrite and Pyrrhotite

For both pyrite and pyrrhotite of the 74-88 μm size fraction the combustion pulses observed were almost exclusively of the A3 type as indicated in Figures 6.28 and 6.29. For the results reported in Table 6.2, the A3 combustion pulses were split into three sub-classifications, "A3-Increasing" (A3I), A3 and "A3-decreasing" (A3D), as described earlier in Section 6.2.1.2. The shape and maximum temperature recorded for the A3 combustion pulses were quite reproducible, with the mean maximum temperatures being 2392 and 2395K respectively for pyrite and pyrrhotite pulses recorded (see Table 6.2). The average temperatures of the A3I and A3D sub-classifications tended to be lower with more scatter due to these particles leaving or entering the pyrometer's view at a temperatures below the peak value. In Figures 6.28 and 6.29, the curves for the relative frequency of low intensity combusting particles refer mainly to the A3I and A3D pulses. As may be expected, a greater number of A3I pulses were observed at the shorter reaction times and a larger number of A3D pulses were observed at longer reaction times.

The major difference between pyrite and pyrrhotite combustion in air was the location in the furnace of the main region of combustion. Pyrite was observed to combust at 70-170mm whereas pyrrhotite combusted at between 110 and 290mm. Accounting for

the difference in density these combustion zones correspond to calculated residence times of 95-220ms and 147-385ms, for pyrite and pyrrhotite respectively. From Figure 6.30, the average pulse lengths are mostly between 10 and 22ms. The calculated maximum pulse lengths of 19.8 and 20.3ms for pyrite and pyrrhotite (82 μ m spheres) respectively are in reasonable agreement with the measured results.

The calculated apparent diameters of the individual particles are typically between 40 and 150 μ m. Due to the apparent expansion observed during combustion, both unexpanded and expanded particles are recorded. To be consistent, wherever possible the diameter of the particle before expansion has been considered. As a result, the apparent diameters of the A3 and A3I particles (generally unexpanded), given in Table 6.2 and Figure 6.30c, were less than those calculated from the A3D combustion pulses (generally expanded). From Table 6.2 the average diameter of the A3 and A3I particles are, for pyrite, 55 and 53 μ m respectively, and for pyrrhotite 69 and 70 μ m respectively are comparable with the average particles sizes of the feed materials (Table 4.3) of 85 and 80 μ m for pyrite and pyrrhotite respectively. The apparent particle diameter calculated from the pyrrhotite A3D combustion pulses was 125 μ m, with that for pyrite 69 μ m. The particle expansion calculated from the individual particles where combustion both before and after expansion was recorded is plotted against an arbitrary data number in Figure 6.31. For the individual particles a similar level of expansion, of 1.8-3.5 times, was observed for both pyrite and pyrrhotite combustion. From Table 6.2 the average particle expansion was 2.57 and 2.65 times respectively for pyrite and pyrrhotite. The similarity of the apparent particle expansion calculated from A3 pulses recorded during the combustion of both galena and Brunswick concentrate is also shown.

The calculated apparent diameters for pyrite and pyrrhotite do not appear dependent on measured particle temperature.

6.2.2.3 Air Experiments - Sullivan Concentrate

The particle type and temperature results for the combustion of 63-74, 74-88, 88-105 and 105-125 μm size fractions of Sullivan concentrate in air are given in Figures 6.32 to 6.33. For the commercial concentrates, several different types of combustion pulses are observed. Some pulses characteristic of the individual mineral species (ie A1 and A3 pulses) are observed, as well as a large number of A2 combustion pulses.

For all the size fractions combustion occurred at a similar location between ~100 and 300mm with many A1 pulses being observed. The location and temperatures of the A1 combustion pulses are similar to the results for galena, with temperatures mainly between 1350 and 1650K (see Table 6.2). At shorter combustion distances, a number of low intensity pulses were recorded, possibly due to the combustion of smaller particles which have broken free of the agglomerates. High intensity pulses are only a very small fraction of the total number of recorded pulses, however, unlike galena, most of the high intensity pulses were recorded at a longer combustion distances of between 200 and 300mm and their frequency, as a fraction of the total, tended to decrease with increasing feed size. These pulses were generally of the A2 or A3 type, with the A2 combustion pulse probably due to larger agglomerate combustion. The longer combustion distances of the A3 pulses are similar to those for pyrrhotite, the predominant iron species present in the Sullivan concentrate.

Due to the large range of particle sizes and densities it is difficult to calculate the residence times of the commercial concentrate particles accurately, and therefore the calculation can be little more than a guide to the actual residence times of combusting particles. When presented, residence times for the commercial concentrates were calculated considering the individual particles to be spheres of galena.

The disintegration of agglomerates is suggested by the numerous small streaks in Figure 6.3. The increasing number of smaller particles would tend to reduce the number of larger particles, as a fraction of the total, and therefore their relative combustion frequency (as observed experimentally in Figures 6.32 to 6.33). Even at their most frequent, with the 63-74 μm size fraction, higher intensity pulses represent only 7.5% of the total. For the two largest size fractions no A3 and A4 pulses and only a few higher intensity A2 combustion pulses were recorded. It is also possible that the larger number of high intensity combustion pulses observed with the smallest size fraction is due to a greater number of individual iron sulphide grains (see Figure 4.8) being present.

The average pulse lengths for the different pulse types presented in Figure 6.34b are mostly between 10 and 20ms and again suggest similar size particles are being measured with all the size fractions. Again, with increasing particle size an increasingly larger proportion of the measured pulses become longer than the calculated maximum particle pulse length.

The calculated apparent particle diameter for the different size fractions as pulse type averages are given in Figure 6.34c. The average calculated apparent particle diameters appear to correlate with the pulse classification but does not seem to depend on the concentrate size fraction. The diameters of most of the individual particles were between 50 and 200 μm . However, some A1 pulses with very large apparent diameters (500-700 μm) and pulse temperatures of below 1400K were recorded, mainly with the 74-88 μm size fraction. The average measured particle diameters tended to decrease in the order A1 to A2 to A3 which also reflects the order of increasing particle temperature. The calculated apparent particle diameter versus measured particle temperatures for the 63-74 μm size fraction, presented as an example is given in Figure 6.35. The observed increase in apparent particle diameter with decreasing combustion temperatures for the

A1 pulses below ~1600K is similar to the results for galena. There appears little temperature dependence for both the A2 and A3 particles of measured temperature greater than 1700K.

6.2.2.4 Air Experiments - Brunswick Concentrate

The temperature and pulse type classifications for the combustion of Brunswick concentrate of size fractions between 63 and 125 μ m are given in Figures 6.36 to 6.37. A greater number of high temperature combustion pulses, are observed with Brunswick concentrate than Sullivan. For the 63-74 μ m size fraction, shown in Figure 6.36a, the main region of combustion is located between 60 and 140mm down the furnace, with an almost equal number of high and low intensity pulses being observed. At longer distances, (140-210mm), a smaller number of predominantly low intensity A1 pulses were recorded. The high intensity pulses were mostly of the A3 type, with combustion temperatures of 2000 to 2500K. The location of the zone of high intensity combustion pulses is similar to that for pure pyrite, which suggests that the combustion of predominantly pyrite particles is being observed. The temperature and location of the later A1 combustion pulses suggest that the combustion of predominantly galena particles is being observed. The difference between the combustion behaviour of Brunswick and Sullivan concentrate appears consistent with the increased quantity of iron sulphide (and corresponding decrease in galena) and its presence as pyrite, rather than pyrrhotite, in the Brunswick concentrate. The A2 combustion pulses observed with Brunswick concentrate tended to have more characteristics of the higher intensity A3 pulses than those recorded with Sullivan concentrate.

The proportion of high intensity combustion pulses recorded with Brunswick concentrate decreased as a fraction of the total with increasing feed size. Very few A3 combustion pulses were observed with the 105-125 μ m size fraction but A2 pulses with particle temperatures of between 1600 and 2200K were recorded with increasing

frequency. A similar combustion zone, between 80 and 200mm, was observed with each of the different size fractions. As with Sullivan concentrate, particle disintegration is suggested by the multiple combustion streaks observed in the time exposure photographs (Figure 6.4). From Figures 6.36 and 6.37 it appears that the location of the maximum number of high intensity combustion pulses moves to longer combustion distances with increasing feed size, from ~100mm for the 63-74 μ m size fraction to ~180mm for the 105-125 μ m size fraction.

From Figure 6.38a the average reaction temperatures of the various pulse classifications were similar for all the size fractions examined. The temperature ranges of the different pulse types appeared to be clearly defined with averages of ~1600, ~1800 and ~2200K for the A1, A2 and A3 combustion pulses respectively. Relatively few A4 combustion pulses were recorded (except with the 74-88 μ m size fractions). For the A4 pulses, measured temperatures were typically 1700 to 2000K.

The average reaction pulse lengths for the different size fractions and pulse classifications are generally quite similar (see Figure 6.38b) being mostly between 10 and 20ms. This, along with the combustion pulse shape, indicates that only a portion of the overall combustion peak is being recorded. From the results in Figure 6.38c, there does not appear to be a strong dependence of the average calculated particle diameters on feed size, with most of the average particle diameters for the different pulse classifications being 50 and 120 μ m. The dependence of the apparent particle diameter on either particle temperature or pulse type appears slight (see Figure 6.39).

Although the chemical analysis of the feed materials (Table 4.1) suggest little difference between the various size fractions, the number of A3 combustion pulses observed declined rapidly with increasing feed size. It is probable that the number of agglomerates consisting predominantly of pyrite decreases with increasing feed size due to the greater number, and random association of the different mineral particles in the

individual agglomerates. The combustion of large quantities of smaller particles which have become detached from the agglomerates would explain the apparently similar combustion distances at which all the size fractions combust. The presence of large quantities of smaller combusting particles, would also tend to obscure the combustion of the smaller number of original larger particles.

The average calculated particle expansion of the A3 pulses recorded with the 63-74, 74-88 and 88-105 μm size fractions of Brunswick concentrate given in Figure 6.31 are mostly between $\times 1.5$ and $\times 3.5$, with average particle expansions of $\sim \times 2.3$ in each case. The similarity of these expansions to the $\sim \times 2.5$ expansion typically observed with pyrite suggests the combustion of primarily pyrite grains is being observed.

6.2.3 Air Experiments - Heating and Cooling Rates

The measured heating and cooling rates of the different combustion pulses were determined graphically from the particle temperature-time plots. The accuracy of the measurements was estimated to be about $\pm 0.5 \times 10^4 \text{ K/s}$. A considerable variation exists between the heating and cooling rates of the different pulse classifications. The measured heating and cooling rates of the individual A1, A2 and A3 combustion pulses are given in Figures 6.40 to 6.42. For each of the different pulse types, the individual data points, have been plotted against an arbitrary, incremental counter.

From the combustion pulses present in Section 6.2.1 it is clear that the heating and cooling rates are seldom linear. As a first attempt at quantifying the results the heating and cooling rates have been taken as an average of the period recorded. Although this data is useful in categorising the overall combustion pulses there is too much variation in measurements of the individual particles to use averaged data directly when modelling individual particles, and in such cases the original combustion pulses should be examined.

For the A1 combustion pulses, the combustion temperatures remained relatively constant, with most heating rates therefore of zero. The results appear as a blur on the lower axis of Figure 6.40a. Measurable heating and cooling rates were observed for a smaller number of A1 combustion pulses. The heating and cooling rates recorded were mostly less than $\sim 3 \times 10^4 \text{ K/s}$ and $\sim 5 \times 10^4 \text{ K/s}$ respectively. These results, along with the maximum pulse temperature of $\sim 1600\text{K}$ clearly link the combustion of galena to a mechanism in which the temperatures (and probably rate) are limited by *PbS* vaporisation (boiling point 1609K [30]).

The heating and cooling rates for the A3 combustion pulses are given in Figure 6.41. Although considerable scatter exists in the results, a range of heating and cooling rates, distinct to A3 combustion pulses, are visible. The measured heating rates were mostly $\sim 1 - 5 \times 10^4 \text{ K/s}$ for all the feed materials. In the case of galena, however, most A3 heating rates were below $3 \times 10^4 \text{ K/s}$. The cooling rates recorded for the A3 combustion pulses were similar, (see Figure 6.41b), with most rates between 8 and $20 \times 10^4 \text{ K/s}$. The heating and cooling rates are similar for both pyrite and pyrrhotite.

The measured heating rates of the A2 combustion pulses recorded show considerable variation and are plotted in Figure 6.42a. The measured heating rates varied from 0 to $\sim 4 \times 10^4 \text{ K/s}$; with a considerable number of particles of relatively constant combustion temperature. The cooling rates of the A2 combustion pulses (see Figure 6.42b) also vary considerably from 1 to $10 \times 10^4 \text{ K/s}$, but most were $< 5 \times 10^4 \text{ K/s}$. Little difference was apparent between the results for either Brunswick or Sullivan concentrates. As suggested by the pulse classification, the heating and cooling rates of the A2 combustion pulses tend to range between those observed with the A1 and A3 combustion pulses.

It was quite difficult to determine accurate heating and cooling rates for the A4 combustion pulses. Of the few for which it was possible to calculate the heating and cooling rates, considerable uncertainty exists, due to the very large temperature changes and very short duration of the pulses from which they were obtained. Both, the measured heating and cooling rates varied considerably between extremes of 0 and $100 \times 10^4 K/s$, but were most commonly ~ 10 to $30 \times 10^4 K/s$.

6.2.4 Summary of Results of Air Experiments

A summary of the results of the air series of experiments is given in Table 6.3.

6.3 OXYGEN EXPERIMENTS

A new series of combustion pulse classifications was necessary to adequately describe the more intense reaction and particle disintegration observed during combustion in oxygen. The characteristics of the four different oxygen combustion pulse classifications are detailed in Table 6.4. As in the case of air, combustion pulses corresponding to galena combustion (O1), pyrite/pyrrhotite combustion (O3), agglomerate combustion (O2) and energy spikes (O4) were identified. "T" and "S" sub-classifications referring to characteristic combustion pulses with twin or multiple energy peaks, are also given in Table 6.4 but these have not generally been identified in the Figures. A number of pulses having "Air Type" characteristics were also observed during combustion in oxygen.

The rapid reaction of the minerals in oxygen makes the distinction between high and low intensity pulses less meaningful. Complete combustion often occurs in times shorter than the pyrometer measurement period. Unfortunately, however, it was not possible to measure a sufficiently large range of particle temperatures (energy) using a single pyrometer gain setting to record the complete thermal history of a given particle.

6.3.1 Oxygen Combustion Pulse Classification

6.3.1.1 Galena Combustion - "Type O1" Pulses

Examples of O1 combustion pulses commonly observed during the combustion of galena in oxygen are given in Figures 6.43 and 6.44. In most cases the pulses had relatively short pulse lengths, typically of less than 10ms, with maximum temperatures of ~1800 and 2400K. These temperatures are higher than the 1500-1700K recorded with the analogous A1 combustion pulses and, unlike the air pulses a period of constant combustion temperature was seldom observed. The moderate maximum temperatures and rapid rates of reaction often allowed the complete thermal history of the particle (above ~1100K) to be recorded. The particles are generally observed to heat and cool very rapidly, typically at rates of $\sim 10 - 90 \times 10^4 \text{K/s}$ and $10 - 40 \times 10^4 \text{K/s}$ respectively. An arrest in the measured particle energy and temperature was generally observed during heating resulting in an O1T (twin) combustion pulse sub-classification (see Table 6.4). As observed with the O1T combustion pulses in Figures 6.43 and 6.44 the second of the energy maxima is generally the larger. The initial arrest generally occurs at a temperature of 1800-1900K and the peak temperatures are typically ~2050 to 2400K.

The rates of energy and temperature change observed with O1(T) combustion pulses are extremely high. Due to the finite response time of the pyrometer and the large quantities of reaction fume probably produced, the accuracies of the measured energies and temperatures calculated during the periods of rapid energy increase and decrease are open to question. Reservations, therefore, also exist as to the validity of the relative changes in the apparent particle area calculated during these periods. Figure 6.44c presents the relative changes in apparent area calculated from the combustion pulse energy and temperature traces. The change in area has been calculated relative to that at 4ms and suggests that during the period of rapid energy increase a dramatic decrease ($\sim \times 20$) in apparent area occurs. The initial energy (and temperature) maximum results in

only a small transient peak corresponding to a relative apparent area $\sim x5$ that of the higher intensity second energy peak. The results strongly suggest that the rapid formation of large quantities of fume is occurring giving considerable errors in the relative apparent area calculations. In consequence, further relative apparent area calculations for the lead concentrates are not presented.

It is probable that the first energy and temperature arrest relates to the initial disintegration and intense lead sulphide volatilisation as the temperature of the particle reaches the boiling point of *PbS* (1609K). The subsequent more intense combustion maximum then relates to the combustion of the resulting cluster of smaller particles, as seen in Figure 6.1b.

Galena combustion pulses with a number of energy spikes, suggesting several material ejections were sometimes observed, and classified as sub-type O1S.

6.3.1.2 Pyrite and Pyrrhotite Combustion - "Type O3" Pulses

The combustion of pyrite and pyrrhotite in oxygen was similar and characterised by very intense and high temperature reactions (see Figure 6.2c). Typical examples of the combustion pulse, classified as "type-O3" are given in Figures 6.45 and 6.46. The energy pulse shape is characterised by an increasingly rapid rate of energy rise, up to the maximum, followed by an equally rapid decline in pulse energy. Maximum peak temperatures were generally 3100 to 3300K and quite reproducible. Due to the low gain settings used it was not possible to record the particle temperatures below ~ 2000 K. The combustion times appears much greater than for galena combustion in oxygen. Longer pulse lengths are typically 10-14ms in length and generally truncated suggesting a considerably longer combustion time. The measured heating and cooling rates are high, typically $10 - 50 \times 10^4$ and $\sim 10 - 70 \times 10^4$ K/s respectively, and often relatively linear.

For many of the combustion pulses the energy increase terminates in an almost instantaneous, typically 2-fold increase in energy which suggests that particle disintegration or material ejection is occurring (Figure 6.46). Twin energy spikes (O3T) such as observed in Figure 6.46 are relatively uncommon; however, the discrete decreases in apparent particle area after each sudden energy increase suggests that material ejection is occurring.

The results for the combustion pyrite and pyrrhotite in oxygen were indistinguishable except for the presence of a small energy spike at the beginning of the pyrite energy pulse. These energy spikes typically result in a temperature spike with a maximum of ~2400-3000K. The temperature at which this phenomenon begins was not established due to the very low signal intensities. This phenomenon is probably due to the combustion of sulphur gas resulting from the thermal decomposition of the pyrite.

6.3.1.3 Brunswick and Sullivan Concentrate Combustion - "Type O2" Pulses

During the combustion of the commercial concentrates in oxygen the number of identifiable pure mineral combustion pulses (O1 and O3) observed was considerably less than for combustion in air. Most pulses were grouped in a O2 classification which encompassed pulses having intermediate characteristics to the pure mineral species. The pulse shape of this classification group was not clearly defined and no dependence on feed material size was apparent.

A typical example of an O2 pulse recorded during the combustion of the Sullivan concentrate is given in Figures 6.47. For Sullivan the temperatures measured were mostly similar to those for galena at ~1800-2600K, however some O2 combustion pulses of temperature 2600-3600K were also recorded. The combustion pulses were typically 5 to 10ms in duration and therefore longer than those of galena. Large energy peaks without corresponding temperature perturbation, such as seen in Figure 6.47 are often observed

with Sullivan O₂ combustion pulses. The results suggest a transient change in area is occurring as would be expected with intense vaporisation and the combustion of lead species in a cloud. Similar to the case for galena (see Figure 6.43c) interference due to fume reaction products appeared to be considerable and therefore considerable error probably exists in particle temperatures calculated at low signal intensities and the calculated changes in relative area during combustion. An example of an O₂ combustion pulse recorded during the combustion of Brunswick concentrate is given in Figure 6.48. The combustion peaks were often very acute suggesting material ejection is occurring. A large range of maximum temperatures between ~2200 to 3200K were recorded and the average for the Brunswick concentrate combustion pulses was higher than for Sullivan. Similarly, the Brunswick O₂ combustion pulses were, at 8-12ms duration, typically longer than those of Sullivan, again probably indicating the higher concentration of iron sulphide present in the particles.

Figure 6.49 is an example of multiple spike combustion pulse, classified as O₂S, commonly observed during combustion of both Sullivan and Brunswick concentrates in oxygen and are probably due to the combustion of ejected material.

The measured heating and cooling rates of the O₂ combustion pulses recorded with both concentrates were typically $\sim 10 - 50 \times 10^4 K/s$. The relatively low and constant cooling rate after ejection, from the combustion pulse in Figure 6.48 of $\sim 7.5 \times 10^4 K/s$ suggest reactions have not ceased completely.

6.3.1.4 Material Ejection and Sparks - "Type O4" Pulses

A considerable number of very short (<4ms) high intensity combustion pulses, classified as "O4" pulses, were recorded during the combustion of all the feed materials. These are due to the combustion of ejected material and typically appeared similar to a single peak shown in Figure 6.49 with peak temperatures ranging from 2000-3600K and suggests the combustion of both lead and iron sulphides materials is being observed. It is

probable that the accuracy of the measured temperature is poor due to the very high rates of signal change which typically correspond to heating and cooling rates varying from $\sim 0 - 100 \times 10^4 K/s$.

6.3.2 Temperature Measurement Experiments for Combustion in Oxygen

6.3.2.1 Galena

The temperature measurements for the combustion of 63-74 μm size fraction galena in oxygen are presented in Figure 6.50, and as averages in Table 6.5. The main region of combustion, located between 70 and 150mm, is earlier than observed in air (160-260mm). Mostly the pulses were of the O1-type with relatively low combustion temperatures ranging from 1700 to 2400K. Those combustion pulses where a single peak temperature maximum was discernible were more reproducible, with temperatures typically between 1950 and 2150K. A few higher temperature combustion pulses were recorded at the start of combustion at ~ 72 mm. These were mainly O3 and O4 pulses; possibly suggesting early disintegrations, or the combustion of iron sulphide impurities.

Temperature measurements for the 74-88 and 105-125 μm size fractions are given in Figure 6.51. Again, in both cases, primarily O1 and O1T combustion pulses of temperatures between 1700 and 2400K were recorded. Similar to the results for air, spiked combustion pulses (O1S) suggesting material ejection and high intensity pulses (see relative frequency of combustion particle curves) were more common at larger size fractions. The main region of combustion is similar for the two smaller size fractions but extends to longer combustion distances (100-260mm) for the 105-125 μm size fraction.

From the average results in Figure 6.52, the O1 pulse temperatures were similar for the 63-74 and 77-88 μm size fractions, at 2004 and 2036K respectively, but increased to 2319K for the 105-125 μm size fraction. The large difference between the O1 and O3 pulse temperatures is also apparent. The combustion pulse lengths are generally less than

10ms, and appear to increase slightly with feed size but seem relatively independent of pulse type. In all cases the maximum pulse lengths are considerably shorter than those calculated. This information and the apparent increase in pulse length with increasing particle size suggest that many complete combustion peaks are being recorded.

The calculated apparent particle diameter of different galena feed sizes reported in Figure 6.52c are between 15-75 μm and relatively independent of pulse classification. The calculated apparent diameters do however appear to decrease with increasing feed size from an average of $\sim 50\text{-}60\mu\text{m}$ to $\sim 30\mu\text{m}$ for the 63-74 μm and 105-125 μm screen fractions respectively. These results conflict with the observed increasing pulse lengths which suggests that particle size is increasing with increasing feed size.

An inverse relationship between the calculated particle diameter and measured particle temperature was observed in oxygen (as with air) for all the size fractions, as shown from the results for the 63-74 μm size fraction presented in Figure 6.53. This relationship however persisted up to temperatures in excess of 2400K which is considerably higher than $\sim 1700\text{K}$ in air. The calculated particle diameters of the O₃ combustion pulses typically appeared relatively independent of combustion temperature.

The measured heating and cooling rates for the different size fractions of galena combusting in oxygen are given in Figure 6.54. The measured heating rates varied considerably, ranging between $10 - 100 \times 10^4 \text{ K/s}$. The results suggest that the measured heating rates tend to decline with increasing size fraction. This is possibly due to the larger thermal mass and smaller surface area to volume ratio. The measured cooling rates were mostly between $10 - 50 \times 10^4 \text{ K/s}$. The average cooling rates do not appear strongly dependent on feed size.

6.3.2.2 Pyrite and Pyrrhotite

The temperatures and main region of combustion recorded for pyrite and pyrrhotite in oxygen are given in Figures 6.55. The combustion pulses recorded were almost

exclusively of the O₃ classification detailed in Table 6.4. Pyrite combustion occurred over a much narrower zone and at much shorter combustion distances, between <40 and 90mm, than with pyrrhotite, where combustion is mainly located between 80 and 230mm. Unlike galena these regions of combustion are only slightly earlier than combustion in air. The temperatures measured for both pyrite and pyrrhotite were, however, considerably hotter than combustion in air and again quite reproducible at between ~3000 and 3400K. As indicated in Figure 6.56, the average temperatures for the O₃ combustion pulses were 3174 and 3232K for pyrite and pyrrhotite respectively.

The O₃ combustion pulses were of between ~2 to 16ms duration, with averages of 8.2 and 7.3ms for pyrite and pyrrhotite respectively (see Figure 6.56) and appeared mostly to be only a fraction of the complete combustion peak. The pulse lengths are typically less than the ~15ms average for combustion in air and considerably shorter than the calculated maximum pulse length of ~21ms.

The calculated apparent particle diameters for the O₃ combustion pulses are quite similar for both pyrite and pyrrhotite, typically being between ~40 and 80 μ m. From Figure 6.56 the average apparent O₃ particle diameters of 58 and 60 μ m respectively for pyrite and pyrrhotite in oxygen, are quite similar to the averages for air of 55 and 69 μ m. This gives some credibility to the apparent diameter calculations, at least for the iron sulphides and also suggests significant particle disintegration does not occur prior to reaction. Similar to the case for air there is also no apparent correlation between the calculated particle diameters and the measured particle temperatures.

Unlike combustion in air, large and permanent apparent particle expansions were not observed during the combustion of pyrite or pyrrhotite in oxygen. For only a few particles were regions of both heating and cooling observed allowing apparent area increases to be calculated. In these cases transient changes in particle diameter of x0.4 to

1.7 were measured. As seen in Figures 6.45 and 6.46 the transient increase in particle area corresponds to the position of maximum pulse temperature and energy suggesting that particle disintegration is being recorded.

The measured heating and cooling rates of the O3 combustion pulses recorded with pyrite and pyrrhotite are given in Figure 6.57. The measured heating rates varied enormously from the extremes of $\sim 1 - 90 \times 10^4 \text{K/s}$, but for both pyrite and pyrrhotite most heating rates were between $10 - 40 \times 10^4 \text{K/s}$. Cooling rates similarly ranged considerably, generally being between $10 - 50 \times 10^4 \text{K/s}$. Individual pulses with measured cooling rates of $> 100 \times 10^4 \text{K/s}$ were, however, recorded. The heating and cooling rates were often not constant, tending to increase on heating towards, and decrease on cooling after, peak temperature. Close to peak temperature instantaneous heating and cooling rates of up to $200 \times 10^4 \text{K/s}$ were recorded.

6.3.2.3 Sullivan Concentrate

The temperature measurement results for the 63-74 and 105-125 μm size fractions of Sullivan concentrate in oxygen are presented in Figure 6.58. In both cases the main region of combustion was located at a similar furnace position, and consists mainly of O1 and O2 combustion pulses with temperatures between 1800 and 2400K. Combustion occurs at shorter combustion distances in oxygen than air but the combustion zones are of similar size (see Figures 6.32 and 6.33). Although a larger number of higher temperature O2, O3 and O4 combustion pulses were recorded with the 63-74 μm size fraction, the intensity of the pulses for the larger size fraction were generally higher. From Figure 6.59 it can be seen that average particle temperatures for the O1, O2 and "air-type" combustion pulses were similar at 1900 to 2200K for all three size fractions examined.

The average pulse lengths were relatively short, typically being less than 10ms but increased with increasing feed size (see Figure 6.59). Except for the O4 combustion pulses, which by definition are of short duration, the pulse lengths appeared independent

of pulse type. The increase in pulse length with feed size suggests that the combustion (often complete within the limits of pyrometer sensitivity) of increasingly larger particles is being observed. These pulses are generally shorter than the 10-20ms pulse lengths typically observed during combustion in air (Figure 6.34).

The calculated apparent particle diameters were mostly 40 to 110 μm with an average of $\sim 75\mu\text{m}$ and appeared independent of both feed size and pulse type (Figure 6.59). The results are therefore not in agreement with the increased particle diameter suggested by the pulse length data. The particle diameters appear slightly smaller than those recorded in air (Figure 6.34).

The heating and cooling rates of the O2 combustion pulses are reported in Figure 6.60. For the Sullivan concentrate measured heating rates were mostly between 10 and 30 $\times 10^4\text{K/sec}$. The heating rates, especially for the largest size fraction tended to be lower than either the O1 or O3 combustion pulses but typically a factor of 5-10 greater than A2 combustion pulses. The cooling rates of the O2 pulses were mostly $\sim 5 - 25 \times 10^4\text{K/sec}$. These cooling rates are typically only x2-4 more rapid than those of the A2 combustion pulses.

6.3.2.4 Brunswick Concentrate

The results for Brunswick concentrates are presented in Figures 6.61 and 6.62. Combustion of the 63-74 μm size fraction was quite intense with measured temperatures of 1600 to 3200K. All types of combustion pulses were observed and reactions were complete at a combustion distance of less than 100mm. For the 105-125 μm size fraction, mostly O2 combustion pulses with temperatures between 2400 and 2600K were recorded with the zone of combustion extending to distances in excess of 150mm. From Figure 6.62 the distinction between the average temperatures of the different pulse classifications is evident with average combustion pulse temperatures increasing in the following order: Air-type < O1 < O2 < O3/O4, relatively independent of feed size. The

reactions in oxygen occurred at combustion distances about half that in air but the combustion zones were of similar length. With both Brunswick and Sullivan concentrates, the total number of particle combustions observed during combustion in oxygen appeared fewer than with air. This is possibly due to the more intense reaction in oxygen resulting in the very rapid combustion of whole particles rather than allowing disintegration to occur prior to reaction (cf Figures 6.4a and b).

Most of the combustion pulses were of lengths ~2-14ms (see Figure 6.62 and Table 6.5) and there appears to be a general trend towards increasing pulse length with increasing feed size. The "air" type combustion pulse lengths tended to be of longer duration, typically 10-20ms which is similar to the case for air. The average calculated particle diameters also appeared to increase with feed size, generally 20-90 μm and 40-130 μm for the 63-74 and 105-125 μm size fractions respectively. No clear trend in the apparent diameters calculated for the "Air-Type" pulses was apparent. Both this and the general increase in pulse length with increasing feed size suggests that, on average, the combustion of larger sized particles is being observed. Similar to the case for combustion in air, the calculated apparent diameter appeared independent of particle temperature.

The heating and cooling rates of O₂ combustion pulses, observed with Brunswick concentrates, are shown in Figure 6.60. Most heating rates were similar to those observed with Sullivan concentrates at $5 - 30 \times 10^4 \text{K/s}$, however a greater number of combustion pulses with heating rates in excess of $30 \times 10^4 \text{K/s}$ were observed than with Sullivan. Similarly, the measured cooling rates at $\sim 5 - 60 \times 10^4 \text{K/s}$ tended to be higher than those observed during Sullivan combustion. The O₂ heating and cooling rates were similar to those of O₃ combustion which probably reflects the high concentration of iron sulphide in the feed. The heating and cooling rates of the Brunswick O₃ combustion pulses, given in Figure 6.57, were typically $10 - 50 \times 10^4 \text{K/s}$ and $10 - 100 \times 10^4 \text{K/s}$ which is also similar to those observed during pyrite and pyrrhotite combustion.

6.3.2.5 Summary of the Results of the Oxygen Experiments

A summary of the results of the oxygen series of experiments is given in Table 6.6.

6.4 The Effect of Oxygen Concentration on the Combustion of Pyrite and Galena

Individual combustion pulse data for the experiments examining the effects of oxygen concentration (balance nitrogen) on the combustion of galena and pyrite are presented in Tables 6.7 and 6.8.

6.4.1 Galena Combustion

6.4.1.1 Variation in Pulse Shape

With increasing oxygen concentration, the shape of the galena combustion pulses gradually changed from A1 associated with combustion in air (<30% oxygen), to the O1-type associated with the combustion in oxygen (>60% oxygen). At oxygen concentrations of 30-65%, a number of combustion pulses with characteristics intermediate to those of Air and Oxygen-type pulses were recorded. These ragged pulses, often with twin energy maxima as shown in Figures 6.63 and 6.64, have been classified as "Type A/O1". These combustion pulses are generally shorter than observed with air, typically being <10ms, and have peak temperatures of ~1600 to 2000K. At the higher oxygen concentrations, the initial energy maximum of the A/O1T and O1T combustion pulses often corresponds to a low temperature arrest or peak at ~1600-1800K, and the later energy maxima to a higher temperature peak at ~1800-2400K.

6.4.1.2 Temperature Measurement Results

The variation in combustion pulse temperature and pulse type with oxygen concentration is shown in Figure 6.65 and Table 6.9. The most rapid change in maximum pulse temperature was recorded in the intermediate region, between ~40 and 65% oxygen where the A/O1 combustion pulses were observed. Below ~40% the A1 pulse temperatures were relatively constant at ~1500-1700K. The temperatures of the A/O1

combustion pulse varied considerably from ~1500 to 2000K without an apparent dependence on oxygen concentration. Above 65% oxygen, the temperature of the O1 combustion pulses increased from ~1800-2000K, with increasing oxygen concentration, to ~1900-2200K at 100% oxygen.

The combustion pulse lengths decreased rapidly with increasing oxygen concentration from an average of ~17ms at 10% to ~5ms for concentrations in excess of 50% (see Figure 6.66 and Table 6.9).

The calculated diameter of the A1 and A/O1 combustion pulses, shown in Figure 6.67, are mostly between 50 and 150 μm , with the average particle diameter remaining relatively constant ~87-102 μm (see Table 6.9). The apparent diameters associated with the O1 combustion pulses were typically 25-70 μm , decreasing slightly with increasing oxygen concentrations above 50%. There appeared less spread in the O1 data than for the Air-type pulses. As seen in Figure 6.67b, similar to the air experiments there is a strong inverse dependence of the apparent particle size on temperature. Again this is probably due to the larger proportion of the total energy resulting from fume and its increasing effect on the calculated apparent area with the lower temperature particles.

The temperature of the twin maxima of the A/O1T and O1T combustion pulses (see Figures 6.43, 6.44, 6.63 and 6.64) recorded are listed in Table 6.10. For oxygen concentrations of less than ~50%, the temperatures at the two energy maxima of the A/O1T combustion pulses were often similar at ~1550-1700K, and the ratio of the apparent diameters, (d_{p2}/d_{p1}), varied considerably from ~0.45 to 1.5. At higher oxygen concentrations the temperature of the initial energy maximum remained relatively low, typically ~1600-1700K, but the second energy maxima generally corresponded to a higher temperature of ~1750-2200K. The calculated diameter ratio of the two energy maxima was typically 0.45-0.8 and appeared to decrease with increasing peak temperature. From Table 6.10 no gradual transition in the heating and cooling rates from

those of air to those of oxygen was observed with increasing oxygen concentration. The heating and cooling rates for A/O₁ combustion pulses varied considerably, but were typically intermediate, at $5 - 20 \times 10^4 K/s$, to the A₁ combustion pulses ($< 1 \times 10^4 K/s$) and the O₁ combustion pulses ($\sim 10 - 50 \times 10^4 K/s$).

6.4.2 Pyrite Combustion

6.4.2.1 Variation in Pulse Shape

Examination of the energy pulses recorded during the combustion of pyrite in atmospheres of between 10 and 100% oxygen revealed only A₃ and O₃ shapes. Below 80% oxygen A₃ combustion pulses similar to those shown in Figures 6.8 to 6.10 were observed. For oxygen concentrations of less than 21%, the peak associated with the rapid energy increase is generally broader and more rounded than for air, as shown in Figures 6.68 (10% oxygen). The period of energy increase associated with the region of expansion also tends to decrease with increasing oxygen concentration from 2-3ms at 10% oxygen, to $< 0.8ms$ for oxygen concentrations $> 35%$ as indicated by a sharper and more intense peak. Figure 6.69 shows the temperature traces for a series of combustion pulse recorded at different oxygen concentrations. The measured temperatures of the A₃ combustion pulses increased from $\sim 2000K$ to 3000-3200K with an increase in oxygen concentrations from 10 to 40% above which the A₃ peak temperature remained relatively constant. Apparent particle diameter increases were typically $\times 1.5 - \times 3$. Above 40% oxygen the heating rate however increased rapidly. The peak temperatures of 3000-3400K and the general peak characteristics of the O₃ combustion pulse were identical to those observed during pyrite combustion in oxygen.

6.4.2.2 Temperature Measurement Results

The effects of oxygen concentration on the combustion temperatures is given in Figure 6.70a and Table 6.11. The reproducibility of the measurements, and linear increase in maximum temperature from ~ 2000 to 3100K with increasing oxygen

concentrations between 10 and 40% oxygen can be clearly seen. A linear regression of the average measured temperature over this range has a regression coefficient of 0.98 and the mathematical relationship is given by :

$$T_{A_3}(\text{max}) = 1542 + 48.2 [\%O_2] \quad 10 \leq \%O_2 \leq 40 \quad (6.1)$$

At 80% oxygen a mixture of A3 and O3 combustion pulses were recorded, however the peak temperature of the individual pulses was similar for both pulse types. For the case of pure oxygen a slight increase in the average of the O3 combustion pulse temperature to 3300K was recorded.

From Figure 6.70b, most pulse lengths are between 12 and 22ms, with those recorded at 10% oxygen tending to be the longest at between 20 and 28ms, and those for pure oxygen shortest at 5 to 15ms. The maximum measured lengths of the A3 combustion pulses are in reasonable agreement with the calculated maximum pulse lengths of 20ms in air (21ms in pure oxygen). The gradual decrease with increasing oxygen concentration is probably associated with both the shorter time for complete combustion and the reduced pyrometer sensitivity at the higher gain settings used to record the more intense signals.

From Figure 6.71a there is relatively good agreement between the feed size (nominally 85 μm) and the measured apparent diameters which are mostly 40-100 μm and do not appear dependent on either oxygen concentration or pulse type. As was the case in the previous pyrite experiments, no correlation between calculated particle diameter and the measured pulse temperature was observed (see Figure 6.71b).

For air-type pulses apparent expansions (diameter increase) of ~ 1.5 to $\times 3$ are typically observed, irrespective of the oxygen concentration (see Figure 6.72). For O3 combustion pulses size reduction rather than particle expansion is typically observed.

The measured heating and cooling rates are enhanced with increasing oxygen concentration, as indicated in Table 6.11, and Figures 6.73a and b. The heating rates increase modestly from ~ 3.5 to $6 \times 10^4 \text{K/s}$ between 10 and 30% oxygen. A relatively constant heating rate was often observed. However, a secondary, more rapid heating rate was sometimes observed prior to the attainment of the maximum temperature as seen for the trace recorded at 25% oxygen in Figure 6.69. The heating rates given in Figure 6.73a are an average over the complete period recorded. Between 30 and 65% oxygen there is a general increase in heating rate; however, much more scatter in the results is observed, with heating rates varying between $\sim 4 - 20 \times 10^4 \text{K/s}$. Above 80% oxygen heating rates recorded were again more reproducible. The results given in Figure 6.73b suggest a strong correlation between the measured cooling rates and the maximum pulse temperature. The cooling rates increase rapidly from $\sim 3.5 \times 10^4 \text{K/s}$ at 10% oxygen to $\sim 10 - 17 \times 10^4 \text{K/s}$ at 25% oxygen. At 30 to 50% oxygen there is a larger spread of results, but above 50% oxygen the rate is relatively constant at $\sim 20 \times 10^4 \text{K/s}$.

6.5 Reaction Product Analysis

6.5.1 Chemical Analysis/X-ray Diffraction Results

The results of the chemical analyses and powder X-ray diffraction analyses for the products of the galena, Sullivan and Brunswick concentrates in air and oxygen are given in Table 6.12 to 6.14 and Figures 6.74 to 6.78. For the galena experiments, zinc was the major impurity and therefore the relative amounts of the different chemical species present were calculated using a zinc balance assuming that no zinc vaporisation occurred. Iron, due to its greater abundance, was used as the reference for the commercial concentrates. The ratio of Fe/Zn , given in Table 6.13 remains relatively constant for all of the experiments and the assumption that no zinc or iron vaporisation occurred appears valid for all but the longest combustion distances.

The main regions of chemical reaction indicated by the reaction product chemical analyses coincide with the combustion zones determined by pyrometry experiments. Similar to the work of Salomon de Friedberg [44], the quantity of feed material collected tended to decrease with increasing combustion distance and suggests the amount of reaction which has occurred (most of the fine fume reaction product is not collected in the solids trap). Ejected material also tended to leave the central axis of the reactor and therefore was not collected by the sampler.

From the slope of the species elimination vs distance curves given in Figures 6.74 to 6.78 it is possible to derive bulk reaction rates in mols/mm and an estimate of mols/s. Owing to the large range of particle sizes present in the feed materials the reaction rates of the individual particles vary considerably and would tend to be very much faster than the bulk reaction rate (not presented).

From the x-ray results in Table 6.14, the relative intensity of the peaks was used to classify whether the mineral species were major or minor constituents of the reaction product. No attempt was made to quantify the amounts present using the relative peak intensities.

6.5.1.1 Air Experiments

The main regions of combustion of the 74-88 μm and 105-125 μm size fractions of galena combustion in air are given in Figure 6.74. The results suggest that during the earlier region of reaction sulphur elimination is considerably more rapid than lead vaporisation. Due to the relative purity of the galena this initial loss of sulphur, without a corresponding lead loss, suggests that the formation of a lead rich *Pb-S* (or *Pb-PbS*) melt is probably occurring and that lead sulphide vaporisation is not the main reaction mechanism during the initial period of reaction. The later similar rates of sulphur and lead decrease are, however, consistent with a reaction mechanism involving the vaporisation of lead sulphide.

The X-ray diffraction analysis of the products of galena combustion in air (Table 6.14) indicate the increasing degree of oxidation of the product with increasing combustion distance. Increasing quantities of anglesite ($PbSO_4$) and lanarkite ($PbO.PbSO_4$) and also minor amounts of dibasic lead sulphate ($2[PbO].PbSO_4$) were detected with increasing combustion distances. At the longer combustion distances the intensity of the galena X-ray diffraction pattern is reduced owing to the large quantities of lead vaporised from the samples, with zinc species becoming predominant. The sphalerite present appeared to react little, with only small quantities of zincite (ZnO) observed at the longer combustion distances.

The X-ray diffraction results (see Table 6.14) indicate that the fume reaction product was mainly anglesite ($PbSO_4$). The mol ratio of $Pb:S:O$ in the fume, assuming the fraction of the total weight missing in Table 6.12 is oxygen, would be 1 : 0.67 : 4.6 which suggests the presence of a basic lead sulphate.

The results for Sullivan concentrate combustion in air are given in Figure 6.75. For both the 74-88 and 105-125 μ m size fractions most of the sulphur and lead loss occurred between combustion distances of 120 and 200mm. The rapid decrease in the amount of ferrous iron present at longer combustion distances, suggests the formation of ferric oxides (eg. magnetite and hematite). The amount of metallic lead formed was similar to the galena experiments, with a maximum of <10% being recorded. The decrease in the S/Pb ratio (see Table 6.13) from ~1.88 (feed) to ~<0.7 beyond 200mm suggests that preferential iron sulphide combustion is occurring over the same range. The X-ray diffraction results (Table 6.14) indicate that the pyrrhotite and small amounts of pyrite in the feed rapidly react, primarily to magnetite. Galena reaction results primarily in the formation of anglesite ($PbSO_4$). At longer combustion distances the sphalerite appears to react to form small amounts of zincite.

The results for the combustion of 74-88 μm and 105-125 μm size fractions of Brunswick concentrate in air are given in Figure 6.76. Due to the large amount of pyrite present, and its more rapid combustion the *S:Pb* mol ratio initially declined rapidly (see Table 6.13). Rapid lead vaporisation follows. However, the *S:Pb* ratios remain high. The total amount of metallic lead formed was less than ~8%. Similar to the Sullivan concentrate it is only during this later stage that the iron tends to oxidise to the trivalent state. From a comparison of the results for Brunswick and Sullivan concentrates in air (see Table 6.14) the effects of the increased pyrite concentration can be detected. The pyrite reacted rapidly, initially to pyrrhotite, and then forming magnetite. At most combustion distances both anglesite (PbSO_4) and lanarkite ($\text{PbO} \cdot \text{PbSO}_4$) were present in varying amounts.

6.5.1.2 Oxygen Experiments

Owing to the very rapid combustion of the concentrates in oxygen few samples corresponding to the intermediate portions of the reaction were collected. For the combustion of 63-74 μm galena (see Figure 6.77) most of the lead (and presumably sulphur) elimination occurs between 100 and 130mm. The large decrease in the weight of product collected between 85 and 102mm suggests that either; i) particle disintegration is occurring with the ejected material not being collected, or ii) particles which ignite, react almost instantaneously whereas those remaining are unreacted. The X-ray analyses (see Table 6.14) indicated the species present are similar to those observed for combustion in air, with anglesite (PbSO_4) appearing to be the main reaction product. The sphalerite appears to react to form zincite (ZnO) and owing to lead vaporisation the amount of zinc present in the reaction product increases.

For the combustion of Sullivan and Brunswick concentrate in oxygen, reactions occur over similar distances (see Figure 6.78) and earlier than with galena. Greater lead loss was recorded for Brunswick combustion than Sullivan, with ~55% of the original

lead rapidly being eliminated. For Sullivan combustion ~44% of the sulphur and ~31% of the lead was rapidly eliminated and with increasing combustion distances sulphur elimination occurred at a relatively constant rate but little more lead loss was recorded. The quantity of metallic lead formed was small (>5% of total) and was recorded at the earlier combustion distances. The iron present in the ferrous form declined rapidly (due to oxidation to ferric iron) at the later stages of reaction. The X-ray diffraction analysis results indicate the formation of magnetite and later hematite. The combustion product of the galena present is anglesite ($PbSO_4$) and the sphalerite appears to react to form zinc ferrite ($ZnFe_2O_4$) rather than zincite (ZnO), possibly due to its presence in the agglomerates. The preferential oxidation of sulphur from the Brunswick concentrate, due to the thermal decomposition and earlier combustion of pyrite, can be seen by the rapid decline in the S/Pb mol ratio (Table 6.13) from 6:1 to ~1:1 between 70 and 85mm.

6.5.2 Scanning Electron Microscopy (SEM), Energy and Wavelength Dispersive X-ray Spectroscopy (EDX/WDX) Studies

On a microscopic level, little difference was observed between the reaction products sampled at the different combustion distances with the solid samples tending to consist mainly of differing proportions of unreacted and fully reacted particles. Examples of the variation in product could be observed in samples taken at any combustion distance, and therefore, the combustion distance at which the particles were collected is not generally reported.

6.5.2.1 Air Experiments

Typical micrographs of the reaction products of galena combustion in air are presented in Figure 6.79. Prior to melting a thin layer of oxide or sulphate reaction product is sometimes observed on the galena particles. At the initiation of reaction, the particles gradually melt and form liquid droplets, which appear as spheres or ellipsoids in the quenched product often with a slight porosity. EDX/microprobe analysis indicated

that these particles are mainly unreacted *PbS*. During reaction these particles appear to shrink rapidly and spheres of a range of sizes were typically found in the product (Figure 6.79a). At the longer reaction times the proportion of unreacted feed tended to decrease rapidly. The large quantities of sub-micron fume reaction product (lead sulphate) tended to adhere to the larger particles and also to form large loosely associated clumps.

Often, as seen in the back-scattered electron images in Figures 6.79b and c, some microstructure structure can be resolved within the individual particles, probably due to the rejection of solute impurities on solidification. Using the back-scattered electron image, regions containing elements of high atomic number appear lighter therefore allowing phases of different chemical composition to be identified. For the galena particles dark rims are commonly seen around a lighter centre, indicating the presence of a sulphur-rich phase around a lead-rich metallic phase. The microprobe studies show the sulphide phase to be 20-50 atomic percent sulphur (balance lead) and the metallic phase to be less than 10% sulphur. From the *Pb-S* phase diagram given in Figure 2.5 such phases would be expected to separate out from a sulphur deficient *Pb-S* melt on cooling [35,49] and similar metallic lead spheres, within a sulphide, were observed by Wuth [64]. A solidified *Pb-Zn-S* melt is shown in the upper right corner of Figure 6.79c where a higher melting point zinc-rich phase appears to have solidified around a *Pb-S* phase with the final formation of a lead-rich core.

Sphalerite particles were observed in the reaction product of galena combustion (Figure 6.79d), and due to *PbS* volatilisation, increased in abundance in the more reacted samples. The sphalerite is present as discrete grains or intimately associated with galena (as indicated by the darker regions in back-scattered electron image in Figure 6.79c). At longer combustion distances the discrete sphalerite particles tend to have a thin, uneven oxide shell inside which the primarily unreacted particle remains.

For pyrite particles, the initial stage of reaction is the thermal decomposition of pyrite to pyrrhotite with the liberation of gaseous sulphur. As indicated in Figure 6.80a to c, this occurs gradually, progressing from the outside to the core of the particle. The reaction product appears porous and often the particle is split into two reacted wings of pyrrhotite with an unreacted pyrite kernel sometimes observed (see Figure 6.80a and c). The presence of a pyrrhotite reaction product surrounding an unreacted pyrite core is indicated by the EDX scan in Figure 6.80b of the relative quantity of sulphur across the partially reacted particle shown in Figure 6.80a (taken at the upper white line bisecting the photograph). These partially decomposed particles were most common at shorter combustion distances. Optical microscopy often indicated a reddish tinge around the outside of the porous pyrrhotite suggesting that some solid state oxidation of the sulphide had occurred at the surface prior to thermal decomposition. The porous pyrrhotite particles then melt followed by rapid oxidation of the sulphur and iron in the melt. Relatively little gas-solid reaction of the dense pyrrhotite mineral was observed prior to melting with the unreacted particles tending to have a fractured appearance as indicated in Figure 6.80d. Once molten, however, the reaction products of pyrrhotite combustion appeared indistinguishable from those of pyrite combustion. Examples of reaction products obtained are shown in Figure 6.81. The quenched samples were primarily iron oxide of several different shapes. A number of elongated particles were found (see Figures 6.81a and b) often with necks in them suggesting the formation of several smaller particles was about to occur. Iron oxide spheres of many sizes were observed in the product. The sphere shown in Figure 6.81b has a diameter of $\sim 210\mu\text{m}$ which is $\sim 2.7\text{x}$ greater than the average diameter of the feed material and in good agreement with the degree of expansion suggested by the pyrometer measurements. These larger spheres are often found cracked, and appear to be iron oxide shells a few microns thick (see Figure 6.84d for Brunswick concentrate). These shells have been observed by other researchers

(notably Jorgensen et al. [81]) and have been referred to as "cenospheres". Within the cenosphere shell fragments, debris is often found. Cenospheres form only a small portion of the total number of particles observed. The smaller particles observed are typically 30 to 50 μm in diameter and many exhibit ruptures which might be the result of the ejection of gas or liquid through the solid shell (Figure 6.81c and d). Although hollow, the shells of these particles are generally thicker than those of the larger cenospheres.

Typical examples of the reaction products observed during the combustion of Sullivan concentrates in air are shown in Figures 6.82a and b. The various stages of combustion of the agglomerates can be seen. Many smaller particles (5-50 μm) were also found in the reaction product (not shown), which probably result from the combustion of individual grains produced by the disintegration of agglomerates. In Figure 6.82a the gradual melting and dissolution of the individual grains of lead and iron sulphide, from the edge to the centre of the grain can be seen. The darker grains of zinc sulphide appear not to dissolve readily in the lead-iron sulphide melt, and can often be seen distinctly within the melt. With the progression of reaction, hollow centres form in many of the particles. Their formation does not appear rapid, but rather as a gentle expansion with the wall remaining relatively thick at ~10-30 μm . With the progression of reaction, lead vaporisation occurs and the wall become predominantly iron oxide. Unsectioned, reacted agglomerates appear roughly spherical, often with large pits in them. No examples of thin-walled cenospheres were observed. Fine particulate matter (probably lead sulphate fume) was present in the reaction product.

The larger quantities of iron and its presence as pyrite rather than pyrrhotite distinguish the combustion of Brunswick concentrate from that of Sullivan. Figure 6.82c shows two grains of pyrite during the early stages of reaction, with cracking and spalling of pyrrhotite layers. Below that is an iron-lead-zinc sulphide agglomerate particle which appears unreacted. With increased reaction melting occurs and also thick-walled hollow

spheres form. The thick-walled hollow iron oxide spheres in Figure 6.82d, although similar to those of Sullivan (Figure 6.82b) appear to have many smaller perforations as well as the larger pits (as shown by the particle in the lower left corner Figure 6.82d). Examples of iron oxide shells resulting from combustion are shown in Figures 6.83. In most cases these probably result from the combustion of predominantly iron sulphide particles. In Figure 6.83a the original particle shell appears to have been shattered and a shell then reformed. Relatively small particles with smooth and skeletal structures (see Figures 6.83b and c) were also recorded. Occasionally large thin-walled iron oxide cenospheres (as observed with pyrite and pyrrhotite combustion) were observed (Figure 6.83d).

6.5.2.2 Oxygen Experiments

In oxygen the reaction of galena is very fast (see Figure 6.84) and the material collected at the earlier stages of combustion usually consisted of large unreacted particles and many smaller partially reacted particles and reaction fume. The large amounts of fume produced tends to coat the larger particles (Figure 6.84b), possibly after quenching in the collector. This fume often forms large clumps within which many small ($<10\mu\text{m}$) unreacted galena spheres are found. The presence of many smaller spheres of lead sulphide in the product is consistent with the pyrometer results and visual observations which suggest that soon after ignition the galena particle disintegrates and the resulting debris rapidly vaporises and combusts. WDX studies and back-scattered electron results (see Figure 6.84c) suggest that some sulphur depletion, either overall or as cores, occurs during reaction (sulphur concentrations of 10-50%). The products resulting from reaction of galena in both air and oxygen appear to be similar except for the much larger number of these very small, partially reacted particles with oxygen. The back-scattered image in Figure 6.84d shows a particle during the very early stages of combustion in oxygen. The cracked material represents the original unmelted *PbS* (WDX analysis *Pb*-61%, *S*-33%,

O-5%) and the lighter patches on the surface are *PbO* ((WDX analysis *Pb*-50%, *S*-0%, *O*-50%) and the melt at the bottom of the particle appears to be a basic lead sulphate (WDX analysis *Pb*-54%, *S*-30%, *O*-16%). This micrograph indicates that an oxide surface layer can form and on melting gets incorporated into the melt but reacts slowly. The result also suggests that the separation of several droplets during the early stage of melting possibly occurs. The initial stages of reaction in air are probably similar.

Examples of the reaction product of pyrite and pyrrhotite combustion in oxygen are given in Figure 6.85. Due to the intensity of the reactions considerable size reduction occurred with the formation of many small spheres and elongated particles, as indicated in Figure 6.86a where both reacted spheres and much larger unreacted grains of pyrite are present. The elongated particles, and others showing signs of necking, suggest many particles were frozen in the process of splitting into several smaller particles. For most of the reacted particles little sulphur was detected suggesting an iron oxide composition. Quantitative microprobe studies (WDX) on polished pyrite and pyrrhotite reaction products, indicated that the particles were iron and oxygen. The mol ratio of *Fe:O* varied from 1.0-1.8:1. These results suggest that oxygen deficient iron oxide may form, however, quantitative oxygen determination is difficult. Typically the total detector counts in the samples were 10 to 20% lower than from the *Fe* and *O* standards. No other major elements were, however, detected to account for this discrepancy. Similar to combustion in air a number of porous particles were observed (Figure 6.85c), but no large cenospheres were observed. Most of the particles of reacted material were less than 50 μ m in diameter and generally spherical. The shell of the particle shown in Figure 6.85d appears to have been shattered some time after freezing, again probably due to an internal force.

The products resulting from the combustion of the commercial concentrates tended to have less distinct morphology than obtained from combustion in air. With Sullivan concentrate the lead tended to vaporise rapidly producing a considerable amount of lead sulphate fume which coated the products. Small iron oxide spheres, considerably smaller than the feed material, were commonly observed and few hollow particles were recorded. The reaction of the agglomerates appeared rapid and few partially reacted lead-iron-zinc sulphide particles were seen. Figure 6.86 shows the electron micrograph and lead, iron and zinc X-ray maps of the cross-section of a partially reacted particle consisting of a lead-iron-zinc sulphide matrix within which distinct lead and zinc sulphide phases are present. The results suggest that the lead sulphide phase was present, undissolved, in the melt prior to quenching and the formation of a void is evident. It is possible that rapid gas generation (PbS vaporisation) within the PbS phase, could result in the disintegration of the surrounding droplets.

Examples of the reaction products of Brunswick combustion in oxygen are given in Figure 6.87. Initially the extremities of particles appear to melt (see Figure 6.87a). At later stages large molten droplets form which tend to remain attached to the granular unmelted agglomerate material. It is possible that these spheres, probably of iron oxide, result either from the melting and reaction of predominantly iron sulphide grains or molten material coalescing into a drop. With other particles the surface of the agglomerate melts first (Figure 6.87c) which, on quenching, appears as a skin over the unmelted agglomerate particles within. At later stages of reaction, the product appears as relatively smooth spheres of iron oxide (see Figure 6.87d). In general some size reduction was observed, with most of the product being 20 to 60 μm in diameter. Unlike reaction in air no hollow reaction products were observed.

TABLE 6.1 Classifications of Pyrometer Output Signal Pulses Recorded During Particle Combustion in Air.
($T_{\text{FURNACE}}=1130\text{K}$)

Combustion Peak Type	PULSE CHARACTERISTICS		Mineral Species or Physical Phenomena
	Energy	Temperature	
A1	-relatively constant -low intensity	1400-1700K -relatively constant	Galena
	-low level "tail" on energy pulse	~furnace temperature	-reaction products trailing particle
A2	-indistinct -intermediate energy level and pulse shape	1700-2400K -a range of heating and cooling rates $0 - 4 \times 10^4 \text{K/s}$ heating rate $1 - 10 \times 10^4 \text{K/s}$ cooling rate	Brunswick, Sullivan concentrates - multiphase mineral particles or agglomerates.
A3	Stage 1: gradual increase	<1800~2350K $1 - 5 \times 10^4 \text{K/s}$ heating rate.	Pyrite and Pyrrhotite
	Stage 2: sudden 5-10 fold increase	2250-2600K peak temperature	5-10 fold increase in apparent area
	Stage 3: very rapid decrease	~2350-<1600K $8 - 20 \times 10^4 \text{K/s}$ cooling rate.	
A4	-very short pulse -high intensity -may be superimposed on other particle types	1800-2500K -rapid increase and decrease in temperature	Material ejection. -sparks -disintegrations
A5	-periodic variation -relatively constant	1600-2100K (often similar to A1) -periodic fluctuations may or may not be present	periodic variation in particle area and/or temperature -area pulsation? or rotation? -pulsating flame front?

TABLE 6.2 Average Temperatures, Pulse Lengths and Calculated Particle Diameter of the Different Pulse Classifications for the Combustion of the Different Feed Materials in Air.

($T_{\text{FURNACE}}=1130\text{K}$)

Sample standard deviations ()

Average for Each Pulse Type

Feed Material	Size Fraction (μm)	Pulse Types	#	T pulse (K)	t pulse (ms)	Calculated dp (μm)	A3 dp Increase	
Galena	63-74	A1	47	1535(62)	12.1(2.0)	112(33)	-	
		A4	3	1864(305)	5.8(2.8)	98(87)	-	
	74-88	A1	25	1463(59)	14.7(6.2)	112(31)	-	
		A4	1	-	-	-	-	
	88-105	A1	33	1591(110)	14.0(3.2)	108(41)	-	
		A3	11	2188(133)	15.7(2.8)	77(26)	2.4(0.7)	
		A3I/D	9	1945(197)	15.2(1.8)	69(15)	-	
		A4	5	2003(275)	5.2(2.2)	52(42)	-	
		A2	2	-	-	-	-	
	105-125	A1	39	1547(104)	11.1(2.9)	139(55)	-	
		A3	11	2281(132)	13.6(3.9)	92(52)	2.2(0.5)	
		A3I	9	2009(188)	13.0(1.4)	91(12)	-	
		A4	5	1461(126)	4.3(1.1)	183(74)	-	
		A2	4	1901(191)	12.7(3.0)	81(35)	-	
	Pyrite	74-88	A3	38	2392(57)	15.5(3.5)	55(14)	2.7(0.3)
			A3I	14	2129(240)	17.6(3.0)	53(13)	-
A3D			12	1986(262)	13.6(5.2)	69(27)	-	
Pyrrhotite	74-88	A3	42	2395(104)	15.7(3.8)	69(27)	2.6(0.4)	
		A3I	27	2199(97)	15.0(5.4)	70(13)	-	
		A3D	12	2235(95)	9.2(2.7)	125(39)	-	
Sullivan	63-74	A1	41	1550(111)	15.1(2.2)	119(48)	-	
		A2	22	1761(151)	16.1(2.6)	82(30)	-	
		A3	7	2061(95)	15.0(4.2)	63(22)	-	
		A5	1	-	-	-	-	
	74-88	A1	14	1464(143)	17.0(5.8)	237(174)	-	
		A2	16	1839(153)	13.0(5.0)	84(27)	-	
		A3	6	2080(237)	17.3(2.0)	61(44)	-	
		A4	7	2007(261)	5.2(2.6)	54(39)	-	
	88-105	A1	47	1535(89)	15.1(3.4)	115(72)	-	
		A2	12	1737(95)	14.0(1.8)	81(29)	-	
		A3	1	-	-	-	-	
	105-125	A1	21	1560(88)	15.4(3.3)	106(32)	-	
		A2	28	1636(70)	13.5(3.4)	132(34)	-	
	Brunswick	63-74	A1	16	1602(121)	14.6(4.5)	92(22)	-
			A2	21	1838(168)	15.2(7.7)	84(38)	-
			A3	31	2170(185)	17.0(3.7)	59(18)	2.3(.5)
A5			1	-	-	-	-	
74-88		A1	18	1579(108)	14.0(3.2)	121(56)	-	
		A2	33	1801(127)	15.9(3.8)	80(33)	-	
		A3	27	2202(184)	14.6(4.6)	49(22)	2.3(0.7)	
		A4	7	1865(117)	4.3(2.2)	77(31)	-	
88-105		A1	17	1571(55)	17.1(2.9)	109(23)	-	
		A2	13	1777(177)	18.3(5.5)	95(38)	-	
		A3	20	2237(187)	12.8(3.3)	81(22)	2.3(0.4)	
105-125		A1	18	1636(124)	16.5(3.1)	101(32)	-	
		A2	21	1818(83)	17.2(3.0)	99(24)	-	
		A3	1	-	-	-	-	

TABLE 6.3 Summary of the Air Series Pyrometry Results.
($T_{\text{FURNACE}}=1130\text{K}$)

Concentrate Type	Mesh Size ($\mu\text{m.}$)	Relative # high/low Intensity Pulses	Combustion Zone (mm)	Calculated Reaction Time (ms)	Peak Temp. (K)	Peak Type
Galena	63-74	(LI)	160-280	200-300	1400-1650	A1
	74-88	(LI)	160-270	162-273	1350-1600	A1
	88-105	(LI)	120-300	98-244	1400-1700	A1,A2,A3
	105-125	1(LI) 0.08(HI)	150-360 150-280	99-233 -	1300-1700 2000-2400	A1 A3
Pyrite	74-88	(HI)	70-170	100-200	2000-2500	A3
Pyrrhotite	74-88	(HI)	120-290	200-350	~2200-2550	A3
Sphalerite	74-88		-	-	-	-
Sullivan	63-74	1(LI) 0.07(HI)	150-290 200-280	175-350 -	1400-1700 1800-2200	A1 A2,A3
	74-88	(LI)	100-260	101-263	1300-1700	A1,A2
	88-105	(LI)	100-270	75-225	1400-1700	A1,A2
	105-125	(LI)	120-220	80-144	1400-1700	A1,A2
Brunswick	63-74	1(LI) 0.8(HI)	50-160 60-160	75-200 -	1400-2500	A2,A1 A3
	74-88	1(LI) 0.38(HI)	80-180 80-160	80-180 -	1400-2500	A2,A1 A3
	88-105	1(LI) 0.1(HI)	80-200 120-210	70-170 -	1400-2500	A1,A2 A3
	105-125	1(LI) 0.1(HI)	100-250 140-250	67-160 -	1400-1900	A2,A1 A3

TABLE 6.4

Classifications of Pyrometer Output Signal Pulses Recorded During Particle Combustion in Oxygen.
($T_{\text{FURNACE}}=1130\text{K}$)

Combustion Peak Type	PULSE CHARACTERISTICS		Mineral Species or Physical Phenomena
	Energy	Temperature	
(O1)	-short pulses -rapid change	1800-2400K -rapidly changing -heating/cooling rates $20 - 60 \times 10^4 \text{K/s}$	Galena -rapid vaporisation and combustion
O1T	-twin energy maxima(O1T)	-1700-2000K thermal arrest -2000-2400K temperature peak	-vaporisation and disintegration -combustion of fragment cluster
(O1S)	-Many Energy Spikes(O1S)	Corresponding Temperature Peaks	combustion of ejected material
O2	-indistinct -intermediate energy level and pulse shape - many spiked combustion pulses	1800-3400 K -a range of heating and cooling rates $10 - 40 \times 10^4 \text{K/s}$ -temperatures increase with increasing iron concentration	Brunswick, Sullivan concentrates - multiphase mineral particles or agglomerates.
O3 (O3T) (O3S)	Stage 1 (pyrite only)-small initial energy spike	-corresponding temperature spike $\sim 2000\text{-}3000\text{K}$	Pyrite thermal decomposition and sulphur combustion
	Stage 2: rapid accelerating increase	$<2000\text{-}3200 \text{K}$ -heating rate $\sim 10 - 40 \times 10^4 \text{K/s}$	Pyrite and Pyrrhotite
	Stage 3: (sometimes present) sudden rapid 1-3x increase	3000-3400K peak temperature	-particle disintegration
	-two or more energy peaks	-corresponding maximum temperature peaks	-multiple ejections of material
	Stage 4: rapid decrease	$\sim 3200\text{-}1600\text{K}$ -range of cooling rates $10 - 70 \times 10^4 \text{K/s}$	-extinction of combusting particles or debris
O4	-very short pulse -high intensity	-rapid temperature increase/decrease 1800-2500K (galena) 2600-3500K (iron sulphides)	Material ejection. -sparks

TABLE 6.5 Average Temperatures, Pulse Lengths and Calculated Particle Diameter of the Different Pulse Classifications for Combustion in Oxygen
($T_{\text{FURNACE}}=1130\text{K}$)

Sample standard deviation ()

Average for Each Pulse Type

Feed Material	Size Fraction (μm)	Pulse Types	#	T pulse (K)	t pulse (ms)	Calculated dp (μm)
Galena	63-74	O1	68	2004(181)	4.5(2.4)	52(20)
		O3	3	2921(365)	5.1(0.4)	59(11)
		O4	1	-	-	-
	74-88	O1	41	2036(224)	5.9(3.6)	48(20)
		O3	5	3226(220)	6.9(2.2)	37(20)
		O4	1	-	-	-
	105-125	O1	38	2319(348)	7.8(3.0)	33(15)
Pyrite	74-88	O3	16	3174(67)	8.2(3.5)	58(16)
		O3S	25	3153(107)	6.6(3.3)	61(21)
		O3I	17	3145(135)	6.4(1.2)	64(13)
		O3D	2	3124(499)	12.3(5.6)	55(3.5)
Pyrrhotite	74-88	O3	38	3232(165)	7.3(2.3)	60(19)
		O3S	18	3156(112)	6.0(1.7)	67(25)
		O3I	2	3125(35)	7.6(1.3)	61(28)
		O3D	2	3090(410)	9.8(3.7)	50(5)
		O4	4	3354(224)	2.8(1.7)	61(29)
Sullivan	63-74	O1	41	1935(112)	4.6(1.5)	78(29)
		O2	32	2234(422)	5.0(1.8)	65(27)
		O3	1	-	-	-
		O4	5	2555(329)	1.9(0.7)	68(32)
		AIR	5	2015(215)	7.5(2.0)	82(36)
	74-88	O1	21	2043(129)	6.5(1.7)	87(33)
		O2	19	2130(381)	7.2(2.5)	70(27)
		O3	-	-	-	-
		O4	1	-	-	-
AIR	8	1903(111)	8.4(2.4)	77(27)		
105-125	O1	18	2072(90)	7.4(1.7)	82(29)	
	O2	25	2139(128)	11.1(2.1)	70(26)	
	O3	-	-	-	-	
	O4	1	-	-	-	
AIR	2	2098(4)	11.3(3.9)	77(51)		
Brunswick	63-74	O1	8	2116(138)	4.8(1.6)	55(17)
		O2	32	2325(275)	5.3(2.3)	56(24)
		O3	15	2899(203)	7.4(3.1)	59(21)
		O4	6	2908(262)	2.3(0.9)	24(23)
		AIR	15	1857(198)	10(4.0)	69(21)
	74-88	O1	4	2047(347)	5.9(0.8)	74(46)
		O2	19	2313(302)	7.4(2.4)	59(42)
		O3	20	3005(218)	7.2(3.0)	76(15)
		O4	-	-	-	-
	AIR	11	1868(232)	14.1(5.2)	80(38)	
	88-105	O1	5	2140(202)	7.2(3.3)	98(20)
		O2	34	2400(235)	8.6(3.6)	93(34)
O3		1	-	-	-	
O4		-	-	-	-	
AIR		6	2012(268)	13.5(4.1)	63(16)	

TABLE 6.6**Summary of the Oxygen Series Pyrometry Results**
($T_{\text{FURNACE}}=1130\text{K}$)

Concentrate Type	Mesh Size ($\mu\text{m.}$)	Relative # high/low Intensity Pulses	Combustion Zone (mm)	Calculated Reaction Time (ms)	Peak Temp. (K)	Peak Type
Galena	63-74	LI	70-150	92-197	1800-2400	O1
	74-88	LI	80-140	87-153	1800-2400	O1
	105-125	(LI)	90-260	65-184	1800-2400	O1
Pyrite	74-88	(HI)	50-90	71-125	3000-3400	O3
Pyrrhotite	74-88	(HI)	80-230	114-324	~3000-3400	O3
Sphalerite	74-88		-	-	-	-
Sullivan	63-74	1(LI)	50-120	65-157	1800-2200	O1
		0.35(HI)	50-120	-	2000-3000	O2,O4
	74-88	1(LI)	60-100	66-109	1800-2200	O1
		0.3(HI)	60-100	-	1800-3000	O2
	105-125	1(LI)	60-130	43-93	1800-2200	O1
		1(HI)	60-130	-	2000-2400	O2
Brunswick	63-74	1(LI)	<50-100	<65-131	1600-2400	O1,A
		1(HI)	<50-100	-	2200-3200	O3,O4
	74-88	1(LI)	50-100	54-109	1600-2400	A,O1
		1.57(HI)	50-100	-	2600-3400	O3
	105-125	1(LI)	70-150	50-107	1800-2600	A,O1
		1.3(HI)	70-170	-	-	O2

TABLE 6.7 Compiled Results of Experiments Examining the Effects of Oxygen Concentration on the Combustion of 74-88 μ m Galena Particles.
($T_{\text{FURNACE}}=1130\text{K}$)

% Oxygen [Lf=(mm)]	Data File #	D710 Gain Setting	Pulse Type	Pulse Length (ms)	Pulse Temp (K)	D710 Output (V)	Calc. dp (μ m)
10% [Lf=160mm]	575	8.23	A1	12.6	1430	0.6	150
	576	8.23	A1	16	1460	0.65	135
	577	8.23	A1	17.2	1620	0.51	61
	578	8.23	A1	19.6	1640	0.64	63
	579	8.23	A1	17.4	1670	0.72	60
	580	8.23	A1	19.3	1560	0.54	79
	581	8.23	A1	12.5	1550	0.8	100
	582	8.23	A1	20	1640	0.64	64
	583	8.23	A1	14.6	1420	0.42	132
	584	8.23	A1	17	1590	0.47	65
21% [Lf=160mm]	500	8.23	A1	8	1780	0.56	36
	501	8.23	A1	13.2	1620	0.9	80
	502	8.23	A1	10.8	1540	0.9	112
	503	8.23	A1	7.8	1600	0.8	83
	504	8.23	A1	9.4	1550	0.9	106
	505	8.23	A1	11.6	1590	0.5	67
	506	8.23	A1S	11	1530	0.6	95
	507	8.23	A1	10.9	1610	0.9	83
	508	8.23	A1	14.2	1560	1.15	115
	509	8.23	A1	14	1540	0.59	92
30% Lf=160mm	510	8.23	A1	14	1640	1.75	104
	511	8.23	A1	12.8	1530	1	121
	512	8.23	A1	13	1530	1.15	129
	513	8.23	A1S	10	1580	0.9	94
		8.23	A1	7	1490	0.65	118
	514	8.23	A/O1T	5.8	1640	1.7	102
	515	8.23	A/O1T	8	1750	1.45	64
	516	8.23	A1	12.4	1560	0.75	93
	517	8.23	A1	14.3	1700	0.9	59
	518	8.23	A1	11.8	1620	1.15	91
519	8.23	A1	10.8	1600	0.95	89	
40% Lf=135mm	520	8.23	A/O1T	8	1900	2.1	49
	521	8.23	A/O1T	5	1710	3.1	106
	522	8.23	A/O1	16	1700	0.72	54
	523	8.23	A/O1T	9	1650	1	77
	524	8.23	A/O1S	10	1540	1.8	157
	525	8.23	A1	11	1530	2	173
	526	8.23	A1	8.4	1590	0.56	71
	527	8.23	A/O1	7.6	1630	1.5	100
	528	8.23	A/O1T	8	1580	1.3	113
	529	8.23	A/O1S	7	1500	0.8	125

TABLE 6.7 continued

% Oxygen [Lf=(mm)]	Data File #	D710 Gain Setting	Pulse Type	Pulse Length (ms)	Pulse Temp (K)	D710 Output (V)	Calc. dp (μm)
50% Lf=120mm	530	8.23	O1	4	1660	1.5	89
	531	8.23	A/O1T	4.8	1710	1.32	70
	532	8.23	A/O1T	3.6	1690	2.5	104
	533	8.23	A/O1	6	1600	1.5	110
	534	8.23	A1	15	1570	1.6	131
	535	8.23	A/O1T	6	1980	1.75	36
	536	8.23	A/O1T	3.8	1880	2.3	54
	537	8.23	A/O1T	10	1750	2.9	91
	538	8.23	A/O1	5.5	1630	1.4	96
	539	8.23	A1	8.6	1600	0.9	87
65% Lf=120mm	540	8.23	O1	8.5	2060	4.5	47
	541	8.23	A/O1	10	1780	1.1	51
	542	8.23	O1	4	1880	2.8	60
	543	8.23	O1T	3.5	1860	2.3	57
	544	8.23	A/O1	3.9	1640	1.2	86
	545	8.23	O1	5	1950	2.8	50
	546	8.23	O1T	4.5	1750	1.7	70
	547	8.23	O1	3.3	1820	2.7	70
	548	8.23	O1T	5.5	1840	3	71
	549	8.23	O1	3	1810	3	76
80% Lf=120mm	550	8.23	O1	6	1920	3.5	60
	551	8.23	O1	4.3	1780	2.4	76
	552	8.23	O1	9.5	1800	1.8	61
	553	8.23	O1	4.8	2090	7.7	58
	554	8.23	O1	3.8	2070	2.8	36
	555	8.23	O1	10	1870	1.1	39
	556	8.23	O1T	5	1820	2.95	73
	557	8.23	O1	3.5	1950	3.6	56
	558	8.23	O1	3.6	2100	3.1	36
	559	8.23	O1	5.8	1940	2.7	50
560	8.23	O1	2.8	1810	1.8	59	
100% Lf=120mm	561	8.23	O1	10.3	1990	2.4	41
	562	8.23	O1T	4.6	2200	5.45	38
	563	8.23	O1	3.1	2050	4.8	50
	564	8.23	O1T	3.2	2210	2.7	26
	565	8.23	O1	4.7	2100	5	45
	566	8.23	O1	3.8	2060	1.3	25
	567	8.23	O1	3.4	2200	3.9	32
	568	8.23	O1	10.3	2000	2.7	43
	569	8.23	O1	2.8	2120	5.4	45
	570	8.23	O1	9	1800	1.7	59
	571	8.23	O1	4.6	1990	0.9	25
	572	8.23	O1	10	1950	1.8	40
	573	8.23	O1	6	1970	1.1	29
	574	8.23	O1T	5.6	1920	2.4	49
	574	8.23	O1	3	2090	3.9	41

TABLE 6.8 Compiled Results of Experiments Examining the Effects of Oxygen Concentration on the Combustion of 74-88 μ m Pyrite Particles.
($T_{\text{FURNACE}}=1130\text{K}$)

% Oxygen [Lf(mm)]	FILE #	D710 Gain Setting	Pulse Type	Pulse Length (ms)	Pulse Temp (K)	D710 Output (v)	Calc. dp (μm)	Dp Expansion	Heating Rate $\times 10^4 \text{K/s}$	Cooling Rate $\times 10^4 \text{K/s}$
10% [200mm]	264	6.73	A3	26	2000	1.1	77	1.24	4.9	
	265	6.73	A3	22	2190	0.28	25	2.43	3.5	4.7
	266	6.73	A3	21	1970	0.45	53	1.90		3.2
	267	6.73	A3	27	1950	0.5	59	1.93	2.4	2.9
	268	6.73	A3	23	1970	0.45	53	2.04	2.6	3.6
15% [140mm]	312	4.73	A3	16	2290	0.27	80	2.36	3.3	5.6
	313	4.73	A3	17.2	2310	0.2	66	2.36	3.5	9.3
	314	4.73	A3	19.5	2400	0.22	59	2.34	3.7	10.2
	315	4.73	A3	13	2280	0.2	70	2.04	5.1	12.5
	316	4.73	A3	18	2280	0.195	69	2.14	4.5	6.9
21% [120mm]	200	5.23	A3	17	2460	0.6	62	2.17	6.3	15
	201	5.23	A3	17	2500	0.5	53	2.47	3.4	11.4
	202	5.23	A3	17	2540	0.4	44	2.70	5.3	16
	203	5.23	A3	19	2590	0.295	36	2.59	3.6	14.3
	204	5.23	A3	19	2470	0.4	50	2.26	5	15.5
	251	5.23	A3	21	2470	0.8	70	2.06	3.9	11.8
	252	5.23	A3	21	2350	0.75	84	1.64		12.8
	253	5.23	A3	15	2510	0.8	66	2.50	5.6	12
	254	5.23	A3	11	2500	0.6	57	2.74	4.3	13.5
	255	5.23	A3	16	2450	1	81	2.05		10.9
25% [120mm]	305	4.73	A3	20	2820	0.6	52	2.78	6.3	16.7
	306	4.73	A3	15	2810	1.5	83	2.58	3.5	18.2
	307	4.73	A3	15	2810	1.6	86	2.44	5.6	14.5
	308	4.73	A3	16	2830	1.4	78	2.38	6.4	15
	309	4.73	A3	16	2800	0.9	65	2.85		17.5
	310	4.73	A3	16.3	2800	1.1	71	2.73	5.8	13.4
	311	4.73	A3	14	2690	2.1	116	1.76	5.4	11.4
		4.73	A3		2770	9	214			
30% [115mm]	269	5.23	A3	18.5	2600	1	64	1.26	10	24
	270	5.23	A3	14	3180	0.9	30	2.67	4.7	16.4
	271	5.23	A3	12	3060	1.1	38	2.24	8	29
	272	5.23	A3	16	3000	1	38	3.12		22
	273	5.23	A3	18	3220	0.6	23	2.58	6	30
	274	5.23	A3	14	3000	1.5	47	2.46	1.2	11
	275	5.23	A3	16	2840	2.3	70	1.42		33

TABLE 6.8 continued

% Oxygen [Lf(mm)]	FILE #	D710 Gain Setting	Pulse Type	Pulse Length (ms)	Pulse Temp (K)	D710 Output (v)	Calc. dp (μm)	Dp Expansion	Heating Rate $\times 10^4 \text{K/s}$	Cooling Rate $\times 10^4 \text{K/s}$
40% [100mm]	276	5.23	A3	17.6	3050	2.3	55	1.71	7.5	
	277	5.23	A3	19	3040	3	64	2.30	5.6	17.1
	278	5.23	A3	18	3130	3.4	61	2.24	17.4	20
	279	5.23	A3	17.8	3020	3	65	2.29	5	16.7
	280	5.23	A3	18.4	3080	2.8	58	2.01	4	16.9
	281	5.23	A3	16	3150	3.4	60	2.32	15.4	15
50% [100mm]	282	4.73	A3	16	3210	4	86	2.24	21.3	28.6
	283	4.73	A3	18	3490	4	67	2.23	8.3	22
	284	4.73	A3	21	3240	10	133			14.8
		4.73	A3		2990	10	172			
	285	4.73	A3	16.5	3220	4.4	90	2.27	17	16.7
	286	4.73	A3	16	3230	10	134	1.80	11.1	10
	287	4.73	A3	15.8	3280	6	99	2.23	5.2	14.3
	288	4.73	A3	14.8	3140	2.7	76	2.27	7	20
	289	4.73	A3	14.3	3200	2.2	65	2.48	12.5	23
	290	4.73	A3	14.1	3140	2.4	72	2.30	11.8	17.7
65% [100mm]	291	4.73	A3	14.3	3090	1.6	62		7.5	
	292	4.73	A3	12.8	3170	2.4	70	2.70	9.3	23.5
	293	4.73	A3	21	3070	2.3	76	2.68	8.3	25
		4.73	A3		3150	3.3	83	2.50	12	18.2
	294	4.73	A3	13	3210	2.4	67	2.74	20	20
	295	4.73	A3	15.2	3050	4	102	2.07	6.75	16.7
	296	4.73	A3	13.3	3240	2.1	61	2.51	9.5	
	297	4.73	A3	13.8	3180	3.6	85	2.64	8.5	18.7
	298	4.73	A3	14.1	3260	2.1	60	2.36	11.1	17.9
	299	4.73	A3	13.8	3160	2.8	76	2.90	6.9	22.2
80% [100mm]	300	4.73	O3	14.9	3200	2.75	72	1.08	7.6	11.4
	301	4.73	A3	21	3000	1.95	75	3.72	9.5	21.1
	302	4.73	A3	14.6	3080	5.4	115	2.32	8.5	16.7
	303	4.73	O3	10.2	3190	3.5	82	1.09	7.9	10
	304	4.73	O3	13	3300	5.8	95		6.6	6
100% [75mm]	244	5.23	O3	12.6	3280	4	57	1.16	12.5	19
	245	5.23	O3	11	3490	7.8	66	0.67	14.9	
	246	5.23	O3S	10.7	3200	2.6	50		14.3	
	247	5.23	O3S	13.8	3350	4.4	56	1.06	14.2	25
	248	5.23	O3	12.4	3330	3	47	1.36	15.2	24
	249	5.23	O3	14.6	3200	4.2	63	0.62	15.4	10
	250	5.23	O3T	5	3540	10	72		50	
	256	5.23	O3T	6.8	3230	1.7	39		57	95
	257	5.23	O3S	7.7	3290	4.5	60			

TABLE 6.2 Averaged Results of the Experiments Examining the Effect of the Oxygen concentration on the Combustion of 74-88 μ m Galena Particles.
($T_{\text{FURNACE}}=1130\text{K}$) Sample standard deviation ()

Percent Oxygen	# of Pulses	Pulse Length (ms)	Measured Temperature (K)	Apparent Diameter (μm)
10	10	16.6(2.4)	1557(92)	91(36)
21	10	11.1(2.3)	1591(74)	87(23)
30	11	11.0(2.8)	1601(78)	96(22)
40	10	9.0(3.0)	1625(115)	102(41)
50	10	6.7(3.6)	1707(132)	87(27)
65	11	4.7(2.7)	1836(108)	63(13)
80	11	5.4(2.3)	1934(122)	55(14)
100	15	5.6(2.8)	2043(115)	39(10)

TABLE 6.10 Measured Particle Expansions, Heating Rates and Cooling Rates for the Combustion of 74-88 μ m Galena in Different Oxygen concentrations.
($T_{\text{FURNACE}}=1130\text{K}$)

FILE #	Percent Oxygen	Pulse Type	First Energy Maxima Temp. (K)	Second Energy Maxima Temp. (K)	Twin Peak Expansion Ratio (d_{p2}/d_{p1})	Heating Rate (10^4K/s)	Cooling Rate (10^4K/s)
502	21	A1	1534				2
507	21	A1	1610				3
511	30	A1	1530				2.3
514	30	A/O1T	1640	1610	0.45		
515	30	A/O1T	1750	1600	0.45		
516	30	A1	1560				2.25
517	30	A1	1710				2.5
518	30	A1	1620				4.3
520	40	A/O1T	1900	1630	1.3		
521	40	A/O1T	1710	1510	0.77		5.6
523	40	A/O1T	1580	1650	0.9		
527	40	A/O1	1630				5.2
528	40	A/O1T	1580	1580	1.4		
530	50	O1	1660			11.4	
531	50	A/O1T	1670	1710	0.71		
532	50	A/O1T	1610	1690	0.71	15.5	19.4
533	50	A/O1	1600				5.3
534	50	A1	1570				3.6
535	50	A/O1T	1610	1980	0.45		17
536	50	A/O1T	1690	1880	0.55	16	
537	50	A/O1T	1590	1750	1.3		
542	65	O1	1880				11.4
543	65	O1T	1640	1860	0.5		
544	65	A/O1	1640				5.6
545	65	O1	1950				12.5
546	65	O1T	1620	1750	1.0		
548	65	O1T	1580	1840	0.8		
551	80	O1	1780				11.9
556	80	O1T	1820	1690	0.7		
558	80	O1	2100				15
559	80	O1	1940				10
560	80	O1	1810			14.3	33
561	100	O1	1990				8.5
562	100	O1T	1710	2200	0.2	33	27
563	100	O1	2050			50	40
564	100	O1T	1680	2210	0.2	45	
567	100	O1	2200			57	
568	100	O1	2000				10
569	100	O1	2120				31
573	100	O1T	1650	1920	0.2		
574	100	O1	2090				22

TABLE 6.11 Averaged Results of the Experiments Examining the Effect of the Oxygen concentration on the Combustion of 74-88 μ m Pyrite Particles.
($T_{\text{FURNACE}}=1130\text{K}$) Sample standard deviation ()

Percent Oxygen	# of Pulses	Pulse Length (ms)	Measured Temperature (K)	Apparent Diameter (μm)	Apparent Expansion (d_p2/d_p1)	Heating Rate $\times 10^4 \text{K/s}$	Cooling Rate $\times 10^4 \text{K/s}$
10	5	23.8(2.6)	2013(101)	54(19)	1.9(0.4)	3.4(1.1)	3.6(0.8)
15	5	16.7(2.5)	2310(49)	69(8)	2.3(0.2)	4.0(0.8)	8.9(2.7)
21	10	17.3(3.0)	2483(63)	60(16)	2.3(0.3)	4.7(1.0)	13.3(1.8)
25	8	16.0(1.9)	2791(46)	96(51)	2.5(0.3)	5.5(1.1)	15.2(2.4)
30	7	15.5(2.3)	2985(211)	44(17)	2.3(0.6)	6.0(3.3)	23.6(7.9)
40	6	17.8(1.0)	3077(53)	60(3)	2.1(0.2)	9.2(5.8)	17.1(1.8)
50	10	16.3(2.1)	3214(125)	99(36)	2.2(0.2)	11.8(5.3)	18.6(5.5)
65	10	14.6(2.5)	3157(71)	74(14)	2.6(0.2)	10.0(3.9)	20.3(3.0)
80	5	14.7(4.0)	3154(116)	88(17)	2.1(1.2)	8.0(1.1)	13.0(5.9)
100	9	10.5(3.3)	3324(121)	57(10)	1.0(0.3)	14.4(1.1)*	19.5(6.9)*

* - heating and cooling rates of Py250 and Py256 ($> 50 \times 10^4 \text{K/s}$) not included.

TABLE 6.12 Chemical Analyses of the Galena, Sullivan and Brunswick Concentrates Combusted in Air and Oxygen. ($T_{\text{FURNACE}}=1130\text{K}$)
(original chemical composition of the feed materials given in Table 4.1)

i) Air

Feed Material	Size Fraction (μm)	Lf (mm)	Pb _{TOTAL} (%)	Pb ⁰ (%)	Fe _{TOTAL} (%)	%Fe as Fe(II)	S _{TOTAL} (%)	Zn _{TOTAL} (%)	%S as SO ₄ ²⁻	
Galena	74-88	160	84.5	1.2	0.3	0.3	13.0	0.9	<0.1	
		190	83.6	-	0.3	0.3	11.4	1.0	0.3	
		230	85.8	-	0.3	0.3	10.1	1.0	<0.1	
		270	80.0	-	1.4	-	-	4.7	-	
	105-125	200	83.8	0.9	0.5	0.5	13.6	1.1	<0.1	
		282	84.8	9	0.6	0.6	10.7	1.2	0.2	
		320	82.6	-	0.9	0.9	8.5	1.9	0.6	
		400	61.0	-	5.7	-	-	15.0	-	
Fume	-	-	68.1	-	0.4	-	7.1	-	-	
Sullivan	74-88	120	62.7	2.1	9.5	9.4	16.5	5.4	0.2	
		160	59.3	4.3	12.8	11.0	12.1	7.2	0.1	
		200	44.6	2.5	20.3	17.0	4.4	11.3	0.3	
		253	39.5	0.7	23.0	8.4	2.3	12.0	0.9	
	105-125	100	63.8	2.5	9.2	9.9	16.7	4.6	0.8	
		140	62.6	5.3	10.6	10.6	12.5	5.4	0.5	
		180	54.8	5.2	15.2	15.2	7.7	7.4	0.7	
		231	44.1	-	20.6	10.0	2.8	10.6	0.8	
		282	38.2	0.7	23.1	4.9	2.1	10.2	1.7	
		-	-	-	-	-	-	-	-	-
Brunswick	74-88	80	30.4	0.8	18.8	2.6	30.2	12.1	2.0	
		120	29.9	2.2	22.8	20.6	19.4	16.8	0.4	
		160	15.4	1.0	31.2	30.4	13.0	22.5	0.2	
		217	11.5	-	35.9	23.8	12.0	-	<0.1	
	105-125	163	38.5	2.0	21.6	-	14.1	10.4	1.5	
		233	17.5	0.9	36.5	-	6.7	14.8	0.6	
		315	13.2	0.7	35.7	-	8.2	18.3	0.1	
		415	11.5	0.2	37.8	-	3.8	13.8	1.5	
		-	-	-	-	-	-	-	-	-
		-	-	-	-	-	-	-	-	-

ii) Oxygen

Feed Material	Size Fraction (μm)	Lf (mm)	Pb _{TOTAL} (%)	Pb ⁰ (%)	Fe _{TOTAL} (%)	Fe ²⁺ as %Fe _{TOTAL}	S _{TOTAL} (%)	Zn _{TOTAL} (%)	SO ₄ ²⁻ as %S _{TOTAL}
Galena	63-74	85	84.7	0.7	0.3	0.3	14.1	0.8	<0.1
		102	84.6	-	0.2	0.2	12	0.8	-
		125	71.0	-	1.4	-	-	2.5	-
Sullivan	74-88	55	61.6	2.5	9.8	9.8	17.7	5.6	0.6
		70	55.8	2.2	12.5	12.2	13.3	7.3	1.5
		85	57.1	2.9	13.1	13.0	10.3	6.8	1.0
		102	51.9	0.4	14.1	0.8	4.4	6.9	4.0
Brunswick	74-88	55	29.9	0.7	19.4	3.4	28.8	12.5	1.9
		70	30.8	0.9	18.8	3.2	28.6	12.4	1.9
		85	22.7	-	29.8	12.6	3.7	19.1	1.0
		102	21.5	-	32.8	9.0	3.2	13.5	1.4

TABLE 6.13 Results of Chemical Analyses for the Combustion of Galena, Sullivan and Brunswick Concentrates in Air and Oxygen. ($T_{\text{FURNACE}}=1130\text{K}$)
(concentrations of the different reaction products are given in Table 6.12)

i) Air

Feed Material	Size Fraction (μm)	Lf (mm)	Product Weight (as % of W_{FEED})	% of Original Lead	% of Original Sulphur	%Pb as Metallic Lead	%Fe as Fe(II)	Fe/Zn Ratio	S/Pb Molar Ratio	
Galena	74-88	160	99	100	94	1.4	100	0.33	1.00	
		190	86	89	74	-	100	0.30	0.88	
		230	57	91	65	-	100	0.30	0.76	
		270	8	18	-	-	-	0.30	-	
	105-125	200	71	100	97	1.1	100	0.45	1.05	
		282	28	92	70	10.6	100	0.50	0.82	
		320	-	57	35	-	100	0.47	0.67	
		400	2.75	5	-	-	-	0.38	-	
Sullivan	74-88	120	71	102	91	3.3	99	1.76	1.70	
		160	44	72	49	7.3	86	1.78	1.32	
		200	23	34	11	5.6	84	1.80	0.64	
		253	18	27	5	1.8	37	1.92	0.38	
	105-125	100	87	99	90	3.9	100	2.00	1.69	
		140	76	84	58	8.5	100	1.96	1.29	
		180	38	51	25	9.5	100	2.05	0.91	
		231	15	30	7	-	48	1.94	0.41	
282	34	23	4	1.8	21	2.26	0.36			
	Brunswick	74-88	80	85	99	95	2.6	14	1.55	6.43
			120	45	80	50	7.4	90	1.36	4.20
			160	29	30	25	6.5	97	1.39	5.46
217			9	20	20	-	66	-	6.75	
105-125	163	-	92	40	5.2	-	2.07	2.37		
	233	-	25	11	5.3	-	2.47	2.48		
	315	-	19	14	5.4	-	1.95	4.02		
	415	-	16	6	1.4	-	2.74	2.14		

ii) Oxygen

Feed Material	Size Fraction (μm)	Lf (mm)	Product Weight (as % of W_{FEED})	% of Original Lead	% of Original Sulphur	Metallic Lead as %Pb _{TOTAL}	Fe ⁺² as %Fe _{TOTAL}	Fe/Zn Ratio	S/Pb Molar Ratio
Galena	63-74	85	97	87	92	0.8	100	0.38	1.08
		102	27	87	78	-	100	0.25	0.92
		125	8	23	-	-	-	0.56	-
Sullivan	74-88	55	97	97	94	4.1	100	1.75	1.86
		70	18	69	56	3.9	98	1.71	1.54
		85	42	68	41	5.1	99	1.93	1.17
		102	22	57	16	0.8	6	2.04	0.55
Brunswick	74-88	55	87	95	88	2.3	18	1.55	6.23
		70	86	100	90	2.9	17	1.52	6.01
		85	21	47	7	3.0	42	1.56	1.05
		102	10	40	6	-	27	2.42	0.96

TABLE 6.14 X-ray Diffraction Analysis of Reacted Material(T_{FURNACE}=1130K)

M = major amounts s = minor amounts

G = galena (PbS)

A = anglesite (PbSO₄)L = Lanarkite (PbO.PbSO₄)

D = Dibasic lead Sulphate

(2[PbO].PbSO₄)

S = sphalerite (ZnS)

Z = zincite (ZnO)

ZF = zinc ferrite (ZnFe₂O₄)Py = pyrite (FeS₂)

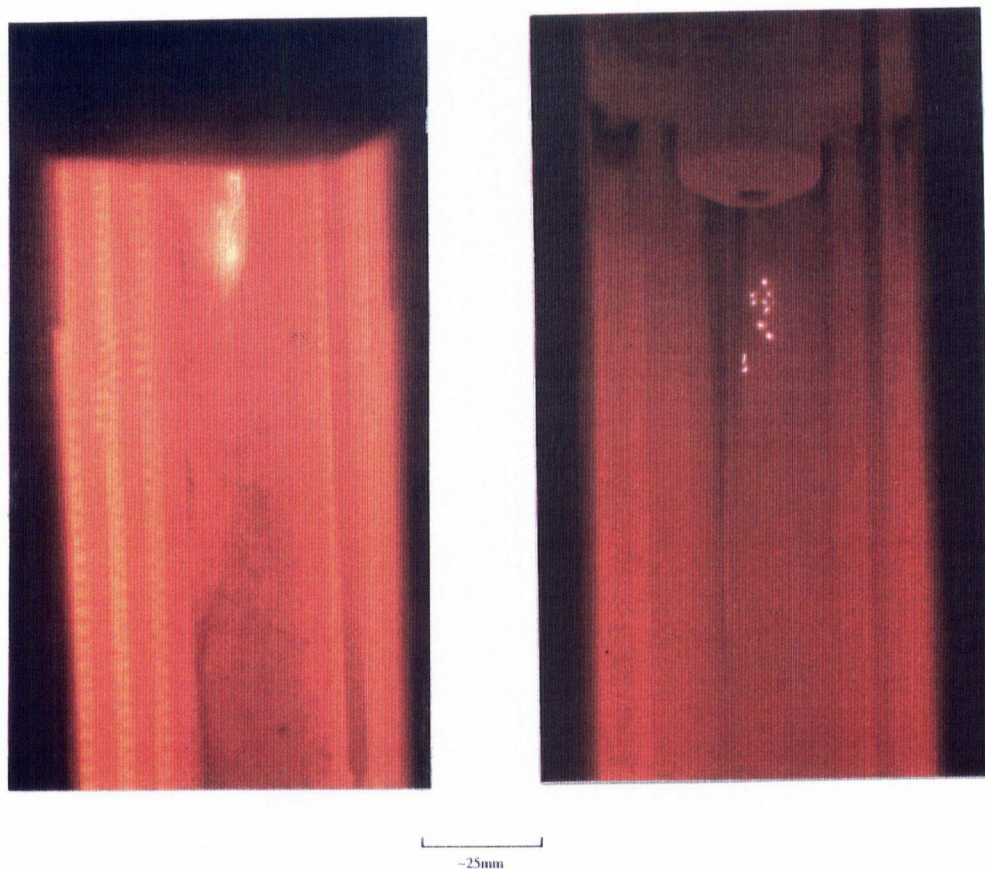
Ph = pyrrhotite (FeS)

Mag = magnetite (Fe₃O₄)He = hematite (Fe₂O₃)**i) AIR**

Feed Material	Size Fraction (μm)	Combustion Distance (mm)	G	A	L	D	S	Z	Py	Ph	Mag	He	Appearance
Galena	74-88	160	M	s	-	-	s	-	-	-	-	-	black(feed) blackish grey fine beige powder
		180	M	s	s	-	s	-	-	-	-	-	
		230	M	s	s	-	s	s	-	-	-	-	
		270	s	M	s	s	M	s	-	-	-	-	
	105-125	200	M	-	-	-	s	-	-	-	-	-	black(feed) grey grey/white yellowish/brown
		282	M	s	-	-	s	s	-	-	-	-	
		320	s	M	M	s	s	s	-	-	-	-	
		400	s	M	M	-	M	s	-	-	-	-	
Fume	-	-	-	M	-	-	-	-	-	-	-	fine white powder	
Sullivan	74-88	120	M	s	s	-	M	s	s	s	-	-	black(feed) black(feed) white flecks white flecks
		160	M	s	-	-	M	s	-	-	M	-	
		200	M	s	-	-	M	s	-	-	M	-	
		252	s	s	-	-	s	s	-	-	M	-	
	105-125	100	M	s	-	-	M	-	s	M	-	-	black(feed) greyish greyish grey/white white/grey
		140	M	s	-	-	M	s	-	-	M	-	
		180	M	s	-	-	-	s	-	-	M	-	
		230	M	M	-	-	-	s	-	-	M	-	
		28.2	s	M	-	-	-	-	-	M	s		
Brunswick	74-88	80	M	s	s	-	M	-	M	M	-	-	grey/black(feed) black white flecks grey/white fleck
		120	M	s	s	-	M	s	s	s	s	-	
		160	M	M	-	-	M	s	-	s	M	-	
		217	s	M	s	-	s	s	-	-	M	-	

ii) OXYGEN

Feed Material	Size Fraction (μm)	Combustion Distance (mm)	G	A	L	S	Z	Py	Ph	Mag	He	ZF	Appearance	
Galena	63-74	85	M	-	s	s	-	-	-	-	-	-	black/grey grey fine beige powder	
		102	M	s	s	-	s	-	-	-	-	-		
		125	s	M	-	-	s	-	-	-	-	-		
Sullivan	74-88	55	M	s	-	M	-	s	s	-	-	-	black(feed) grey grey/brown brown/grey	
		70	M	M	-	M	-	-	-	s	M	s		
		85	M	M	-	s	-	-	-	-	M	s		s
		102	-	M	-	-	-	-	-	-	s	M		s
Brunswick	74-88	55	M	M	-	M	-	M	s	s	s	-	grey/black(feed) brown/black grey/white fleck	
		70	s	s	-	M	-	s	s	M	s	-		
		85	s	M	-	M	s	-	-	-	s	M		s



(a) air

(b) oxygen

Figure 6.1 Time exposure photographs of galena combustion in air and oxygen.
a) 63-74 μm screen fraction, air, $T_{\text{FURNACE}}=1123\text{K}$ $t_{\text{exp}}=0.125\text{s}$.
b) 63-74 μm screen fraction, oxygen, $T_{\text{FURNACE}}=1023\text{K}$ $t_{\text{exp}}=0.067\text{s}$.

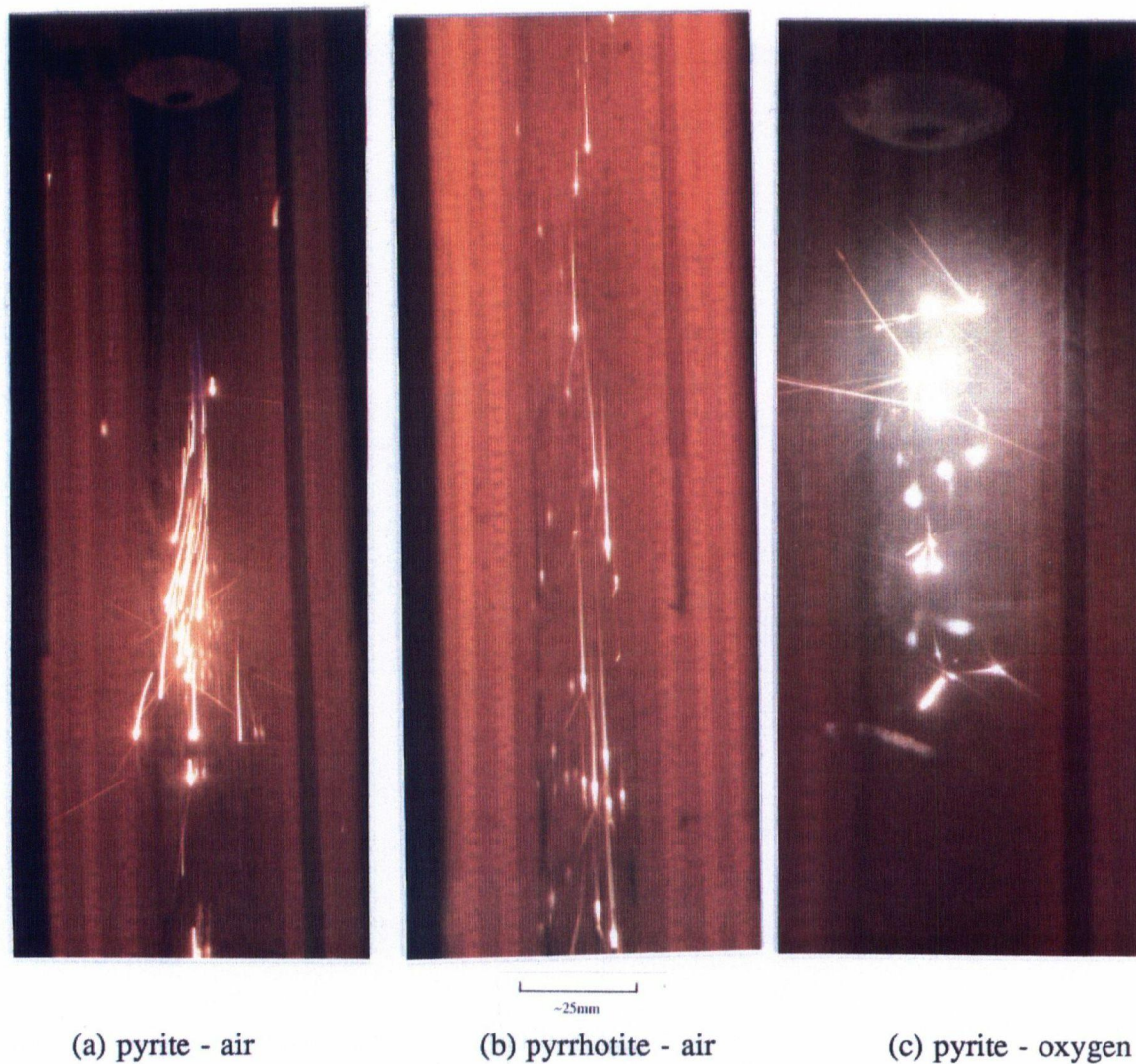
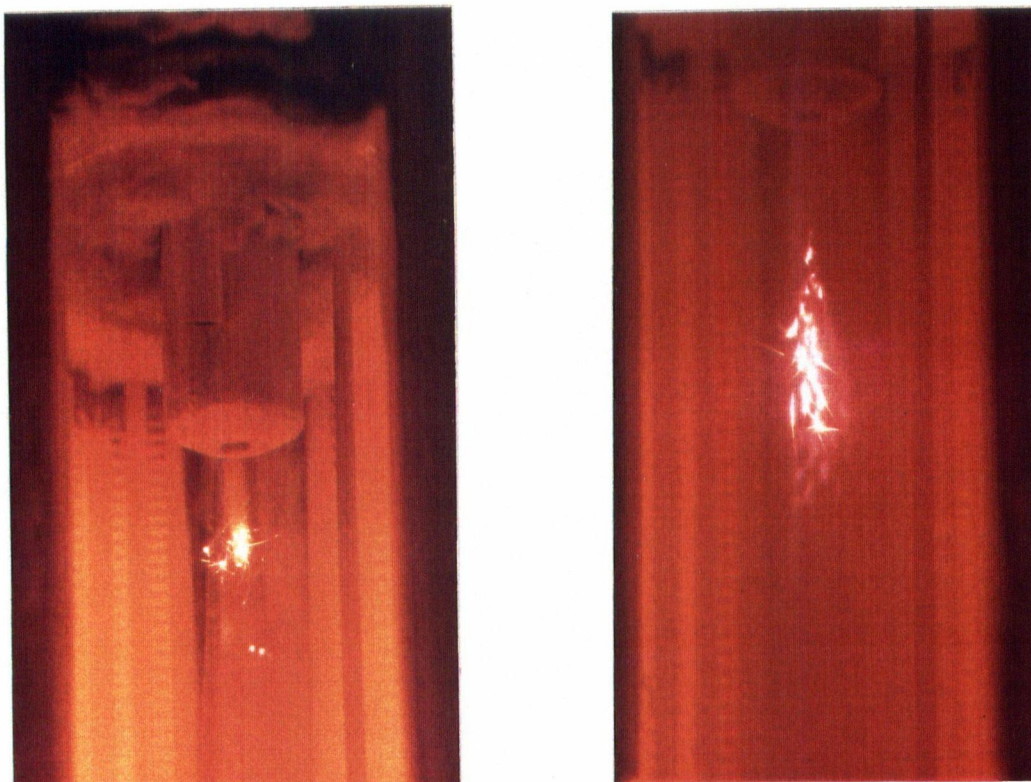


Figure 6.2 Time exposure photographs of pyrite and pyrrhotite combustion in air and oxygen.

a) Pyrite, 74-88 μm screen fraction, air, $T_{\text{FURNACE}}=1023\text{K}$, $t_{\text{exp}}=0.125\text{s}$.

b) Pyrrhotite, 74-88 μm screen fraction, air, $T_{\text{FURNACE}}=1123\text{K}$, $t_{\text{exp}}=0.125\text{s}$.

c) Pyrite, 74-88 μm screen fraction, oxygen, $T_{\text{FURNACE}}=1023\text{K}$, $t_{\text{exp}}=0.067\text{s}$.



~25mm

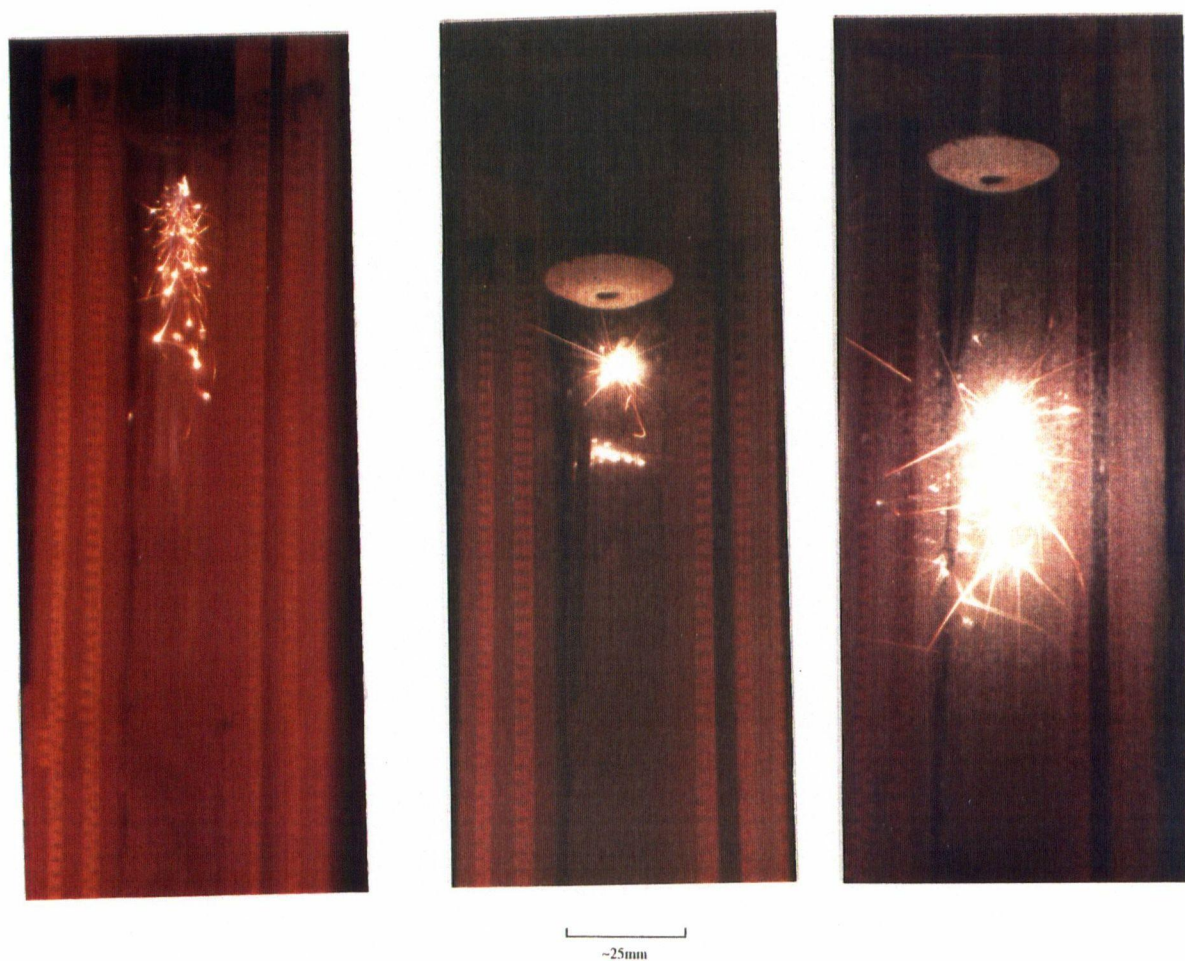
(a) air

(b) oxygen

Figure 6.3 Time exposure photographs of Sullivan concentrate combustion in air and oxygen.

a) 63-74 μ m screen fraction, air, $T_{\text{FURNACE}}=1123\text{K}$ $t_{\text{exp}}=0.125\text{s}$,

b) 63-74 μ m screen fraction, oxygen, $T_{\text{FURNACE}}=1023\text{K}$ $t_{\text{exp}}=0.125\text{s}$.



(a) air

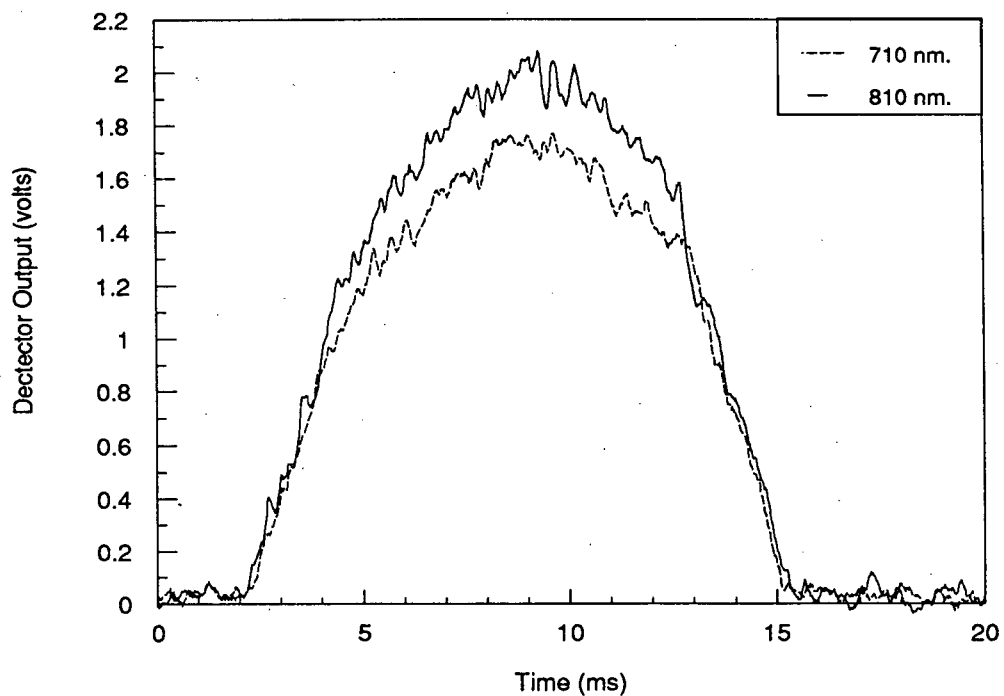
(b) oxygen - 63-74 μm (c) oxygen - 105-125 μm

Figure 6.4 Time exposure photographs of Brunswick concentrate combustion in air and oxygen.

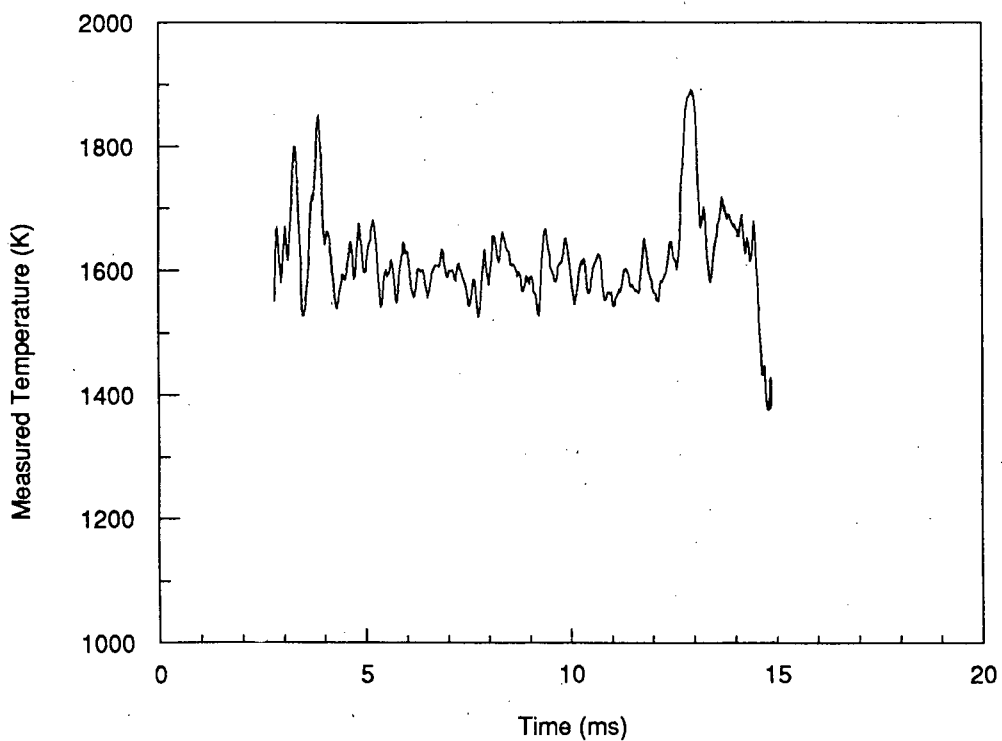
a) 63-74 μm screen fraction, air, $T_{\text{FURNACE}}=1023\text{K}$ $t_{\text{exp}}=0.125\text{s}$.

b) 63-74 μm screen fraction, oxygen, $T_{\text{FURNACE}}=1023\text{K}$ $t_{\text{exp}}=0.067\text{s}$.

c) 105-125 μm screen fraction, oxygen, $T_{\text{FURNACE}}=1023\text{K}$ $t_{\text{exp}}=0.067\text{s}$.

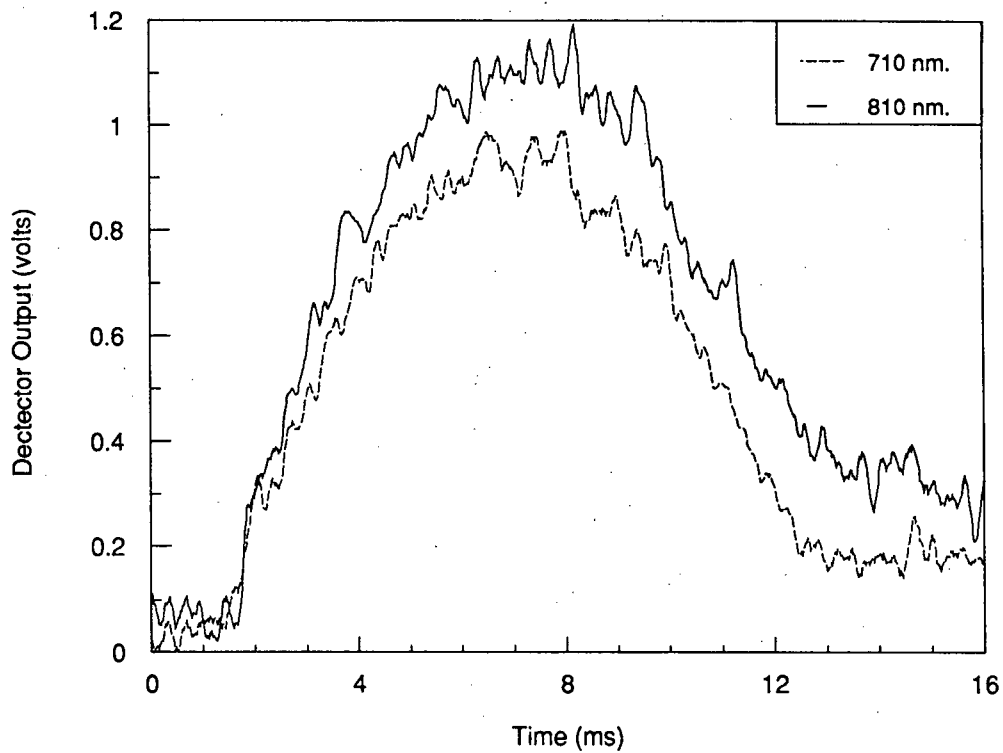


(a)

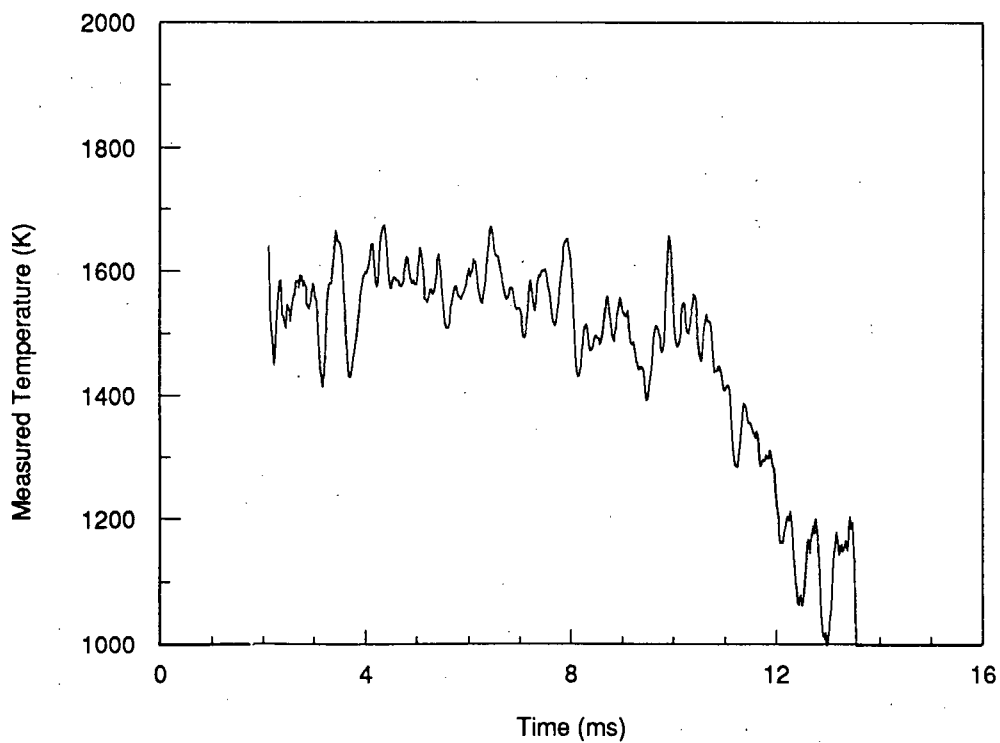


(b)

Figure 6.5 A1 combustion pulse recorded during the combustion of galena in air. a) pyrometer output and b) measured temperature. (63-74 μ m, $T_{\text{FURNACE}}=1130\text{K}$, $C_{\text{VAL}}=1.42$, data#=G237.dat).



(a)



(b)

Figure 6.6 A1 combustion pulse recorded during the combustion of galena in air. a) pyrometer output and b) measured temperature. ($63\text{-}74\mu\text{m}$, $T_{\text{FURNACE}}=1130\text{K}$, $C_{\text{VAL}}=1.42$, data#=G352.dat).

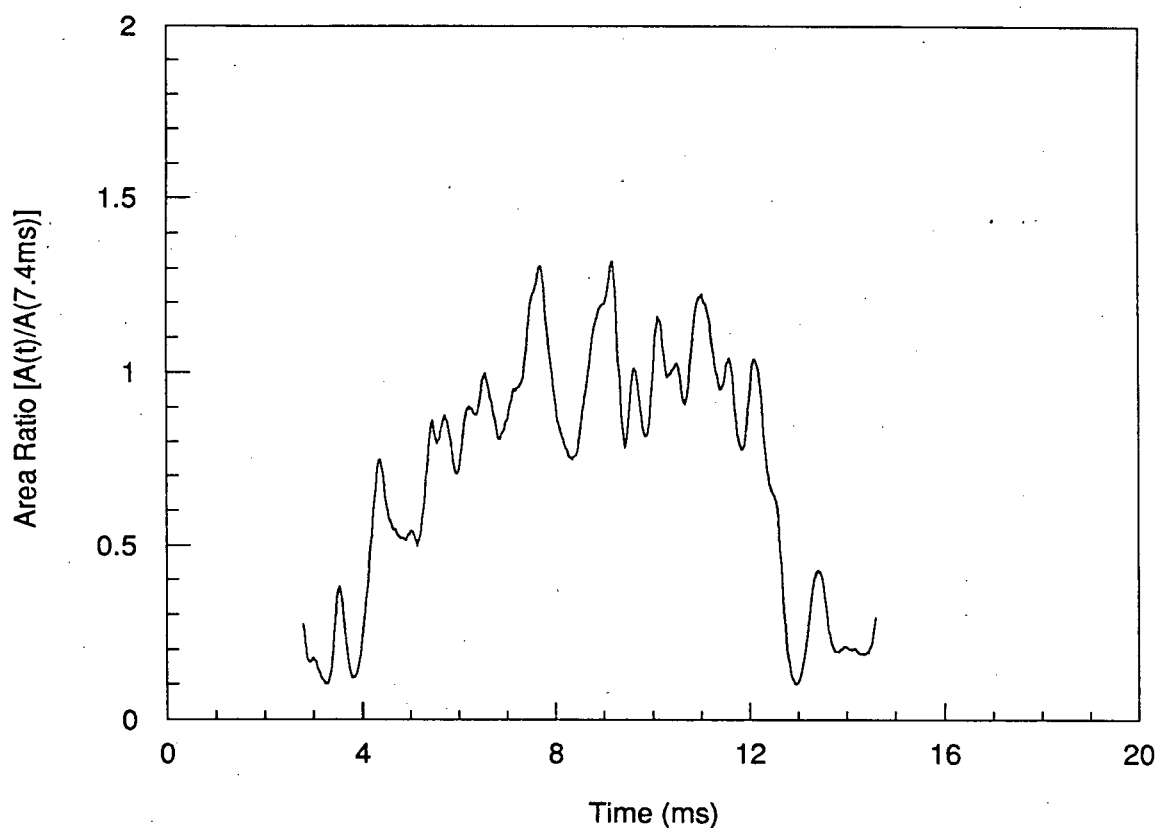


Figure 6.7 Variation in apparent relative area from the A1 galena combustion pulse shown in Figure 6.5. Particle area calculated relative to that at 7.4ms. (63-74 μm , $T_{\text{FURNACE}}=1130\text{K}$, $C_{\text{VAL}}=1.42$, data#=G237.dat).

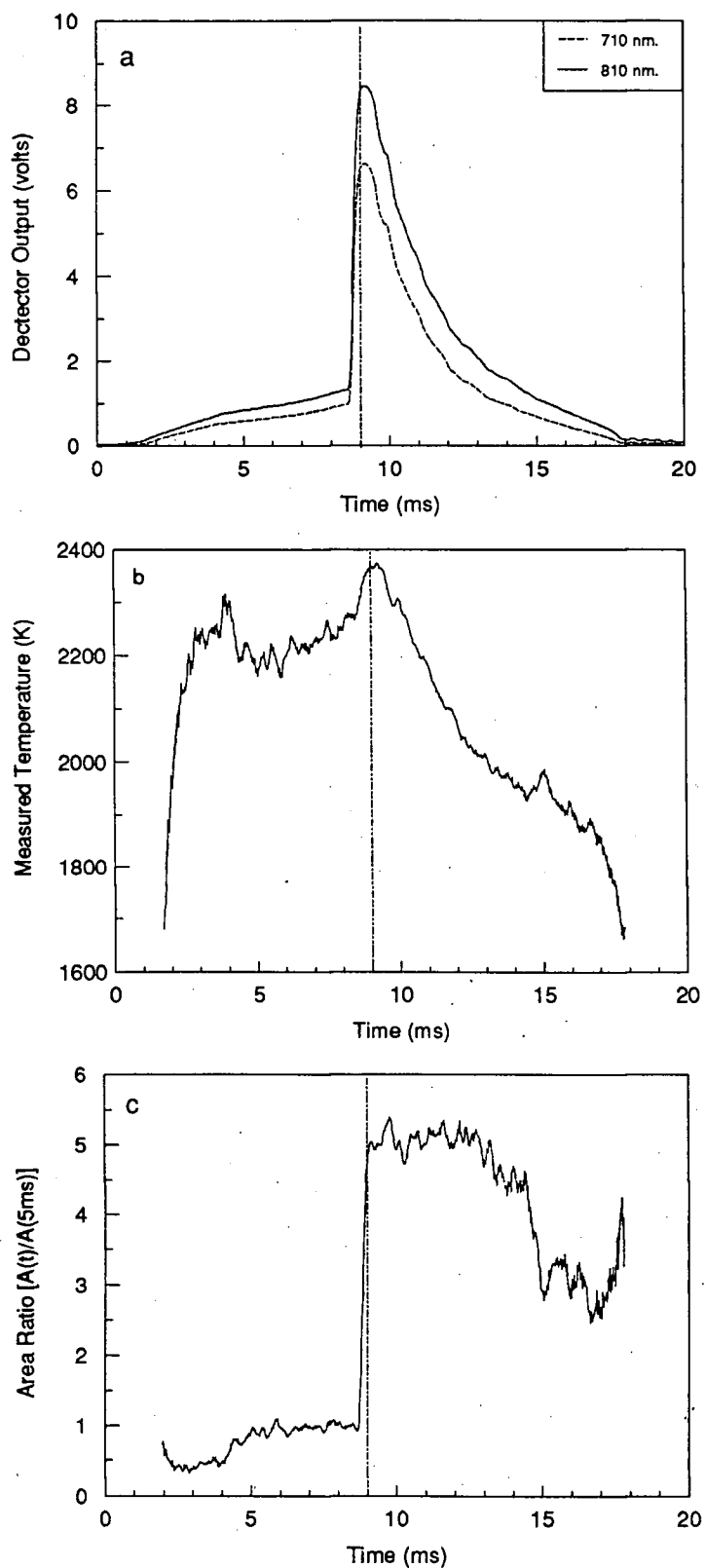


Figure 6.8 A3 combustion pulse recorded during the combustion of pyrrhotite in air, a)pyrometer output, b)measured temperature and c)apparent area relative to that at 5ms.
 (74-88 μ m, $T_{\text{FURNACE}}=1130\text{K}$, $C_{\text{VAL}}=1.01$, data#=PH126.dat).

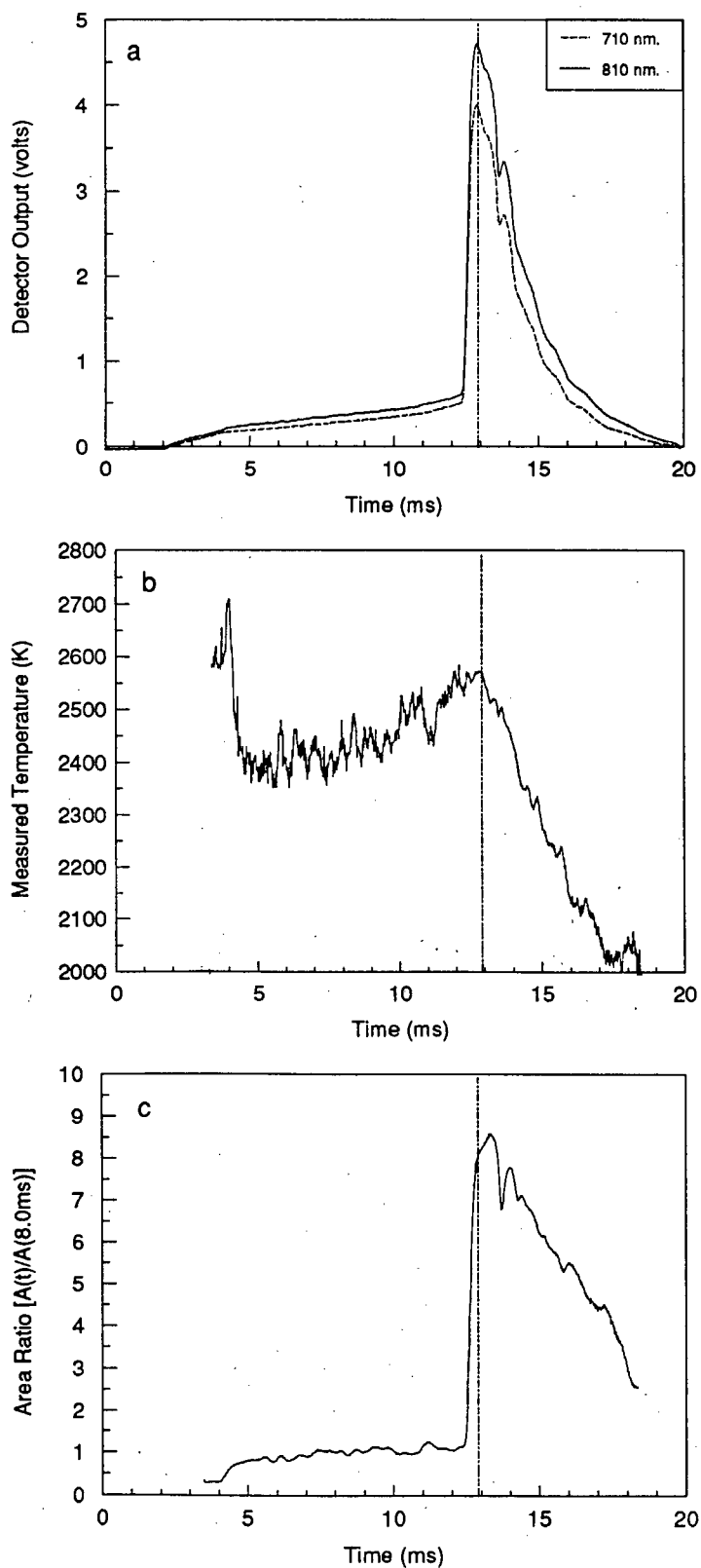


Figure 6.9 A3 combustion pulse recorded during the combustion of pyrite in air. a) pyrometer output, b) measured temperature and c) apparent area relative to that at 8ms. ($74-88\mu\text{m}$, $T_{\text{FURNACE}}=1130\text{K}$, $C_{\text{VAL}}=0.81$, data#=PY201.dat).

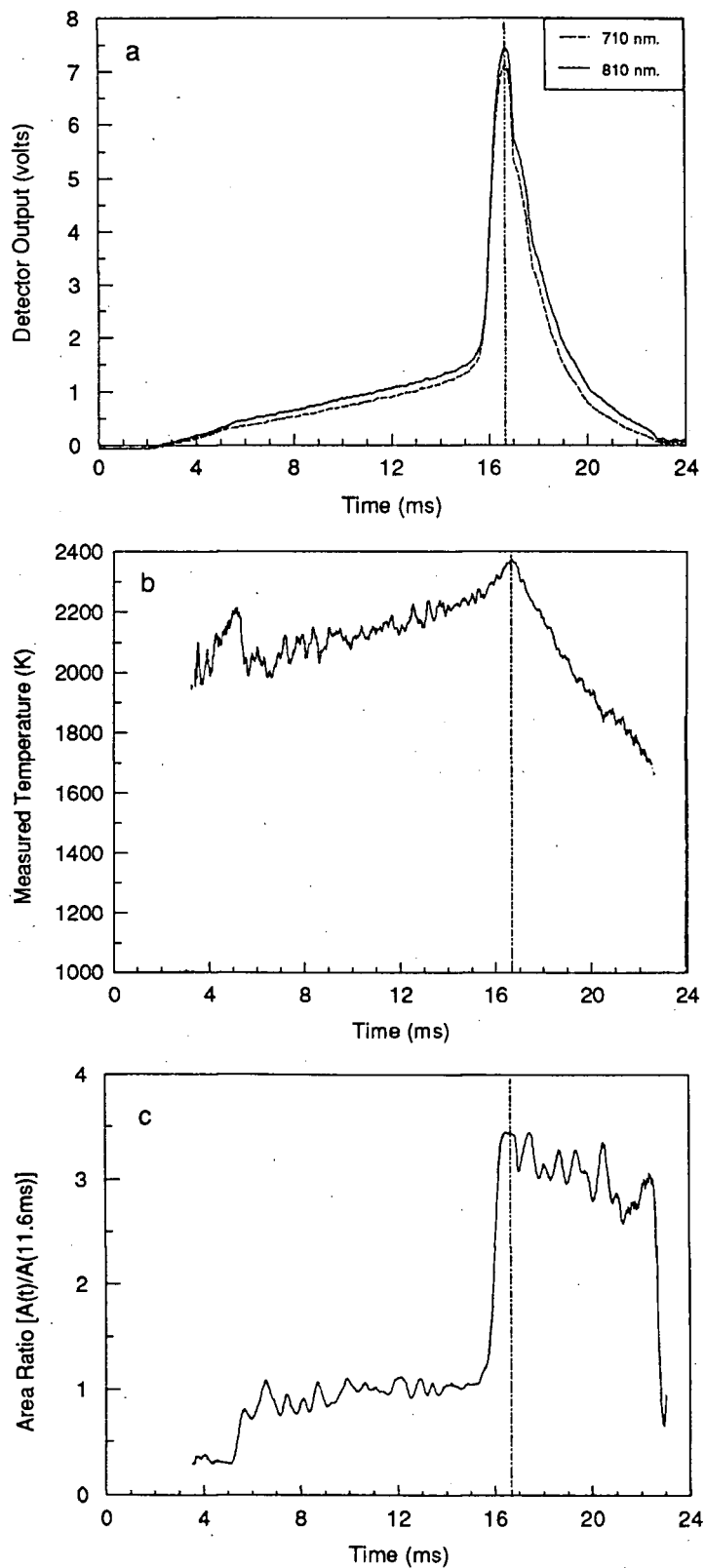
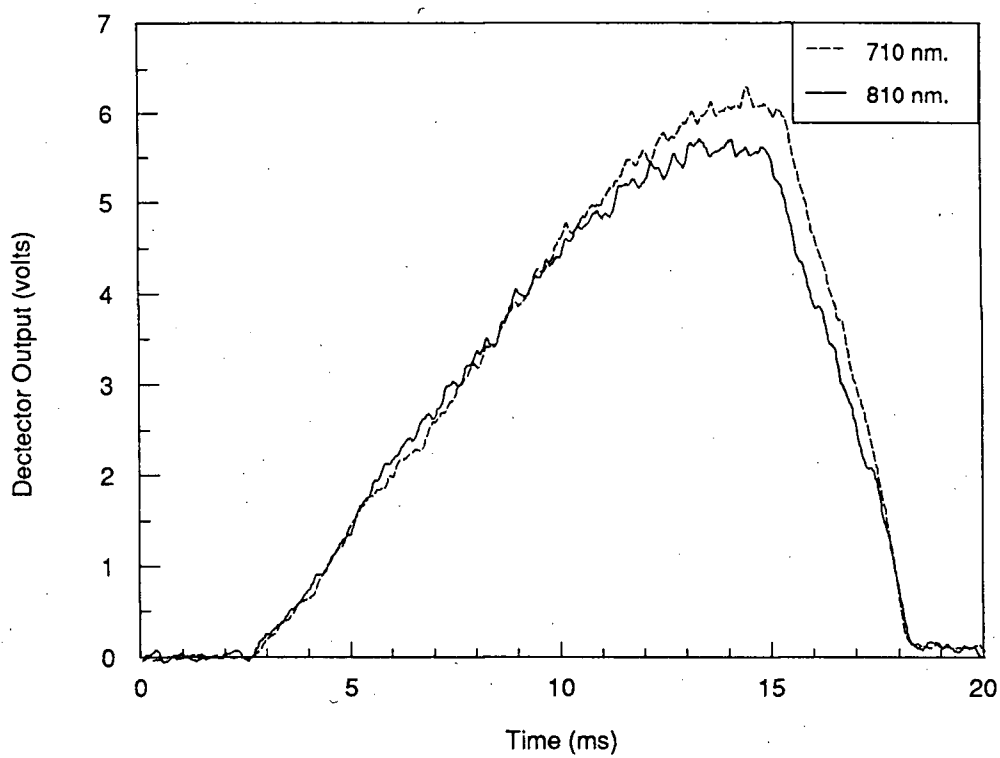
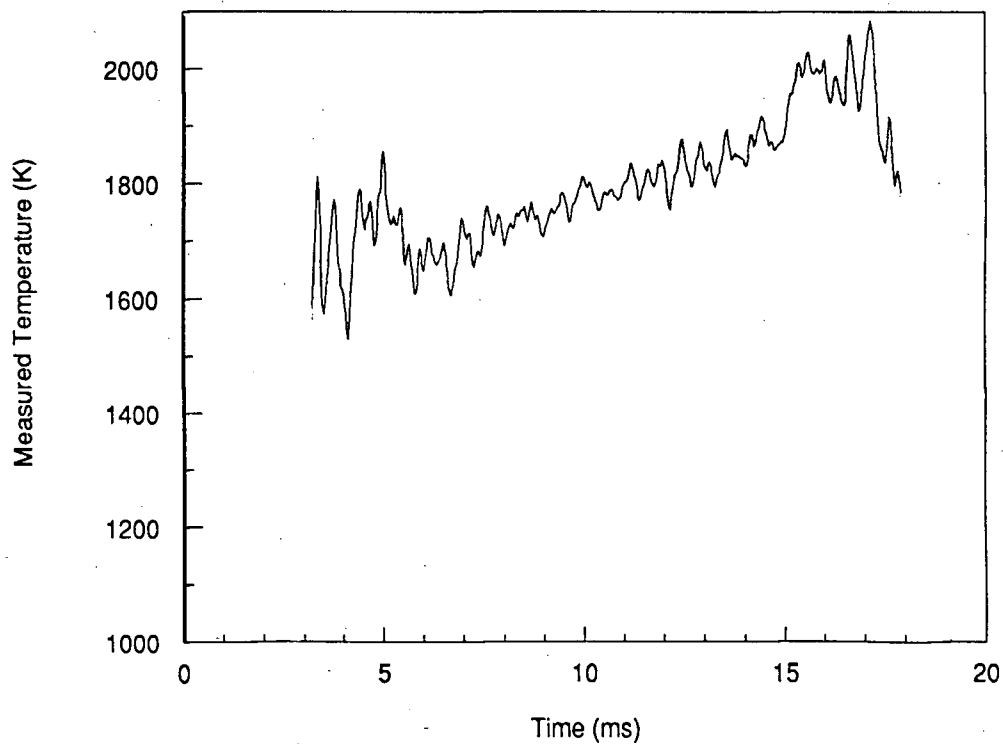


Figure 6.10 A3 combustion pulse recorded during the combustion of Brunswick concentrate in air a)pyrometer output, b)measured temperature and c)apparent area relative to that at 11.6ms. ($74\text{-}88\mu\text{m}$, $T_{\text{FURNACE}}=1130\text{K}$, $C_{\text{VAL}}=1.01$, data#=NB414.dat).

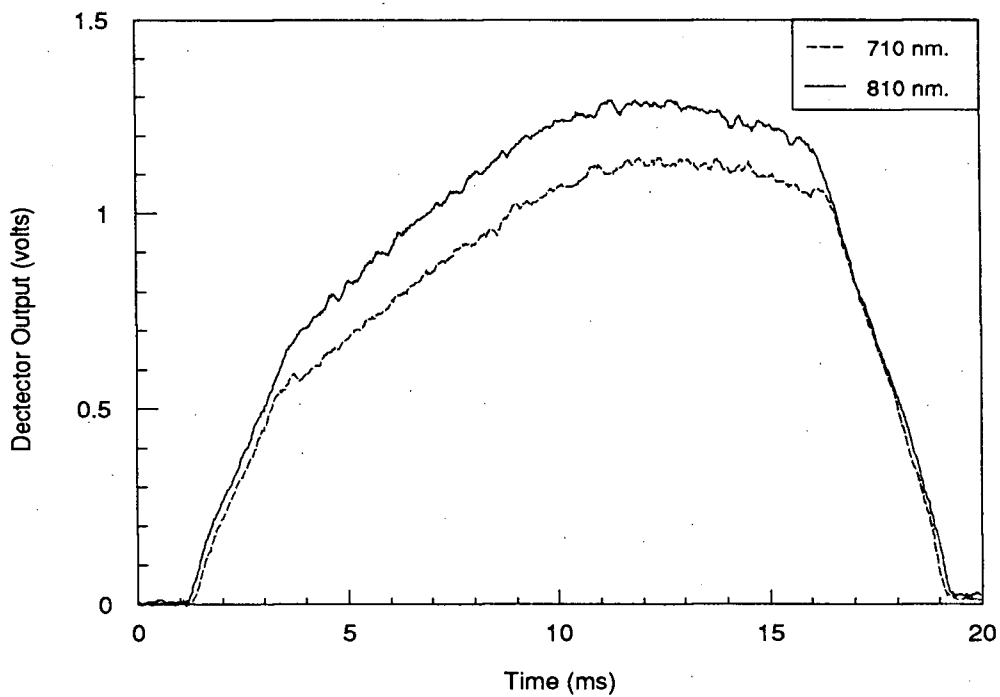


(a)

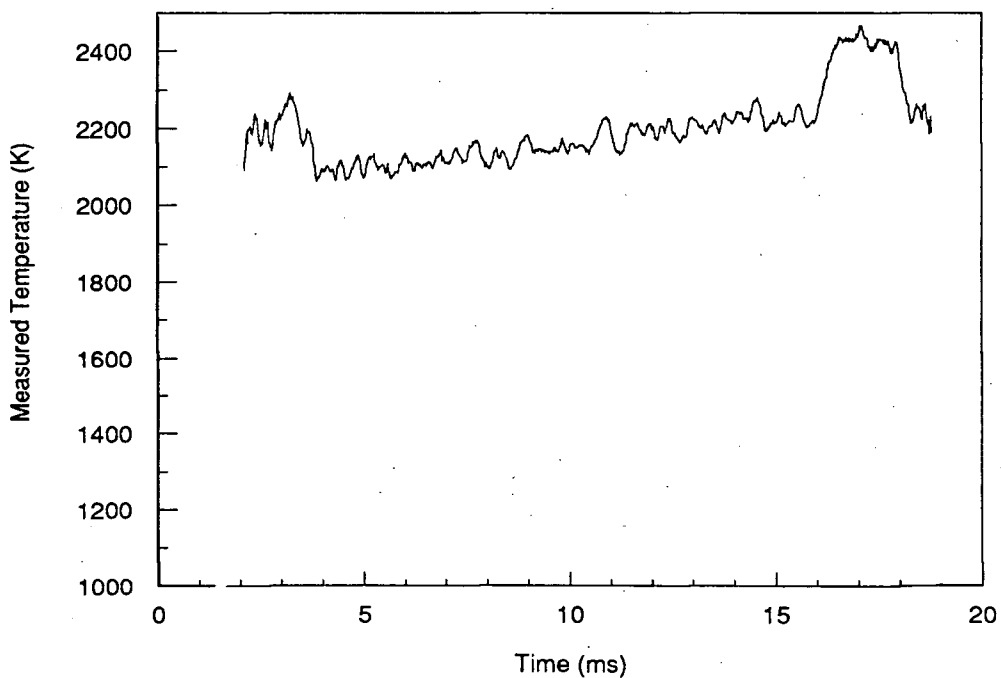


(b)

Figure 6.11 A3I combustion pulse recorded during the combustion of pyrrhotite in air. a)pyrometer output and b)measured temperature. (63-74 μ m, $T_{\text{FURNACE}}=1130\text{K}$, $C_{\text{VAL}}=1.42$, data#=PH81.dat).



(a)



(b)

Figure 6.12 A3I combustion pulse recorded during the combustion of pyrrhotite in air, a)pyrometer output and b)measured temperature. (74-88 μ m, $T_{\text{FURNACE}}=1130\text{K}$, $C_{\text{VAL}}=1.01$, data#-PH176.dat).

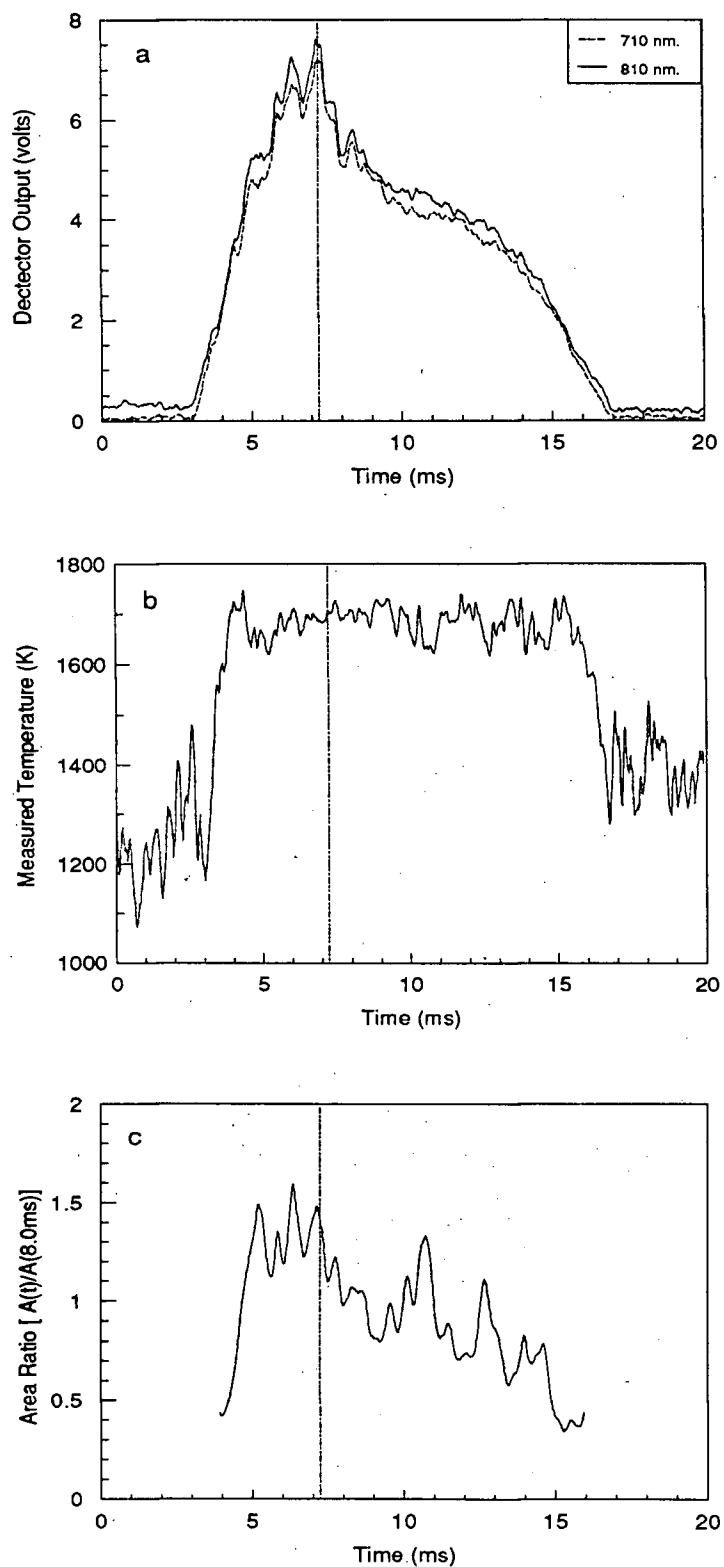


Figure 6.13 A2 combustion pulse recorded during the combustion of Sullivan concentrate in air, a) pyrometer output, b) measured temperature and c) apparent area relative to that at 8.0ms. (105-125 μ m, $T_{\text{FURNACE}}=1130\text{K}$, $C_{\text{VAL}}=1.42$, data#=S436.dat).

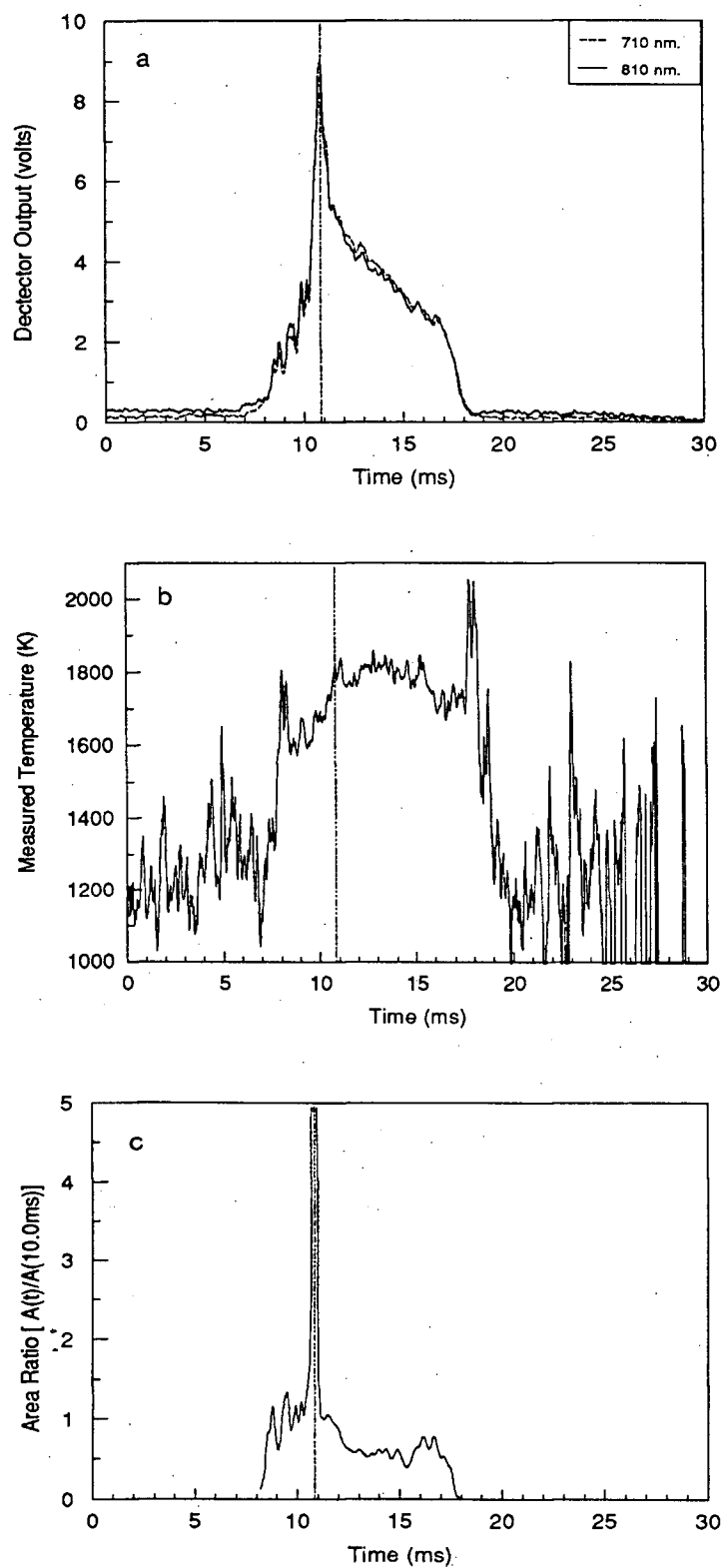


Figure 6.14 A2 combustion pulse recorded during the combustion of Brunswick concentrate in air, a) pyrometer output, b) measured temperature and c) apparent area relative to that at 10.0ms. (63-74 μ m, $T_{\text{FURNACE}}=1130\text{K}$, $C_{\text{VAL}}=1.42$, data#=NB284.dat).

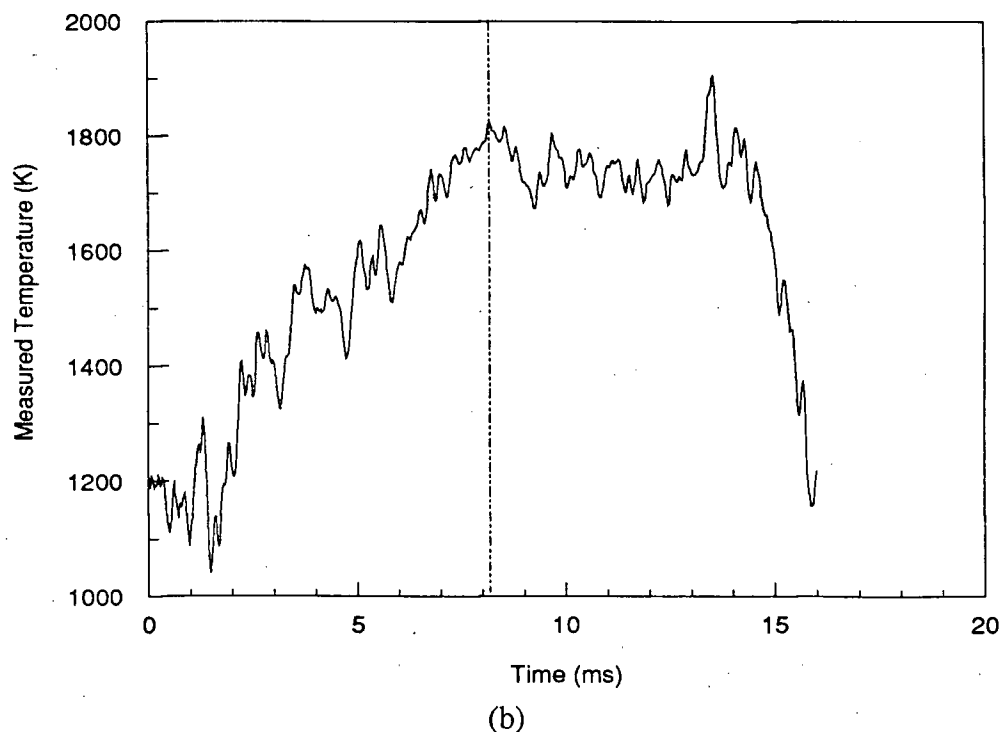
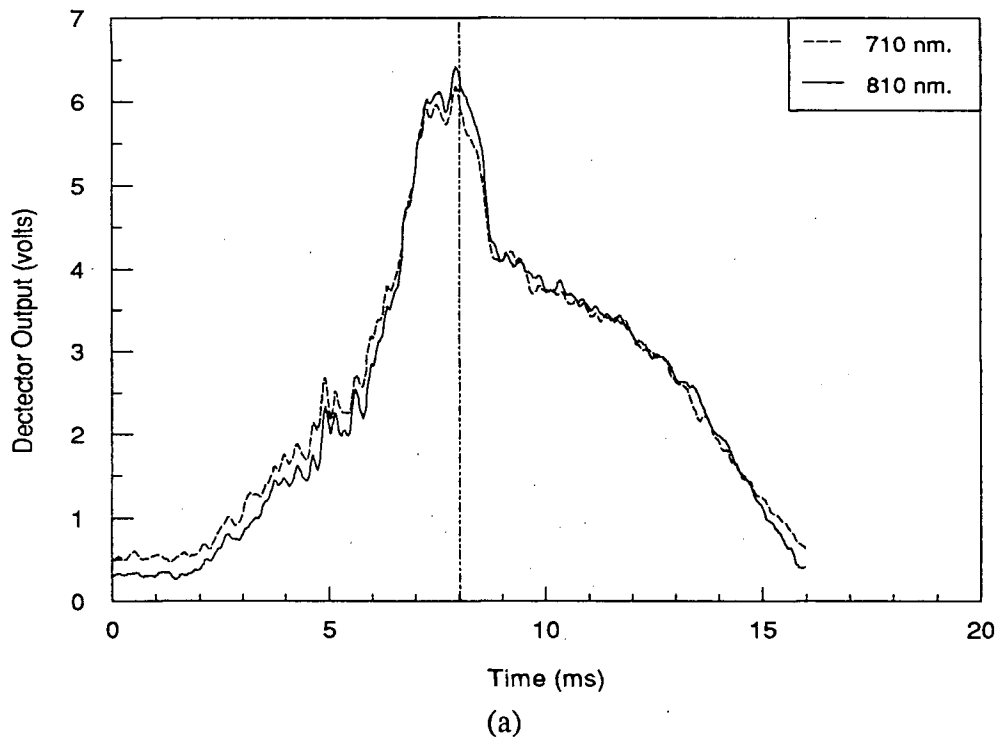
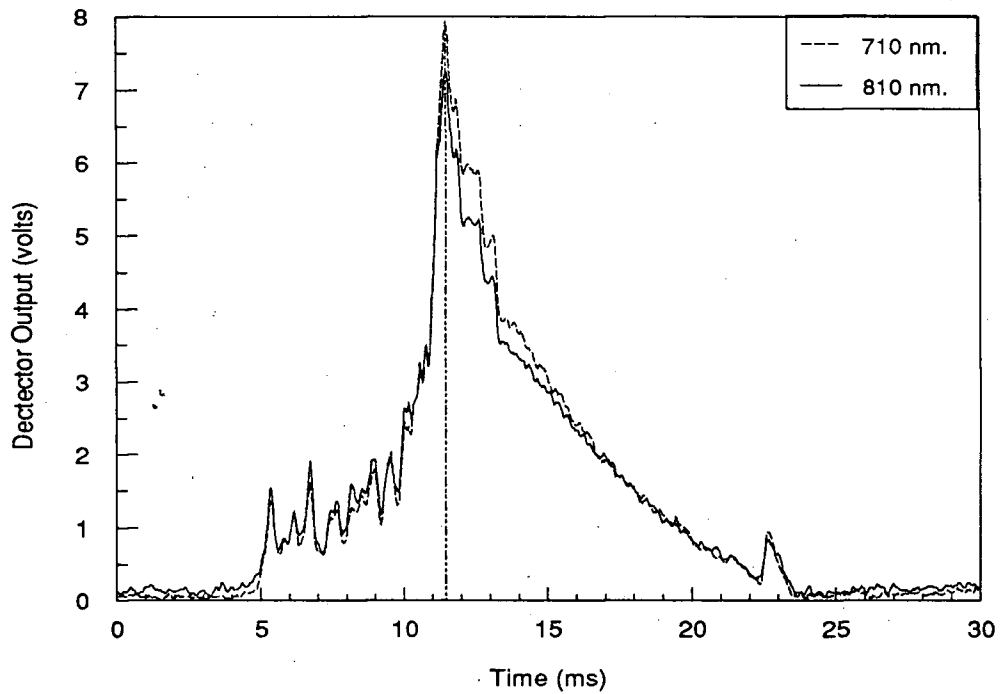
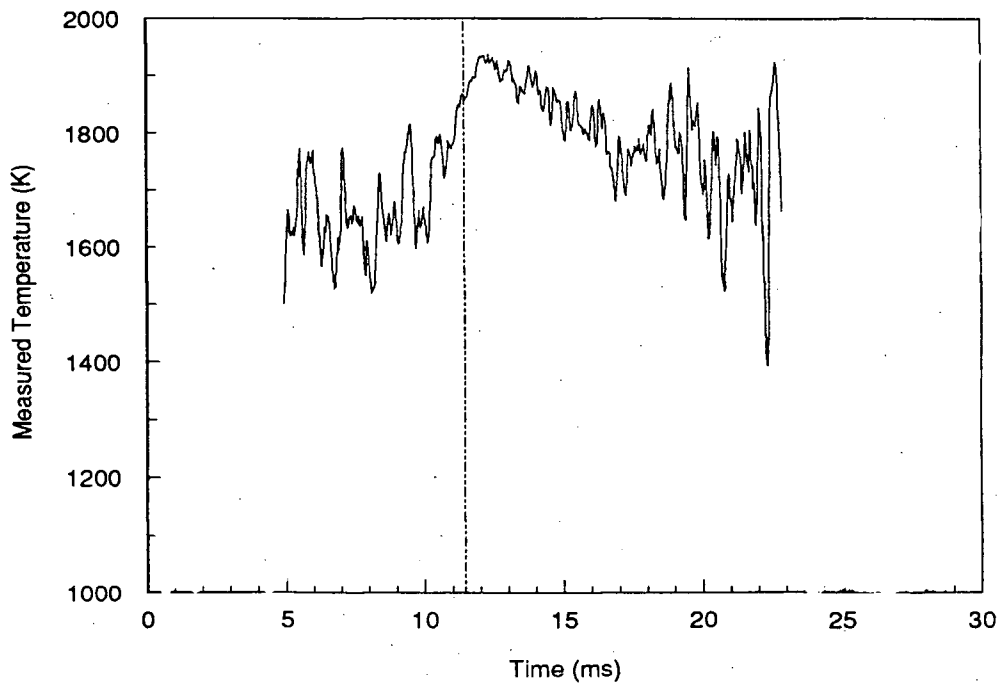


Figure 6.15 A2 combustion pulse recorded during the combustion of Sullivan concentrate in air.
 a) pyrometer output and b) measured temperature.
 (88-105 μ m, $T_{\text{FURNACE}}=1130\text{K}$, $C_{\text{VAL}}=1.42$, data#=S966.dat).



(a)

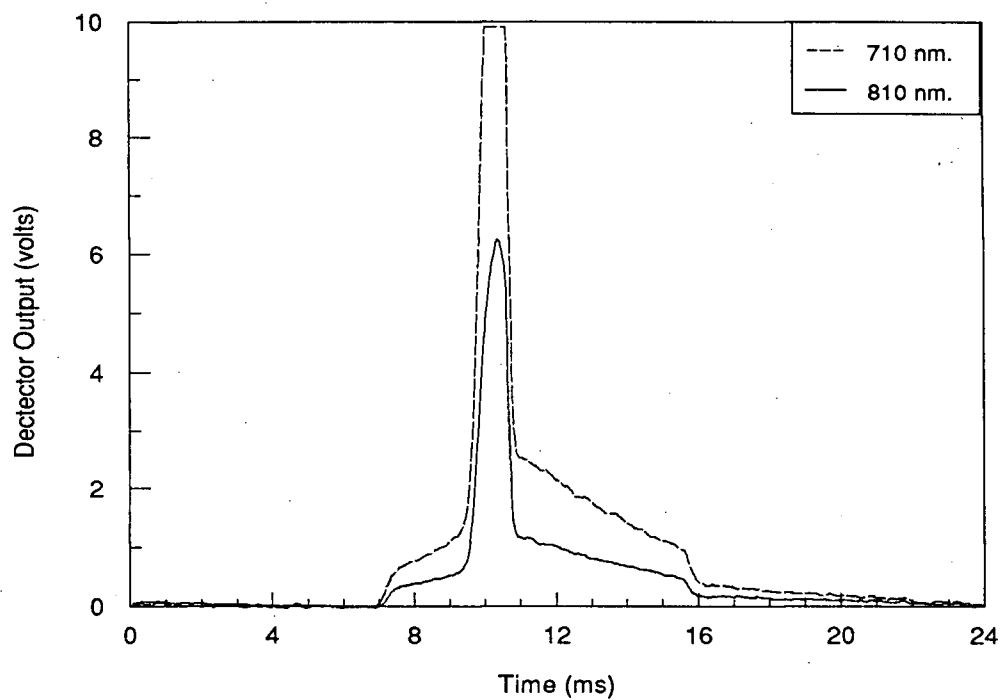


(b)

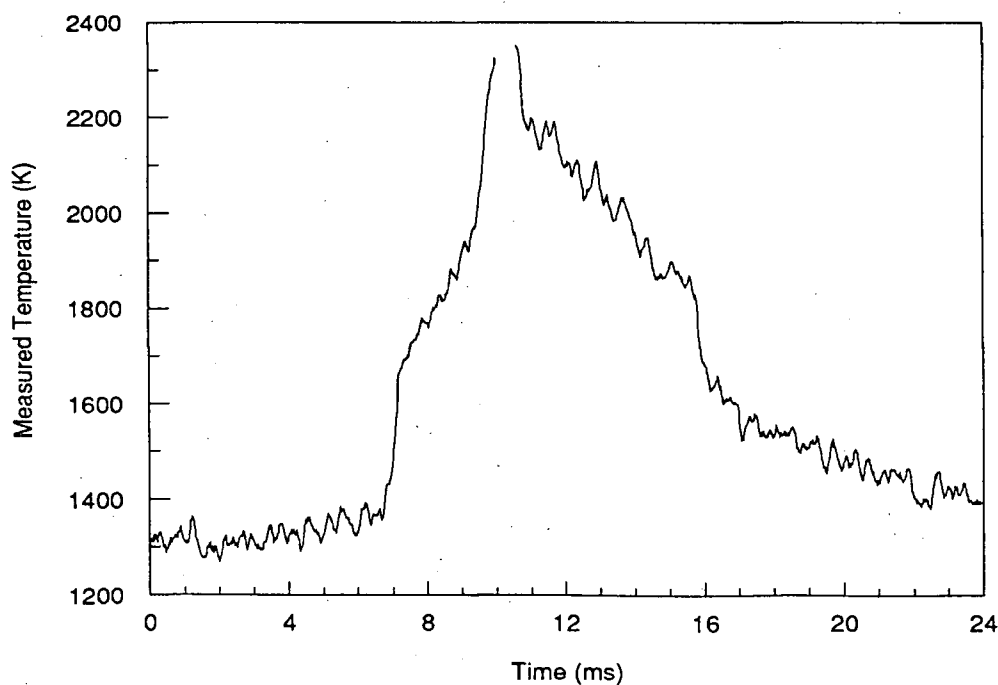
Figure 6.16 A2 combustion pulse recorded during the combustion of Brunswick concentrate in air.

a) pyrometer output and b) measured temperature.

(74-88 μ m, $T_{\text{FURNACE}}=1130\text{K}$, $C_{\text{VAL}}=1.42$, data#=NB313.dat).



(a)



(b)

Figure 6.17 A4 combustion pulse recorded during the combustion of galena in air, a) pyrometer output and b) measured temperature. (74-149 μ m, $T_{\text{FURNACE}}=1130\text{K}$, data#=G70.dat).

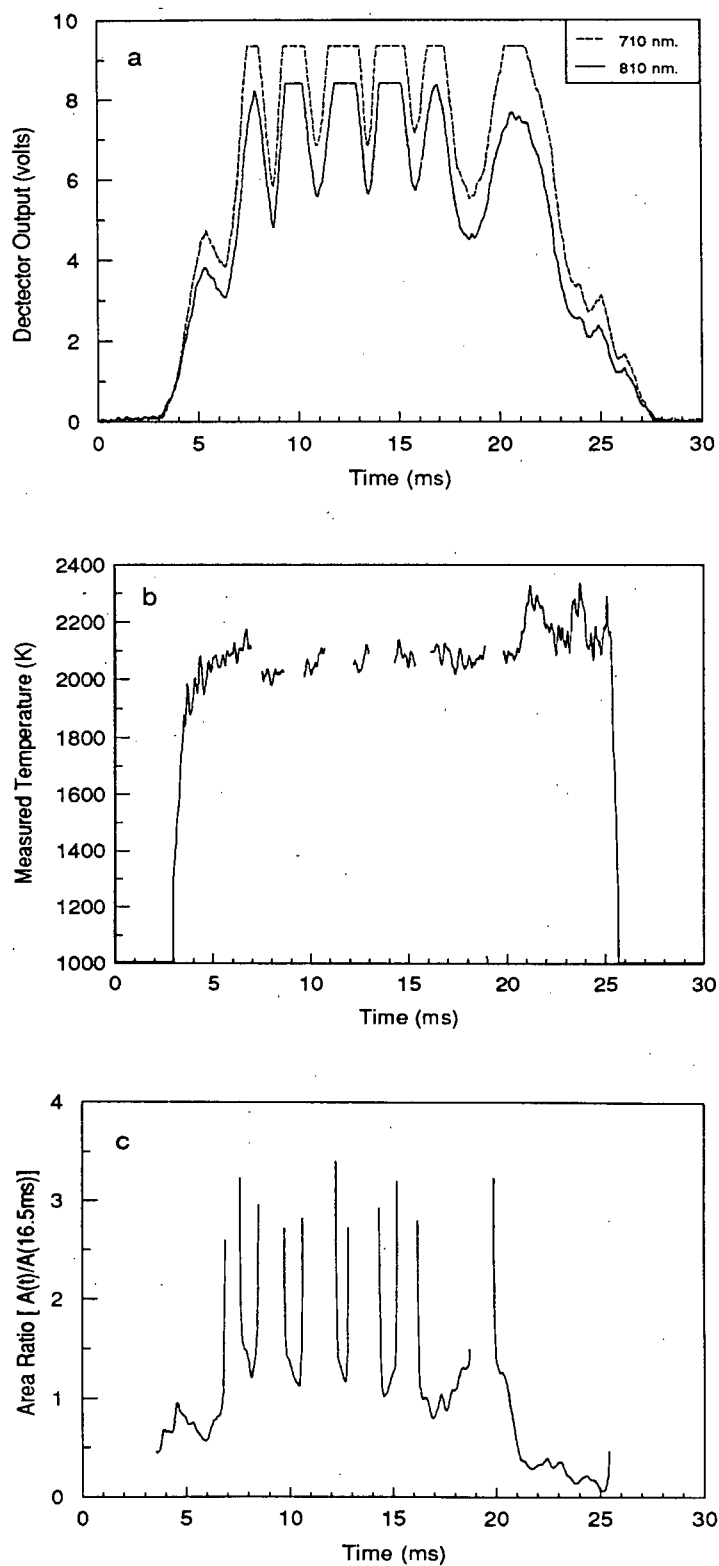


Figure 6.18 A5 combustion pulse recorded during the combustion of Sullivan concentrate in air, a) pyrometer detector output, b) measured temperature and c) apparent area relative to that at 16.5ms. ($63\text{-}74\mu\text{m}$, $T_{\text{FURNACE}}=1130\text{K}$, $C_{\text{VAL}}=1.42$, data#=S234.dat).

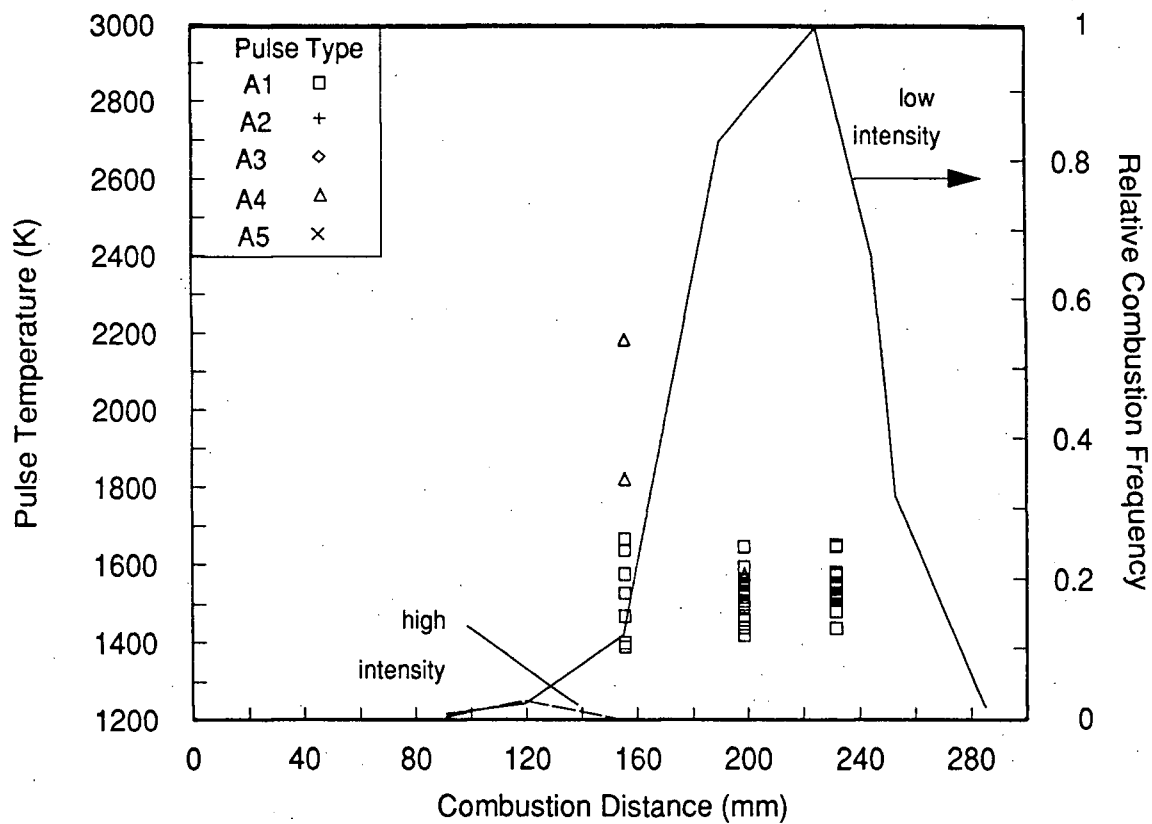
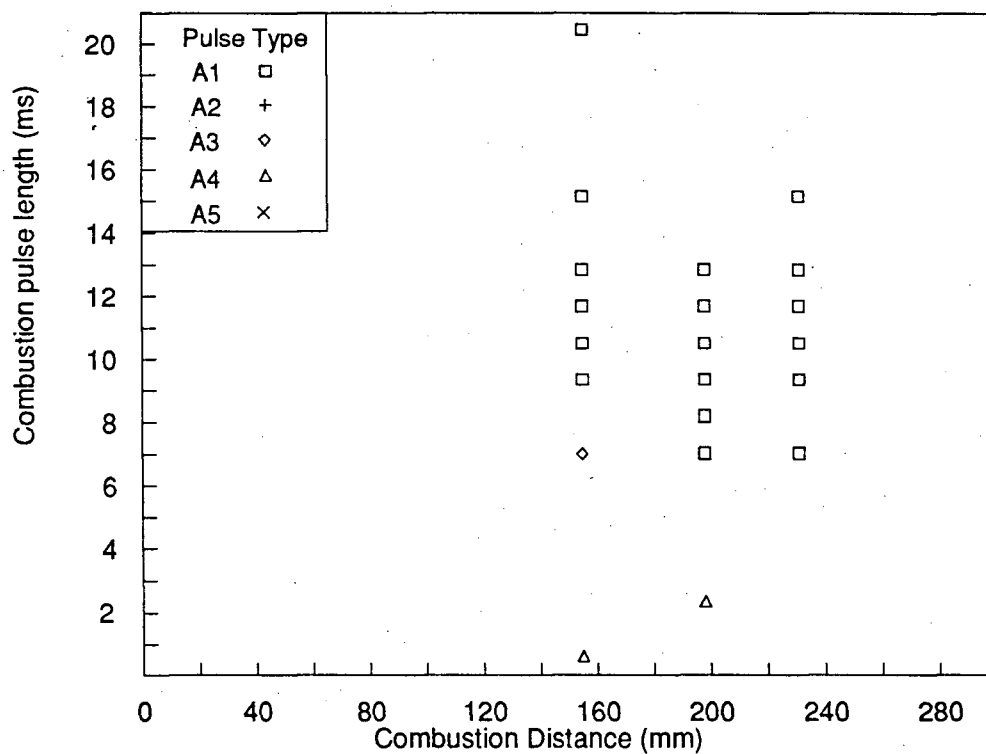
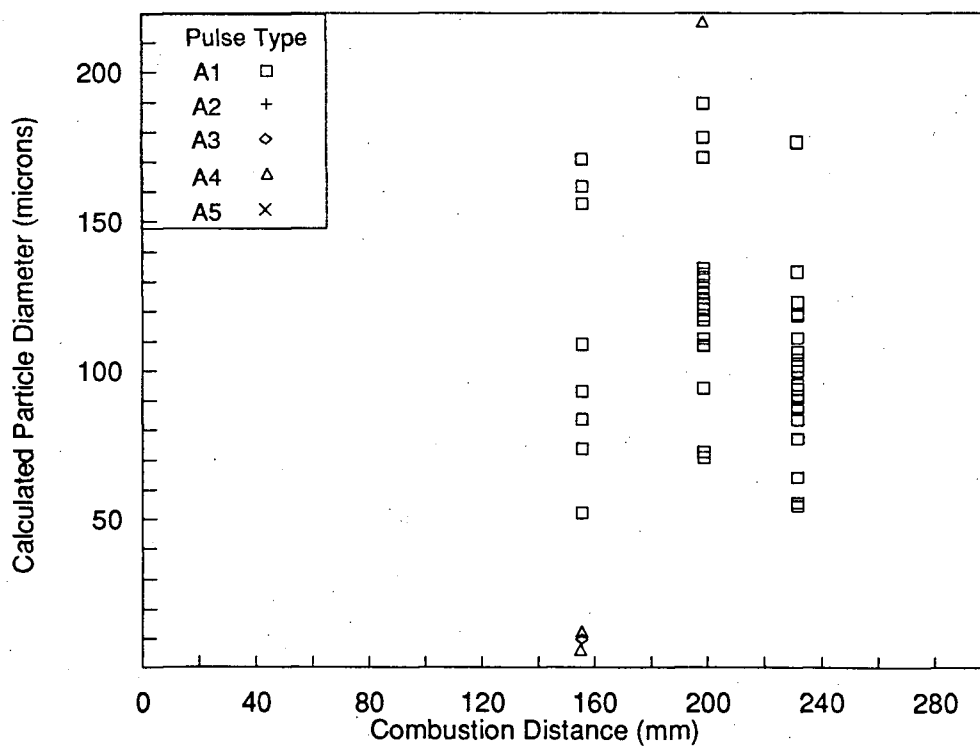


Figure 6.19 Combustion of galena 63-74 μ m in air at $T_{\text{FURNACE}}=1130\text{K}$ - pulse type, temperature and relative frequency as a function of furnace combustion distance.



(a)



(b)

Figure 6.20 Combustion of galena 63-74 μm in air at $T_{\text{FURNACE}}=1130\text{K}$; a) pulse length and b) calculated particle diameter, as a function of furnace combustion distance.

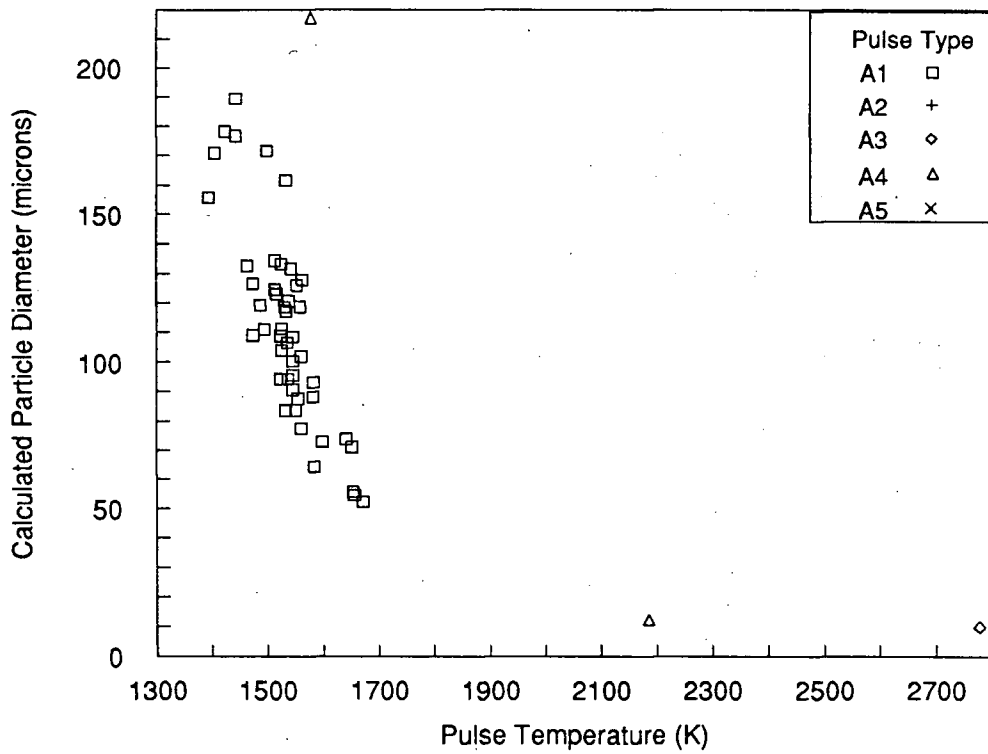


Figure 6.21 Combustion of galena 63-74 μ m in air at $T_{\text{FURNACE}}=1130\text{K}$ - apparent particle diameter versus measured particle temperature.

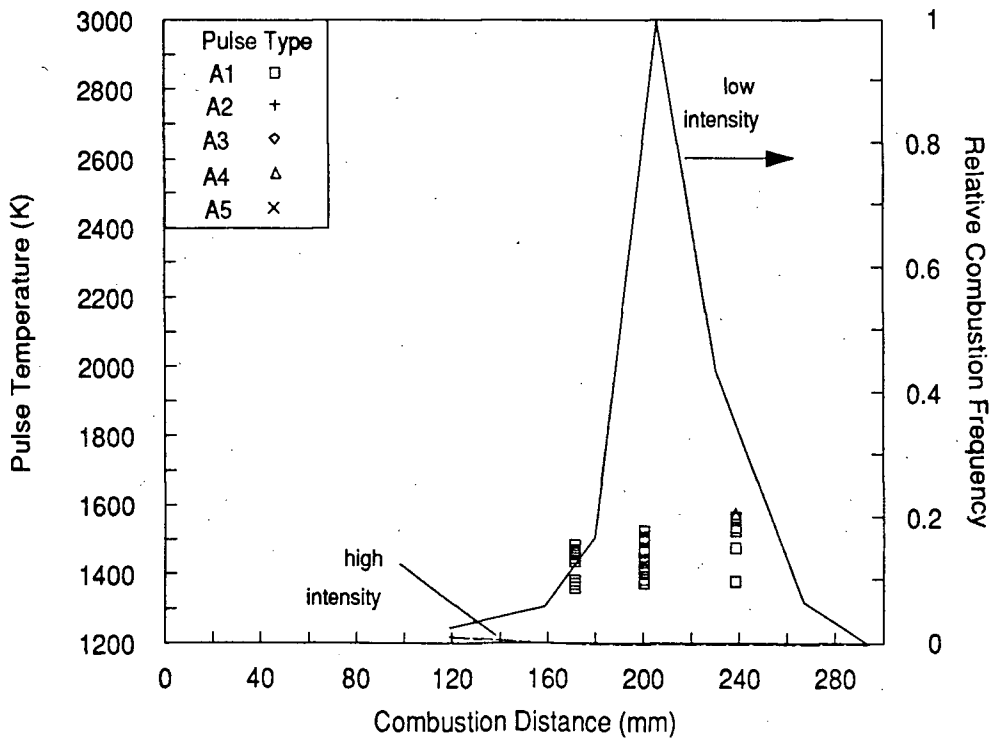


Figure 6.22 Combustion of galena 74-88 μ m in air at $T_{\text{FURNACE}}=1130\text{K}$ - pulse type, temperature and relative frequency as a function of furnace combustion distance.

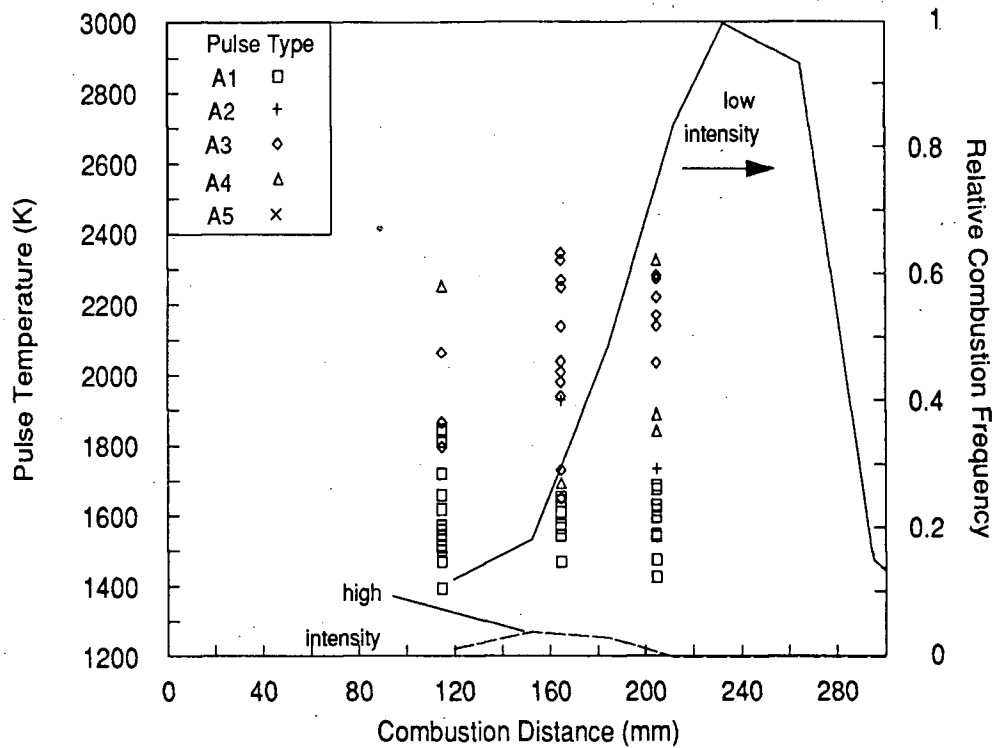


Figure 6.23 Combustion of galena 88-105µm in air at $T_{\text{FURNACE}}=1130\text{K}$ - pulse type, temperature and relative frequency as a function of furnace combustion distance.

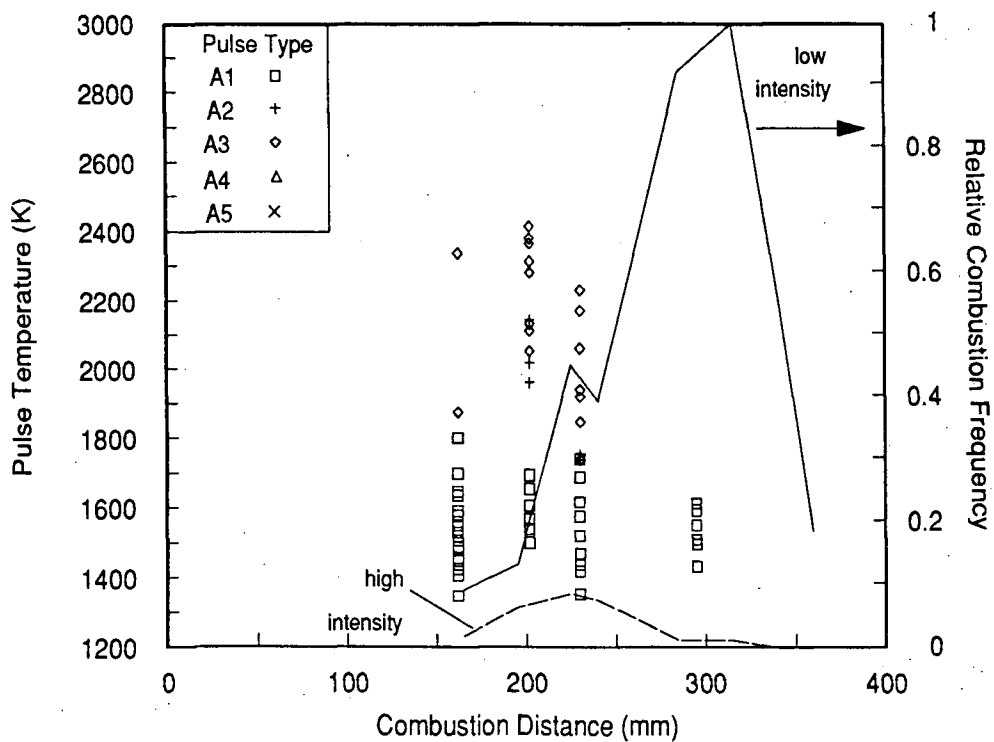


Figure 6.24 Combustion of galena 105-125µm in air at $T_{\text{FURNACE}}=1130\text{K}$ - pulse type, temperature and relative frequency as a function of furnace combustion distance.

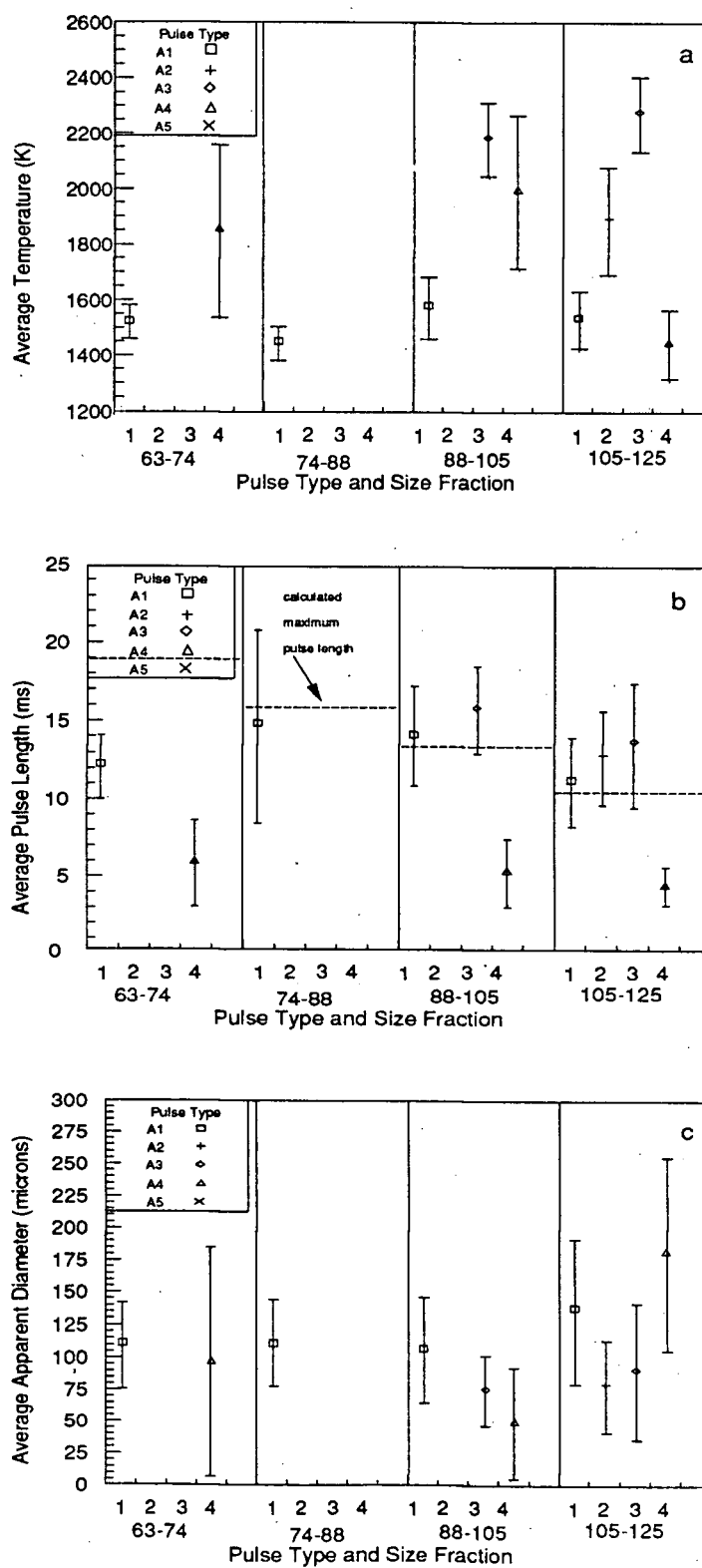


Figure 6.25 Pulse type averaged combustion pulse data as a function of feed size for galena combustion in air, a) pulse temperatures, b) pulse lengths and c) apparent diameters. ($T_{\text{FURNACE}}=1130\text{K}$).

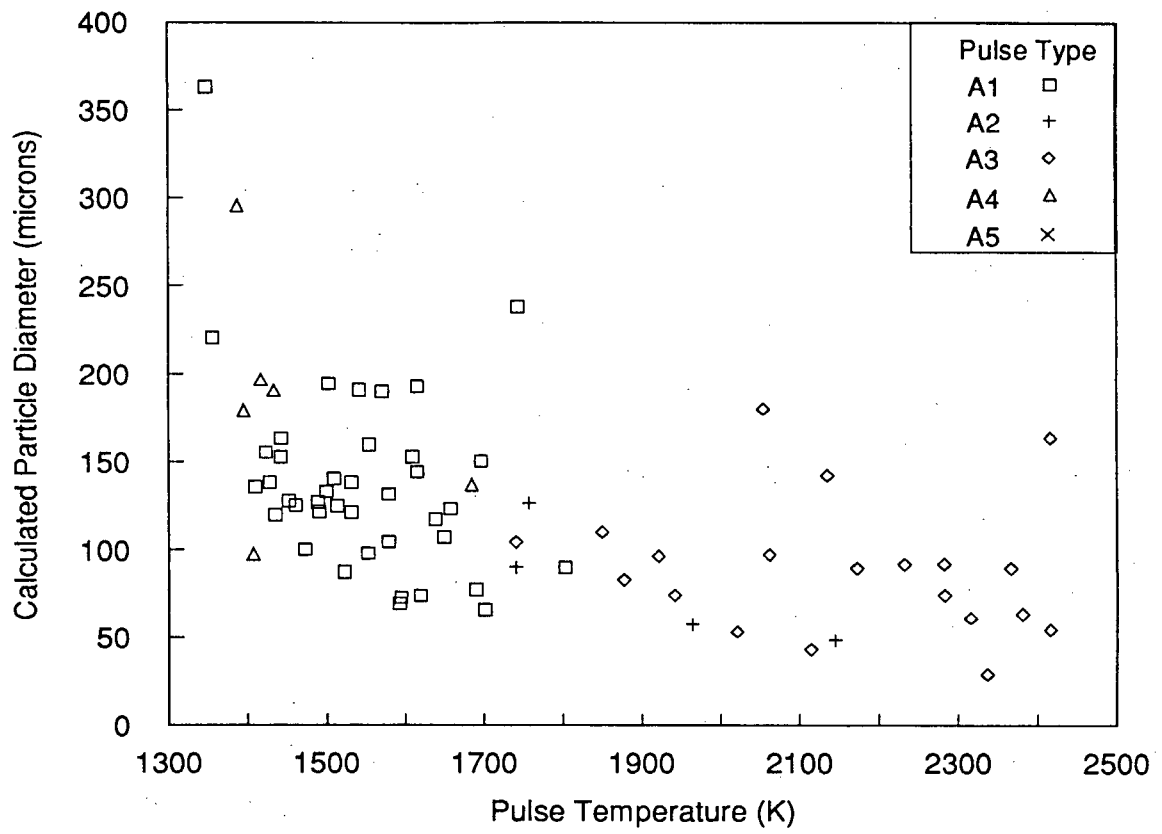
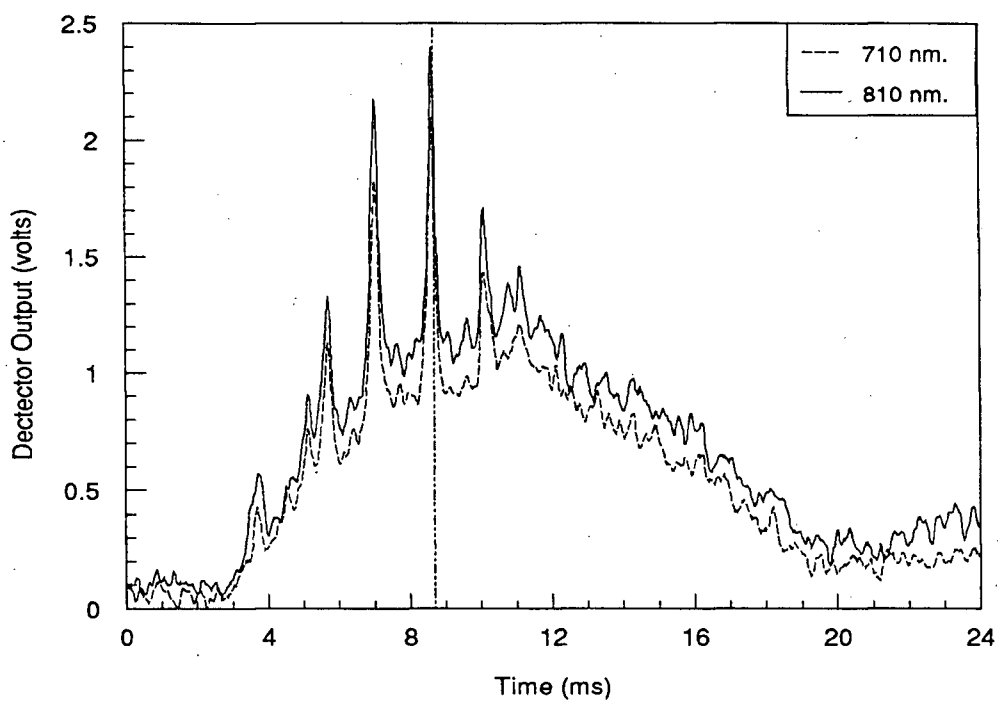
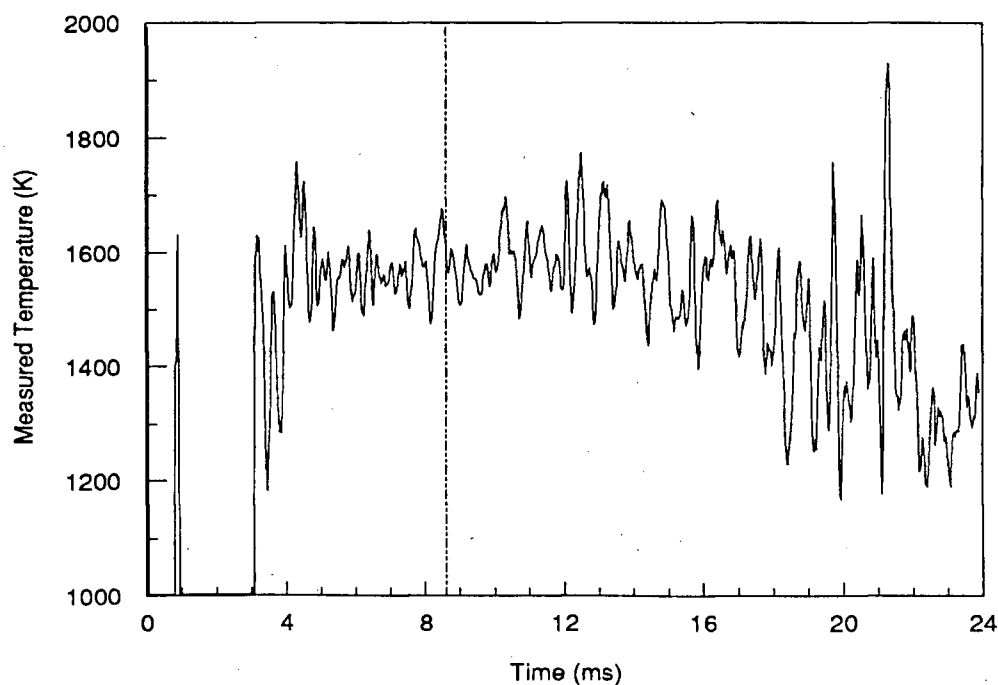


Figure 6.26 Combustion of galena 105-125 μ m in air at $T_{\text{FURNACE}}=1130\text{K}$ - apparent particle diameter versus measured particle temperature.



(a)



(b)

Figure 6.27 A1 combustion pulse recorded during the combustion of 88-105 μ m galena in air showing the presence of energy spikes, a) pyrometer output and b) measured temperature. (74-88 μ m, $T_{\text{FURNACE}}=1130\text{K}$, $C_{\text{VAL}}=1.42$, data#=G156.dat).

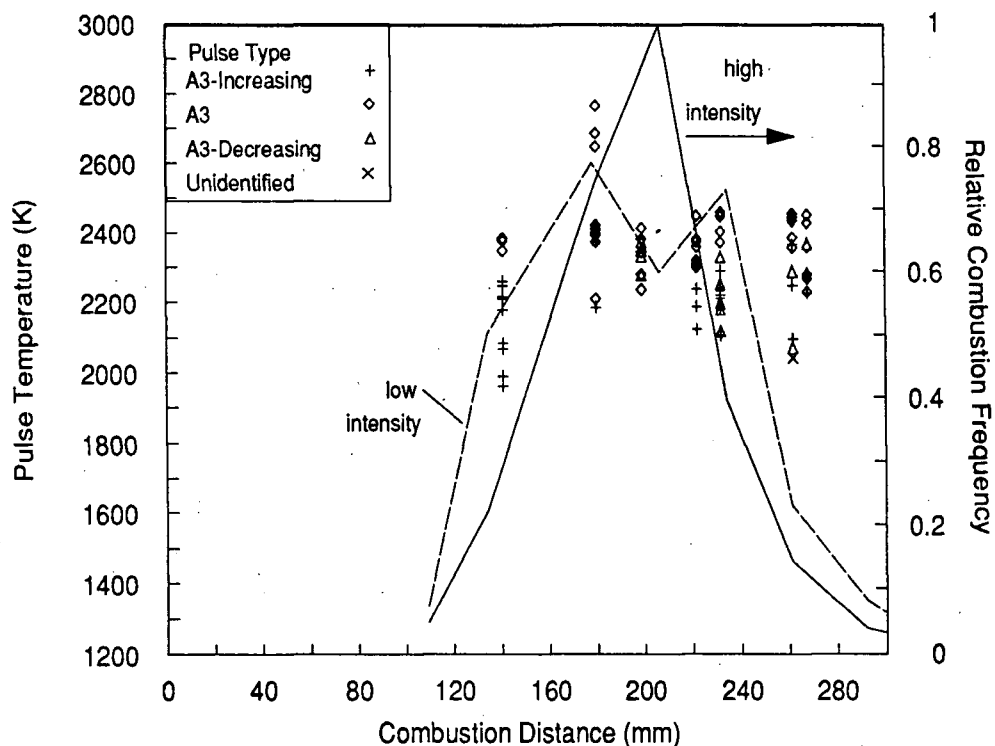


Figure 6.28 Combustion of 74-88 μm pyrrhotite in air at $T_{\text{FURNACE}}=1130\text{K}$ - pulse type, temperature and relative frequency as a function of furnace combustion distance.

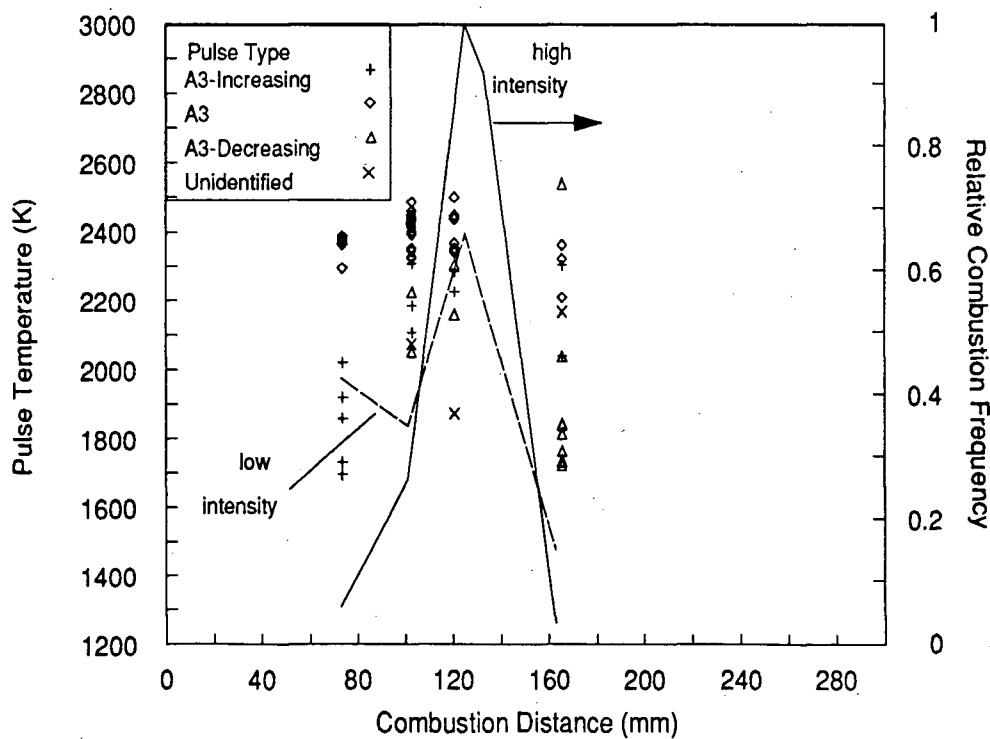


Figure 6.29 Combustion of 75-88 μm pyrite in air at $T_{\text{FURNACE}}=1130\text{K}$ - pulse type, temperature and relative frequency as a function of furnace combustion distance.

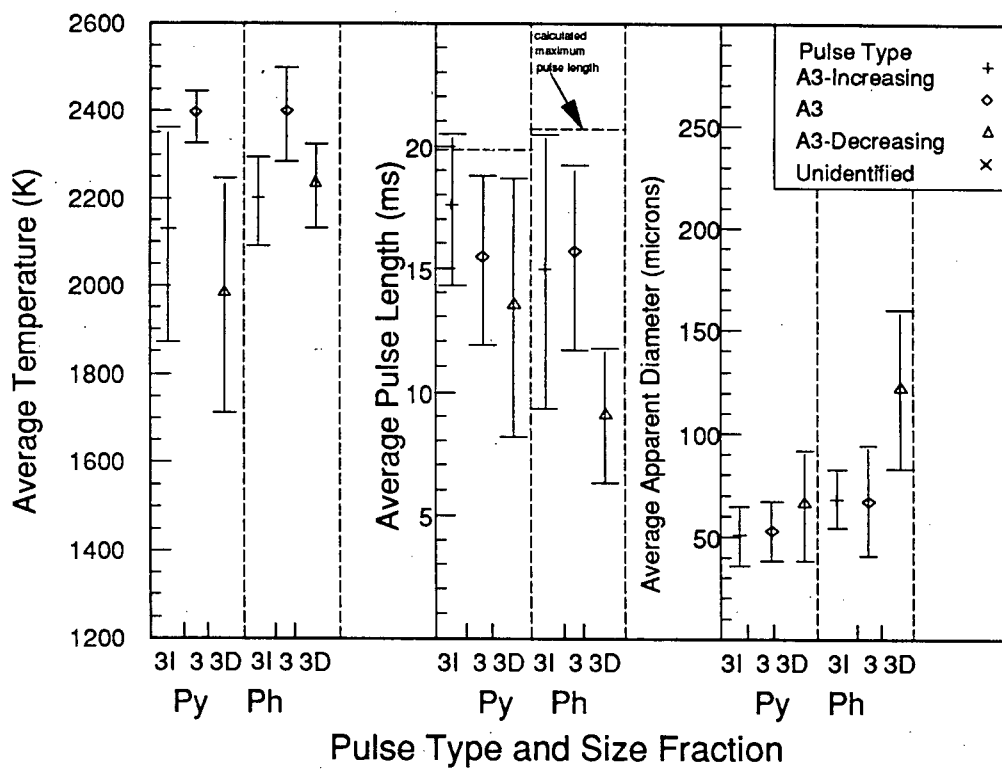


Figure 6.30 Pulse type averaged combustion pulse data for pyrite and pyrrhotite combustion in air, a) pulse temperatures, b) pulse lengths and c) apparent diameters. ($T_{\text{FURNACE}} = 1130\text{K}$).

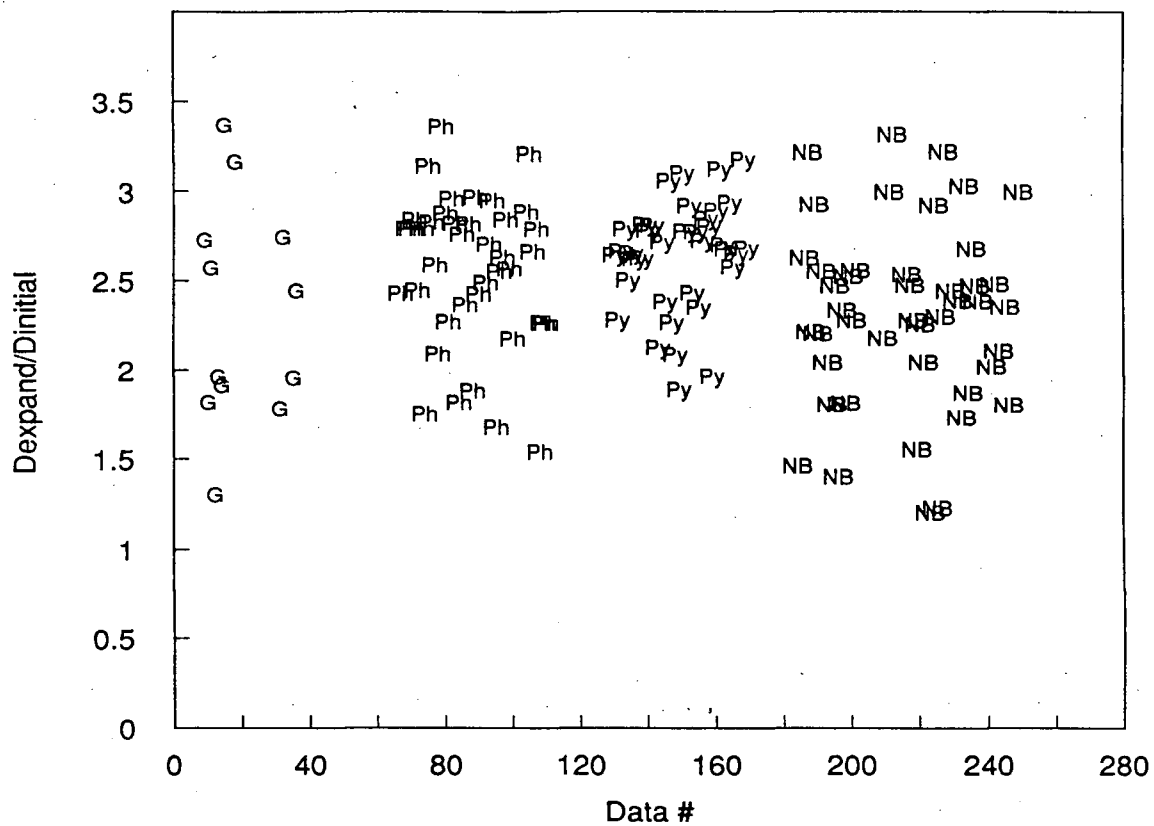
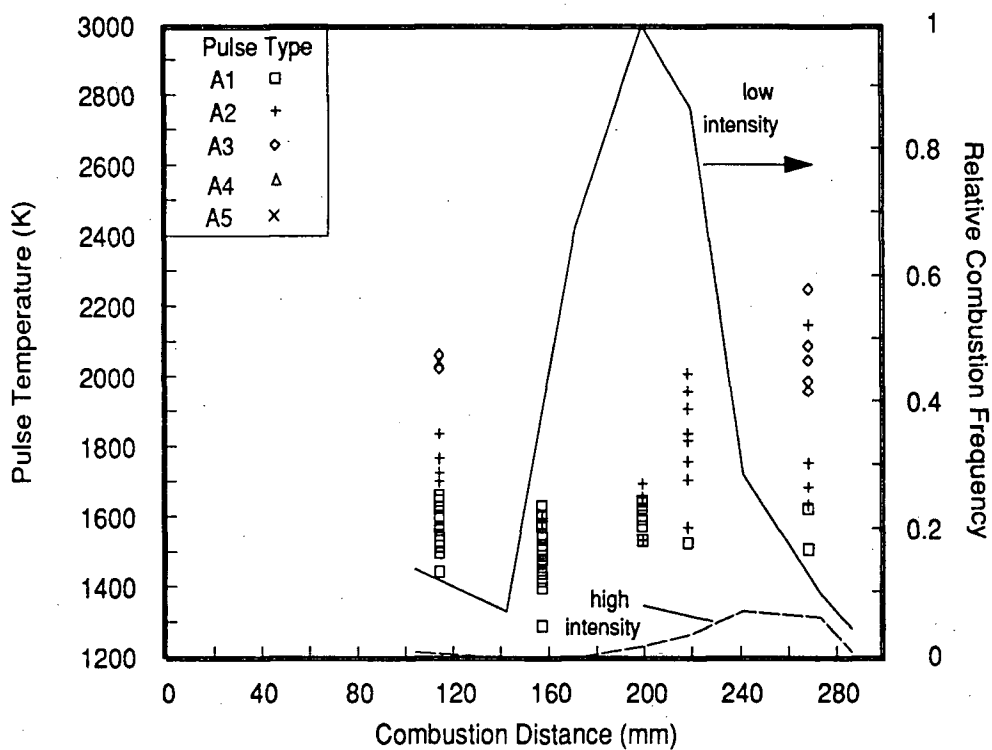
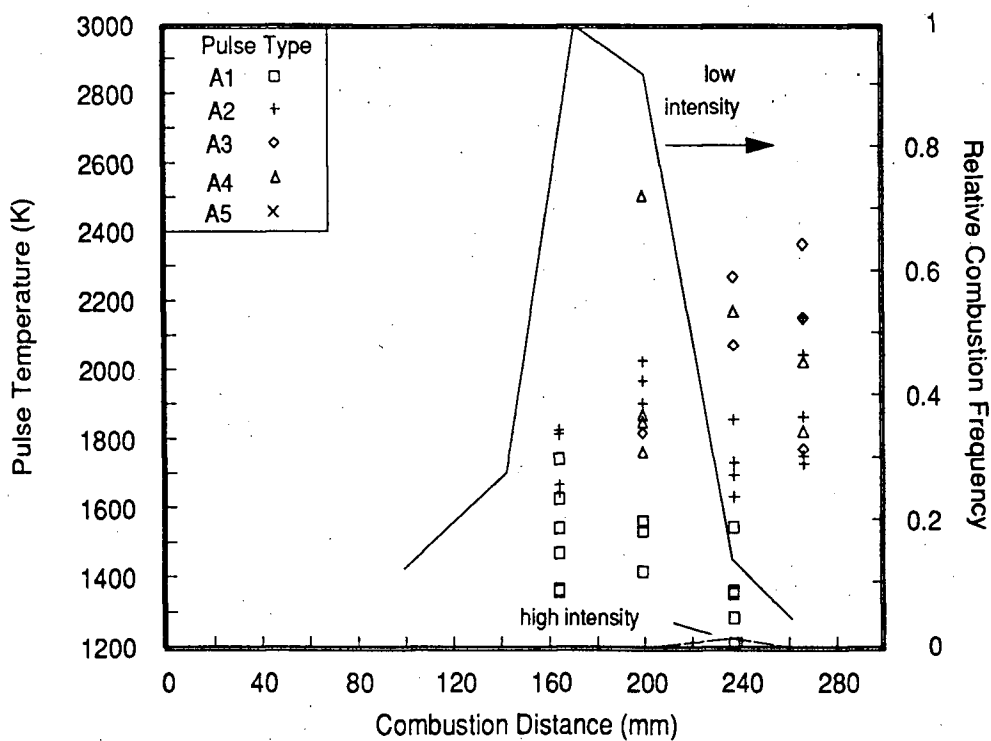


Figure 6.31 Calculated apparent particle expansion for A3 combustion pulses recorded during the combustion of pyrite(Py), pyrrhotite(Ph), galena(G) and Brunswick(NB) concentrate in air at $T_{\text{FURNACE}}=1130\text{K}$, as a function of an arbitrary data#.

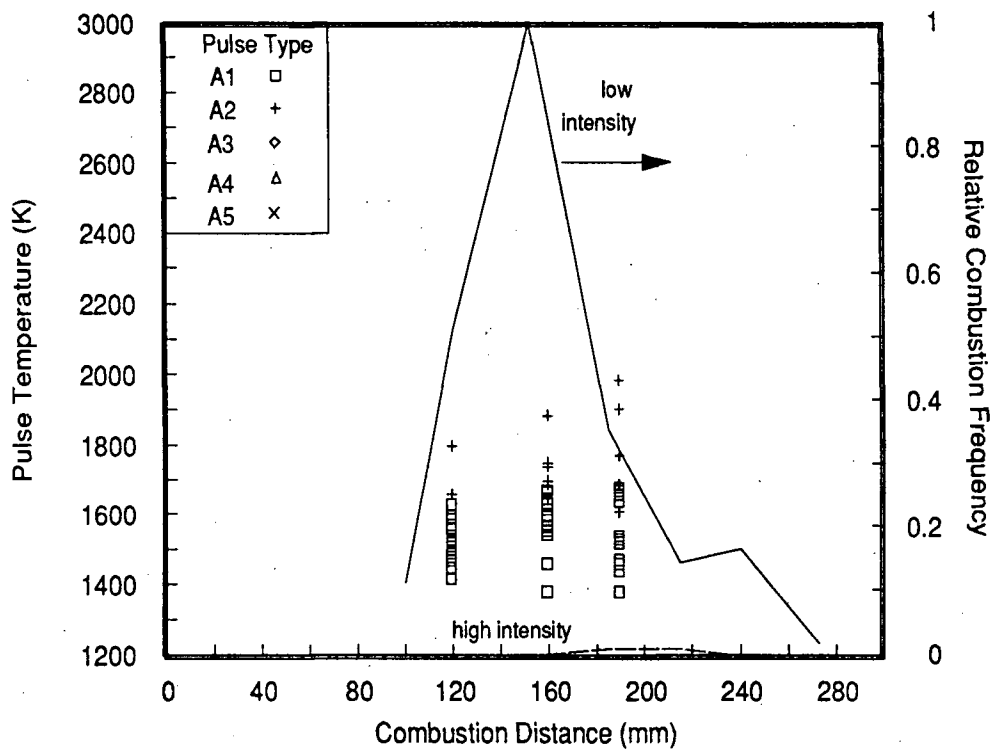


(a)

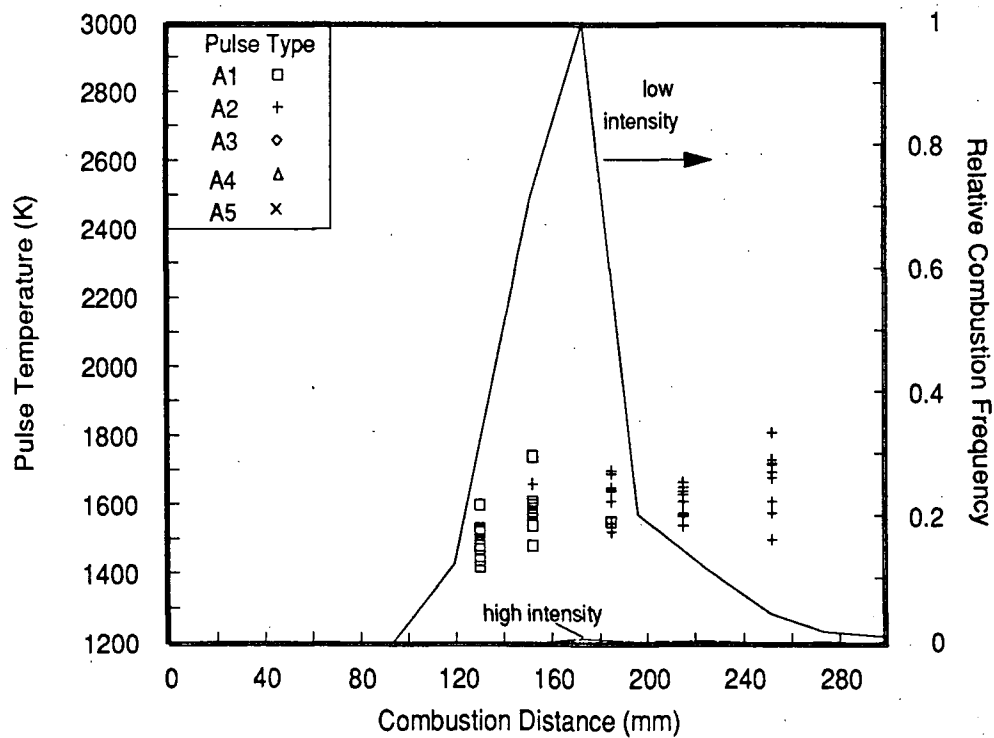


(b)

Figure 6.32 Combustion of a) 63-74 μm and b) 74-88 μm Sullivan concentrate in air at $T_{\text{FURNACE}}=1130\text{K}$ - pulse type, temperature and relative frequency as a function of furnace combustion distance.



(a)



(b)

Figure 6.33 Combustion of a) 88-105 μ m and b) 105-125 μ m Sullivan concentrate in air at $T_{\text{FURNACE}}=1130\text{K}$ - pulse type, temperature and relative frequency as a function of furnace combustion distance.

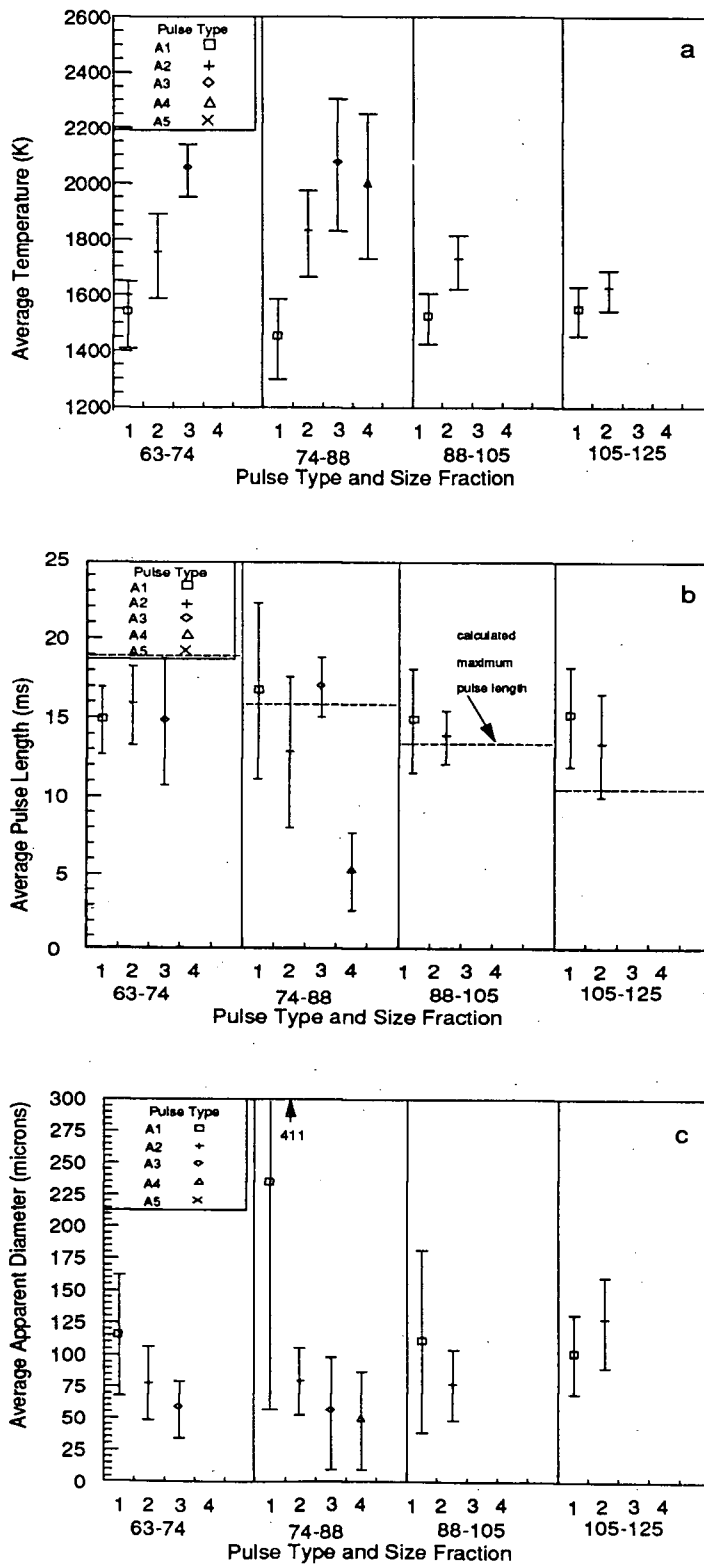


Figure 6.34 Pulse type averaged combustion pulse data as a function of feed size for Sullivan concentrate combustion in air, ($T_{\text{FURNACE}}=1130\text{K}$). a) pulse temperatures, b) pulse lengths and c) apparent diameters.

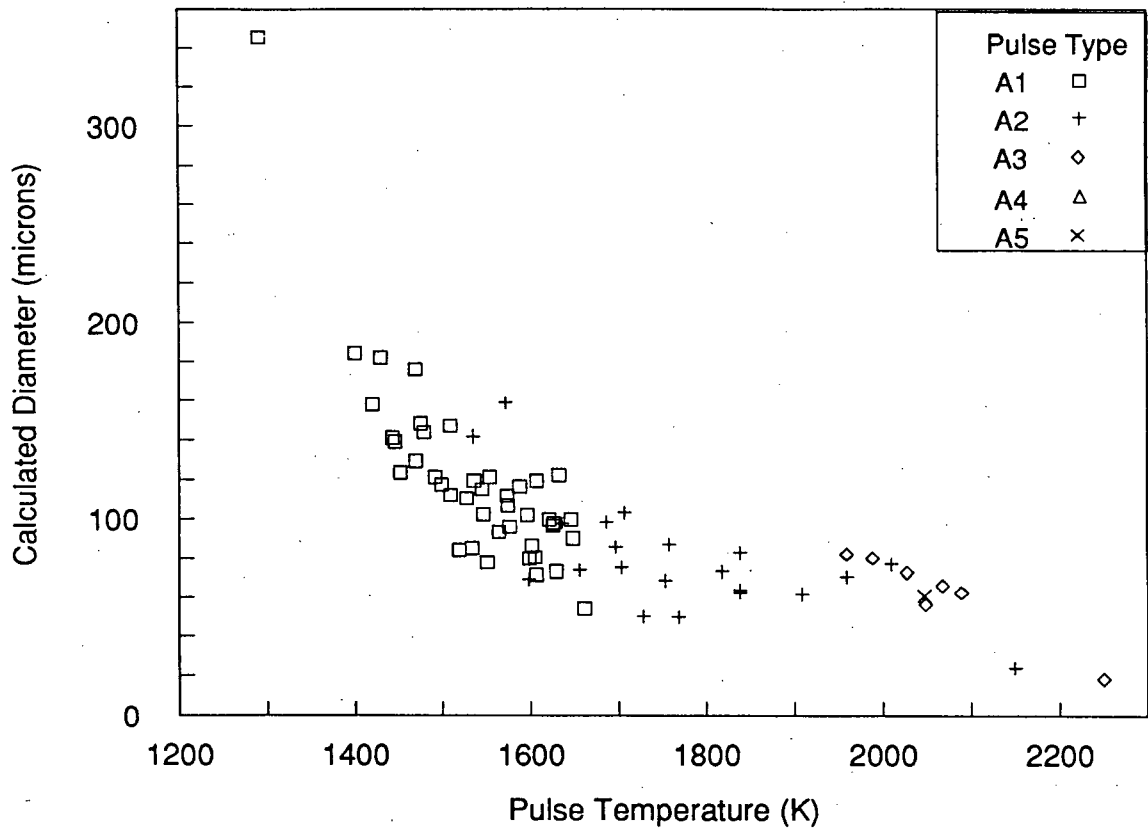
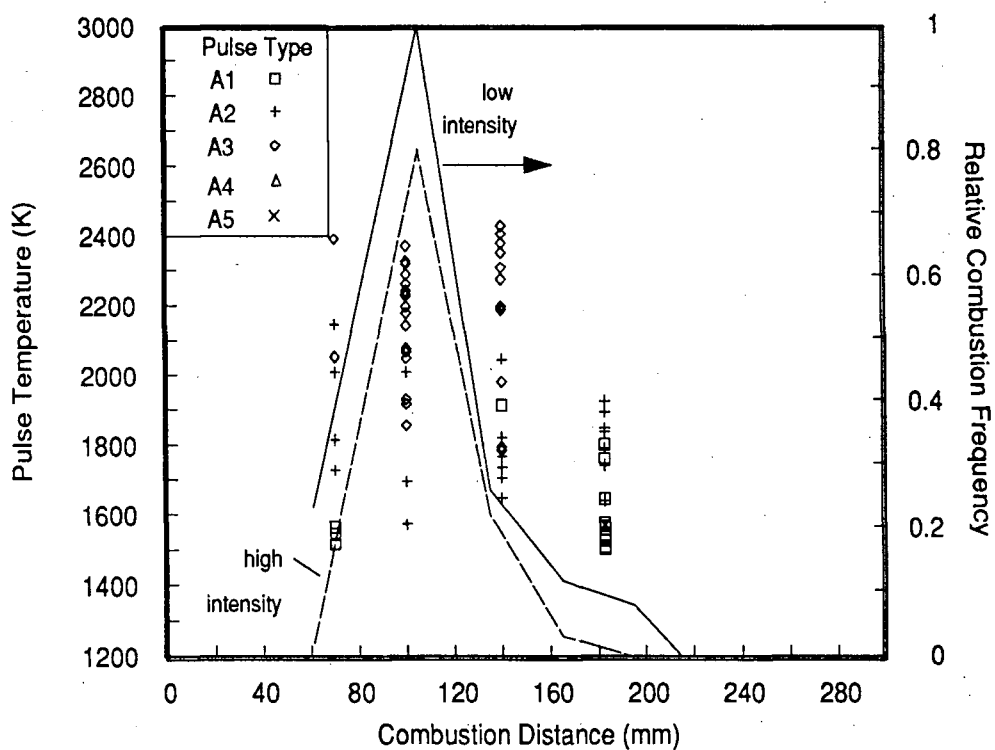
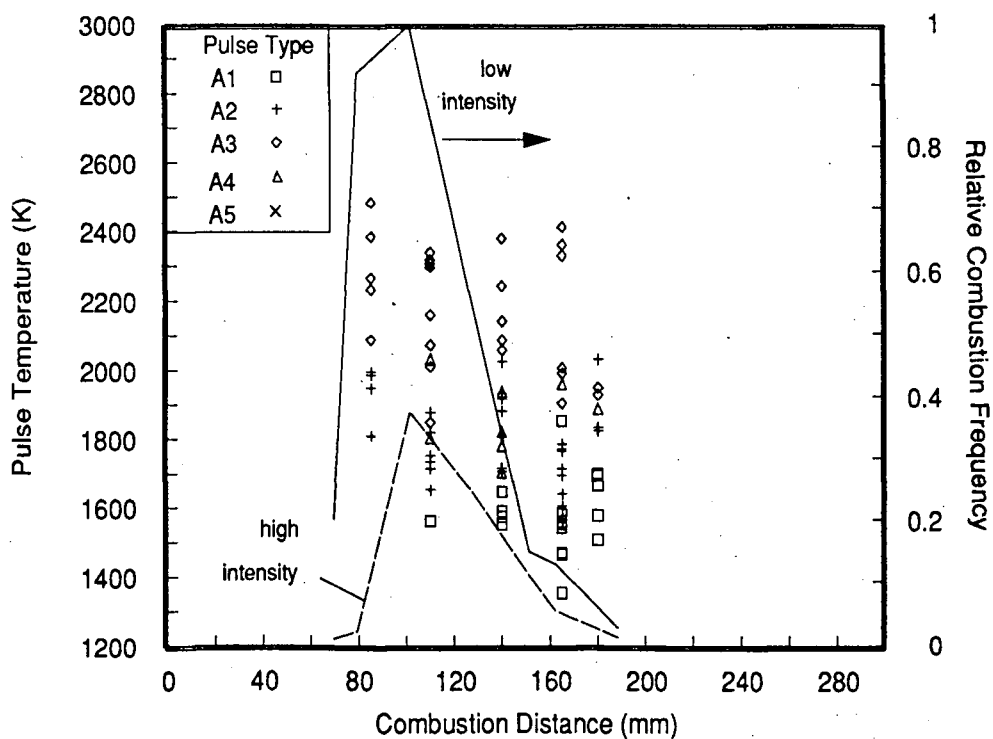


Figure 6.35 Combustion of 63-74 μ m Sullivan concentrate in air at $T_{\text{FURNACE}}=1130\text{K}$ -apparent particle diameter versus measured particle temperature.

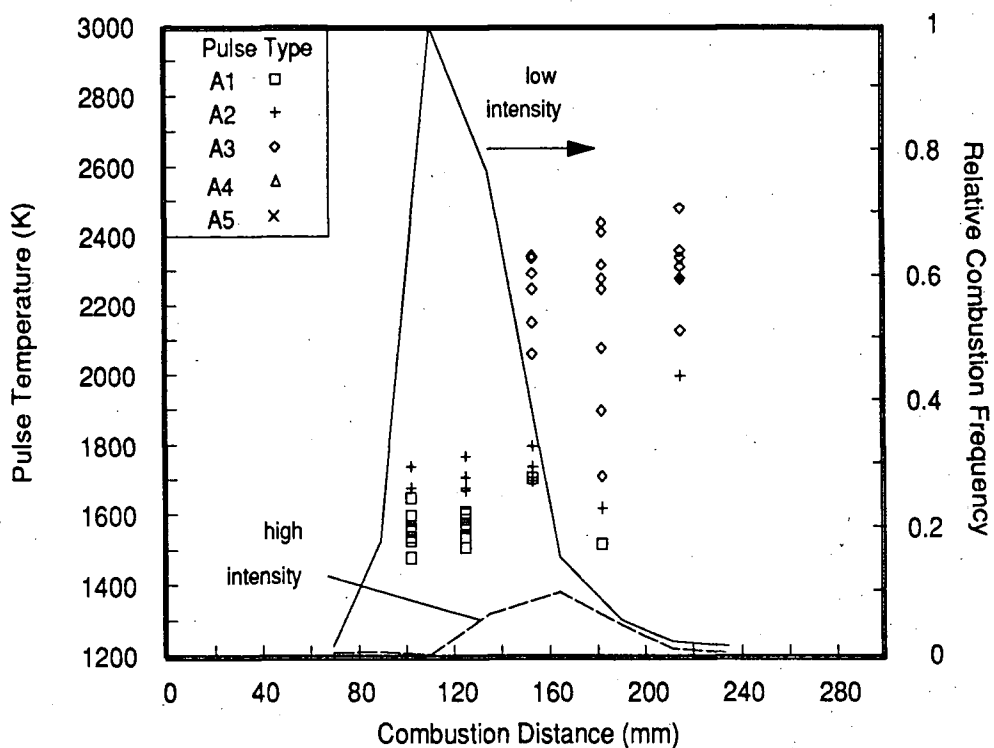


(a)

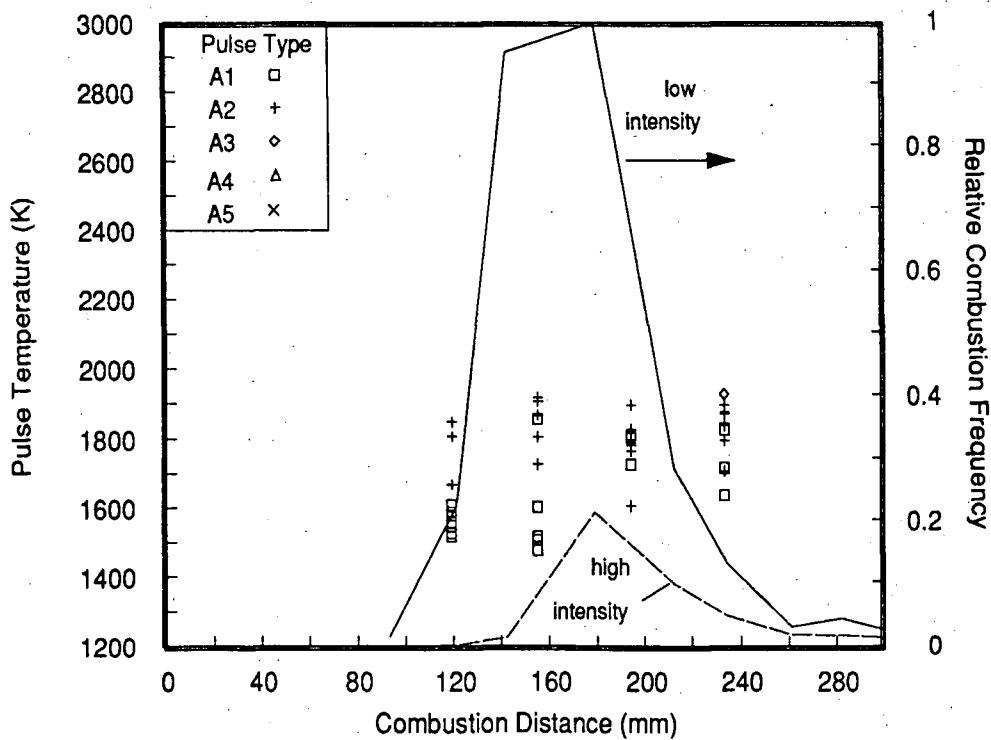


(b)

Figure 6.36 Combustion of a)63-74 μ m and b)74-88 μ m Brunswick concentrate in air at $T_{\text{FURNACE}}=1130\text{K}$ - pulse type, temperature and relative frequency as a function of furnace combustion distance.



(a)



(b)

Figure 6.37 Combustion of a) 88-105 μm and b) 105-125 μm Brunswick concentrate in air at $T_{\text{FURNACE}}=1130\text{K}$ - pulse type, temperature and relative frequency as a function of furnace combustion distance.

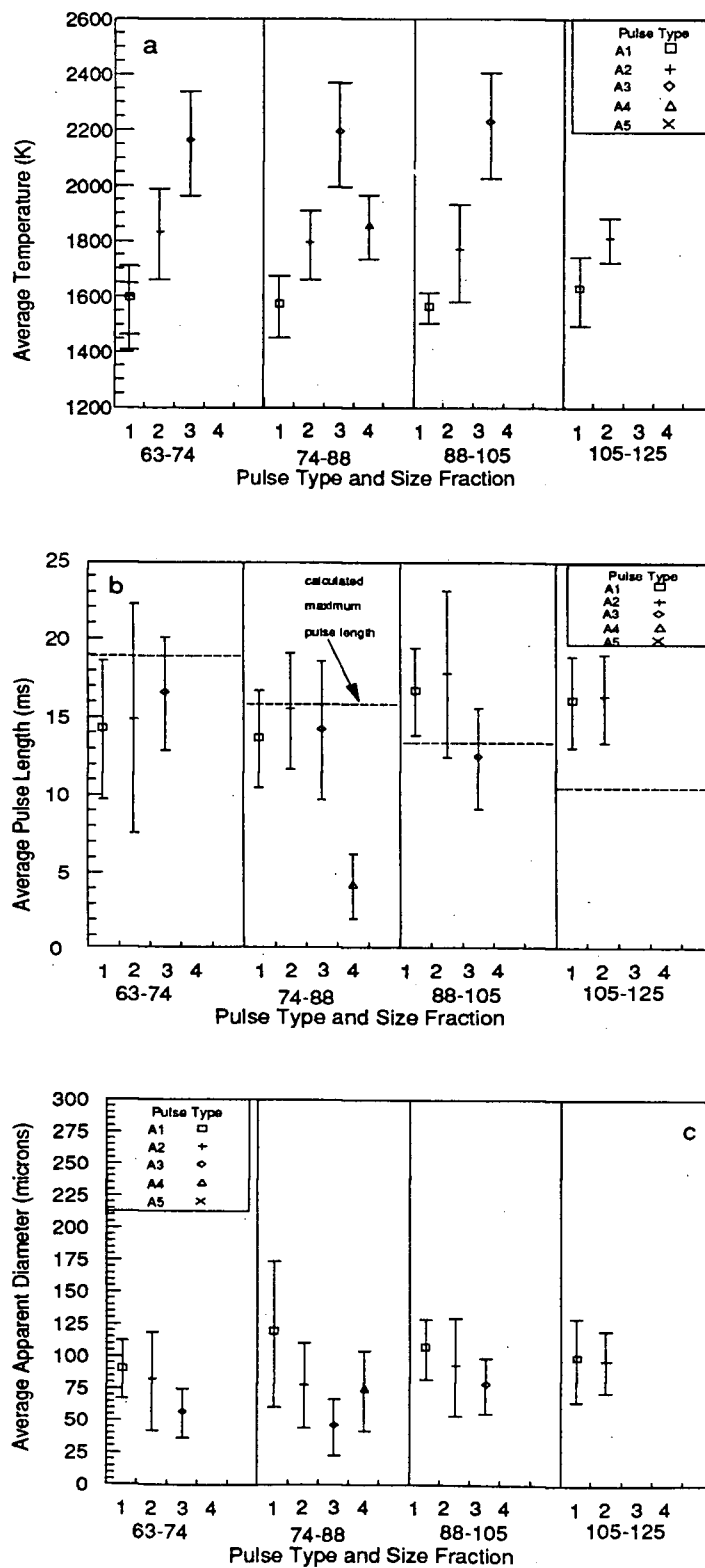


Figure 6.38 Pulse type averaged combustion pulse data as a function of feed size for Brunswick concentrate combustion in air, ($T_{\text{FURNACE}}=1130\text{K}$).
 a) pulse temperatures, b) pulse lengths and c) apparent diameters.

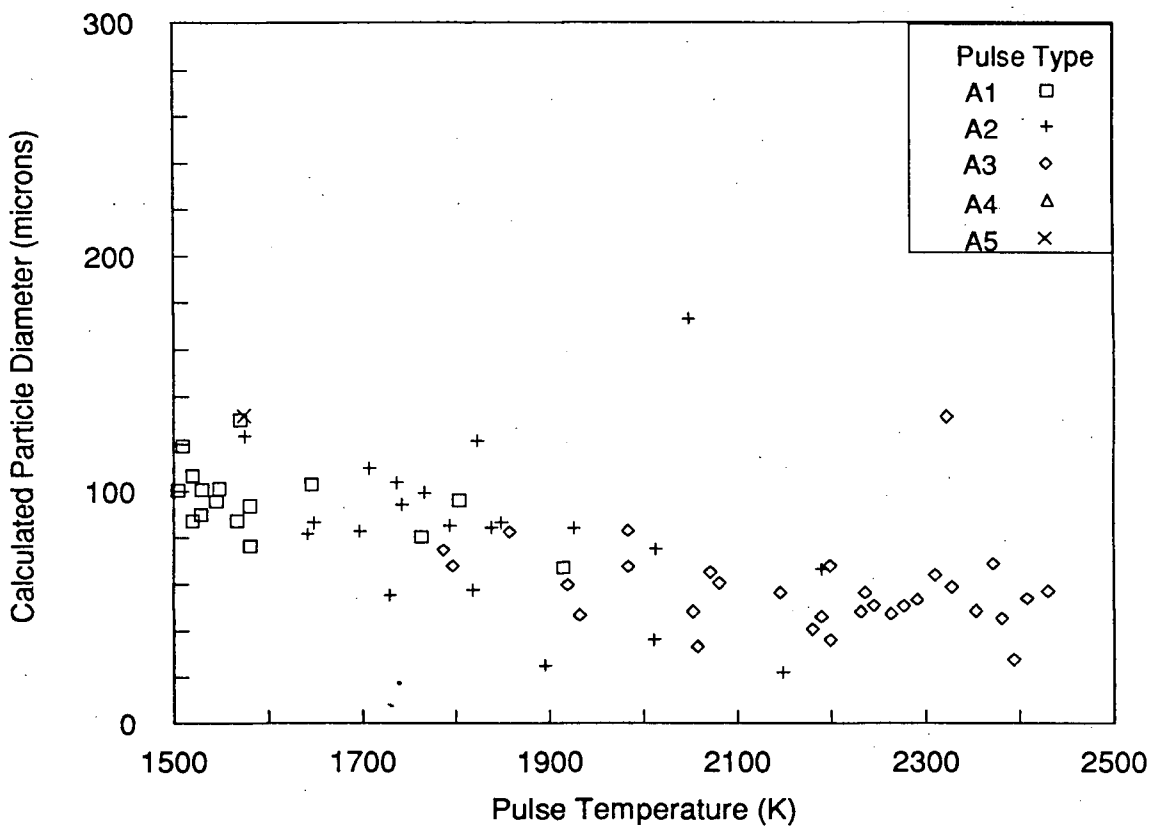
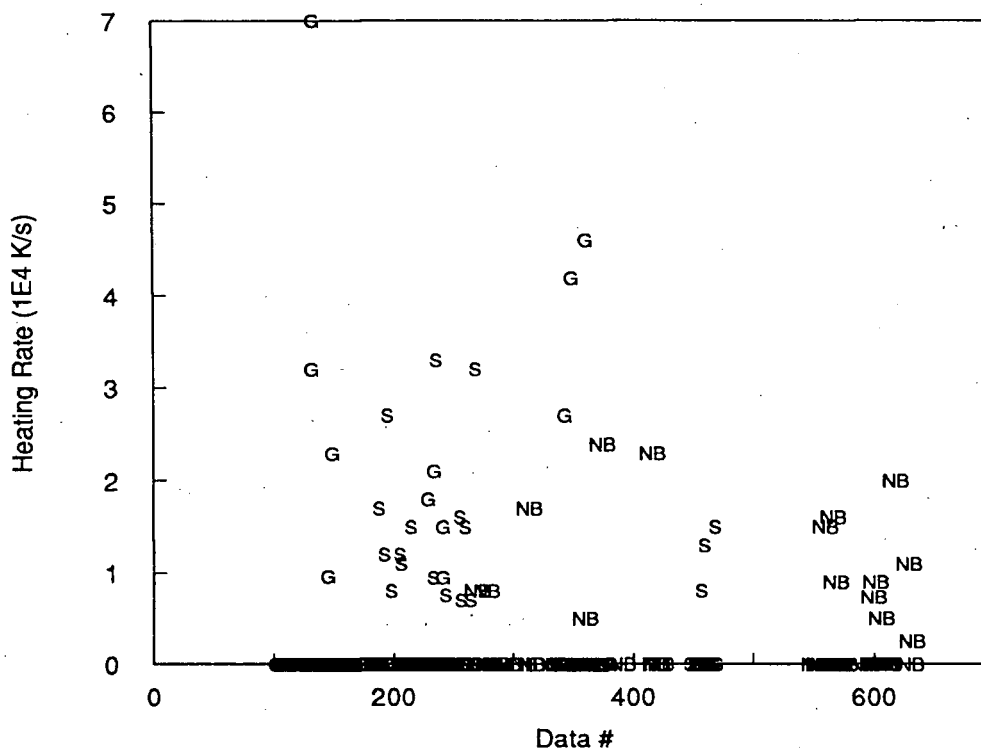
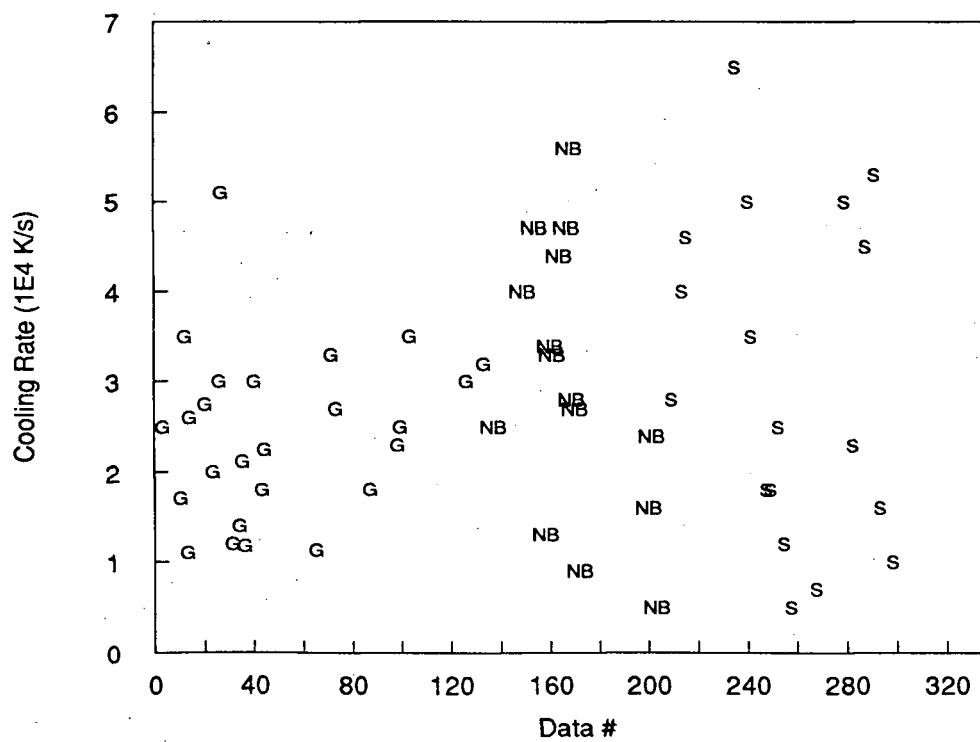


Figure 6.39 Combustion of 63-74 μm Brunswick concentrate in air at $T_{\text{FURNACE}}=1130\text{K}$ -apparent particle diameter versus measured particle temperature.

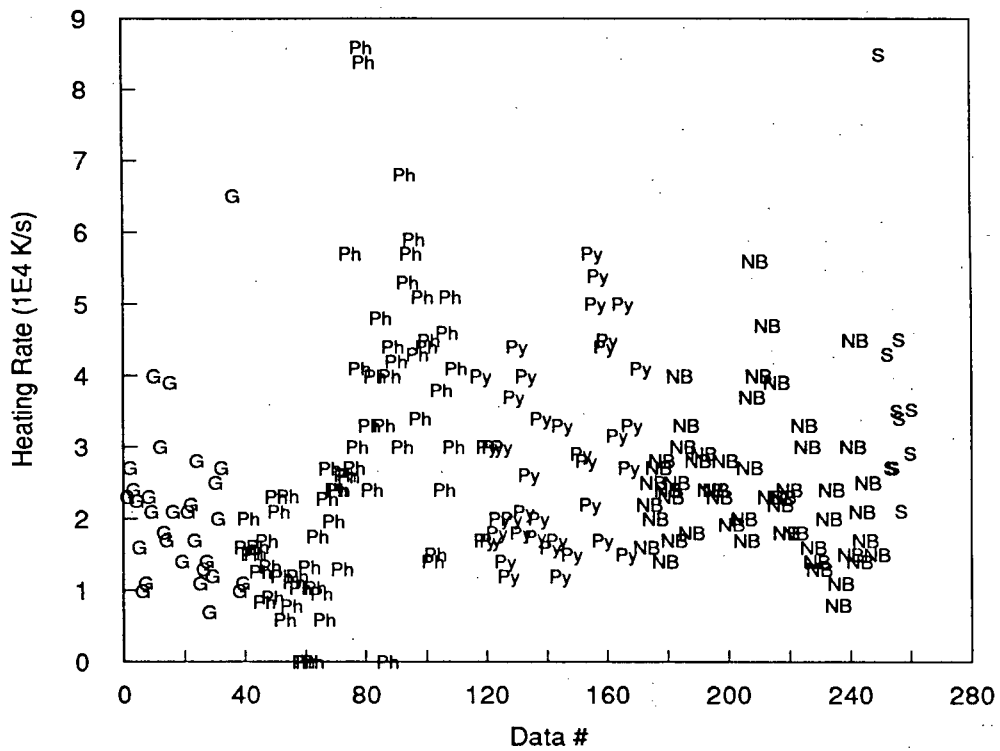


(a) heating rates

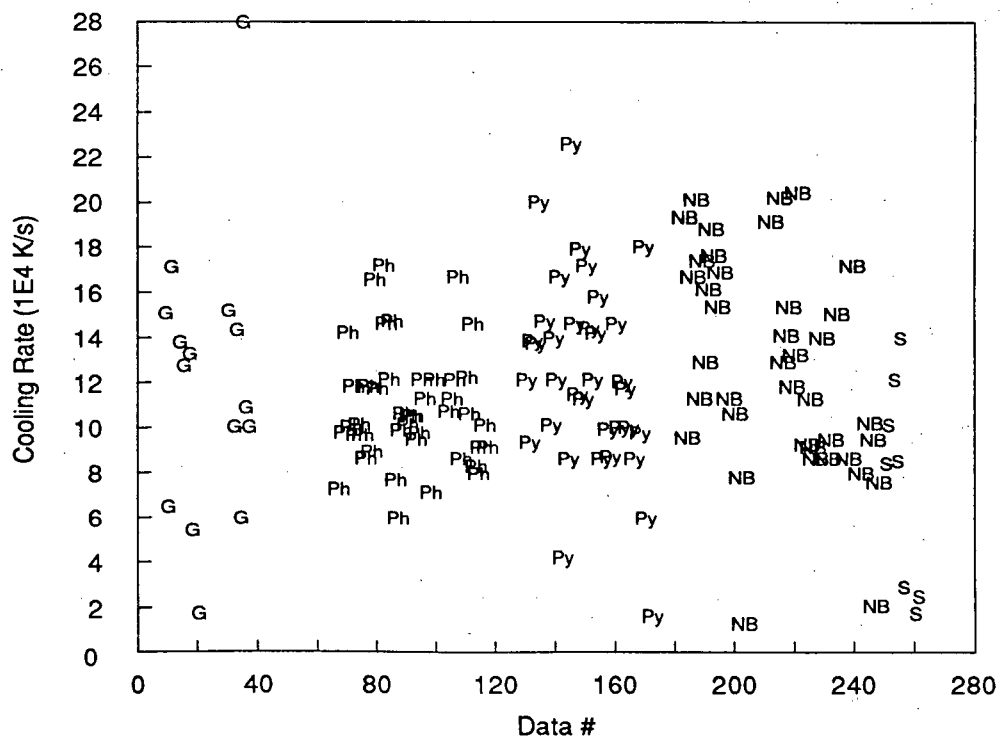


(b) cooling rate

Figure 6.40 Heating and cooling rates of the Al combustion pulses recorded during the combustion of the galena(G), Sullivan(S) and Brunswick(NB) feed materials in air at $T_{\text{FURNACE}}=1130\text{K}$ (plotted vs an arbitrary data number).

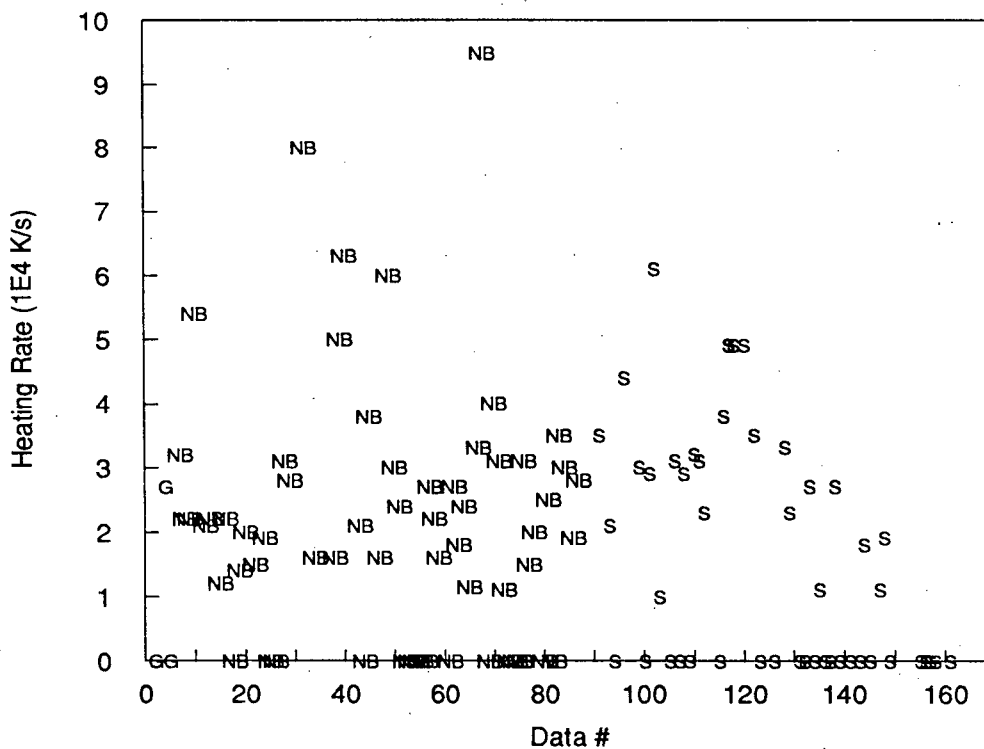


(a) heating rates

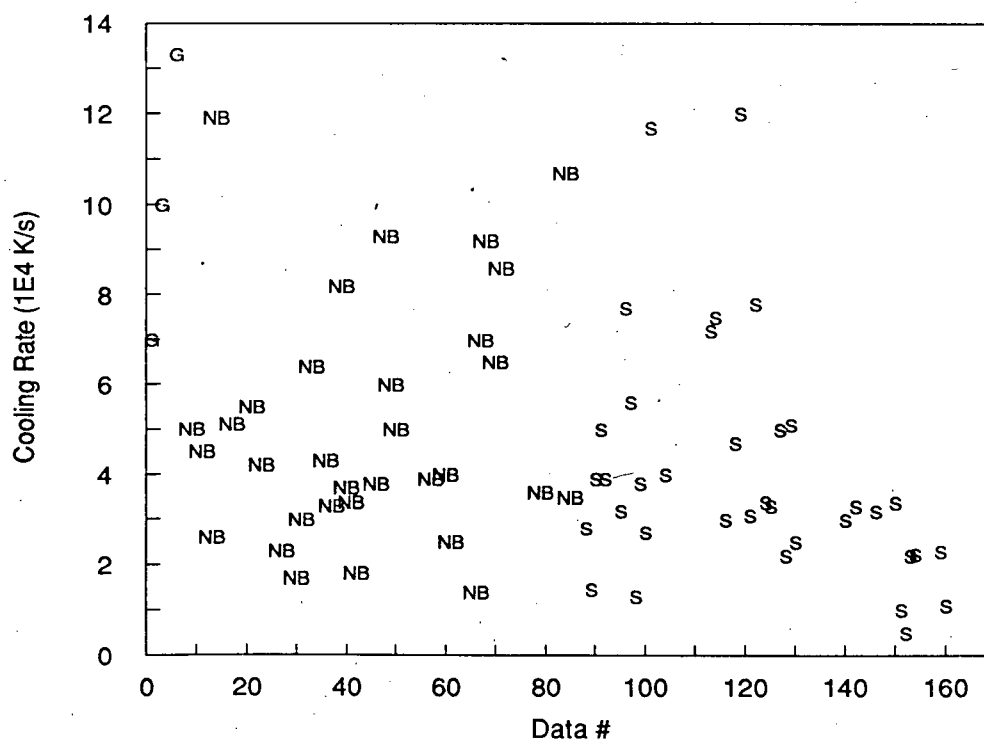


(b) cooling rate

Figure 6.41 Heating and cooling rates of the A3 combustion pulses recorded during the combustion of Pyrite(Py), Pyrrhotite(Ph), galena(G), Sullivan(S) and Brunswick(NB) feed materials in air at $T_{\text{FURNACE}}=1130\text{K}$ (plotted vs an arbitrary data number).



(a) heating rates



(b) cooling rate

Figure 6.42 Heating and cooling rates of the A2 combustion pulses recorded during the combustion of galena(G), Sullivan(S) and Brunswick(NB) feed materials in air at $T_{\text{FURNACE}}=1130\text{K}$ (plotted vs an arbitrary data number).

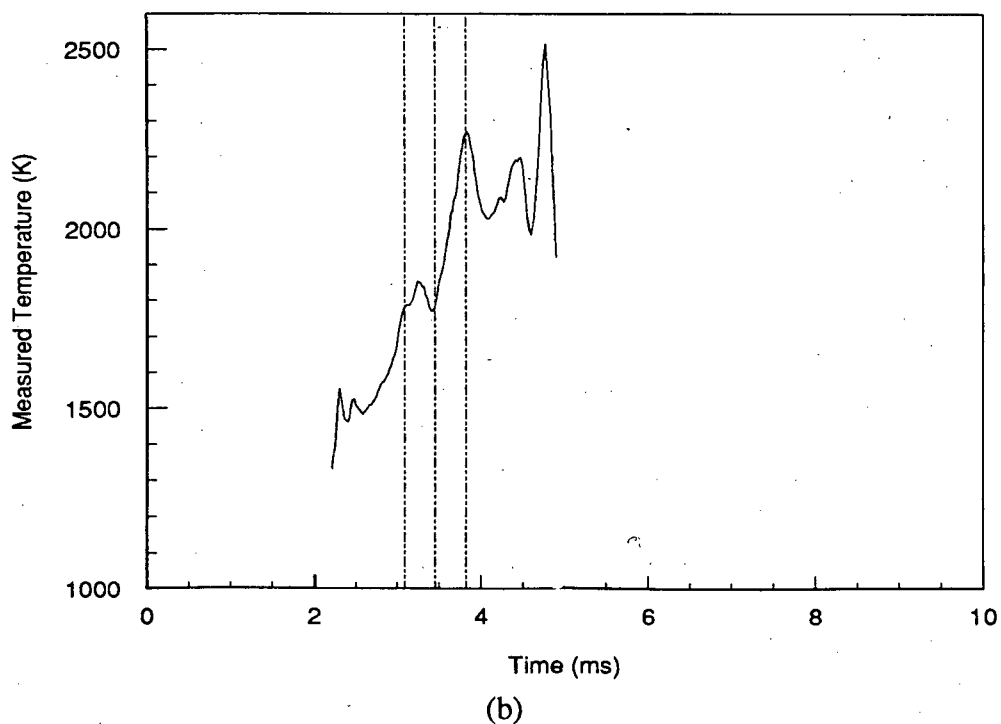
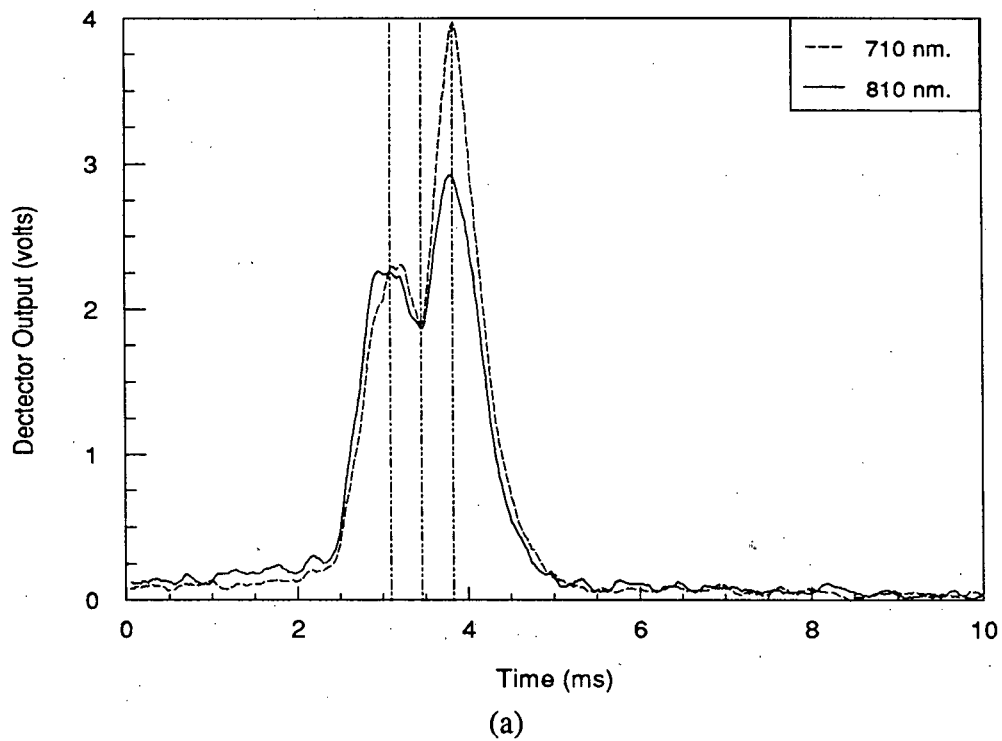


Figure 6.43 OIT combustion pulse recorded during the combustion of galena in oxygen,
a) pyrometer output and b) measured temperature.
(63-74 μm , $T_{\text{FURNACE}}=1130\text{K}$, $C_{\text{VAL}}=1.42$, data#=G316.dat).

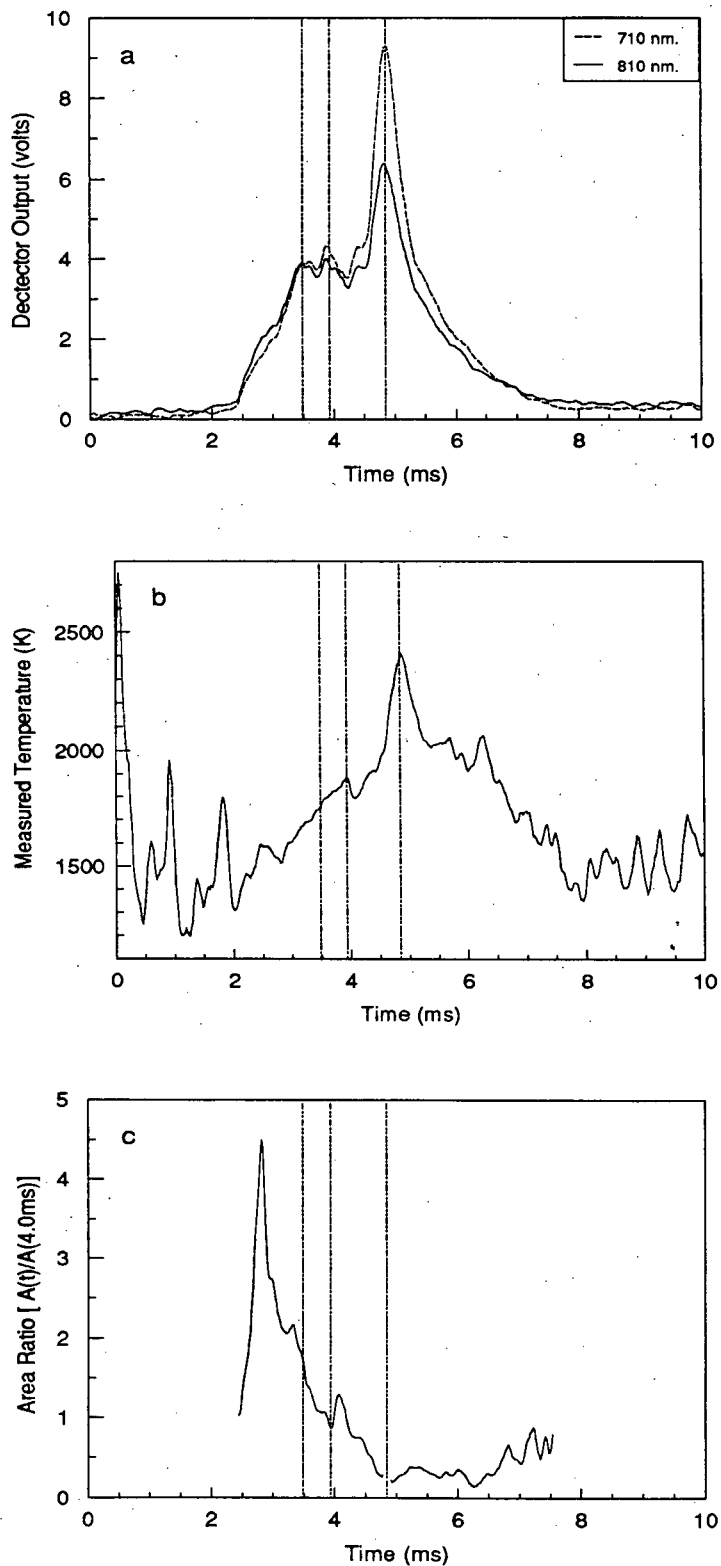


Figure 6.44 OIT combustion pulse recorded during the combustion of galena in oxygen, a)pyrometer detector output, b)measured temperature and c)apparent area relative to that at 4ms. (105-125 μ m, $T_{\text{FURNACE}}=1130\text{K}$, $C_{\text{VAL}}=1.42$, data#=G455.dat).

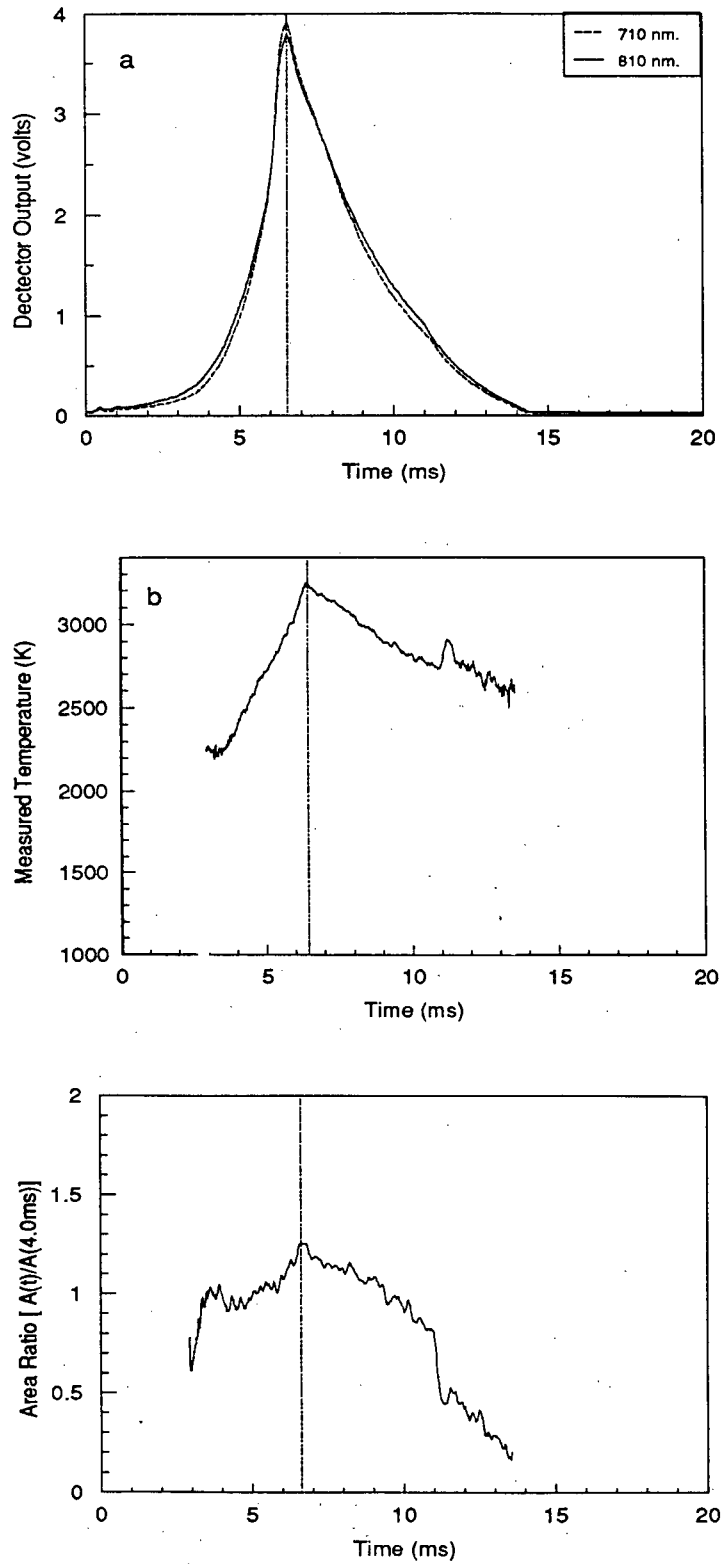


Figure 6.45 O₃ combustion pulse recorded during the combustion of pyrrhotite in oxygen, a) pyrometer output, b) measured temperature and c) apparent area relative to that at 4ms. ($74-88\mu\text{m}$, $T_{\text{FURNACE}}=1130\text{K}$, $C_{\text{VAL}}=0.81$, data#=PH224.dat).

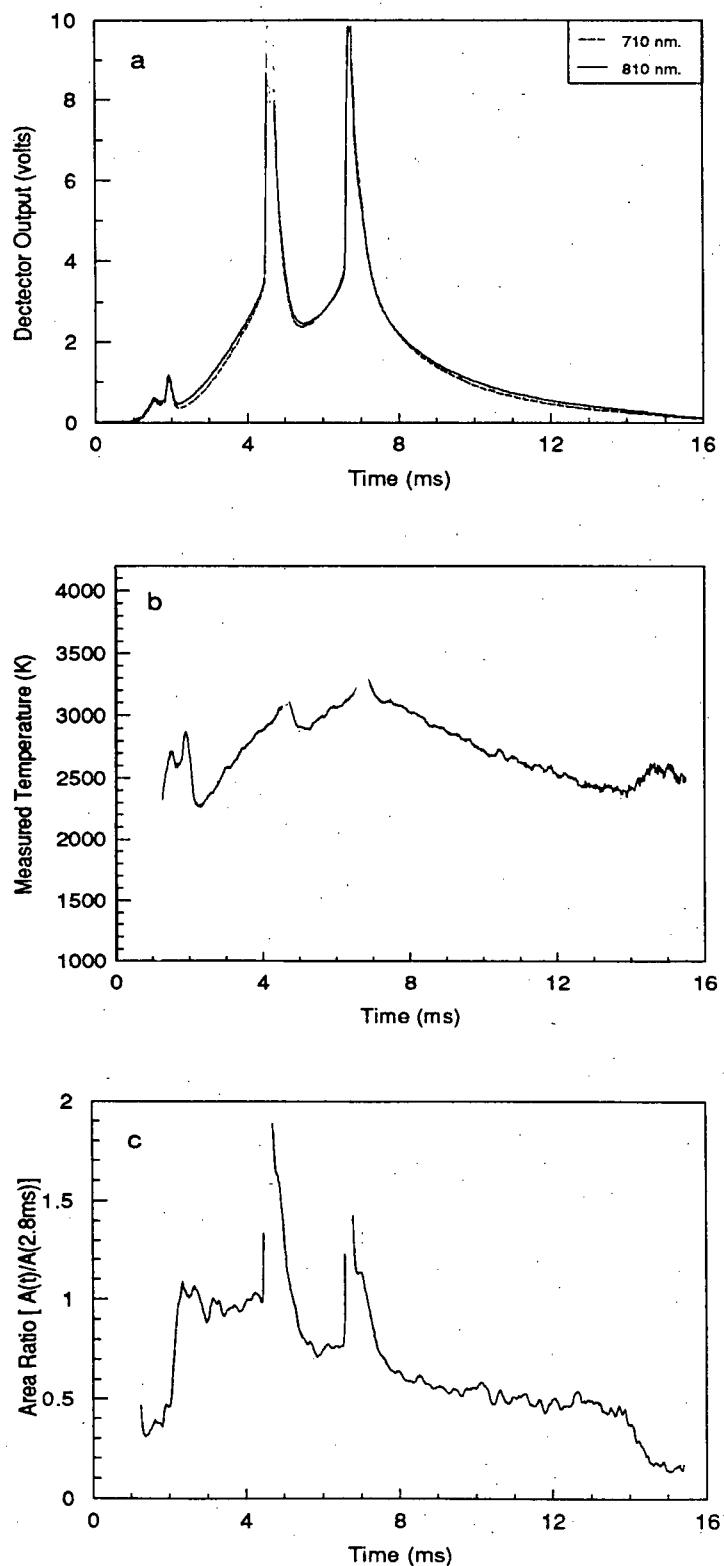


Figure 6.46 O₃ combustion pulse recorded during the combustion of pyrite in oxygen, a) pyrometer output, b) measured temperature and c) apparent area relative to that at 2.8ms. (74-88 μ m, $T_{\text{FURNACE}}=1130\text{K}$, $C_{\text{VAL}}=0.81$, data#=PY84.dat).

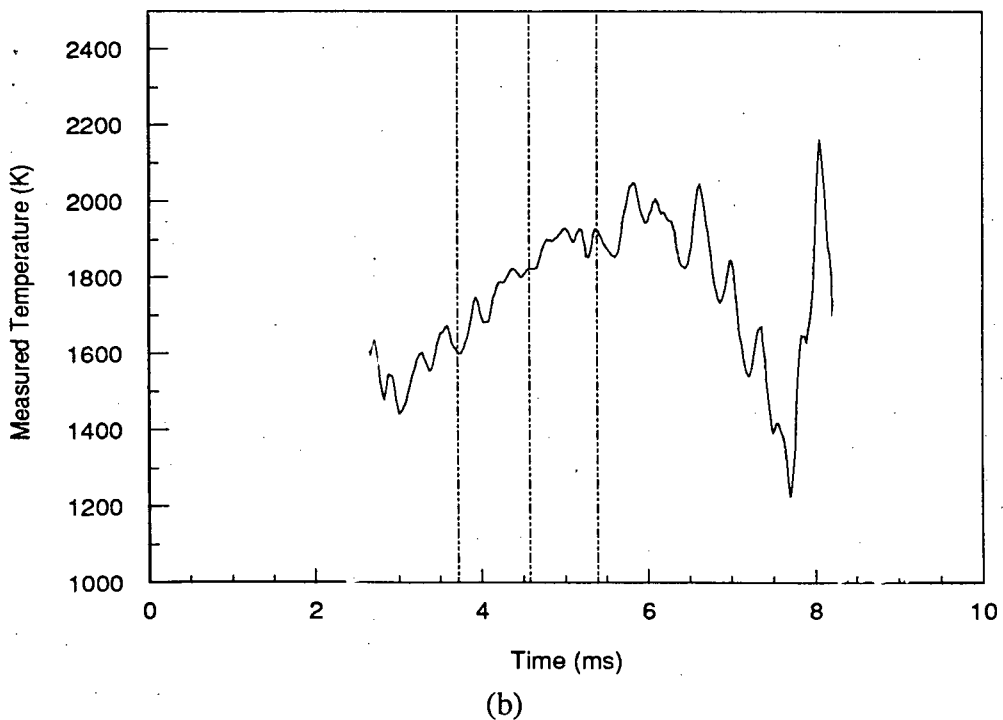
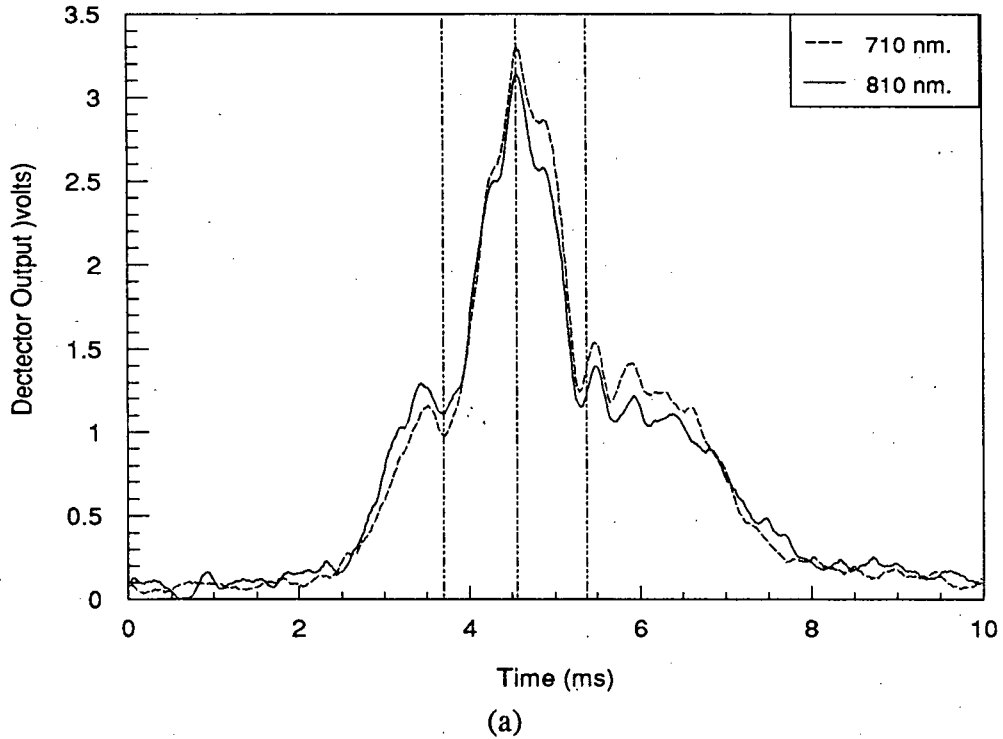


Figure 6.47 O₂ combustion pulse recorded during the combustion of Sullivan concentrate in oxygen, a) pyrometer output and b) measured temperature. (63-74 μ m, $T_{\text{FURNACE}}=1130\text{K}$, $C_{\text{VAL}}=1.42$, data#=S324.dat).

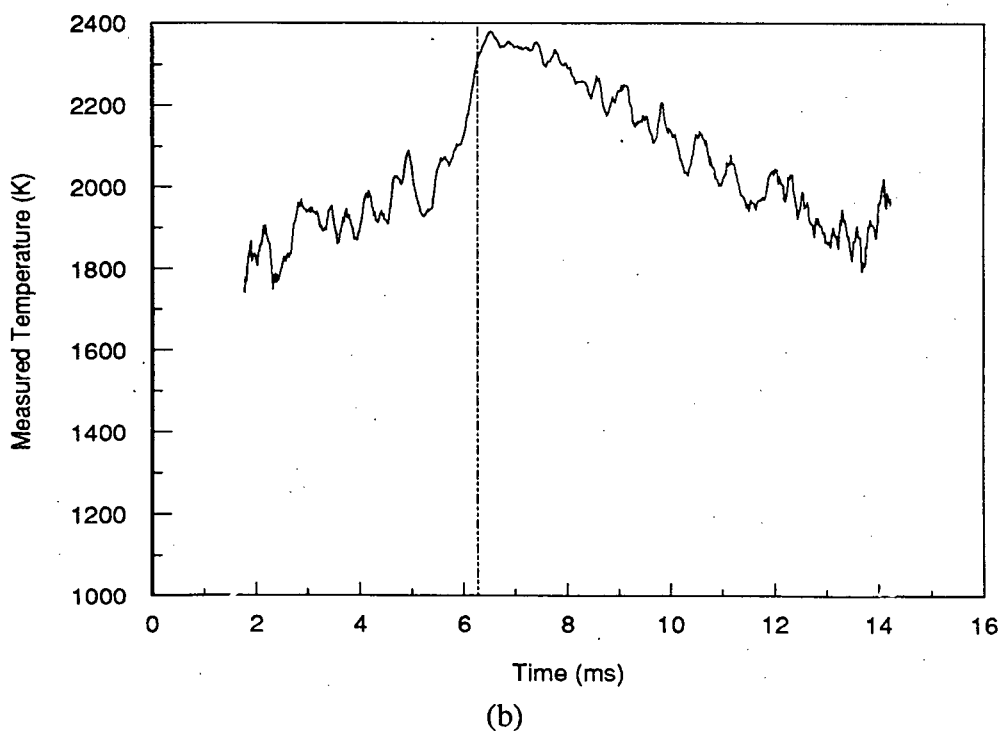
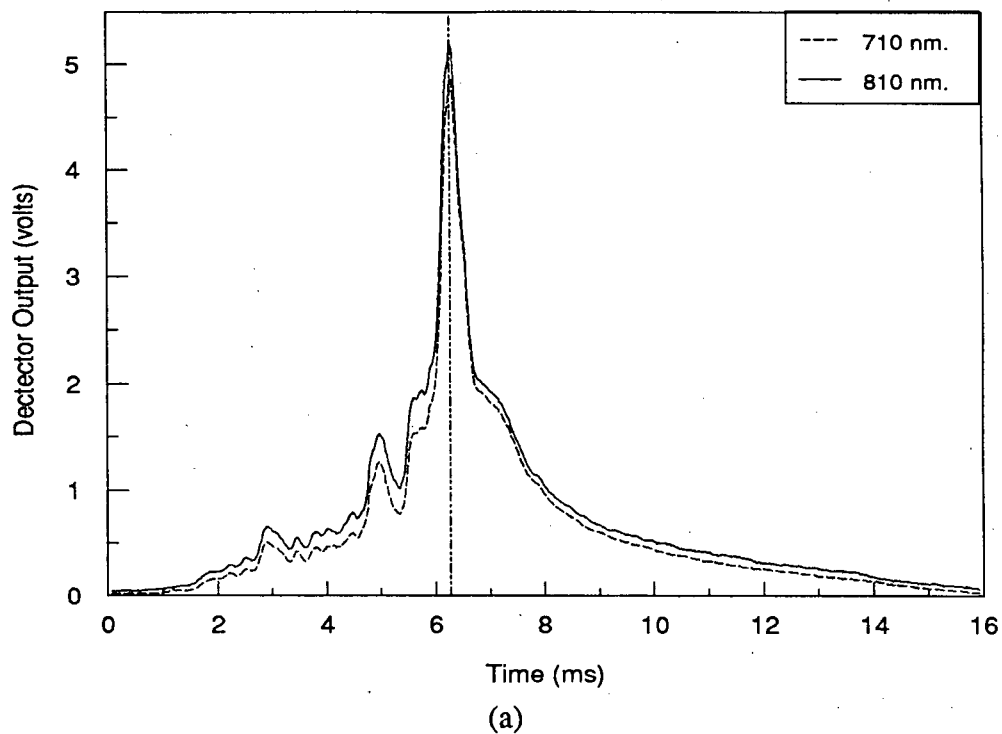


Figure 6.48 O₂ combustion pulse recorded during the combustion of Brunswick concentrate in oxygen, a) pyrometer output and b) measured temperature. (105-125 μm , $T_{\text{FURNACE}}=1130\text{K}$, $C_{\text{VAL}}=1.01$, data#=NB669.dat).

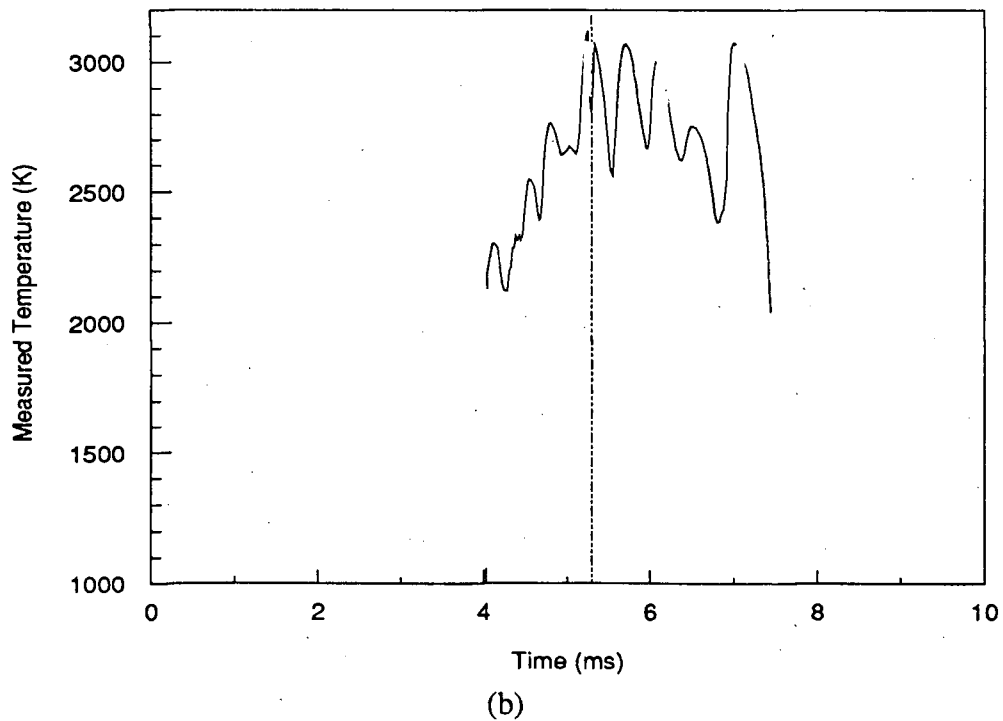
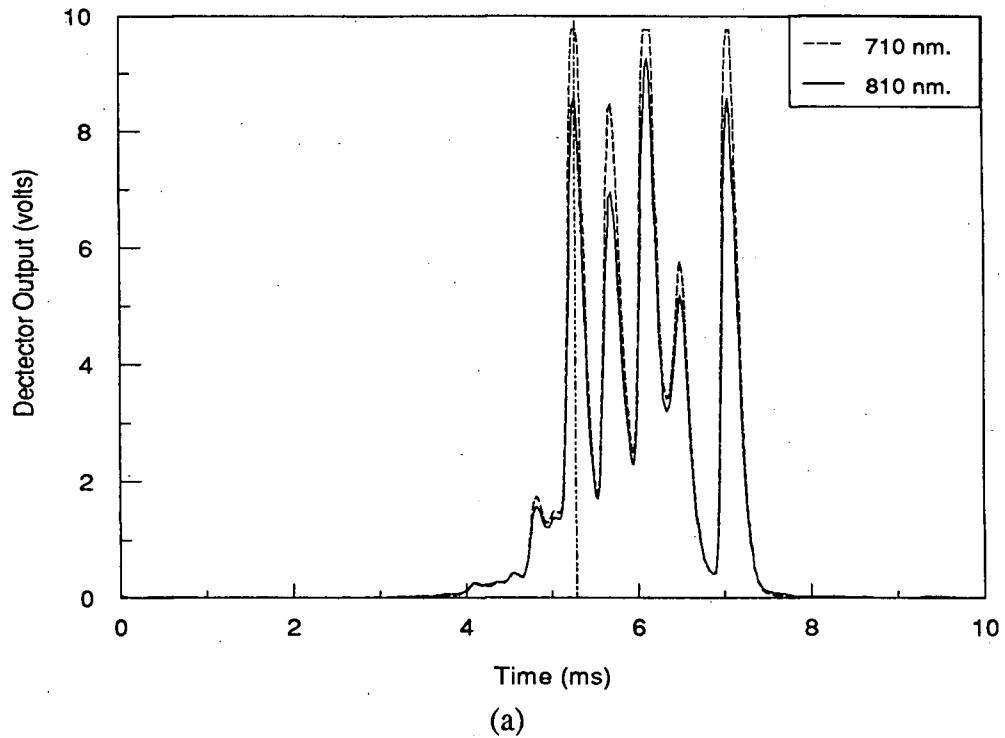


Figure 6.49 O₂S combustion pulse recorded during the combustion of Sullivan concentrate in oxygen, a) pyrometer output and b) measured temperature. (63-74 μm , $T_{\text{FURNACE}}=1130\text{K}$, $C_{\text{VAL}}=1.01$, data#=S303.dat).

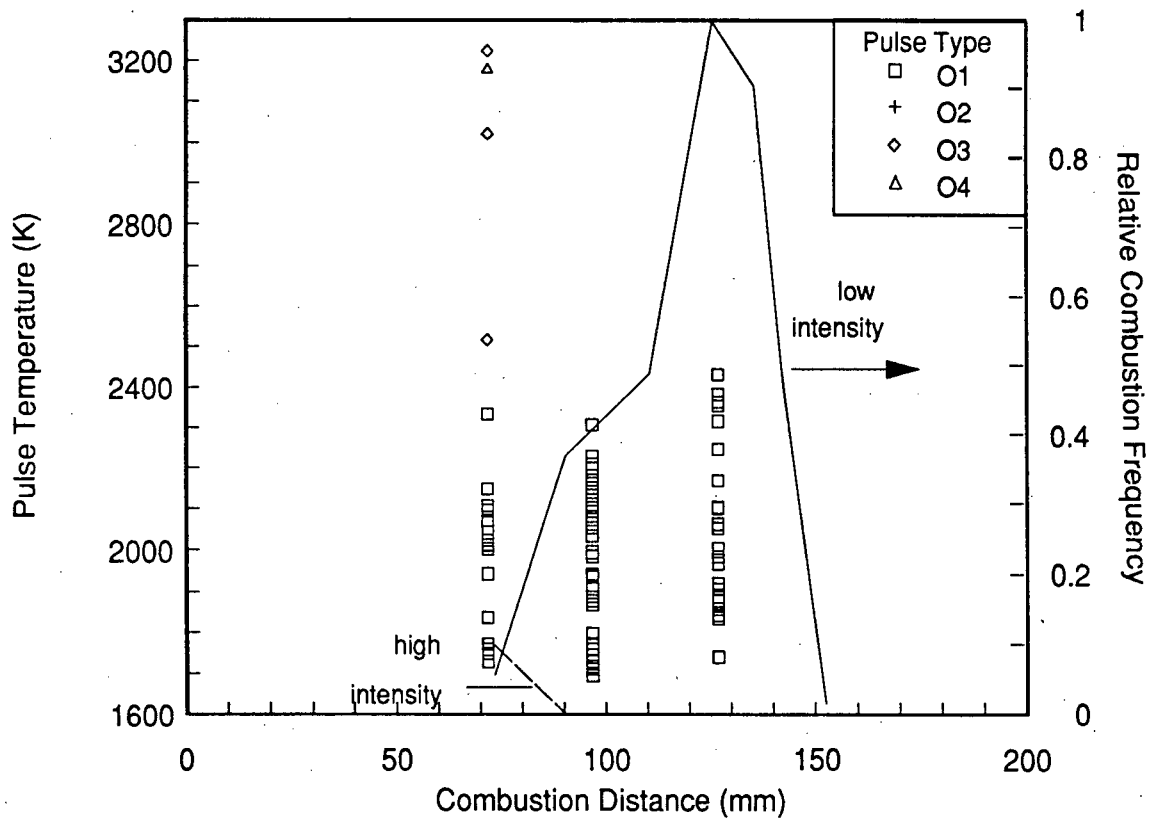
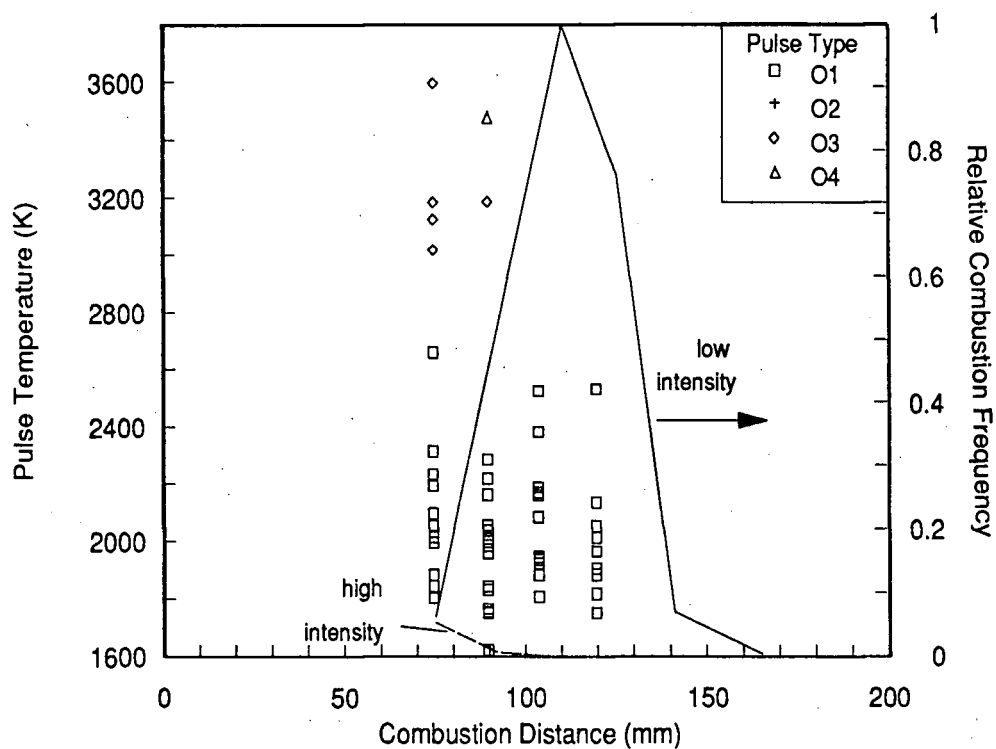
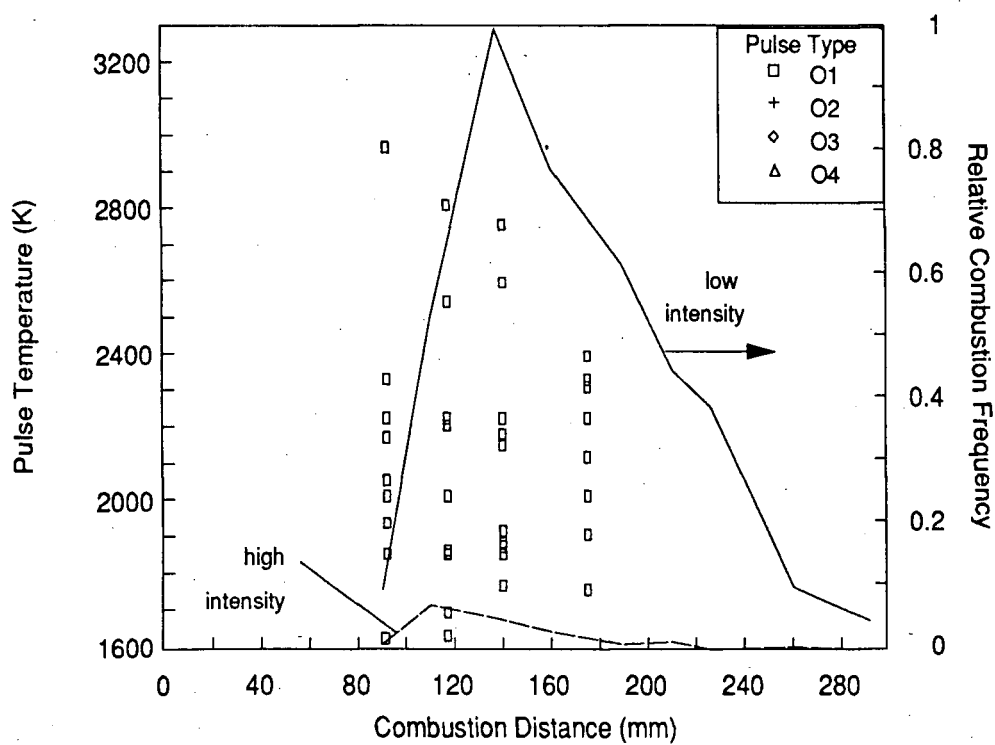


Figure 6.50 Combustion of 63-74 μ m galena in oxygen at $T_{\text{FURNACE}}=1130\text{K}$ - pulse type, temperature and relative frequency as a function of furnace combustion distance.



(a)



(b)

Figure 6.51 Combustion of a) 74-88 μm and b) 105-125 μm galena in oxygen at $T_{\text{FURNACE}}=1130\text{K}$ - pulse type, temperature and relative frequency as a function of furnace combustion distance.

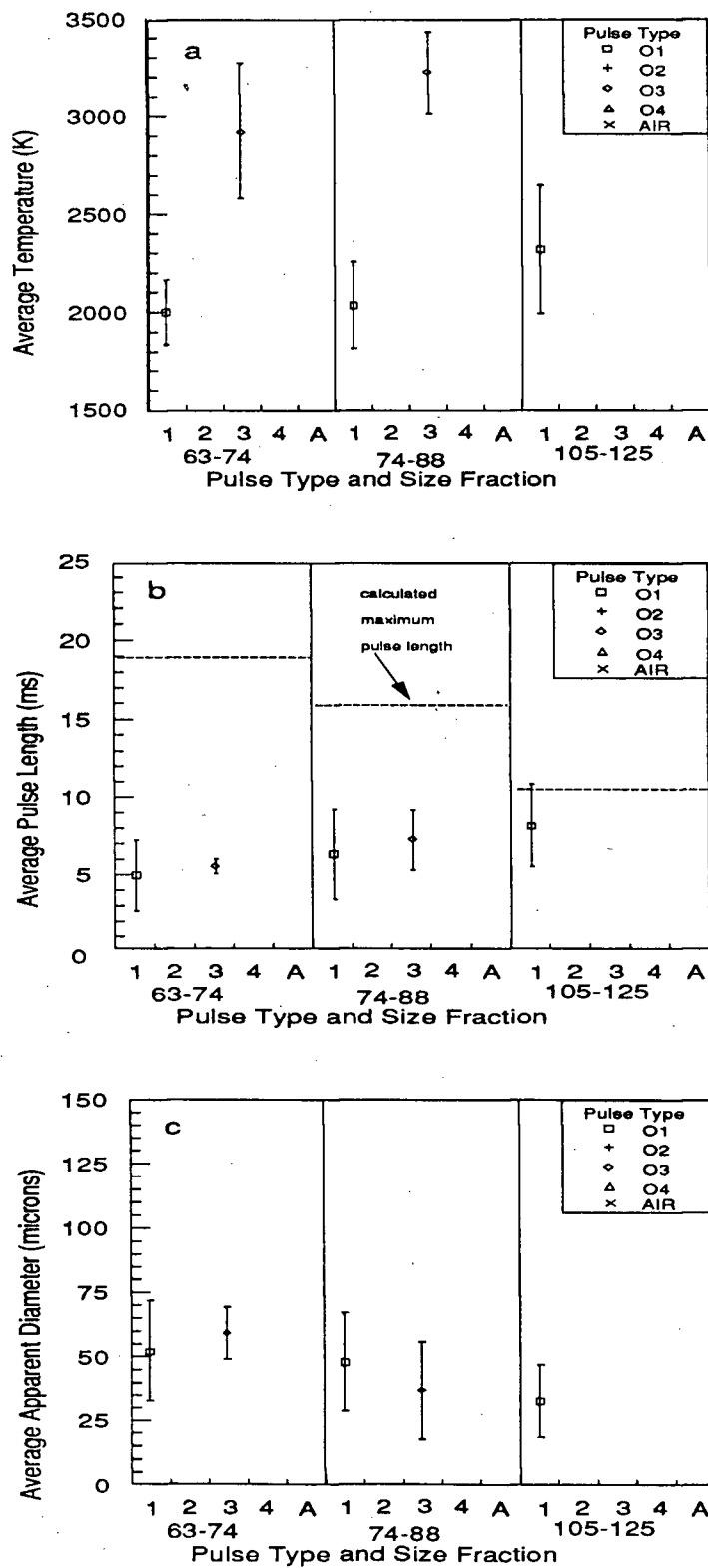


Figure 6.52 Pulse type averaged combustion pulse data as a function of feed size for galena combustion in oxygen, a) pulse temperatures, b) pulse lengths and c) apparent diameters. ($T_{\text{FURNACE}}=1130\text{K}$).

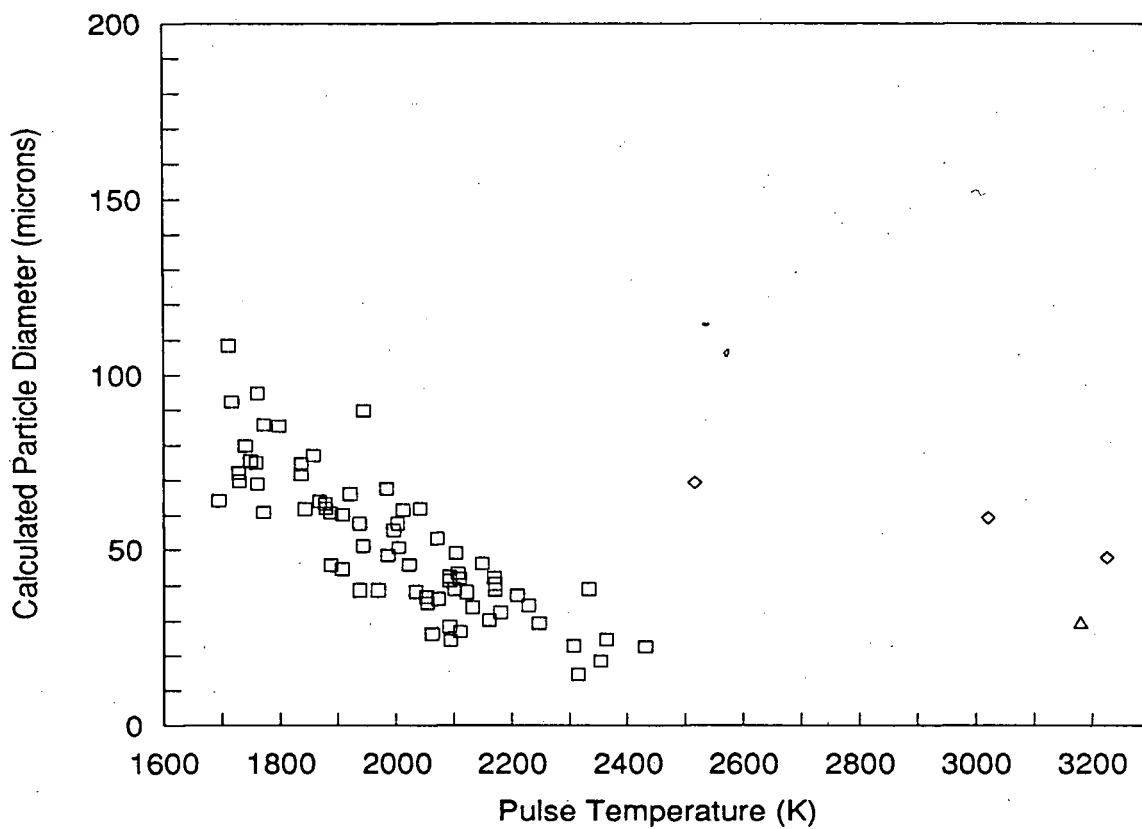
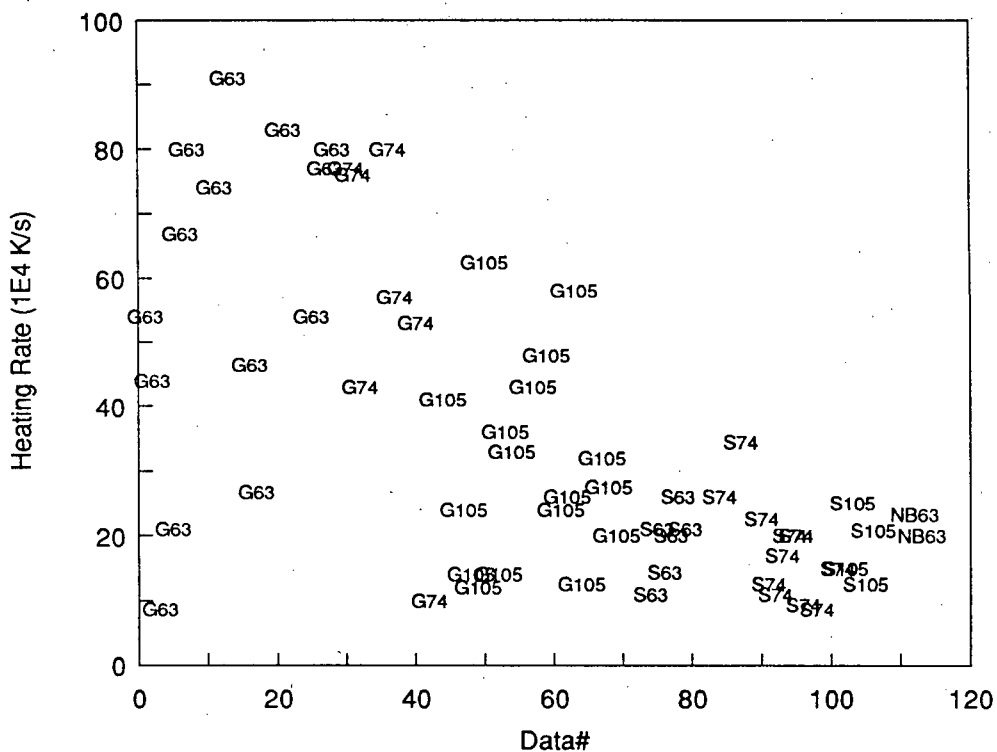
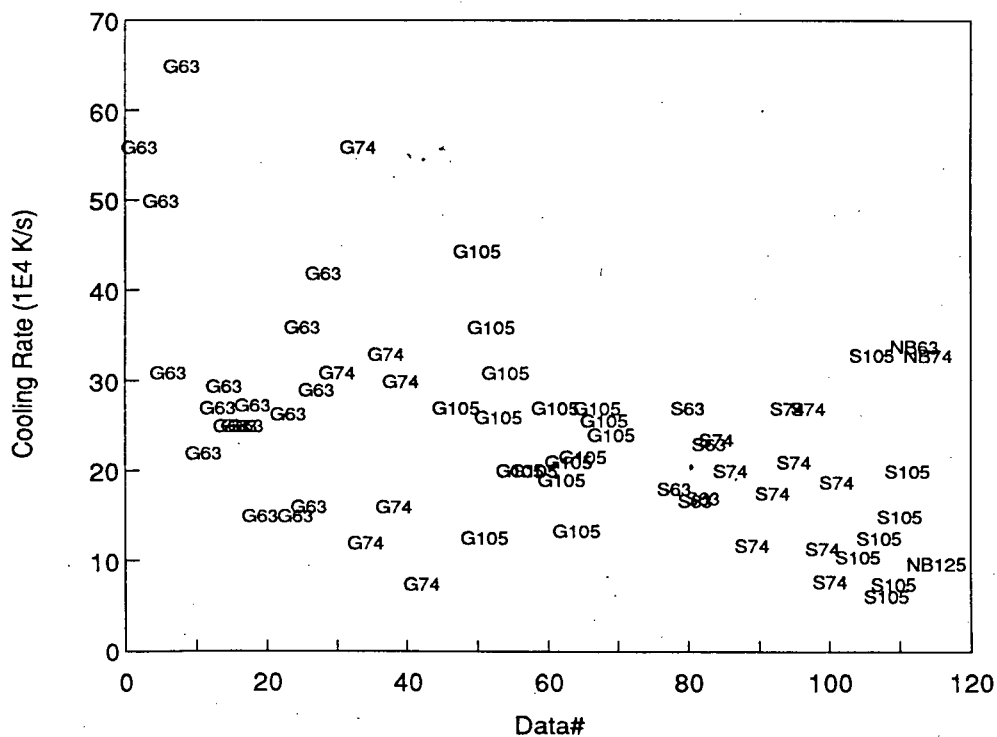


Figure 6.53 Combustion of 63-74 μm galena in oxygen at $T_{\text{FURNACE}}=1130\text{K}$ - apparent particle diameter versus measured particle temperature.

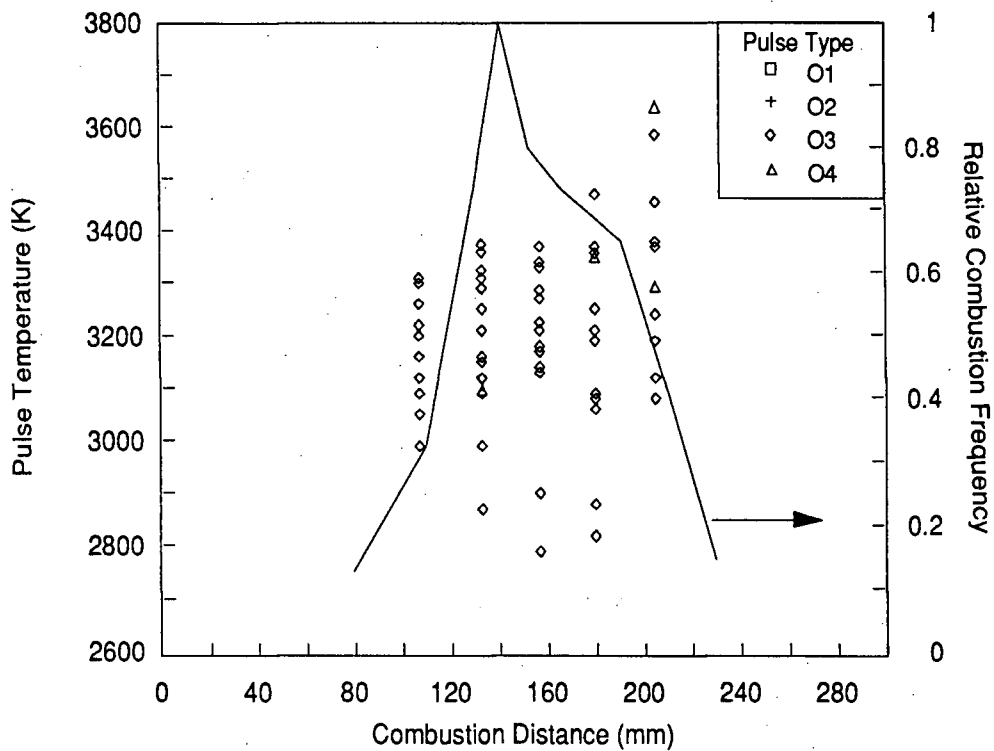


(a) heating rates

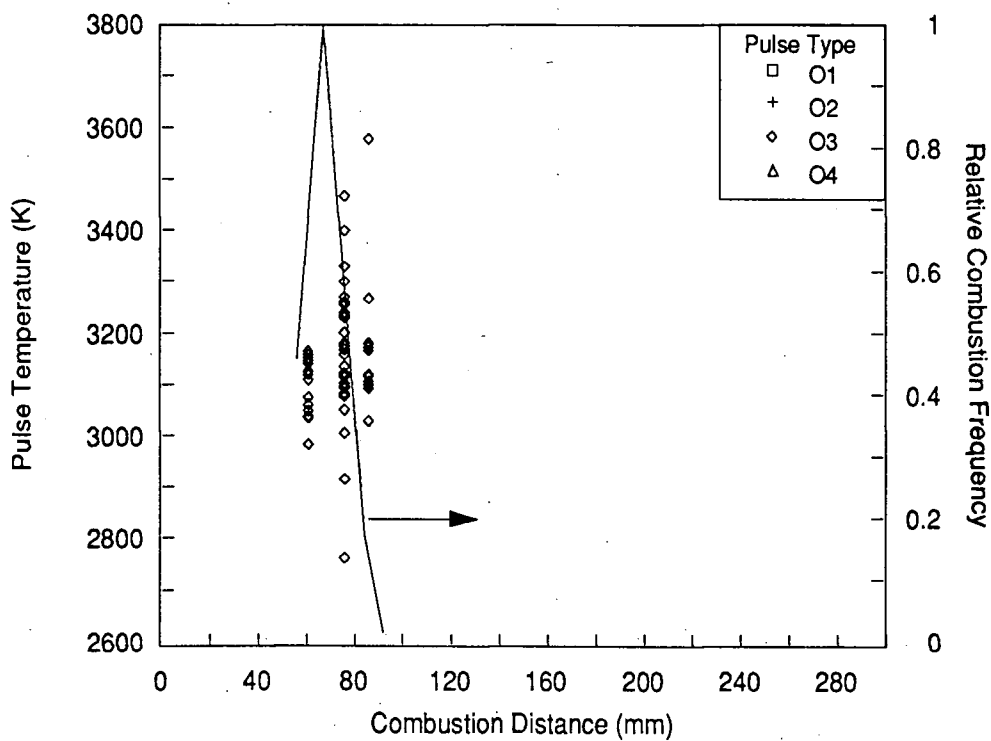


(b) cooling rate

Figure 6.54 Heating and cooling rates of the O1 combustion pulses recorded during the combustion of galena(G), Sullivan(S) and Brunswick(NB) feed materials in oxygen at $T_{\text{FURNACE}}=1130\text{K}$ (plotted vs an arbitrary data number).



(a)



(b)

Figure 6.55 Combustion of 74-88 μ m a)pyrrhotite and b)pyrite in oxygen at $T_{\text{FURNACE}}=1130\text{K}$ - pulse type, temperature and relative frequency as a function of furnace combustion distance.

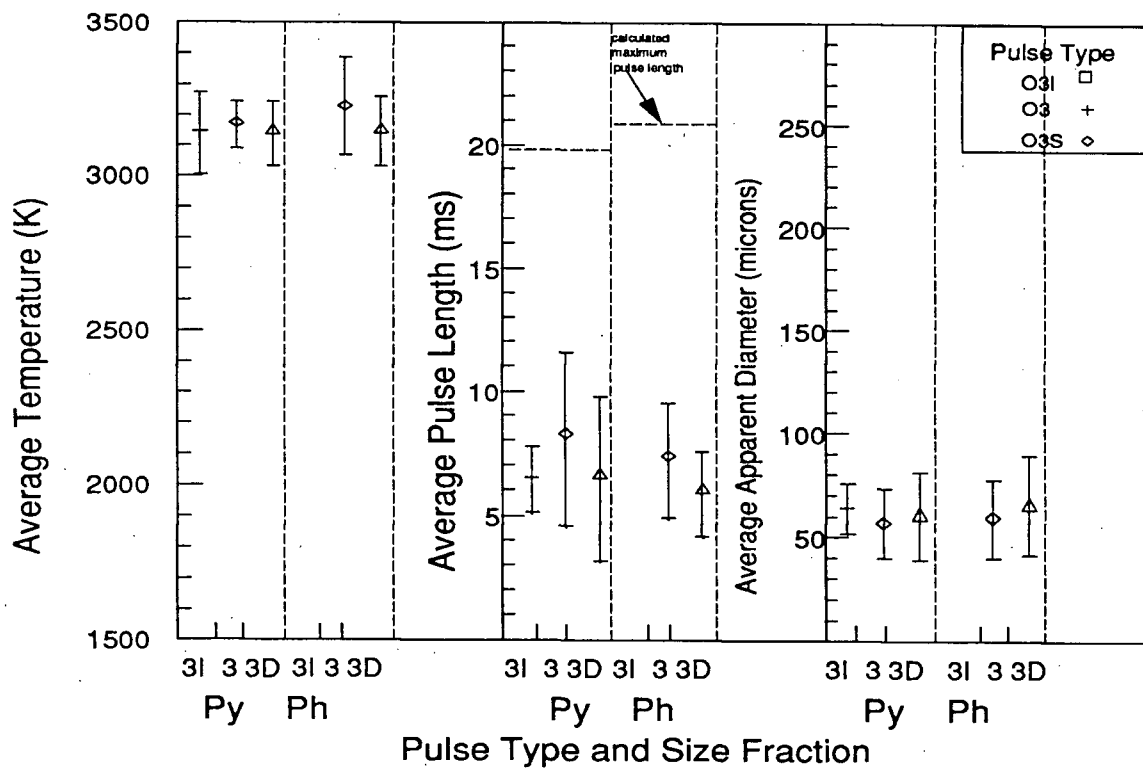
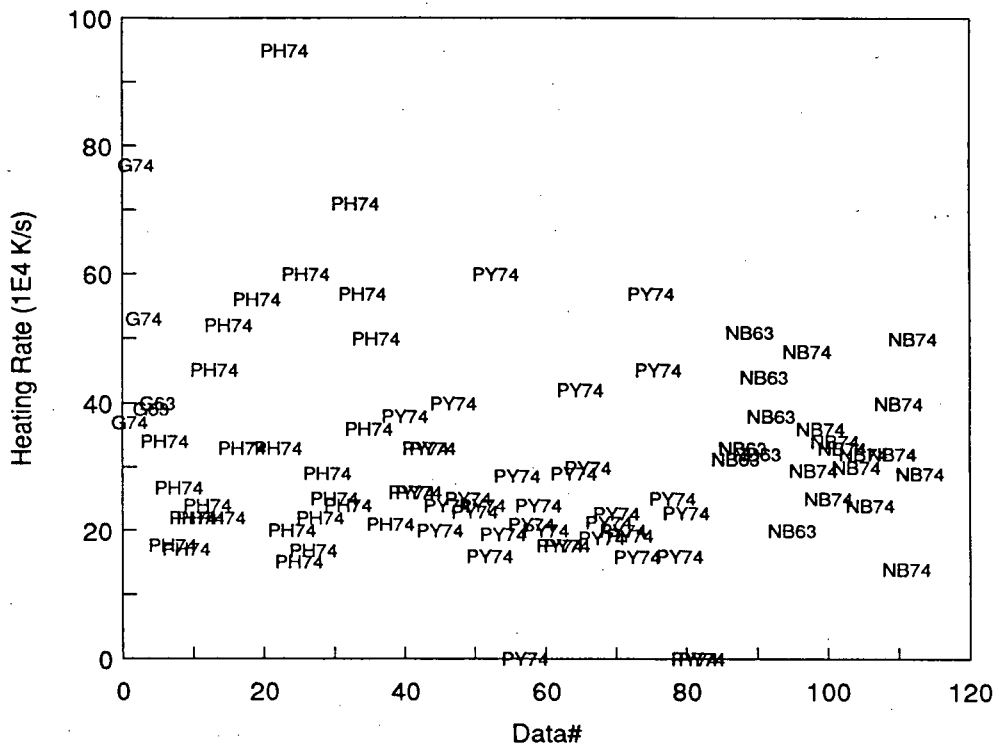
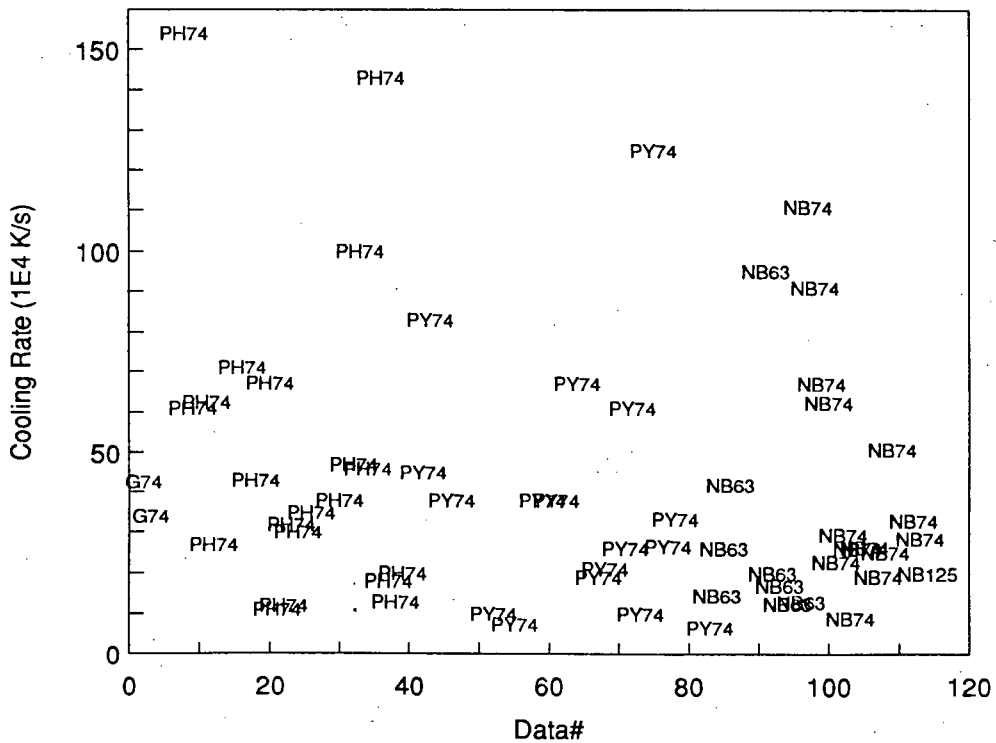


Figure 6.56 Pulse type averaged combustion pulse data for the combustion of pyrrhotite and pyrite in oxygen, a) pulse temperatures, b) pulse lengths and c) apparent diameters. ($T_{\text{FURNACE}}=1130\text{K}$).

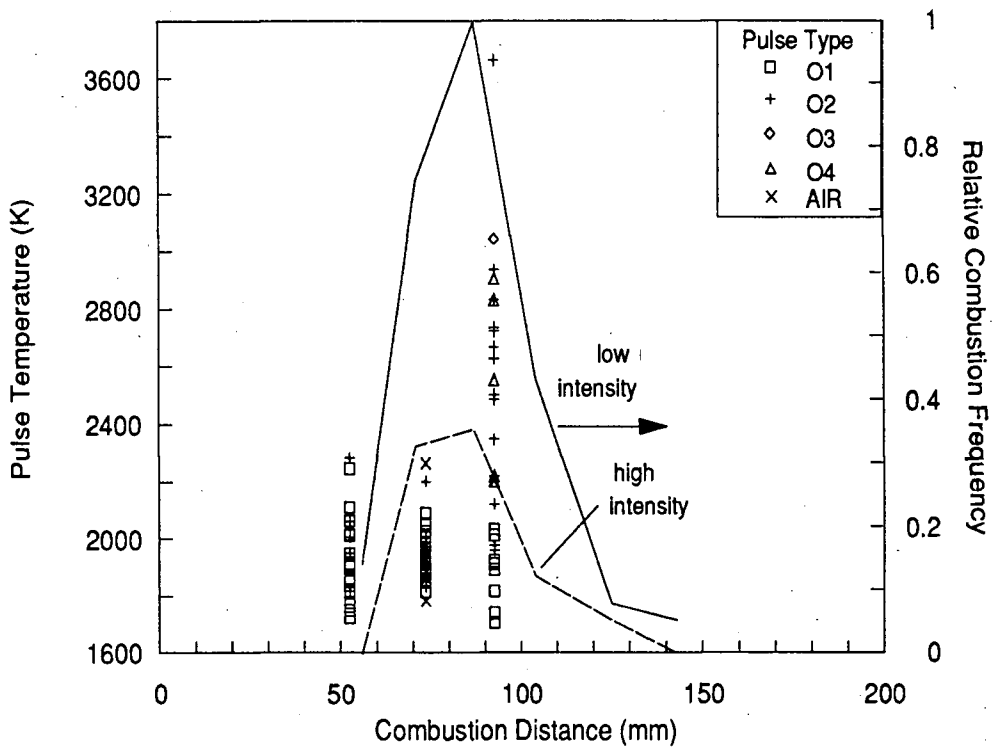


(a) heating rates

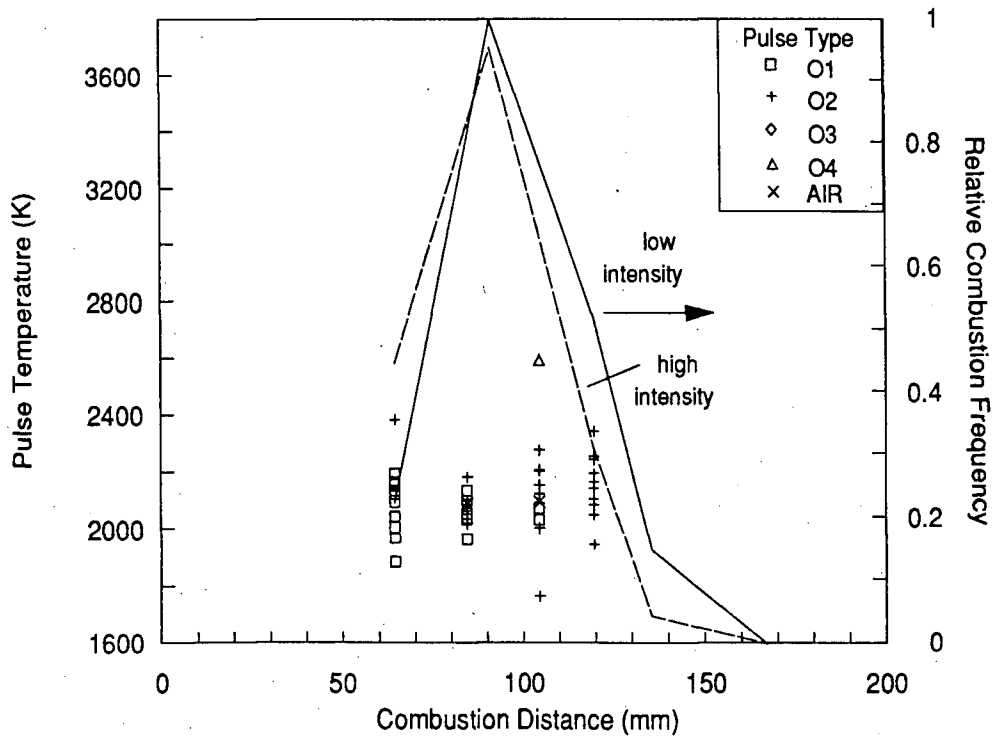


(b) cooling rate

Figure 6.57 Heating and cooling rates of the O₃ combustion pulses recorded during the combustion of pyrite(Py), pyrrhotite(Ph), galena(G) and Brunswick(NB) feed materials in oxygen at $T_{\text{FURNACE}}=1130\text{K}$ (plotted vs an arbitrary data number).



(a)



(b)

Figure 6.58 Combustion of a) 63-74 μm and b) 105-125 μm Sullivan concentrates in oxygen at $T_{\text{FURNACE}}=1130\text{K}$ - pulse type, temperature and relative frequency as a function of furnace combustion distance.

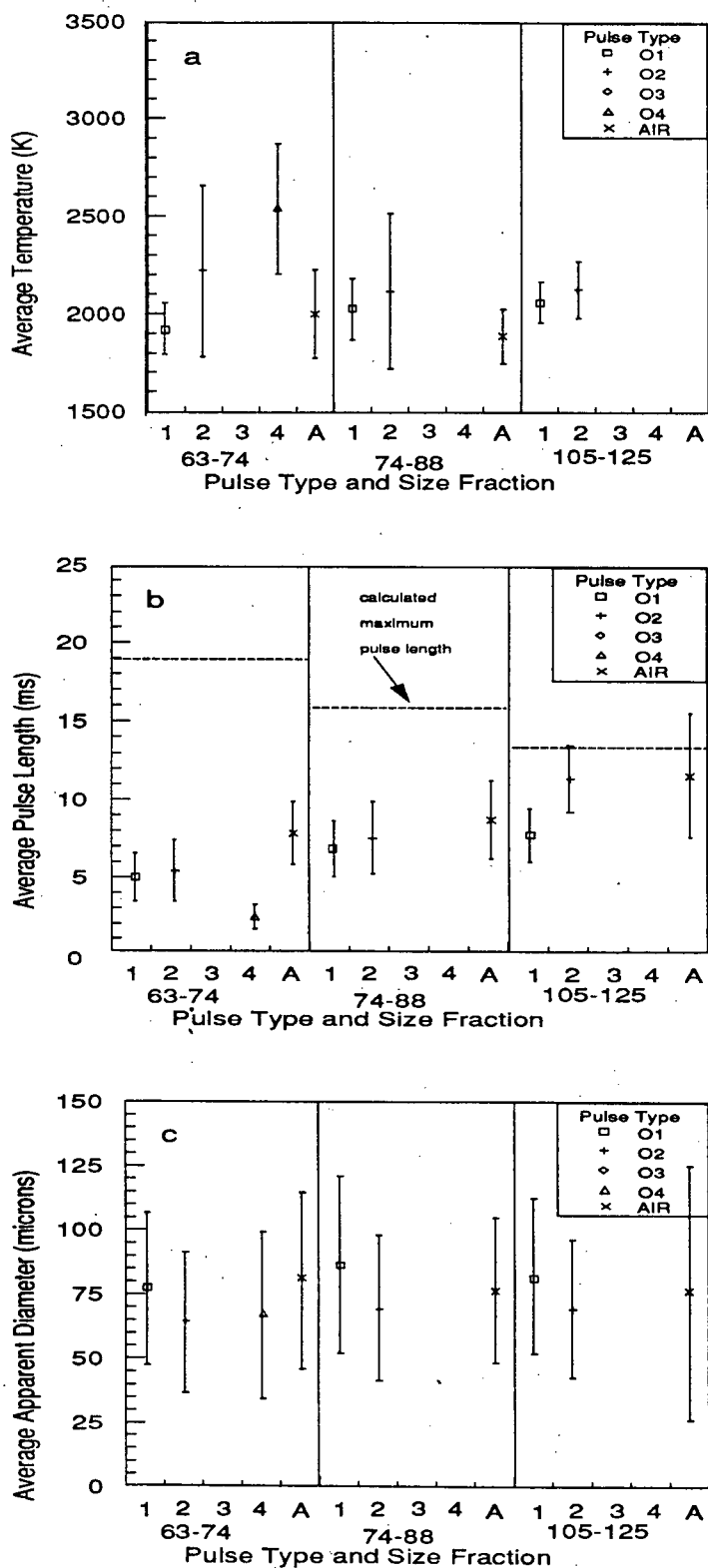
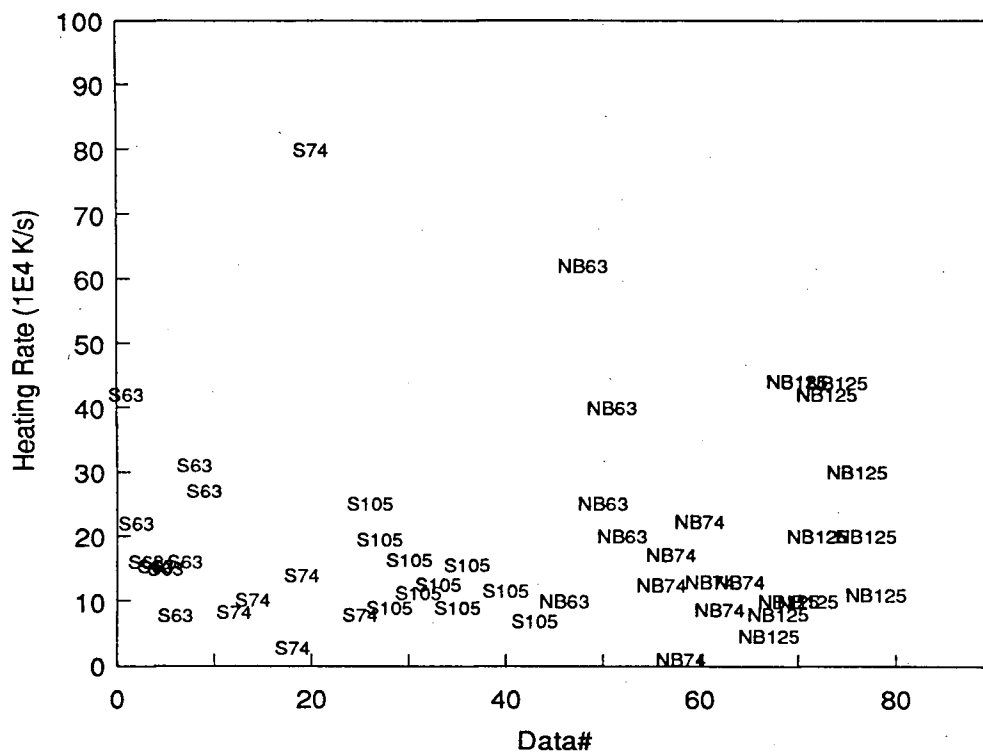
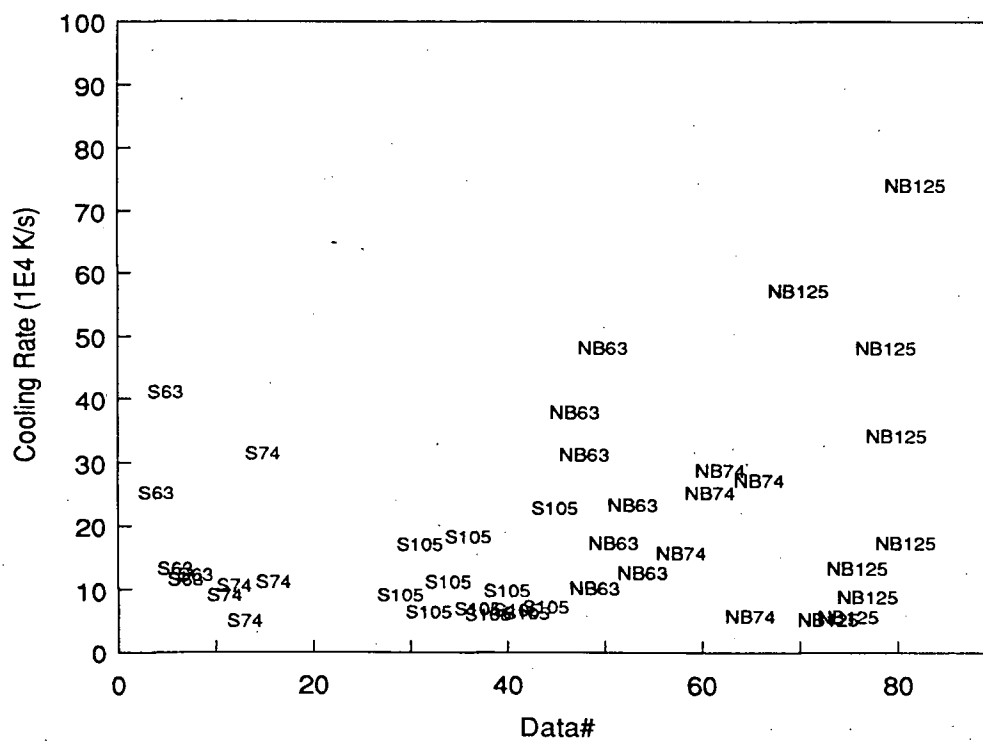


Figure 6.59 Pulse type averaged combustion pulse data as a function of feed size for Sullivan concentrate combustion in oxygen, a) pulse temperatures, b) pulse lengths and c) apparent diameters. ($T_{\text{FURNACE}}=1130\text{K}$).

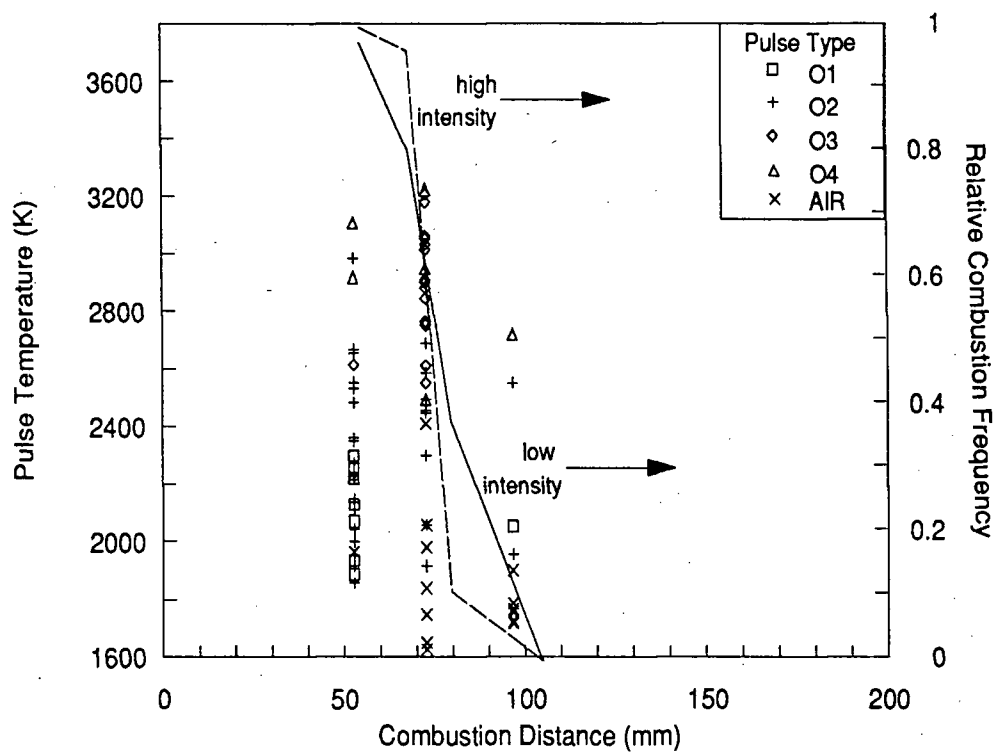


(a)heating rates

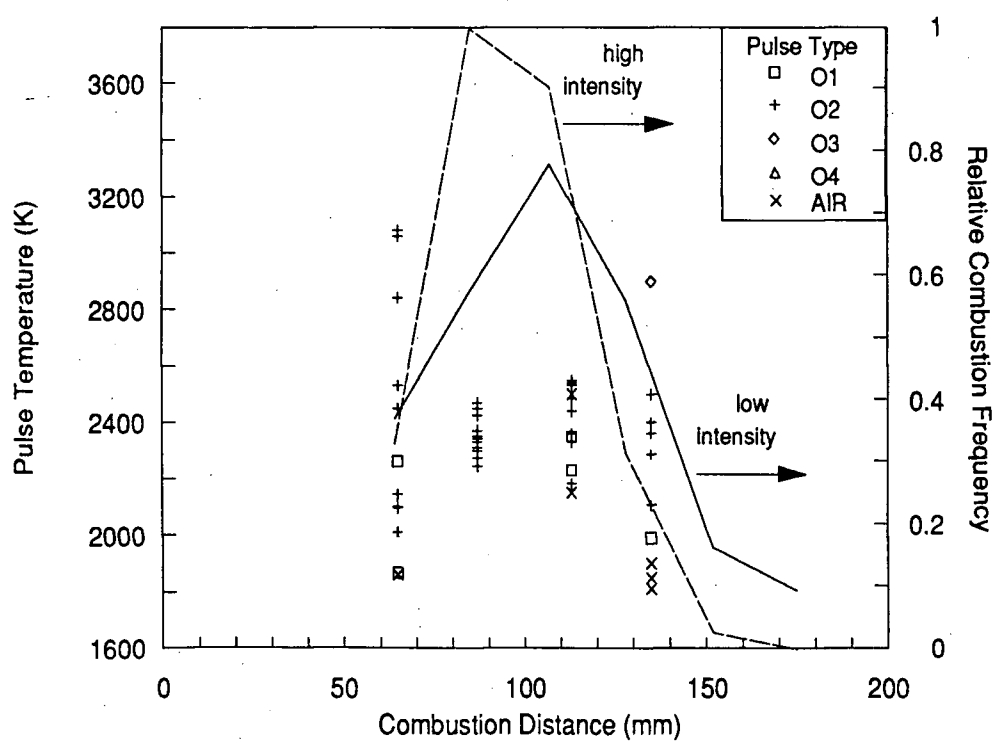


(b)cooling rate

Figure 6.60 Heating and cooling rates of the O₂ combustion pulses recorded during the combustion of the commercial concentrates in oxygen at $T_{\text{FURNACE}}=1130\text{K}$ (plotted vs an arbitrary data number).



(a)



(b)

Figure 6.61 Combustion of a)63-74 μ m and b)105-125 μ m Brunswick concentrates in oxygen at $T_{\text{FURNACE}}=1130\text{K}$ - pulse type, temperature and relative frequency as a function of furnace combustion distance.

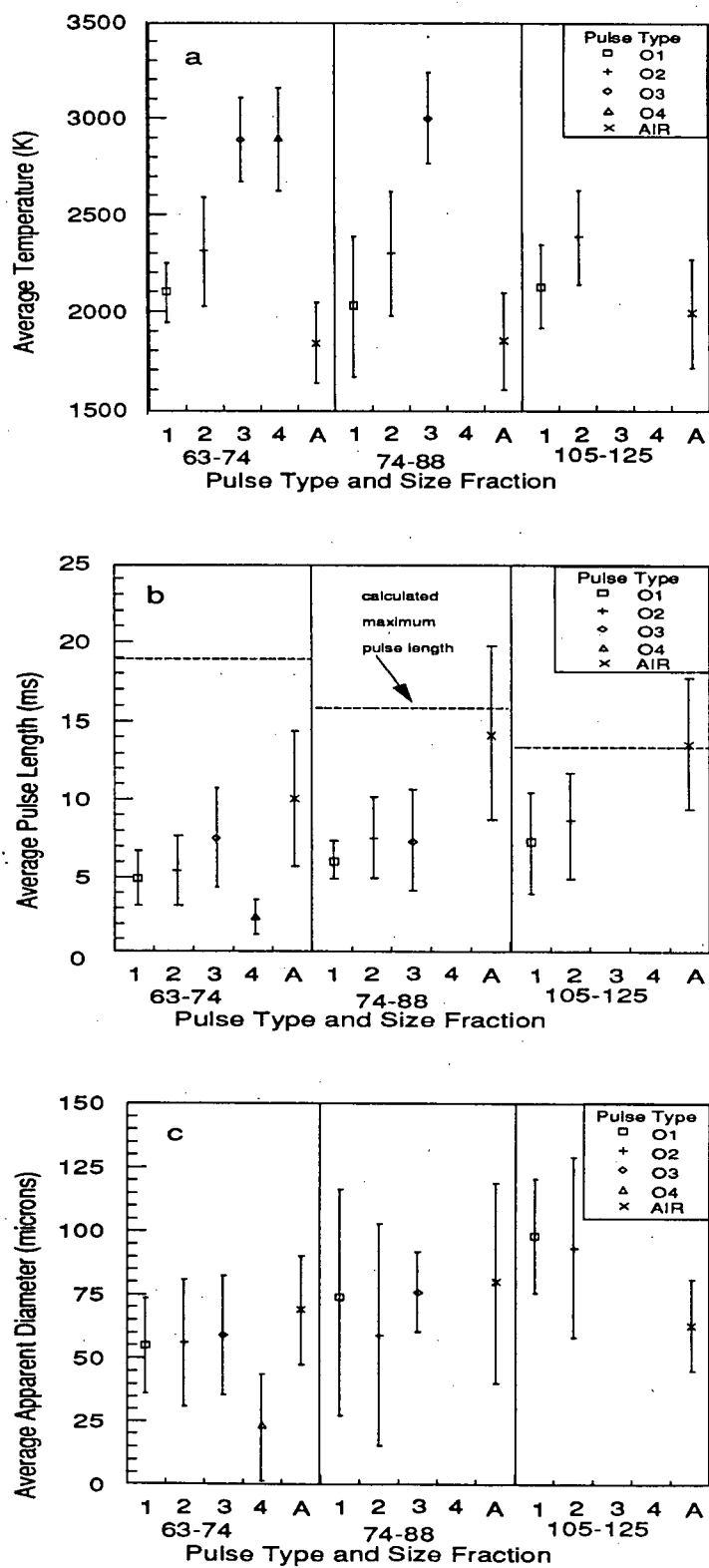


Figure 6.62 Pulse type averaged combustion pulse data as a function of feed size for Brunswick concentrate combustion in oxygen, a) pulse temperatures, b) pulse lengths and c) apparent diameters. ($T_{\text{FURNACE}}=1130\text{K}$).

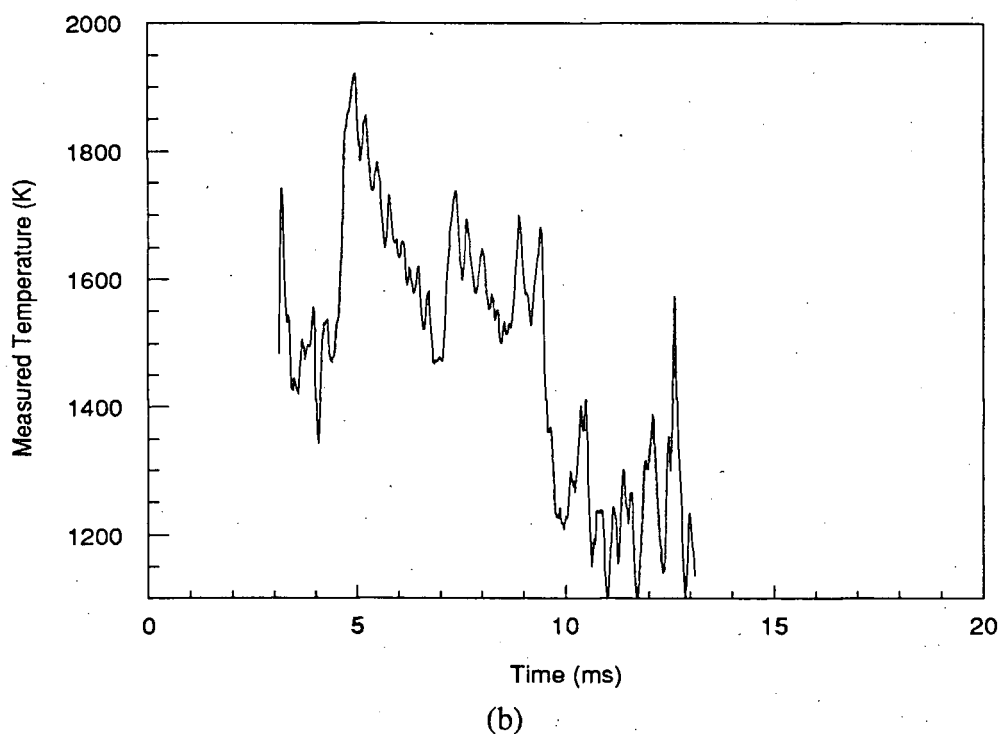
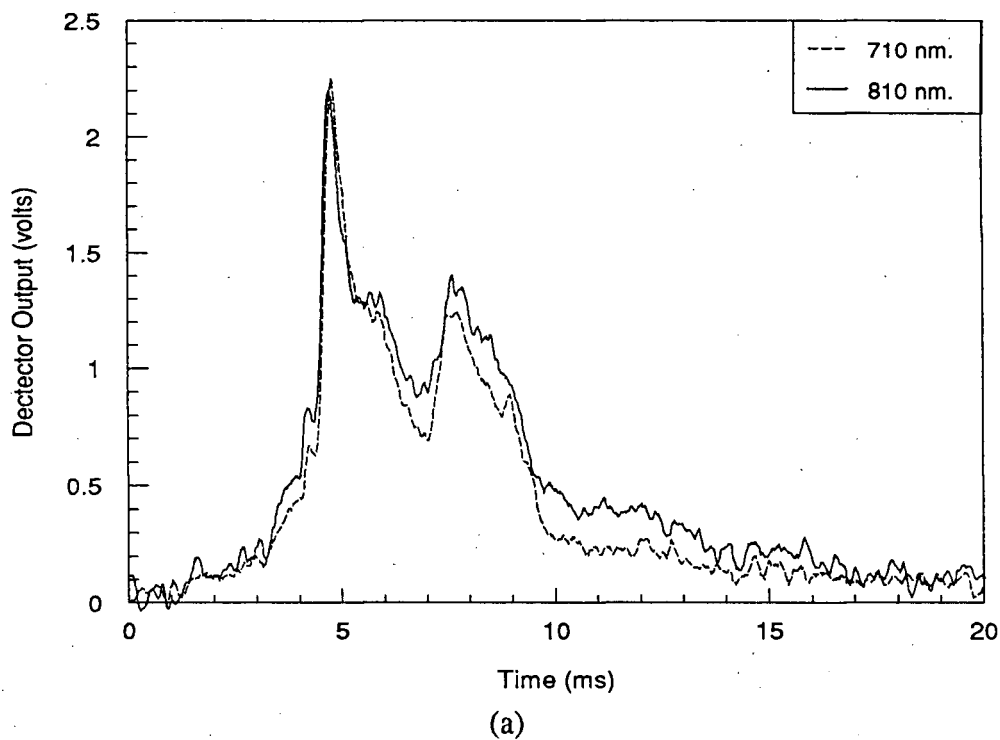
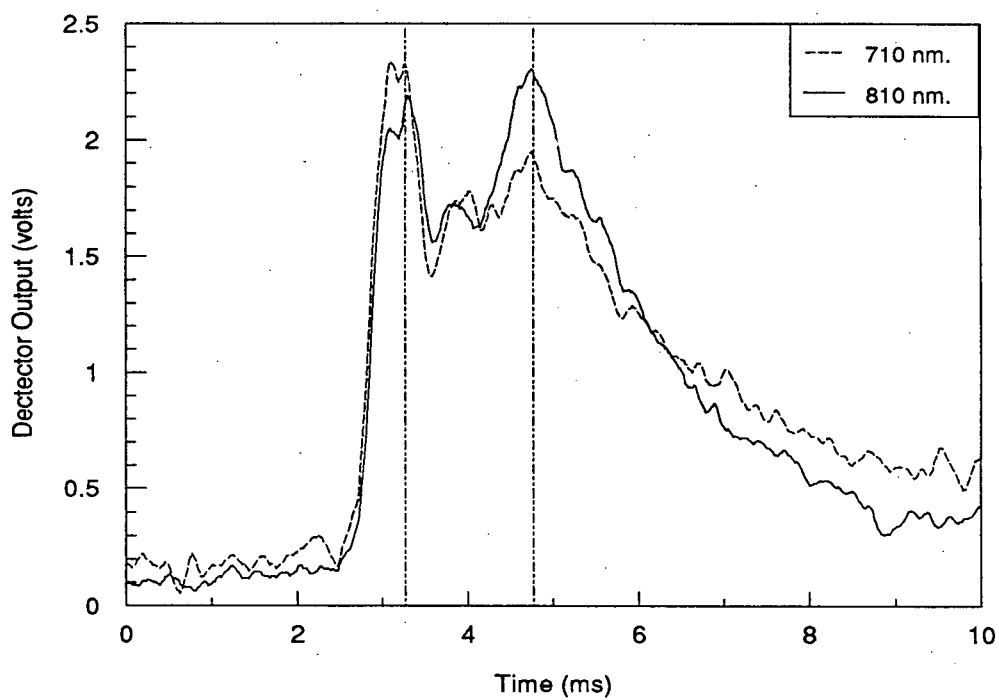
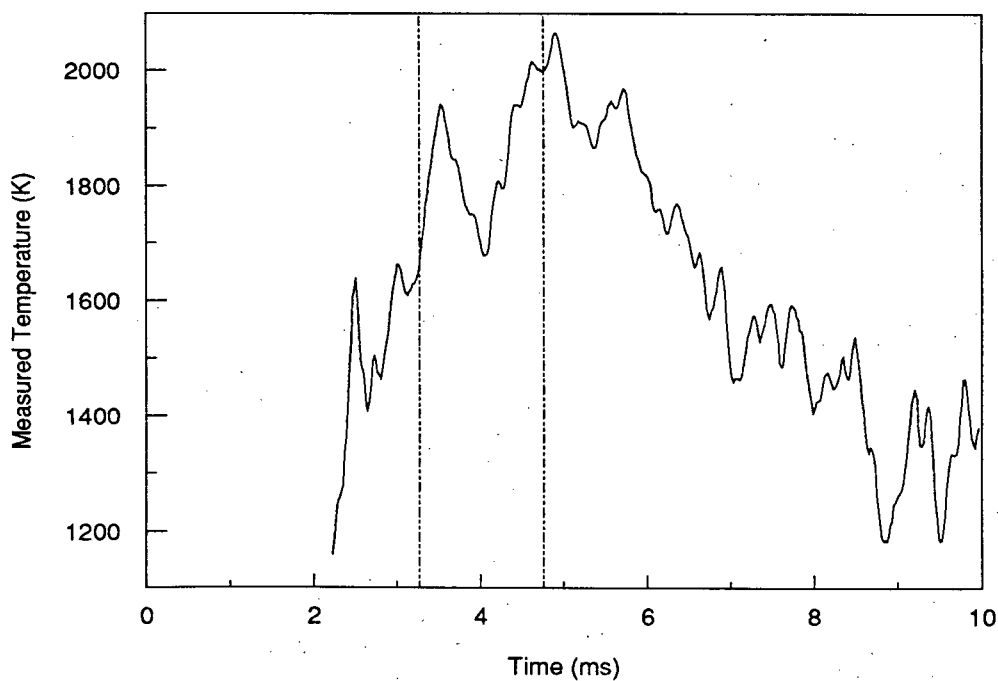


Figure 6.63 A/OIT combustion pulse recorded during the combustion of 74-88 μm galena in 40% oxygen,
 a) pyrometer output and b) measured temperature.
 ($T_{\text{FURNACE}}=1130\text{K}$, $C_{\text{VAL}}=1.42$, data#=G520.dat).



(a)



(b)

Figure 6.64 A/O1T combustion pulse recorded during the combustion of 74-88 μm galena in 50% oxygen, a)pyrometer output and b)measured temperature. ($T_{\text{FURNACE}}=1130\text{K}$, $C_{\text{VAL}}=1.42$, data#=G535.dat).

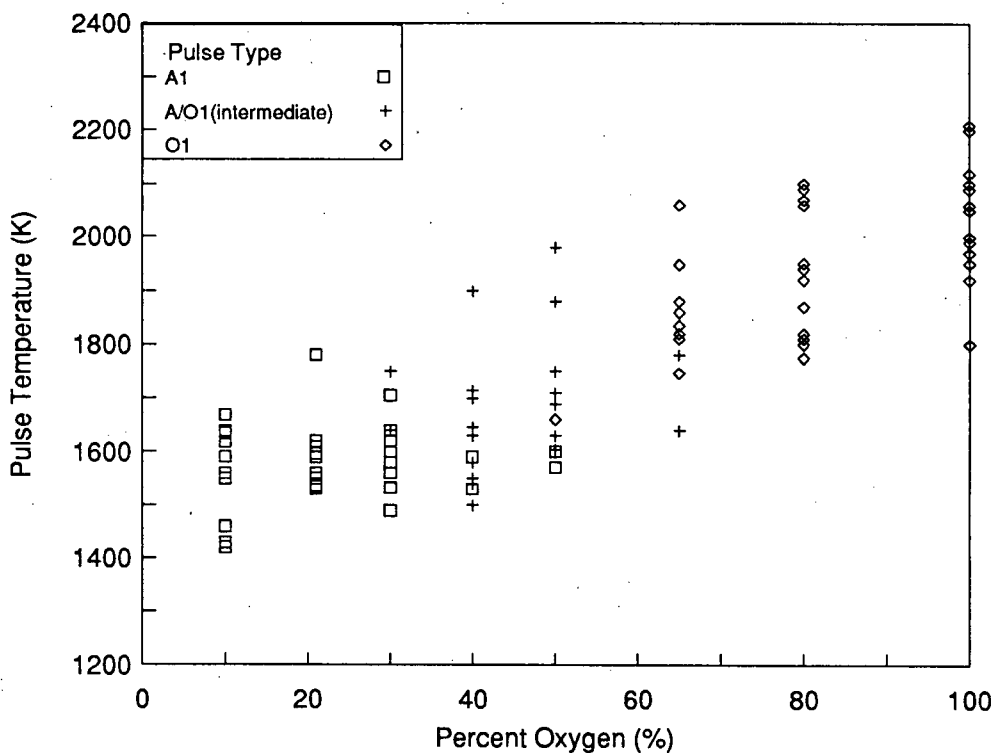


Figure 6.65 The effect of oxygen concentration on the combustion of 74-88 μ m galena at $T_{\text{FURNACE}}=1130\text{K}$ - combustion pulse type and temperature.

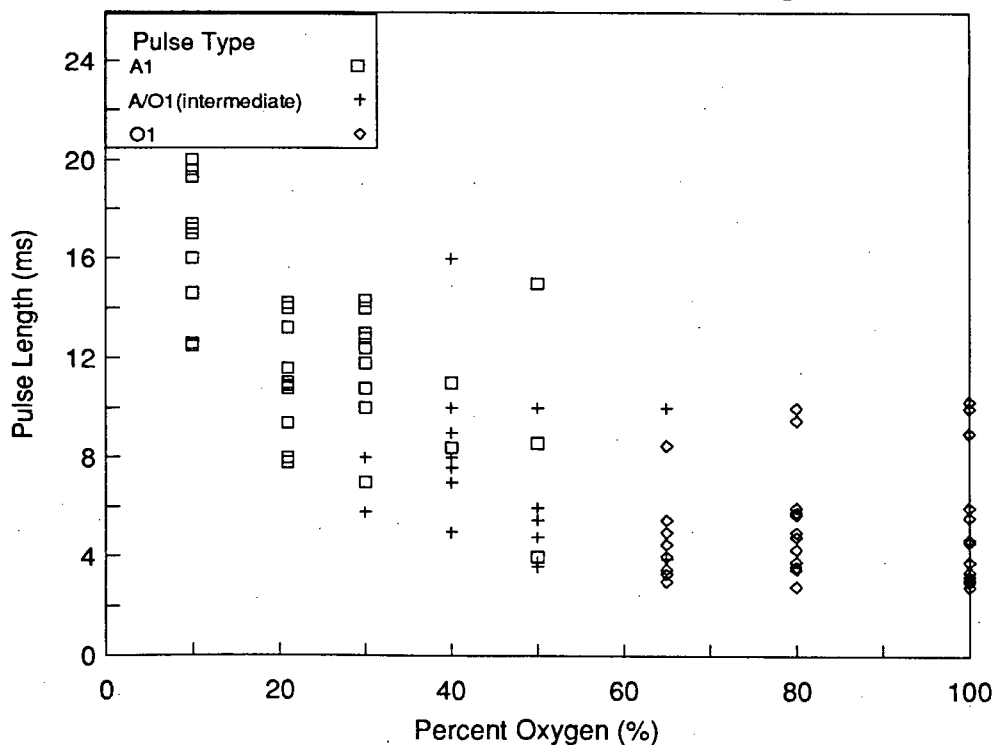


Figure 6.66 The effect of oxygen concentration on the combustion of 74-88 μ m galena at $T_{\text{FURNACE}}=1130\text{K}$ - combustion pulse length.

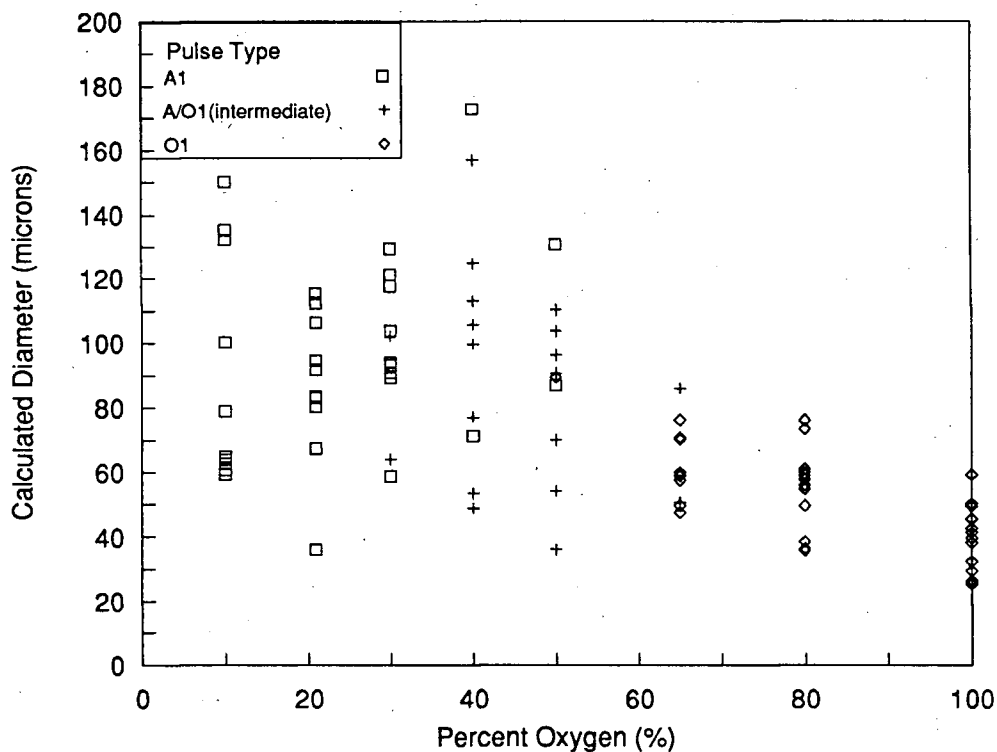


Figure 6.67a The effect of oxygen concentration on the combustion of 74-88 μ m galena at $T_{\text{FURNACE}}=1130\text{K}$ - calculated apparent particle diameter.

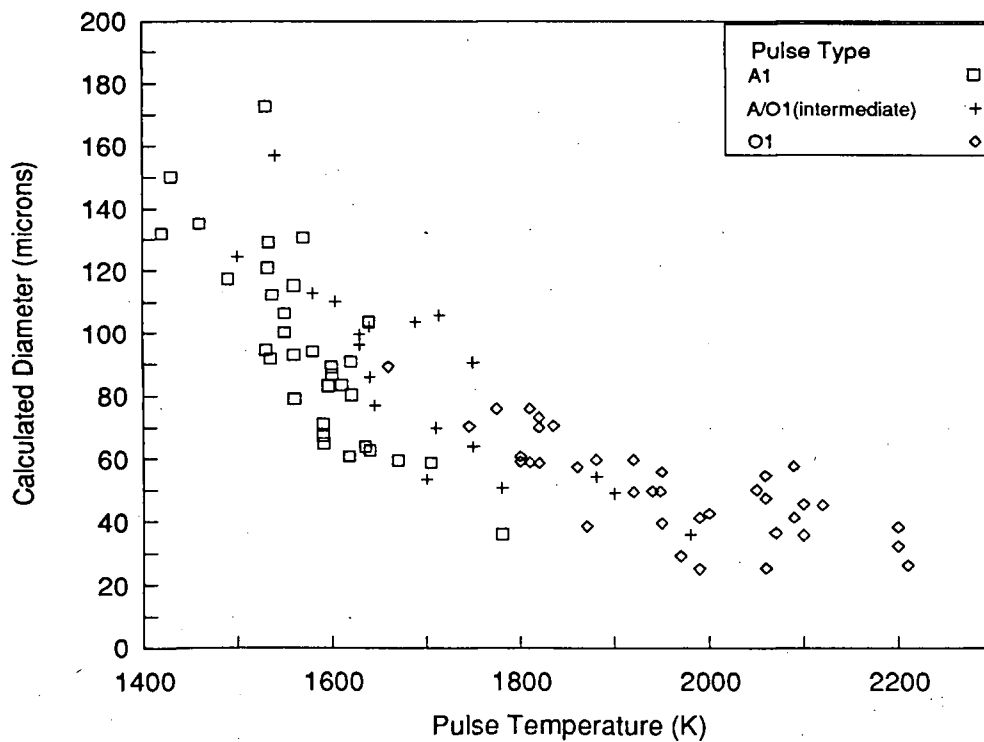
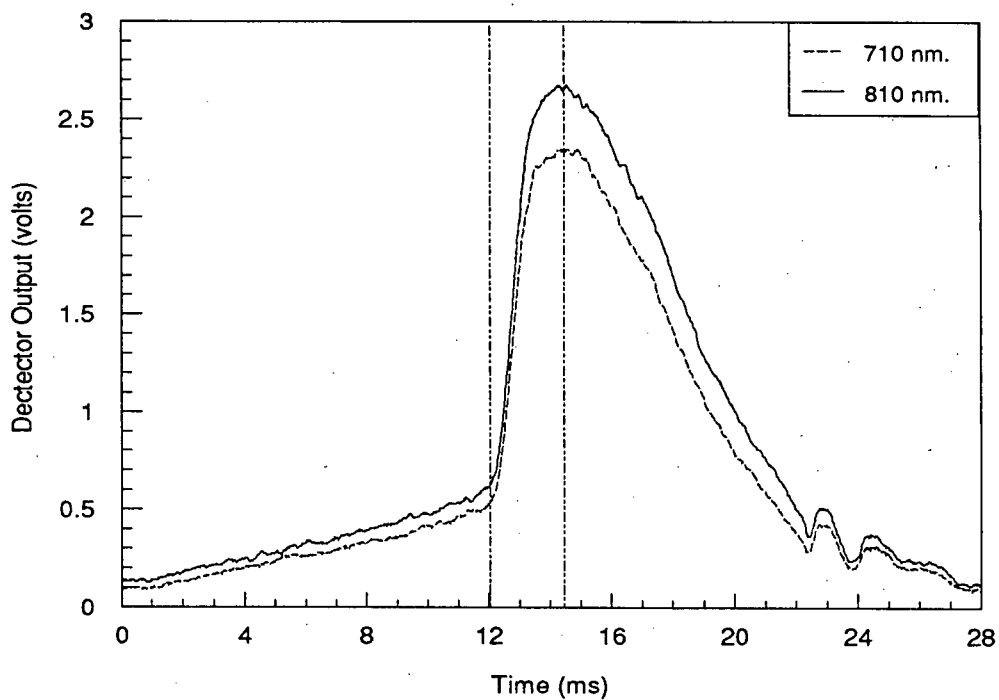
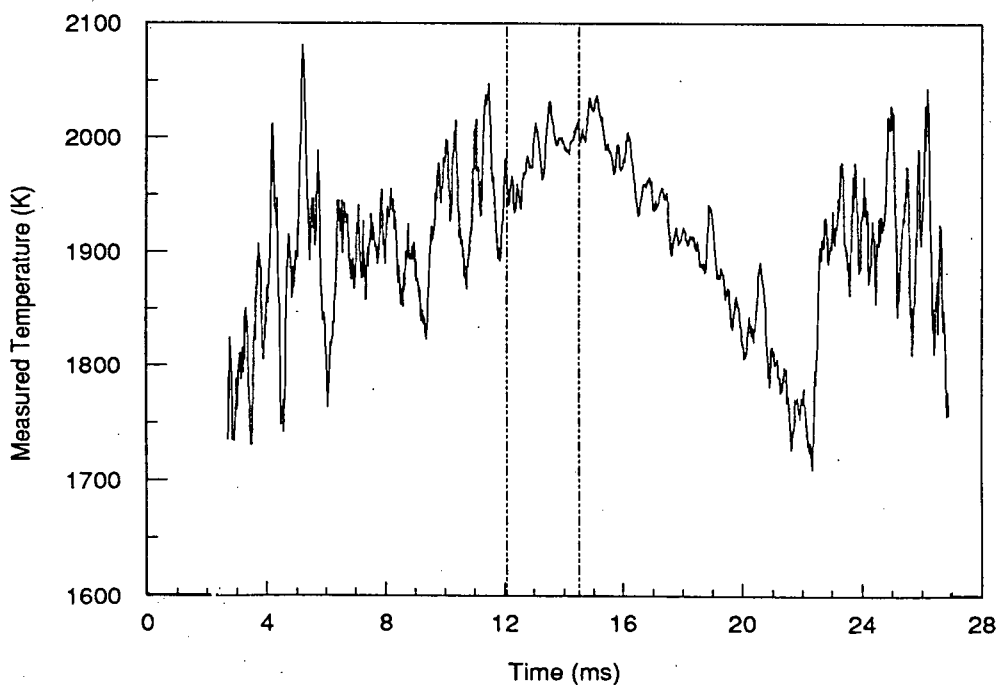


Figure 6.67b The effect of oxygen concentration on the combustion of 74-88 μ m galena at $T_{\text{FURNACE}}=1130\text{K}$ - calculated apparent particle diameter vs particle temperature.



(a)



(b)

Figure 6.68 A3 combustion pulse recorded during the combustion of 74-88 μ m pyrite in 10% oxygen, a) pyrometer detector output and b) measured temperature. ($T_{\text{FURNACE}}=1130\text{K}$, $C_{\text{VAL}}=1.12$, data#-PY267.dat).

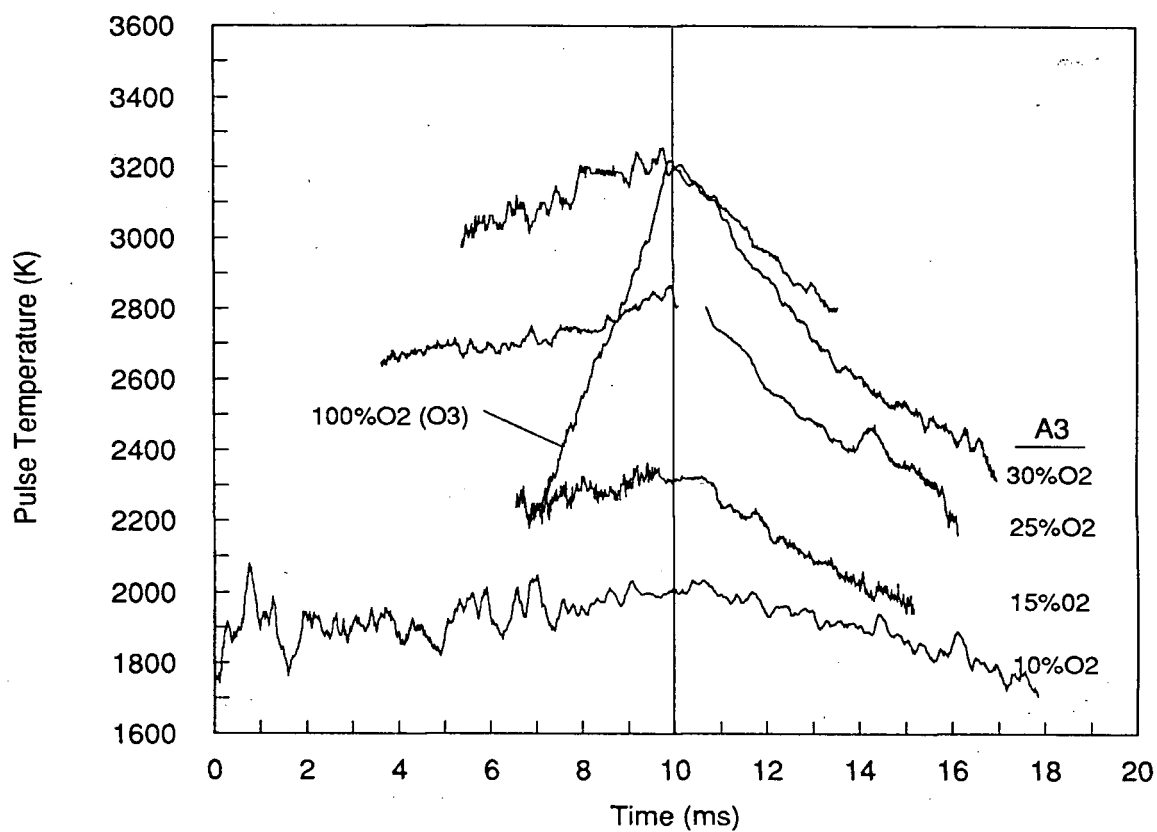


Figure 6.69 Temperatures of A1 and O1 combustion pulse recorded during the combustion of 74-88 μ m pyrite at various oxygen concentrations at $T_{\text{FURNACE}}=1130\text{K}$.

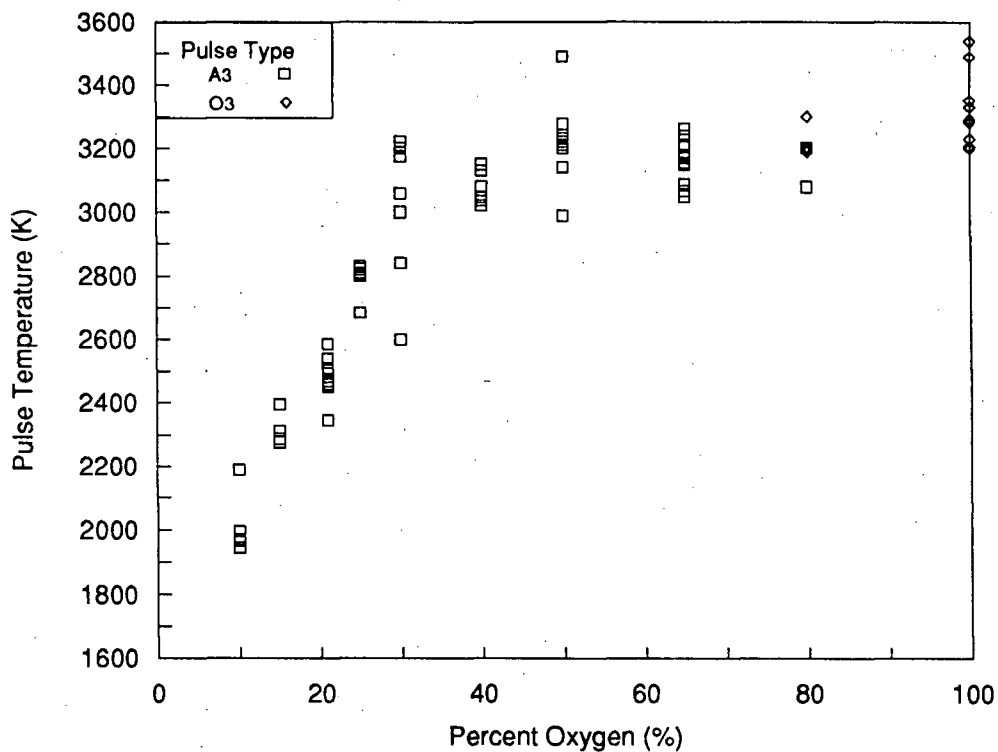


Figure 6.70a The effect of oxygen concentration on the combustion of 74-88 μ m pyrite at $T_{\text{FURNACE}}=1130\text{K}$ - combustion pulse type and temperature.

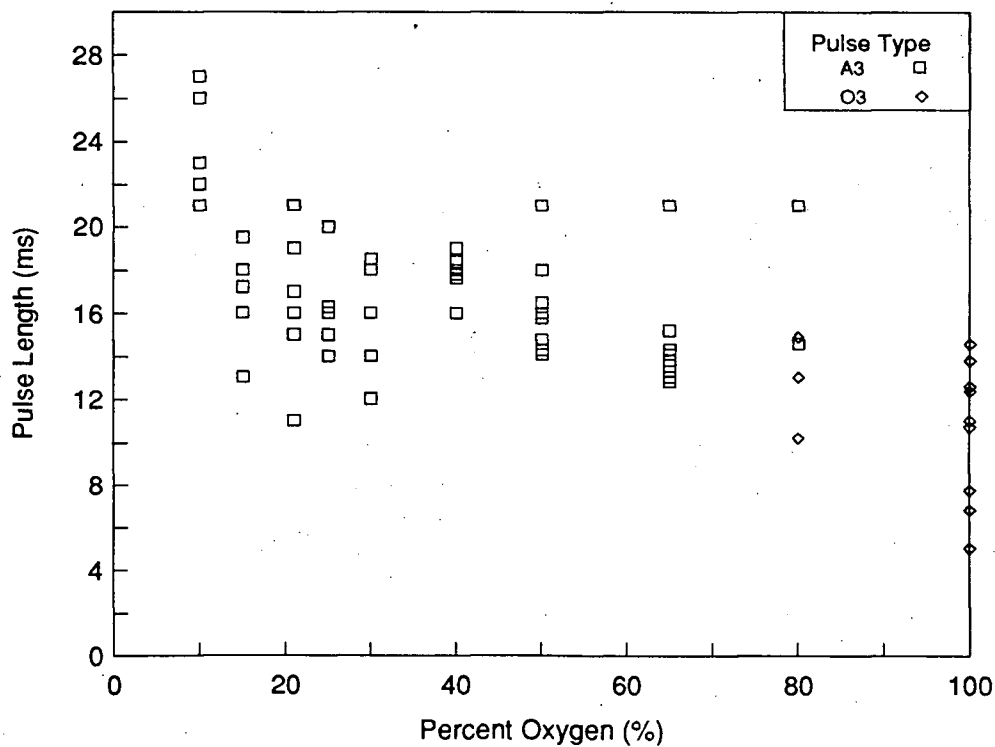


Figure 6.70b The effect of oxygen concentration on the combustion of 74-88 μ m pyrite at $T_{\text{FURNACE}}=1130\text{K}$ - combustion pulse length.

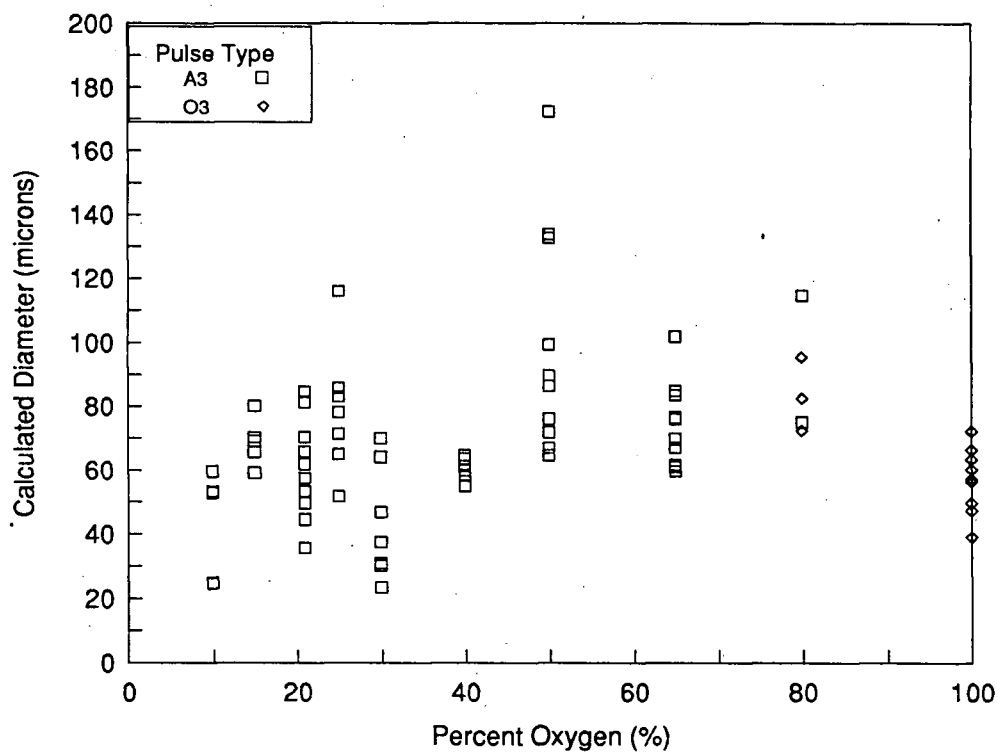


Figure 6.71a The effect of oxygen concentration on the combustion of 74-88 μ m pyrite at $T_{\text{FURNACE}}=1130\text{K}$ - calculated apparent particle diameter.

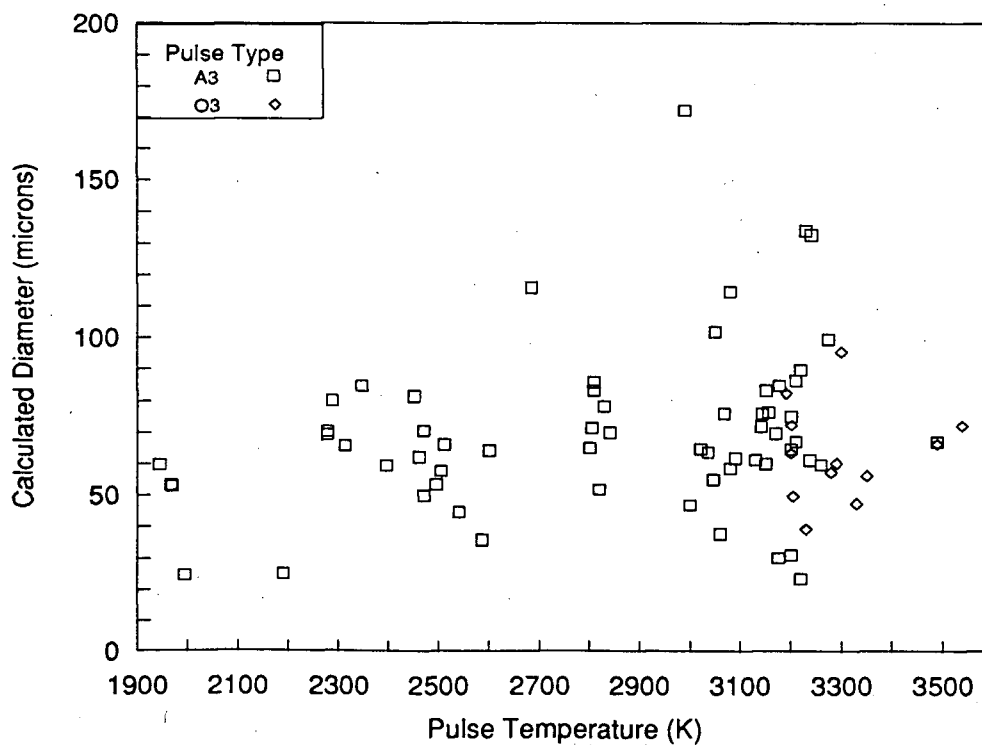


Figure 6.71b The effect of oxygen concentration on the combustion of 74-88 μ m pyrite at $T_{\text{FURNACE}}=1130\text{K}$ - calculated apparent particle diameter vs particle temperature.

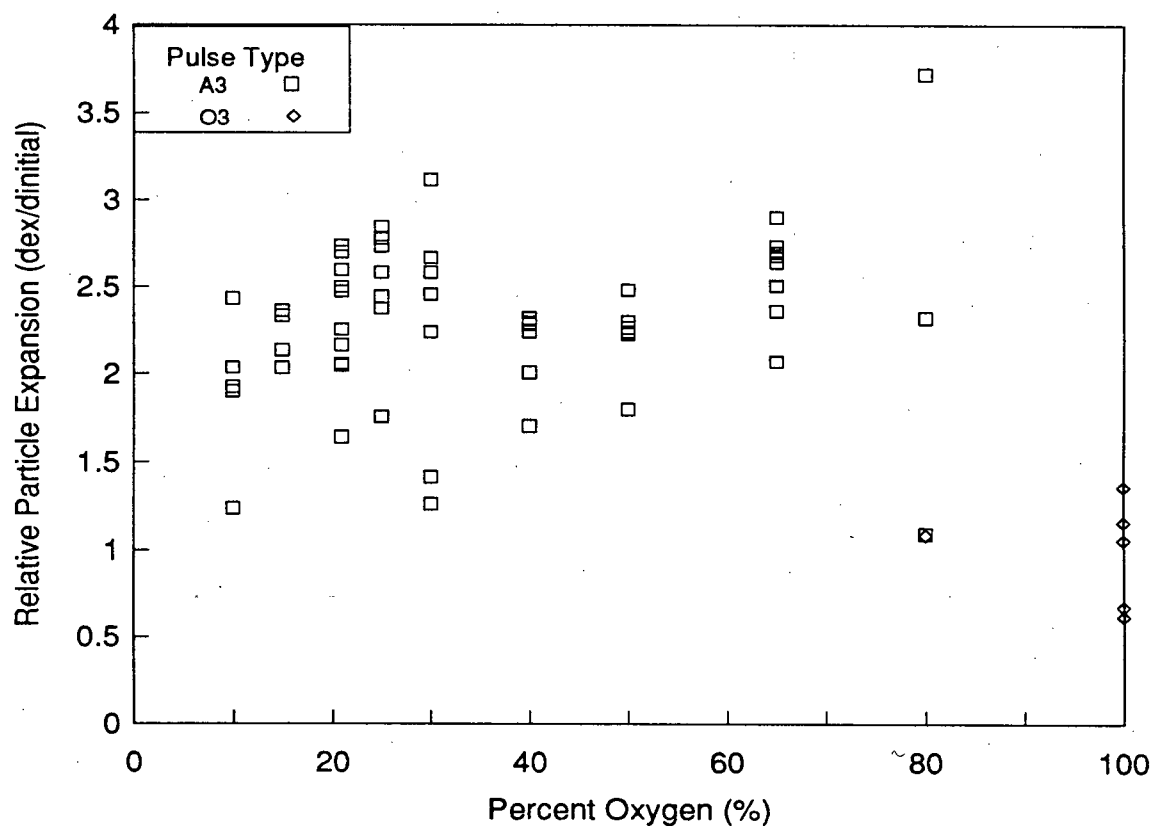
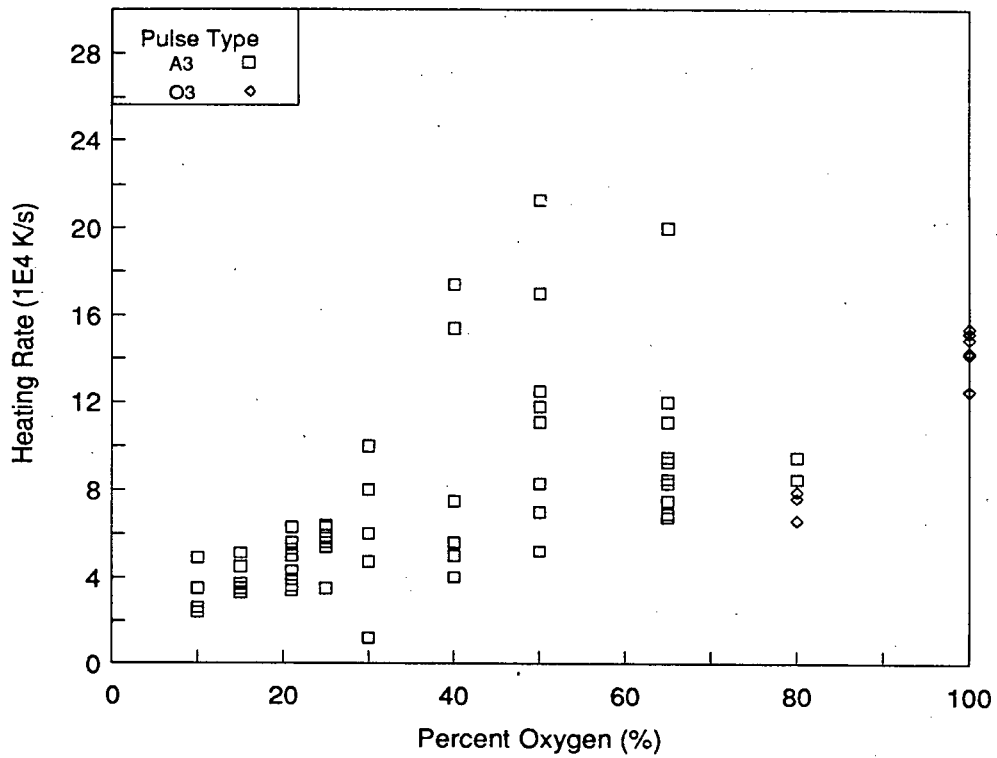
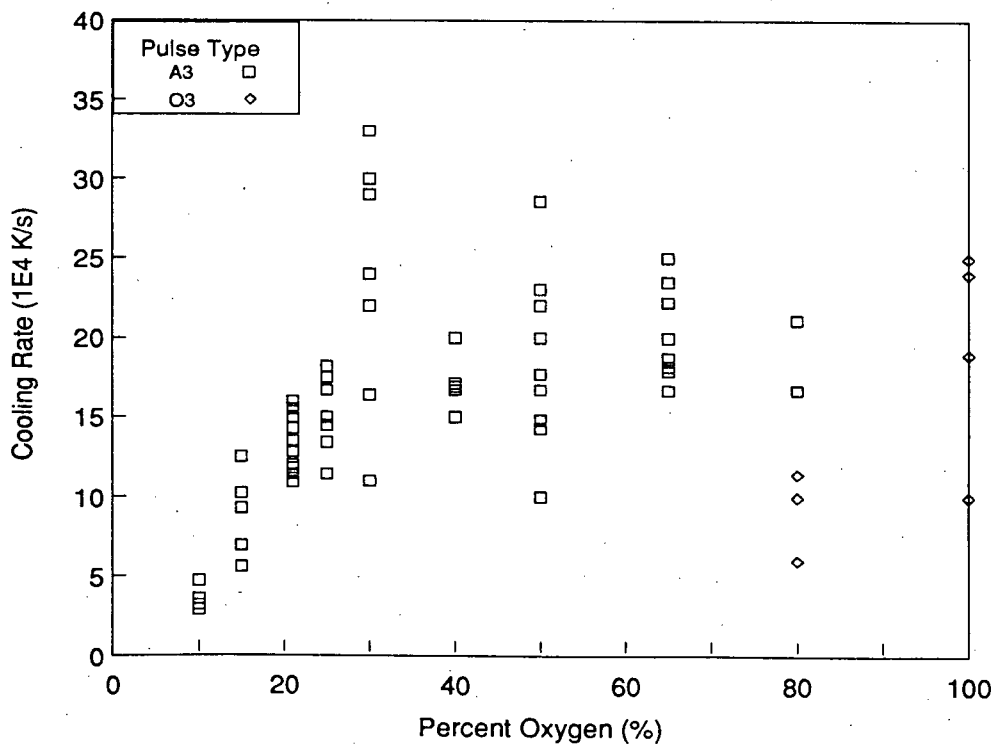


Figure 6.72 The effect of oxygen concentration on the combustion of 74-88 μm pyrite at $T_{\text{FURNACE}}=1130\text{K}$ - calculated apparent particle expansion.

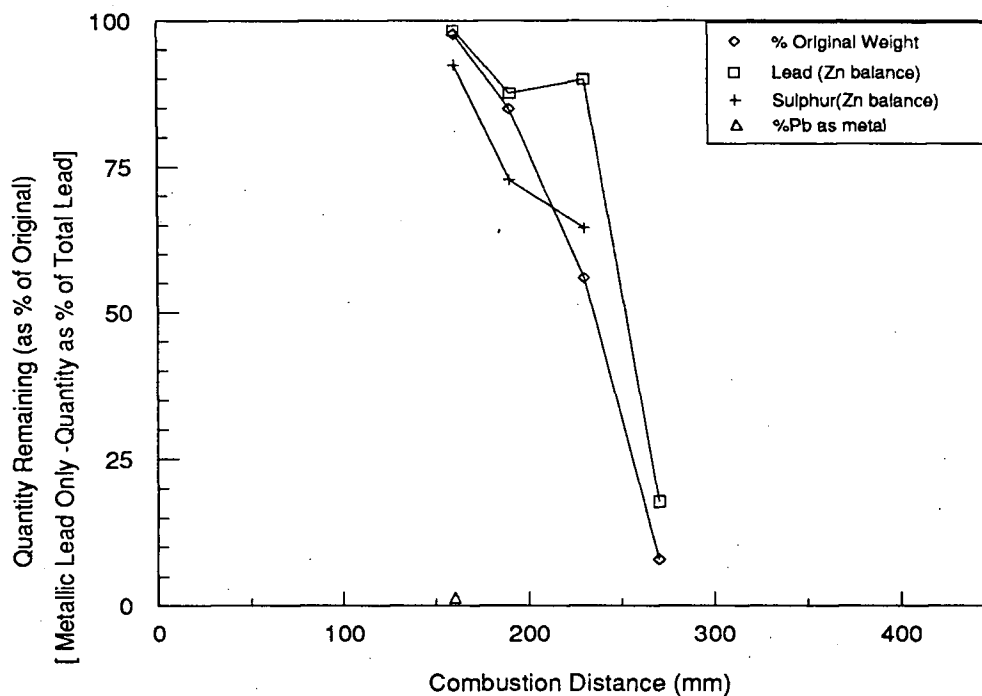


(a) heating rates

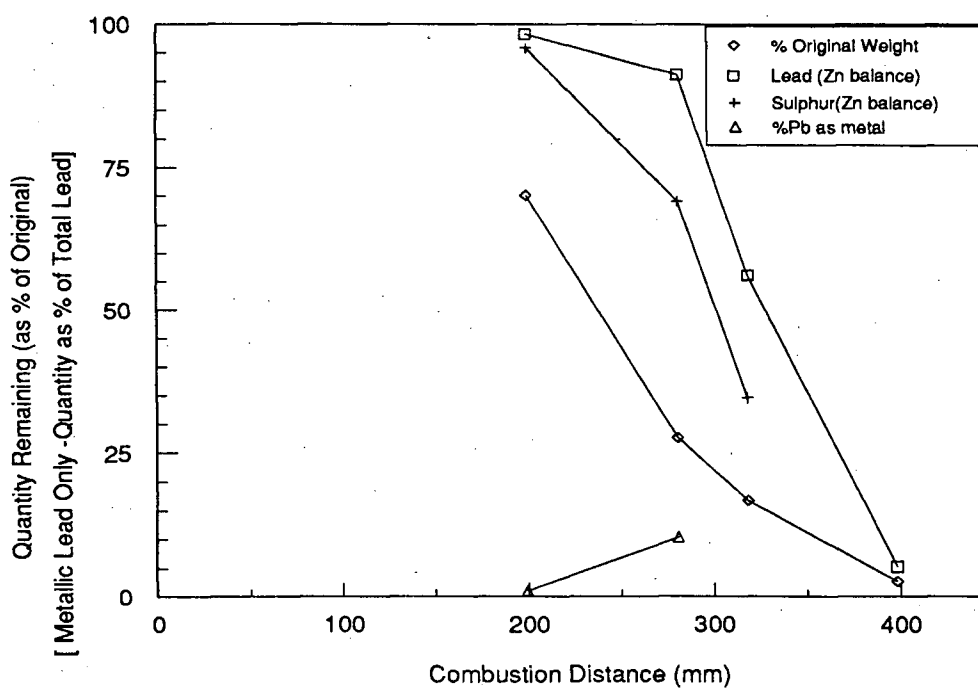


(b) cooling rate

Figure 6.73 The effect of oxygen concentration on the combustion of 74-88 μ m pyrite at $T_{\text{FURNACE}}=1130\text{K}$ on the heating and cooling rates.

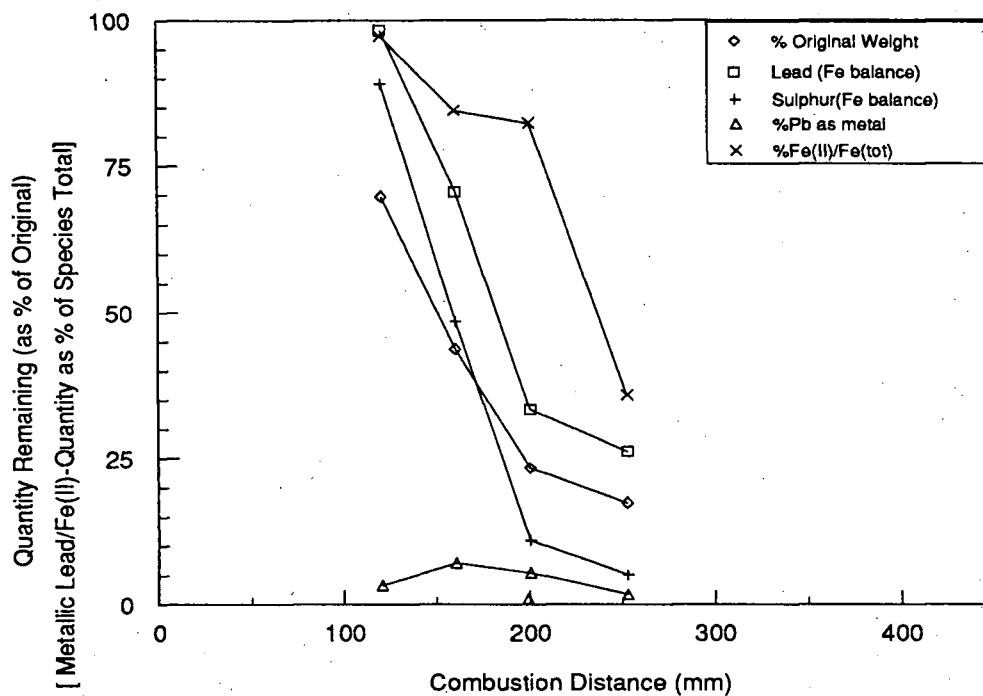


(a)

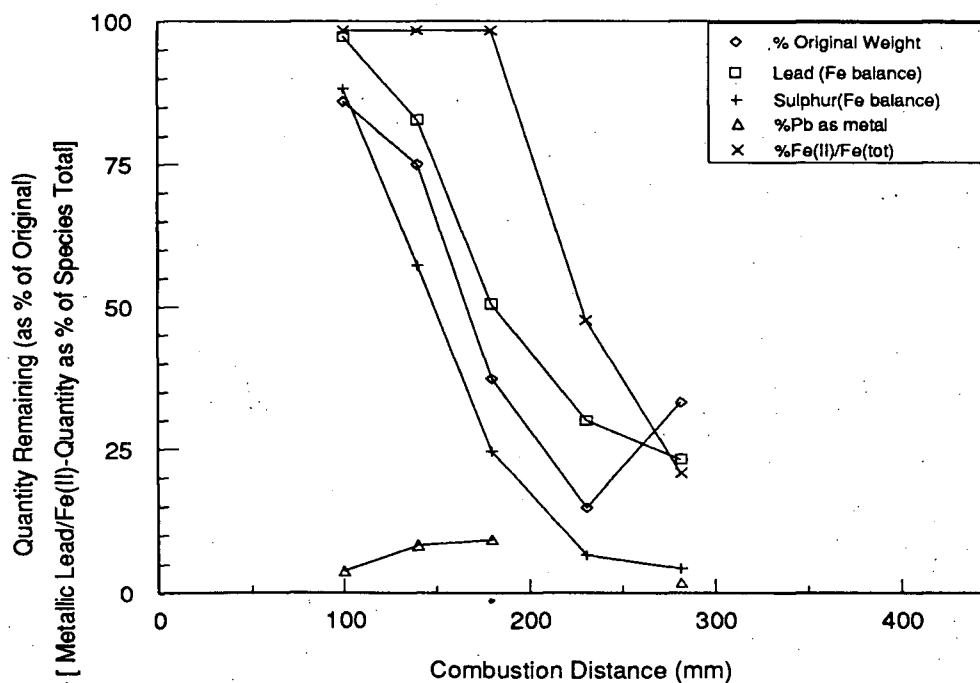


(b)

Figure 6.74 Chemical analyses of the reaction products of galena combustion in air at $T_{\text{FURNACE}}=1130\text{K}$, a) 74-88 μm and b) 105-125 μm screen fractions. Sulphur, lead and product weight as percentage of original, metallic lead as percent of total lead.

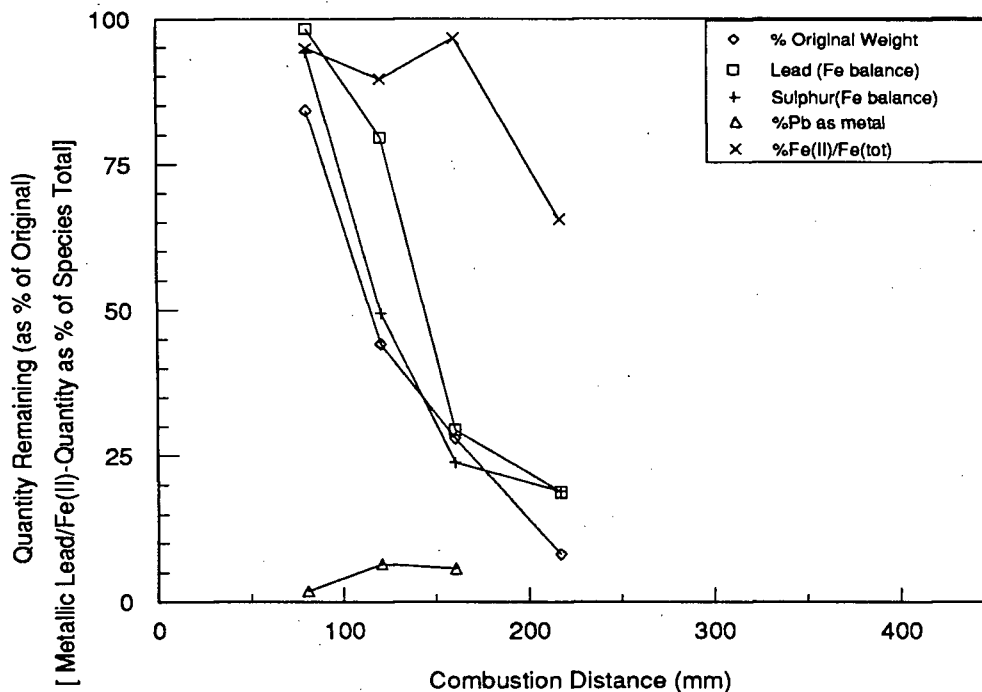


(a)

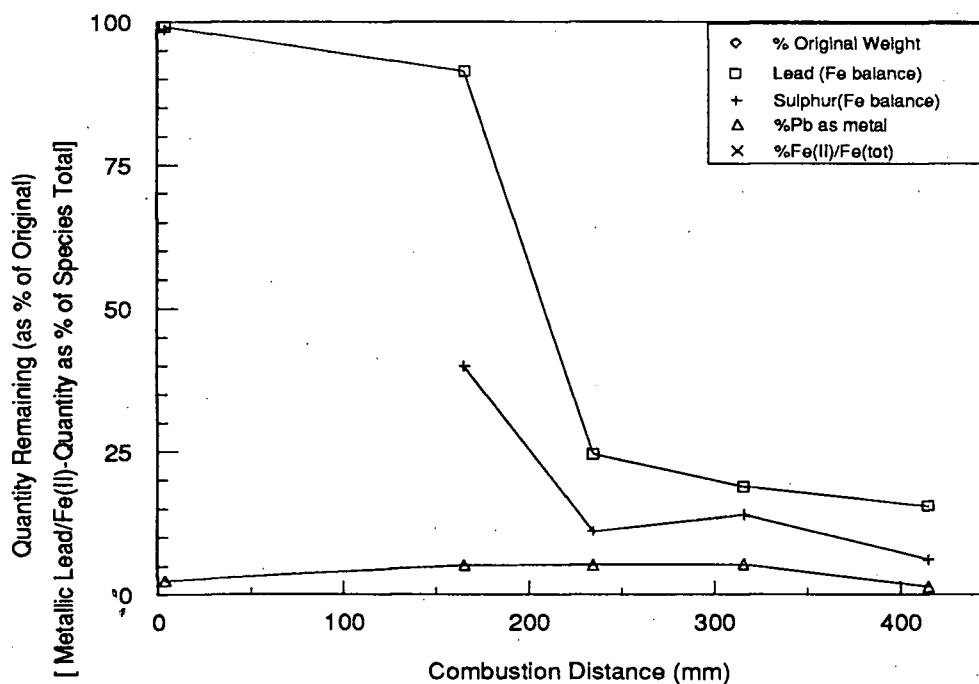


(b)

Figure 6.75 Chemical analyses of the reaction products of Sullivan concentrate combustion in air at $T_{\text{FURNACE}}=1130\text{K}$, a) $74\text{-}88\mu\text{m}$ and b) $105\text{-}125\mu\text{m}$ screen fractions. Sulphur, lead and product weight as percentage of original, Fe(II) and metallic lead as percent of species total.



(a)



(b)

Figure 6.76 Chemical analyses of the reaction products of Brunswick concentrate combustion in air at $T_{\text{FURNACE}}=1130\text{K}$, a) $74-88\mu\text{m}$ and b) $105-125\mu\text{m}$ screen fractions. Sulphur, lead and product weight as percentage of original, Fe(II) and metallic lead as percent of species total.

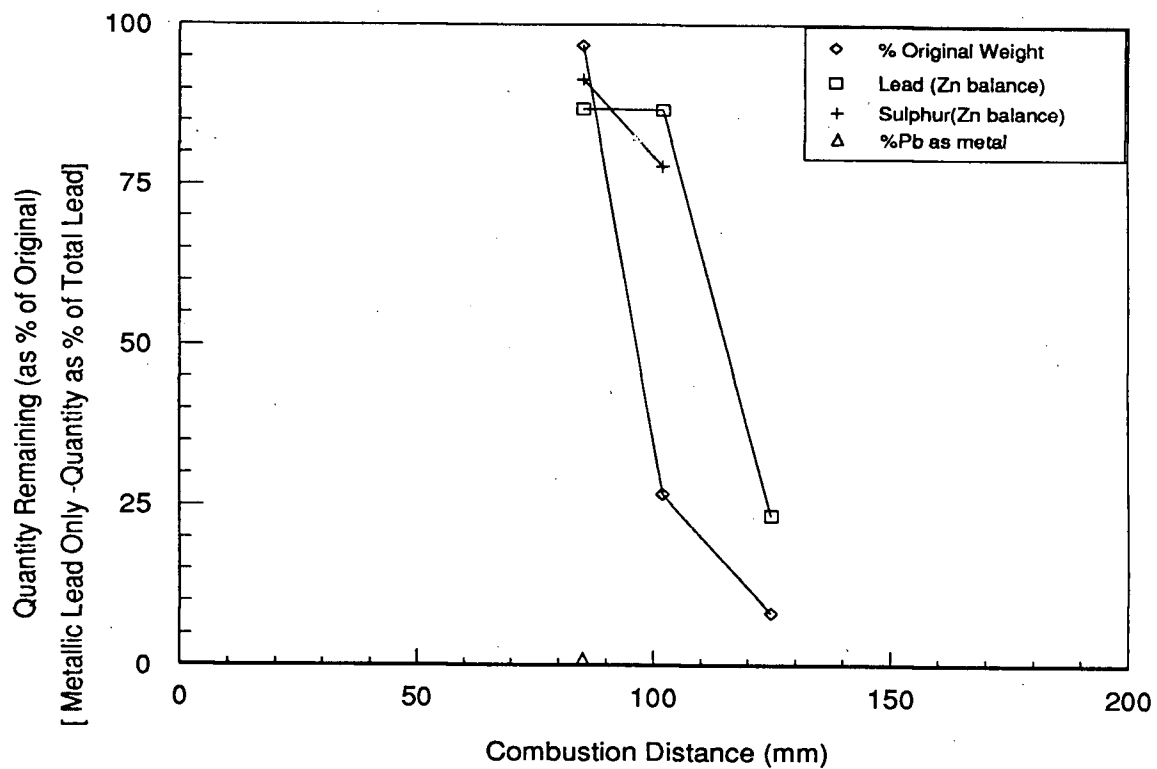
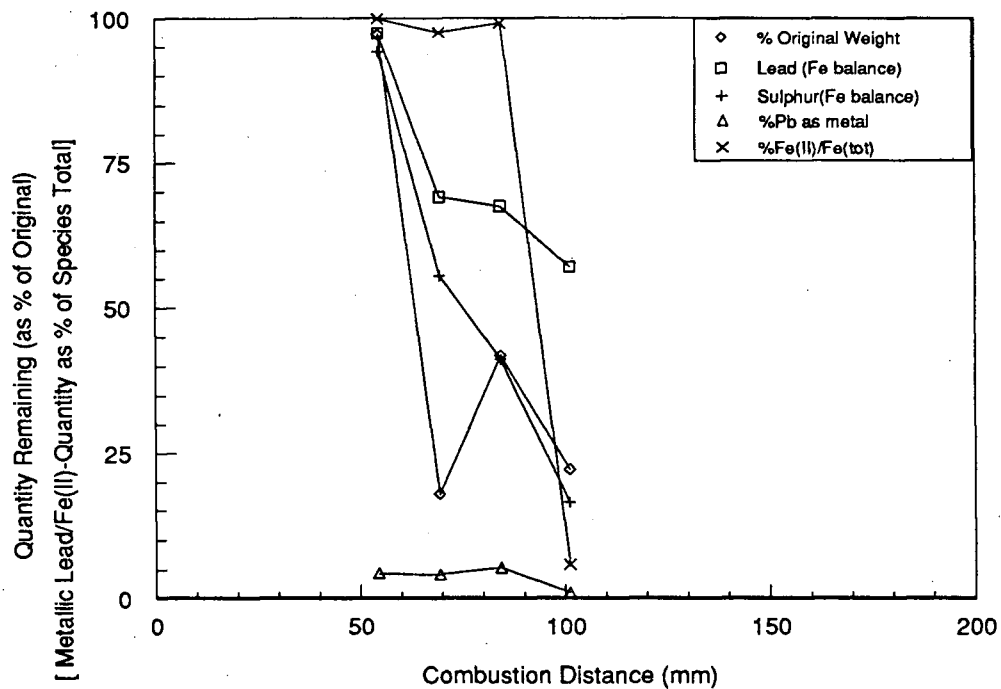
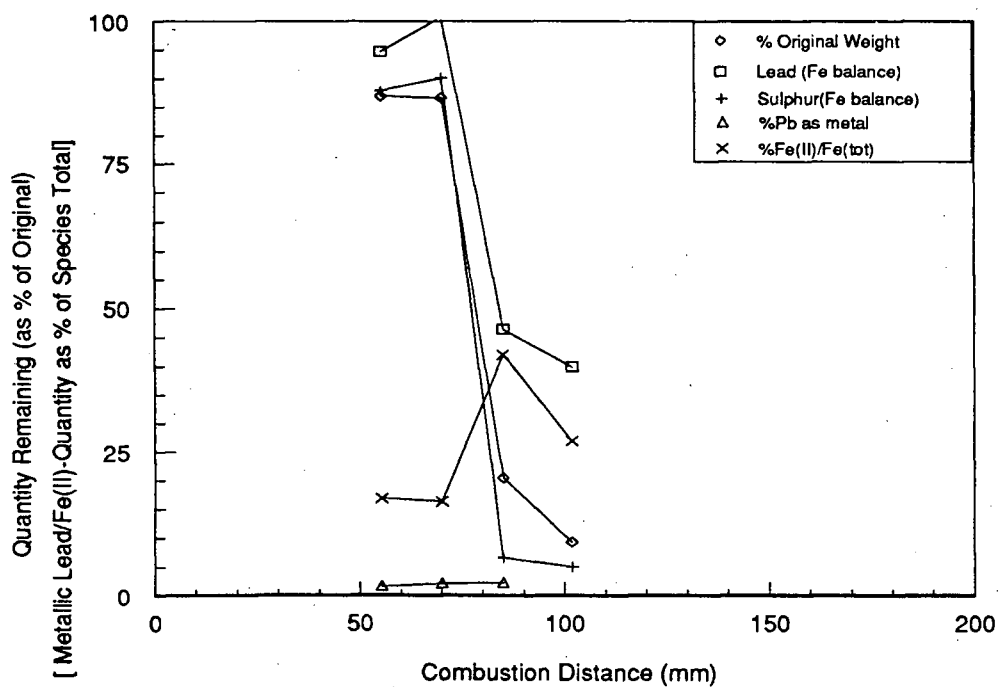


Figure 6.77 Chemical analyses of the reaction products of 63-74 μ m galena combustion in oxygen at $T_{\text{FURNACE}}=1130\text{K}$. Sulphur, lead and product weight as percentage of original, metallic lead as percent of total lead.

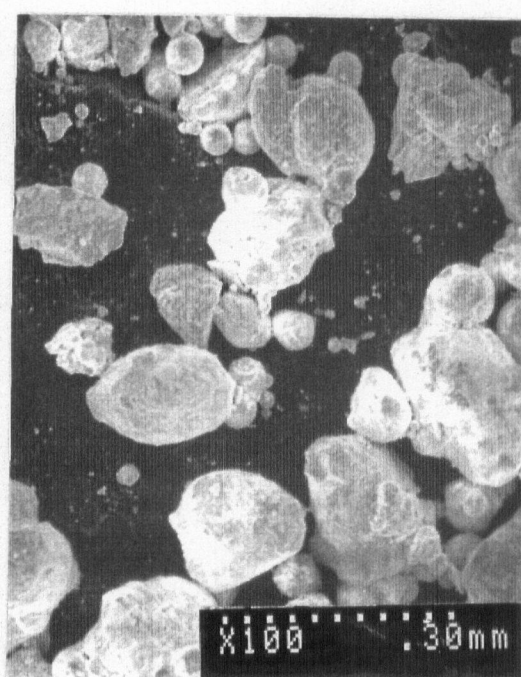


(a)

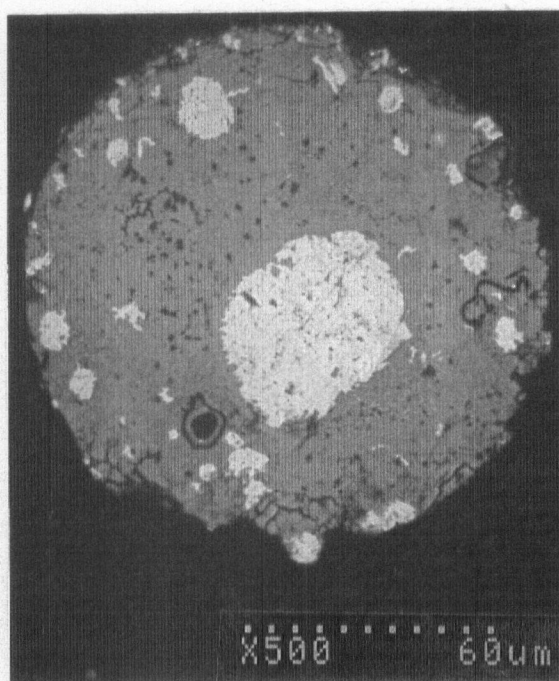


(b)

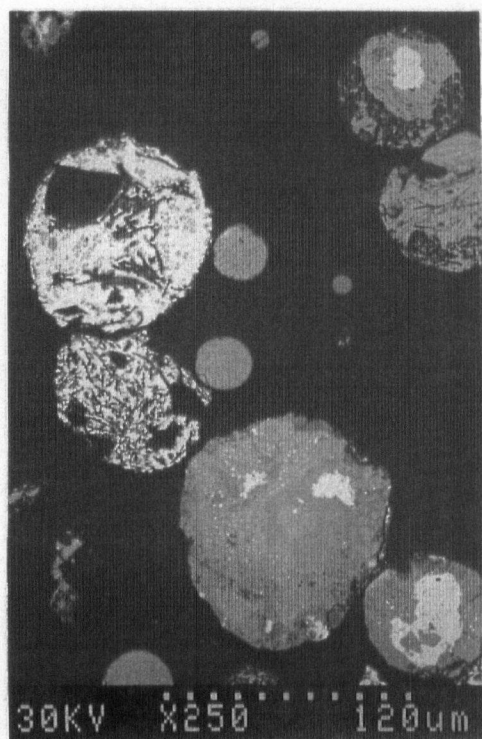
Figure 6.78 Chemical analyses of the reaction products of 74-88 μm screen fractions of a) Sullivan, and b) Brunswick concentrate, combustion in oxygen at $T_{\text{FURNACE}}=1130\text{K}$. Sulphur, lead and product weight as percentage of original, Fe(II) and metallic lead as percent of species total.



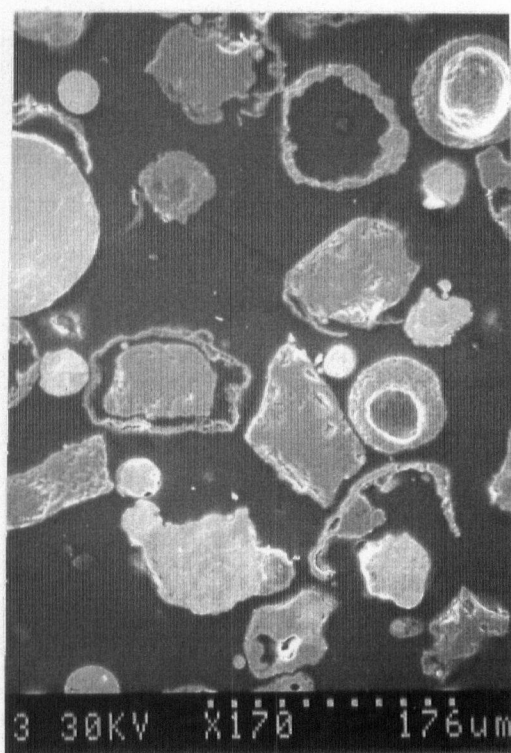
(a)



(b)



(c)



(d)

Figure 6.79

SEM photomicrographs of reaction products of galena combustion in air at $T_{\text{FURNACE}}=1130\text{K}$. a) 74-149 μm screen fraction, b) and c) back-scattered electron image showing sulphur deficient Pb cores (light areas), 74-88 μm , and d) zinc oxide shells, 74-88 μm .

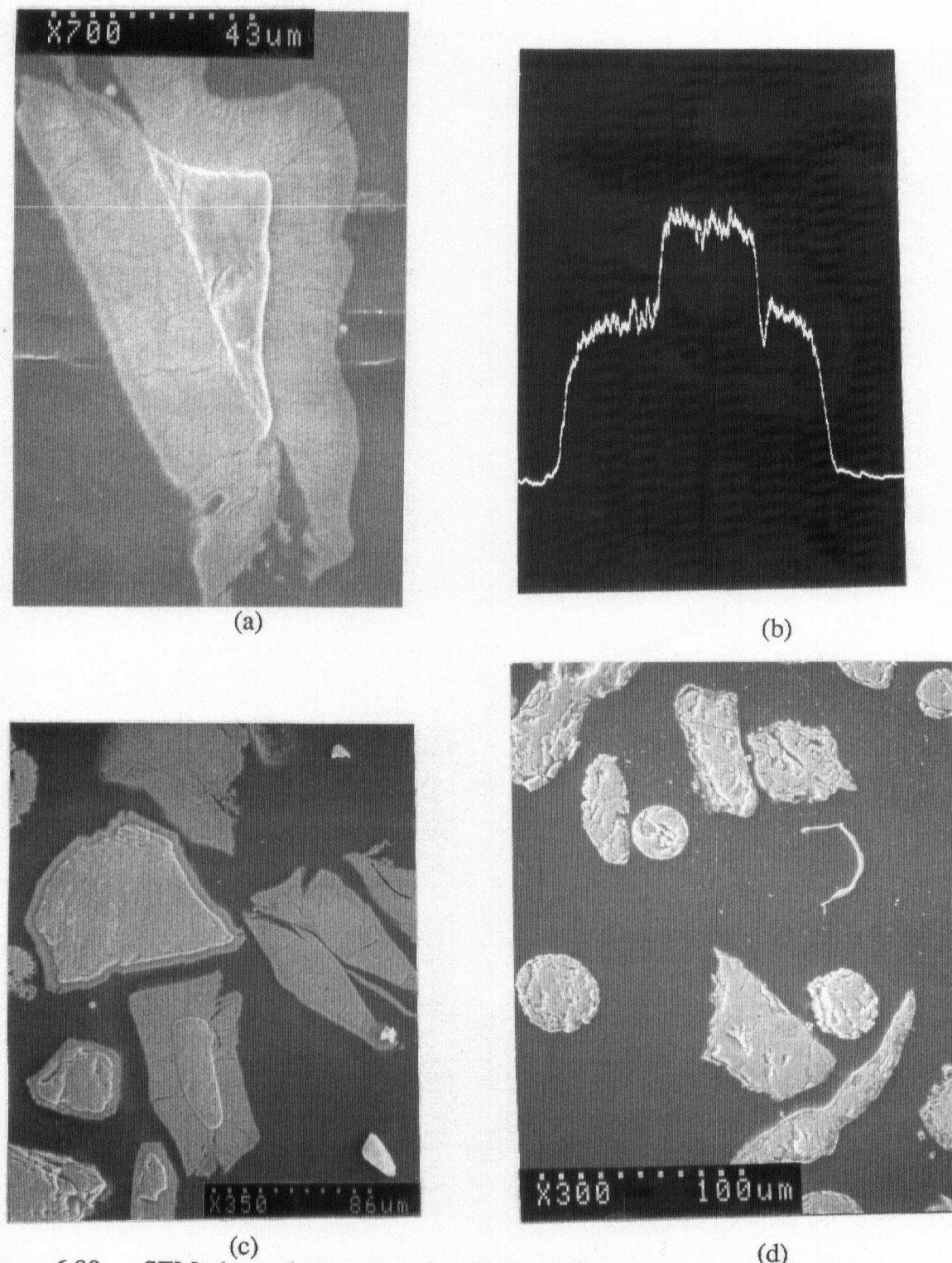
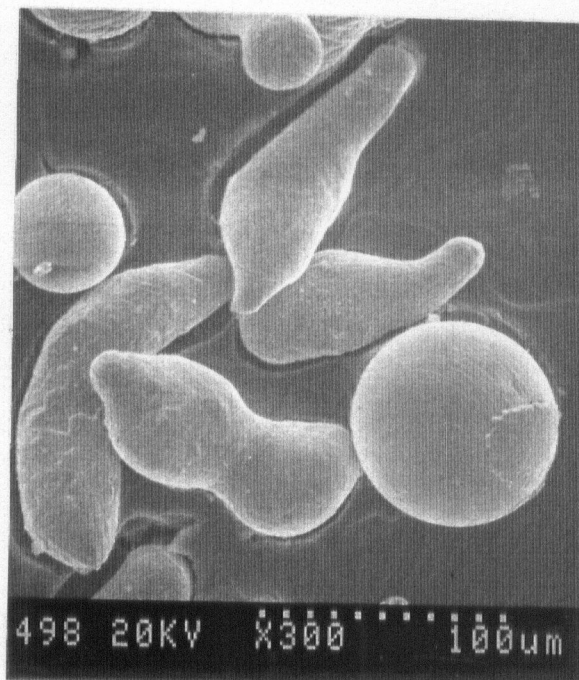
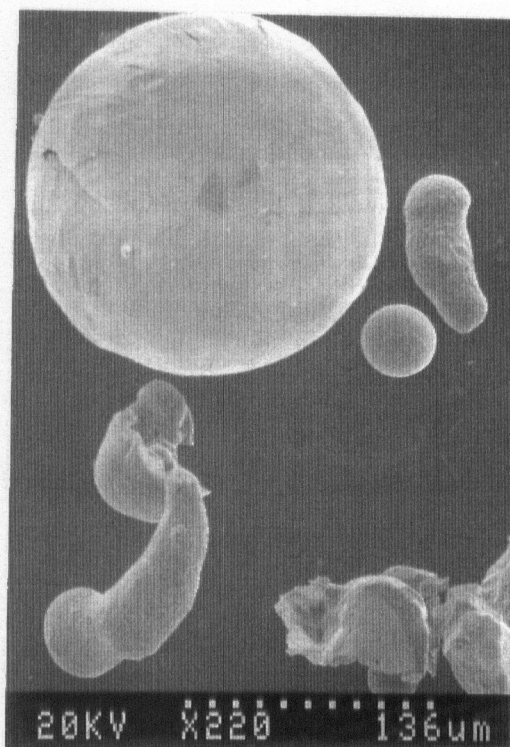


Figure 6.80

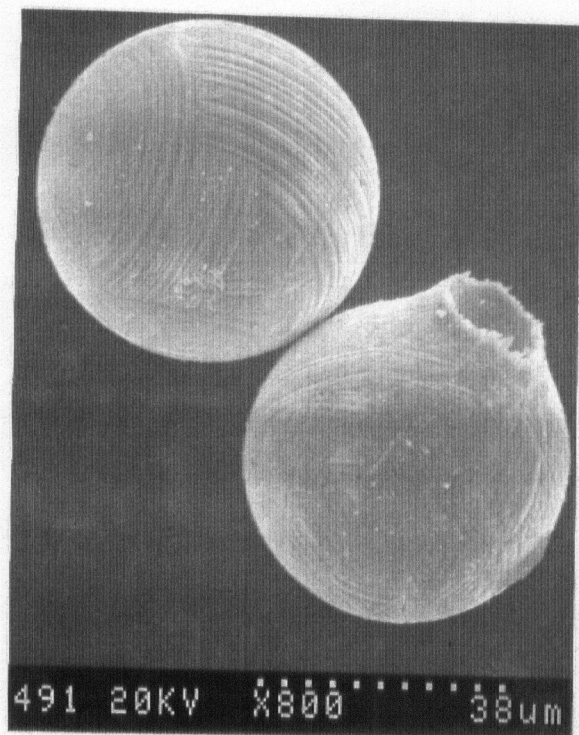
SEM photomicrographs of partially reacted pyrite and pyrrhotite grains prior to melting (74-88 μm , air, $T_{\text{FURNACE}}=1130\text{K}$). a) porous pyrrhotite surrounding pyrite core, b) Relative sulphur concentration across particle in a), c) partially thermally decomposed pyrite grains, and d) pyrrhotite grains.



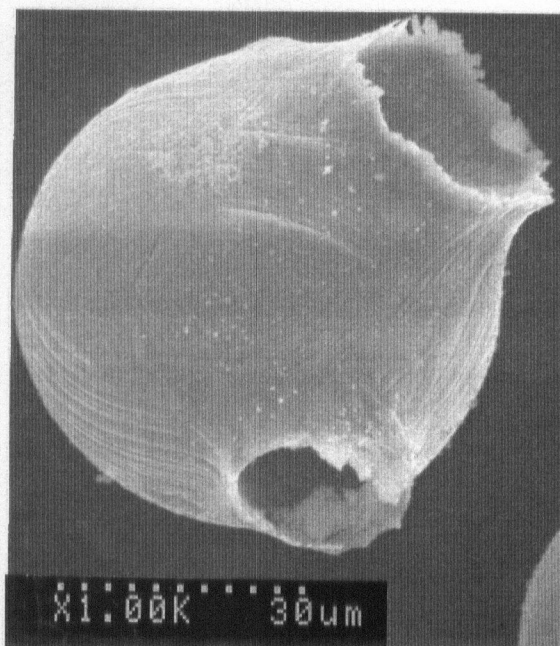
(a)



(b)

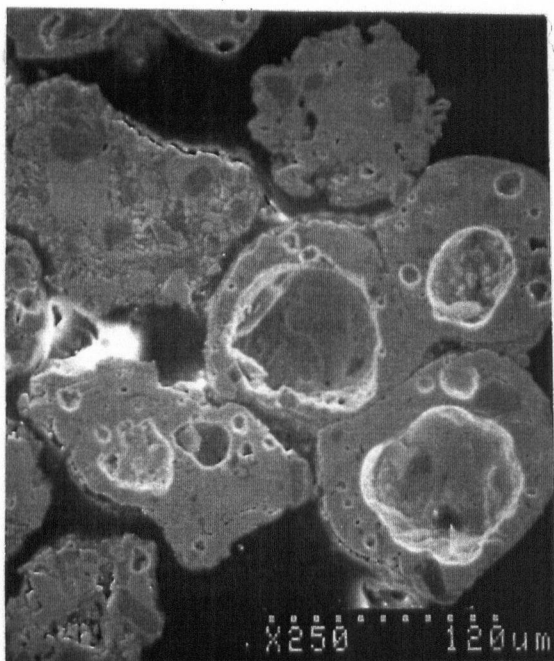


(c)

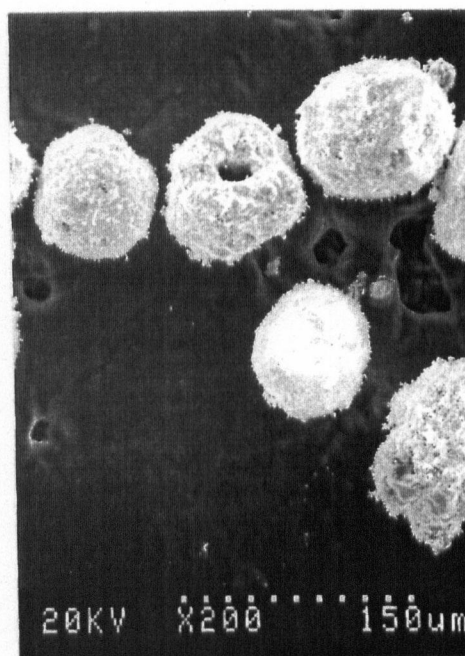


(d)

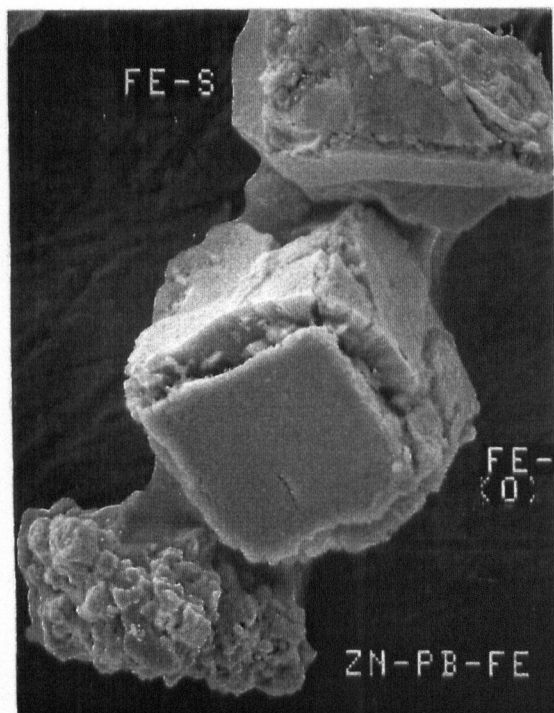
Figure 6.81 SEM photomicrographs of iron oxide reaction products of 74-88 μ m screen fraction pyrite and pyrrhotite combustion in air at $T_{\text{FURNACE}}=1130\text{K}$.



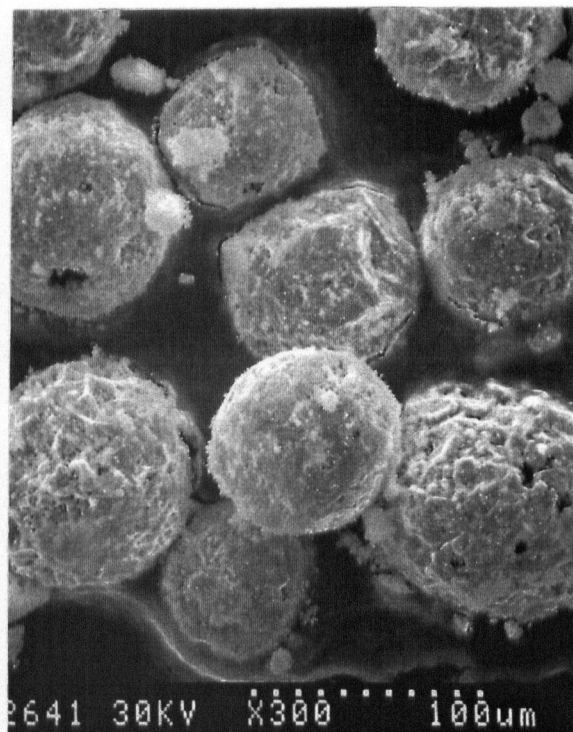
(a)



(b)

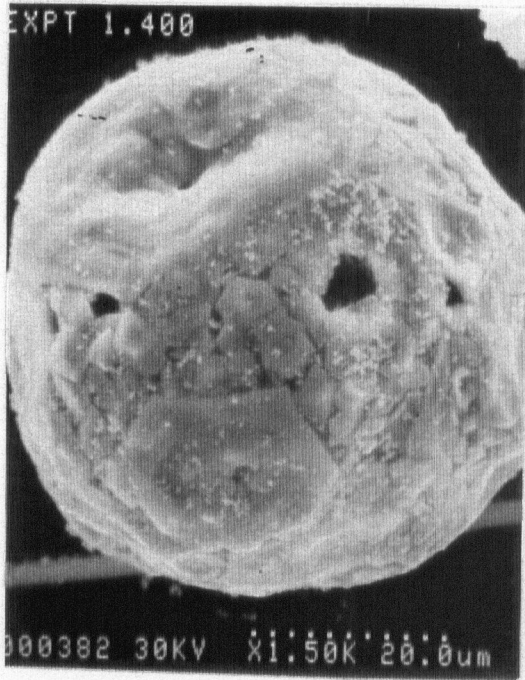


(c)

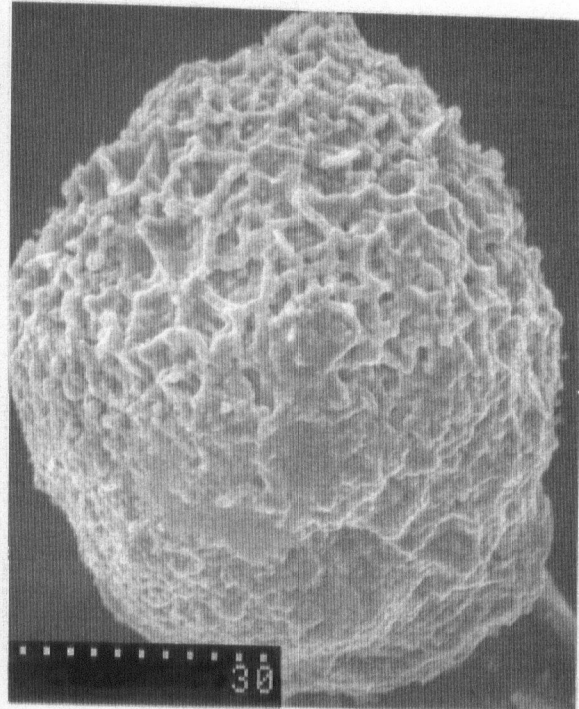


(d)

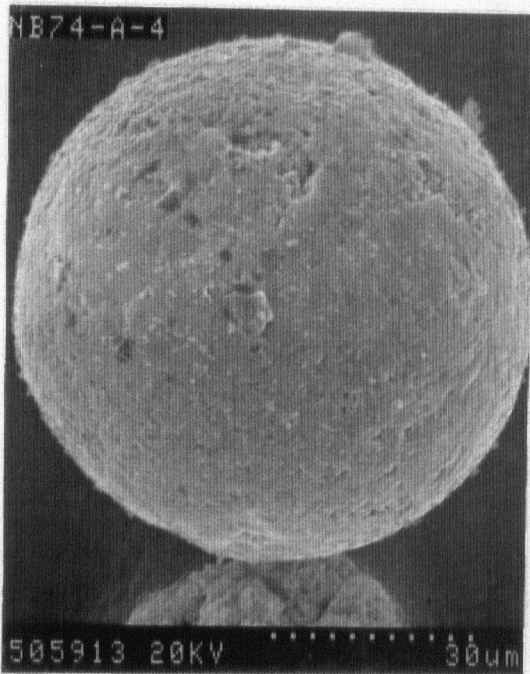
Figure 6.82 SEM photomicrographs of commercial concentrate combustion in air at $T_{\text{FURNACE}}=1130\text{K}$. a) Sullivan Pb-Fe-S melt (105-125 μm), b) Sullivan, iron oxide shells (105-125 μm), c) Brunswick, partially reacted iron sulphide particles (74-88 μm), and d) Brunswick iron oxide shells (74-88 μm).



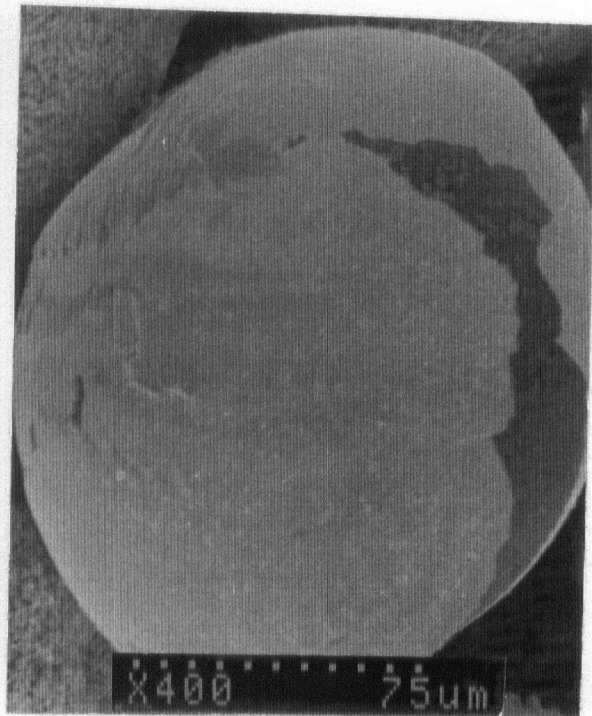
(a)



(b)



(c)



(d)

Figure 6.83 SEM photomicrographs of iron oxide shells found in the products of 74-88 μm Brunswick concentrate combustion in air at $T_{\text{FURNACE}}=1130\text{K}$.

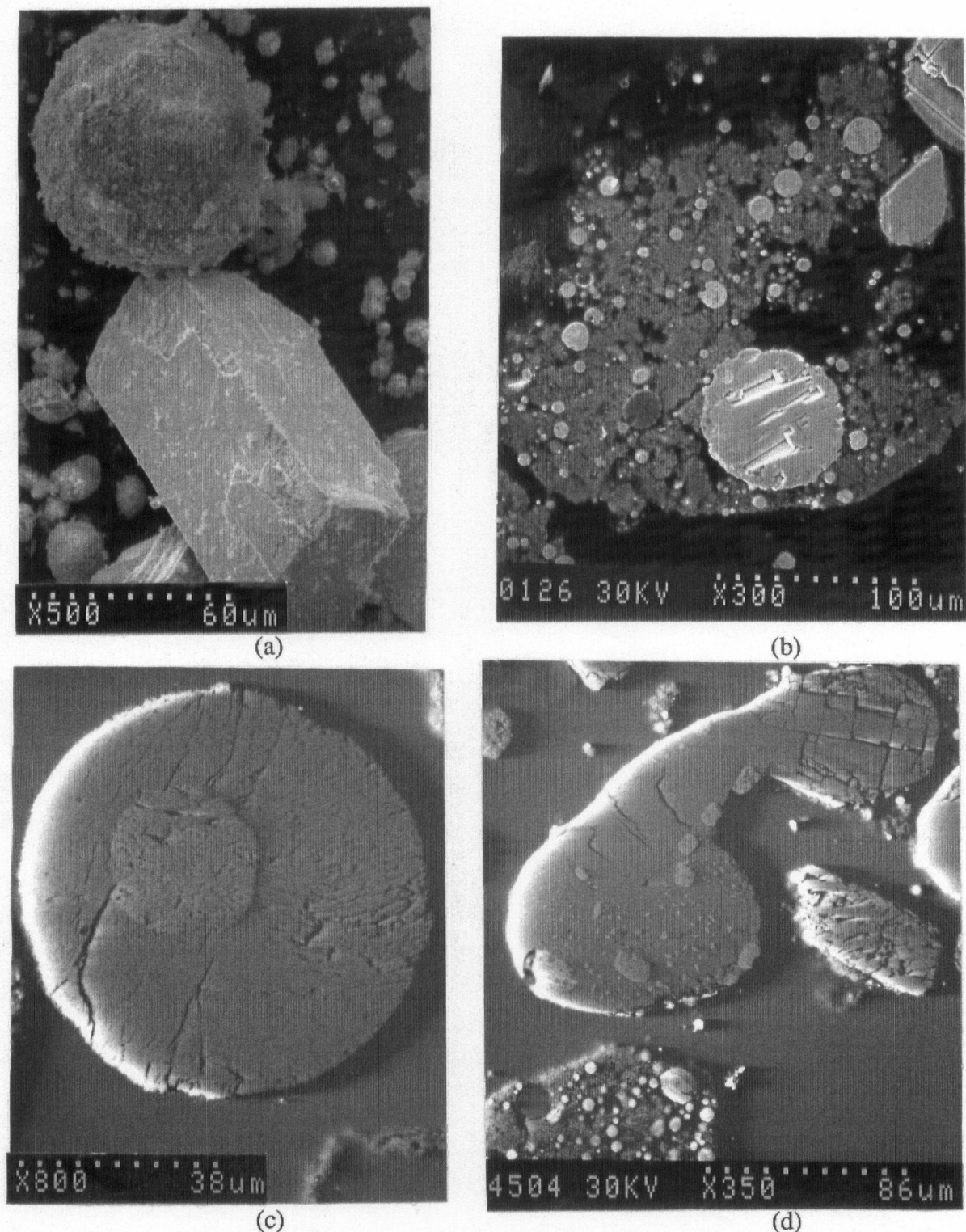
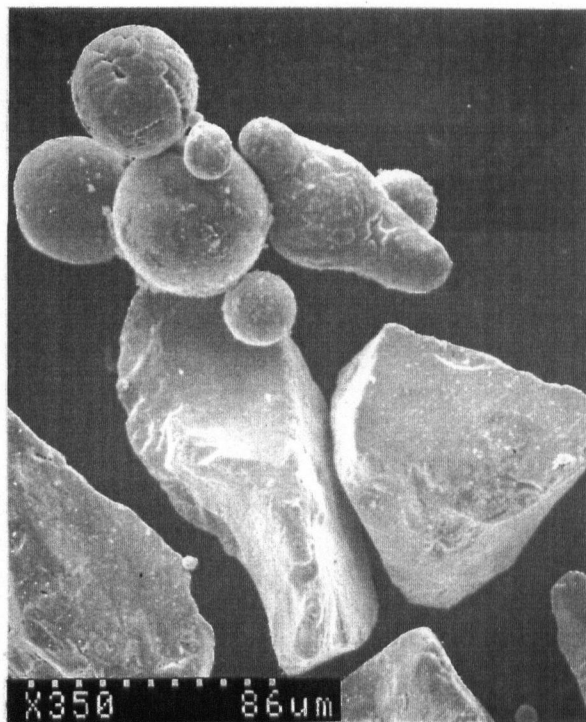
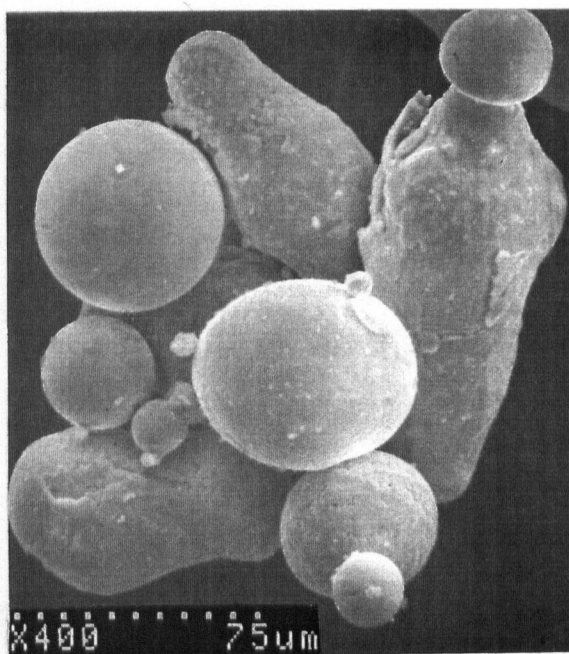


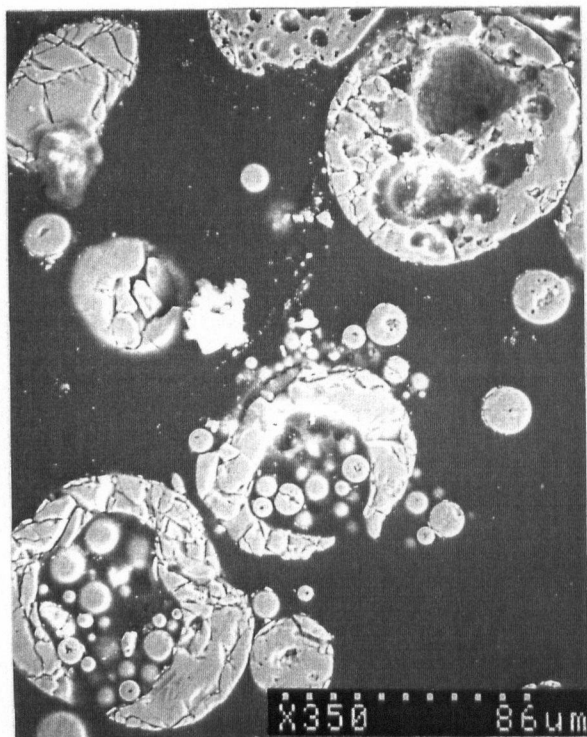
Figure 6.84 SEM photomicrographs of the reaction products of 63-74 μm screen fraction galena combustion in oxygen at $T_{\text{FURNACE}}=1130\text{K}$. a) unsectioned, b) part-reacted particles (light) in fume clump, c) B-S image of Pb rich core in PbS drop, d) B-S images of a partially melted PbS particle, unmelted material (fractured) and original surface oxide (light patches).



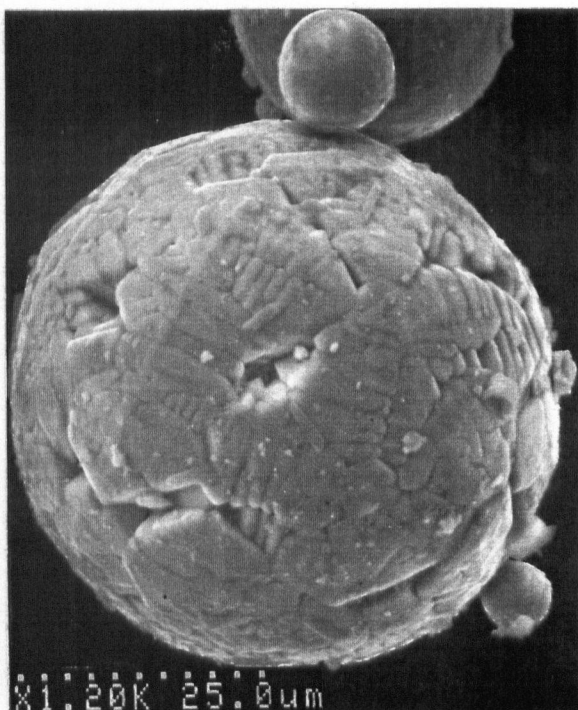
(a)



(b)

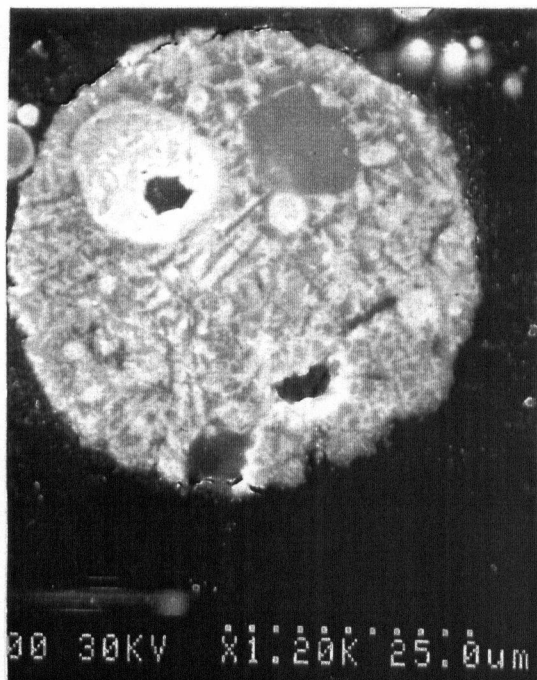


(c)

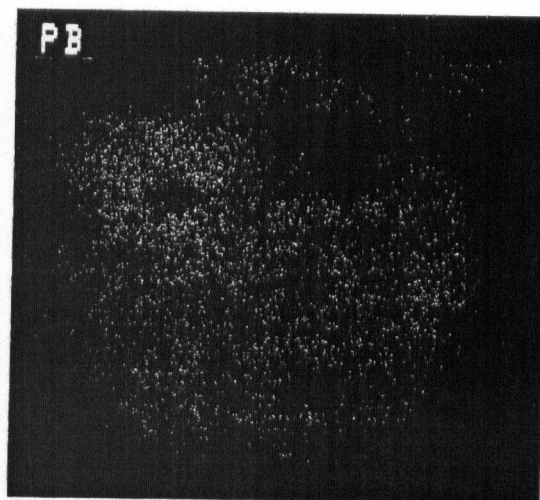


(d)

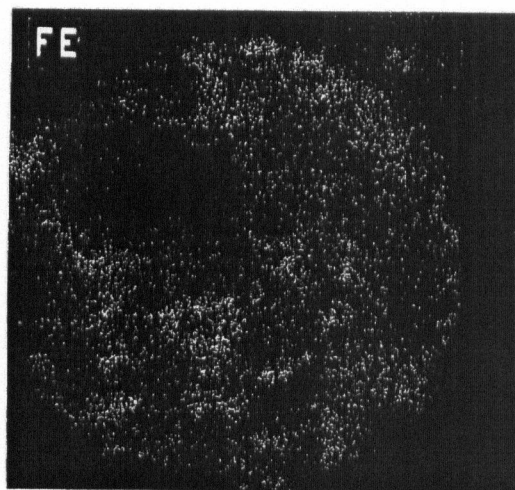
Figure 6.85 SEM photomicrographs of the reaction products of 74-88 μm screen fraction pyrite and pyrrhotite combustion in oxygen at $T_{\text{FURNACE}}=1130\text{K}$. a),c)-d))pyrite, and b) pyrrhotite.



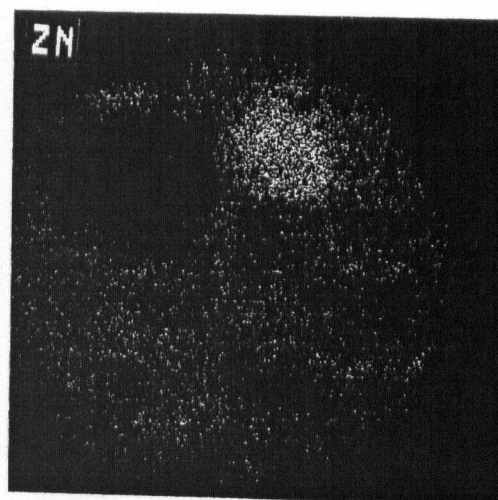
(a)



(b)

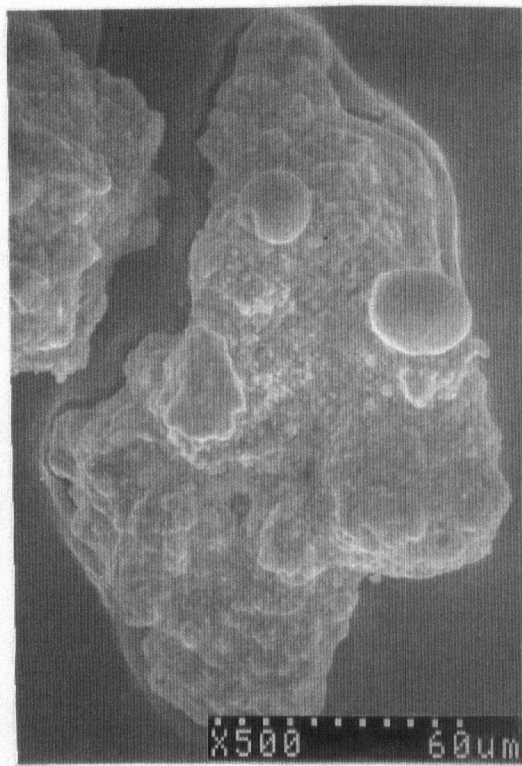


(c)

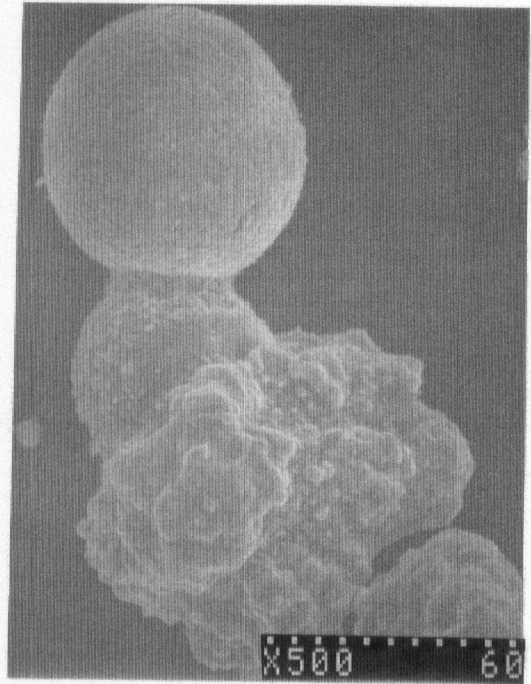


(d)

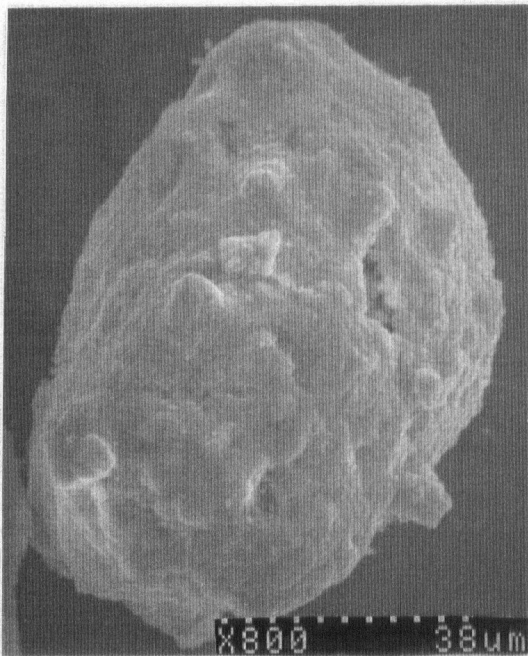
Figure 6.86 SEM photomicrographs and x-ray maps of a sectioned, partially reacted, Pb-Fe-Zn-S particle. Sullivan feed, 74-88 μ m, oxygen, $T_{\text{FURNACE}}=1130\text{K}$.



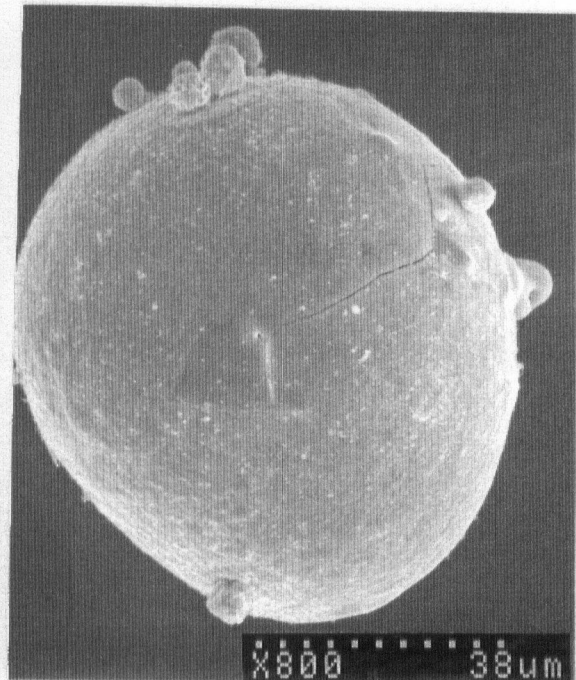
(a)



(b)



(c)



(d)

Figure 6.87 SEM photomicrographs of the products of 74-88 μ m screen fraction of Brunswick concentrate combustion in oxygen at $T_{\text{FURNACE}}=1130\text{K}$.

CHAPTER 7

Discussion of Results

7.1 Important Findings in the Experimental Results

From an examination of the experimental results, the following findings were identified as important to an understanding of the combustion mechanisms of the different feed materials:

- i) During the combustion of galena, in both air and oxygen, large quantities of reaction fume were observed and the vaporisation of lead species appears very important to the combustion mechanism. In air, relatively constant temperatures of 1500-1700K were recorded for most of the time ignited (often in excess of 30ms), suggesting that the combustion temperature is limited by the vaporisation of lead sulphide (bpt. 1609K) (Section 6.1 and 6.2.2.1). *PbS* vaporisation is also suggested by the similar rates of lead and sulphur loss observed during combustion as indicated by the chemical analyses (see Section 6.5.1). The reaction product collected (SEM studies, see Section 6.5.2) consisted of a mixture of large spherical particles of effectively unreacted *PbS* and a fine sub-micron reaction product of lead sulphate. In oxygen the combustion of galena is extremely fast with complete combustion, after ignition, occurring in less than 10ms (Section 6.3.1.1). The combustion pulses typically have twin maxima with the first corresponding to a thermal arrest at ~1700-2000K prior to the maximum of ~2000-2400K. Visual observations and examination of the product suggest that the particles disintegrate during combustion but still react by vaporisation of *PbS*, with lead sulphate being the final form of the reaction product (Sections 6.5.1 and 6.5.2).
- ii) The similar energy pulses (A3) observed during the combustion of both pyrite and pyrrhotite in air are distinctive and very reproducible. The maximum temperatures recorded, ~2300 to 2600K, coincide with a large increase in the energy emitted from the particle (Section 6.3.1.2). The energy increase is equivalent to a x1.5 to

x3 increase in apparent particle diameter; and cenospheres, suggesting a similar increase, were found in the reaction product (Section 6.5.2.1). The ejection of molten material on cooling was observed in the time exposure photographs (Section 6.1) and smaller particles with ragged holes consistent with material ejection were also found in the reaction product. The reactions in oxygen are more intense with the particles heating rapidly to peak temperatures of 3000-3400K and appearing to terminate in disintegration (Sections 6.3.1.2) with the formation of a product consisting mainly of small iron oxide spheres. For pyrite and pyrrhotite particle combustion appears to be of relatively long duration in both air and oxygen, with the glowing particles estimated to be visible often >80ms in air and >20ms in oxygen.

- iii) For the commercial concentrates, the combustion behaviour appears to be determined by the relative amounts of the iron and lead sulphide present, with characteristics of both pure minerals identified (the A2 and O2 combustion pulses see Sections 6.2.1 and 6.3.1). This appears to be due to the presence of a large number of particles which are agglomerates of many smaller individual grains. Brunswick concentrate was found to react more rapidly, and with more similarities to the iron sulphides, than the Sullivan concentrate. This was considered due to the much larger amount of iron sulphide in the Brunswick concentrate, and its presence as pyrite rather than pyrrhotite. During heating in air the agglomerates have a tendency to disintegrate prior to ignition (Section 6.1, 6.2.2.3 and 6.2.2.4). In oxygen molten droplet disintegration appears more common (Section 6.1 and 6.5.2.2). In air the reaction products consisted mainly of thick-walled iron oxide shells, whereas in oxygen the more violent reactions result in predominantly small iron oxide spheres being formed.

- iv) The effect of oxygen concentration on the combustion behaviour is pronounced. With increasing oxygen concentration the reactions tend to become more intense, resulting in higher combustion temperatures, shorter reaction times and an increased tendency for particle disintegration to occur. For galena the transition from the air-type (A1) combustion pulses to the oxygen-type (O1) combustion pulses occurred mostly between oxygen concentrations of 40 and 65%. Over this range the most significant increase in the average combustion temperature (~1600 to 1850K) and a reduction in combustion pulse length was observed. The gradual development of a twin energy maxima in the combustion pulse (O1T) and an associated increase in particle disintegration and vaporisation also occurred over this concentration range (Section 6.5.1). For pyrite the transition from A3 to O3 combustion pulse shape occurred at ~80% oxygen and no transitional pulse shapes were observed. Although similar shaped A3 combustion pulses were observed up to an oxygen concentration of 80%, between 10 and 35% oxygen the maximum pulse temperature increased linearly from ~1900 to ~3000K. At higher oxygen concentrations relatively constant maximum temperatures of 3000-3400K were observed irrespective of pulse type and it is probable that oxide or metal vaporisation is limiting the reactions or causing disintegration. The measured heating rates appear to increase gradually with increasing oxygen concentration, whereas the cooling rates have a similar trend to the peak temperature and remain relatively constant at oxygen concentrations above 30% (Section 6.5.2).
- v) The calculated reaction times in Table 6.3 and 6.6 show that the order of ignition was similar in both air and oxygen with pyrite reacting first followed by galena and pyrrhotite. Sphalerite did not ignite under the conditions of these experiments. The ignition of the Brunswick and Sullivan concentrates seemed to be initiated by

the iron sulphides present in these concentrates. This is supported by the chemical analyses (section 6.5.1) which show significant sulphur elimination prior to lead vaporisation.

- vi) The large range of particle sizes in the feed materials (Table 4.3) make it difficult to identify the effects of particle size on the combustion behaviour. For reactions in air, the first particles are observed to ignite at distances of between 50 and 200mm down the furnace. In each case, however, the ignition and combustion of the remainder of the particles occurs over a further 100 to 200mm, with the individual particles typically being observed as visible streaks (Figures 6.1 to 6.4) over distances of 20 to 50mm. A similar trend was also observed with the oxygen results. For any specific size fraction, the distance travelled by the individual particles before ignition occurs, can therefore vary by up to a factor of two, and the time to ignition is generally the largest portion of the total reaction time. This is also suggested by the mixture of unignited (essentially unreacted) and completely reacted material (see Figures 6.84 and 6.85) observed in the reaction products at all but the longest combustion distances.
- vii) The similar position of the combustion zones for the different size fractions suggests (possibly erroneously) that the total combustion time for large particles was shorter than for small particles (see Tables 6.3 and 6.6). In general, the results do not suggest that the combustion behaviour (pulse shape), and possibly even temperature, are extremely sensitive to particle size. In air, the combustion of galena becomes more violent with increasing feed size (Section 6.2.2.1.1) whereas with the commercial concentrates less violent disintegrations were seen with the larger size fractions (Sections 6.2.2.3 and 6.2.2.4)
- viii) The presence of metallic lead was detected in the products of galena, Sullivan and Brunswick concentrate combustion in air. Individual particles with metallic lead cores, which appeared to have been rejected from a sulphur deficient melt, were

commonly observed (6.5.2). The incorporation of oxide surface layers into the melt and possibly the occurrence of a roast reaction was identified from the reaction products (Figure 6.84d). From the chemical analyses of the bulk samples, however, a maximum of less than 10% metallic lead was recorded and seemed to occur during the early stages of reaction prior to lead (sulphide) vapourisation. Smaller amounts of metallic lead ($\sim <5\%$) were detected in the products of combustion in oxygen (Section 6.5.1).

- ix) The more rapid ignition of pyrite than pyrrhotite (Sections 6.2.2.2 and 6.3.2.2), in both air and oxygen, is the main difference between the two. This is probably due to the rapid thermal decomposition of pyrite, with the release of sulphur, and the formation of porous pyrrhotite; specimens of which were found in the solid samples (Section 6.5.2.1). A violet glow observed in the time exposure photographs of pyrite combustion in air and a small initial energy spike on the O₃ combustion pulses indicate the external combustion of labile sulphur produced by the thermal decomposition of pyrite.
- x) At a furnace temperature of 1130K sphalerite did not ignite. Reaction product analyses indicated that detached oxide shells formed around unmelted zinc sulphide grains were present at longer combustion distances. The sphalerite in the commercial concentrate agglomerates slowly dissolved into the melt and reacted (Section 6.5.2.1).

From the results it is clear that considerable differences exist in the combustion behaviour among the different feed materials, especially the lead and iron sulphides. These differences, and the series of pulse classifications resulting from the pyrometer study, (see Tables 6.1 and 6.4) provide information about the reaction kinetics and the combustion mechanisms for the different materials. The pyrometer results also furnish information about phenomenological events that are occurring during reaction such as

material ejection and particle disintegration which also appear very important to the overall combustion behaviour. Effects of mineral composition and gaseous oxygen concentration are both identifiable from the results.

Of the experimental results only the pyrometer measurements of the individual combusting particles provide quantitative information about the kinetics of the reactions occurring. The average results, determined from the solid samples (such as chemical analyses, X-ray analyses etc.) are of little use to determine the reaction kinetics directly, owing to the large range of particle sizes present in all of the feed materials. The scanning electron microscopy, EDX and microprobe (WDX) studies of individual particles give clues to both the reaction mechanism and the kinetics but their thermal history prior to collection is unknown. Little information on the gas-solid reactions during the initial period of rapid heating prior to ignition and melting is obtainable from the present study.

7.1.1 Comparison of the Pyrometer Results with Previous Studies

Prior to a detailed analysis of the findings it is useful to compare the results of the present investigation with those of similar research published in the literature, especially the pyrometer studies of Jorgensen et al [43,78-83](see Section 2.3.4). Such a comparison, as well as determining the level of consistency between the two, allows the areas where the present work is novel to be emphasised and thus the significance of the present work to be identified.

Despite the use of different pyrometer filter wavelengths there is generally good agreement between the particle temperatures measured in the present study and those presented by Jorgensen [43,78]. Similar to the results of this investigation, average temperatures of 1625K for the combustion of galena in air and ~1800 to 1950K for the combustion of lead concentrate (2.5% Fe and 3.3% Zn) in oxygen, were reported by Happ and Jorgensen [43]. Although the importance of lead species vaporisation to the reaction was identified, no individual lead sulphide combustion pulses have been published with which the results of the present study can be compared directly.

Excellent agreement was obtained between the experimental results for pyrite combustion in this study and the work of Jorgensen [78-79,81-82]. Maximum temperatures of $\sim 2375\text{K}$ were reported by Jorgensen [79] for the combustion of $40\mu\text{m}$ pyrite particles in air at 1130K . Similarly, the shape of the combustion pulses (pyrometer output signal) appeared identical to those recorded in the present study (see Figure 2.14a). The resolution of the measured particle temperature is, however, considerably greater in the present study owing to the much higher sampling rate used such that reproducible trends in the heating and cooling rates could be identified (cf Jorgensen [78] Figure 2.14). The rapid particle temperature increase with increasing oxygen concentration up to $\sim 35\%$ oxygen was also observed by Jorgensen [79], however the maximum temperature recorded of $\sim 2650\text{K}$ for the combustion in oxygen (Figure 2.14b) is considerably less than the $3000\text{-}3400\text{K}$ measured in the present study. Similar to the results of the present investigation the formation of thin wall cenospheres during pyrite combustion in air has been observed by a number of previous researchers [66-67,81].

The combustion times reported by Jorgensen et al. [43,78-79,80], appear shorter than in the present study. The total reaction times of $\sim 33\text{-}46\text{ms}$ and $\sim 15\text{-}45\text{ms}$, for the $37\text{-}53\mu\text{m}$ size fraction galena in air and oxygen respectively (see Figure 2.12), are considerably shorter than the $200\text{-}300$ and $92\text{-}200\text{ms}$ estimated from the present results for the $63\text{-}74\mu\text{m}$ size fraction. Similar discrepancies were also observed for pyrite, where the combustion of the $74\text{-}105\mu\text{m}$ size fraction in air at 973K was observed between $40\text{-}190\text{ms}$ (Jorgensen [80]) was as rapid (see Figure 2.13) as that calculated ($100\text{-}200\text{ms}$) for the $74\text{-}88\mu\text{m}$ size fraction, at 1130K , in the present study. The apparent increase in average particle temperature with decreasing particle size reported by Jorgensen [78] is not readily apparent from the results of the present investigation.

The present work identifies new and important information about the combustion of individual particles. The effect of the different feed materials and the physical constitution of the particles appear identifiable as a series of different combustion pulses.

The effect of oxygen concentration on combustion was also quantified. Unfortunately owing to the large overlap between the results for the different size fractions it is not possible to quantify the effects of particle size on combustion from the present experimental study. Empirical information provided as to maximum particle temperatures and particle disintegration is also of importance.

From this information, attempts were made to develop reaction mechanisms which are in agreement with the kinetic data, and also the phenomenological events observed during typical combustion behaviour. Complete mathematical formulation of the reaction models for individual particles was not performed. However, the heating rates and combustion temperatures determined in the present study will be useful for model verification.

7.2 Particle Heating and Reaction Prior to Ignition

The large variations in particle size present in the individual screen fractions would tend to enlarge the combustion zone through the greater range of terminal velocities (see Table 4.5) and heating rates of the individual particles. The large quantities of fines present in all the feed materials (see Table 4.3) would be expected to result in poor distinction among the results from the different size fractions. From the size analysis results presented in Table 4.3, a general increase in particle size with increasing screen fraction is observed; however a pronounced increase in the furthestmost distance at which the combustion of the last particles occurred was not observed in the experiments. Superficially the results therefore suggest that the *time* for complete combustion of the larger particles decreases with increasing particle size (see Table 6.3). The experimental results indicate that the time to combust once ignited (see Figure 6.2) is a relatively small portion of the total combustion time and therefore disintegration prior to ignition would be necessary to significantly reduce overall combustion times. From the solid sample results there is little indication that, for the pure minerals, significant particle size reduction occurs prior to melting. From the sectioned specimen in Figure 6.84d there is

some indication that in the case of galena the shedding of molten droplets occurs during melting. The time exposure photographs also indicate a relatively short combustion time for galena once ignited (as compared with pyrite see Figure 6.1 and 6.2) possibly suggesting liquid droplet disintegration is occurring, especially for the larger feed sizes. The variation in chemical compositions of the different size fractions (see Table 4.6) is small and does not appear sufficient to alter their reactivities.

In an attempt to elucidate the effect of particle size on combustion the theoretical times to heat to ignition were calculated for various size particles and the results compared with the experimental measurements.

7.2.1 Time to Ignition

From the simple heat balance, (see Appendix 4.1) the heating rates of inert spherical particles were calculated considering only radiative and convective heat transfer and the changes in the gas boundary layer properties. Evaluating the relative magnitudes of the convective and radiative components of heat transfer indicated that for particle heating the radiative component is relatively insignificant (<10%) [75,105].

The calculated effect of particle size on the heating rate of inert particles with the physical properties of galena is shown in Figure 7.1a. The calculated time (and distance) taken to reach the ignition temperatures (see Section 2.3.1) is given in Table 7.1. Also included in Table 7.1 are the experimentally observed combustion zones and estimated particle residence times for similar size fractions. Using this simple model, particles are calculated to ignite much more rapidly than observed experimentally. The discrepancies increase with decreasing particle size, with the ignition of a 63 μm galena particle in air calculated to occur after ~10mm (~13ms), a factor of 10-20 earlier than determined experimentally. From Figure 7.1b, in contrast to the experimental results, the ignition of pyrite was determined to occur at a later time than similarly sized galena particles, despite the lower ignition temperature of the former. The effect of thermal decomposition of pyrite to porous pyrrhotite, on either the physical properties or heat balance was not

however considered. The heating of pyrrhotite would be almost identical ($\rho_{pyrite} = 1.05\rho_{pyrrhotite}$) and thermal decomposition effects would not be important. The effect of increasing oxygen concentration is relatively insignificant to the calculated heating rate but reduces the ignition temperature. The effect of reducing the furnace gas temperature is also shown in Figure 7.1b with the calculated time to ignition increasing dramatically as the gas temperature tends to the particle ignition temperature.

The enthalpy required to melt the mineral, although important, should not effect the time to ignition. Instead once ignited the particle temperature will be limited temporarily by melting (mpt. *PbS* 1392K).

TABLE 7.1 Comparison of Calculated Time to Reach Ignition Temperature and Observed Combustion Zone.

1 - Reference 44 2 - Reference 72

Species	T _{ignition} (K)	Size Fraction (μm)	Calculated Ignition Distance (mm)	Calculated Ignition Time (ms)	Observed Combustion Zone (mm)	Derived Residence Time (ms)
Galena (air)	973 ¹	63-74	10-15	13-17	160-280	200-300
	973 ¹	74-88	15-25	17-23	160-270	162-273
	973 ¹	88-105	25-42	23-31	120-300	98-244
	973 ¹	105-125	42-69	31-42	200-360	132-233
Pyrite	823 ²	88	22	26	70-170	100-200
Galena (oxygen) T _{GAS} =1000K (air)	883 ¹	88	16	16	80-140	87-153
	973 ¹	88	51	47	-	-

The range of particle size in the feed does not explain the apparent delay in particle ignition, and the information obtained in the present study does not appear adequate to determine the precise cause of the discrepancy. The two most probable explanations are:

- i) ignition is delayed by the formation and breakdown of a surface layer or;
- ii) the experimental conditions differ from those considered and heating is less rapid than predicted.

It is possible that the formation of surface layers of oxides and sulphates occurs which impedes further reaction. From Figure 6.84d a lighter rim of PbO surrounding parts of the unmelted PbS surface (lower face and upper right corner) is visible. The exact time to ignite may then depend on the kinetics of the formation and possibly decomposition of this layer rather than the precise temperature. Nakamura et al. [53] from DTA studies of galena suggest that the ignition of rapidly heated particles can be retarded by several hundred degrees over those heated at a slower rate. If the reactions are endothermic (cf roast reactions Equations 2.4 and 2.5) the heat requirements for decomposition would again tend to retard ignition. The importance of the surface condition to the ignition of pyrrhotite is also well known [55], with reported ignition temperatures varying from $\sim 688K$ [55] to $\sim 1073K$ [75]. The formation of a thin protective hematite layer on troilite (FeS) was reported by Asaki et al [128] and Thornhill and Pidgeon [129]; this layer retards oxidation until the specimen has transformed to pyrrhotite ($Fe_{0.89}S$). This is followed by the formation of a porous oxide layer and an increase in the rate of oxidation. Jorgensen [73] reports that the initial reaction prior to thermal decomposition of pyrite is retarded by the formation of a magnetite shell. From Figure 6.2a the violet glow indicating thermal decomposition of pyrite can be seen over a distance of $\sim 15mm$ which corresponds to $\sim 35ms$.

If the formation of a surface layer, and the degree to which it temporarily impedes ignition, depend on the properties of the individual particles, very long combustion zones, as observed in the experimental results, could occur. For the commercial concentrates, the higher porosity within the agglomerates could be expected to enhance ignition (as observed experimentally) through greater gas permeability.

It is highly probable that the gas in the vicinity of the feed delivery tube tip is below that of the bulk furnace temperature of $1130K$. It is improbable however that the gas in this region is below $1000K$ (measured feed delivery tube surface temperature, see Section 4.2.2). From Figure 7.1b, the effect of considering a gas temperature of $1000K$ is to

increase the time taken by an 88 μm galena particle to reach an ignition temperature of 973K from 23 to 47ms (25 to 51mm), which is still less than a third that observed experimentally. It is also improbable that velocity increases up to a factor of ten, necessary to account for the discrepancy between the measured and calculated results, could occur.

It is probable that the observed combustion behaviour, which is dominated by the time to ignition, is dependent on both of the above factors. The large range of sizes, densities and reactivities of the particle present in the individual size fractions and also the uncertainties in the furnace conditions result in at best only a rough estimate of the reaction times of the individual combusting particles being possible.

7.2.2 Sphalerite Reaction

Although the ignition of sphalerite was not observed, detached oxide shells surrounding small sulphide cores formed during reaction in both air and oxygen (see Figure 6.79d). Similar products have been reported by Denbigh and Beveridge [130] for the oxidation of zinc sulphide pellets in air, where it is suggested that reaction occurs between zinc and sulphur diffusing outward through the oxide shell and inward diffusing oxygen. Such detached shells have been observed by others (without ignition) for gas temperatures in excess of 1300K [130]. In the present study sphalerite particles within the agglomerates are observed to gradually dissolve in the sulphide melt and zinc ferrites were detected in the commercial concentrate reaction products.

7.3 Combustion Mechanisms

7.3.1 Galena

The experimental results indicate that at higher temperatures the volatilisation and combustion of lead sulphide vapour is the main reaction mechanism for galena combustion, in both air and oxygen. The results also appear consistent with the thermodynamics of the *Pb-S-O* system and the high vapour pressure of lead sulphide [30]. From the WDX study (see Figure 6.84d), however, *PbO* rather than the

thermodynamically predicted basic lead sulphates were identified as the gas-solid reaction products. This appears in agreement with the DTA study of Nakamura et al. [53].

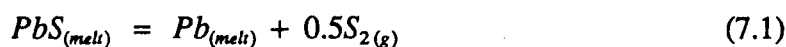
7.3.1.1 Metallic Lead Formation

A maximum of less than 10% metallic lead was recorded in the bulk samples for combustion in air (see Figure 6.74). The metallic lead concentration in individual particles was however considerably higher, as suggested by the presence of sulphur deficient metallic lead cores observed in the WDX/EDX studies (see Figure 6.79 and 6.84). It is probable these different phases separated on cooling. Similar particles with metallic lead cores have been reported by Wuth [64], as have copper and $CuFe_2O_4$ cores surrounded by Cu_2S [63-65].

It is probable that metallic lead forms through a roast reaction (Equations 2.4 and 2.5) between the melt, and the oxides or sulphates formed by gas-solid reactions during particle heating. A 5-10 μ m layer of PbO adhering to unreacted PbS can be seen being gradually incorporated into the PbS melt in Figure 6.84d. It is not clear whether the PbO islands in the melt were incorporated as a solid or molten phase. Although PbO is reported to have a lower melting than PbS (~1158K vs ~1392K [30]) it is possible that the melting point of the $Pb-S-O$ melt (see Section 6.5.2.2) is considerably less than for pure PbS (see Figure 2.4 [46]).

At low temperatures the roast reactions are endothermic [30] and kinetically slow [15], however the rate would probably increase rapidly with increasing temperature. Such a mechanism would suggest that the amount of metallic lead formed would be dependent on the amount of oxide/sulphate formed during heating. Metallic lead formation would also be expected to occur primarily during the early stages of reaction, in general agreement with the experimental findings (see Figure 6.74b). At a later stage of reaction it is possible that metallic lead formation could occur through a back reaction between the oxide reaction products formed in the gas phase and the melt.

It is also possible that metallic lead could form during the early stage of reaction through sulphur vaporisation from the melt. The conditions at the melt surface, owing to the high P_{PbS} and low P_{O_2} within the vaporising PbS layer, is probably represented by the $P_{PbS} - P_{SO_2}$ predominance area diagrams (see Figure 2.3). Sulphur vaporisation from the melt (see Equation 7.1) would result in metallic formation as indicated by Figure 7.2. From Figure 2.1 the P_{S_2} above a PbS melt [34] is however several orders of magnitude lower than the P_{PbS} at the same temperature.



The lower amounts of metallic lead found during combustion in oxygen could be due to faster ignition and less gas-solid reaction occurring, or the more intense reactions may cause metallic lead vaporisation (b.pt. 2017K). In industrial flash smelting, up to 40% metallic lead has been reported [19] to form during combustion in pure oxygen. This difference may be the result of oxygen starvation occurring around the individual particles within the flash smelting flame.

7.3.1.2 Reaction Mechanism

To determine the limits of the combustion temperature, the adiabatic flame temperature was calculated [30] for the combustion of lead sulphide in air, from a reactant temperature of 1130K. Considering all species in their standard states and PbO (m.pt. 1158K, b.pt. 1745K [30]) or $PbSO_4$ (m.pt. 1363 or 1443K and b.pt. unknown [30]) to be the products (see Equations 2.1 and 2.2), adiabatic flame temperatures, in air, of 1701K and 2836K respectively were determined. Although the actual combustion temperature could be considerably less than the adiabatic flame temperature, the similarity of that calculated for PbO (liquid) formation to the measured temperatures and the thermodynamic instability of the sulphate predicted at temperatures above ~1300K suggests that PbO is the main reaction product. If sulphation of the product occurred at a sufficient distance from the particle the heat generated would not be transferred to the particle.

The experimental results suggest that during combustion in oxygen the molten galena particles disintegrate rapidly with the resulting fragments reacting very rapidly, possibly as a cloud. The initial vaporisation and disintegration appears to correspond to the transient thermal arrest at $\sim 1700\text{-}2000\text{K}$ of a few milliseconds duration observed with O1T combustion pulses (see Figure 6.44). It is probable that a large thermal input to a particle already at its boiling point would result in fragmentation due to internal gas generation. Visual observations suggest that 4 to 10 smaller fragments typically result with their subsequent vaporisation and combustion occurring within a 5mm radius of the original particle. This is thought to correspond to the later temperature maximum, of $\sim 2000\text{-}2400\text{K}$, of the O1T pulses. The final temperatures reached are considerably above the boiling point of *PbS*. The total reaction time after ignition also appears to be very short, typically less than 5ms. At these higher combustion temperatures *PbO* would form as a gaseous species, which would then presumably condense and sulphate with increasing distances from the particle. For combustion in oxygen, adiabatic flame temperatures of 2746K and 5385K [30] were determined for oxide and sulphate reaction products respectively.

A schematic diagram of the combustion mechanism proposed for the combustion of galena in $<40\% \text{O}_2$ and $>60\% \text{O}_2$ is shown in Figure 7.3. The main difference between the mechanisms of galena combustion in air and oxygen appears not to be due to different reactions, but rather to the physical phenomena of increased particle disintegration resulting from more intense heat generation with increasing oxygen concentration. The gradual change from air-type (A1) combustion pulses to oxygen-type (O1) combustion pulses, with usually twin maxima (A/O1T and O1T), between 40 and 65% oxygen is the result of heat generation becoming sufficient to cause internal gas generation and disintegration, and also to overcome the thermal barrier required to produce a gaseous, instead of liquid, *PbO* reaction product.

For combustion in air the initial stage prior to melting is long, typically calculated to be between 100 and 200ms, with the time taken appearing dependent on the characteristics of the individual particles. During this period an oxide/sulphate surface layer forms through gas-solid reactions. With increasing temperature particle ignition occurs and the particle rapidly heats to its melting point (Stage 1b). During melting, the shedding of molten droplets from the partially melted particle may occur. At these temperatures the vapour pressure of *PbS* is considerable and vapour phase combustion may be significant even before the completion of particle melting. Combustion of vaporised lead sulphide results in a fine *PbO* (liquid) reaction product forming some distance from the particle surface (Stage 2b). Metallic lead formation probably occurs at this stage due to roast reactions between the melt and the oxides and sulphates formed earlier by gas-solid reactions. The particle temperature rapidly heats to near the boiling point of *PbS* (1609K), and then remains constant, as the excess heat generated by the reaction is consumed in vaporising material. This mechanism of reaction continues as the liquid drop is consumed (Stage 3b) and the *PbS* vapour combusting at approximately a constant temperature (possibly the adiabatic flame temperature of ~1700K) some distance from the surface until vaporisation of the drop is complete (Stage 4b).

For combustion in oxygen the faster reaction rates, result in the particles rapidly igniting. The particles rapidly melt (Stage 1a), and intense gas-liquid reactions and vapour phase combustion of *PbS* occurs. The molten particles rapidly heat to the boiling point of *PbS* and the very high heat input results in internal gas generation and the explosion of the molten droplet (Stage 2a). The rapid expansion and vaporisation associated with the formation of several smaller particles results in an apparent temporary thermal arrest in the range 1700-2000K. The smaller particles then rapidly vaporise and combust forming a gaseous *PbO* reaction product (Stage 3a). The temperature of the combusting 'vapour cloud' quickly rises to 2000-2400K, until combustion is complete.

7.3.1.3 Comparison With Salomon de Friedberg Combustion Model

The reaction mechanism considered by Salomon de Friedberg [44], with lead sulphide vaporisation the rate limiting step, appears in general agreement with the results of the present experimental study. Salomon de Friedberg, however, considered lead sulphate, rather than *PbO*, to be the reaction product with all of the excess heat generated being assumed to report to the particle. The model predicts that for combustion in air, on completion of vaporisation following the $\sim 1609\text{K}$ thermal arrest, 40% of the original lead sulphide is present as a vapour cloud; which for a $100\mu\text{m}$ particle would be 1.7mm in diameter! The subsequent combustion of this cloud then resulted in extremely high temperatures being predicted for combustion in air and oxygen (see Figure 2.15). Unfortunately direct comparison with the results of the present study is not possible as only calculations for furnace temperatures of 978K were reported (see Figure 2.15). Despite the higher rates of heat generation and vaporisation expected through considering a sulphate reaction product the actual lengths of the thermal arrest at $\sim 1600\text{K}$ reported for combustion in air [44], $\sim 40\text{ms}$, appears comparable with the results of the present study ($T_{\text{GAS}}=1130\text{K}$). If, as considered in the present study, *PbO* is the reaction product the lower heat of reaction should result in a much longer combustion time. This discrepancy is possibly a further indication of the formation of multiple liquid droplets at an early stage of reaction as suggested experimentally.

In oxygen the high heating rates and relatively short thermal arrest ($\sim 10\text{ms}$) at $\sim 1609\text{K}$ due to *PbS* vaporisation, predicted by the model shown in Figure 2.15, has similarities to the initial thermal arrest of the OIT combustion pulses (see Figure 6.44). The rapid rise in temperature following the arrest, as the remaining lead sulphide vapour combusts, also resembles the initial part of the second maximum of the combustion peak. The heating rates predicted by his reaction model ($\sim 30 \times 10^4\text{K/s}$ $T_{\text{GAS}}=978\text{K}$) are also similar to those recorded for galena combustion in oxygen (see Figure 6.44). The present

experimental results suggest that part of the more rapid reaction in oxygen is due to the rapid disintegration of the *PbS* droplets at an early stage of combustion, a factor not included in the reaction model.

In general the different stages of reaction proposed by Salomon de Friedberg [44] appear in agreement with the present experimental results. The experimental results however suggest that *PbO* is the reaction product. The experimental results indicate the need to incorporate particle disintegration into the reaction mechanism for combustion in oxygen and also for the larger size fractions in air.

7.3.2 Pyrite/Pyrrhotite

The reproducibility of the combustion pulses observed during the combustion of pyrite and pyrrhotite and their strong dependence on the partial pressure of oxygen allows considerable information about the reaction mechanism to be determined. Both the thermally decomposed pyrite and original pyrrhotite would be expected to form liquids of similar compositions on melting and it is therefore not unforeseen that, as observed experimentally, after melting the reactions of the two would appear indistinguishable. From the time exposure photographs in Figure 6.2a the gradual increase from ignition to peak temperature is estimated, in both cases, to occur over a period of ~80ms, followed by rapid cooling, typically in less than ~20ms.

The combustion of the sulphur resulting from the thermal decomposition of pyrite to pyrrhotite, is visible as a violet glow (see Figure 6.2a) during the early stages of reaction. The shrinking core formation of porous pyrrhotite from pyrite (see Figure 6.80) has been observed at temperatures above 800K by many researchers [66-67,73,78,81], with the porosity being due to the large (~20%) volume change associated with the reaction [73]. Jorgensen reports [73] that the initial magnetite films (which form prior to thermal decomposition) remain relatively adherent and tend to split circumferentially rather than spalling. This partially protective layer may explain the typical "winged" form

of thermally decomposed pyrrhotite (see Figure 6.80a and c). The more rapid ignition of pyrite than pyrrhotite is due to the porous nature of the pyrrhotite product and unoxidised surface.

Predominance area diagrams for the *Fe-S-O* system at 1900, 2500 and 2900K are given in Figures 7.4 [30]. At temperatures below ~1750K hematite (Fe_2O_3) is the stable phase predicted at bulk gas compositions. Between ~1750 and ~2500K, magnetite (Fe_3O_4) is the expected stable phase, and at higher temperatures wustite (FeO) becomes thermodynamically favoured. The range of stability of metallic iron and iron sulphide move to increasingly higher oxygen partial pressures with increasing temperature. Above the melting point of magnetite at 1873K [30] all species are molten. The validity of the predominance area diagrams are probably limited by the uncertainties in the thermodynamic properties above ~2500K. The predominance area diagram for the *Fe-S-O* system at 2500K indicates a considerable sulphur vapour pressure exists (Figure 7.4d).

From the thermodynamics of the system, there appears little to link the strong relationship between the partial pressure of oxygen to the maximum reaction temperatures observed with A3 combustion pulses at oxygen concentrations below 40%. The relatively constant maximum temperature of ~3000-3400K at oxygen concentrations greater than ~40% does however seem to correspond to the boiling point of iron (3300K) and the thermal decomposition of *FeO* (reported at 3400K [145]).

The presence of *Fe-S-O* melts with species at reduced activities will alter the predominance area diagrams and increase the region of stability of lower activity reaction products. It is therefore unrealistic to consider a system containing only the pure oxides and sulphides. Toguri et al. [132] reports that 6% oxygen is typically found in iron sulphide matte. Naldrett [133] reports the minimum melting point for the *Fe-S-O* system as 1188K at 68.2% *Fe*, 24.3% *S*, and 7.5% *O*, (cf mpt. *FeS* 1468K [30]). Complete miscibility between *FeO* and *FeS* is reported [134] at temperatures above ~1680K (see

Figure 7.5). From the *Fe-S* and *Fe-O* binary phase diagrams [136] given in Figure 7.6 it can be seen that at temperatures above the melting point of iron (1811K) miscibility exists for the complete range of sulphur compositions between metallic iron and *FeS*. In contrast, for the *Fe-O* melt, liquid *FeO* was found to separate from the metallic phase at oxygen concentrations greater than a few weight percent, even at temperatures in excess of ~2300K. The *FeO-FeS-SiO₂* ternary phase diagram at 1473K shown in Figure 7.5 [134] indicates that, at lower temperatures the presence of even a few percent of oxide stabilising species, such as silica, can result in the separation of a slag phase.

It is possible that the separation of an oxide phase is important to the reaction mechanism, which through a dependence on the melt composition, could be very sensitive to the experimental conditions. Under conditions of gas phase oxygen mass transfer control the low surface oxygen potential coupled with high liquid phase diffusion rates would tend to promote the formation of a miscible *Fe-S-O* melt. At a later stage however, sulphur depletion in the melt would tend to result in liquid phase diffusion of sulphur limiting the reaction rates and the oxygen potential, and the activity of *FeO* on the surface would increase eventually resulting in oxide formation. The generation of sulphur dioxide at the interface between the sulphide and oxide would provide a mechanism for the cenosphere inflation.

For gas phase oxygen mass transfer control the heating rates (Figure 6.73a) and maximum temperature (Figure 6.70) would be expected to increase with increasing oxygen concentrations as was observed experimentally at concentrations below 40%. The large energy increase observed at the same instant, suggests that termination of heating is related to a phenomological event. The formation and inflation of a thin iron oxide film, resulting in reaction termination and rapid cooling is one possible mechanism which would fit these experimental observations. The enhanced heating rates of the A3 combustion pulses with increasing oxygen concentrations above 40% (see Figure 6.73a), and the constant maximum temperature of 3000-3400K similar to the boiling point of

iron suggest, that the reactions are being terminated through material ejection probably due to intense vaporisation of iron species. This is in agreement with complete particle disintegration observed with O3 combustion pulses (see Figure 6.2), however the A3-type combustion pulses observed at between 40 and 80% oxygen suggest the reactions in this concentration range are terminating without substantial disintegration.

Although a number of intact iron oxide cenospheres were observed in the products collected, their numbers were not sufficient to unequivocally state that the combustion of every iron sulphide particle results in the formation and freezing of a cenosphere. The ejection of material during the later stage of A3 particle cooling (see Figure 6.2a and b), which is commonly observed would tend to rupture these thin shells, as could the quenching/sampling technique. Many particles with a high porosity are also observed in the reaction products of iron sulphide combustion in both air and oxygen (see Figure 6.85c) and would provide an alternative mechanism for expansion.

In general the time taken for the rapid energy increase observed with A3 combustion pulses to occur decreases with increasing oxygen concentration, being ~3 and ~1ms respectively in Figures 6.68 and 6.10 for 10 and 21% oxygen. This suggests that inflation occurs through a gas generating reaction which is enhanced with increasing oxygen concentration. The rejection of gas on cooling due to equilibrium reactions does not appear sufficient for the degree of inflation observed.

Large increases in emissivity, and the delayed separation of an iron oxide phase, has been observed during the oxidation of levitated iron drops [137]. It does not, however, seem very probable that the $\times 4-9$ increase in energy observed with A3 combustion pulses at peak temperature is the result of emissivity changes due to the sudden oxidation of the surface. The emissivity of iron oxide has been reported as 0.65-0.95 [135], and therefore the emissivity of the original *Fe-S* melt would have to be extremely low (less than 0.1, cf cast iron at 0.29 [136]) to result in the necessary increase in energy radiated and associated apparent particle area.

Turkdogan [138] suggests that low surface tension melts and a continuous source of gas generation are necessary for bubble inflation. The relatively small amount of information which is available on the physical properties of *FeO-FeS* melts at temperatures in excess of 2000K does not suggest a tendency for bubble formation. Turkdogan [138] reports that mattes are very fluid with viscosities similar to those of molten metal ($\sim 1 - 5 \times 10^{-3} \text{ kg} \cdot \text{m}^{-1} \text{ sec}^{-1}$) and surface tensions of *FeS* and *FeO* are similar being reported [138] as $575 \times 10^{-3} \text{ N} \cdot \text{m}^{-1}$ (at 1523K) and $340 \times 10^{-3} \text{ N} \cdot \text{m}^{-1}$ (at 1673K) respectively. The bubble formation may however be the result of surface impurities, which are reported [138], even in trace amounts, to dramatically decrease surface tension and encourage bubble formation.

The formation of cenospheres has also been observed during the combustion of aluminium [141-144]. Similar to the present study at lower oxygen concentrations cenosphere formation was observed, whereas at oxygen concentration in excess of ~40% there was a transition to particle fragmentation. The combustion was considered to occur in the vapour phase through aluminium vaporisation and to be limited by the boiling of the oxide [141]. This appears to be a major difference between the combustion of *FeS* and aluminium as the results of the present study do not suggest combustion is occurring at a flame front. Using high speed cinematography Otero [88] has also recorded flame fronts at ~0.5 diameters from the surface of ~50 μm copper concentrate particles (*CuFeS₂*) during combustion in oxygen. It is possible this is the result of copper (bpt 2968K) or sulphur vaporisation from the melt. Copper concentrate combustion also appears to terminate with a sudden increase in intensity possibly due to particle disintegration [88]. In these cases the disintegration at high oxygen concentrations seems consistent with the mechanism proposed in the present study for disintegration through internal vaporisation of the reactants.

It seems probable that once molten the combustion of iron sulphide is gas phase oxygen mass transfer controlled [24-25]. The formation of FeO and SO_2 is the favoured reaction at higher temperature [30]. It is possible, however, that due to kinetic constraints other reactions may occur. Although the formation of sulphur monoxide is thermodynamically less favoured than the formation of SO_2 (see Equations 7.2 and 7.3) better agreement between the lower predicted temperatures and the experimental results (see Figure 2.14b) was taken by Jorgensen [79] as evidence that the reaction proceeded via this species.



$$\Delta H_{R7.2,2800K} = -350 \times 10^3 J \quad \Delta G_{R7.2,2800K} = -160 \times 10^3 J$$



$$\Delta H_{R7.3,2800K} = -59 \times 10^3 J \quad \Delta G_{R7.3,2800K} = -74 \times 10^3 J$$

It is also possible that metallic iron could form owing to sulphur vaporisation from the melt (see Figure 7.7) due to a low surface P_{O_2} under conditions of intense surface oxidation and the relatively high equilibrium sulphur pressure above the melt. It is therefore necessary to examine the feasibility of other species, such as Fe or SO , participating in the reactions. Discontinuous changes in experimental heating rate strongly suggest a change in the chemical reactions has occurred. The sudden rapid increase in temperature sometimes observed over the final few milliseconds of heating with A3 combustion pulses, as that shown in Figure 6.10, would fit with a change in reaction mechanism during the last stage of melt oxidation.

The hypothesis that the reaction of a molten FeS droplet is gas phase oxygen mass transfer controlled can be examined using a simple reaction model and the effects of different overall chemical reactions investigated. In an attempt to examine this and the effects of process variables on the combustion a simple model of combustion similar to that presented by Jorgensen [79] was written. From a comparison of the heating rates,

maximum combustion temperature and reaction times predicted by this model with those measured experimentally further elucidation the mechanism of iron sulphide combustion appears possible.

Jorgensen [138] considered the combustion of a molten droplet of iron sulphide to be controlled by the mass transfer of oxygen in the gas phase. To examine the validity of this assumption it is necessary to estimate the relative magnitudes of the flux of oxygen in the gas phase and that of sulphur in the liquid phase to the reaction interface.

Approximate calculations, considering diffusion to be through a stagnant film in both the gas and liquid phase (Appendix 4) indicate that this assumption is probably valid, at least at higher temperatures. Eventually the decline in reacting species (S) in the $Fe-O-S$ melt would result in liquid phase mass transfer becoming the limiting step. It is implicit in such a control mechanism that the mass transfer of the reaction products, in either the gas or liquid phase, is not rate limiting.

7.3.2.1 Combustion Model

The particle heat balance given in Appendix 4 can be extended to include heating due to chemical reaction, expressed in terms of the rate of oxygen mass transfer as given by Equation 7.4.

$$-\frac{\pi}{6} d^3 \rho_s C_p \frac{dT}{dt} = \pi d^2 h_{con} (T_p - T_{gas}) + \pi \sigma \epsilon d^2 (T_p^4 - T_{wall}^4) + \Delta H_R \frac{dM_{O_2}}{dt} \quad (7.4)$$

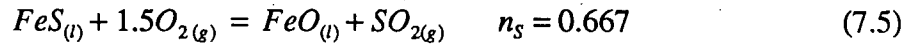
where $\Delta H_R = \text{Enthalpy of reaction (J/mol } O_2)$

$\frac{dM_{O_2}}{dt} = \text{Oxygen mass transfer rate (mols } O_2/\text{s)}$

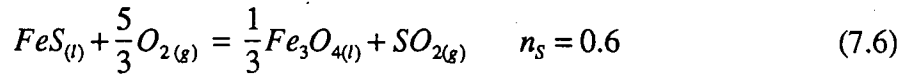
As the initial rates of reaction of the solid during melting are unknown, and probably chemically controlled, the model has been simplified by considering only gas phase mass transfer limited combustion of a molten particle above 1200K. As a first approximation for the mass balance, the droplet is initially considered to be stoichiometric FeS . The specified reaction (Equations 7.5 to 7.8) is considered to proceed until all liquid phase reactants are consumed, after which the chemical reactions cease.

Cooling then occurs through convective and radiative heat transfer only, with heat evolved during phase transformations or solidification ignored. The physical properties of the melt during reaction are determined from an average of those of the reactants and products based on mole fraction as calculated from the mass balance.

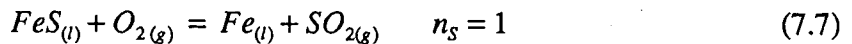
The following overall combustion reactions were considered:



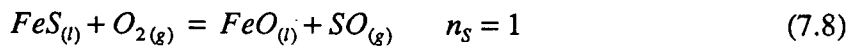
$$\Delta H_{R7.5, 2800K} = -320 \times 10^3 \text{ J/mol}O_2 \quad K_{7.5, 2800K} = \frac{a_{FeO} P_{SO_2}}{a_{FeS} P_{O_2}^{1.5}} = 4.6 \times 10^4$$



$$\Delta H_{R7.6, 2800K} = -336 \times 10^3 \text{ J/mol}O_2 \quad K_{7.6, 2800K} = \frac{a_{Fe_3O_4}^{1/3} P_{SO_2}}{a_{FeS} P_{O_2}^{5/3}} = 3.2 \times 10^4$$



$$\Delta H_{R7.7, 2800K} = -224 \times 10^3 \text{ J/mol}O_2 \quad K_{7.7, 2800K} = \frac{a_{Fe} P_{SO_2}}{a_{FeS} P_{O_2}} = 500$$



$$\Delta H_{R7.8, 2800K} = -176 \times 10^3 \text{ J/mol}O_2 \quad K_{7.8, 2800K} = \frac{a_{FeO} P_{SO}}{a_{FeS} P_{O_2}} = 1.1 \times 10^3$$

where n_S = stoichiometric factor ($FeS_{(l)} + \frac{1}{n_S}O_{2(g)} = FeO_{X(l)} + SO_{Y(g)}$)

The standard enthalpies of reaction are relatively insensitive to temperature over the range examined [30,79] and were therefore considered constant. The FeS in the melt was also considered at unit activity throughout. Owing to the uncertainties involved in the calculations changes in mechanism during reaction were not considered with the present model.

Considering equimolar counter diffusion through a stagnant film (see Appendix 4) the gas phase oxygen mass transfer rate can be expressed as [79,105]:

$$\frac{dM_{O_2}}{dt} = \frac{2\pi D_{O_2-SO_2/N_2} d_p (P_{O_2 \text{ bulk}} - P_{O_2 \text{ surface}})}{RT_{\text{film}}} \quad \text{molsO}_2/\text{s} \quad (7.9)$$

Under conditions of gas phase oxygen mass transfer control the surface oxygen concentration in Equation 7.9 can be considered to be zero. Incorporating Equation 7.9 and the heat transfer coefficient given by Equation A.4.3 in Equation 7.4 and rearranging, the final form of the heat balance, similar to that derived by Jorgensen [79] is given in Equation 7.10:

$$\frac{dT}{dt} = -\frac{6}{\rho C_p} \left\{ 2k_{\text{gas}} \cdot \frac{1}{d_p^2} \cdot (T_p - T_{\text{wall}}) + \sigma \epsilon \cdot \frac{1}{d_p} \cdot (T_p^4 - T_{\text{wall}}^4) + 2D_{O_2-SO_2/N_2} \cdot \frac{1}{d_p^2} \cdot \frac{P_{O_2 \text{ bulk}}}{RT_{\text{film}}} \cdot \Delta H_R \right\} \quad (7.10)$$

Depending on the reaction stoichiometry the oxygen mass transfer through a boundary layer can be enhanced due to bulk fluid motion resulting from non-equimolar diffusion. For the formation of wustite/ SO_2 and magnetite/ SO_2 in oxygen (Equations 7.5 and 7.6), the calculated enhancement of the oxygen diffusion rate was estimated to be 22 and 28% respectively (see Appendix A.4.4). Due, however, to the many approximations used in the calculations, such a level of refinement was not felt justified and therefore the effects of non-equimolar counter diffusion were not considered.

The rate of consumption of the liquid phase reactants is related to the rate of oxygen mass transfer through the stoichiometry factor n_s , given in Equations 7.5 to 7.8 such that:

$$\frac{dM_{FeS}}{dt} = -n_s \frac{dM_{O_2}}{dt} \quad (7.11)$$

7.3.2.2 Combustion Model Predictions

The calculated variations in particle temperature with time for combustion in air, based on the different overall reaction mechanisms given in Equations 7.5 to 7.8, are shown in Figure 7.7. In each case a similar trend is predicted with the relative heating rates being determined by the different enthalpies of reaction. Both heat and mass balance considerations influence the maximum temperatures predicted. For the formation of magnetite/ SO_2 and wustite/ SO_2 the temperatures are similar at ~2700K and 2650K for a

65 μm droplet of emissivity 0.7. The reactions considering the formation of metallic iron/ SO_2 or wustite/ SO result in lower maximum temperatures of ~ 2250 and 2000K respectively. The predicted heating rates are given in Figure 7.8a and range from above $10 \times 10^4 \text{ K/s}$ for the initial magnetite/ SO_2 reaction to less than $1 \times 10^4 \text{ K/s}$ for the reactions at the point of termination. The shorter combustion times predicted for the Fe/SO_2 and FeO/SO reactions are the result of the higher sulphur removal per mol oxygen given by the stoichiometries of reactions 7.7 and 7.8. Since all reactions are considered to cease at the start of cooling, the cooling rates predicted at any specific temperature are similar (see Figure 7.8b).

A typical measured A3 combustion pulse (from Figure 6.10) is included in Figure 7.7 for comparison with predicted results. The agreement between the measured and predicted thermal histories is poor. It would be surprising if this simple model adequately predicted the combustion behaviour as, among other things, the amount of sulphur removed prior to the formation of the sulphide melt is unknown. As the total amount of fuel available for reaction is unknown the maximum temperature achievable by the different reaction mechanism cannot be calculated. In theory, if gas phase oxygen mass transfer control was limiting throughout, the temperature at which the reactions cease would lie at some point along one of the curves already shown in Figure 7.7. Based on this rationale, finite final heating rates would be expected to exist at peak temperature. This appears in agreement with the measured combustion pulse shown in Figure 7.7 where both a sizeable heating rate and an abrupt transformation to particle cooling occurring at peak temperature. It is possible for gas phase oxygen mass transfer to limit throughout if either the reaction is terminated prior to completion by a physical phenomena such as particle disintegration, or alternatively, if liquid phase diffusion is fast enough to allow gas phase oxygen mass transfer to dominate throughout the reaction.

The measured temperature of the combustion pulse shown in Figure 7.7 is higher than the maximum predicted for the formation of Fe/SO_2 or FeO/SO . This does not preclude a certain amount of the reaction progressing through these routes. Similarly measured heating rates intermediate to those predicted may indicate a fraction of the reaction is occurring through the different reaction mechanisms.

For magnetite/ SO_2 and wustite/ SO_2 combustion reactions the results are similar and only those for wustite formation are presented in later Figures. In theory, below $\sim 2500K$ the formation of magnetite instead of wustite should be considered. Of the lower pair, only the curve for metallic iron/ SO_2 reaction is presented for convenience. Unless otherwise indicated a particle surface emissivity of 0.7 (as used in the apparent particle size calculations from the experimental results) is considered.

In Figure 7.9 the measured heating rates for the two A3I combustion pulses given in Figures 6.11 and 6.12 have been superimposed on the calculated wustite/ SO_2 and metallic iron/ SO_2 curves shown in Figure 7.9. For combustion in air, the measured heating rates ($< 3 \times 10^4 K/s$) are generally lower than those predicted by the heat balance and it is only at temperatures above $\sim 2000K$ for the Fe/SO_2 and $\sim 2400K$ for the FeO/SO_2 reactions that the declining predicted heating rates becomes similar to those measured experimentally. The lack of agreement at lower temperatures possibly suggests that gas phase oxygen mass transfer control does not occur until higher temperatures or an alternate low temperature chemical reaction is occurring.

The calculated effect of initial particle size on the combustion temperature, considering only the FeO/SO_2 overall reaction is shown in Figure 7.10. The model predicts that combustion is strongly dependent on particle size with a $30\mu m$ particle calculated to react about 5 times as fast as a $65\mu m$ particle. Cooling is also predicted to be considerably enhanced for the smaller particles as indicated in Figure 7.8b.

The calculated effect of using a particle emissivity of 1 and of a particle diameter expansion of x2.5 (at peak temperature) is also shown in Figure 7.10 for a 65 μ m particle. The most apparent effect of increasing the particle emissivity from 0.7 to 1 is to reduce the maximum calculated temperature from ~2650 to ~2530K. Although less noticeable the cooling rate increases by ~16% as indicated in Figure 7.8b. In this case the predicted radiative cooling accounts for only ~40% of the total at 2500K and the emissivity effects are consequently proportionally reduced and diminish rapidly as the particle cools. Considering the particle to expand by a factor of 2.5 at the termination of reaction, results in over a four fold increase in cooling rate from ~8 to ~34 $\times 10^4$ K/s at 2400K. The large effect of particle expansion is the result of enhancement of both the radiative and conductive cooling (see Equation 7.10).

To examine whether or not emissivity changes or particle expansion could account for the large energy increase observed at peak temperature the calculated heating and cooling rates for a number of experimentally measured combustion pulses are shown Figures 7.11. To aid in the comparison cooling is assumed to begin as soon as the calculated particle temperature reaches the experimentally measured maximum. The particle heating rates for both the *FeO/SO₂* and *Fe/SO₂* reactions are shown, as are the calculated cooling rates for both expanded and unexpanded particles. The particle size and expansion determined from the experimental results, using an emissivity estimate of 0.7 are used as the inputs to the heat balance. In general the measured heating rates are typically intermediate to those calculated for *FeO* ($2 - 4 \times 10^4$ K/s) and *Fe* ($< 0.5 \times 10^4$ K/s) formation. Often the rate for the final 1-2ms of heating (which corresponds to the experimentally observed large energy increase) increases to nearer that predicted by the wustite reaction.

The measured cooling rate is typically intermediate to that predicted considering and neglecting particle expansion. The measured cooling rate for the combustion pulse shown in Figure 7.11a, at ~16.4 $\times 10^4$ K/s, is identical to that calculated for a particle of

69 μm in diameter which expands by the measured value of 1.8 at the onset of cooling. This is much greater than predicted with the maximum possible unexpanded radiative cooling rate (ie emissivity one) of $\sim 9.3 \times 10^4 \text{K/s}$ (see Figures 7.8b). For the combustion pulses shown in Figures 7.11b and c the measured cooling rates are less rapid than that predicted considering expansion, and the possibility of the energy increase being the result of an emissivity change cannot be dismissed immediately. The large increase in energy observed experimentally would, however require a corresponding increase in particle emissivity, and therefore, the initial emissivity during heating would have to be very low ($\sim 0.1-0.2$). Such a low emissivity would however result in the calculated diameter of the reacting particle (see Appendix 2, Equation A.2.8) being $\sim 1.8-3$ times greater than the value determined using an emissivity of 0.7. From the heat balance the predicted cooling rates of such large particles would then tend to be lower than those measured experimentally. This apparent anomaly arises because the pyrometer only measures the radiative component, but variations in apparent particle diameter also affect the convective/conductive cooling component and the particle mass. Although the apparent particle diameter calculations are open to large errors, a considerable systematic error would also have to exist in the initial pyrometer calibration for emissivity changes to be the cause of the large energy increase observed with A3 combustion pulses. These calculations therefore strongly suggest that the large energy increase observed experimentally is the result of cenosphere or particle expansion.

The predicted results for particle combustion in oxygen are shown in Figure 7.12. Over a comparable temperature range the measured and calculated heating rates are similar ($\sim 20 - 40 \times 10^4 \text{K/s}$). The maximum temperatures calculated considering FeO/SO_2 and $\text{Fe}_3\text{O}_4/\text{SO}_2$ reactions is $\sim 4800\text{K}$, much higher than the 3000-3400K maximum observed experimentally with both the O3 and higher oxygen concentration A3 combustion pulses. This discrepancy can be accounted for by vaporisation reactions at, or above the boiling point of iron, which result in the disintegration of the particles, and

which have not been considered in the reaction model. To allow comparison, the particles were considered to cease reaction, and begin cooling immediately on reaching a temperature of 3300K (the boiling point of iron).

Figures 7.13a to c show the measured and calculated results for three different O₃ combustion pulses. The measured heating rates shown ($\sim 20 - 40 \times 10^4$ K/s see Figure 6.57) are similar to those predicted for the Fe/SO_2 and FeO/SO_2 reactions. The experimentally measured cooling rates shown in Figure 7.13 appears comparable to those predicted, despite the disintegration of the droplets casting doubt on what is actually being measured by the pyrometer. Measured cooling rates greater than $\sim 20 \times 10^4$ K/s are often recorded (see Figure 6.57) and are probably due to the disintegration of the particles, prior to the completion of reactions.

The maximum temperature predicted by the combustion model as a function of oxygen concentration (considering the different overall reactions and the heat balance), and the experimentally measured peak temperatures (from Section 6.4.2) are shown in Figure 7.14. At higher oxygen concentrations the very high temperatures predicted considering the wustite/ SO_2 reaction can be seen. At lower oxygen concentrations there is reasonable agreement between the experimental temperature and those predicted by the model considering this reaction. Although it is not possible to predict the maximum combustion temperature a priori it is still possible to examine the effect of oxygen concentration on combustion through the change in heating rates observed experimentally at the maximum temperature. The oxygen dependence of the heating rate at maximum combustion temperature was obtained from the experimental data presented in Section 6.4.2 and is shown in Figure 7.15. For comparison, the heating rate calculated for a 65 μ m diameter particle considering the Fe_3O_4/SO_2 overall reaction for peak temperatures below 2400K, and the FeO/SO_2 reaction for peak temperatures above 2400K is also shown. At 10% oxygen (and therefore probably below) the calculated particle temperature just achieves the experimentally measured maximum. The relatively modest dependence of

the heating rate on oxygen concentration between ~10 and 30% oxygen, corresponds to the region over which the large increases in maximum temperature were observed experimentally. Over this region the measured temperatures are close to the maximum predicted (from mass balance considerations) where the calculated rates of heating are beginning to slow. Above this oxygen concentration the maximum temperatures measured remains relatively constant at 3300K however the calculated heating rate increases rapidly and approximately linearly. Only the experimental pulses where a considerable period of heating was observed have been shown in Figure 7.15; and the heating rates were determined only from the linear portion of the combustion pulses ignoring the final increase in heating rate sometimes observed (see Figure 7.10). Owing to these criteria the heating rates tend to be lower than those shown in Figure 6.73a, despite being calculated from the same data.

The agreement between the calculated and experimental heating rates shown in Figure 7.15 appears reasonable for oxygen concentrations below 50% with the most significant increase in heating rate occurring between 30 and 50% oxygen. At higher oxygen concentrations the measured heating rates tend to be lower than predicted, but there is some scatter in the results and it is less clear whether increasing heating rates are generally observed. In pure oxygen the measured heating rates increase to a value near those calculated (see Figure 6.57).

The increasing initial cooling rate with increasing particle temperature, as observed in Figures 6.73b, is to be expected if all chemical reactions cease on reaching peak temperature. The cooling rates of all the A3 combustion pulses have been plotted in Figure 7.16, as a function of temperature (only the cooling rates from the A3 combustion pulses have been plotted, due to the disintegration observed with O3-type combustion). For reference the calculated cooling rates of a 65 μm diameter droplet considering both no inflation and a x2.5 increase in diameter are also shown. Most of the measured cooling rates lie between the two curves, suggesting that particle expansion normally occurs.

Considerable inaccuracies, however, exist in the experimental results and derived properties. As a result a poor correlation was obtained between predicted cooling rates calculated by incorporating the experimentally determined particle size and inflation and those measured.

Through this simple reaction model the combustion behaviour of both the A3 and O3 pulses observed during iron sulphide combustion appears explainable. The similarity of the predicted and measured heating rates suggests that the reactions are gas phase oxygen mass transfer controlled, at least at the higher temperatures. The calculated cooling rates were also in reasonable agreement with the experimental results and suggest that the cooling is enhanced by cenosphere formation rather than through emissivity changes. The model is, however, unable to predict the maximum combustion temperature especially at high oxygen concentrations where reactions terminate in disintegration. The heat balance suggests that the overall reaction proceeds through the formation of iron oxide and sulphur dioxide. A portion of the reaction could however occur through the formation of metallic iron or sulphur monoxide.

7.3.2.3 Overall Pyrite/Pyrrhotite Reaction Model

A mechanism based on the formation of an iron oxide surface layer and, at higher oxygen concentrations, disintegration due to superheating and vaporisation, appears capable of explaining most of the experimental results and the different characteristics of the A3 and O3 combustion pulses. A schematic diagram of the postulated reaction mechanism for iron sulphide combustion in varying oxygen concentrations is given in Figure 7.17. It is considered that iron sulphide particles initially heat rapidly, with, in the case of dense pyrrhotite, little oxidation occurring (1b). In the case of pyrite thermal decomposition occurs to produce porous pyrrhotite and labile sulphur (1a). Despite the overall heating and melting of pyrrhotite taking much longer than pyrite, both species eventually form a *Fe-S* melt (stage 2). The *Fe-S* droplet reacts very rapidly under conditions of gas phase oxygen mass transfer control forming a miscible *Fe-S-O* melt and

sulphur dioxide. The overall chemical reactions probably involve the formation of iron oxide and SO_2 but there is a possibility that at higher temperatures an iron rich melt and sulphur monoxide (as an intermediate species) form. The heating rate and maximum temperature reached is dependent on the oxygen concentration. At lower oxygen concentrations (<75%), sulphur concentrations in the melt decline sufficiently during combustion that liquid phase mass transfer becomes significant and the oxygen front contacts the surface, quickly reacting to form an oxide coating (stage 3b). Sulphur however is still diffusing outwards and when this S comes in contact with the oxide it reacts to form a gas which inflates the cenosphere (stage 4b). Any reactions then cease and rapid cenosphere cooling occurs. During cooling small amounts of molten material is sometimes ejected (stage 5b). At higher oxygen concentrations the particle heating rates increase and the particle reaches temperatures in excess of 3300K (the boiling point of iron) with a relatively high sulphur content. Due to super heating of the liquid and internal vaporisation (stage 3a) complete particle disintegration occurs (stage 4a) as seen in O₃ combustion pulses.

7.3.3 Commercial Concentrates

It is difficult to quantify the results of the commercial concentrates due to the large and unknown range of chemical/mineral compositions and sizes of the individual particles. This problem is worse than the case for the pure mineral feeds owing to the large proportion of agglomerates in the commercial concentrates and their tendency to disintegrate on heating. The combustion of individual mineral grains and agglomerates consisting primarily of a single mineral species appear adequately described by the mechanisms presented for the pure minerals. This discussion will thus be limited to the effects of mineral and gas composition on the mechanism of agglomerate combustion.

The reaction of agglomerate particles is strongly dependent on composition and in consequence on the specific mineral composition of commercial concentrate from which they are formed. The larger amount of iron sulphide and its presence as the more reactive

pyrite (rather than pyrrhotite), in Brunswick concentrate is evident, in air, as earlier combustion than with Sullivan concentrate. The porosity of the agglomerates would be expected to enhance gas-solid reactions. On melting however, the gas-liquid reactions should only depend on the overall composition of the melt. Agglomerate combustion differs from that of the pure minerals in that the oxidation occurs from a multicomponent lead, iron and possibly zinc sulphide melt. The activities of the species in the melt and their heats of reaction will be important. The results also indicate the importance of the vaporisation of lead species from the melt, both to the reaction rate and combustion temperature, and also phenomenologically through its involvement in disintegration.

The results suggest that the gas-solid reactions of the individual grains within the agglomerates, during particle heating, are similar to those observed with the pure minerals. Reactions probably occur between the individual grains, either at their interface or through vapour phase transport in the interstices. Hsiao et al. [45] reports roast reactions (Equations 2.4 and 2.5) between solid lead oxides/sulphates and lead/iron/zinc sulphides occurs in pellets. Both chemical and physical changes, such as thermal decomposition, occurring during particle heating probably encourage the agglomerates to disintegrate due to volume change, stresses etc. It is evident from the SEM studies that melting does not occur homogeneously (see Figure 6.82a). Individual grains are gradually incorporated into the melt depending on their location, mineralogy, temperature etc. During this period the combustion behaviour could be quite different than if a homogeneous melt had formed.

It is probable that melting within the agglomerates, between touching grains, occurs at relatively low temperatures, with miscible $FeS-PbS$ and $ZnS-PbS$ melts forming (see Figure 2.5 [2]). The experimental results however suggest ZnS grains remained unreacted in the $Pb-Fe-S$ melts (see Figure 6.82a) possibly due to slow dissolution kinetics. It is probable that similar to the case for galena metallic lead formation is the result of a roast reactions between the oxides and sulphates formed by gas-solid reactions and the

sulphide melt (Equations 2.4 and 2.5). Chemical analysis indicate a few percent of sulphate (probably associated with the lead species) is present in the feed, and the porous nature of the agglomerates would also tend to encourage sulphate (or oxide) formation during heating. From the superimposed *Fe-S-O* and *Pb-S-O* systems at 1500K shown in Figure 7.18 the lower stability for the *FeS* phase as compared with the *PbS* can be seen. For the pure phases, iron sulphide oxidation is favoured and also its reduction of lead oxide (Equation 7.12).



$$\Delta G_{R7.12\ 1500K} = -439\ kJ$$

$$\Delta H_{R7.12\ 1500K} = +664\ kJ$$

The similar quantities of metallic lead observed during the early stages of combustion of both galena and the commercial concentrates suggests that a similar reaction route for metallic lead formation is occurring in both cases, and therefore the presence of iron sulphide is not important to the reaction. As with galena combustion metallic lead formation could also occur directly through sulphur vaporisation [34,48] (see Equation 7.1), or through back reaction between the *PbO/PbSO₄* vapour phase reaction product and the melt.

The heat generated by the initial preferential iron oxidation would be expected to result in considerable lead species vaporisation. As the particle temperature exceeds the boiling point of the *PbS* (1609K) an expanding cloud of lead sulphide vapour is produced similar to that observed during galena combustion. In such a case the reaction temperature would be limited by vaporisation which in turn would be limited by heat generation. During this period of vaporisation and gas phase reaction, oxidation of the liquid melt surface should cease. Only when the vaporisation reactions had abated would direct oxidation of the melt surface recommence. These later gas-liquid reactions would also tend to result in the vaporisation of the remaining lead species (*Pb* or *PbO*) in the melt.

The pyrometer results clearly indicate that the vaporisation of lead species from the multicomponent melt, during the early stages of reaction, is very important. This is most evident with the Sullivan A2 combustion pulses in Figures 6.13 and 6.15. For Brunswick combustion in air (see Figures 6.14 and 6.16), and oxygen combustion pulses in general, the larger number of disintegrations and more intense reactions probably result in internal lead species vaporisation. The SEM electron micrographs and x-ray maps in Figure 6.86 (for the product of Sullivan combustion in oxygen) show the presence of a small predominantly *PbS* droplet within the iron-lead sulphide melt and an associated void, and possibly indicates a particle quenched immediately prior to disintegration.

Analysis of the reaction products shows very little lead remains in the final thick walled hollow shells, which are primarily iron oxide. These thick-walled hollow spheres and sink-holes, most commonly observed in the product of Sullivan combustion in air (see Figure 6.40), are not thought to be the result of material ejection. It is thought that these large central voids form through the coalescence of the interstices between the agglomerate grains as melting proceeds. Growth of these voids could then result from gas generating reactions such as lead vaporisation.

With Brunswick it is possible the particles with shattered skins (Figure 6.83a) or many blow holes (6.82d) are the product of relatively low temperature ejections due to the melting and reaction of a sulphide core within a solid oxide shell as proposed by Kim and Themelis [138] for chalcopyrite combustion. Higher temperature material ejection observed probably occur through internal gas generation and disintegration of an *Fe-Pb-S* melt. The more intense reactions and particle disintegrations observed during combustion in oxygen are also suggested by the form of the reaction products which tend to be small spheres (<25 μm) of iron oxide. The intense heating of the agglomerates during reaction in oxygen appears to result in surface melting during the early stages of reaction as

shown in Figure 6.86c. Surface melting possibly prevents the disintegration of the agglomerates during particle heating, and the enclosing of unreacted lead species would result in internal gas generation and particle explosion.

A schematic diagram of the proposed reaction mechanism for the combustion of agglomerates found in *PbS-FeS/FeS₂-(ZnS)* commercial concentrates is given in Figure 7.19. On entering the furnace the particles are heated rapidly by the gas. For combustion in air considerable disintegration occurs with many small particles being detached and rapidly combusting (stage 1b). The porosity of the agglomerates also encourages sulphation reactions. The particles rapidly reach a temperature at which melting can occur through the gradual fusion of different mineral grains. Gradually a melt is formed within which solid *ZnS* grains and bubbles are present (stage 2b). It is probable metallic lead formation occurs through a roast reaction between lead oxides/sulphates present and the now molten sulphides. The iron sulphide rapidly oxidises, with the intense gas-liquid reactions probably being gas phase oxygen mass transfer controlled. The heat generated and increasing droplet temperature result in lead sulphide vaporisation (stage 3b). As the temperature exceeds the boiling point of *PbS* (~1609K) intense vaporisation occurs resulting in the formation of a reacting, outwardly expanding vapour cloud similar to that postulated for galena combustion. For agglomerates of higher iron content the intensity of the reactions result in internal gas generation and material ejection, and it is probable the shattered shells sometimes observed in the product are formed at this stage. During the period of an expanding *PbS* vapour cloud direct oxidation of the melt would cease, recommencing only after lead sulphide vaporisation stops. This later oxidation would tend to vaporise any lead species remaining in the melt. The zinc sulphide gradually dissolves during the later stage of reaction and also further oxidation of the iron to hematite and zinc ferrite (*ZnFe₂O₄*) occurs. In the cases where particle disintegration does

not occur internal interstices and bubbles produced by reaction and vaporisation tend to coalesce to form a central void (stage 4b). On cessation of reaction sink holes sometimes collapse into the lower pressure of the cooling void.

During combustion in oxygen the initial reactions are so intense that the surface of the agglomerates melt very rapidly (stage 1a). The reaction and thermal decomposition of the grains trapped within the molten shell result in material being ejected and the rapid disintegration of the particle (stage 2a). Massive vaporisation and combustion of *PbS* follows disintegration, and the molten debris quickly oxidises to form small iron oxide spheres and lead sulphate fume.

Of special importance to flash smelting is whether the particle interactions encourage metallic lead formation or lead vaporisation and fume production. There is no indication from the present study that the presence of mineral species other than galena enhance the formation of metallic lead; however they influence the reaction rate and therefore the required shaft height. If, as the results suggest, the formation of metallic lead is the result of a roast reaction between the oxides/sulphates formed during particle heating, and the sulphide melt, the amount of reaction prior to ignition will be of importance to the quantity formed. The quantity of fume produced will be dependent on the concentrate mineral composition through the heat of reaction of the feed material and the amount of lead vaporised. The present results for agglomerate combustion suggest that the reaction temperatures are limited by lead vaporisation, which is in agreement with the industrial and pilot plant data where higher heat inputs tend to result in greater lead vaporisation as opposed to increased furnace temperatures [28,27]. Similar temperatures but shorter combustion distances and higher dust recycle were observed in pilot plant studies with Brunswick as compared to Sullivan concentrate [27]. This would suggest that the amount of lead vaporised could be minimised by adjusting the feed composition such that excess heat input and therefore lead vaporisation is minimised.

Such operation may also encourage gas-solid reactions prior to melting. The operation of the Portovesme Kivcet plant [8] seems in agreement with low recycles being obtained with low heat feed materials.

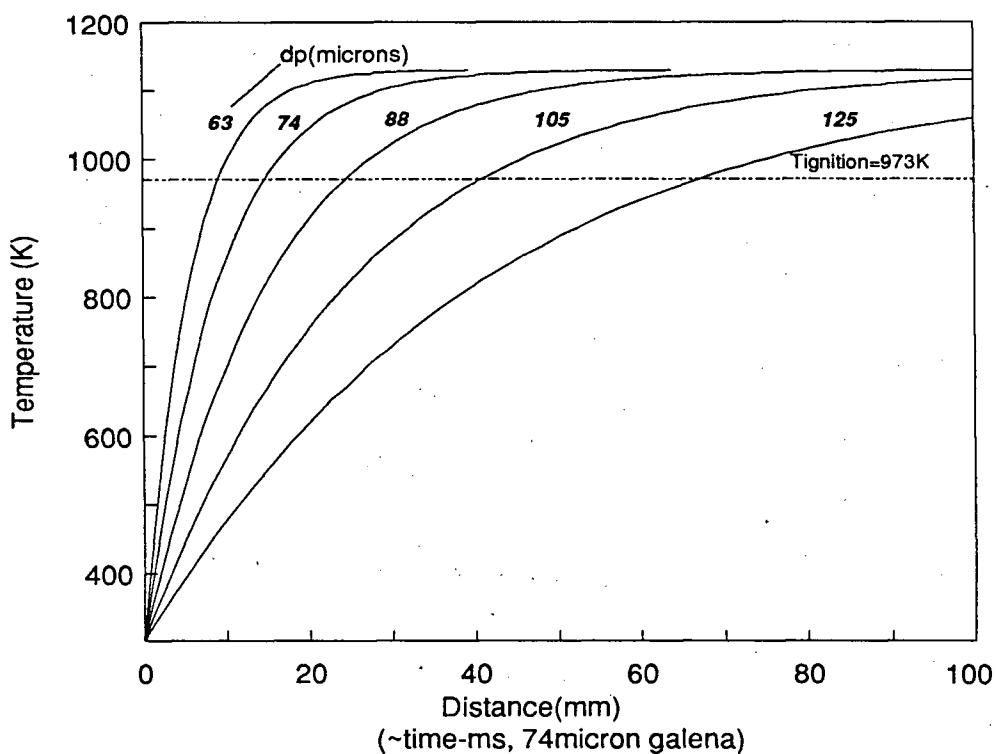


Figure 7.1a Calculated heating rates for various size particles of density equivalent to galena ($\rho=7500 \text{ kgm}^{-3}$, $\epsilon=0.7$ and $T_{\text{FURNACE}}=1130\text{K}$).

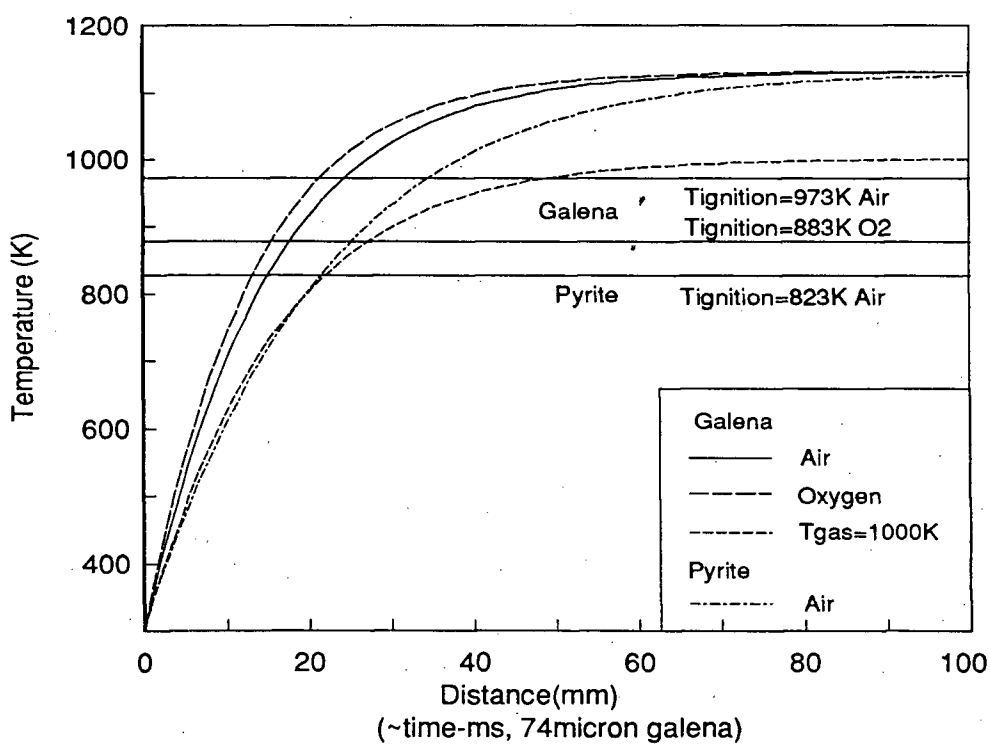


Figure 7.1b Calculated heating rates for particles of different densities, different furnace gas temperatures and furnace gas compositions ($d_p=74\mu\text{m}$, $\rho=7500 \text{ kgm}^{-3}$, $\epsilon=0.7$ and $T_{\text{FURNACE}}=1130\text{K}$).

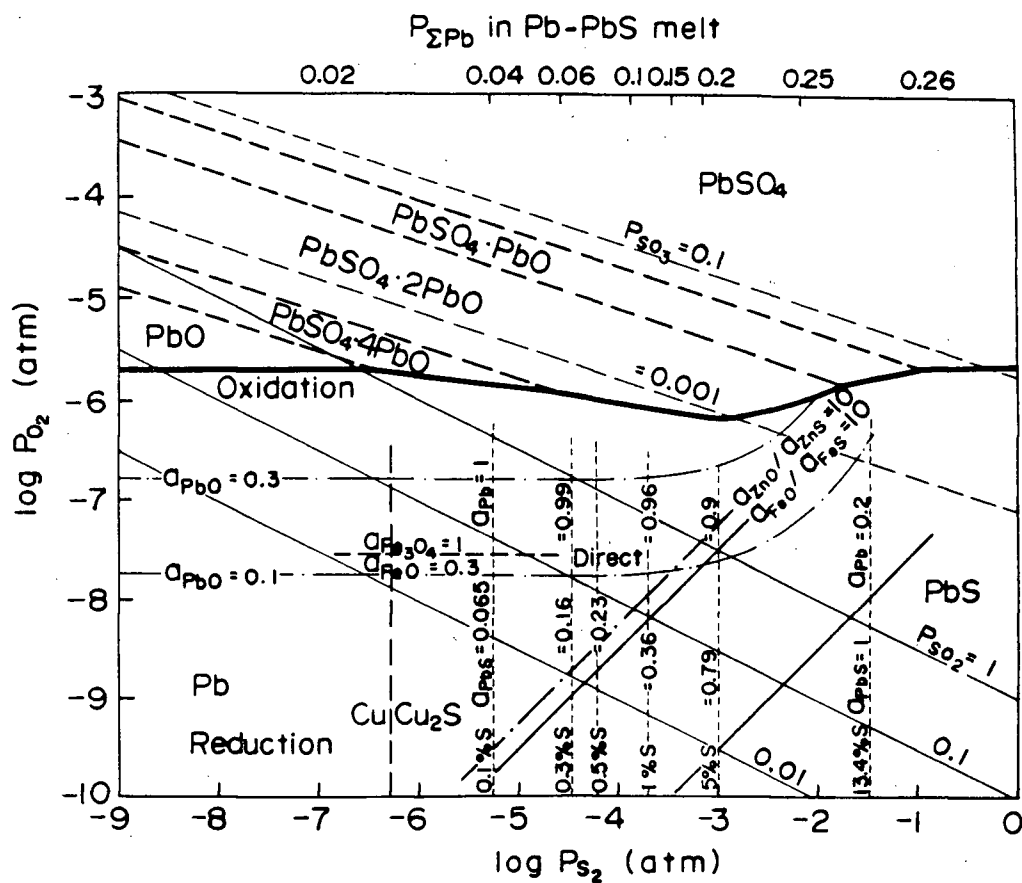


Figure 7.2 The sulphur-oxygen potential diagram for Pb-S-O system at 1473K (from Yazawa [38]).

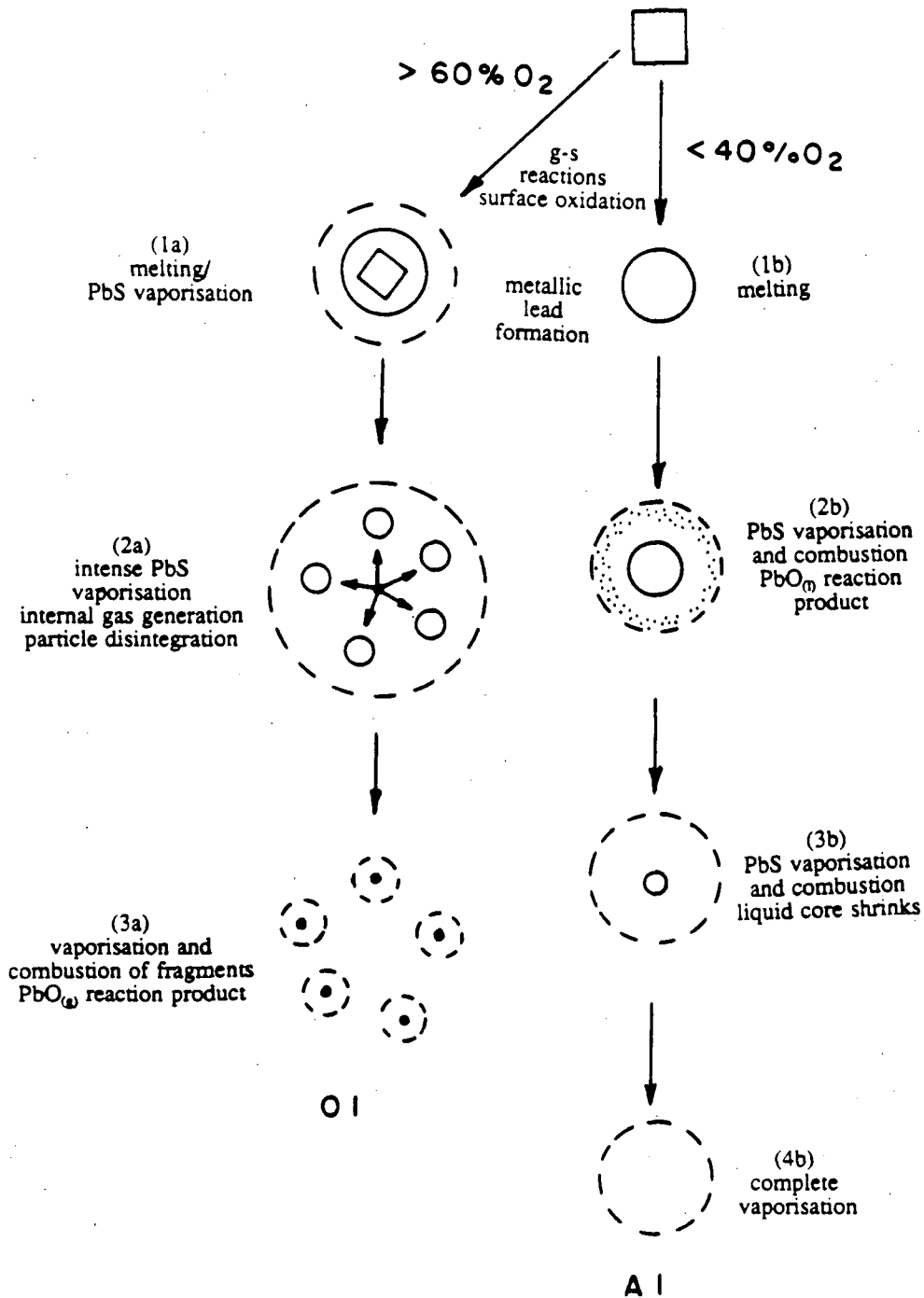


Figure 7.3 Schematic diagram of the galena combustion mechanism in air and oxygen at 1130K.

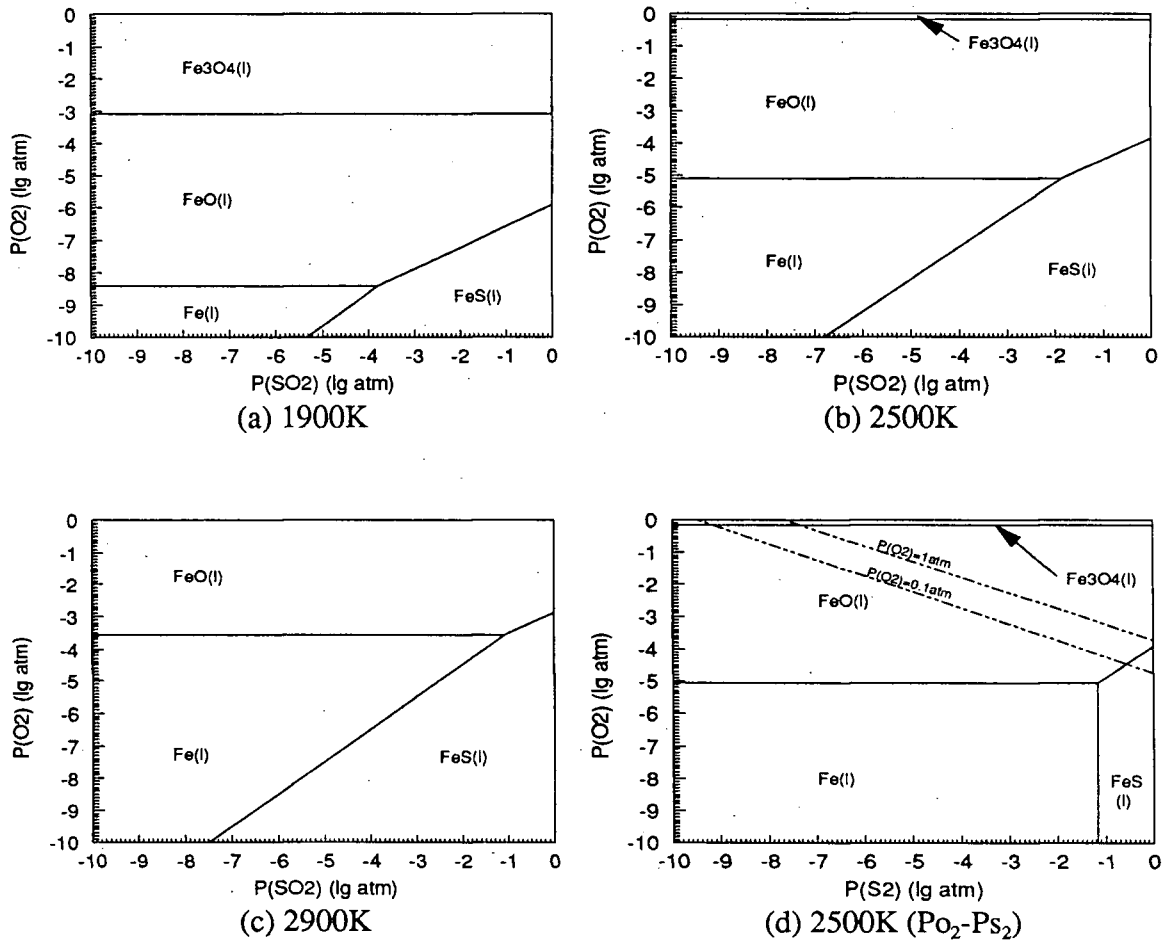


Figure 7.4 Oxygen-sulphur dioxide/sulphur potential diagrams for the Fe-S-O system at several temperatures (from F*A*C*T [30]).

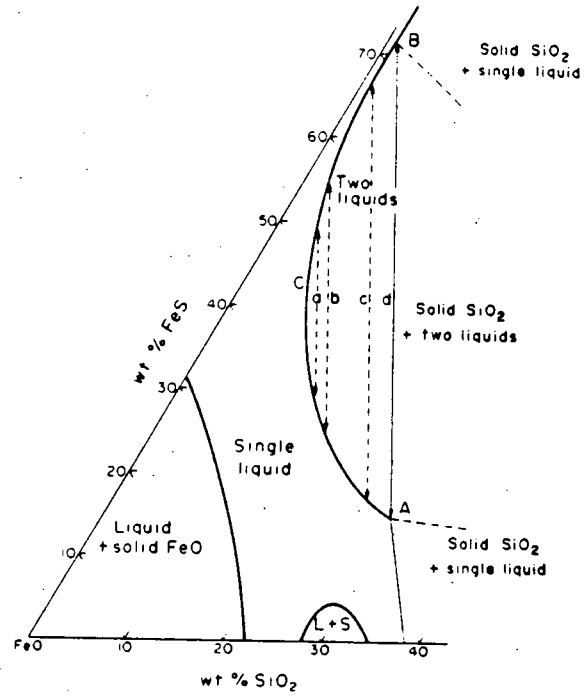
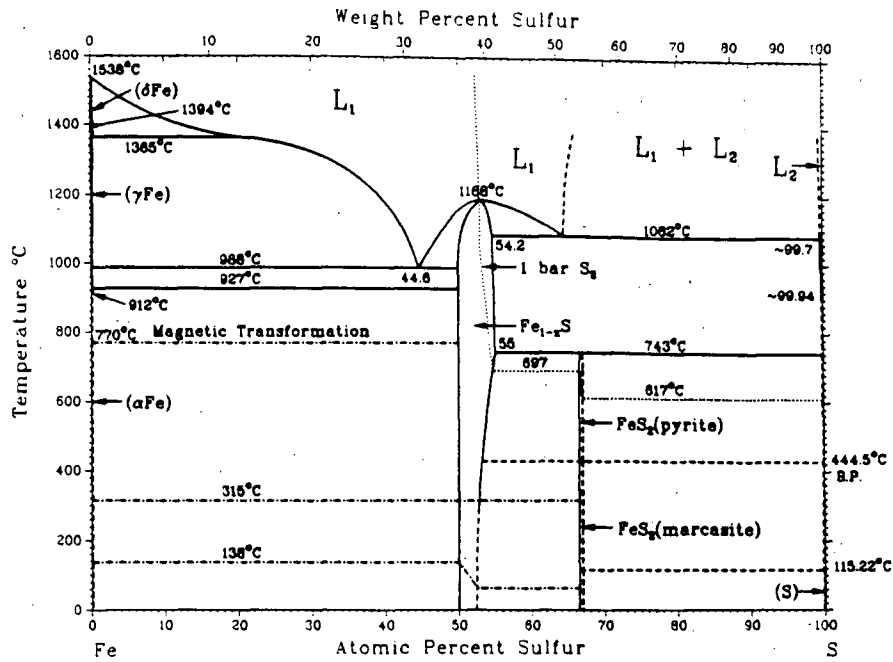
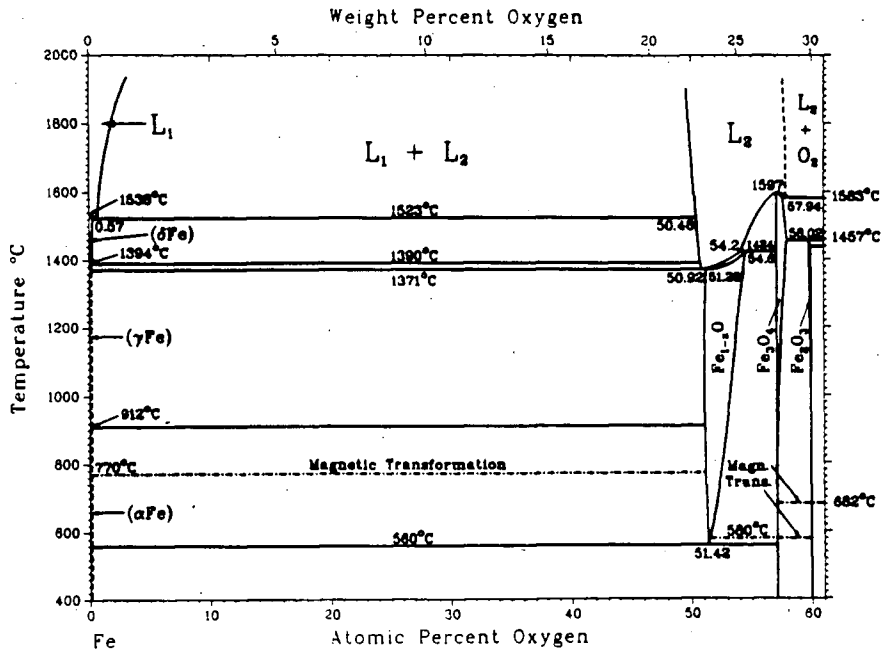


Figure 7.5 The FeS-FeO-SiO₂ system ternary phase diagram at 1473K (from Biswas et al. [134])



(a)



(b)

Figure 7.6 Binary phase diagrams a) Fe-S and b) Fe-O systems (from [136]).

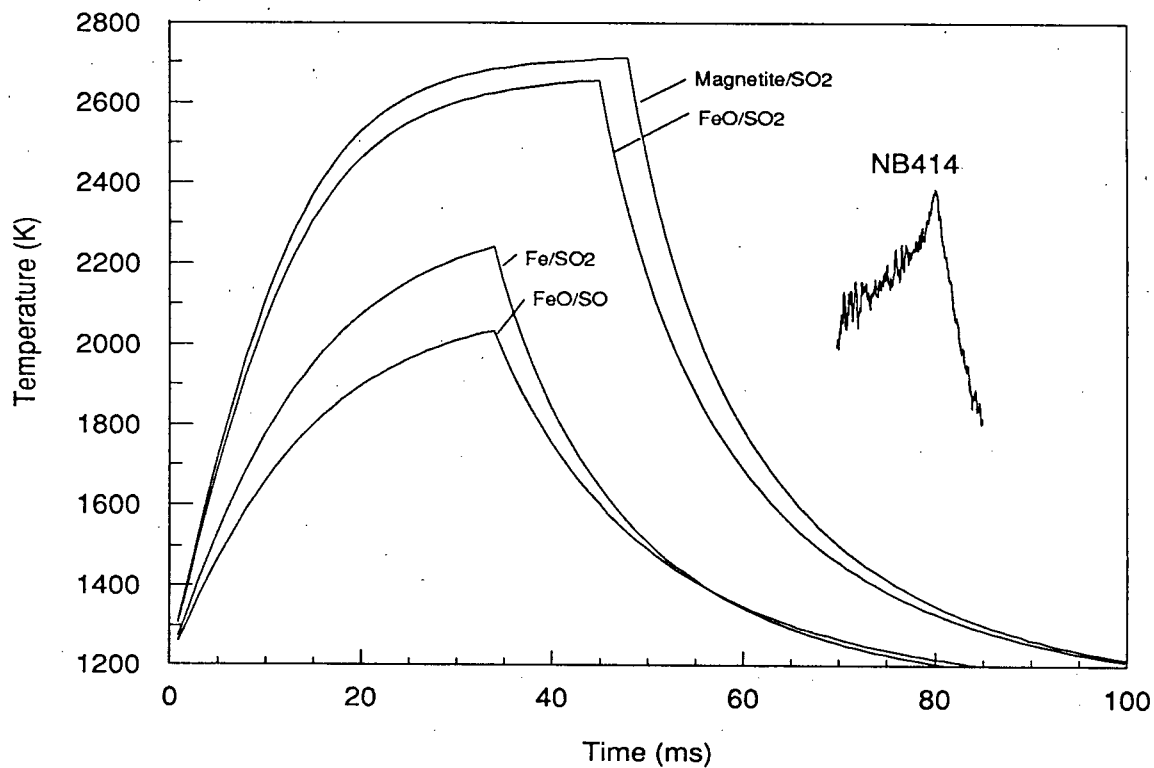


Figure 7.7 Calculated temperature histories for 65 μ m FeS particles combusting in air ($T_{\text{FURNACE}} = 1130\text{K}$, $\epsilon=0.7$) considering the formation of different reaction products (after Jorgensen [79]).

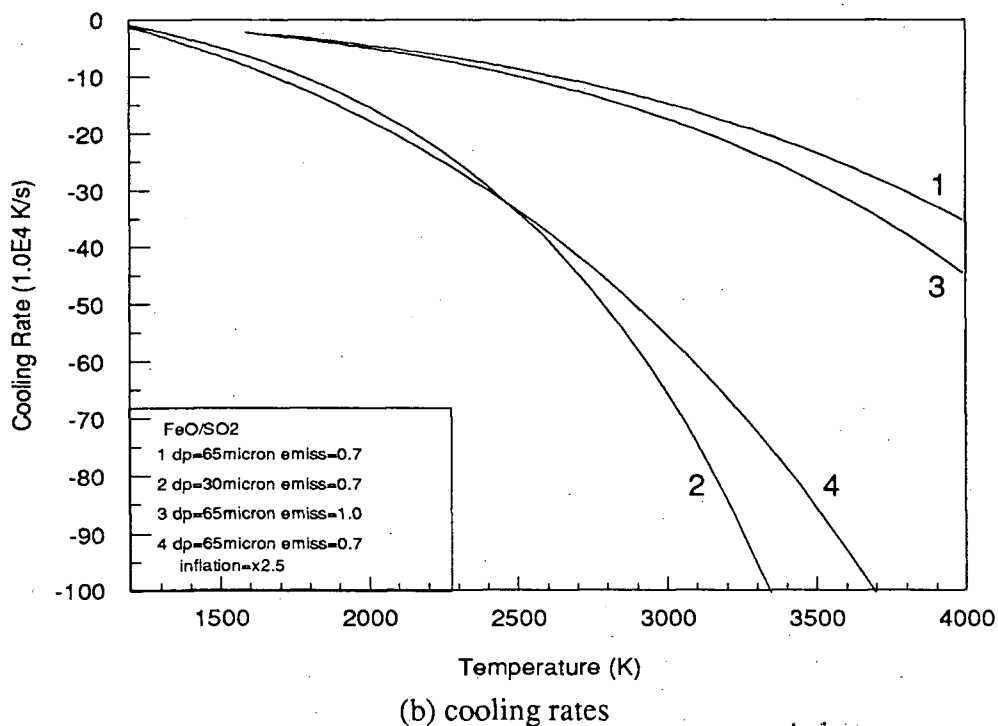
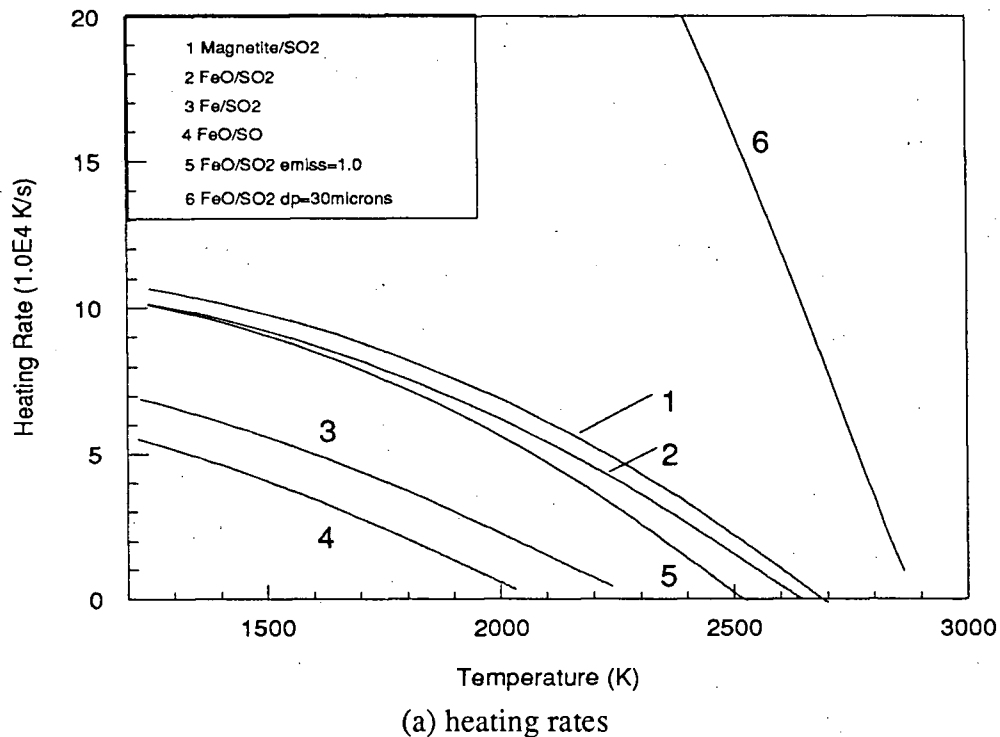


Figure 7.8 Calculated heating and cooling rates as a function of particle temperature for variations in reaction mechanism, particle emissivity and diameter for particles combusting in air at $T_{\text{FURNACE}} = 1130\text{K}$ and $\epsilon=0.7$ (unless otherwise stated).

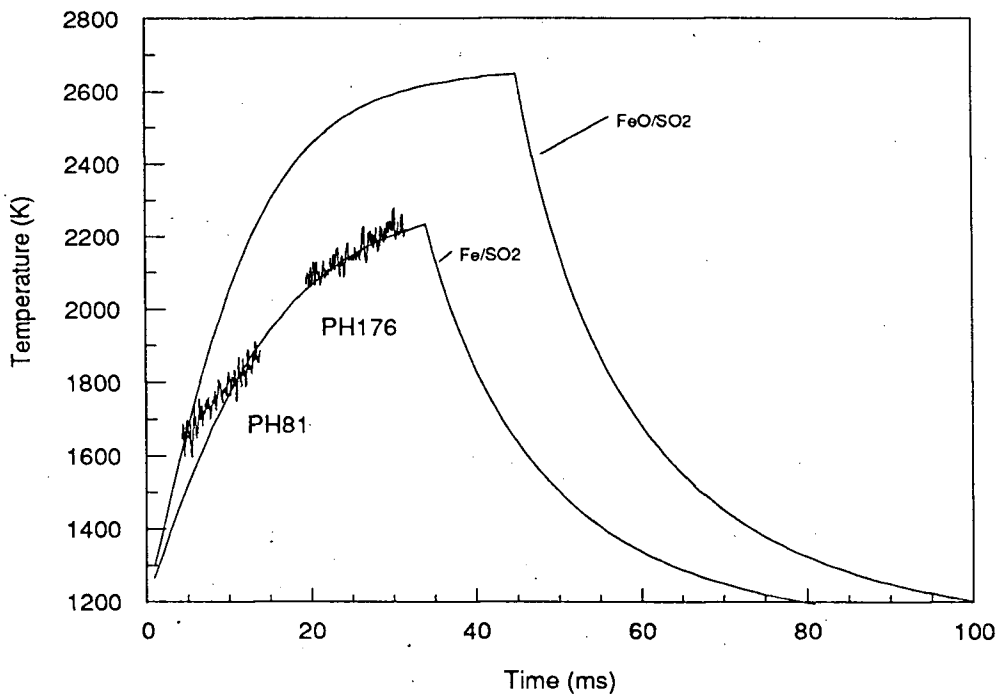


Figure 7.9 A comparison of calculated thermal histories for the combustion of FeS particles in air ($d_p=65\mu\text{m}$, $T_{\text{FURNACE}} = 1130\text{K}$ and $\epsilon=0.7$) and measured A3I combustion pulses for 74-88 μm pyrrhotite particles.

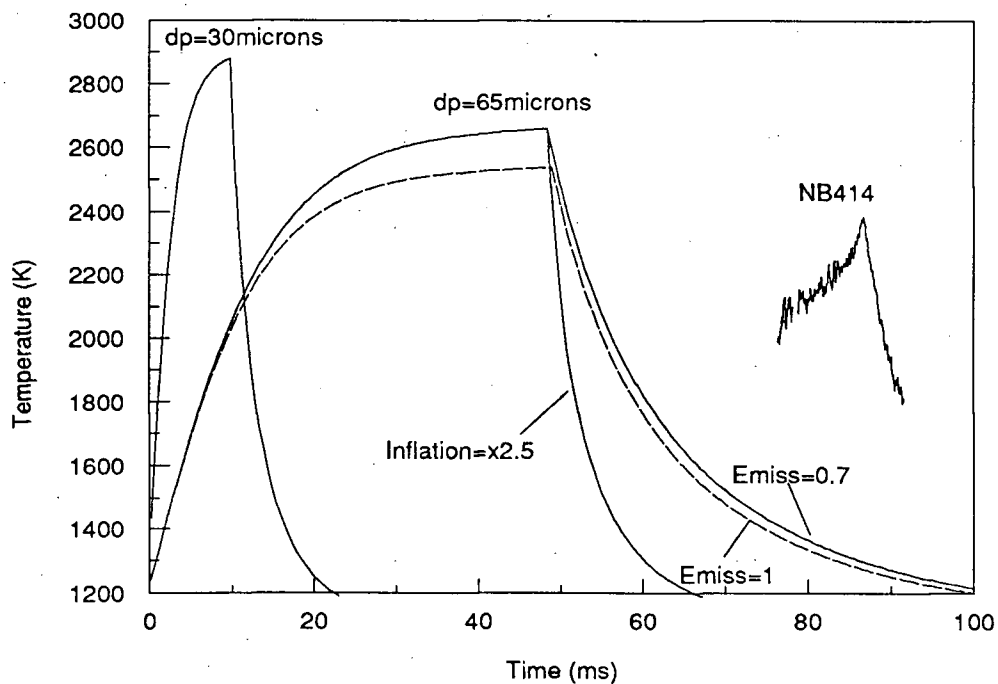


Figure 7.10 Calculated thermal histories for 30 and 65 μm FeS particles combusting in air ($T_{\text{FURNACE}} = 1130\text{K}$, $\epsilon=0.7$) and the effect of a) emissivities variations ($\epsilon=0.7$ and 1) and b) $\times 2.5$ diameter increase on cooling.

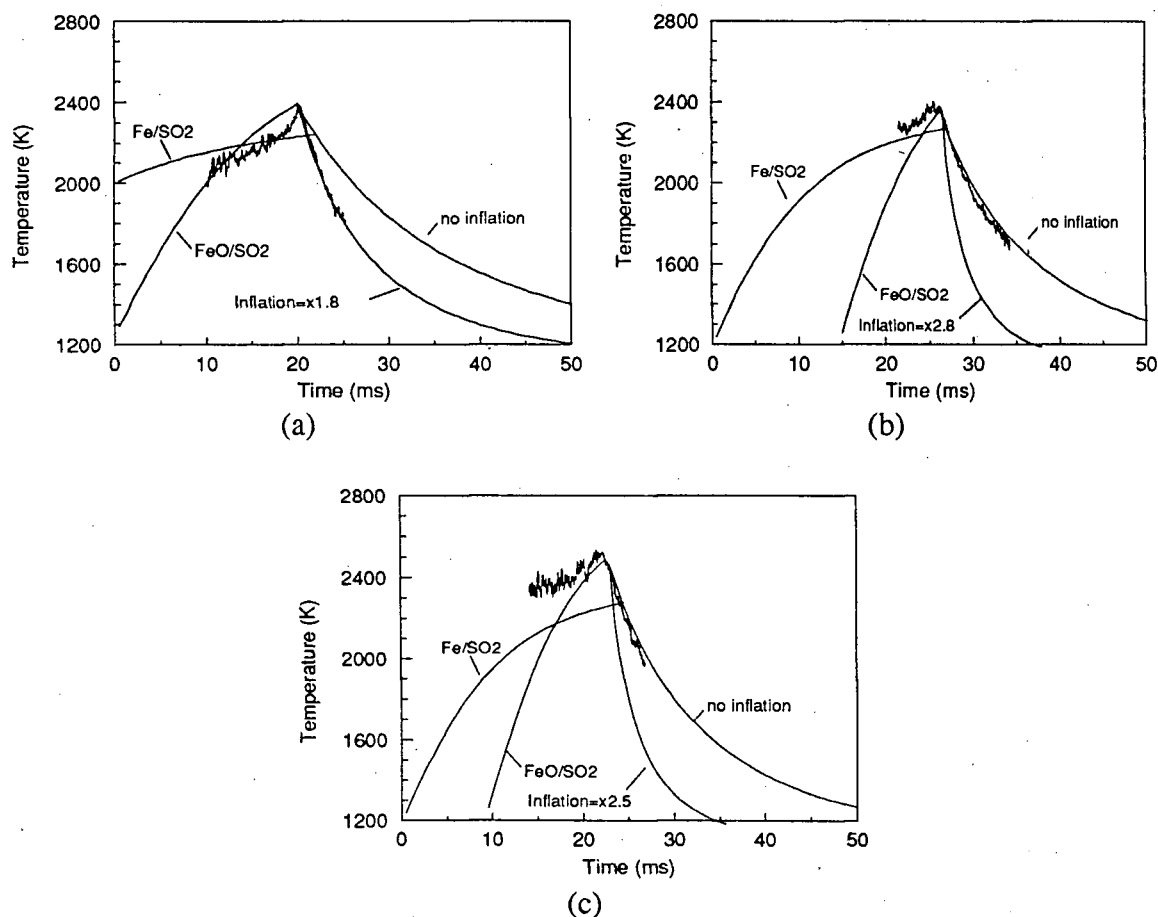


Figure 7.11 Measured and predicted combustion temperatures for specific FeS particles in air ($\epsilon=0.7$) (a) NB414 $d_p=69\mu\text{m}$ inflation $\times 1.7$, (b) PY123 $d_p=55\mu\text{m}$ inflation $\times 2.8$ and (c) PY201 $d_p=53\mu\text{m}$ inflation $\times 2.5$.

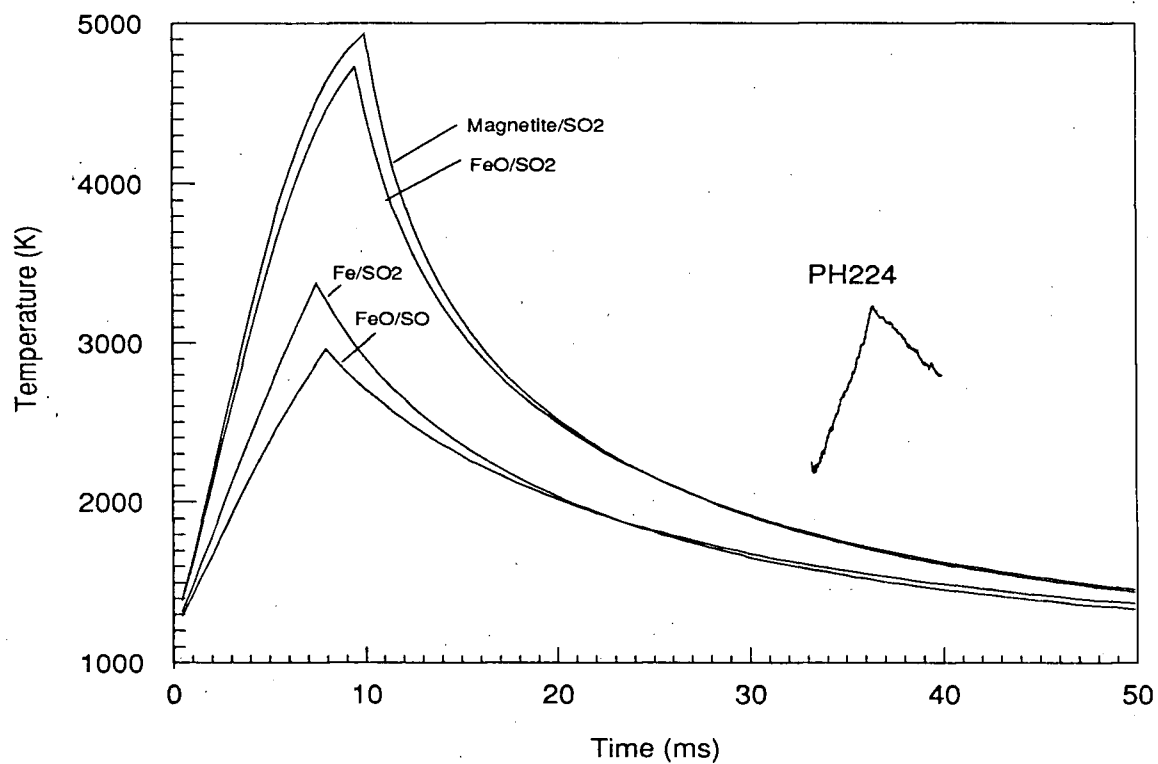


Figure 7.12 Calculated temperature histories for 65µm FeS particles combusting in oxygen ($T_{\text{FURNACE}} = 1130\text{K}$, $\epsilon=0.7$) considering the formation of different reaction products.

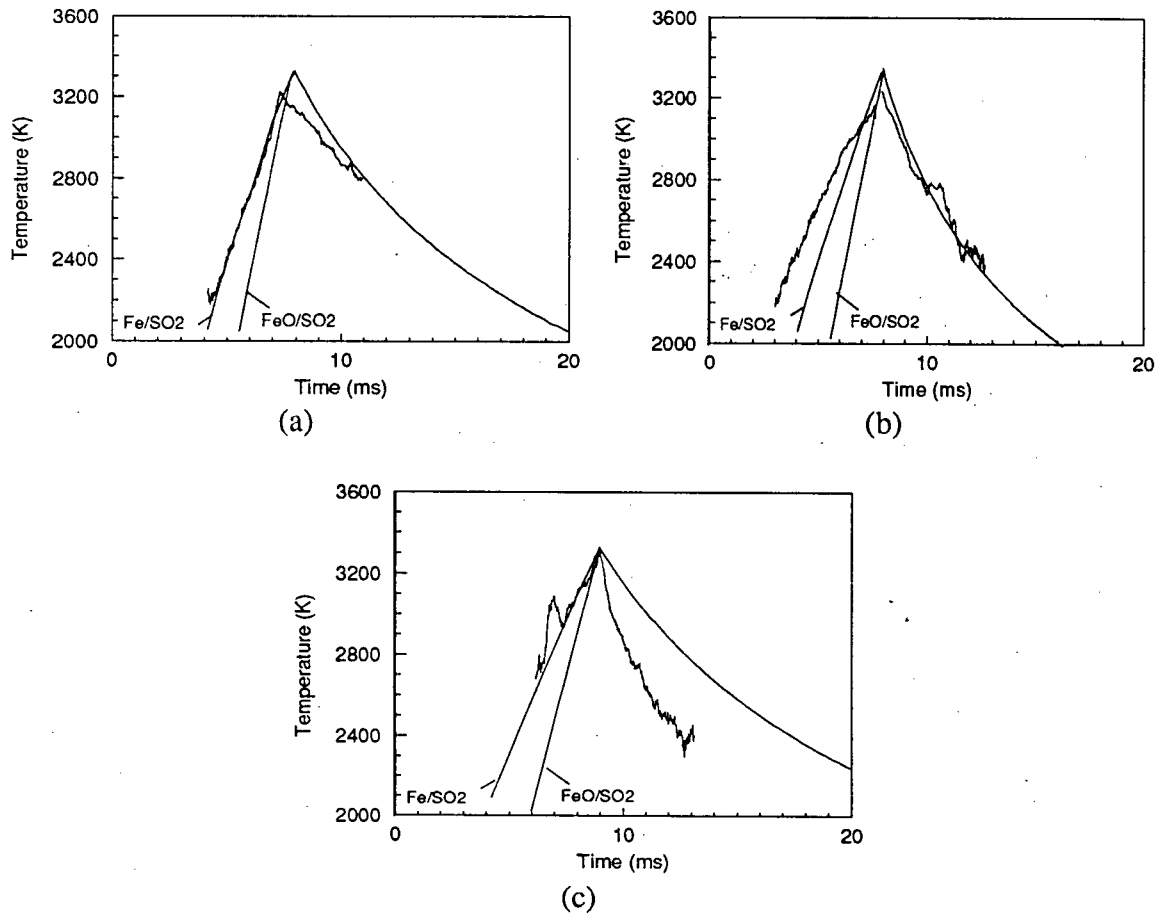


Figure 7.13 Measured and predicted combustion temperatures for specific FeS particles in oxygen ($\epsilon=0.7$, x1 inflation) (a) PH224 $d_p=60\mu\text{m}$, (b) PH222 $d_p=61\mu\text{m}$ and (c) PY216 $d_p=68\mu\text{m}$.

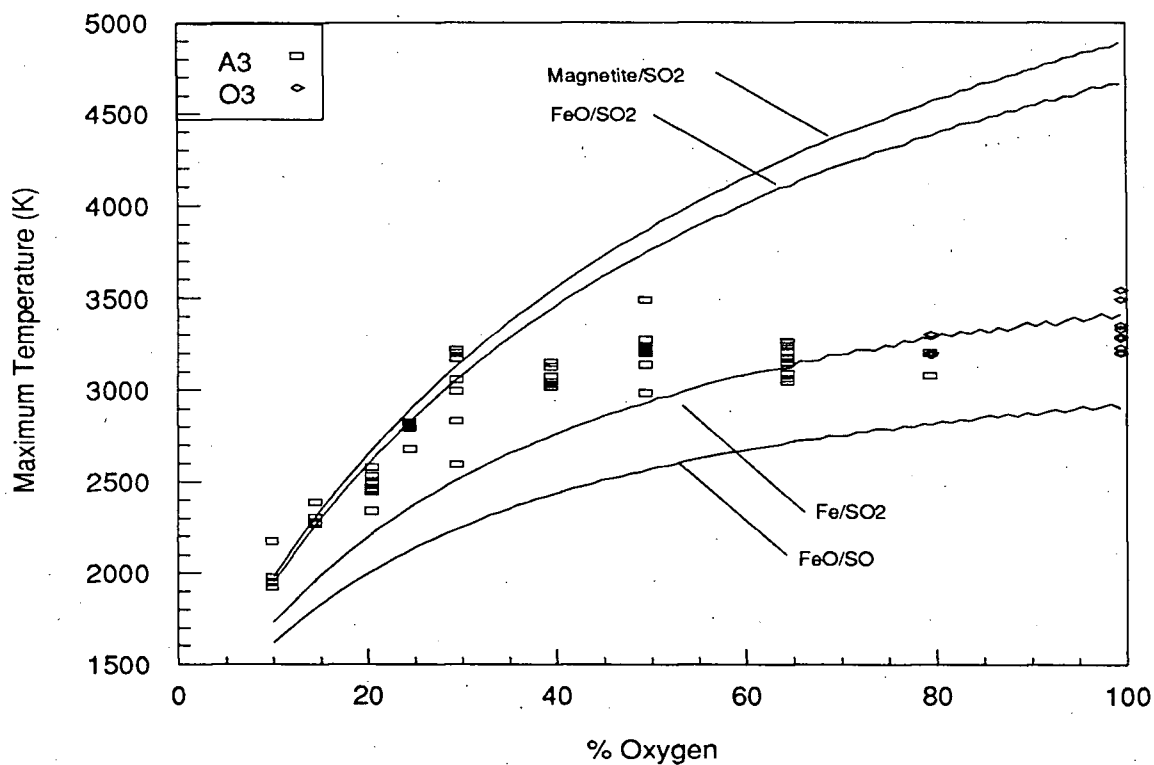


Figure 7.14 Calculated* and measured maximum temperatures for $65\mu\text{m}$ FeS particles as a function of oxygen concentration for the different reaction mechanism ($T_{\text{FURNACE}} = 1130\text{K}$, $\epsilon = 0.7$) considering the formation of different reaction products.
 * based on the mols of reacting species present, therefore an over-estimate.

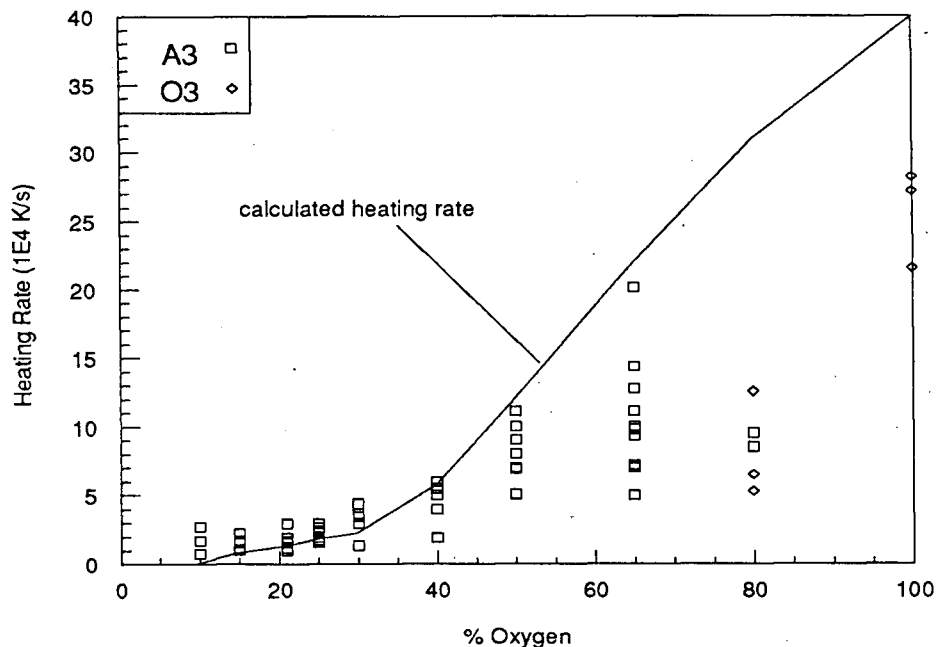


Figure 7.15 A comparison of calculated and measured heating rates at peak combustion temperature as a function of oxygen concentrations ($d_p=65\mu\text{m}$, $T_{\text{FURNACE}} = 1130\text{K}$ and $\epsilon=0.7$).

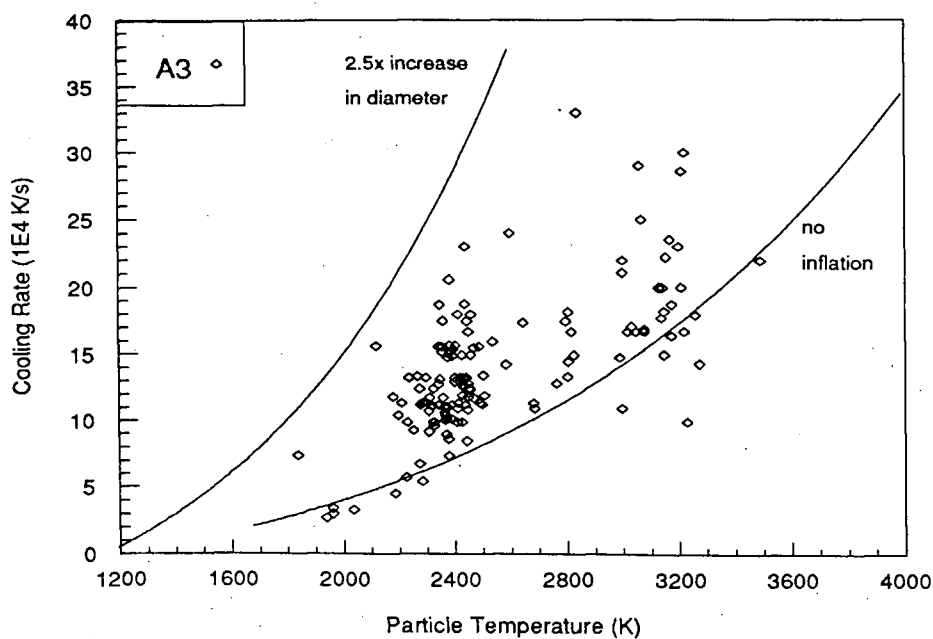


Figure 7.16 Measured cooling rates of the A3 combustion pulses as a function of combustion temperature. The calculated cooling rates for $65\mu\text{m}$ FeS particles considering x1 and x2.5 particle inflation ($T_{\text{FURNACE}} = 1130\text{K}$, $\epsilon=0.7$) are also included for comparison.

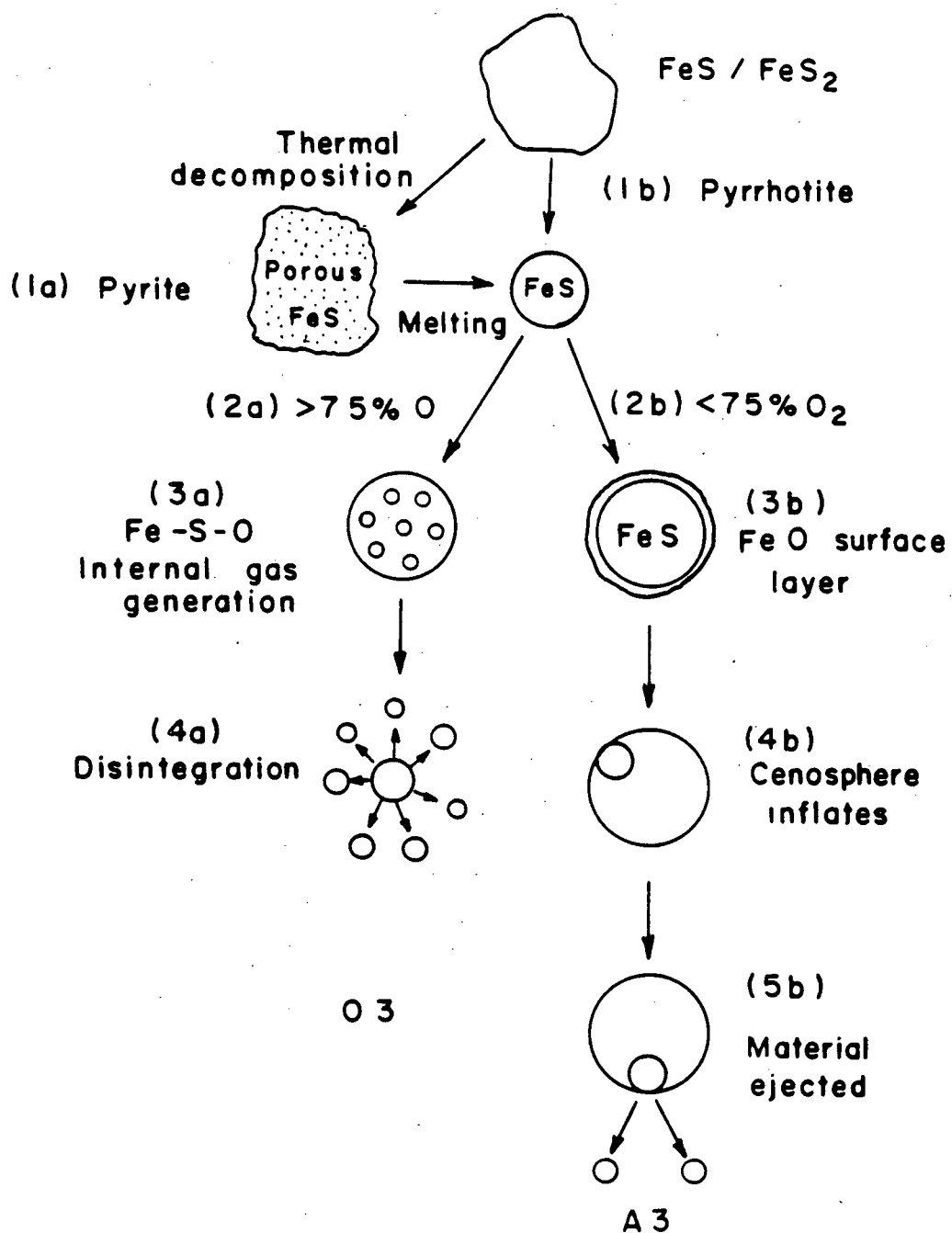


Figure 7.17 Schematic diagram of pyrite/pyrrhotite combustion in air and oxygen at 1130K.

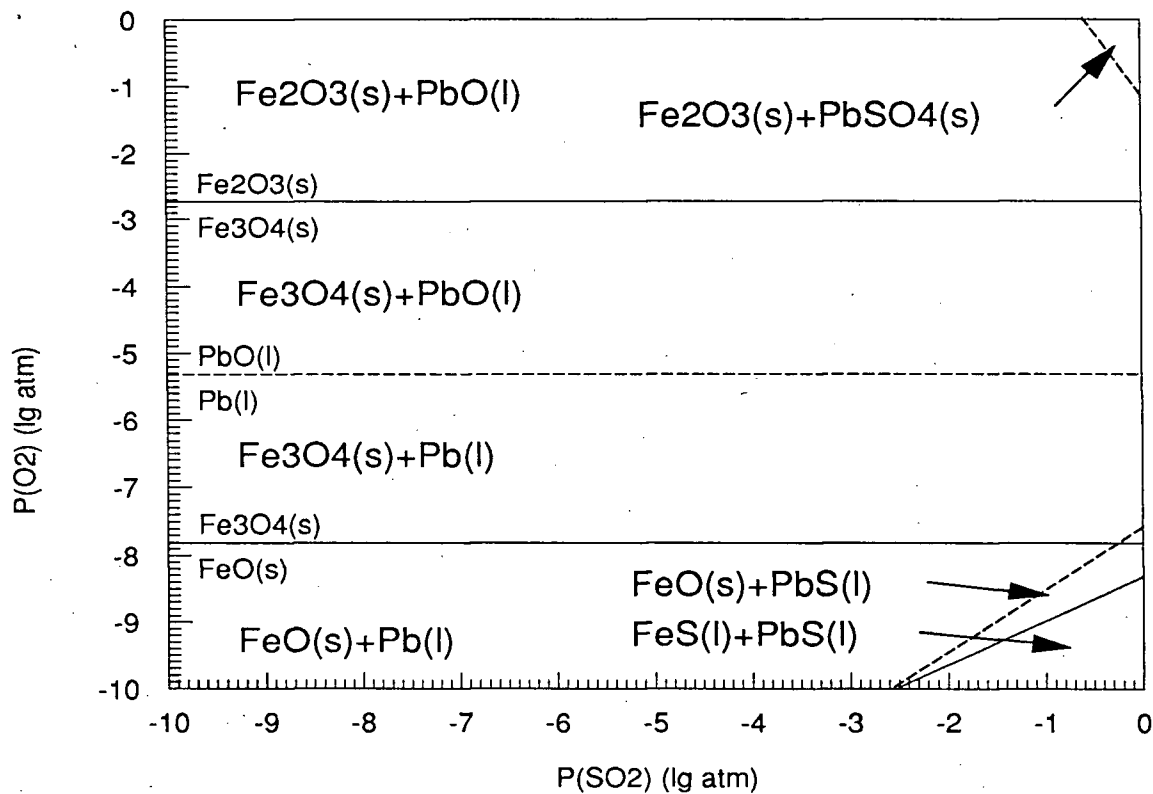


Figure 7.18 Superimposed oxygen-sulphur dioxide potential diagrams for the Fe-S-O and Pb-S-O systems at 1500K.

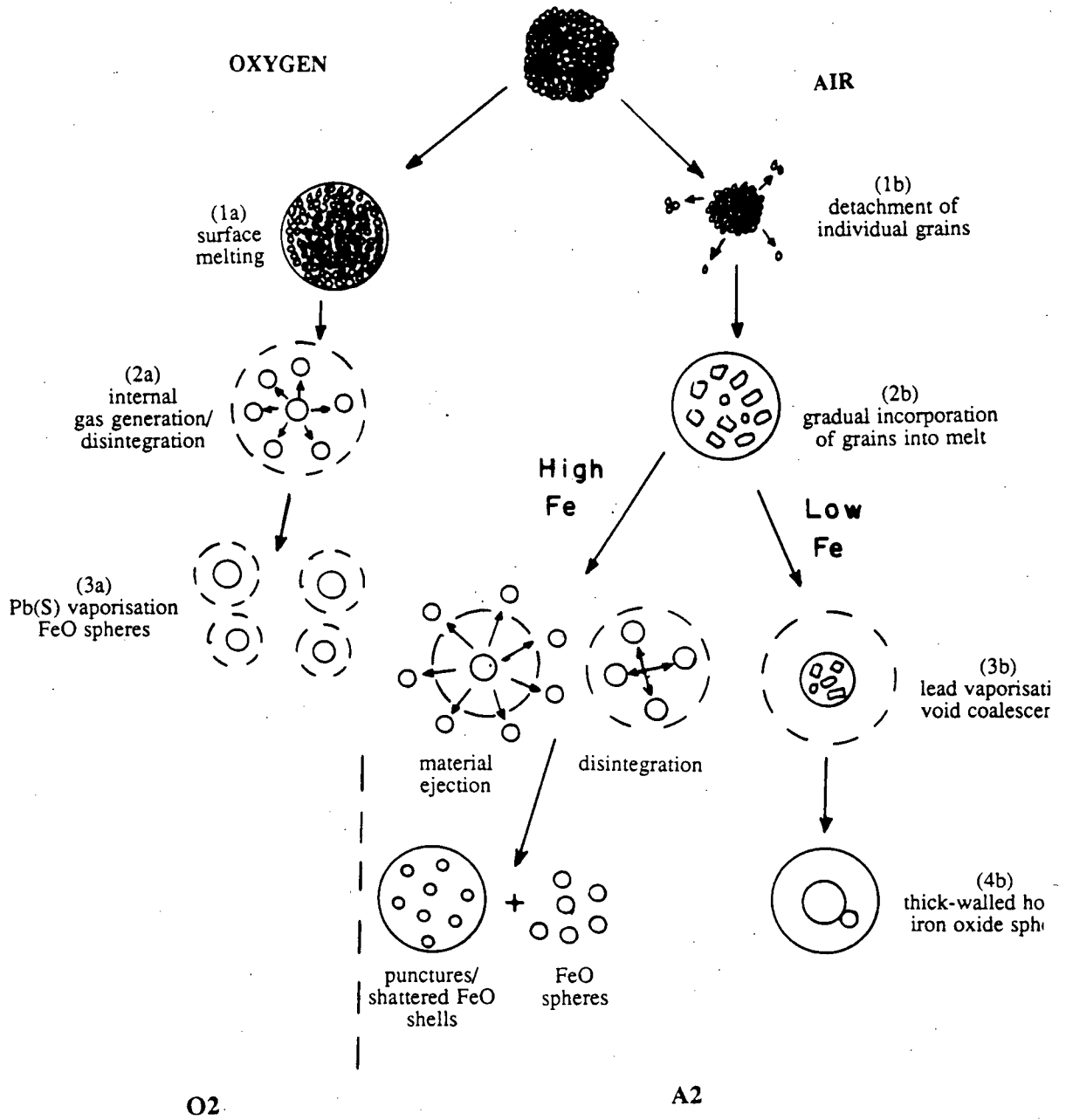


Figure 7.19 Schematic diagram of the combustion lead-iron-zinc sulphide agglomerates in air and oxygen at 1130K.

CHAPTER 8

Conclusions

A considerable amount of information about the mechanisms and kinetics of the reactions occurring during the combustion of lead concentrates has been obtained from this study. The fast response, two-wavelength radiation pyrometer and "laminar flow" furnace constructed for this study functioned satisfactorily allowing variations in the particle temperature and heating rates during reaction to be determined. Through the identification of the differences between the feed materials information about the mechanisms of combustion of the individual mineral species was obtained.

It was not possible to examine the effect of particle size on combustion due to large variation in size within the individual screen fractions and the considerable over-lap which existed.

The following are the important findings of the study:

- i) Differences between the combustion of the individual mineral species and commercial concentrates were identifiable and led to the classification of different combustion pulses.
- ii) The reactions were strongly dependent on the gaseous oxygen concentration, with the intensity and temperature of combustion tending to increase with increasing oxygen concentration.
- iii) Vaporisation reactions appear very important to the combustion of sulphide minerals, with the maximum combustion temperature being limited either directly (galena PbS vaporisation) or indirectly (through associated physical phenomena, e.g. particle disintegration of iron sulphides or galena).
- iv) The ignition and combustion of the individual particles were observed to occur over a much larger range of distances (times) than expected. It was proposed that this spread (and delay) is the result of surface oxide/sulphate layers, formed by gas-solid reactions

during heating which present a temporary resistance to ignition. Uncertainties in the experimental conditions may also contribute to the discrepancies between the measured and predicted time to ignition.

- v) The combustion of galena appears limited by the vaporisation of PbS, with combustion in air having a relatively constant temperature of 1500-1700K. During combustion in oxygen the reactions are very intense. Internal gas generation results in a thermal arrest at 1700-2000K and disintegration of the molten droplets, followed by rapid combustion of the debris at 2000-2400K. Transition from air-type combustion to oxygen-type combustion occurred between ~40 and 65% and is thought to be due to transition from a liquid to gaseous PbO product in the reaction cloud.
- vi) The formation of metallic lead was observed during the early stages of galena combustion probably through reaction on melting between oxides/sulphates formed by gas-solid reactions during heating and unreacted PbS.
- vii) The initial stage of pyrite reaction is the thermal decomposition to porous pyrrhotite. The ignition of this porous product tends to be more rapid than for dense pyrrhotite. Once molten, the combustion of pyrite and pyrrhotite is indistinguishable and very reproducible.
- viii) For iron sulphide combustion in air the molten particles heat rapidly up to a peak temperature of 2400-2600K at which point a large increase in apparent particle diameter and rapid particle cooling is observed. With increasing oxygen concentration the peak combustion temperature increased linearly up to 3000-3400K at ~35% oxygen above which a relatively constant temperature was obtained. At oxygen concentrations in excess of 80% particle disintegration occurs. The heating rate remained relatively constant for oxygen concentrations below ~35% but increased rapidly at higher oxygen concentrations. Maximum cooling rates appeared to correlate with peak combustion temperature.

ix) A simple reaction model for the combustion of a molten iron sulphide, considering gas phase oxygen mass transfer control and the formation of iron oxide/SO₂, was in reasonable agreement with the experimental results. Considering several different overall reaction mechanisms, the measured heating rates suggested a portion of the reaction may proceed through less exothermic reactions, such as the formation of metallic iron or sulphur monoxide. This simple model was unable to predict maximum combustion temperature due to the importance of physical phenomena (expansion and disintegration) to reaction termination. A comparison of predicted and measured cooling rates suggested that particle expansion was occurring during combustion at oxygen concentrations below ~80%.

x) Analysis of the results suggest that for oxygen concentrations up to 80% the termination of the reaction is associated with the expansion of a thin iron oxide cenosphere typically of x1.5-x3 the original diameter. This appears explicable through a mechanism in which the transition from gas phase to liquid phase mass transfer control results in the formation of a surface oxide layer, and gas generation at the oxide-sulphide interface inflates the skin.

xi) The different mineralogy of individual commercial concentrates is evident in their combustion behaviour. Lead concentrates higher in iron sulphide (with a higher enthalpy of reaction) combust more intensely and at higher temperatures. The presence of agglomerates within the commercial concentrates modifies the combustion behaviour considerably, with agglomerate combustion typically being intermediate between those of the mineral constituents (generally iron and lead sulphides). The iron sulphides in the molten droplet tends to react first with the heat of reaction vaporising the lead species present, and the final form of the reaction product typically being iron oxide spheres.

In total this information provides a basis from which to address the combustion of the commercial concentrates as a population of individual particles rather than as a uniform group of particles of average properties. In this respect the information on

agglomerates combustion is new and appears of considerable importance to the overall combustion behaviour of the commercial concentrates. Other information such as the heat transfer and fluid dynamics within the flame will, however, also be necessary for the development of a mathematical model capable of describing the overall system.

Possibly the other critical result of the present study has been to quantify the role of particle disintegration in the combustion behaviour of a number of sulphide minerals and to correlate this to the oxygen concentration of the gas. This information and also the linkage of the disintegration behaviour to physical phenomena involving the vaporisation of species within the melt will be of considerable importance to any later modelling study.

The galena results indicate the importance of two competing reactions to the overall combustion behaviour. These reactions are the vaporisation and gas phase combustion of lead sulphide and the formation of metallic lead within the melt. For flash smelting, maximising metallic lead formation is important for minimising both dust formation and lead oxide formation which requires reduction at a later stage. The results also suggest metallic lead formation is the result of a roast reaction between surface oxides formed during heating and the unreacted PbS. A slower heating rate, with more surface oxidation prior to melting, should result in more metallic lead formation and less PbS vaporisation. The comparison between Sullivan and Brunswick commercial concentrates suggest that feeds with higher heats of combustion result in greater lead vaporisation and dust formation, in agreement with the U.B.C. pilot plant results [27] and industrial operation [9].

References

1. Bray J.L., Non-Ferrous Production Metallurgy, 2nd. Ed. John Wiley & Sons, New York, 1947, pp274-339.
2. Hofman H.O., Metallurgy of Lead, McGraw-Hill Book Company, New York, 1918.
3. Collins H.F., The Metallurgy of Lead, Charles Griffin & Co. Ltd., London, 1910.
4. Reimers J.H. and Taylor J.C., "The Future of Lead Smelting". in Advances in Sulphide Smelting, vol. 1, Eds. H.Y. Sohn, D.B. George and A.D. Zunkel. Met. Soc. AIME, 1983, pp 529-551.
5. Matyas A.G. and Mackey P.J., "Metallurgy of the Direct Smelting of Lead", Journal of Metals 28 pp10-15 (1976).
6. Hoffmann J.E., "Update on Emerging Lead Smelting Processes", Journal of Metals 36 pp29-35 (1984).
7. Morrison B.H., "A Review of New Technologies for Lead and Zinc Reduction Plants" Canadian Metallurgical Quarterly, 23,(4), pp377-381, (1984).
8. Perillo A., Carminati A., Carlini G. and Ibba R., "The Kivcet Lead Smelter at Portovesme. Commissioning and Operating Results", Met. Soc. AIME. TMS Technical paper #A88-2 (1987).
9. Ferri P.F. and Perillo A., "The New Lead Smelter at Portovesme", in Extraction Metallurgy'85, IMM, London, 1985, pp891-903.
10. Fischer P. and Maczek H., "The Present Status of Development of the QSL-Lead Process", Journal of Metals, 34, pp60-64, (1982).
11. Nermes, E.O and Talon, T.T. "Flash Smelting of Lead Concentrates", Met.Soc.AIME-TMS Preprint #A83-35 (1983)
12. Bryk P., Malmstrom R. and Nyholm E. "Flash Smelting of Lead Concentrates", Journal of Metals 18 pp1298-1302 (1965).
13. Krogerus E., Sulanto J. and Talonen T., "The Outokumpu Lead Flash Smelting Process", Symp. on Extractive Metallurgy in Australas. IMM Melbourne Branch, Nov. 1984, pp303-307.
14. Makinen T. and Kyto M., "Pilot and Mini-Pilot Tests of Flash Reactions", in Flash Reaction Processes, Eds. D.G.C. Robertson, H.Y. Sohn and N.J. Themelis. Univ. of Utah, Salt lake City, Utah, 15-17th June 1988. Pub. Center for Pyrometallurgy, Fulton Hall, Univ. Missouri-Rolla, Rolla, MO. pp69-98.
15. Fuller F.T., "Process for the Direct Smelting of Lead Concentrates", Journal of Metals, 20, pp26-30 (1968).
16. Quarm T.A.A., "Submerged Smelting of Lead Merits Longer Look", E/MJ 7 pp60-61 (1974).

17. Errington W.J., Fewings J.H., Keran V.P. and Denholm W.T., "The Isasmelt Lead Smelting process", in Extraction Metallurgy'85, IMM, London, 9-12 September 1985, pp199-218.
18. Chaudhuri K.B. and Melcher G., "Comparative View of the Metallurgy of the Kivcet-CS and other Direct Smelting Processes", CIM Bull. 71 pp126-130 (1978).
19. Chaudhuri K.B. and Melcher G., "Comparative View of the Metallurgy of the Kivcet-CS and other Direct Smelting Processes", CIM Bull. 71 pp126-130 (1978).
20. Chaudhuri K.B., Koch M. and Patino J.L., "The Technical-Scale Realization of the Kivcet Process for Lead", CIM Bull. 73 pp146-150 (1980).
21. Muller E., "How Kivcet-CS Shaft Furnace Simultaneously Smelts Pb-Zn", World Mining 4 pp46-49,99 (1977).
22. Chaudhuri K.B. and Torres N., "Direct Smelting of Lead Concentrates - The Kivcet Process", Met. Soc. AIME-TMS Preprint #A82-? (1982).
23. Anon. "Kivcet Process for Complex Ores", World Mining, 6, pp26-27 (1974).
24. Themelis N.J. and Kellogg H.H., "The Principles of Sulphide Smelting". in Advances in Sulphide Smelting, vol 1, Eds. H.Y. Sohn, D.B. George and A.D. Zunkel. Met. Soc. AIME, 1983, pp 1-29.
25. Themelis N.J., "Transport Phenomena in High-Intensity Smelting Furnaces". Trans. IMM 96, pp C179-C184 (1987).
26. Toop G.W., Cominco Ltd. Private Communications, (1985).
27. Shook. A.A., Richards G.G. and Brimacombe J.K. "Pilot-Plant Study of Lead Flash Smelting", in Flash Reaction Processes, Eds. D.G.C. Robertson, H.Y. Sohn and N.J. Themelis. Univ. of Utah, Salt lake City, Utah, 15-17the June 1988. Pub. Center for Pyrometallurgy, Fulton Hall, Univ. Missouri-Rolla, Rolla, MO. pp99-123.
28. Sychev A.P., "Oxygen-Electrothermic Treatment of Lead Concentrate in the Kivset-TsS Unit" Tsvetnye Metally 18 (7) pp7-14 (1977).
29. Kubaschewski O. and Alcock C.B., Metallurgical Thermochemistry, 5the. Ed., New York, NY, Pergamon Press, 1979.
30. Thomson W.T., Pelton A.D. and Bale C.W., F*A*C*T Data System, 1987.
31. Nagamori M. and Chaubal P.C., "Thermodynamics of Copper Matte Converting: Part III. ", Met.Trans.B 13B pp 319-329 (1982).
32. Hager J.P., Shanks R. and Castro R.Z., "The Fuming of Lead and Germanium Sulphide ", in Flash Reaction Processes, Eds. D.G.C. Robertson, H.Y. Sohn and N.J. Themelis. Univ. of Utah, Salt lake City, Utah, 15-17the June 1988. Pub. Center for Pyrometallurgy, Fulton Hall, Univ. Missouri-Rolla, Rolla, MO. pp367-389.
33. Elliott J.F. and Gleiser M., Thermochemistry for Steelmaking, Vol.2, Addison-Wesley Pub. Co., USA, 1960.

34. Sharma R.C., Lin J.C. and Chang Y.A., "A Thermodynamic Analysis of the Pb-S System and Calculation of the Pb-S Phase Diagram", *Met. Trans.B* 18B pp 237-244 (1987).
35. Kullerud G., "The Lead-Sulphur System", *American Journal of Science* 267-A pp 233-256 (1969).
36. Schuhmann R., Chen P-C., Palanisamy P. and Sarma D.H.R., "Thermodynamics of Converting Lead Sulphide ", *Met. Trans.B* 7B pp 95-101 (1976).
37. Yazawa A. and Gubcova A., "Diagrammatic Representation of Equilibrium Relations in the Lead-Sulphur-Oxygen System ", *Trans.Met.AIME* 239 pp 2004-2005 (1967).
38. Yazawa A., "Thermodynamic Evaluation of Extractive Metallurgical Processes", *Met. Trans.B* 10B pp 307-321 (1979).
39. Kellogg H.H. and Basu S.K., "Thermodynamic Properties of The System Pb-S-O to 1100K." *Trans.Met.AIME*, 218 pp70-81 (1960).
40. Tuffley J.R. and Russell B., "Sulphate Formation during the Roasting of Lead Sulphide ", *Trans.Met.AIME* 230 pp 950-956 (1964).
41. Tuffley J.R and Russell B., "The Oxidation of Lead Sulphide ", *Journal Austral.Inst.Metals* 7 pp 122-129 (1962).
42. Kellogg H.H., "Critical Evaluation of the Thermodynamic Properties of Lead Sulphates", *Met. Trans.B* 20B pp 77-85 (1989).
43. Happ J.V. and Jorgensen F.R.A. "Experimental Study of Flash Smelting of Broken Hill Lead Concentrate", in Flash Reaction Processes, Eds. D.G.C. Robertson, H.Y. Sohn and N.J. Themelis. Univ. of Utah, Salt lake City, Utah, 15-17the June 1988. Pub. Center for Pyrometallurgy, Fulton Hall, Univ. Missouri-Rolla, Rolla, MO. pp215-242.
44. Salomon de Friedberg A.M., "Kinetics of Lead Concentrate Oxidation in a Stagnant Gas Reactor", M.A.Sc. Thesis, Univ. British Columbia. November 1987.
45. Hsiao H.C., Jorgensen F.R.A. and Wright S., "A Study of the Reaction Between Lead Sulphate and a Number of Base Metal Sulphides", in Symposium on Reaserch and Development in Extractive Metallurgy, Australasian IMM, Adelaide Branch, May 1987, pp69-76.
46. Rosenqvist T., "Phase Equilibria in the Pyrometallurgy of Sulphide Ores", *Met. Trans.B* 17B pp 51-60 (1986).
47. Hansen M. and Anderko K., Constitution of Binary Alloys, 2nd Ed., McGraw-Hill Book Co. Inc., New York, 1958, pp1099-1100.
48. Esdaile J.D., "Thermodynamics and Phase Diagram of the Lead-Lead Sulphide Binary System ", *Proc.Australas.IMM* 241 pp 63-71 (1972).
49. Willis G.M., "The Physical Chemistry of Lead Extraction", in Lead-Tin-Zinc '80, Eds J.M. Cigan, T.S. Mackey and T.J. O'Keefe, AIME, 1980, pp457-476.

50. Condina V.K., Jorgensen F.R.A., Moyle F.J. and Turner T.M., "Ignition of Elura Lead Concentrate Under Flash Drying Conditions", in Symposium on Research and Development in Extractive Metallurgy, Australasian IMM, Adelaide Branch, May 1987, pp61-68.
51. Sychev A.P., Kopylov N.I., Margulis E.V. and Noveselova V.N., "Mathematical Dependence of the Ignition Temperature of Sulphides on the Process Conditions", Soviet Non-ferrous Metals Research 5 pp228-230 (1975).
52. Sychev A.P., Kopylov N.I., Margulis E.V. and Noveselova V.N., "Ignition of Copper, Zinc, Iron and Lead Sulphides", Soviet Non-ferrous Metals Research 5 pp185-187 (1975).
53. Nakamura T., Noguchi F., Ueda Y. and Ito H., "A Basic Study of the Oxidation Smelting of Lead Sulphide", in Symposium on Research and Development in Extractive Metallurgy, Australasian IMM, Adelaide Branch, May 1987, pp85-94.
54. Dunn J.G., Jayaweera A. and Davies S.G., "Development of Techniques for the Study of Flash Smelting Reactions Using Differential Thermal Analysis and Gravimetry", Bull. Proc. Australas. IMM 290 (4) pp 75-82 (1985).
55. Reimers G.W. and Pomroy W.H., "Spontaneous Combustion Susceptibility of Sulphide Minerals", U.S. Bureau of Mines. Information Circular # IC9206 pp54-60 (1988).
56. Henley R.G., Hsiao H.C. and Jorgensen F.R.A., "Suspension Smelting Studies on Mount Isa Copper Concentrate". in Advances in Sulphide Smelting, vol 1, Eds. H.Y. Sohn, D.B. George and A.D. Zunkel, AIME, 1983, pp 81-98.
57. Jorgensen F.R.A., "Investigation of Shaft Reactions in Nickel Flash Smelting at 0.5 kg/min Scale", in Pyrometallurgy'87, IMM, London, 21-23rd September 1987, pp627-645.
58. Partelpoeg E.H., "Flash Smelting Reactions at the Phelps Dodge Hidalgo Smelter", in Flash Reaction Processes, Eds. D.G.C. Robertson, H.Y. Sohn and N.J. Themelis. Univ. of Utah, Salt lake City, Utah, 15-17th June 1988. Pub. Center for Pyrometallurgy, Fulton Hall, Univ. Missouri-Rolla, Rolla, MO. pp35-45.
59. Kermori N., Ojima Y. and Kondo Y., "Variation of the Composition and Size of Copper Concentrate Particles in the Reaction Shaft", in Flash Reaction Processes, Eds. D.G.C. Robertson, H.Y. Sohn and N.J. Themelis. Univ. of Utah, Salt lake City, Utah, 15-17th June 1988. Pub. Center for Pyrometallurgy, Fulton Hall, Univ. Missouri-Rolla, Rolla, MO. pp47-68.
60. Kimura T., Ojima Y., Mori Y. and Ishii Y., "Reaction Mechanism in the Flash Smelting Reaction Shaft", in The Reinhardt Schuhmann International Symposium, Eds. D.R. Gaskell, J.P. Hager, J.E. Hoffmann and P.J. Mackey, The Metallurgical Society of AIME, 1986, pp403-418.
61. Kim Y.H. and Themelis N.J., "Effects of Phase Transformation and Particle Fragmentation on the Flash Reactions of Complex Metal Sulphides", in The Reinhardt Schuhmann International Symposium, Eds. D.R. Gaskell, J.P. Hager, J.E. Hoffmann and P.J. Mackey, The Metallurgical Society of AIME, 1986, pp349-369.

62. Themelis N.J., Wu L. and Jiao Q., "Some Aspects of Mathematical Modelling of Flash Smelting Phenomena", in Flash Reaction Processes, Eds. D.G.C. Robertson, H.Y. Sohn and N.J. Themelis. Univ. of Utah, Salt lake City, Utah, 15-17th June 1988. Pub. Center for Pyrometallurgy, Fulton Hall, Univ. Missouri-Rolla, Rolla, MO. pp263-285.
63. Sen M. and Wuth W., "Distribution of Minor Elements from Copper Concentrates in Laboratory Flash Experiments", in Flash Reaction Processes, Eds. D.G.C. Robertson, H.Y. Sohn and N.J. Themelis. Univ. of Utah, Salt lake City, Utah, 15-17th June 1988. Pub. Center for Pyrometallurgy, Fulton Hall, Univ. Missouri-Rolla, Rolla, MO. pp191-200.
64. Wuth W., "High Temperature Oxidation of Sulphur Particles", in Mineral Processing and Extractive Metallurgy, Eds. J.M. Jones and P. Gill. Kunming, Yunnan Province, Peoples Republic of China, 27th Oct. to 3rd Nov. 1984, IMM. pp369-379.
65. Kang J-S. and Pyun S-I, "High-Temperature Oxidation Processes in Dispersed Particle Jet System of Cu-Fe-S Mineral Bearing Concentrates", Trans. IMM C97 pp C198-C206 (1988).
66. Hagni R.D. and Vierrether C.B., "Sulphide and Oxide Mineralogy, Textures and Reactions in Suspended Particles from Experimental and Production Flash Furnace Reaction Shafts", in Flash Reaction Processes, Eds. D.G.C. Robertson, H.Y. Sohn and N.J. Themelis. Univ. of Utah, Salt lake City, Utah, 15-17th June 1988. Pub. Center for Pyrometallurgy, Fulton Hall, Univ. Missouri-Rolla, Rolla, MO. pp245-262.
67. Hagni R.D., Vierrether C.B. and Sohn H.Y., "Process Mineralogy of Suspended Particles from a Simulated Commercial Flash Smelter", Met. Trans B, 19B, pp719-729 (1988).
68. Tuffrey N.E., Salomon de Friedberg A.M., Brimacombe J.K.B. and Richards G.G., "The Reaction Kinetics of Lead Sulphide Particles During Combustion", in Flash Reaction Processes, Eds. D.G.C. Robertson, H.Y. Sohn and N.J. Themelis. Univ. of Utah, Salt lake City, Utah, 15-17th June 1988. Pub. Center for Pyrometallurgy, Fulton Hall, Univ. Missouri-Rolla, Rolla, MO. pp331-366.
69. Jorgensen F.R.A., "Combustion of Chalcopyrite, Pyrite, Galena and Sphalerite under Simulate Suspension Smelting Conditions", Australia-Japan Extractive Metallurgy Symp. Sydney, Australia, 1980, pp41-51.
70. Gray N.B., Stump N.W., Boundy W.S. and Culver R.V., "The Sulphation of Lead Sulphide", Trans. Met. AIME 239 pp1835-1840 (1967).
71. Gray N.B., Harvey M.R. and Willis G.M., "Roasting of Sulphides in Theory and Practice", in Physical Chemistry of Process Metallurgy: the Richardson Conference, eds. J.H.E. Jeffes and R.J. Tait, Inst. Min. Metall., London, 1974, pp19-32.
72. Jorgensen F.R.A., "The Ignition Temperature of a Nickel Concentrate from Kambalda under Simulated Flash Smelting Conditions", Proc. Australas. IMM 268 (12) pp 47-55 (1978).

73. Jorgensen F.R.A., Moyle F.J. And Wadsley M.W., "The Ignition of Chalcopyrite and Pyrite During Flash Smelting", in Flash Reaction Processes, Eds. D.G.C. Robertson, H.Y. Sohn and N.J. Themelis. Univ. of Utah, Salt lake City, Utah, 15-17th June 1988. Pub. Center for Pyrometallurgy, Fulton Hall, Univ. Missouri-Rolla, Rolla, MO. pp167-190.
74. Jorgensen F.R.A. and Segnit E.R., "Copper Flash Smelting Simulation Experiments", Proc.Australas.IMM 261 (3) pp 39-46 (1977).
75. Jorgensen F.R.A., "Heat Transfer Mechanism in Ignition of Nickel Sulphide Concentrate Under Simulated Flash Smelting Conditions", Proc.Australas.IMM 271 (9) pp 21-25 (1978).
76. Jorgensen F.R.A. and Sengit E.R., "Some Results of Flash Smelting Simulation Experiments", The Aus.I.M.M Melbourne Branch, Symposium on Extractive Metallurgy. Melbourne, Australia, 1975, ppvi.6.1-vi6.9.
77. Jorgensen F.R.A., "Vaporization During the Combustion of a Complex Copper Concentrate", Bull.Proc.Australas.IMM 290 (1) pp 91-98 (1985).
78. Jorgensen F.R.A., "Combustion of Pyrite Concentrate under Simulated Flash Smelting Conditions", Trans. IMM (London) 90 ppC1-C9 (1981).
79. Jorgensen F.R.A., "On Maximum Temperature Attained During Single Particle Combustion of Pyrite", Trans. IMM (London) 90 ppC10-C16 (1981).
80. Jorgensen F.R.A., "Single Particle Combustion of Chalcopyrite", Proc.Austal.IMM 288 (12) pp 37-46 (1983).
81. Jorgensen F.R.A., "Cenosphere Formation During the Combustion of Pyrite", Proc.Austal.IMM 276 (12) pp 41-47 (1980).
82. Jorgensen F.R.A. and Zuiderwyk M., "Two-Colour Pyrometer Measurement of the Temperature of Individual Combusting Particles", J.Phys. E.:Sci. Instrum., 18 pp486-491 (1985).
83. Jorgensen F.R.A. and Zuiderwyk M., "Some Applications of Two-Colour Pyrometry to Pyrometallurgical Research", The Aus.I.M.M Melbourne Branch, Symposium on Extractive Metallurgy, Melbourne, Australia, 1984, pp317-321.
84. Otsuka K. and Soma T., "Suspension Roasting of Pyrite and Copper Concentrate", Australia-Japan Extractive Metallurgy Symp. Sydney, Australia, 1980, pp233-243.
85. Jokilaakso A., Suominen R., Hackman H., Taskinen P. and Lillus k., "The Behaviour of Tetrahedrite in Simulated Suspension Smelting Conditions", in Flash Reaction Processes, Eds. D.G.C. Robertson, H.Y. Sohn and N.J. Themelis. Univ. of Utah, Salt lake City, Utah, 15-17th June 1988. Pub. Center for Pyrometallurgy, Fulton Hall, Univ. Missouri-Rolla, Rolla, MO. pp201-213.
86. Themelis N.J. and Gauvin W.H., "Reduction of Iron Oxide in Gas-Conveyed Systems ", Journal A.I.Ch.E., 8 (4) pp437-444 (1962).
87. Themelis N.J. and Gauvin W.H., "A Two-Wavelength Pyrometer for Temperature Measurements in Gas-Solid Systems ", Canadian Journal of Chemical Engineering, 40-41 pp157-161 (1962).

88. Otero A., Brimacombe J.K. and Richards G.G., "Flash Smelting" (Video Cassette), University of British Columbia (1989).
89. Timothy L.D., Sarofim A.F. and Beer J.M., "Characteristics of Single Particle Coal Combustion", Nineteenth Symp. (International) on Combustion, The Combustion Institute, 1982, pp1123-1130.
90. Ayling A.B. and Smith I.W., "Measured Temperature of Burning Pulverized-Fuel Particles, and the nature of the Primary Reaction Product", Combustion and Flame, **18** pp173-184 (1972).
91. Ayling A.B., Mulcahy M.F.R. and Smith I.W., "The Temperature of Burning Pulverized-Fuel Particles", CSIRO Division of Mineral Chemistry, Sydney Laboratory, P.O. Box 175, Chatswood, N.S.W. Aust., Investigative Report **88** May 1971 pp1-26.
92. Tichenor D.A., Mitchell R.E., Hencken K.R. and Niksa S., "Simultaneous in Situ Measurement of the Size, Temperature and Velocity of Particles in a Combustion Environment", Twentieth Symp. (International) on Combustion, The Combustion Institute, 1984, pp1213-1221.
93. Grosshandler W.L., "The Effect of Soot on the Pyrometric Measurements of Coal Particle Temperature", Combustion and Flame, **55** pp59-71 (1984).
94. Babii V.I. and Ivanova I.P., "The Temperature of Coal Particles During Combustion", Thermal Engineering, **15** (12) pp46-50 (1968).
95. Bach J.H., Street P.J. and Twamley C.S., "Temperature Measurement of Particulate Surfaces", Journal of Sci. Instruments, **3** pp281-286 (1970).
96. Hahn Y.B. and Sohn H.Y., "Radiative Heat Transfer in a Flash Smelting Furnace", in Flash Reaction Processes, Eds. D.G.C. Robertson, H.Y. Sohn and N.J. Themelis. Univ. of Utah, Salt lake City, Utah, 15-17th June 1988. Pub. Center for Pyrometallurgy, Fulton Hall, Univ. Missouri-Rolla, Rolla, MO. pp287-317.
97. Hahn Y.B. and Sohn H.Y., "Prediction of the Behaviour of a Particle-Laden Gas Jet as Related to the Flash-Smelting Process", in The Reinhardt Schuhmann International Symposium, Eds. D.R. Gaskell, J.P. Hager, J.E. Hoffmann and P.J. Mackey, The Metallurgical Society of AIME, 1986, pp469-499.
98. Hahn Y.B. and Sohn H.Y., "mathematical Modelling of the Combined Turbulent Transport Phenomena, Chemical Reactions and Thermal Radiation in a Flash-Furnace Shaft", in Mathematical Modelling of Materials Processing Operations, Eds. J. Szekeley, L.B. Hales, H. Henein, N. Jarret, K. Rajamani and I. Samarsekera, Met. Soc. AIME, 1988, pp799-834.
99. Ruottu S., "The description of a Mathematical Model for the Flash Smelting of Copper Concentrate", Combustion and Flame, **34** pp1-11 (1979).
100. Fukunaka Y., Nakashita S., Asaki Z. and Kondo Y., "A Modelling Study on The Pyrite Smelting Process", in World Mining and Metals Technology, Vol.1, Eds. A. Weiss, The Metallurgical Society of AIME, 1976, pp481-503.
101. Asaki Z., Mori S., Ikeda M. and Kondo Y., "Oxidation of pyrrhotite Particles Falling Through a Vertical Tube", Met. Trans. B **16B** pp 627-638 (1985).

102. Surges L.J. Brunswick Mining and Smelting Co. Private Communications (1987).
103. Bazin C. Brunswick Mining and Smelting Co., (formerly of Universite de Laval), Draught Chapter from Ph.D. Thesis (1988).
104. Poling G. Private communications. Department of Mining and Mineral Processing, University of British Columbia (1988).
105. Szekely J. and Themelis N.J., Rate Phenomena in Process Metallurgy, Wiley-Interscience, New York, NY, 1971, pp602-609.
106. Perry R.H and Green D., Perry's Chemical Engineering Handbook, 6th Ed, McGraw-Hill Book Co., New York, NY, 1984.
107. Tuffrey N.E., "Laser Doppler Anemometry/Mathematical modelling Studies of the Laminar Flow Furnace" Unpublished Work (1986).
108. Crowe C.T., "Gas-Particle Flow" in Pulverized-Coal Combustion and Gasification, Eds L.D. Smoot and D.T. Pratt., Plenum Press, New York N.Y., Chapter 6, 1979, pp107-119.
109. Beckwith P.J. and Crane K.C.A., "Two-wavelength Infrared Pyrometry for Large and Rapid Temperature Changes ", Review of Scientific Instruments 53, (6) pp871-875 (1982).
110. Ohse R.W., Babelot J-F., Kinsman P.R. Long K.A and Magill J., "High-speed Pyrometry and Spectroscopy in Laser-pulse Heating Experiments at Extreme Rates of Evaporation", High Temperature-High Pressures 11, pp225-239 (1979).
111. Mitchell R.E. and McLean W.J., "On the Temperature and Reaction Rate of Burning Pulverized Fuels", Nineteenth Symposium (International) on Combustion, The Combustion Institute, 1982, pp1113-1122.
112. Pasta M., Ruffino G. and Soardo P., "New Two-Colour Pyrometer", High Temperature -High Pressures 5, pp99-104 (1973).
113. Bolsaitis P., Spjut R.E. and Elliot J.F., "The Measurement of Temperature of Particles Under Conditions Simulating Flash Smelting", in "Flash Reaction Processes", Eds. D.G.C. Robertson, H.Y. Sohn and N.J. Themelis. Univ. of Utah, Salt Lake City, Utah, 15-17th June 1988. Pub. Center for Pyrometallurgy, Fulton Hall, Univ. Missouri-Rolla, Rolla, MO. pp319-330.
114. Spjut R.E., Bar-Ziv E., Sarofim A.F. and Longwell J.P., "Electrodynamic Thermogravimetric Analyzer", Rev. Sci. Instrum. 57 (8) pp1604-1610 (1986).
115. Spjut R.E., "Transient Response of One- and Two-colour Optical Pyrometry", Optical Engineering. 26 (5) pp467-472 (1987).
116. Electro-Optics Handbook, 2nd. Eds. F.J. Gardiner, RCA Commercial Engineering, Harrison, NJ, 07029, 1968.
117. Research Proposal #P-35. Canatech Electronic Research Corp. Richmond, B.C. submitted to U.B.C. 6th. January 1985.

118. Technical Literature Anarad Inc., 534 E. Ortega St., Santa Barbara, CA, 93103, 1984.
119. Shelton R.D., Nielson A.H and Fletcher W.H., *J.Chem.Phys.*, 21, p2178 (1953).
120. Baker H.D., Ryder E.A. and Baker N.H., Temperature Measurement in Engineering, Vol.I and II, John Wiley and Sons, Inc, New York, NY. Chap.4 pp131-165 and Chap.13, 1961, pp424-447.
121. Branstetter J.R., "Some Practical aspects of Surface Measurement by Optical and Ratio Pyrometers", NASA Technical Note D-3604, September 1966, pp1-67.
122. Kostkowski H.J. and Lee R.D., "Theory and methods of Optical Pyrometry", NBS Monograph #41, National bureau of Standards, United States Department of Commerce, 1st March 1962, pp1-28.
123. Kostkowski H.J., "The Accuracy and Precision of Measuring Temperatures Above 1000K", in Proc. Int. Symp. on High Temperature Technology, McGraw-Hill Book Co., New York, 1959, pp33-44.
124. Latyev L.N., Chekhovskoi V.Y. and Shestakov E.N., "Monochromatic Emissivity of Tungsten in the Temperature Range 1200-2600K and in the Wavelength Range 0.4-4 micrometers", *High Temperature-High Pressures* 2, pp175-181 (1970).
125. Stair R., Johnston R.G. and Halbach E.W., "Standard Spectral Radiance for the Region of 0.25 to 2.6 μ m", *Journal of Research of the National Bureau of Standards- A Physics and Chemistry*, 64A, (4) pp291-296 (1960).
126. Ealing Optics Catalogue, The Ealing Corporation, Pleasant Street, South Natick, MA. 01760, 1985.
127. "CRC Handbook of Chemistry and Physics", 61st. Edition, Eds. R.C. Weast and M.J. Astle, CRC Press, Inc., Boca Raton, Florida. 33431, 1980, ppE-400 (1980).
128. Asaki Z., Matsumoto K., Tanabe T. and Kondo Y., "Oxidation of Dense Iron Sulphide", *Met.Trans.B* 14B pp 109-116 (1983).
129. Thornhill P.G. and Pidgeon L.M., "Micrographic Studies of Sulphide Roasting", *Journal of Metals*, 9 pp 989-995 (1957).
130. Denbigh K.G. and Beveridge G.S.G, "The Oxidation of Zinc Sulphide Spheres in An Air Stream", *Trans.Instn Chem. Engrs* 40 pp 23-34 (1962).
131. Turkdogan E.T., Grieveson P. and Darken L.S., "Enhancement of Diffusion-Limited Rates of Vaporisation of Metals", *Journal of Physical Chemistry*, 67, pp 1647-1654 (1963).
132. Toguri J.M., Themelis N.J. and Jennings P.H., "A Review of Recent Studies on Copper Smelting", *Canadian Metallurgical Quarterly*, 3 (3), pp 197-220 (1964).
133. Naldrett A.J., "A Portion of the System Fe-S-O between 900°C and 1080°C and its Application to Sulphide Ore Magmas", *Journal of Petrology*, 10, (2) pp 171-201 (1969).

134. Biswas A.K. and Davenport W.G., Extractive Metallurgy of Copper, 2nd. Ed., Pergamon Press, Oxford, 1980, pp 80-99.
135. Kazantsev E.I., Industrial Furnaces, MIR Publishers, Moscow, USSR, 1977, pp283-289.
136. Binary Alloy Phase Diagrams, Volume 1, Ed. T.B. Massalki, American Society of Metals, Metals Park, Ohio, 1986, p559.
137. Robertson D.G.C, Warner N.A. and Jenkins A.E., "Basic Oxygen and Spray Steelmaking- Some Research on the Mechanisms of the Reactions", Chemica'70, Instn. Chem. Eng. Melbourne and Sidney, Aust. Butterworths, 1970, pp54-69.
138. Turkdogan E.T., Physical Chemistry of High Temperature Technology, Academic Press. New York, 1980.
139. Geiger G.H. and Poirier D.R., Transport Phenomena in Metallurgy, Addison-Wesley Publishing Company, Reading Mass. 1973.
140. Clift R., Grace J.R. and Weber M.E., Bubbles, Drops and Particles, Academic Press, New York, 1978.
141. Law C.K., "Models for Metal Particle Combustion with Extended Flame Zones", Combustion Science and Technology, 12, pp113-124 (1976).
142. Friedman R. and Macek A., "Ignition and Combustion of Aluminium Particles in Hot Gases", Combustion and Flame, 6, 9-19 (1962)
143. Friedman R. and Macek A., "Combustion Studies of Single Aluminium Particles", The Ninth Symposium (International) on Combustion, The Combustion Institute, pp 703-712 (1962)
144. Bartlett R.W., Ong J.N., Fassell W.M., "Estimating Aluminium Particle Combustion Kinetics", Combustion and Flame, 7, 227-234 (1963)
145. Samsonov G.V., The Oxide Handbook , IFI/Plenum, New York, 1973.
146. Siegel R. and Howell J.R., Thermal Radiation Heat Transfer, 2nd. Ed., McGraw-Hill Book Co., New York, 1981, pp1-34.
147. Distin P.A, Hallett G.D. and Richardson F.D., "Some Reactions between Drops of Iron and Flowing Gases", Journal of the Iron and Steel Institute. 206 pp467-472 (1968).
148. Tamura K., Iwamura T. and Kurita K., "Improvement of Traceability for Radiation Pyrometers in the Steel Industry", in Temperature Its Measurement and Control in Science and Industry, Vol.5, Part 1, Ed. J.F. Schooley, American Institute of Physics, New York, NY, 1982, pp479-483.
149. Temperature Measurement Handbook and Encyclopedia, OMEGA Engineering Inc., Stamford, CT, USA, 1985, pH-3 .

APPENDIX 1

Two-Wavelength Pyrometry

A.1.1 Theory

The relationship between monochromatic radiation from a blackbody and the blackbody temperature is expressed by Planck's Law [120-123] as follows:

$$W_{\lambda_{bb}} = \frac{2\pi hc^2 \lambda^{-5}}{\exp\left(\frac{ch}{k\lambda T}\right) - 1} = \frac{C_1 \lambda^{-5}}{\exp\left(\frac{C_2}{\lambda T}\right) - 1} \quad (Wm^{-2}m^{-1}) \quad (A.1.1)$$

If $\exp(C_2/\lambda T)$ is much greater than unity, Equation A.1.1 can be simplified to the Wien's Law approximation :

$$W_{bb\lambda} = C_1 \lambda^{-5} \exp\left(\frac{-C_2}{\lambda T}\right) \quad (A.1.2)$$

This corresponds to the lefthand portions of the curves given in Figure 5.1.

For a non-blackbody it is necessary to consider the monochromatic emissivity of the object (ϵ_λ), which is defined as:

$$\epsilon_\lambda = \frac{\text{intensity of radiation of non-blackbody at } \lambda T}{\text{intensity of radiation of blackbody at } \lambda T} \quad (A.1.3)$$

therefore,

$$W_\lambda = \epsilon_\lambda C_1 \lambda^{-5} \exp\left(\frac{-C_2}{\lambda T}\right) \quad (A.1.4)$$

The ratio of the intensities at two different wavelengths at the same temperature is

$$\ln\left(\frac{W_{\lambda_1}}{W_{\lambda_2}}\right) = \ln\left\{\left(\frac{\epsilon_{\lambda_1}}{\epsilon_{\lambda_2}}\right) \left(\frac{\lambda_2}{\lambda_1}\right)^5\right\} - \frac{1}{T} \left(\frac{C_2}{\lambda_1} - \frac{C_2}{\lambda_2}\right) \quad (A.1.5)$$

If the assumption that the ratio of the emissivities at two particular wavelengths is temperature independent (grey body behaviour), the relationship between the ratio of the intensities at the two wavelengths and the object temperature is of the form

$$\ln\left(\frac{W_{\lambda_1}}{W_{\lambda_2}}\right) = K \frac{1}{T} + B \quad (\text{A.1.6})$$

In practice a pyrometer can only approximate the theoretical relationships pertinent to monochromatic radiation owing to the finite width of the optical filters. The voltage output from a pyrometer photomultiplier tube detector will depend on both the pyrometer characteristics and the object characteristics. The pyrometer characteristics of importance are the filter centre wavelength λ_1 , optical bandwidth $\Delta\lambda_1$, particle-detector view factor $F_{dp\lambda_1}$ and the overall pyrometer gain G including all the optical and electronic gains and losses. The object-dependent properties are temperature T , area A_p and bandpass emissivity ϵ_{λ_1} . The pyrometer detector output voltage V_{λ_1} then can be expressed through the Wien's Law approximation as

$$V_{\lambda_1} = A_p F_{dp\lambda_1} G_{\lambda_1} \frac{C_1 \epsilon_{\lambda_1}}{\lambda_1^5 \exp\left(\frac{C_2}{\lambda_1 T}\right)} \Delta\lambda_1 \quad (\text{A.1.7})$$

Combining the various factors

$$V_{\lambda_1} = A_p \epsilon_{\lambda_1} K_{2\lambda_1} \exp\left(-\frac{C_2}{\lambda_1 T}\right) \quad (\text{A.1.8})$$

where

$$K_{2\lambda_1} = F_{dp\lambda_1} G_{\lambda_1} C_1 \frac{\Delta\lambda_1}{\lambda_1^5}$$

then combining Equation A.1.8 with the equivalent expression for the detector filtered at λ_2

$$\ln\left(\frac{V_{\lambda_1}}{V_{\lambda_2}}\right) = \ln\left(\frac{\epsilon_{\lambda_1} K_{2\lambda_1}}{\epsilon_{\lambda_2} K_{2\lambda_2}}\right) + \left(\frac{C_2}{\lambda_2} - \frac{C_2}{\lambda_1}\right) \frac{1}{T} \quad (\text{A.1.9})$$

Since the object size is the same for both detectors the temperature measurement is independent of the particle size.

A.1.2 Calculation of Relative Apparent Object Area

Under given experimental conditions, the output signal voltage for a specific two-wavelength pyrometer can often be considered to be dependent only on the object properties (eg temperature, area and emissivity). If this assumption is valid it is possible to calculate relative changes in these properties with time [89]. From Equation A.1.8, the ratio of the pyrometer output signal (V) at time t, to that at a reference time of, t_0 , can be linked to the temperature, area and emissivity of the object at the two instances by:

$$\frac{V_{\lambda_1}(t)}{V_{\lambda_1}(t_0)} = \frac{A_p(t)}{A_p(t_0)} \cdot \frac{\epsilon_{\lambda_1}(t)}{\epsilon_{\lambda_1}(t_0)} \cdot \frac{\exp[-C_2/\lambda_1 T(t)]}{\exp[-C_2/\lambda_1 T(t_0)]} \quad (\text{A.1.10})$$

Equation A.1.10 is given for the output signal from detector 1, an analogous equation can be derived for detector 2.

If the ratio of the emissivities at the two detector wavelengths is considered to remain constant, changes in the signal due to variations in the area-emissivity component can be determined.

$$\frac{A_p(t)}{A_p(t_0)} \cdot \frac{\epsilon_{\lambda_1}(t)}{\epsilon_{\lambda_1}(t_0)} = \frac{V_{\lambda_1}(t)}{V_{\lambda_1}(t_0)} \cdot \exp\left[\frac{C_2}{\lambda_1} \left(\frac{1}{T(t)} - \frac{1}{T(t_0)}\right)\right] \quad (\text{A.1.11})$$

In order to determine relative changes in area it is necessary that the emissivity of the object be considered to remain constant (or its variation be known) both with time, and over a range of temperature. Due to the relative changes in object area being calculated from only one of the two pyrometer detectors, it is the change in the absolute value of emissivity at the specific detector wavelength (as well the ratio of the emissivity at the two detector wavelengths) which is important. For some solids, especially over a limited range of temperatures, this assumption may be valid, allowing relative changes in particle area to be determined. Changes in the apparent relative area of the small objects passing in front of the pyrometer lens will also occur, due to variations in the amount of radiation collected. In many cases, however, large variations in emissivities (and reflectivities) occur, especially when associated with phase changes [129]. The emissivities of rough

solids can decrease by a factor of 3 on melting [105,130]; which if occurring on heating (with the assumption of constant emissivity) would result in a corresponding, imaginary, decrease in the calculated relative particle area. Notwithstanding these limitations, some useful information can be obtained from apparent relative area calculations.

A.1.3 Pyrometer Accuracy

The theoretical difference between the true object temperature, T , and measured temperature, T_m , due to the variation in emissivities can be calculated by assuming the measured energy is equivalent to the true blackbody energy multiplied by the emissivity. For a two wavelength radiation pyrometer the effect of the emissivity ratio is then given by [120-123]:

$$\frac{W_{\lambda_1 T_m}}{W_{\lambda_2 T_m}} = \frac{\epsilon_{\lambda_1 T} W_{\lambda_1 T}}{\epsilon_{\lambda_2 T} W_{\lambda_2 T}} \quad (\text{A.1.12})$$

Substituting for the monochromatic radiative power with relationships of the form of Equation A.1.5 gives:

$$5 \ln \left(\frac{\lambda_2}{\lambda_1} \right) - \frac{1}{T_m} \left(\frac{C_2}{\lambda_1} - \frac{C_2}{\lambda_2} \right) = \ln \left(\frac{\epsilon_{\lambda_1}}{\epsilon_{\lambda_2}} \right) + 5 \ln \left(\frac{\lambda_2}{\lambda_1} \right) - \frac{1}{T} \left(\frac{C_2}{\lambda_1} - \frac{C_2}{\lambda_2} \right) \quad (\text{A.1.13})$$

from which,

$$\frac{1}{T} - \frac{1}{T_m} = \frac{\lambda_1 \lambda_2}{C_2 (\lambda_2 - \lambda_1)} \ln \left(\frac{\epsilon_{\lambda_1}}{\epsilon_{\lambda_2}} \right) \quad (\text{A.1.14})$$

APPENDIX 2

Mathematical Model of the Two-Wavelength Radiation Pyrometer

From the theoretical consideration of the spectral radiance from a blackbody, the emissivity of the temperature source, the spectral transmittance of the interference filters, and the geometric and physical characteristics of the instrument and system, it is possible to calculate the theoretical performance of a two-wavelength radiation pyrometer.

Two versions of a model of the system were developed. The initial model was formulated and used in the design of the pyrometer to determine its sensitivity and the relative importance of the various design parameters. Following construction of the pyrometer, the specific parameters of the pyrometer were incorporated in the model which then was applied to calculate the apparent combusting particle size from the measured pyrometer signals. This appendix contains an outline of the method used to develop the model.

A.2.1 General

The quantity of energy reaching the detector is dependent on:

- i) source (hot object) properties (T_{object} , ϵ_{object} , A_{object});
- ii) the distance from the source to objective lens;
- iii) the optic system and geometry (the absorptivity, reflectivity, transmittivity, diameter, etc. of each of the lenses and the focal lengths and spacing of the lenses);
- iv) filter properties (centre wavelength, band pass and transmission characteristics);
- v) the detector electronic characteristics (efficiency, area and reflectivity).

A schematic diagram of the relationship amongst the various components is given in Figure A.2.1.

For the calculations it is assumed that:

- i) the ratio of the emissivity of the source at the two detector wavelengths is constant and

independent of source temperature;

ii) the optical properties of the lenses are independent of wavelength at the two pyrometer filter wavelengths.

A.2.2 Model Outline

In both versions of the model, the calculations can be divided into four stages.

For the pyrometer design model these consisted of:

- i) calculation of the proportion of the total blackbody radiation at the chosen object temperature which is transferred to the interference filters and detectors based on the selected source-to-objective lens distance, objective lens area and pyrometer optical components;
- ii) calculation of the fraction of total blackbody radiation being transmitted through the filters at the chosen wavelength and object temperature;
- iii) calculation of the power incident on the detectors if particles of diameter, d , and emissivity ϵ_p are considered instead of a blackbody source;
- iv) calculation of limits of temperature measurement errors based on chosen detector signal resolution.

For the model to predict particle area, steps i) and ii) remain the same except specific properties of the pyrometer component properties were used and the calculations are performed for actual measured particle temperatures. Steps iii) and iv) are replaced by:

- iii) calculation of the power incident on the pyrometer detectors from the measured pyrometer output signals, the specific detector sensitivities and gains;
- iv) calculation of apparent particle area by equating the results from steps ii) and iv), and assuming a particle emissivity of 0.7.

A.2.2.1 Energy Transmitted Through the Filter

The total energy emitted from a blackbody at temperature, T_{bb} , which is transmitted through the interference filters can be calculated by integrating the product of the

blackbody spectral radiance and the filter transmissivity over the whole range of wavelengths transmitted. In practice this must be done by numerical integration. The fraction of the total blackbody radiation between λ_{\min} and λ_{\max} at temperature T_{bb} can be calculated using blackbody functions or from polynomial approximations [146].

$$F_{0-\lambda,T} = \frac{15}{\pi^4} \sum_{m=1,2,\dots} \frac{\exp(-m\nu)}{m^4} \{[(m\nu + 6)m\nu + 6]m\nu + 6\} \quad (A.2.1)$$

where

$$\nu = \frac{C_2}{\lambda T} = \frac{1.4388 \times 10^4}{\lambda T} \quad (\mu m.K) \geq 2$$

The fraction of the total blackbody radiation between λ_{\min} and λ_{\max} is therefore

$$F_{\lambda_{\min}-\lambda_{\max}} = F_{0-\lambda_{\max},T} - F_{0-\lambda_{\min},T} \quad (A.2.2)$$

Each filter transmittance range was divided into 14 equal segments and the calculations were performed numerically on each segment. The fraction of the total blackbody radiation transmitted ($F_{\lambda_{\min}-\lambda_{\max}}$) then is multiplied by the total radiant flux from a blackbody at temperature T_{bb} into surroundings at ambient temperature T_a as follows

$$W_{bb,\lambda_{Trans}} = F_{\lambda_{\min}-\lambda_{\max}} \sigma(T_{bb}^4 - T_a^4) \quad (Wm^{-2}) \quad (A.2.3)$$

A.2.2.2 Power Incident on the Detectors

To calculate the radiant power incident on each of the detectors the physical and optical properties of the pyrometer must be included in the calculations. Since it is assumed that the physical and optical properties of the optics are temperature independent these reduce to a single multiplying constant of the blackbody radiation passing through each of the filters.

If grey-body particles are considered instead of a blackbody radiator the power incident on each of the detectors is given by

$$P_{detector 1} = K_{4\lambda_1} \epsilon_{\lambda_1} d_{particle}^2 W_{bb,\lambda_1,trans} \quad (A.2.4a)$$

$$P_{\text{detector 2}} = K_{4\lambda_2} \epsilon_{\lambda_2} d_{\text{particle}}^2 W_{bb, \lambda_2, \text{trans}} \quad (\text{A.2.4b})$$

$K_{4\lambda_1}, K_{4\lambda_2} = \text{constants}$

From these series of equations the pyrometer design calculations were performed and the apparent particle area model developed.

A.2.2.3 Calculated Measurement Error in Pyrometer Temperature

The maximum temperature error calculated as a function of detector resolution, particle size and temperature was required for the pyrometer design. This was calculated using the relationships given in Equations A.1.6 and A.1.9 for a range of detector resolutions. The maximum and minimum possible temperatures measured for a detector resolution of (ΔV) is therefore

$$\frac{1}{T_{\text{max}}} = K_5 \ln \left[\frac{V_{\lambda_1} - \Delta V}{V_{\lambda_2} + \Delta V} \right] - B \quad (\text{A.2.5a})$$

$$\frac{1}{T_{\text{min}}} = K_5 \ln \left[\frac{V_{\lambda_1} + \Delta V}{V_{\lambda_2} - \Delta V} \right] - B \quad (\text{A.2.5b})$$

A.2.2.4 Apparent Particle Area Calculation

To calculate the apparent particle area it is necessary to equate the energy incident on the pyrometer detector, as calculated from the detector output signal and the pyrometer detector calibration equations (Section 5.2.1), to that calculated by Equation A.2.4 for a particle of unknown size of the experimentally determined temperature.

The pyrometer detector sensitivities (S) are related to the pyrometer gain settings (GS) by an experimentally determined equation (Equations 5.1a and b) and are of the form

$$S_{\lambda_1} = \exp_{10}[K_{S1}(GS)_{\lambda_1} + B_{S1}] \left(\frac{V}{\mu W} \right) \quad (\text{A.2.6a})$$

$$S_{\lambda_2} = \exp_{10}[K_{S2}(GS)_{\lambda_2} + B_{S2}] \left(\frac{V}{\mu W} \right) \quad (\text{A.2.6b})$$

The power incident on the pyrometer detector is then related to the measured detector output voltage by

$$P_{\text{detector 1}} = \frac{V_{\lambda_1}}{S_{\lambda_1}} \quad (\text{A.2.7a})$$

$$P_{\text{detector 2}} = \frac{V_{\lambda_2}}{S_{\lambda_2}} \quad (\text{A.2.7b})$$

Combining Equations A.2.4 and A.2.7 the apparent equivalent diameter of the particle can be calculated

$$d_{\text{particle}} = \left\{ \frac{V_{\lambda_1}}{K_{4\lambda_1} S_{\lambda_1} \epsilon_{\lambda_1} W_{bb, \lambda_1, \text{trans}}} \right\}^{0.5} \quad (\text{A.2.8a})$$

$$d_{\text{particle}} = \left\{ \frac{V_{\lambda_2}}{K_{4\lambda_2} S_{\lambda_2} \epsilon_{\lambda_2} W_{bb, \lambda_2, \text{trans}}} \right\}^{0.5} \quad (\text{A.2.8b})$$

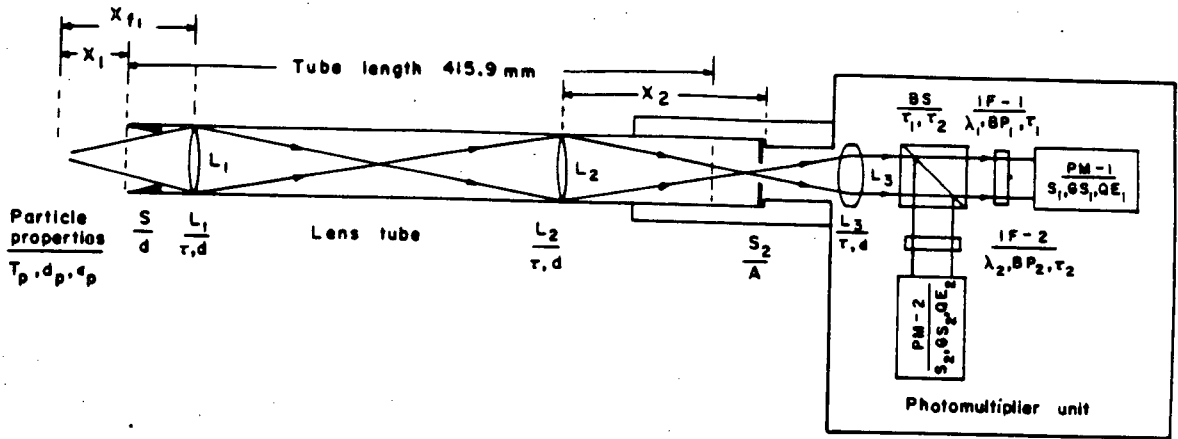


Figure A.2.1 Schematic diagram of the pyrometer optics.

APPENDIX 3

Particle Terminal Velocity and Residence Time Calculations

A.3.1 Particle Terminal Velocity

The terminal velocity of a particle relative to the gas is the result of a balance existing between the gravitational force and the drag force due to differences in the relative motion of particle and the gas. Considering the force balance on a particle travelling at terminal velocity [105,108]:

$$F_{gravitational} = F_{buoyancy} + F_{drag} \quad (A.3.1)$$

for a spherical particle the solution to the equation becomes

$$F_{drag} = F_{gravitational} - F_{buoyancy} = \frac{\pi d_p^3}{6}(\rho_p - \rho_g)g \quad (A.3.2)$$

In general the drag force acting on the particle can be expressed as

$$F_{drag} = C_D A_p \frac{\rho_g}{2} |u_p - u_g| (u_p - u_g) \quad (A.3.3)$$

where C_D is the empirically determined drag coefficient. The drag coefficient is primarily a function of the particle Reynolds number, defined as

$$Re_p = \frac{d_p |u_p - u_g| \rho_g}{\mu} \quad (A.3.4)$$

but may also depend on the particle shape, burning rate and Mach number [108]. The relationship between Re_p and the drag coefficient has been experimentally determined for spherical particles.

For Re_p less than 2 the drag coefficient is given by Stokes Law [105];

$$C_D = \frac{24}{Re_p} \quad (A.3.5.1)$$

For the intermediate range of particle Reynolds Numbers a number of empirical correlations have been proposed [105-106] such as that given by Szekely and Themelis [105] for $2 < Re_p < 500$:

$$C_D \sim \frac{18.5}{Re_p^{0.6}} \quad (A.3.5.2)$$

For $500 < Re_p < 2 \times 10^5$ the drag coefficient is approximately constant [105]:

$$C_D \sim 0.44 \quad (A.3.5.3)$$

If spherical particles are considered the drag force acting on the particles, for the different regions, can be obtained from Equations A.3.3 and A.3.5:

$$Re_p < 2 \quad F_{drag} = 3\pi\mu d_p(u_p - u_g) \quad (A.3.6a)$$

$$2 < Re_p < 500 \quad |F_{drag}| = 2.31\pi\rho_g^{0.4}\mu^{0.6}(u_p - u_g)^{1.4}d_p^{1.4} \quad (A.3.6b)$$

$$500 < Re_p < 2 \times 10^5 \quad |F_{drag}| = 0.055\pi\rho_g(u_p - u_g)^2d_p^2 \quad (A.3.6c)$$

Considering the particle terminal velocity, u_t , from Equation A.3.2 and Equations A.3.6.1 to A.3.6.3

$$Re_p < 2 \quad u_t = u_g + \frac{d_p^2 g (\rho_p - \rho_g)}{18\mu} \quad (A.3.7a)$$

$$2 < Re_p < 500 \quad u_t = u_g + \left\{ \frac{d_p^{1.6} g (\rho_p - \rho_g)}{13.86\rho_g^{0.4}\mu^{0.6}} \right\}^{0.7143} \quad (A.3.7b)$$

$$500 < Re_p < 2 \times 10^5 \quad u_t = u_g + \left\{ 3d_p g \left(\frac{\rho_p}{\rho_g} - 1 \right) \right\}^{0.5} \quad (A.3.7c)$$

A.3.2 Particle Residence Time Calculations

Particles from the particle feeder fall through the stagnant, cool gas in the feed delivery tube before entering the hot gas in the reactor tube (see Figures 4.1 and 4.2). In the stagnant gas of the feed delivery tube the particles tend towards their terminal falling velocity and, after attaining some fraction of this velocity, enter the hot gas in the

furnace. From this velocity the particles are then accelerated or decelerated by the forces acting on them from the flowing gas until a final terminal velocity relative to the hot gas is reached and the forces are balanced.

If several simplifying assumptions are made it is possible to calculate the variation in particle velocity and residence time in the furnace from the simple force balance given in Equation A.3.1. The following simplifications or assumptions were made:

- i) the falling particles are not influenced by each other, and during their flight through the furnace they are considered to travel through two different regions; first through the stagnant cool gas in the feed delivery tube and then into the hot flowing gas in the reactor tube;
- ii) the gas properties were considered constant in each of the regions and the variations in gas velocity due to flow development along the reactor tube was neglected;
- iii) virtual mass effects, Basset forces, Magnus effects and Saffman lift forces were not considered in the force balance [108];
- iv) initially the particles were considered to have no effect on the gas and only the effects of particle heating on the mean gas boundary layer temperature was considered, see Section A.4.2).

Using these assumptions the equation of motion was solved for the falling particles. From Newton's second law the acceleration of the falling particle is given by

$$a_{particle} = \frac{F_{acc}}{m_{particle}} \quad (A.3.8)$$

For a falling particle the force, at any instant, accelerating it towards its terminal velocity is the residual of all the forces acting on the particle and from equation A.3.1

$$F_{acc} = F_{gravitational} - F_{buoyancy} - F_{drag} \quad (A.3.9)$$

combining Equations A.3.8, A.3.9 and A.3.2

$$a_{particle} = \frac{du_p}{dt} = \frac{1}{\left(\frac{\pi}{6}d_p^3\rho_p\right)} \cdot \left\{ \frac{\pi}{6}d_p^3(\rho_p - \rho_g)g - F_{drag} \right\} \quad (A.3.10)$$

where F_{drag} is defined by Equation A.3.6a to A.3.6c depending on the particle Reynolds number. By integrating Equation A.3.10 the particle velocity with respect to time is obtained:

$$u_p(t) = \int_{t_1}^{t_2} \frac{1}{\left(\frac{\pi}{6} d_p^3 \rho_p\right)} \left\{ \frac{\pi}{6} d_p^3 (\rho_p - \rho_g) g - F_{\text{drag}} \right\} dt \quad (\text{A.3.11})$$

A computer model was written in FORTRAN to solve this equation and the position of the particle in the furnace with respect to time. Equation A.3.11 was solved using a fourth order Runge-Kutta subroutine, and a "marching" technique was used to calculate the change in particle position with each time step. The variation of Re_p with changes in particle velocity and gas properties was considered.

The residence time of the particles for the specific furnace dimensions, experimental conditions and feed materials used in the experiments were then calculated.

APPENDIX 4

Combusting Particle Modelling

A.4.1 Particle Heat Balance

From the unsteady heat balance, the rate of heat accumulation is dependent on the rate of heat transfer to the particle through convection from the gas, radiation from the system and heat generated by chemical reaction. Neglecting the temperature dependence and time dependence of the physical properties of a combusting particle the heat balance on the system can be described by Equation A.4.1.

$$-V_p \rho_p C_p \frac{dT}{dt} = A_p h (T_p - T_{wall}) + \sigma \epsilon A_p (T_p^4 - T_{wall}^4) + \sum n_{sx} \Delta H_{R_x} \frac{dM_x}{dt} \quad (A.4.1)$$

where

n_{sx} = a stoichiometric factor related to the over-all reaction considered (see Equation A.4.9)

ΔH_{R_x} = enthalpy of reaction (kJ mol^{-1})

M_x = mols of species x

A.4.2 Heat Transfer Correlations

Using the Rantze-Marshall correlation [105] for heat transfer to a small particle the convective heat transfer coefficient, h , has been correlated through the following equation:

$$Nu = 2 + 0.6 Re_p^{0.5} Pr^{0.33} \quad (A.4.2)$$

where the gas properties are determined at the average boundary layer temperature (T_{film}) given by:

$$T_{film} = \frac{T_{particle} + T_{gas}}{2} \quad (A.4.3)$$

For particles of small diameter and consequently low terminal velocities the product of the Reynolds number and Prandtl number is very small and the Nusselt number tends to a value of two. In the present study a maximum value for the Nusselt number of 2.6

was calculated for a 125 μm galena particle and declined rapidly with decreasing particle size and density. The heat transfer coefficient for convection between the particle and the gas was therefore approximated by:

$$h = \frac{2k_{\text{gas}}}{d_p} \quad (\text{A.4.4})$$

The rate of heat generation due to chemical reaction given by the third term on the right-hand side of Equation A.4.1 is more complex, being dependent on the specific chemical reaction occurring and may vary during the reaction.

A.4.3 Mass Transfer Correlations

For gas phase mass transfer between a particle and the gas a correlation similar to that for heat transfer has been determined [105].

$$Sh = 2 + 0.6Re_p^{0.5}Sc^{0.33} \quad (\text{A.4.5})$$

For particles of small diameter and consequently low terminal velocities the product of the Reynolds number and Schmidt number is very small and the Sherwood number tends to a value of two. The mass transfer coefficient between the particle and the gas can therefore approximated by:

$$k_g = \frac{2D_{A-B}}{d_p} \quad (\text{A.4.6})$$

From the film model of mass transfer [105] for the diffusion of species in a liquid droplet, the mass transfer coefficient can be described by Equation A.4.7 where, δ_l is the stagnant film thickness.

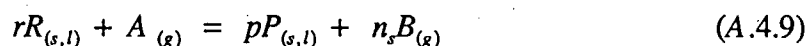
$$k_l = \frac{D_{S-FeS}}{\delta_l} \quad (\text{A.4.7})$$

For the size of droplet considered in this study (10-100 μm) internal circulation of the fluid is negligible [140] and therefore it can be considered a rigid sphere with the droplet radius being equivalent to the stagnant film thickness and therefore

$$k_l = \frac{2D_{S-FeS}}{d_p} \quad (\text{A.4.8})$$

A.4.3.1 The Effects of Non-Equimolar Diffusion on Mass Transfer

A system is considered in which reactant R in the particle is reacting with a gas A to produce a condensed phase reaction product P and a gaseous reaction product B according to the generalised reaction.



i) Equimolar Counter Diffusion.

For equimolar counter diffusion of reactant and product, the stoichiometry factor, n_s , equals one (i.e. the flux of gas reactants, A (O_2), to the reaction interface is equal and opposite to the flux of gaseous product, B (SO_2), away from it).

If the boundary layer around a particle is considered to be small in comparison to its diameter the unidirectional molar flux of species A (in species B) due to diffusion down a concentration gradient is given by [105]:

$$N_A = -cD_{A-B} \frac{dX_A}{dy} + X_A(N_A + N_B) \quad (\text{A.4.10})$$

For a binary system under equimolar counter diffusion:

$$N_A = -N_B \quad (\text{A.4.11})$$

and therefore

$$N_A = -cD_{A-B} \frac{dX_A}{dy} \quad (\text{A.4.12})$$

Solving Equation A.4.12 for the boundary conditions

$$\text{at } Y=0 \text{ (surface)} \quad X_A = X_{A \text{ surface}}$$

$$\text{at } Y=Y_{bl} \text{ (boundary layer)} \quad X_A = X_{A \text{ bulk}}$$

the following is obtained

$$N_A = -\frac{cD_{A-B}}{Y_{bl}} (X_{A \text{ bulk}} - X_{A \text{ surface}}) \quad (\text{A.4.13})$$

ii) Non-equimolar counter diffusion

In the case of non-equimolar counter diffusion

$$n_s \neq 1 \quad (\text{A.4.14})$$

$$n_s N_A = -N_B \quad (\text{A.4.15})$$

Substituting into Equation A.4.10 gives

$$N_A = -\frac{cD_{A-B}}{[1 - (1 - n_s)X_A]} \frac{dX_A}{dy} \quad (\text{A.4.16})$$

and integrating over the same limits as before

$$N_A = \frac{cD_{A-B}}{Y_{bl}(1 - n_s)} \ln \left[\frac{(1 - (1 - n_s)X_{A \text{ bulk}})}{(1 - (1 - n_s)X_{A \text{ surface}})} \right] \quad (\text{A.4.17})$$

The enhancement of oxygen mass transfer due to the bulk movement of fluid in the gas boundary layer, as the result of non-equimolar diffusion, is dependent on the reaction stoichiometry. For the formation of wustite and magnetite, in oxygen (Equations 7.3 and 7.4), relative increases of 22 and 28% were calculated.

iii) Diffusion of a dilute species in a bulk medium

At lower oxygen concentrations (balance nitrogen) it is possible to consider the diffusion of oxygen to be through a stagnant film and to neglect the outward diffusion of the small quantities of reaction product. Under such conditions

$$N_B \sim 0 \quad (\text{A.4.18})$$

therefore following a similar analysis [105]

$$N_A = \frac{cD_{A-B}}{Y_{bl}} \ln \left[\frac{(1 - X_{A \text{ bulk}})}{(1 - X_{A \text{ surface}})} \right] \quad (\text{A.4.19})$$

As the boundary layer is being considered in a binary system

$$X_B = 1 - X_A \quad (\text{A.4.20})$$

Equation A.4.19 can be rewritten as:

$$N_A = \frac{cD_{A-B}}{Y_{bl}} \ln \left[\frac{X_{B \text{ bulk}}}{X_{B \text{ surface}}} \right] \quad (\text{A.4.21})$$

The logarithmic mean concentration of the non diffusing gas can be defined as:

$$(X_B)_{lm} = \frac{X_{B \text{ bulk}} - X_{B \text{ surface}}}{\ln \left[\frac{X_{B \text{ bulk}}}{X_{B \text{ surface}}} \right]} \quad (\text{A.4.22})$$

which substituting in to Equation A.4.21 gives

$$N_A = \frac{cD_{A-B}}{Y_{bl}(X_B)_{lm}} (X_{B \text{ bulk}} - X_{B, \text{surface}}) \quad (\text{A.4.23})$$

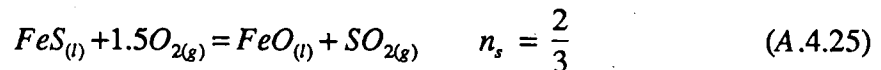
and substituting for X_B

$$N_A = -\frac{cD_{A-B}}{Y_{bl}(X_B)_{lm}} (X_{A \text{ bulk}} - X_{A \text{ surface}}) \quad (\text{A.4.24})$$

A.4.4 Estimate of Relative Magnitude of Gas Phase and Liquid Phase Mass Transfer

In an attempt to determine the rate limiting step in the combustion of iron sulphide, an estimate of relative magnitudes of the limiting rates of mass transfer in the gas and liquid phases are necessary. The transfer of oxygen in the gas phase, and of sulphur in the liquid phase to the reaction interface were considered.

At temperatures above $\sim 2000\text{K}$, the reaction of iron sulphide (to wustite and sulphur dioxide) was considered to occur through the overall reaction given in Equation A.4.25.



For pure oxygen, considering the effects of non-equimolar diffusion in the gas phase (Equation A.4.17.), the flux of reactants to the gas-liquid interface due to gas and liquid phase mass transfer can be approximated by Equation A.4.26 [105].

$$N_{\text{O}_{2(g)}} = -1.5N_{\text{S}_{(l)}} = 3k_g c_g \ln \left[\frac{(3 - X_{\text{O}_2 \text{ bulk}})}{(3 - X_{\text{O}_2 \text{ surface}})} \right] = 1.5k_l (c_{s \text{ bulk}} - c_{s \text{ surface}}) \quad (\text{A.4.26})$$

For air a similar equation was derived considering dilute species diffusion as described by Equation A.4.24.

The mass transfer coefficients for small particles were calculated using empirical correlations given in Equations A.4.6 and A.4.7. Comparing mass transfer under limiting conditions in which surface concentrations are zero, for gas phase mass transfer to be limiting the following inequality must be satisfied:

$$2\alpha \frac{D_{O_2-SO_2/N_2}}{d_p} c_g \ll 1.5 \frac{D_{S-FeS}}{\delta_l} c_{S_{bulk}} \quad (A.4.28)$$

where

$\alpha = 1.2$ for oxygen

$\alpha = (1.12 \times 0.21) = 0.24$ for air

$\alpha = 1.0$ for equimolar counter diffusion

As a rough check, as to the thickness of the liquid phase concentration boundary layer, δ_l , the thickness was calculated from the liquid phase mass transfer coefficient, k_l , of carbon in iron of $3.2 \times 10^{-4} \text{ m s}^{-1}$, reported by Distin et al. [147] for the combustion of carbon impurities in levitated iron drops. From Equation A.4.7, estimating the value of the diffusion coefficient for carbon in iron to be $10^{-8} \text{ m}^2 \text{ s}^{-1}$ (for C in Fe-3.5% C [105]) a boundary layer thickness, δ_l , of $\sim 31 \mu\text{m}$ is calculated. For the calculations the apparent radius of the droplet was therefore considered as equivalent to the diffusion distance δ_l .

From the experimental values and temperature dependence of the diffusivities presented by Gieger and Poirier [139] and Szekeley and Themelis [105], it is estimated that:

i) Liquid phase diffusion of sulphur

$$D_{S-FeS} = 10^{-8} - 10^{-7} \text{ m}^2 \text{ s}^{-1} \text{ at } 2000\text{K.}$$

$$= 10^{-7} - 10^{-6} \text{ m}^2 \text{ s}^{-1} \text{ at } 3000\text{K.}$$

ii) Gas phase diffusion of oxygen in oxygen/nitrogen

$$D_{O_2-SO_2/N_2} = \sim 2 - 4 \times 10^{-4} \text{ m}^2 \text{ s}^{-1} \text{ at } T_{\text{film}} = 1565\text{K}$$

$$= \sim 4 - 6 \times 10^{-4} \text{ m}^2 \text{ s}^{-1} \text{ at } T_{\text{film}} = 2065\text{K.}$$

Considering a particle of 32.5 μm radius combusting in a gas stream at 1130K; the following comparison is obtained for Equation A.4.28:

$$T_{\text{PARTICLE}} = 2000\text{K}$$

<i>Liquid phase mass transfer</i>	>	<i>gas phase mass transfer (mols m² s⁻¹)</i>
25 – 250		13 (Air)
	(> ?)	109 (Oxygen)

$$T_{\text{PARTICLE}} = 3000\text{K}$$

250 – 2500	>	135 (Oxygen)
------------	---	--------------

These calculations indicate that it is probable that gas phase mass transfer control is limiting the reaction at these temperatures.

APPENDIX 5

Pyrometer Calibration

A.5.1 Calibrated Temperature Sources Available

Ultimately the accuracy of calibration possible from any calibration source will depend on the accuracy to which the source itself was calibrated. This primary calibration of the temperature source can be performed either by a Standards Laboratory or using standard techniques outlined by Kostkowski and Lee [122].

Two types of calibration source commonly used to calibrated pyrometers are blackbody cavity furnaces and tungsten filament lamps [121,122]. Each technique suffers from its own inherent problems and is more suited to certain applications or temperature ranges. The spectral radiation from a blackbody as a function of wavelength and temperature is generally accepted to be accurately described by Plank's radiation Equation A.1.1, and therefore blackbodies are generally used as primary calibration sources. Blackbodies are however not particularly convenient to use and those commercially available are not suitable for use at temperatures above $\sim 1000^{\circ}\text{C}$. At higher temperatures tungsten filament lamps are often used. These sources are relatively stable and easy to use. The lamps spectral radiation dependence on wavelength and temperature differs from that predicted by Plank's radiation equation and therefore it is necessary to calibrate the lamp at both the temperatures and wavelengths of interest before use. The calibration, against a blackbody temperature source, is normally performed at a Standards Laboratory [122].

Most researchers measuring the temperature of combusting particles have used calibrated tungsten strip lamps for pyrometer calibration [82]. Typically tungsten filament lamps are calibrated for temperature between $800\text{-}2800^{\circ}\text{C}$ [124,125]. For two-wavelength radiation pyrometry the lamp should be calibrated at both detector

interference filter wavelengths. The accuracy of the lamp temperature measurement is reported as typically <0.5% [121]. If the measured temperature must be corrected for the differences in the emissivity of tungsten at the two wavelengths greater errors will result.

It was decided at an early stage to design and construct a series of blackbody cavities to allow the pyrometer to be calibrated over a range of temperature. The main reason for rejecting the much easier to use calibrated tungsten lamp was the difficulty in finding a supplier of such lamps. The National Bureau of Standards (NBS, Washington, D.C.) the main supplier, was reluctant to supply calibrated lamps due to quality problems with the type of lamp normally used.

The accuracy of pyrometer calibration using the constructed blackbody will depend both on the intrinsic limitations of the blackbody furnace design and also on the accuracy to which the blackbody itself was calibrated. The accuracy of the blackbody calibration furnace is therefore discussed after the specifics of the design has been presented.

A.5.2 Blackbody Temperature Sources

For an opaque surface, radiation incident on the surface can be absorbed or reflected. A blackbody is an object which absorbs all radiation incident on it and emits radiation in accordance with that predicted by Plank's radiation Equation. The emissivity, ϵ_λ , and absorptivity, α_λ , of a blackbody are equal such that:

$$\epsilon_\lambda = \alpha_\lambda = 1 \quad (\text{A.5.1})$$

Few surfaces approximate a blackbody as in general a proportion of the incident radiation is reflected. The reflectivity, ρ_λ , is related to the emissivity and absorptivity by

$$\epsilon_\lambda = \alpha_\lambda = 1 - \rho_\lambda \quad (\text{A.5.2})$$

The apparent emissivity of a surface can be greatly increased by viewing into a cavity rather than a flat surface [121,122]. The radiation reflected from the cavity tends to be incident on other parts of the cavity such that only a very small portion of the initial radiation is not absorbed after multiple reflections. In general, the greater the surface area

of the cavity with respect to the area of the hole the nearer the cavity will approach a blackbody ($\epsilon_\lambda = 1$). As well as the cavity-to-hole area ratio the apparent emissivity will depend on the apparent surface emissivity which is dependent on the roughness of the cavity. The apparent emissivity of cylindrical cavities as a function of a number of parameters has been tabulated both from analytical calculations and experimental measurements [121]. The effects of i) length to diameter ratio, ii) surface emissivity, iii) surface roughness and iv) radial position have been examined. For length/diameter (L/D) ratios greater than 5 and surface emissivities greater than 0.7 cavity emissivities of greater than 0.99 are predicted. With increasing L/D ratio or surface emissivity the value of cavity emissivity rapidly approaches unity (see Figure A.5.1).

To use a blackbody cavity as a temperature source it is also necessary that the walls of the cavity be isothermal and that the temperature can be measured accurately. One solution to this problem is to use the melting point and the latent heat released during freezing of a metal to produce an isothermal blackbody of a defined temperature. This technique, using the melting point of gold and silver, has been used by the NBS to produce very accurate primary calibration sources [122]. Blackbodies relying on the melting points of copper, aluminium, zinc, tin and alloys of known melting point have also been used [134], with a lesser degrees of accuracy. This technique is not suitable for calibrations over a range of temperatures. To calibrate the pyrometer over a range of temperatures a cavity blackbody is often used, the temperature of which is determined by a thermocouple or another pyrometer which has been calibrated against a primary temperature source.

Considering the various requirements and limitations of blackbody cavity calibration sources a series of blackbody cavities were designed and constructed to allow calibration of the pyrometer over a range of temperatures. Three blackbody cavity furnaces were constructed to verify calibration and to allow calibration over a wide range of pyrometer detector gain settings. The furnaces constructed were:

- 1) copper freezing point furnace - $T_{\text{furnace}}=1358\text{K}$;
- 2) low-temperature blackbody furnace - $T_{\text{furnace}}=1100\text{-}1550\text{K}$;
- 3) high-temperature induction heated blackbody furnace - $T_{\text{furnace}}=1500\text{-}1950\text{K}$.

The copper-freezing-point blackbody furnace was considered the primary standard. The Type-S thermocouple used for this experiment was then used as the secondary standard with which the temperature of the other blackbody cavities were measured.

A.5.3 Copper Freezing Point Blackbody

Primary calibration of the pyrometer was performed using a copper freezing point blackbody cavity. The design of the blackbody is detailed in Figure A.5.2. The cavity consisted of a 9mm OD, 7mm ID closed end alumina tube 187mm long. The alumina tube was inserted in a 127mm x 36.5mm ID mullite crucible containing 670g of reagent grade copper shot (>99.9% Cu) resulting in an immersion depth of 66mm. Powdered graphite was placed on top of copper bath to prevent oxidation of the copper metal. A Pt-Pt/10%Rh thermocouple mounted in a 5mm OD, 3mm ID alumina sheath was also inserted into the copper bath to measure the bath temperature and to give a reference point for thermocouple calibration. The mullite crucible was enclosed in a machined graphite susceptor and heated by induction. The susceptor was insulated with 75mm of Fibrefrax blanket. The pyrometer was mounted on a frame vertically above the alumina cavity and attached using a specially constructed lens tube incorporating a 1mm diameter aperture stop. This 1mm diameter aperture limits the pyrometer view to an area at the bottom of the cavity completely immersed in the molten copper. The walls of the cavity were coated with lamp black to increase emissivity and a low flow of argon was purged through the lens tube to prevent oxidation.

The cavity L/D ratio was 9.4 and the estimated emissivity of lamp black is 0.99 [122] resulting in a effective cavity emissivity of >0.999 (from Figure A.5.1). Using a value of ~0.47 [105] for the emissivity of alumina the same cavity would have a effective emissivity of ~0.99 [121].

The results of a typical cooling experiment obtained during copper solidification are given in Table A.5.1 and Figure A.5.3. The melting point of copper measured by the type-S thermocouple was 1358.2K which can be compared with the literature value of 1358.03K [134,135]. The error of $\sim 0.015\%$ between the measured and literature value is negligible and therefore no temperature corrections were made.

A.5.4 Low Temperature Resistance Heated Blackbody Furnace

A diagram of the low temperature blackbody cavity furnace is given in Figure A.5.4. A 89mm x 12.5mm diameter cavity was drilled in a 150mm x 32mm OD graphite block. A 7.9mm diameter hole was drilled through the two plugs at one end to allow the central cavity to be observed. A smaller hole was drilled into the plugs at the other end such that a 5mm alumina sheath containing the calibrated thermocouple could be positioned a fraction of a millimeter behind the cavity wall. The graphite block was mounted inside of a 300mm x 32mm ID 'clamshell', Kanthal wound furnace insulated with 100mm of insulating brick. The furnace was capable of supplying 1200 watts and had an upper temperature limit of 1500K. Power was controlled manually by a Variac transformer. In an attempt to reduce temperature gradients in the blackbody cavity a series of compartments were constructed within the furnace using alumina discs. Fibrefrax plugs were positioned at the ends. A quartz window was sealed over the blackbody cavity viewing hole and the whole furnace was purged with argon to prevent oxidation of the graphite.

To sight the pyrometer directly into the blackbody the cavity was viewed through a 3mm diameter aperture fixed in front of the quartz viewing window (see Figure A.5.4) and an aperture of variable size rotated between the blackbody and the pyrometer lens. Varying the diameter of the aperture between 0.33 and 2mm varied the amount of radiation reaching the pyrometer detectors such that calibration could be performed for a range of detector gain settings.

As the diameter of the cavity is greater than the aperture, the ratio of the cavity length to aperture diameter is used. The L/D ratio for the cavity was 11.2 and considering the high emissivity of graphite [105] the apparent emissivity of the cavity is >0.999 [121].

The experimental results of the low-temperature blackbody cavity furnace calibration experiments are reported in Table A.5.2. As well as indicating the reproducibility of calibration, the results also indicate that similar calibration constants were determined using both the calibration lens tube and the actual water-cooled lens tube used for the experimental measurements.

A.5.5 High Temperature Induction Heated Blackbody Furnace

A schematic diagram of the high temperature blackbody furnace is given in Figure A.5.5. The 75 x 12.5mm diameter cavity drilled in a 150 x 37.5mm diameter graphite rod was mounted in a 127mm OD mullite tube filled with Safil insulation. A 150 x 6.35mm ID alumina tube was inserted into the graphite block to allow the pyrometer to be sighted, via the lens tube, through the 6.35mm diameter aperture into the cavity. The temperature of the block was measured with a type S thermocouple mounted in a 5mm OD alumina sheath positioned a fraction of a millimeter behind the viewed surface. The blackbody was horizontally mounted within the coils of an induction furnace capable of supplying up to 12 kilowatts. The L/D ratio of the cavity is 12 which corresponds to an apparent emissivity of >0.999 [121].

Temperature measurements were made after the furnace power was shut off and the calibration results were taken at the inflection between blackbody heating and cooling as measured by the thermocouple. The results of the series of calibration experiments are reported in Table A.5.3.

A.5.6 Calibration Accuracy

The calibration accuracy of the pyrometer will ultimately depend on the accuracy of calibration of the blackbody. For the blackbodies described their accuracy as temperature source will depend on both their design and the accuracy to which the thermocouple was calibrated.

From an examination of the blackbody designs, the L/D ratios and emissivities it is estimated that the apparent cavity temperature is within $\pm 0.25\%$ of that recorded by the thermocouple.

The same type-S thermocouple was used to measure the temperature in all three blackbody furnaces. The reported accuracy [149] of the type-S thermocouple used is $\pm 1.5^\circ\text{C}$ or $\pm 0.25\%$. The platinum wire was joined to copper directly in an icebath and therefore no errors were introduced through the use of compensation wire. The temperature measured by the thermocouple in the copper freezing point test was 1358.2K with a standard deviation of 0.18 as compared with the literature value of 1358.02K [136]. The agreement is to within $\pm 0.015\%$, however considering i) the slight uncertainty which exists as to the exact melting point of the 99.99% pure copper saturated with carbon [136,149,127] and ii) the errors associated with a single point calibration, the reported accuracy of $\pm 0.25\%$ was considered more realistic.

The overall limit of error of the measurement of the true blackbody temperature was considered to be the sum of the errors of both the thermocouple calibration and those intrinsic in the blackbody design. The overall blackbody temperature errors were therefore estimated at $\sim \pm 0.5\%$ representing an error of $\pm 10\text{K}$ at 2000K. The effects of this error and the overall accuracy of the pyrometer measurements is discussed in Section 5.2.8.

Table A.5.1 Pyrometer Calibration Test Data - copper freezing point calibration test.
 $GS_{710}=8.23$, $GS_{810}=9.9$

Time (s)	V_{710} (V)	V_{810} (V)	C_{val}	$\ln(V_{810}/V_{710})$	T(K)	1/T (K^{-1})
20	0.415	0.605	1.416	0.3776	1394.15	7.17E-04
40	0.325	0.491	1.414	0.4130	1368.15	7.31E-04
60	0.288	0.444	1.407	0.4333	1358.25	7.36E-04
80	0.288	0.442	1.413	0.4278	1358.25	7.36E-04
100	0.286	0.442	1.404	0.4363	1358.35	7.36E-04
120	0.286	0.442	1.404	0.4363	1358.35	7.36E-04
140	0.283	0.442	1.396	0.4449	1358.35	7.36E-04
160	0.286	0.439	1.410	0.4308	1358.35	7.36E-04
180	0.283	0.439	1.401	0.4394	1358.35	7.36E-04
200	0.286	0.437	1.415	0.4252	1358.35	7.36E-04
220	0.286	0.437	1.415	0.4252	1358.35	7.36E-04
240	0.286	0.432	1.427	0.4140	1357.95	7.36E-04
260	0.286	0.435	1.422	0.4196	1357.85	7.36E-04
280	0.283	0.432	1.418	0.4226	1357.95	7.36E-04
300	0.288	0.435	1.430	0.4111	1358.05	7.36E-04
320	0.286	0.432	1.427	0.4140	1358.15	7.36E-04
340	0.286	0.432	1.427	0.4140	1358.05	7.36E-04
360	0.281	0.432	1.410	0.4312	1358.15	7.36E-04
380	0.283	0.427	1.430	0.4112	1358.15	7.36E-04
400	0.278	0.427	1.412	0.4286	1358.15	7.36E-04
420	0.278	0.425	1.418	0.4229	1357.95	7.36E-04
440	0.273	0.420	1.412	0.4290	1357.85	7.36E-04
460	0.278	0.430	1.407	0.4343	1358.05	7.36E-04
480	0.286	0.432	1.426	0.4140	1358.35	7.36E-04
500	0.278	0.427	1.412	0.4286	1358.35	7.36E-04
520	0.276	0.422	1.415	0.4259	1358.35	7.36E-04
540	0.276	0.422	1.415	0.4259	1358.25	7.36E-04
560	0.276	0.422	1.415	0.4259	1358.15	7.36E-04
580	0.273	0.422	1.406	0.4348	1358.35	7.36E-04
600	0.273	0.422	1.406	0.4348	1358.35	7.36E-04
620	0.269	0.420	1.393	0.4470	1358.35	7.36E-04
640	0.269	0.420	1.393	0.4470	1358.45	7.36E-04
660	0.271	0.417	1.408	0.4321	1358.35	7.36E-04
680	0.269	0.417	1.399	0.4412	1358.35	7.36E-04
700	0.269	0.415	1.405	0.4353	1358.45	7.36E-04

Table A.5.2 Pyrometer Calibration Test Data.

1) Rotating disc and resistance heated low temperature blackbody cavity Furnace calibration test

d_{hole} (mm)	GS ₇₁₀	GS ₈₁₀	V ₇₁₀ (V)	V ₈₁₀ (V)	C _{val}	$\ln(V_{810}/V_{710})$	T(K)	1/T (K ⁻¹)
2	8.23	9.9	0.176	0.405	1.427	0.8353	1105	9.05E-4
2	8.23	9.9	0.276	0.618	1.399	0.8060	1134	8.82E-4
2	8.23	9.9	0.283	0.625	1.411	0.7916	1135	8.81E-4
2	8.23	9.9	0.393	0.840	1.402	0.7592	1157	8.64E-4
2	8.23	9.9	0.669	1.321	1.414	0.6803	1194	8.38E-4
2	8.23	9.9	1.035	1.929	1.418	0.6223	1226	8.16E-4
2	8.23	9.9	1.887	3.293	1.407	0.5568	1273	7.86E-4
2	8.23	9.9	2.866	4.761	1.405	0.5074	1307	7.65E-4
2	8.23	9.9	4.778	7.483	1.402	0.4486	1351	7.40E-4
1	8.23	9.9	1.843	2.690	1.411	0.3782	1397	7.16E-4
1	8.23	9.9	2.837	3.899	1.419	0.3180	1439	6.95E-4
1	8.23	9.9	3.984	5.227	1.422	0.2715	1476	6.78E-4
1	8.23	9.9	5.449	6.978	1.407	0.2472	1511	6.62E-4
1	8.23	9.9	6.819	8.469	1.409	0.2168	1538	6.50E-4
2	6.73	8.4	0.046	0.127	1.150	1.0068	1159	8.63E-4
2	6.73	8.4	0.078	0.205	1.123	0.9651	1197	8.35E-4
2	6.73	8.4	0.115	0.293	1.100	0.9373	1227	8.15E-4
2	6.73	8.4	0.220	0.505	1.126	0.8329	1276	7.84E-4
2	6.73	8.4	0.330	0.718	1.130	0.7783	1310	7.63E-4
2	6.73	8.4	0.552	1.147	1.113	0.7322	1355	7.38E-4
2	6.73	8.4	0.833	1.653	1.109	0.6858	1393	7.18E-4
1	6.73	8.4	0.317	0.593	1.108	0.6255	1442	6.93E-4
1	6.73	8.4	0.457	0.813	1.111	0.5770	1481	6.75E-4
1	6.73	8.4	0.623	1.077	1.101	0.5478	1516	6.60E-4
1	6.73	8.4	0.757	1.292	1.088	0.5344	1541	6.49E-4
1	8.23	9.9	3.984	5.227	1.422	0.2715	1476	6.78E-4
1	7.73	9.4	1.904	2.817	1.299	0.3917	1478.5	6.76E-4
1	7.23	8.9	0.933	1.494	1.219	0.4713	1479	6.76E-4
1	6.73	8.4	0.457	0.813	1.111	0.5770	1481	6.75E-4
1	6.23	7.9	0.227	0.452	0.999	0.6878	1482	6.75E-4
2	5.73	7.4	0.491	1.069	0.906	0.7789	1484	6.74E-4
2	5.23	6.9	0.247	0.596	0.801	0.8820	1485	6.73E-4
2	4.73	6.4	0.127	0.334	0.714	0.9687	1486	6.73E-4
1	8.23	9.9	6.819	8.469	1.409	0.2168	1538	6.50E-4
1	7.73	9.4	3.247	4.495	1.299	0.3251	1539	6.50E-4
1	7.23	8.9	1.550	2.373	1.199	0.4257	1539	6.50E-4
1	6.73	8.4	0.757	1.292	1.088	0.5344	1541	6.49E-4
1	6.23	7.9	0.378	0.706	0.998	0.6230	1542	6.49E-4
2	5.73	7.4	0.798	1.653	0.893	0.7277	1542.5	6.48E-4
2	5.23	6.9	0.398	0.911	0.792	0.8278	1543	6.48E-4
2	4.73	6.4	0.198	0.513	0.667	0.9527	1544	6.48E-4

Table A.5.2 (continued)

d_{hole} (mm)	GS ₇₁₀	GS ₈₁₀	V ₇₁₀ (V)	V ₈₁₀ (V)	C _{val}	$\ln(V_{810}/V_{710})$	T(K)	1/T (K ⁻¹)
-	-8.23	9.9	0.339	0.493	1.421	0.3738	1393	7.18E-4
-	8.23	9.9	0.366	0.522	1.435	0.3553	1396.5	7.16E-4
-	8.23	9.9	0.422	0.601	1.436	0.3520	1398	7.15E-4
-	8.23	9.9	0.474	0.676	1.428	0.3562	1401	7.14E-4
-	8.23	9.9			1.430		1426	7.01E-4
*	5.23	6.9	0.508	1.334	0.813	0.9655	1406	7.11E-4
*	5.23	6.9	0.943	2.465	0.808	0.9613	1413	7.08E-4
*	5.23	6.9	0.510	1.343	0.809	0.9678	1407	7.11E-4
*	5.73	7.4	2.468	0.905	0.905	0.8710	1407.65	7.10E-4
*	5.73	7.4	2.466	0.908	0.908	0.8680	1407.65	7.10E-4
*	6.23	7.9	4.575	0.997	0.997	0.7786	1408	7.10E-4
*	6.23	7.9	4.538	0.998	0.998	0.7776	1408	7.10E-4
*	6.23	7.9	4.965	1.006	1.006	0.7683	1409	7.10E-4
*	6.73	8.4	9.850	1.104	1.104	0.6690	1410	7.09E-4

* Water-cooled Lens Tube

Table A.5.3 Pyrometer Calibration Test Data.

2) Induction heated high temperature blackbody calibration test

GS ₇₁₀	GS ₈₁₀	V ₇₁₀ (volts)	V ₈₁₀ (volts)	Cval	$\ln(V_{810}/V_{710})$	T(K)	1/T (K ⁻¹)
8.23	9.9	1.653	1.992	1.413	0.1867	1563	6.40E-4
8.23	9.9	2.412	2.864	1.428	0.1716	1563	6.40E-4
8.23	9.9	1.873	2.307	1.422	0.2087	1533	6.52E-4
8.23	9.9	1.584	1.987	1.426	0.2265	1513	6.61E-4
8.23	9.9	3.066	3.569	1.417	0.1519	1593	6.28E-4
8.23	9.9	2.615	3.123	1.412	0.1775	1573	6.36E-4
8.23	9.9	2.229	2.715	1.413	0.1972	1553	6.44E-4
8.23	9.9	1.863	2.336	1.415	0.2265	1523	6.57E-4
8.57	9.9	4.250	3.025	1.929	-0.3402	1573	6.36E-4
8.57	9.9	3.376	2.483	1.928	-0.3074	1543	6.48E-4
8.57	9.9	2.844	2.148	1.922	-0.2806	1523	6.57E-4
8.57	9.9	2.397	1.848	1.924	-0.2602	1503	6.65E-4
8.57	9.9	2.012	1.582	1.926	-0.2403	1483	6.74E-4
8.42	9.78	3.264	2.515	1.850	-0.2609	1573	6.36E-4
8.42	9.78	2.813	2.205	1.853	-0.2435	1553	6.44E-4
8.42	9.78	2.397	1.917	1.855	-0.2239	1533	6.52E-4
8.42	9.78	2.034	1.660	1.855	-0.2029	1513	6.61E-4
8.42	9.78	1.721	1.436	1.856	-0.1815	1493	6.70E-4
7.55	9.3	2.192	2.930	1.187	0.2899	1693	5.91E-4
7.55	9.3	1.794	2.463	1.186	0.3168	1663	6.01E-4
7.55	9.3	1.462	2.061	1.188	0.3429	1633	6.12E-4
7.55	9.3	1.270	1.826	1.186	0.3636	1613	6.20E-4
7.55	9.3	1.082	1.577	1.192	0.3772	1593	6.28E-4
7.73	9.4	2.678	3.149	1.332	0.1621	1673	5.98E-4
7.73	9.4	2.317	2.776	1.332	0.1807	1653	6.05E-4
7.73	9.4	2.004	2.449	1.331	0.2002	1633	6.12E-4
7.73	9.4	1.729	2.148	1.332	0.2175	1613	6.20E-4
7.73	9.4	1.472	1.873	1.329	0.2406	1593	6.28E-4
7.4	9.05	2.651	3.079	1.285	0.1494	1743	5.74E-4
7.4	9.05	2.698	3.130	1.286	0.1486	1743	5.74E-4
7.4	9.05	2.373	2.800	1.285	0.1655	1723	5.80E-4
7.4	9.05	2.075	2.483	1.289	0.1794	1703	5.87E-4
7.4	9.05	1.741	2.141	1.278	0.2070	1683	5.94E-4
7.23	8.9	2.979	3.491	1.235	0.1588	1793	5.58E-4
7.23	8.9	2.424	2.920	1.232	0.1860	1763	5.67E-4
7.23	8.9	2.129	2.610	1.231	0.2037	1743	5.74E-4
7.23	8.9	1.863	2.324	1.230	0.2213	1723	5.80E-4
7.23	8.9	1.626	2.065	1.229	0.2392	1703	5.87E-4

Table A.5.3 (continued)

GS ₇₁₀	GS ₈₁₀	V ₇₁₀ (volts)	V ₈₁₀ (volts)	Cval	ln(V ₈₁₀ /V ₇₁₀)	T(K)	1/T (K ⁻¹)
7.08	8.73	2.473	2.942	1.213	0.1736	1803	5.55E-4
7.08	8.73	2.183	2.642	1.211	0.1909	1783	5.61E-4
7.08	8.73	1.924	2.363	1.212	0.2057	1763	5.67E-4
7.08	8.73	1.687	2.109	1.211	0.2234	1743	5.74E-4
7.08	8.73	1.477	1.880	1.210	0.2412	1723	5.80E-4
6.73	8.4	1.973	2.454	1.138	0.2182	1843	5.43E-4
6.73	8.4	1.726	2.178	1.139	0.2324	1823	5.49E-4
6.73	8.4	1.531	1.965	1.137	0.2499	1803	5.55E-4
6.73	8.4	1.350	1.760	1.137	0.2653	1783	5.61E-4
6.73	8.4	1.189	1.577	1.136	0.2825	1763	5.67E-4
6.6	8.2	1.794	2.097	1.186	0.1559	1863	5.37E-4
6.6	8.2	1.594	1.892	1.185	0.1713	1843	5.43E-4
6.6	8.2	1.414	1.707	1.183	0.1883	1823	5.49E-4
6.6	8.2	1.260	1.541	1.185	0.2012	1803	5.55E-4
6.6	8.2	1.108	1.379	1.183	0.2187	1783	5.61E-4
6.23	7.9	1.257	1.687	1.034	0.2940	1883	5.31E-4
6.23	7.9	1.072	1.470	1.026	0.3158	1863	5.37E-4
6.23	7.9	0.955	1.328	1.026	0.3302	1843	5.43E-4
6.23	7.9	0.845	1.196	1.023	0.3480	1823	5.49E-4
6.23	7.9	0.750	1.077	1.024	0.3622	1803	5.55E-4
5.73	7.4	0.640	0.950	0.925	0.3952	1893	5.28E-4
5.73	7.4	0.569	0.857	0.925	0.4097	1873	5.34E-4
5.73	7.4	0.510	0.776	0.929	0.4197	1853	5.40E-4
5.73	7.4	0.479	0.737	0.924	0.4323	1843	5.43E-4
5.73	7.4	0.452	0.698	0.928	0.4356	1833	5.46E-4
5.23	6.9	0.356	0.579	0.822	0.4845	1913	5.23E-4
5.23	6.9	0.320	0.522	0.830	0.4908	1893	5.28E-4
5.23	6.9	0.288	0.476	0.832	0.5023	1873	5.34E-4
5.23	6.9	0.256	0.430	0.833	0.5165	1853	5.40E-4
5.23	6.9	0.227	0.388	0.828	0.5363	1833	5.46E-4
4.73	6.4	0.200	0.352	0.730	0.5631	1933	5.17E-4
4.73	6.4	0.178	0.320	0.722	0.5847	1913	5.23E-4
4.73	6.4	0.159	0.291	0.716	0.6047	1893	5.28E-4
4.73	6.4	0.225	0.396	0.714	0.5658	1953	5.12E-4
4.73	6.4	0.200	0.356	0.716	0.5769	1933	5.17E-4
8.23	9.9	6.018	6.416	1.430	0.0640	1673	5.98E-4
8.23	9.9	5.168	5.627	1.427	0.0851	1653	6.05E-4
8.23	9.9	4.795	5.266	1.428	0.0937	1643	6.09E-4
8.23	9.9	7.891	8.130	1.430	0.0299	1713	5.84E-4
8.23	9.9	6.865	7.200	1.429	0.0476	1693	5.91E-4
8.23	9.9	9.077	9.165	1.433	0.0096	1733	5.77E-4

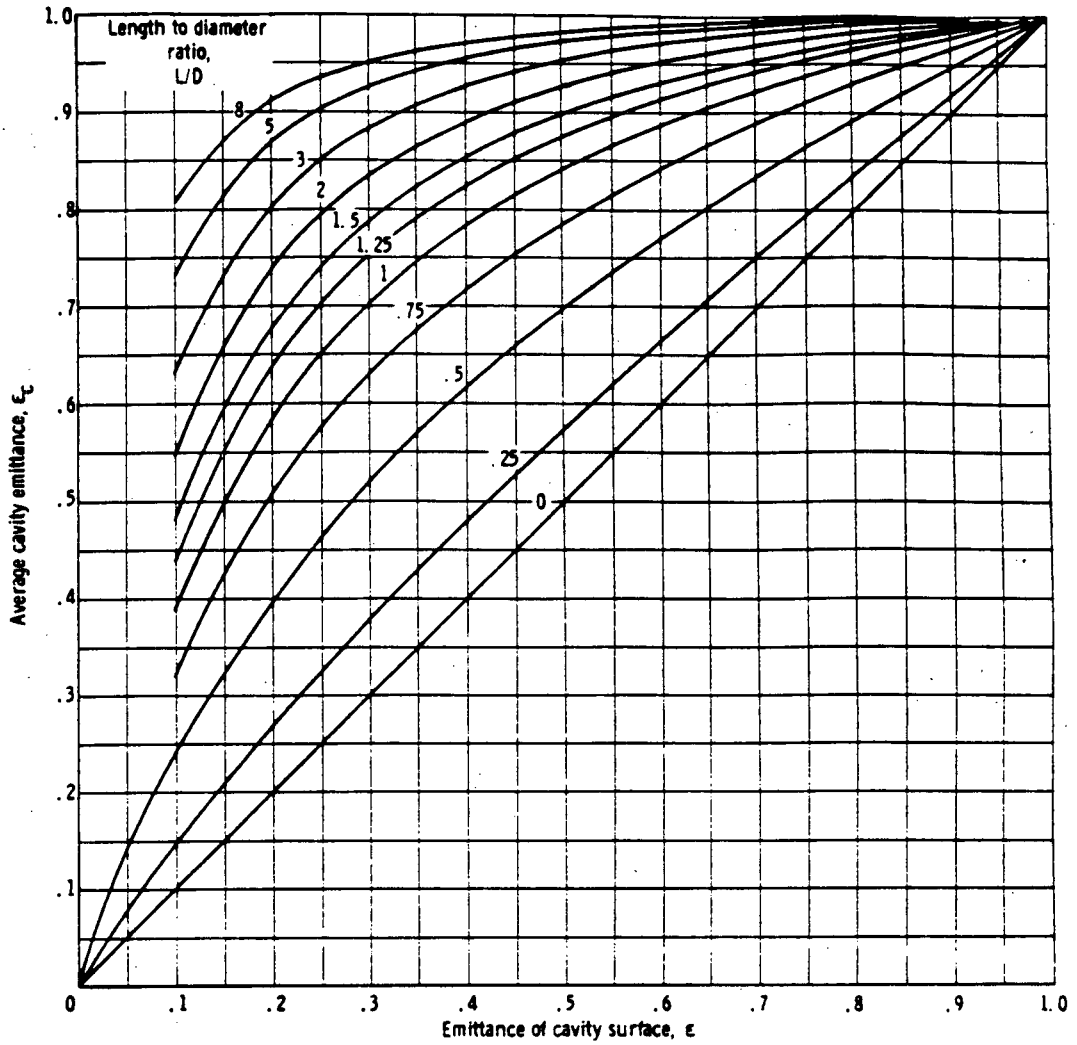


Figure A.5.1 Theoretical blackbody emissivity as a function of cavity L/D ratio and surface emissivity (from Brandsetter [121]).

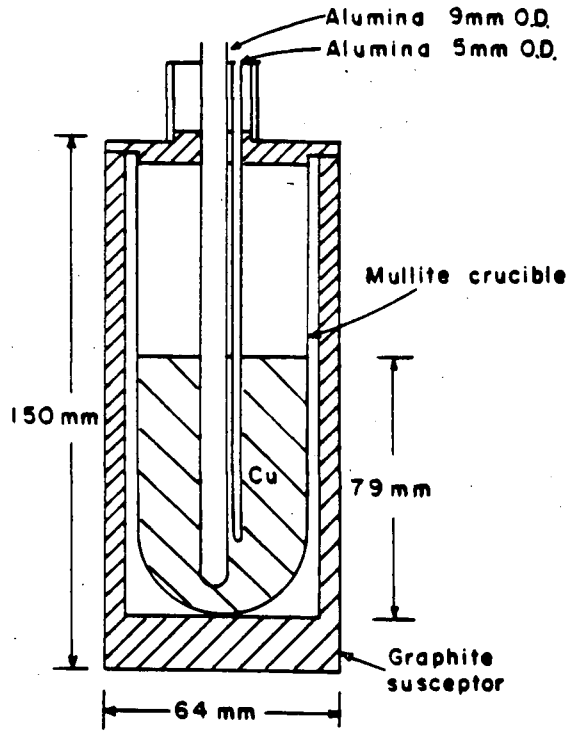


Figure A.5.2 Schematic diagram of copper freezing point blackbody cavity.

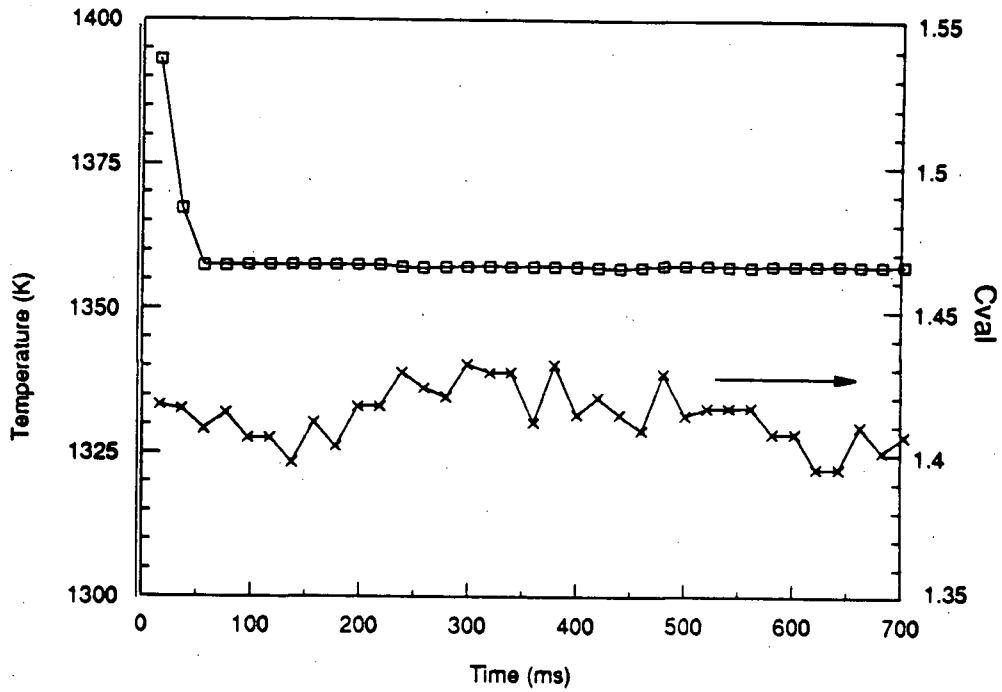


Figure A.5.3 Typical variation in measured temperature and derived calibration constant observed with the copper freezing point blackbody cavity (for $G_{710}=8.23$ $G_{810}=9.9$).

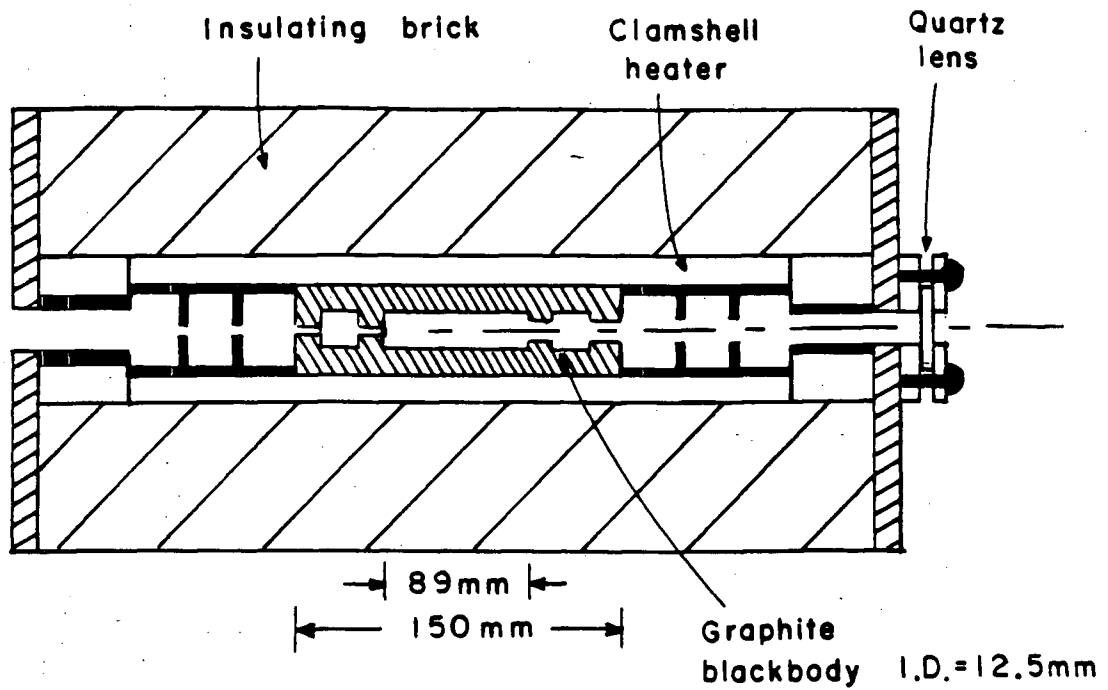


Figure A.5.4 Schematic diagram of low temperature, resistance heated, blackbody cavity.

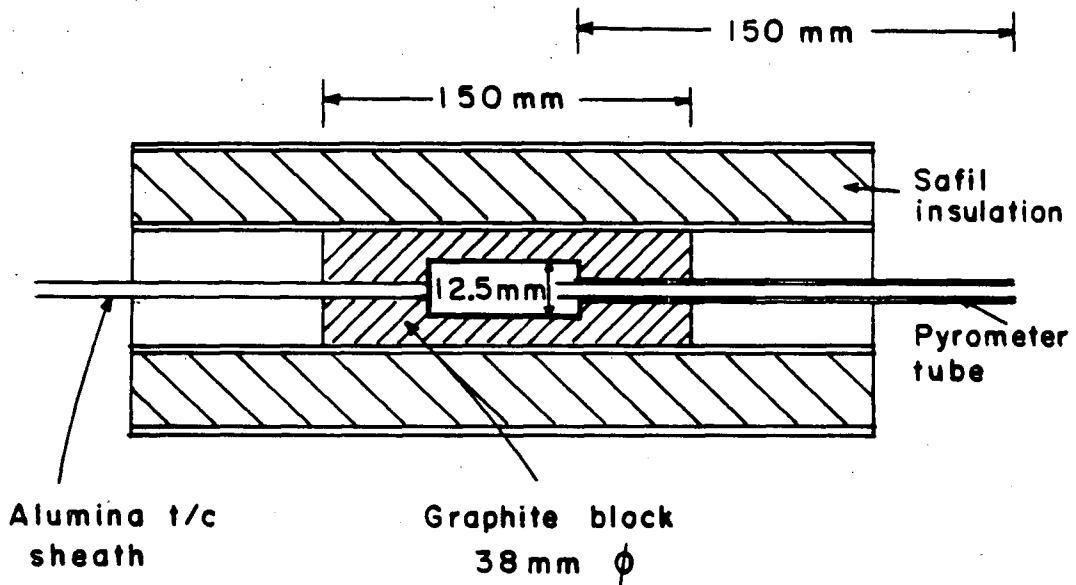


Figure A.5.5 Schematic diagram of high temperature, induction heated, blackbody cavity.

APPENDIX 6

Tungsten Emissivity Data

The emissivity of most materials is dependent on both temperature and wavelength. Tungsten, due to its importance in calibration lamps, is however one of the few materials where data on the variation of emissivity with temperature and wavelength has been published [124,127]

Latyev et al. [124] measured the variation in monochromatic emissivity for temperatures between 1200 and 2600K and wavelengths between 0.4 and 4 μ m. Tungsten emissivities, taken from this data, for wavelengths of 710 and 810nm and temperatures between 1200 and 2600K are plotted in Figure A.6.1a. The emissivities are 0.40-0.45 and decline with increasing wavelength and temperature. From two-wavelength pyrometry theory it is the ratio of the emissivities at the two wavelengths which is important and deviations from unity will result in temperature measurement errors. The temperature measurement error associated with the variation in tungsten emissivity can be calculated by incorporating the filter wavelengths of 710 and 810nm into Equation A.1.14, resulting in the equation

$$\frac{1}{T} - \frac{1}{T_m} = 9.210 \times 10^{-4} \log_{10} \left(\frac{\epsilon_{\lambda_{810}}}{\epsilon_{\lambda_{710}}} \right) \quad (\text{A.6.1})$$

The ratio of the emissivities at monochromatic wavelengths of 810nm and 710nm, and associated temperature error as a function of temperature are given in Figure A.6.1a. There is no clear trend in the emissivity ratio and for the temperature range shown it varies between 0.957 and 0.960. The measured temperature is increasingly overestimated with increasing temperature reaching an error of 4.5% at 2600K.

The results were extrapolated to higher temperatures to allow calculation of the true temperature of the tungsten lamp filament used in the calibration experiments (see Section 5.2.5.1).

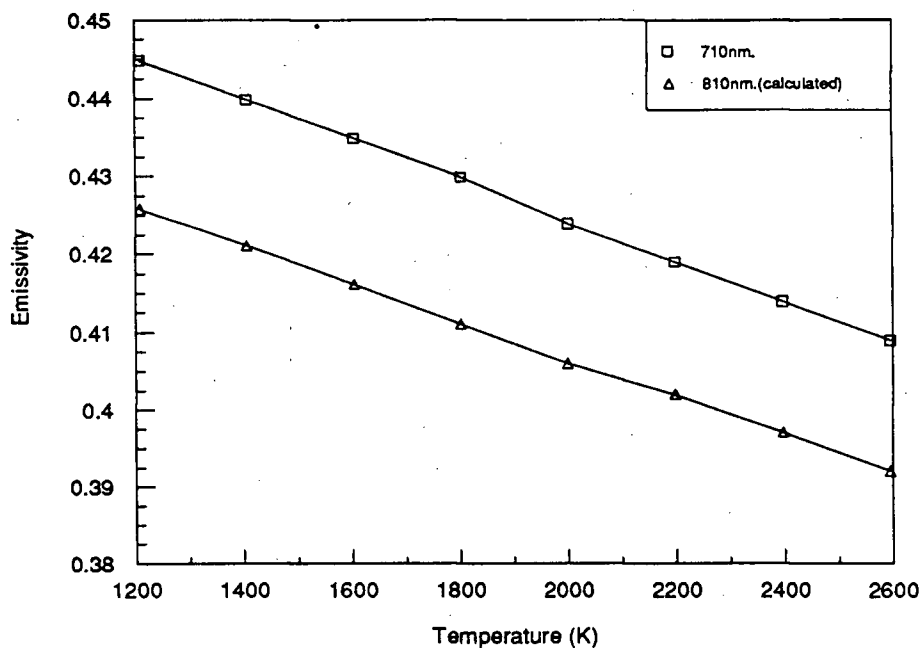


Figure A.6.1a Variation in the monochromatic emissivity of tungsten with temperature (from Latyev et al. [124]).

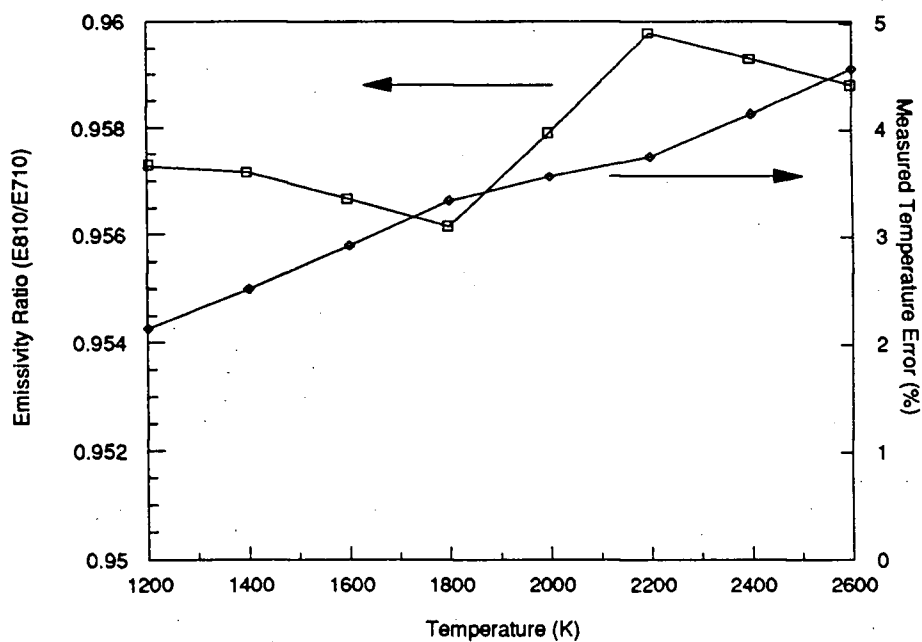


Figure A.6.1b Variation in the ratio of the monochromatic emissivity of tungsten at 710 and 810nm, and associated measured temperature error as a function of temperature (from Latyev et al. [124]).